

Non-Destructive
Testing in Civil
Engineering
Edited by **2000**
Taketo Uomoto



ELSEVIER

Non-Destructive Testing in Civil Engineering 2000

Elsevier Science Internet Homepage

<http://www.elsevier.nl> (Europe)

<http://www.elsevier.com> (America)

<http://www.elsevier.co.jp> (Asia)

Consult the Elsevier homepage for full catalogue information on all books, journals and electronic products and services.

Elsevier Titles of Related Interest

ABE & TSUTA

AEPA '96: Proceedings of the 3rd Asia-Pacific Symposium on Advances in Engineering Plasticity and its Applications (Hiroshima, August 1996).

ISBN: 008-042824-X

CARPINTERI

Handbook of Fatigue Crack Propagation in Metallic Structures.

ISBN: 0-444-81645-3

CARPINTERI

Minimum Reinforcement in Concrete Members.

ISBN: 008-043022-8

JONES

Failure Analysis Case Studies.

ISBN: 008-043338-3

KARIHALOO *ET AL.*

Advances in Fracture Research: Proceedings of the 9th International Conference on Fracture (Sydney, April 1997).

ISBN: 008-042820-7

LÜTJERING & NOWACK

Fatigue '96: Proceedings of the 6th International Fatigue Congress (Berlin, May 1996).

ISBN: 008-042268-3

MACHA *ET AL.*

Multiaxial Fatigue and Fracture.

ISBN: 008-043336-7

MARQUIS & SOLIN

Fatigue Design of Components.

ISBN: 008-043318-9

MARQUIS & SOLIN

Fatigue Design and Reliability.

ISBN: 008-043329-4

RAVICHANDRAN *ET AL.*

Small Fatigue Cracks: Mechanics, Mechanisms & Applications.

ISBN: 008-043011-2

RIE & PORTELLA

Low Cycle Fatigue and Elasto-Plastic Behaviour of Materials.

ISBN: 008-043326-X

VOYIADJIS *ET AL.*

Damage Mechanics in Engineering Materials.

ISBN: 008-043322-7

VOYIADJIS & KATTAN

Advances in Damage Mechanics: Metals and Metal Matrix Composites.

ISBN: 008-043601-3

Related Journals

Free specimen copy gladly sent on request. Elsevier Science Ltd, The Boulevard, Langford Lane, Kidlington, Oxford, OX5 1GB, UK

Acta Metallurgica et Materialia

Cement and Concrete Research

Composite Structures

Computers and Structures

Corrosion Science

Engineering Failure Analysis

Engineering Fracture Mechanics

International Journal of Fatigue

International Journal of Impact Engineering

International Journal of Mechanical Sciences

International Journal of Non-Linear Mechanics

International Journal of Plasticity

International Journal of Pressure Vessels & Piping

International Journal of Solids and Structures

Journal of Applied Mathematics and Mechanics

Journal of Construction Steel Research

Journal of the Mechanics and Physics of Solids

Materials Research Bulletin

Mechanics of Materials

Mechanics Research Communications

NDT&E International

Scripta Metallurgica et Materialia

Theoretical and Applied Fracture Mechanics

Tribology International

Wear

To Contact the Publisher

Elsevier Science welcomes enquires concerning publishing proposals: books, journal special issues, conference proceedings, etc. All formats and media can be considered. Should you have a publishing proposal you wish to discuss, please contact, without obligation, the publisher responsible for Elsevier's mechanics and structural integrity publishing programme:

Dean Eastbury

Senior Publishing Editor, Engineering and Technology

Elsevier Science Ltd

The Boulevard, Langford Lane

Kidlington, Oxford

OX5 1GB, UK

Phone: +44 1865 843580

Fax: +44 1865 843920

E.mail: d.eastbury@elsevier.co.uk

General enquires, including placing orders, should be directed to Elsevier's Regional Sales Offices – please access the Elsevier homepage for full contact details (homepage details at the top of this page).

Non-Destructive Testing in Civil Engineering 2000

(SEIKEN SYMPOSIUM No. 26)

Edited by

Taketo Uomoto
*Center for Collaborative Research,
University of Tokyo, Japan*

Tokyo, Japan
25 - 27 April 2000

2000



ELSEVIER

Amsterdam - Lausanne - New York - Oxford - Shannon - Singapore - Tokyo

ELSEVIER SCIENCE Ltd
The Boulevard, Langford Lane
Kidlington, Oxford OX5 1GB, UK

© 2000 Elsevier Science Ltd. All rights reserved.

This work is protected under copyright by Elsevier Science, and the following terms and conditions apply to its use:

Photocopying

Single photocopies of single chapters may be made for personal use as allowed by national copyright laws. Permission of the Publisher and payment of a fee is required for all other photocopying, including multiple or systematic copying, copying for advertising or promotional purposes, resale, and all forms of document delivery. Special rates are available for educational institutions that wish to make photocopies for non-profit educational classroom use.

Permissions may be sought directly from Elsevier Science Rights & Permissions Department, PO Box 800, Oxford OX5 1DX, UK; phone: (+44) 1865 843830, fax: (+44) 1865 853333, e-mail: permissions@elsevier.co.uk. You may also contact Rights & Permissions directly through Elsevier's home page (<http://www.elsevier.nl>), selecting first 'Customer Support', then 'General Information', then 'Permissions Query Form'.

In the USA, users may clear permissions and make payments through the Copyright Clearance Center, Inc., 222 Rosewood Drive, Danvers, MA 01923, USA; phone: (978) 7508400, fax: (978) 7504744, and in the UK through the Copyright Licensing Agency Rapid Clearance Service (CLARCS), 90 Tottenham Court Road, London W1P 0LP, UK; phone: (+44) 171 631 5555; fax: (+44) 171 631 5500. Other countries may have a local reprographic rights agency for payments.

Derivative Works

Tables of contents may be reproduced for internal circulation, but permission of Elsevier Science is required for external resale or distribution of such material.

Permission of the Publisher is required for all other derivative works, including compilations and translations.

Electronic Storage or Usage

Permission of the Publisher is required to store or use electronically any material contained in this work, including any chapter or part of a chapter.

Except as outlined above, no part of this work may be reproduced, stored in a retrieval system or transmitted in any form or by any means, electronic, mechanical, photocopying, recording or otherwise, without prior written permission of the Publisher.

Address permissions requests to: Elsevier Science Rights & Permissions Department, at the mail, fax and e-mail addresses noted above.

Notice

No responsibility is assumed by the Publisher for any injury and/or damage to persons or property as a matter of products liability, negligence or otherwise, or from any use or operation of any methods, products, instructions or ideas contained in the material herein. Because of rapid advances in the medical sciences, in particular, independent verification of diagnoses and drug dosages should be made.

First edition 2000

Library of Congress Cataloging in Publication Data

A catalog record from the Library of Congress has been applied for.

British Library Cataloguing in Publication Data

A catalogue record from the British Library has been applied for.

ISBN: 0 08 043717 6

♻️ The paper used in this publication meets the requirements of ANSI/NISO Z39.48-1992 (Permanence of Paper).
Printed in The Netherlands.

CONFERENCE COMMITTEES

International Scientific Committee

Prof. Shozo. Amasaki	Ritsumeikan University, Japan
Prof. J. H. Bungey	University of Liverpool, UK
Prof. O. Buyukozturk	Massachusetts Institute of Technology, USA
Prof. M. C. Forde	University of Edinburgh, UK
Dr. M. Krause	Federal Institute for Materials Research and Testing, Germany
Prof. A. E. Long	The Queen's University, UK
Prof. Chitoshi Miki	Tokyo Institute of Technology, Japan
Prof. Toyoaki Miyagawa	Kyoto University, Japan
Prof. Hiroaki Niitsuma	Tohoku University, Japan
Prof. Masayasu Ohtsu	Kumamoto University, Japan
Prof. Keitetsu Rokugo	Gifu University, Japan
Prof. G. Schickert	German Society of Non-Destructive Testing, Germany
Prof. Taketo Uomoto	University of Tokyo, Japan
Dr. H. Wigggenhauser	Federal Institute for Materials Research and Testing, Germany

Organizing Committee

Chairman:

Prof. Taketo UOMOTO University of Tokyo

Members:

Prof. Shozo AMASAKI	Ritsumeikan University
Prof. Nobuaki OTSUKI	Tokyo Institute of Technology
Mr. Hiroataka KAWANO	Public Works Research Institute, Ministry of Construction
Prof. Kazuo KURODA	University of Tokyo
Prof. Torao KEMI	Ashikaga Institute of Technology
Dr. Kazuo TATEISHI	University of Tokyo
Prof. Hiroaki Niitsuma	Tohoku University
Dr. Hidenori HAMADA	Port and Harbour Research Institute, Ministry of Transport
Prof. Chitoshi MIKI	Tokyo Institute of Technology
Dr. Kazuo YAMADA	Aichi Institute of Technology
Dr. Hirotake KURIHARA	KAJIMA CORPORATION
Mr. Kennosuke WATANABE	TAISEI CORPORATION
Dr. Takayoshi OTA	SHIMIZU CORPORATION
Mr. Kiyoshige NISHIBAYASHI	OBAYASHI CORPORATION
Dr. Kunio MAEDA	NKK CORPORATION
Mr. Shoichiro NUMATA	Technology Center of Metropolitan Expressway
Mr. Kunio IIDA	Hanshin Expressway Management Technology Center
Dr. Masaharu KATO	SHO-BOND CORPORATION
Dr. Harumitsu TAMANO	SYUKOU ENGINEERING CO.,LTD.
Mr. Hidekatsu ITAGAKI	SHOWA ENGINEERING CO.,LTD.
Mr. Hideo ISHII	TAIYO DORO CO.,LTD
Mr. Tsunehiro OHUCHI	DEC CO.,LTD.
Mr. Mamoru ENOMOTO	TOKYO ROAD ENGINEERING CO.,LTD.
Mr. Ikuo OKADA	DOURO TECHNO SERVICE CO.,LTD.
Mr. Tadao OKAMOTO	ROAD REFRE CO.,LTD.

Executive Committee

Chairman:

Dr. Kazuo TATEISHI University of Tokyo

Members:

Dr. Yoshihiro ITO SATO KOGYO CO.,LTD.
Dr. Sadamu ONO Constec Engineering Co.,Ltd.
Dr. Futoshi KATSUKI Shibaura Institute of Technology
Dr. Yoshitaka KATO University of Tokyo
Dr. Toshiharu KISHI University of Tokyo
Dr. Junichi KOSEKI University of Tokyo
Mr. Noboru SATO Sankyo Co.,Ltd.
Dr. Yoshiaki NAKANO University of Tokyo
Dr. Takafumi NOGUCHI University of Tokyo
Ms. Ayako NOGUCHI KAIHATSU CONSULTANT CO.,LTD.
Mr. Kenichi HIDA Chiyoda ENGINEERING CONSULTANTS CO.,LTD
Dr. Shigenori YUYAMA Nippon Physical Acoustics, Ltd.
Mr. Masaru YOSHIZAWA Technology Center of Metropolitan Expressway

CO-SPONSORS

Architectural Institute of Japan
Federal Institute for Materials Research and Testing, Germany
Japan Concrete Institute
Japan Society for the Promotion of Science
Japan Society of Civil Engineers
Japanese Society of Non-Destructive Inspection
Japanese Society of Steel Construction
The British Institute of Non-Destructive Testing, UK
The Foundation for the Promotion of Industrial Science
The Japanese Geotechnical Society
University of Liverpool, UK

FINANCIAL SUPPORTERS

DEC CO.,LTD.
Hanshin Expressway Management Technology Center
KAJIMA CORPORATION
ROAD REFRE CO.,LTD.
DOURO TECHNO SERVICE CO.,LTD.
SAKAI IRON WORKS CO.,LTD.
SHIMIZU CORPORATION
SHO-BOND CORPORATION
SHOWA ENGINEERING CO.,LTD.
SYUKOU ENGINEERING CO.,LTD.
TAISEI CORPORATION
TAIYO DORO CO.,LTD.
Technology Center of Metropolitan Expressway
TOKYO ROAD ENGINEERING CO.,LTD.

PREFACE

One of the original objectives of the NDT-CE (Non-Destructive Testing in Civil Engineering) symposium is to provide an opportunity for discussing current issues and future perspectives of NDT and for promoting mutual understanding among engineers and researchers. This symposium is organized as SEIKEN SYMPOSIUM No. 26, sponsored by Institute of Industrial Science, University of Tokyo.

The idea of holding a symposium for exchanging information and views on NDT was realized in 1991, and the first international symposium on NDT-CE was held in Berlin, Germany in 1991. With that as a start, four symposiums were organized; the second in Liverpool, UK in 1993, the third in Berlin, Germany in 1995 and the fourth in Liverpool, UK in 1997. Following these symposiums hosted by European countries, the fifth symposium will be held in Tokyo, Japan.

Asia is one of the key regions for further developments of NDT. The symposium in Japan will be a good opportunity not only to exchange technical information on NDT, but to promote worldwide friendship between engineers in the Asian countries and other nations of the world.

This volume contains 70 papers including 5 keynote papers from the worldwide range of 20 countries. They provide the most recent research results and findings. The papers are grouped under the following areas: 1) keynote papers, 2) magnetic/electric, 3) steel structures, 4) integrated test, 5) moisture, 6) strength, 7) acoustic emission, 8) various tests, 9) ultrasonic, 10) impact echo, 11) radar, 12) quality and 13) corrosion/cover. The writing format of the paper varies from author to author, because the proceedings were produced by offset printing from the manuscripts provided by the authors. However we believe that the authors are able to get their message across to the readers.

We would like to express our gratitude to all the key note speakers, International Scientific Committee members, Organizing Committee members, Executive Committee members, co-sponsoring organizations and financial supporters for their efforts and commitments. I would like to send my sincere thanks especially to Dr. K.Tateishi, the chairman of the executive committee, and Mr. M. Yoshizawa for arranging the symposium in details.

Taketo UOMOTO
Chairman, Organizing Committee
Professor of University of Tokyo

This Page Intentionally Left Blank

CONTENTS

Preface	vii
---------------	-----

KEYNOTE PAPERS

Maintenance of Concrete Structures and Application of Non-Destructive Inspection in Japan T. Uomoto	1
Nondestructive Testing for Steel Bridges in Japan C. Miki and H. Shirahata	13
Research in Non-Destructive Testing in Civil Engineering at BAM H. Wiggenhauser	23
Non-Destructive Testing in the UK J.H. Bungey	41
High-Resolution Geophysical Methods as NDT for Civil Engineering Applications T. Takahashi	51

MAGNETIC/ELECTRIC

Experimental Research for Estimating Erection Stress of Steel Bridge Using Magnetic Anisotropy Sensor Y. Sakai and N. Tamura	61
Inversion of Borehole Magnetic Survey Data for Estimating the Depth of Pile Y.H. Cha and J.H. Suh	71
Application of the Dielectric Measurement for Non-Destructive Test of Mortar S. Yagihara, N. Shinyashiki, Y. Hayashi, M. Asano, M. Shiotsubo, Y. Kato, T. Uomoto, M. Arino, T. Tokunaga, K. Noto, S. Tsuda and W. Kimura	79
Highly Accurate Low Frequency Elastic Wave Measurement Using Magnetstrictive Devices S. Hattori, T. Shimada, R. Taniguchi and K. Matsuhashi	87
Non-Destructive Localisation of Prestressing Steel Fractures in Post-Tensioned Concrete B. Hillemeier and H. Scheel	99

STEEL STRUCTURES

Measurement of Axial-Stress in High Tension Bolts by Acoustoelastic Velocity-Ratio Method H. Toda, Y. Go, K. Yokoyama, O. Yosikawa and T. Yawata	109
Fatigue Crack Propagation Monitoring in Steel Structures with Intelligent Systems M.S. Rahman, T. Oshima, S. Mikami, T. Yamazaki and N. Takada	117
Non-Destructive Testing Being Essential Part of the Safety Assessment of Steel Bridges K. Brandes, J. Herter and R. Helmerich	127
Detection of Structural Damage by Ambient Vibration Measurement using Laser Doppler Vibrometer K. Kaito, M. Abe, Y. Fujino and H. Yoda	135

INTEGRATED TEST

Radar and Seismic Tomographies on Gypsum Pillars X. Dérobert and O. Abraham	145
Investigation on Several Non-Destructive Inspection Methods about Strength Degradation of Reinforced Concrete Beam T. Tomokiyo, T. Hikichi, K. Hida and T. Uomoto	151
Advanced NDT of Reinforced Concrete Members by Ultrasonics and Acoustic Emission M. Uchida, M. Ohtsu and T. Okamoto	161
Application of Various Non-Destructive Inspection for Existing Reinforced Concrete Structures T. Uomoto, S. Tomizawa and H. Tanaka	171

MOISTURE

Investigation of the Drying Process of Moist Building Materials by Means of Heat Flux Density Measurements H. Rogass and U. Fischer	181
A Microwave-Sensor for Monitoring the Moisture Content of Concrete B. Jannsen and A.F. Jacob	191
Moisture Measurements in Building Materials with Microwaves H. Kääriäinen, M. Rudolph, D. Schaurich, K. Tulla and H. Wiggerhauser	199
Measurement of the Moisture and Salt Content of Building Materials W. Leschnik and U. Schlemm	209

A New Microwave Sensor System for Moisture and Salt Content Measurements at Building Materials to Reduce Disturbances by Inhomogeneities U Schlemm and W. Leschnik	219
-----------------------------------------------------------------------------------------------------------------------------------------------------------------------------	-----

STRENGTH

NDT for Assessing Concrete Strength A.P. Ferreira and P.F. Castro	229
New Test Method for Pullout Strength for the Hardend Concrete using Post settled Pullbolt M. Arazoe, Y. Ito and F. Katsuki	239
Evaluation of the Strength Characteristics of Building Materials I.E. Shkolnik, H.M. Aktan, H.C. Wu and D.A. Russell	245
A Proposal of Control Method on Shotcrete Strength by Pin Penetration Test Using Air Pressure K. Iwaki, A. Hirama, K. Mitani, S. Kaise and K. Nakagawa	253
Evaluation of Concrete in Structures with Small Core Specimen Y. Kasai, N. Yuasa, M. Kunimoto and T. Mano	263

ACOUSTIC EMISSION

Quantitative Diagnosis of Reinforced Concrete Structures by AE-SiGMA Analysis M. Shigeishi, D. Yukawa and M. Ohtsu	273
Evaluation of Fatigue Damage in Reinforced Concrete Slab by Acoustic Emission S. Yuyama, Z.W. Li, M. Yoshizawa, T. Tomokiyo and T. Uomoto	283
Quantitative Evaluation of Fracture Processes in Concrete by the Use of Improved <i>b</i> -Value T. Shiotani, S. Yuyama, Z.W. Li and M. Ohtsu	293

ULTRASONIC

Ultrasonic Imaging of Concrete Members Using an Array System M. Krause, F. Mielentz, B. Milman, H. Wiggenhauser, W. Müller and V. Schmitz	303
Influence of Aggregates on Ultrasonic Elastic Waves Propagation in Concrete N. Otsuki, M. Iwanami, S Miyazato and N. Hara	313
Differential Approach to Ultrasonic Testing of Strength and Homogeneity of Concrete E. Nesvijski, T Nesvijski and A. Lorenzi	323
Measurements of Thickness and Crack Depth in Concrete by Ultrasonic Methods T. Yamaguchi and T. Yamaguchi	331

Basic Study for an Ultrasonic Testing Methods of PC Grouting Condition N. Sato	341
Ultrasonic Nondestructive Testing Method for Heavy Plate Butt Welds Using Low Frequency Broadband Angle Probe and Synthetic Aperture Focusing Technique S. Wadaka, M. Koike, T. Kimura, S. Kameyama and Y. Manome	347
Simulation for Ultrasonic Evaluation of a Welding Defect in a Thick Plate S. Hirose, K. Kimoto and C. Miki	357
The Use of Surface Waves for the Non Destructive Testing of Concrete Structures O. Abraham, H. Pedersen, G. Hevin, X. Kergadallan and Ph. Côte	367
Fracture Mechanics Approach to Crack Depth Determined through Ultrasonic Method T. Kamada, M. Kunieda and K. Rokugo	375
Detection of Ultrasonic Pulse Echo through Steel Bar in Concrete Crack Depth Measurement T. Hirata and T. Uomoto	383
New Ultrasonic Computerized Tomography Technologies for Nondestructive Testing and Diagnostics of Bridges Welded Structures V. Koshovy, Z. Nazarchuk, E. Krivin, V. Kuriy and I. Romanyshyn	391
VARIOUS TESTS	
High Elevation Inspection Vehicle N. Tamura and K. Takada	401
Analysis of Concrete using LIBS H. Wiggenshauser, G. Wilsch, D. Schaurich and J. Wöstmann	407
High Resolution Seismic Imaging as a NDT Tool for the Shallow Subsurface Survey B. Piwakowski and Ch. Leonard	415
Determination of Thermophysical Parameters of Building Components and Buildings A. Donath	425
Measurement of a Spatial Distribution of Radon Emanations through a Fracture – A New Non-destructive Testing Technique of Concrete Materials T. Hatsukari and N. Tsuchiya	435
Evaluation of Concrete with FRP Sheet under Accelerated Degradation Environments A. Hattori, A. Etoh, Y. Ohnishi and T. Miyagawa	443
IMPACT ECHO	
Spectral Imaging of Impact Echo Technique for Grouted Duct in Post-Tensioning Prestressed Concrete Beam T. Watanabe and M. Ohtsu	453

Use of a Time–Frequency Analysis Approach in Impact Echo Method Example of Application: Detection of Faults in Concrete Slabs O. Abraham, Ch. Leonard, Ph. Côte and B. Piwakowski.....	463
Automated Impact-Echo and Method Improvement: 2- and 3-D Imaging of Concrete Elements C. Colla, G. Schneider and H. Wiggenhauser	471

RADAR

Application of Ground Penetrating Radar for Evaluation of Sub-Surface Airfield Pavement Conditions K.R. Maser and I. Sande	481
Statewide Bridge Deck Survey Using Ground Penetrating Radar K.R. Maser and M. Bernhardt.....	491
Using Ground Penetrating Radar to Evaluate Pavement Structures I.L. Al-Qadi, A. Loulizi and M.D. Oosterbaan.....	499
GPR Calibration Facility I.L. Al-Qadi, S. Lahouar and A. Loulizi	509
Dielectric Properties of Concrete and Their Influence on Radar Testing M.N. Soutsos, J.H. Bungey, S.G. Millard, M.R. Shaw and A. Patterson	519
Radar Investigations of Historical Structures Ch. Maierhofer, J. Wöstmann and D. Schaurich	529
Estimation of Thickness and Width of Void under Concrete Slab using Radar Image Processing S.K. Park and T. Uomoto	539
Evaluation of Concrete Strength using Radar Method on Structures S. Oota, T. Fujiwara, K. Matsuyama and Y. Kanemoto	549
Radar Technique for Detecting Voids under Concrete Pavement K. Matsuyama, S. Oota, M. Kawamorita and I. Tamura	559
GPR Experiments Using Small Tub and Application for Determining Fracture H. Imai and J. Kawakami	567
Detection of Steel Reinforcing Bars Inside Concrete Using Radar H.C. Rhim	577

QUALITY

In-Situ Strength Assessment of Concrete – The European Concrete Frame Building Project M.N. Soutsos, J.H. Bungey, A.E. Long and G.D. Henderson	583
---------------------------------------------------------------------------------------------------------------------------------------------------------	-----

Identification of Convective Heat Transfer Coefficient from Field Test T. Shiina, N. Nishida, K. Matsui and T.F. Smith	593
A Quality Control Method of Thick Embankment by a Failing Weight Test K. Oniki, K. Fujisaki and K. Yasumoto	605
CORROSION/COVER	
Compensated Half-Cell Potential Technique for NDE of Rebar Corrosion M. Ohtsu and Y. Tomoda	615
Environmental Influences on Linear Polarisation Corrosion Rate Measurement in Reinforced Concrete S.G. Millard, D. Law, J.H. Bungey and J. Cairns	625
A Rapid Field Testing Method for Chloride Ion Content in Concrete using Drilled Powder N. Yuasa and Y. Kasai	637
Macrocell Sensor Systems for Monitoring of the Corrosion Risk of the Reinforcement in Concrete Structures M. Raupach and P. Schiebl	647
Method of Test for Neutralization Depth of Concrete in Structure with Drilling Powder Y. Kasai, N. Yuasa and T. Mano	661
Estimation Method of Corroded Portion of Reinforcing Steel Bar by Natural Potential Measurement E. Tsukahara, R. Koyama, T. Hoshino and T. Uomoto	671
Author Index	679
Keyword Index	681

**MAINTENANCE OF CONCRETE STRUCTURES
AND
APPLICATION OF NON-DESTRUCTIVE INSPECTION IN JAPAN**

Taketo Uomoto

Professor,

Center for Collaborative Research, University of Tokyo

7-22-1, Roppongi, Minato-Ku, Tokyo, 106-8558, Japan

ABSTRACT

Japan has been producing a large amount of concrete structures throughout our country since 1950's. The important structures such as Shinkansen, Highways etc. have been used for more than 35 years, and it is now becoming an important problem to maintain the existing concrete structures. The normal maintenance methods is to inspect the structures periodically, and when the degree of deterioration exceeds certain limit, repair or strengthening of the structures is performed.

To inspect existing concrete structures, visual inspection is the easiest and the most fundamental method. But this method may not be applicable for inspecting defects which does not appear on the surface of concrete. For such defects, non-destructive inspection is the only method which can be applied. This paper explains briefly the background of the problem, how the maintenance of concrete structures are being done, and introduces some new applications of NDI techniques in Japan.

Keywords: maintenance, non-destructive inspection, civil structures, concrete, evaluation

INTRODUCTION

A large amount of concrete structures have been made in Japan since 1950's. Especially, just before 1964, when Olympic game was held in Tokyo, not only the facilities for the Olympic games but also traffic facilities such as "Shinkansen" (rapid train railways), "Shutokousoku-doro" (metropolitan express way), and "Toumei kousoku-doro"(high way connecting Tokyo and Nagoya) had been made. Many projects has been proposed and numerous facilities has been constructed since then, using concrete. Recently, three huge bridges connecting Honshu island and Shikoku

island (Honshu-Shikoku Renraku-kyo) have been made and people can travel to 4 main islands (Hokkaidou, Honshu, Shikoku and Kyusyu) by land.

Although there are still many structures to be made, one of the most important works to be done by the civil engineers today is to maintain these structures to be used. Such as Shinkansen and Shutokousoku-doro have been in use for more than 35 years and without these important facilities, the economy of Japan can not be maintained.

Recently, spalling of concrete from concrete structures, such as bridges, tunnels, etc., has become a big problem in the field of mass media. Although the spalling of concrete may not be a big problem considering the load carrying capacity of the structure, they may cause traffic accident when cars or trains run underneath at a high speed, such as in the case of Shinkansen which runs at the speed above 210km/hr. In 1999, a block of concrete hit Shinkansen in Fukuoka tunnel, and the top of several cars were damaged partly. The ministry of transportation and port and harbor organized a special committee to investigate the causes, and concluded that a part of the concrete lining spalled off due to insufficient consolidation at the time of construction and formation of inner cracks from the early age. Since then, many engineers and researchers brought a keen interest on non-destructive inspection of existing structures.

1. Change of Durability Problems

Before 1970's, concrete structures are believed to possess high durability compared to steel structures. The main durability items considered in design and construction at that time were: fatigue, freeze-thaw deterioration, abrasion, permeability and chemical attack. As can be easily estimated from these items, the concrete engineers were proud of using concrete as construction material compared to steel. They did not have to consider about corrosion of reinforcing steel bars, which was a big problem in case of steel structures. The steel structure engineers have to consider the rate of corrosion in different environment even at the stage of design.

From 1965 to 1974, due to rapid growth of economy, tremendous amount of structures has been constructed. The construction engineers were too busy to check the quality of materials to be used, design methods, construction procedures, etc., and also due to the lack of river sand and gravel, large amount of sea sand and crushed stone were used as aggregates. Although there were regulations on chloride content, people did not realize the importance of the limitation. To facilitate the casting of concrete and to increase the strength of concrete, not only water content but also cement content was increased. At that time there were no special regulations on reactive aggregates and amount of

alkali content in cements. As a result, many newly constructed concrete structures deteriorated abruptly within 5 to 10 years which was unusual up till then.

After the investigations of these deteriorated concrete structures, the following items were considered important from the durability point of view. Additionally to fatigue, freeze-thaw deterioration, abrasion, permeability and chemical attack, corrosion of reinforcing steel, alkali aggregate reaction, acidic rain, biological attack, etc., were decided important to increase the durability of structures. Not only JSCE (Japan Society of Civil Engineers), AIJ (Architectural Institute of Japan), and JCI (Japan Concrete Institute) recommended many important aspects of the problems but also the Ministries related took prompt counter measures to cope with the situation. A large amount of researches has been done related to the durability of concrete structures. Recently, the concrete committee of JSCE, etc. have been working hard to propose new standards considering the performance based design, construction and maintenance.

2. Methods for Inspection and Evaluation of Concrete Structures in General

The maintenance of concrete structures are done by the owners of the structures. In case of public structures, the ministries, etc. maintain the structure as soon as they are completed. For the time being, the methods for the maintenance differ according to the owners of the structures. Although there are some differences, the main concept of the maintenance can be summarized as in Figure 1.

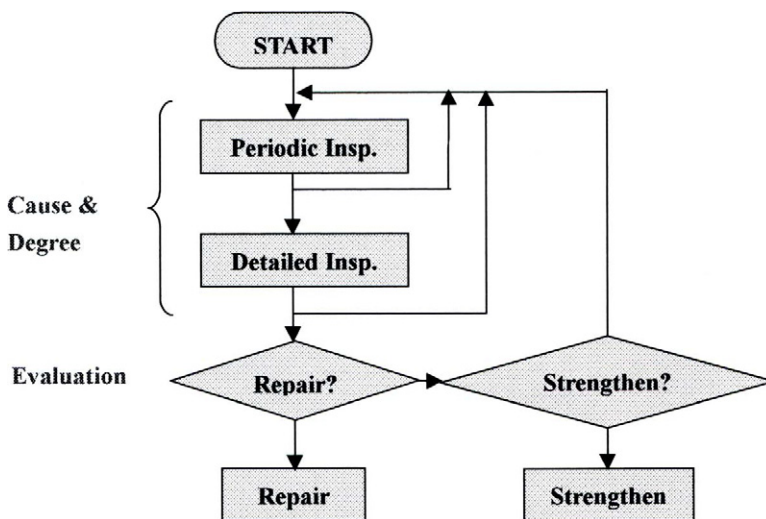


Figure 1 Flow chart for maintenance of concrete structures

2.1 Periodic inspection

Periodic inspection is essential in most cases. The inspectors inspect the structures visually, sometimes with the help of binoculars, once a year or once in several years according to the importance and the time after the structure is completed. In some cases, sonic inspection is carried out along with hammers. The inspectors are mostly trained engineers with experiences.

The periodic inspection covers not only the degree of deterioration but also the estimated main cause of the deterioration. For example, when a crack was found at the corner of openings and increased, the inspector may estimate the main cause as drying shrinkage with restraint. As shown in Table1, in most cases, the appearance and crack formation may offer good data for the inspector. In our laboratory, we developed a system using handy type computers estimating the possible causes and degree of deterioration[1]. The system is composed of sample photographs and questionnaire to be answered by the inspectors by looking at the inspecting concrete structures, and the answers are stocked as individual data to be transported to the main computer from any place within Japan. This system runs with expert system eliminating the personal errors of the inspectors.

In some cases, visual inspection is also used to decide whether further inspection is needed or not. In Tables 1 and 2, an example of the actual visual evaluation making criteria is briefly shown. From

Table 1 Evaluation of deterioration degree by periodic inspection (example)

Degree of deterioration	Steel bar corrosion	Cracks	Spalling
0	none	none	none
1	Some stains on concrete surface	partial cracks	none
2	Stains are observed Partially	Some cracks	Partial rise at surface
3	Fair amount of Stains observed	Fair amount of cracks(width: Several mm)	Partial spalling observed
4	Fair amount of Rusts observed	Large amount of cracks (width: several mm)	Fair amount of rise and spalling
5	Large amount of Rusts observed		Large amount of rise and spalling

Table 2 Evaluation for detailed inspection and need for repair(example)

Deterioration degree	Detailed inspection	Need of repair
0	no	no
1	no	no
2	yes	no (may need)
3	yes	yes
4	yes	yes
5	yes	yes(may strengthen)

these evaluations, when the structure is ranked equal or above 2, careful inspection or detailed inspection of the structure is performed. According to the table, for the sake of simplicity, the items to be inspected are limited to cracks, stains and spallings.

2.2 Detailed inspection

The detailed inspection is done when the estimated degree of deterioration exceeds certain limit, or when some new phenomenon is found during the periodic inspection. The inspection is done normally by using non-destructive tests or taking core samples out from the inspected structure. The purpose of the inspection is to decide the cause of the deterioration and also to evaluate whether repair and/or strengthening is needed or not. In Table 3, the available non-destructive inspection methods being used are listed with some comments of the individual methods.

In case of large concrete structures, such as bridges, tunnels, dams, buildings, etc., the structures are too large to be inspected in details. To overcome the problem, the following methods are being used. 1) Overall inspection techniques, such as using digital still camera, thermography, radar, sonic and laser technique are often used to sweep the whole area to be inspected and find out the distribution of defects within the structure. Then, 2) other techniques, such as X-ray, ultra-sonic, natural potential, acoustic emission, etc. can be applied to get more detailed information.

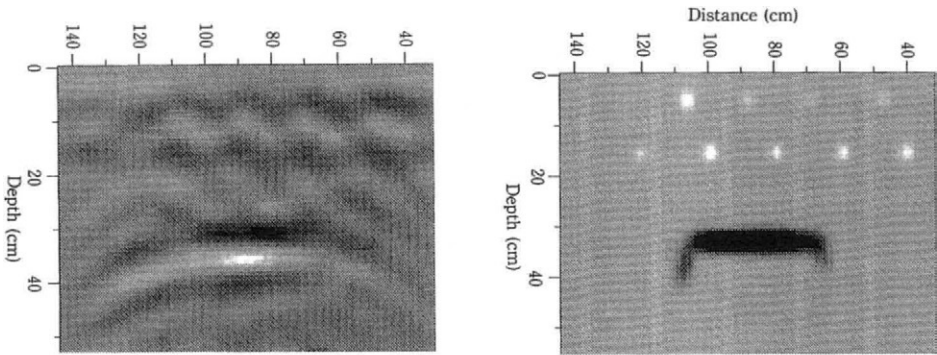
Some movable inspection cars and trains have been developed for the overall inspection 1). In case of tunnel linings, an inspection train mounting both heating facility and thermograph has been developed to obtain the crack distribution and spalling portions for the subways. To inspect the voids at the back of tunnel linings or pavements, radar mounted cars have been developed for railways, waterways and highways. To digitize the surface cracks of reinforced concrete slabs, laser mounted car has been developed by the Technology Center of Metropolitan Expressway. These techniques are important for obtaining inspected data without any personal errors and can be used to check whether the deterioration advanced since the previous inspection.

Table 3 Application of NDI for existing concrete structures [4]

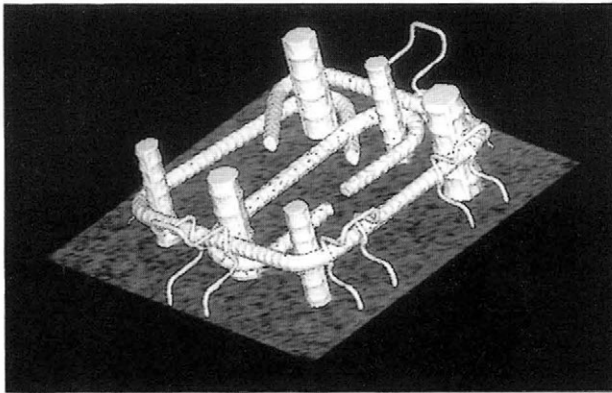
Time	Items	Measurement	Methods	Comments
Just after construction	Dimension	Cross sectional dimension	Measure, Transit, Laser	When the structure is in the open air
			Ultra-sonic, Impact echo, Radar	When a part of the structure is embedded
	Arrangement of steel reinforcement	Concrete cover	Radar, Electro-magnetic, X-ray	Surface bars only
		Bar spacing	Radar, Electro-magnetic, X-ray	Surface bars only
		Bar diameter	Electro-magnetic method	Surface bars only
Structure	Overall stiffness	Oscillation test	Amplitude, frequency	
After several years of usage	Appearance	Deterioration	Visual inspection, Photograph	Stain, cracks,
		Defects (Surface)	Digital still camera, Thermograph	Including honeycomb, cold joints
		Defects (Inside)	Sonic, Thermograph, Radar U-sonic, X-ray, Impact echo	Voids inside and at the back of the structure
	Stress & Strain	Deformation(Macro)	Measure, Transit, Laser	
		Deformation(Micro)	Dial gauge, Strain gauge	
		Vibration	Acceleration Sensor, LVDT Laser deformation measurement	
		Stress	Mold gauge, Optical sensor	
	Strength & Stiffness	Concrete strength	Core sample test	General method
			Rebound hammer, Pull-out test	Problem of accuracy
		Modulus of Elasticity	Core sample test Ultra-sonic velocity	
	Cracks & Spalling	Distribution	Digital still camera, Thermograph	
		Crack width	Digital still camera, Thermograph	Direct measurement possible
		Crack depth	Ultra Sonic	Effect of bars
		Cracking	Acoustic Emission	Continuous measurement required
	Diffusion Depth	Carbonation	Core sample test	Analysis by core samples Limited to concrete surface
		Chlorides	Core sample test	
		Acids	Core sample test	
		Other substances	Multi-spectrum method	
	Permeability	Permeability	On-site permeability test	
	Steel Corrosion	Location	Natural potential	Location at that time
Corrosion degree		Natural potential, Electric current analysis	periodic measurement required	

Note: indicates application of NDI.

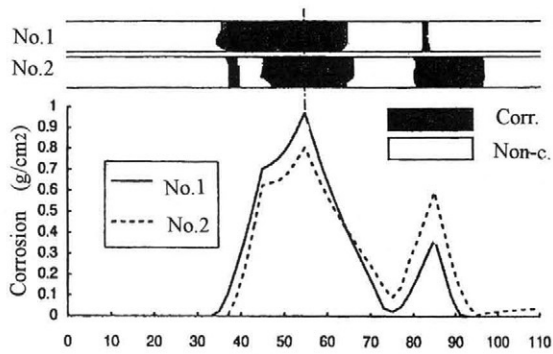
For detailed inspection, many new techniques have been developed. Photographs 1,2 and 3 are the examples being developed using radar, X-ray and natural potentials. The details of the technique can be found in the references [5],[6], and [7].



Photograph 1 Estimated voids and reinforcements by radar technique[5]



Photograph 2 Three dimensional image of reinforcements in concrete by X-ray CT/DR[6]



Photograph 3 Estimated corroded amount from natural potential measurement[7]

2.3 Prediction and Evaluation of Deterioration

The evaluation is one of the most difficult thing to be done. The engineer must predict the remaining life time of the structure if the structure is kept un-repaired. To predict the life time, not only the mechanism of the deterioration must be clarified but also accurate calculation and enough data is needed. Although the data is limited, JSCE and JCI committees have been trying to propose an accurate and practical prediction method to avoid big mistakes in the prediction[2].

The decision, whether the structure can be used as it is or whether repair/strengthening is needed, can be done by the engineers with above mentioned prediction method. But whether to demolish and construct a new structure, must be done considering engineering, social and economical views. Up till now, none of the important structures, such as Shinkansen, highways, Honshu-Shikoku Bridges, etc., deteriorated to a dangerous level but sooner or later we may encounter such a problem in the 21st century. It will become especially important in Japan how to decide such a problem obtaining consensus of the public.

3. Repair and Strengthen of Deteriorated Structures

3.1 Repair of concrete structures

To repair or strengthen the existing structures, design and selection of sufficient materials are important. The design and the selection are different according to the cause and the degree of deterioration. For an example, if the cause is alkali-aggregate reaction and the amount of reactive aggregate is large, the only method to be applied is to reduce the rate of reaction. The most practical method is to apply coatings on the surfaces of concrete to avoid water getting into concrete. In the future, better methods may be developed, but for the time being this method is the only method to reduce the reaction rate. If the concrete contains a large amount of alkali and could not stop the reaction, the structure may be deteriorated in the near future. The structure must be demolished and a new structure must be constructed.

The most popular repair method against corrosion of steel bars due to carbonation is as shown in Figure 2. If the cracked portion of steel bar is not corroded to large extent and the depth of carbonation is less than the cover to reinforcing steel bars, application of coating to the surface of concrete is valid to avoid carbon dioxide penetrating into concrete and to prevent corrosion of the bars. If the carbonation depth at the crack is larger than concrete cover, injection of epoxy resin in the crack is needed. But in case of steel corrosion due to chlorides from the surrounding environment, the highly concentrated portion of concrete must be taken out, anti-corrosive treatment is to be applied to the surface of the bar, and polymer cement mortar is generally used to repair the

concrete before coating the concrete surface.

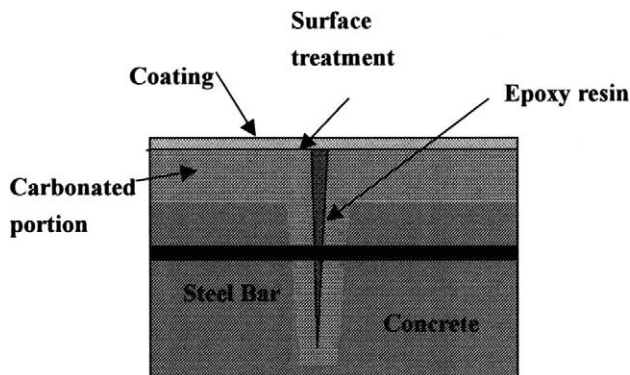


**Figure 2 Repair of concrete by applying coating on the surface of concrete
(Corrosion of steel bars due to carbonation of concrete cover)**

3.2 Strengthening of concrete structures

Strengthening of concrete structures is needed when the load bearing capacity of the structure become lower than the designed value, or when larger loads are going to be applied. Recently in Japan, due to the change of the live loads (cars) from 20tons to 25tons, many beams, slabs and columns were strengthened. The cause was not the deterioration but social need.

After the Great Hanshin-Awaji Earthquake, it was clarified that the shear strength of the columns designed before 1980's were not enough. As can be seen in Figure 3, the allowable shear stress of concrete was reduced tremendously in the standard specification of JSCE in 1980 and 1984[3]. As a result, the existing structures do not possess enough shear strength according to the specification today. Considering the evidence, many bridge piers etc. were strengthened by external reinforcement as shown in Figure 4. The concrete committee of JSCE has published the recommendations for designing of concrete structures for strengthening in general [8] and by using FRP sheets [9].

Reinforced concrete piers for important highways and railways which were constructed using the design standards before 1984 were all strengthened by using either steel plates or FRP sheets after the earthquake. For buildings, some of them are still existing as it was, without any special repair/strengthening. This is mainly due to the problem of owners who can not deal with the fee for repair/strengthening.

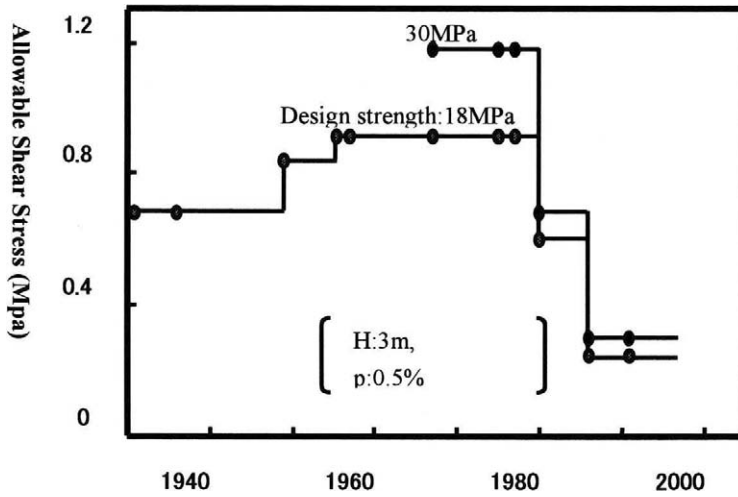


Figure 3 Change of allowable shear stress for concrete by JSCE[3]

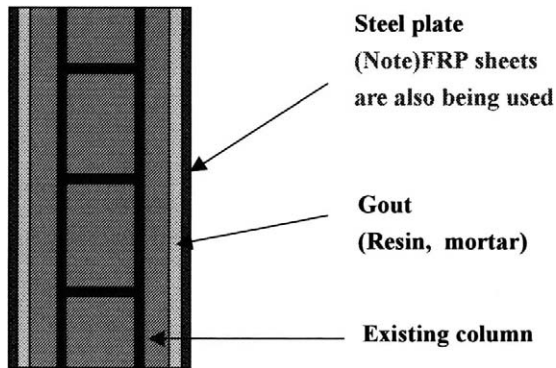


Figure 4 External reinforcement for concrete columns

Concluding Remarks

Engineering is not always complete, and further research works are needed. To set up a good system for maintenance of existing concrete structures, there are still many things to be done: not only researches but also education to the students and engineers about durability and maintenance of concrete structures. I hope this paper may become a help to the concrete engineers and NDI

engineers who are involved in maintaining the existing concrete structures.

References

- [1]T. Uomoto: Development of Deterioration Diagnosis for Reinforced Concrete Structures, Report of Grant-in-Aid from Ministry of Education, IIS, University of Tokyo, March, 1992
- [2]Research Committee on Repair of Concrete Structures: Committee Report on Analysis for Evaluation of Repair Methods, Japan Concrete Institute, October, 1996
- [3]H.Okamura et al: Transition of Seismic Design of Concrete Structures, Proceedings of the Meeting on the Great Hanshin-Awaji Earthquake, JSCE, pp.563-570, January, 1996
- [4]T.Uomoto: Non-destructive Inspection of Concrete Structures, pp.3-11, Dam Engineering, November, 1999
- [5]S.K.Park: Estimation of the Volume of Three-Dimensional Subsurface Voids by Microwave Polarization Method, pp.13-24, JSCE No.592/V-39, 1998.5
- [6]S.Izumi et al: Application of High Energy X-ray CT/DR to Non-Destructive Testing of Thick Concrete Structure, 3rd Non-destructive Symposium using X-rays, 1999 .11
- [7]E.Tsukahara et al: Basic Study on Corrosion of Reinforcement in Cracked Concrete, General Meeting of JSCE, 1999.9
- [8] Concrete committee: Recommendation to Strengthen Concrete Structure, Concrete Library No.95, JSCE, 1999
- [9]Concrete Committee: Recommendation for Design and Construction of Concrete Structures using Continuous Fiber Reinforcing Materials, Concrete Engineering Series 23, JSCE, 1997

This Page Intentionally Left Blank

NONDESTRUCTIVE TESTING FOR STEEL BRIDGES IN JAPAN

Chitoshi MIKI* and Hiromi SHIRAHATA**

**Department of Civil Engineering, Tokyo Institute of Technology,
2-12-1 Oookayama Meguroku Tokyo, 152-8552 Japan*

** *Department of Civil Engineering, Musashi Institute of Technology,
1-28-1 Tamazutsumi Setagayaku Tokyo, 158-8557 Japan*

ABSTRACT

Nondestructive testing plays an important role for quality evaluation. Among nondestructive testing methods, automatic ultrasonic testing is focused in this paper. A brief history of automatic ultrasonic testing systems will be described. Application for evaluation of blow holes in the corner joints of truss chords, detection of fatigue crack from the blow holes will be introduced. Some studies on applicability of automatic ultrasonic testing systems by comparing between radiographic testing and automatic ultrasonic testing will be introduced. Recent collaborative researches on automatic ultrasonic systems aiming to performance and quality based design will be mentioned.

KEYWORDS

nondestructive testing, automatic ultrasonic testing system, weld, detectability, performance based design

INTRODUCTION

The application of thicker plates has been increasing in the bridge construction in Japan. Sometimes plates of up to 100 mm thick are used as the flange plate of bridge girder. Welded joints are more suitable remarkably than bolted joints as field joints. However, radiographic testing (RT) cannot be applicable for the welded joints of thick plates. In addition, the application of RT is unfavorable in site. Instead, automatic ultrasonic testing (AUT) will be applied for inspection.

AUT systems were developed and started to apply to the inspection of bridge members in the 1980s. AUT systems were applied for evaluation of blow holes in the corner joints of truss chord members of Seto Ohashi. It was the first time of application of AUT systems. Since then, AUT systems have been applied for not only corner joints but other types of joints such as field welded joints of orthotropic bridge deck and field welded joints of steel bridge piers. The history of development and application of nondestructive testing, particularly AUT, is reviewed.

REVIEW OF AUTOMATIC ULTRASONIC TESTING SYSTEM UNDER THE HONSHU-SHIKOKU BRIDGE PROJECT

Quality evaluation of corner joint of truss chord members of Seto Ohashi

The construction work of Seto Ohashi was completed in 1988. The concept of permissible sizes of weld defects had been introduced in the quality control program of weld coupling with fatigue design. A large number of full scale and large size fatigue tests were conducted. It turned out that blow holes in corner joints of truss chord members might affect the fatigue performance [1]. Fig.-1 shows a blow hole and fatigue crack in a corner joint. The permissible size of blow holes was determined for 100 year service.

The members were categorized three types such as AA, A and B based on required fatigue performance. Permissible size of blow holes in each category is shown in Fig.-2. Therefore, nondestructive testing systems were required to detect defects of sizes shown in Fig.-2. Since those members had closed section, RT could not be applied. Instead, AUT would be applied. It was the first time that AUT systems were developed [2].

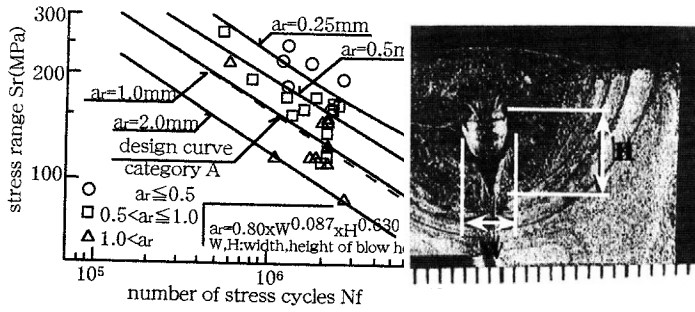


Fig. 1: fatigue strength of corner joint

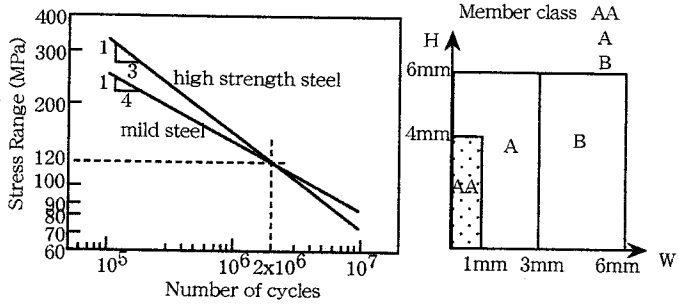


Fig. 2: acceptable size of blow hole

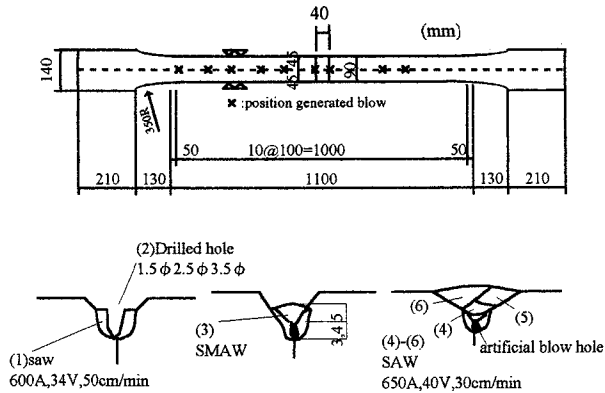


Fig. 3: specimen with simulated blow hole

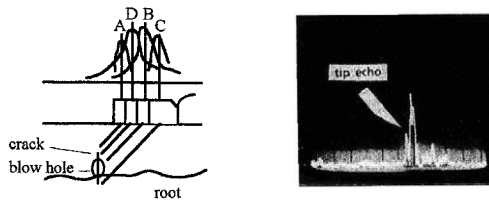
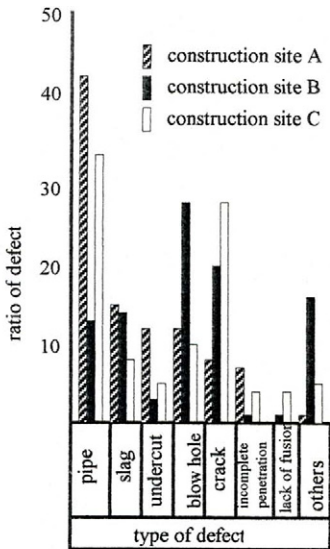


Fig. 4: tip echo method



ratio of defect is calculated by
number of film of the defect/total number of film of defects

Fig. 5: types of defects of steel deck plate

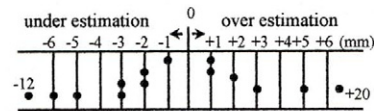


Fig. 6: difference of estimation of defect size

Detection and characterization of fatigue crack in the corner joint of truss chord member

Fatigue cracks would be initiated from blow holes in the corner joint of truss chord. Applicability of AUT systems was investigated to detect fatigue cracks from blow holes. AUT systems were the same as those used for evaluation of blow holes.

Fig.-3 shows a test specimen used in that investigation. This specimen simulates corner joint of truss chord. The specimen was V-groove partial penetration weld. This specimen contained 11 artificial defects modeling blow holes. As shown in Fig.-3, holes were made by a drill. Diameters of artificial blow holes were 1.5, 2.5 and 3.5mm. During fatigue tests, ultrasonic tests were conducted.

The tip echo method was applied in ultrasonic testing. 19 fatigue cracks could be detected out of 44 fatigue cracks by tip echo method. Fig.-4 shows a tip echo on cathode ray tube (CRT). Tip echo is indicated by arrow. Fig.-4 also shows an illustration of a crack initiated from a blow hole. In such case, reflecting points are (A) tip of the crack, (B) blow hole and (D) corner of crack and blow hole. In that study, the minimum size of detection of fatigue cracks by tip echo method was about 8mm, while it depends on the width of incident ultrasonic beam.

Application of Automatic ultrasonic test for steel deck plates

Quality evaluation of field welded joints of steel deck plates had been carried out by RT. AUT systems for truss chord members were applied to steel deck plates of 3 bridges of Seto Ohashi in mid 1980s.

Thickness of deck plates are usually 12mm to 14mm. One side submerged arc weld is applied for field weld of steel deck plates. Fig.-5 shows weld defects which can be seen in steel deck plates [3]. Among those weld defects, hot cracks often can be included. In case of one side weld, cracks caused by the constraint at the end also can be included.

Comparison of testing results between RT and AUT was made. RT was carried out where an unacceptable weld defect was found. The result of comparison is shown in Tab.-1. From Tab.-1, difference of length of defects between radiographic testing and ultrasonic testing was calculated. Fig.-6 shows over- and under-estimation of defect size of AUT judging from RT. The difference of estimation of defect size is ± 2 mm.

Tab. 1: comparison between automatic ultrasonic testing and radiographic testing

result of radiographic testing		result of ultrasonic testing		difference (RT-UT)
type · length	class	class	echo height · length	
crack-- 24mm	4	4	50% · 25mm	-1mm
incomplete penetration --5mm	4	4	30% · 10mm	-5mm
blow hole -- 14mm	4	4	85% · 13mm	+1mm
blow hole -- 90mm	4	4	95% · 85mm	+5mm
blow hole -- 12mm	4	4	75% · 10mm	+2mm
blow hole -- 31mm	4	4	100% · 25mm	+6mm
blow hole -- 28mm	4	4	75% · 25mm	+3mm
blow hole -- 67mm	4	4	100% · 65mm	+2mm
blow hole -- 72mm	4	4	100% · 60mm	+12mm
blow hole -- 8mm	4	3	50% · 5mm	+3mm
not detected	1	4	55% · 20mm	-20mm
blow hole -- 17mm	4	4	100% · 21mm	-3mm
blow hole -- 13mm	4	4	100% · 15mm	-2mm
blow hole -- 2mm	1	1	35% · 3mm	-1mm

APPLICATION OF AUTOMATIC ULTRASONIC TESTING SYSTEMS TO BUTT WELDED SPLICE JOINTS

In 1990, specifications for highway bridges in Japan were revised [4]. It was described that ultrasonic testing could be applied for quality evaluation of welded joints instead of RT. RT takes time to expose the films. On the other hand, testing results can be obtained instantaneously by ultrasonic testing.

In the early 1990s, applicability of AUT for butt welded joints was investigated [5]. As the first step, survey of defects formed in butt welded joints was carried out. Fig.-7 shows results of RT of butt welded joint in a certain shop. Type 1 is volumetric defects such as blow holes. Type 2 is cylindrical defects such as pipe and slag inclusion. Total number of pieces of film recorded from 1985 to 1992 was about 48000. No defect could be detected from 97.9% of 48000. Type 1 defects were detected from 1.45%. Type 2 defects were from 0.24%. Most of those type 1 and 2 defects were classified in class 1 and 2. If welding condition is controlled sufficiently, few type 1 defects of class 3 or 4 can be formed. Defects of class 4 are larger and may cause damage to the structure. Incomplete penetration and crack are classified as class 4. Although the number of incomplete penetration and crack is small, these defects can be formed. Therefore, it is necessary that incomplete penetration and crack should be detected by nondestructive testing.

As the second step, comparisons between RT and AUT for some types of welded joints were made. Tab.-2 shows one of the results. Defects of classes of 3 and 4 are unacceptable. The total number of defects detected either AUT or RT was 403. Agreement between AUT and RT could be seen 66% out of those 403 defects. There were 66 defects (16%) which were judged unacceptable by AUT and acceptable by RT. On the other hand, there were 76 defects (18%) which were judged acceptable by AUT and unacceptable by RT. Most of the defects disagreed were planar defects such as crack and lack of fusion. It was also pointed out that detectability of planar defects were different from each of the AUT systems. Detectability of planar defects by AUT needs to be investigated.

AUTOMATIC ULTRASONIC TESTING SYSTEMS TO FIELD WELDED BUTT JOINTS

In recent years, for economical reason, simplified girder bridges have been constructed in Japan [6]. The number of main girders are decreased two or three. Thickness of flange plate is sometimes more than 80mm. Welding joints of main girders are adopted in order to reduce dead weight of the girder. Weld of main girders would be conducted in site. Fig.-8 shows details of one of the site welding joints. In this type, both upper and lower flanges are welded by flat position.

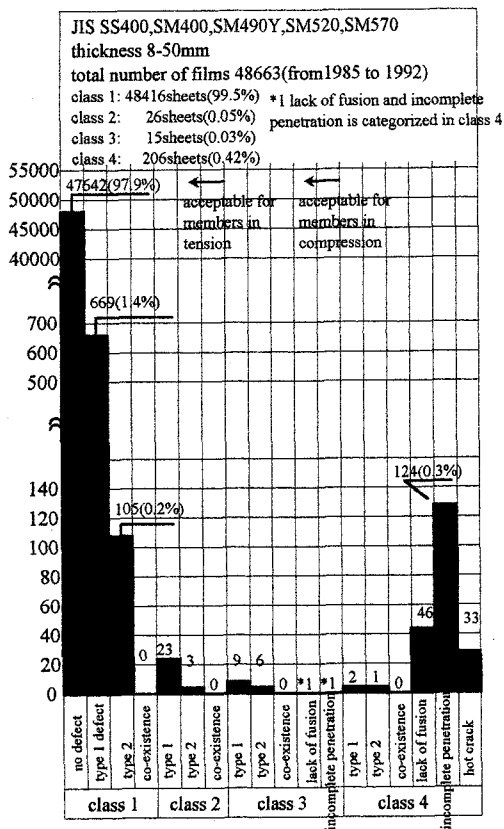


Fig. 7: welded defects in a shop evaluated by radiographic testing

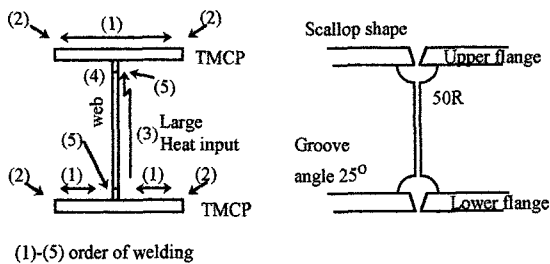


Fig. 8: site welded joint

Tab. 2: comparison between ultrasonic testing and radiographic testing

Radiographic test		JIS Z 3104		JIS SM490 thickness 9-32mm groove I,V,X probe SZ10X10A70 STB A2 L-level detection one-sided test				
		unacceptable	acceptable	no detection	class 1	class 2	class 3	class 4
JIS Z 3104	unacceptable	class 4	type 3	7 (0)	7 (3)	2 (0)	1 (0)	22 (4)
			type 2	3 (0)	11 (1)	13 (2)	37 (4)	39 (10)
	class 3	type 2	3 (0)	7 (1)	5 (2)	4 (1)	11 (2)	
		type 1	5 (0)	8 (2)	2 (1)	8 (2)	7 (1)	
	class 2	type 2	2 (0)	4 (0)	2 (1)	1 (0)	2 (1)	
		type 1	8 (2)	6 (1)	9 (2)	7 (0)	5 (0)	
	class 1	type 2	15 (2)	16 (2)	7 (3)	6 (1)	4 (1)	
		type 1	6 (0)	4 (1)	1 (0)	2 (1)	5 (1)	
	no detection			46 (8)	9 (2)	19 (4)	15 (4)	
				no detection	class 1	class 2	class 3	class 4
			acceptable			unacceptable		

ultrasonic test (JIS Z 3060) () manual ultrasonic test

total data 403 (detected by either RT and UT):403
 accepted by RT and UT :135 264 (66%)
 unaccepted by RT and UT:129

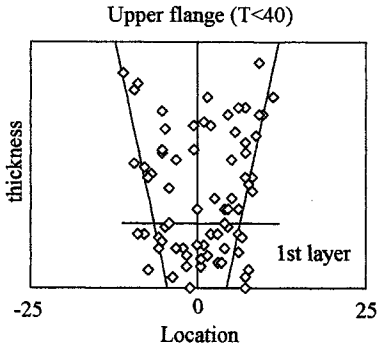


Fig. 9: distribution of defects in welded section

Tab. 3: type of defect in site welded joint

MUT		Real type of defect and number						Correctness %
Type	Number	BH	SI	C	IP	LF	Unclear	
BH	32	24	0	0	0	5	3	82.8
SI	100	4	65	1	0	19	11	73
C	3	0	0	3	0	0	0	100
IP	21	1	1	0	12	3	4	70.6
LF	329	0	13	0	0	284	32	95.9

Correctness of volumetric defect = $(20+4+39)/(21+58) = 70.5\%$

Correctness of planar defect = $(1+12+3+17)/(1+21+135) = 85.6\%$

BH: blow hole IP: incomplete penetration
 SI: slag inclusion LF: lack of fusion
 C: crack

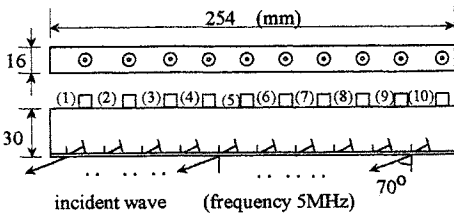


Fig. 10: tandem array transducer

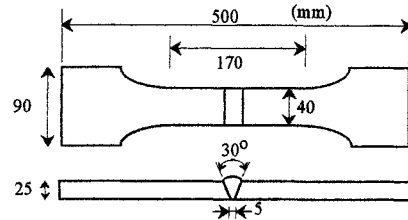


Fig. 11: test specimen

Site welding joints of thick steel plates have never been applied before. Details of welding are different from that of in the past. It is possible that different types of defects would be formed in site welded joints. It is necessary to investigate type of defects, distribution of defects in welded section and distribution of defects along seam line. Fig.-9 shows distribution of defects in welded section. Most of the defects can be found in the first welding layer. Tab.-3 shows type of defect. Tab.-3 is comparison between presumed defect type by manual ultrasonic testing and real defect type. Lack of fusions were found most of all the types of defects. Slag inclusion is the next.

Nondestructive testing also has to be conducted in the field. AUT will be applied because RT may do harm to the surroundings. AUT systems should have performance which is never required before.

NEW TANDEM ARRAY AUTOMATIC ULTRASONIC TESTING SYSTEM

Detection of planar defects such as lack of fusion and crack is important. At planar defects, incident waves will be reflected specularly. Reflected waves sometimes cannot be received by a probe, when one probe is used. Only tip diffracted echoes can be received by the probe because tip diffracted echoes have no directivity [7, 8].

Planar defects can be detected, if reflected waves with strong directivity can be received. It is made to be possible if more than one probes are used. Tandem probe technique is effective to detect planar defects [9]. In tandem probe technique, two probes are mounted in the same direction. Comparing with one probe technique, tandem probe technique needs more calibration and skill of scanning. The system have to be more complicated. In order to avoid complicated scanning process, tandem array transducer was developed. Fig.-10 shows tandem array transducer. The transducer consists of 10 probes aligned. As total, 100 patterns of combination of transmitter and receiver are possible, 10 as the transmitter and 10 as the receiver.

Experiments were carried out with the transducer. The specimen is shown in Fig.-11. The specimen contains

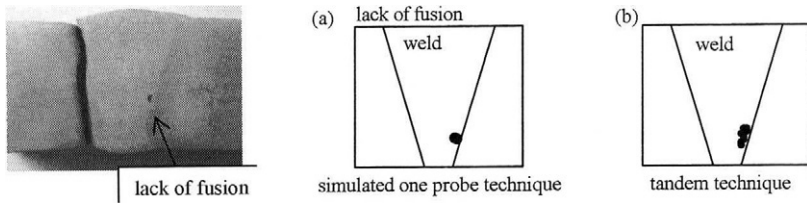


Fig. 12: B-scope displays of lack of fusion by tandem array transducer (a)simulated one probe technique, (b)tandem probe technique

a lack of fusion. Fig.-12 is B-scope displays of the lack of fusion. In 10 out of 100 patterns of combination of transmitter and receiver, the transmitter and the receiver is the same probe. One probe scanning can be simulated by those 10 patterns. Fig.-12(a) means simulated one probe scanning. Comparing with Fig.-12(a) and (b), more echoes are plotted in Fig.-12(b). This means that tandem probe technique has higher detectability than one probe technique.

FATIGUE PERFORMANCE-BASED QUALITY CONTROL DESIGN

Fatigue tests of butt welded joint containing various embedded defects

A feasible quality control program should be established due to recent changes in steel bridge construction such as field welded joints of thicker plates. Butt welded joints has to satisfy Class D JSSC specifications. The degree of significance of weld defects may vary with the type, size, shape, location of defect and joint geometry. The fatigue performance of butt welded joints containing various embedded defects was examined experimentally. Based on these test results, permissible limits of defects would be determined. In this section, some of the test results are described.

Fig.-13 shows the shapes and sizes of test specimens. The specimens simulate field welded joint of main girder. The thickness of the specimens was 25mm, 50mm and 75mm. The steel of the specimens was JIS SM490. The specimens were fabricated by a CO₂ gas shielded arc welding process. The shape of the groove is a single V-groove. A pair of wide plates was welded together. The condition of welding was changed intentionally. Weld defects were made. The locations and sizes of defects in the weld were examined by RT after welding. Based on the results of RT, specimens were cut out from the welded plates such that each defect was located at the center zone.

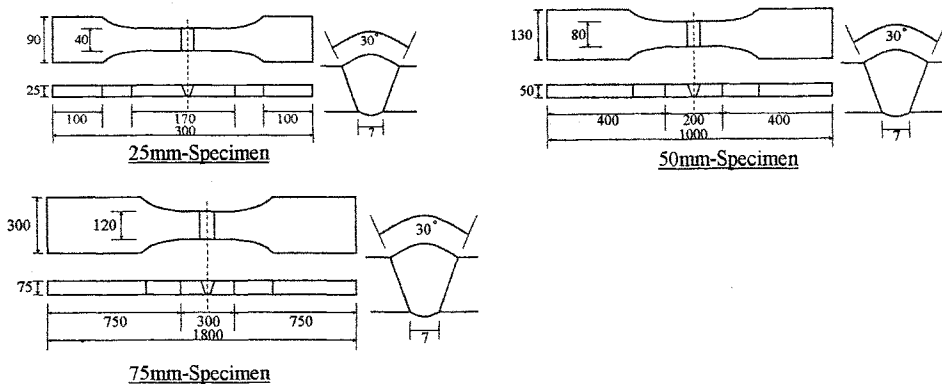


Fig. 13: test specimen of fatigue tests

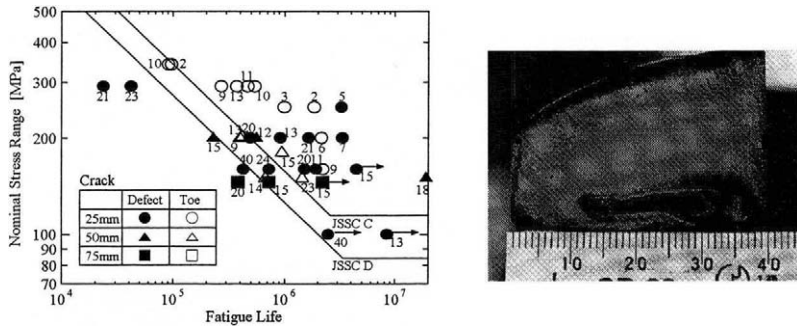


Fig. 14: fatigue test results and failure surface

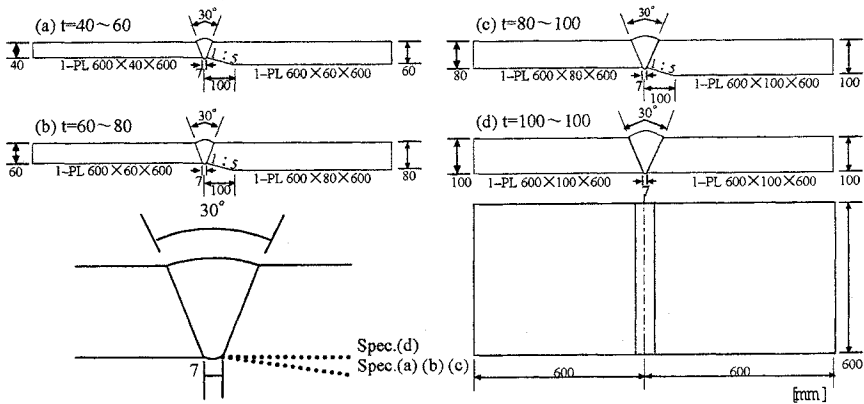


Fig. 15: test specimen of round robin test

Fig.-14 shows the fatigue test results as an S-N diagram. Typical failure surfaces are shown in Fig.-14. The number beside each plot in Fig.-14 indicates the length of defect in the specimen measured along the failure surface. Some of the fatigue cracks initiated from the surface of the weld toe. Some of the fatigue cracks penetrated through the entire section of plate, regardless of the existence of weld defects. The open symbol indicates that the specimen has failed by growth of a fatigue crack that initiated from the weld toe. In such cases, the number beside plot is the maximum size of defect in that specimen. Some fatigue tests are still on-going. The acceptable size of weld defects will be discussed and determined after the fatigue tests.

Round robin test for automatic ultrasonic test

Requirement for AUT systems may change according as the acceptable size of weld defects. Round robin test is conducted as part of a collaborative research project. One of the purposes of the round robin test is to examine the performance of newly developed and existing AUT systems. Sixteen companies are involved in this test program. Specimens used in this program are shown in Fig.-15. Those test specimens simulate field welded joint of main girder. The specimens contains artificial and natural weld defects. The thicknesses of those plates are 40mm, 60mm, 80mm and 100mm. Fig.-16 shows the round robin test.

Another purpose of the test is to establish a manual for nondestructive examination techniques for welded joints. The manual will include methods for approving ultrasonic automatic examination systems and methods for confirming the performance of on-site ultrasonic automatic examination systems. Differences in existing ultrasonic automatic examination systems are transducer characteristics such as frequency, angle and size of crystal, the number of transducers, scanning systems, echo data recording system, imaging system such as A,



Fig. 16: round robin test of automatic ultrasonic test

B, C scope and synthetic aperture method. The round robin test is conducted at the laboratory of the Public Works Research Institute and still under way.

CONCLUSION

In this paper, historical review of automatic ultrasonic testing systems was described. Some studies on applicability of automatic ultrasonic testing in shop and site were introduced. Recent trend of steel bridge was mentioned. Round robin test and fatigue test for performance based design were introduced.

References

- [1] Sakamoto, K., Fukazawa, M., Hamano, M. and Tajima, J. (1985). In : *Proc. of JSCE Structural Eng./Earthquake Eng.*, Vol.2, No.2, pp.209-219.
- [2] Miki, C. (1994). In : *Review of Progress in QNDE*, Vol.13, pp.2071-2082.
- [3] Kanazawa, K. (1987) In : *Honshi Technical Report* Vol.11, No.43, pp.7-11.
- [4] Specifications for Highway Bridges in Japan, 1990.
- [5] Miki, C., Narumiya, T., Morishita, T. and Kato, M. (1994). In : *Proc. of JSSC*, Vol.1, No.4, pp.105-117.
- [6] Takahashi, S., Shimura, T., Tachibana, Y. and Konishi, T. (1996). In : *Bridge and Foundation Engineering*, pp.23-30.
- [7] Thompson, R.B. (1983). In : *Journal of Applied Mechanics*, Vol.50, pp.1191-1201.
- [8] Arakawa, T., Hirose, S. and Senda, T. (1985). In : *NDT International*, Vol.18, No.1, pp.9-16.
- [9] Bowker, K.J., Coffey, J.M., Hanstock, D.J., Owen, R.C. and Wrigley, J.M. (1983). In : *British Journal of NDT*, Vol.25, No.5, pp.249-255.

RESEARCH IN NON-DESTRUCTIVE TESTING IN CIVIL ENGINEERING AT BAM

HERBERT WIGGENHAUSER
Bundesanstalt für Materialforschung und -prüfung
Unter den Eichen 87, D-12205 Berlin, Germany



Figure 1: Aerial view of BAM headquarters in Berlin-Lichterfelde

ABSTRACT

A special group for non-destructive testing in civil engineering was established at BAM in 1990. The tasks of this group, the background for the research and the links between the different disciplines are outlined. The main areas of research, the activities in standardisation, information and conferences are outlined. Examples of recent research results are presented and discussed.

KEYWORDS

Ultrasound, radar, impact-echo, LIBS, compendium

BAM: Federal Institute for Materials Research and Testing

BAM is an institute of the *Ministry of Economics and Technology* with 150 year tradition in materials testing and research. The staff is approx. 1200, with more than 800 scientists working in all areas of materials research. The profile of BAM is described by:

The mission to promote the development of German economy

the function as materials-technological and chemical-technological national institute

the guideline safety and reliability in chemical and materials technologies

the activities research and development, testing, analysis, approvals, consultation and informa-

tion

the tasks in the interacting fields of materials - chemistry - environment - safety

BAM has 10 departments

- I Analytical Chemistry; Reference Materials
- II Chemical Safety Engineering
- III Containment Systems for Dangerous Goods
- IV Environmental Compatibility of Materials
- V Materials Engineering
- VI Performance of Polymeric Materials
- VII Safety of Structures**
- VIII Materials Protection; Non-Destructive Testing
- S Interdisciplinary Scientific and Technological Operations
- Z Administration and Internal Services

The Department VII - Safety of Structures - consists of 4 Divisions:

- VII.1 Building Materials
- VII.2 Building and Structures
- VII.3 Building Diagnosis; Non-Destructive Testing in Civil Engineering**
- VII.4 Corrosion and Corrosion Protection

The Division VII.3 *Building Diagnosis; Non-destructive Testing in Civil Engineering* was established as a link between civil engineering and the NDT laboratories in the department VIII. The main research areas presently are:

- Ultrasound (Pulse Echo)
- Impact-Echo
- Radar
- LIBS (Laser Induced Breakdown Spectroscopy)
- Thermography
- Moisture Measurements

ULTRASONIC PULSE ECHO

The research in Ultrasonic Pulse Echo has the goal to determine the inner geometrical structure of concrete specimens. As opposed to the transmission velocity measurements, this method can be used with one sided access. The method measures the transit time and intensity of ultrasound reflections at inner scatter centres.

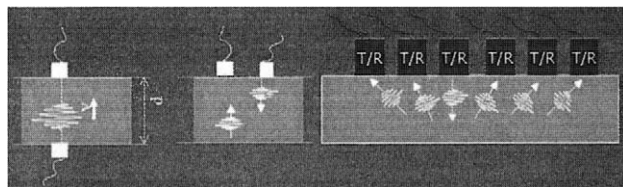


Figure 2: Ultrasound techniques: Transmission (left), Bistatic pulse echo (middle), pulse echo array (right)

US-PE: Principle

- Transmission (velocity measurement)
- Pulse Echo (mono- and bistatic)
- Pulse Echo (array)

In medical applications, ultrasound is a very powerful imaging tool with resolution in the millimetre range. This technique is based on arrays of high frequency focusing transducers and cannot be easily applied to concrete. The problems are:

- High frequencies -> short wavelengths ($\lambda = v/f$)
- The transducer diameter must be much larger than the wavelength to focus the ultrasound, e.g. at 100 KHz and a velocity of $v_L = 4 \text{ km/s}$ the wavelength is $\lambda = 4 \text{ cm}$, resulting in a transducer diameter of more than $d > 15 \text{ cm}$!
- Large diameter transducers cannot be used in practical applications (coupling to surface)

A-Scan

In A-scans (intensity vs. time) the signal is hidden in the surface waves which arrive at the receiving transceiver earlier than waves reflected internally (see figure 3). Coupling of the transducers to the concrete surface is difficult and highly influences the intensity of the signal.

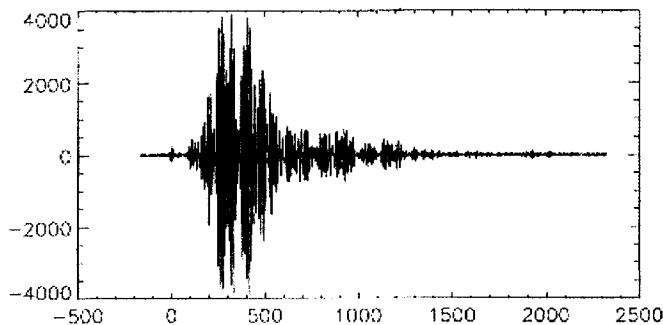


Figure 3: Typical ultrasound A-scan from concrete specimen

Phase Corrected Superposition

The phase corrected superposition technique was applied to obtain a S/N-improvement through the superposition of single measurements with varying transducer distances. Any signals originating from random scatterers are statistical, true reflections are not. The more measurements are taken, the better the S/N-ratio. Therefore multiple meas-

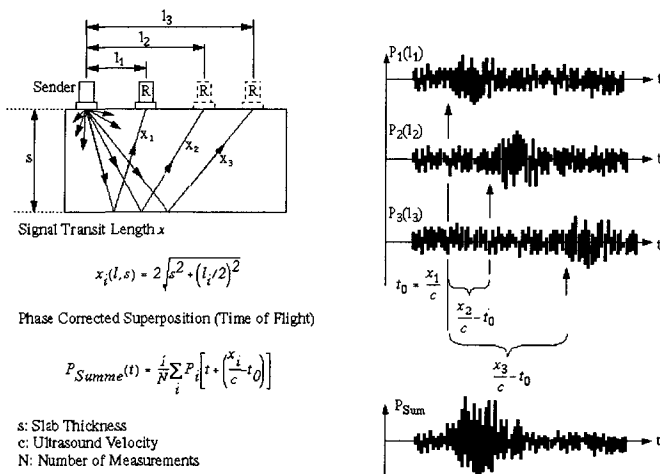


Figure 4: Principle of phase corrected superposition of ultrasound pulse echo experiments on concrete specimen.

urements are required for this technique.

Figure 5: Result of synthesis of phase corrected signal for a range of thicknesses. At the true thickness of the specimen (50 cm), an amplification of the backplane reflection takes place.

An example of a phase corrected superposition of measured signals for different thicknesses is shown in figure 5: the absolute values of calculated synthetic curves are shown as a function of the corresponding slab thickness for which the calculation was performed. At the true thickness of the specimen, an amplification of the signal is observed.

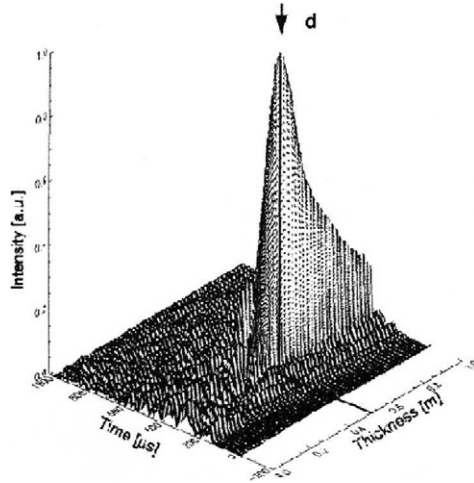
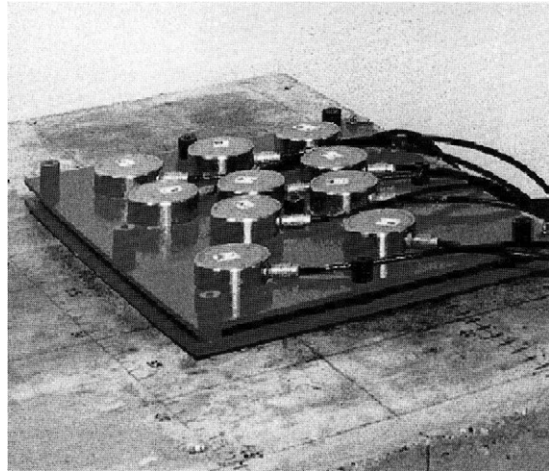


Figure 6: Photograph of the BAM ultrasound array of 10 transducers

The experiment can be time consuming when many readings must be taken in sequence. The position of the transducers must be recorded and the waveforms stored for post-processing. To overcome these problems, a transducer array is used and the transducers employed in both transmitting and receiving mode. In this way, the measurement time can be reduced to less than 5 minutes. The coupling of the transducers is done once and must not be repeated for each single measurement. An array of 10 transducers collects 90 readings which are enough for most applications.



Applications

The thickness measurement with phase corrected superposition has been used in a number of applications on site. It was found that the reinforcement influences the test. For this reason, reinforcement localisation is typically done before, to position the transducers between the reinforcing bars and to minimize interference.

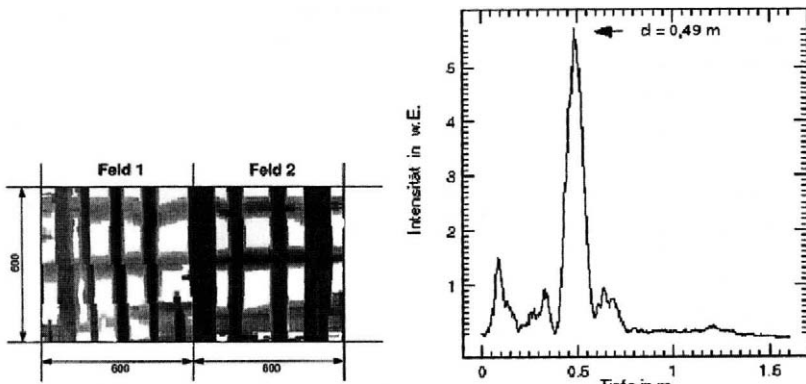
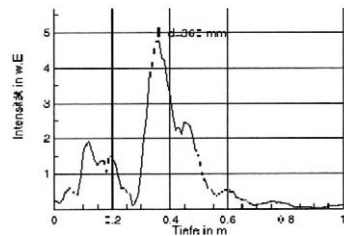
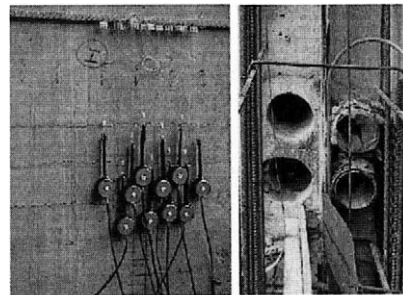


Figure 7: Thickness measurement of a highly reinforced concrete foundation (left: reinforcement position, right: amplitude of phase-corrected reflection signal over thickness).

Figure 8: Localisation of an empty pipe in a highly reinforced concrete tunnel wall. The transducers of the array have been positioned between the reinforcement positions to obtain better signal.

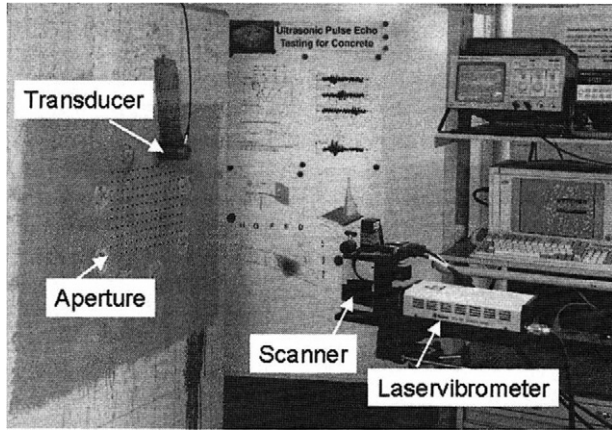


3D-SAFT Reconstruction and automatized measurements with a laser vibrometer

One step further goes the 3D-SAFT (Synthetic Aperture Focusing Technique) reconstruction of a volume under the surface. For this analysis, that part of each A-scan which may originate from a given voxel is calculated and averaged into the voxel. The result is a three dimensional data array, where the values represent the intensity of the reflected ultrasound at this voxel.

Figure 9: Photograph of Laboratory setup for automatized ultrasound tests with 2D aperture and scanning Laser vibrometer

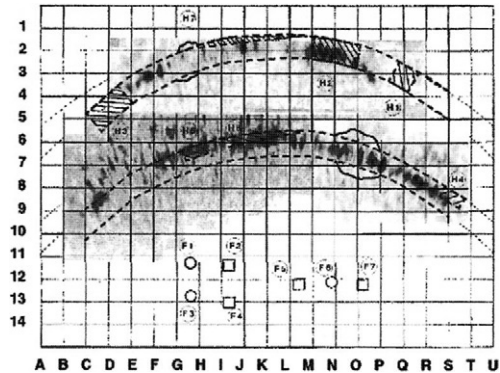
A large number of measurements must be taken for such investigations, typically more than 1000. Such measurements are best automatized with a laser vibrometer. This very sensitive device measures the vibrations of a surface in the direction of the laser beam, which is pointing onto the surface.



3D-SAFT Reconstruction to locate voids in duct

Figure 10: Localization of two ducts in a concrete beam. H1 - H8 indicate the position of intentional and unintentional voids. (Reconstruction by FhG-IZFP, Saarbrücken, specimen: BAsT).

The localization of voids in and around the duct is possible with this time consuming technique which requires many measurements to be taken. Nevertheless it is the only one known which is able to detect voids in metal ducts having a concrete cover of more than 10 cm.



IMPACT-ECHO

Typical tasks for Impact Echo measurements are the same as for ultrasonic echo measurements:

- Thickness measurements of concrete elements with one sided access
- Localization of voids
- Localization of delaminations
- Investigation of ducts

The Impact-Echo principle is based upon the measurement of multiple reflections between the surface and an inner reflector. The sound impulse is generated by a mechanical impact whilst the acoustical intensity is measured with an accelerometer/displacement transducer.

From the measured signal (intensity over time) the frequency components are calculated by a Fast Fourier Transformation. The depth of a reflector is then given by the

formula $d = \frac{v}{2f}$ v: Velocity of sound in the specimen, f: measured frequency)

To exactly determine the depth of an object, the velocity of sound must be known. This is typically obtained by calibrations measurements on a core.

Impact Echo research at BAM was triggered by the fact that three research groups could not correctly measure the position of a duct in a concrete specimen during a round robin test in Germany. The size of the specimen was 2000 x 1500 x 500 mm³, the duct being covered by one layer of reinforcement and having a concrete cover of 10-12 cm on the near side. The diameter of the duct was 12 cm.

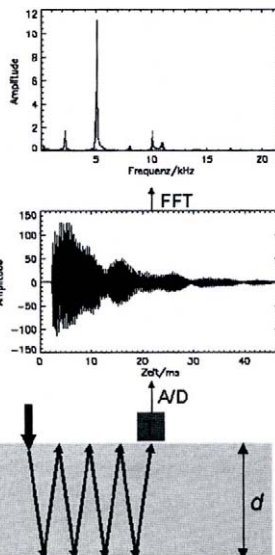
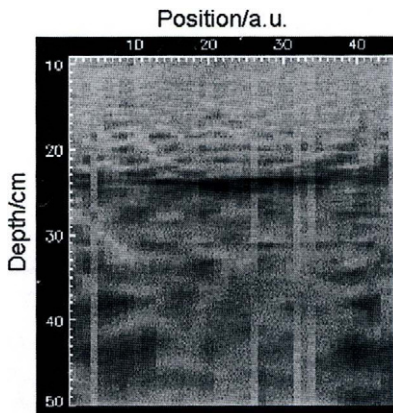


Figure 11: Impact-Echo principle

Figure 12: Example of an Impact-Echo B-scan on a concrete plate with a large delamination

The BAM research proposed and established an automated Impact-Echo with a scanning system to avoid any influence from the operator and to get reproducible results. The advantage of the scanning IE becomes immediately apparent when the data is plotted in a B-scan image, where the amplitude of the frequency function is displayed color coded over position and depth (frequency).

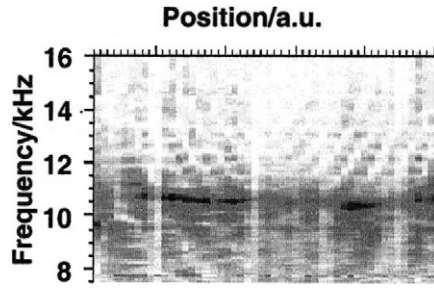
It becomes then very obvious that geometrical effects play an important role at specimens of limited size. Surface waves can mask signals from the interior of the specimen. In single point measurements, there is no possibility to visually distinguish between true reflections signals from the specimen and signals caused by the geometry of the surface. Therefore, scanning IE has several advantages but is more time consuming. It also requires other software for data acquisition and analysis.



Applications of Impact Echo Testing

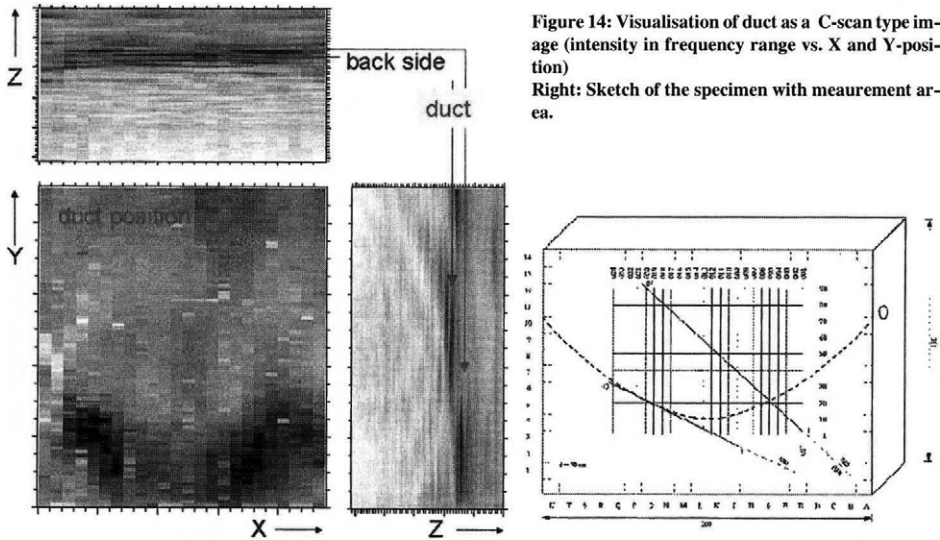
The length of a prism (10 x 10 x 40 cm³) can be measured very easily with IE as shown in figure 11. From a clear signal when the wave velocity is known, the length is determined with high accuracy. Such clear signals are not typical for IE testing in concrete structure applications.

Figure 13: Measurement of the bonding between sleeper and substructure. Geometry effect can be identified in scan mode.



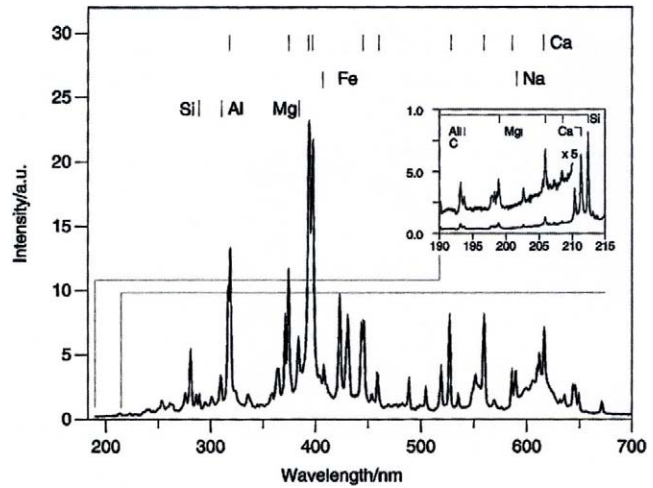
The localization of a duct which has a concrete cover of more than a few centimetres was one task which proved to be more difficult than reports in the literature have indicated. It was not possible to unambiguously identify direct reflections from the duct (10 cm diameter, 12 cm concrete cover) in point measurements. Therefore automatic measurement with a planar aperture (27 x 90 points, 3 measurements averaged at each position, 1 cm distance between points in Y-direction, 5 cm in X-direction) were carried out.

The individual B-scans have been combined in a 3D-data array for data visualisation. No direct signal from the duct was identified, but an indirect indication of the presence of the duct can be seen: the signal from the backside of the wall shows an apparent greater thickness at the position of the duct. By visualizing the signal amplitude in the plane of the wall backside, the duct shows up as an area of smaller amplitude.



**Figure 14: Visualisation of duct as a C-scan type image (intensity in frequency range vs. X and Y-position)
Right: Sketch of the specimen with mearement ar-
ea.**

Figure 17: Typical spectrum of a concrete sample. The spectral lines of characteristic elements are labelled. The inset shows the interesting UV-region around 200 nm with lines of the elements C and Al.



Point Measurement

For point measurements a spectrum is collected at one point on the sample. The wavelength range depends on the measurement task. An example is shown in figure 18, where the presence of Lead was detected in a sample.

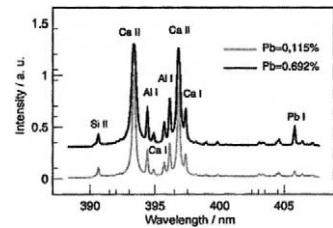


Figure 18: Example: Proof of the presence of Lead in concrete ($\lambda = 405,78$ nm)

Line Scan

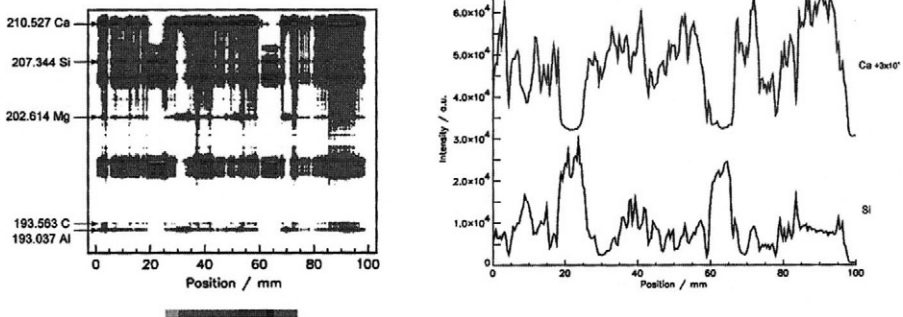


Figure 19: Example for a line scan: the intensities are visualized color coded as a function of position and wavelength (left). The intensity of selected wavelengths are plotted as a function of position (right)

By moving the sample during the measurements, spectra can be collected point by point along a line. Taking the intensity of a selected line (actually the intensity is processed to be corrected for several effects), a concentration profile can be plotted along the measured line (see figure 19).

Area Scan

An area scan is done line by line, taking a spectrum at each point. It can be used to visualize the spacial distribution of a selected element over an area.

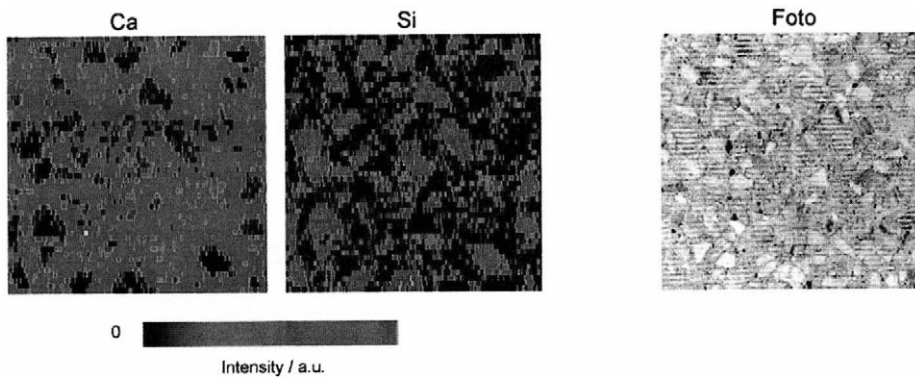
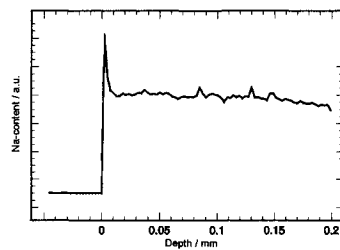


Figure 20: Example for an area scan. The image shows the distribution of Ca (left) and Si (middle) of a broken concrete sample. The picture on the right is a photograph of the specimen.

Depth Profile

A depth profile is collected by shooting with the laser on one point continuously and acquiring data. The intensity of a selected spectral line is then plotted against the depth (number of laser shots)

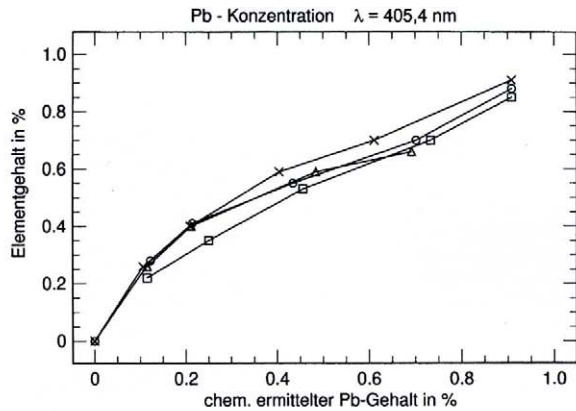
Figure 21: Example of a depth profile: Sodium concentration profile in brick



Metal

The concentration of Lead in mortar was measured with LIBS and the standard laboratory method AAS (Atomic Absorption Spectroscopy). The result gives a calibration curve for the determination of Lead in concrete by LIBS.

Figure 22: Plot of the relative amount of Lead found by LIBS vs. Lead found by AAS



Characterisation of Cement

LIBS can be used to characterize concrete by identifying the composition of the material and visualizing the result in a Rankin diagram. In this diagram, the different types of cement can be distinguished by their position as shown in figure 23 (top left). If cement paste only is measured, the result is visualized in figure 23 (top right). The bottom side of figure 23 shows the result from two concrete samples. Naturally, in concrete the aggregates are composed of SiO₂ causing the results to be distributed along a line from the Si-corner to the cement point. Different concrete compositions result in different slopes of the line. The red values are collected on the smooth side of the concrete, where mainly cement paste covers the surface and only few aggregates can be hit directly by the laser.

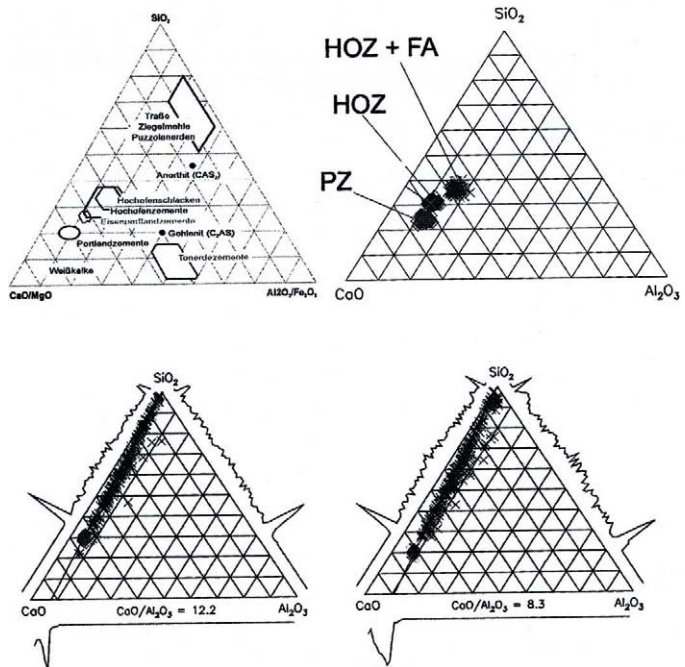


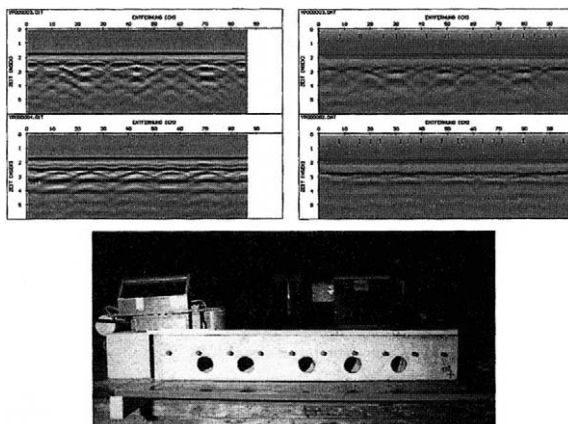
Figure 23: Rankin diagram for cementous materials (top left). LIBS results on cement paste samples (top right). LIBS result from two concrete samples (bottom). The red values are collected on the smooth side of the samples, the blue ones on the broken surface.

RADAR

BAM participated in an European Radar Project with eight partners from four countries: England, Italy, Norway and Germany. In this project, dealing with radar applications for the building industries the dielectric properties of building materials were measured for a large variety of conditions. Also, a high frequency antenna was developed, which proved to give very good results when compared to the ones which are commercially available.

Figure 24: Comparison of GSSI antenna (1.5 GHz) to BAM antenna (1.8 GHz) in two polarization directions. The specimen (HochTief) is shown in the photograph.

In figure 24, a comparison between the GSSI 1.5 GHz antenna (top right) and the BAM antenna (top left) is shown for both polarisation directions. The specimen (from HochTief) was used for comparison of radar systems in their ability to detect ducts below rebars. This specimen is shown in the photograph.



Most radar applications at BAM deal with the location of ducts, voids or other structural elements in concrete. It is one of the most often used tool for non-destructive testing of concrete and masonry structures. It also proved to be valuable in determining the moisture content in historic buildings.

COMPENDIUM ON NDT-CE METHODS

In 1991 BAM published a compendium on NDT-CE methods, describing more than 80 different methods and techniques. The compendium was designed for easy update and expandability: keywords, classifications and a scheme for the description was used for all methods. The content and the links were stored in a database, allowing to produce the compendium through a set of database queries and formatting programs.

The original compendium was soon sold out and in 1998 the compendium was put onto the internet for worldwide free access (www.bam.de/a_vii/vii_3/kompendium/welcome.thml).

Presently, the compendium is under revision and many new method descriptions will be included. A translation into English is planned in cooperation with the FHWA.

The figures show some pages of the NDT-CE compendium on the internet, using Impact-Echo as an example.

PUBLICATIONS

Some selected publications of the NDT-CE group in BAM from recent years;

- 95Kra Krause, M., Maierhofer, C. und H. Wiggenhauser:
Thickness measurement of concrete elements using Radar and Ultrasonic Impulse Echo Techniques
in: Forde, M. C. (Ed.); Proceedings of the 6th International Conference on Structural Faults and Repairs,
London, July 1995, Engineering Technics Press, Vol. 2 (1995) pp.17-24
- 95Kra1 Krause, M., Bärmann, R., Frielinghaus, R., Kretzschmar, F., Kroggel, O., Langenberg, K., Maierhofer,
C., Müller, W., Neisecke, J., Schickert, M., Schmitz, V., Wiggenhauser, H. und F. Wollbold:
Comparison of Pulse Echo Methods for Testing Concrete
in: Schickert, G. and H. Wiggenhauser (Eds.); Proceedings of the International Symposium "Non-Destructive
Testing in Civil Engineering (NDT-CE)" in Berlin, 26.-28. September 95, Berlin: DGZfP, 48.1 (1995)
pp. 281-296
- 95Sch2 Schickert, G. und H. Wiggenhauser:
Proceedings of the International Symposium Non-Destructive Testing in Civil Engineering (NDT-CE)
26.-28.09.95
Schickert, G. and H. Wiggenhauser (Eds.); 26.-28. September 1995 in Berlin, Berlin: DGZfP, BB 48.1,
48.2 (1995) 1346 pp.
- 95Wig1 Wiggenhauser, H., Salzmann, M., Wilsch, G. und D. Schaurich:
Analysis of Concrete with Laser Induced Breakdown Spectroscopy (LIBS)
in: Schickert, G. and H. Wiggenhauser (Eds.); Proceedings of the International Symposium "Non-Destructive
Testing in Civil Engineering (NDT-CE)" in Berlin, 26.-28. September 95, Berlin: DGZfP, 48.1 (1995)
pp. 529-537
- 96Mai Maierhofer, C., Wiggenhauser, H., Brandfaß, M., Pitsch, A. und K. Langenberg:
Localization of Tendon Ducts Behind Reinforcement in Concrete Using Radar in Combination with In-
verse Scattering
in: Proceedings GPR 96, 6th International Conference on Ground Penetrating Radar, 30.09.-3.10.96, Sen-
dai, Japan, pp.257-260
- 97Kra Krause, M., Bärmann, R., Frielinghaus, R., Kretzschmar, F., Kroggel, O., Langenberg, K., Maierhofer,
C., Müller, W., Neisecke, J., Schickert, M., Schmitz, V., Wiggenhauser, H. und F. Wollbold:
Comparison of pulse-echo methods for testing concrete
in: NDT&E International Sonderheft Vol. 30 (1997) 4, pp. 195-204
- 97Kra1 Krause, M. und H. Wiggenhauser:
Ultrasonic Pulse Echo Technique for Concrete Elements Using Synthetic Aperture
in: Bungey, J. H. (Ed.); Proceedings of the International Conference NDT in Civil Engineering in Liver-
pool, Northampton: The British Institute of NDT Vol. 2 (1997) pp. 135-142
- 97Mai2 Maierhofer, C., Krause, M. und H. Wiggenhauser:
Non-destructive investigation of sluices using radar and ultrasonic impulse echo
in: Forde, M. C. (Ed.); Proceedings of 7th International Conference on Structural Faults and Repair, 08.
Juli 1997, Edinburgh: Engineering Technics Press, Vol. 2 (1997) pp. 467-474
- 97Wig Wiggenhauser, H., Wilsch, G. und D. Schaurich:
LIBS for Non-Destructive Testing of Element Distributions on Surfaces
in: Bungey, J. H. (Ed.); Proceedings of the International Conference NDT in Civil Engineering, Liverpool,
Northampton: The British Institute of NDT (1997)
- 98Bue Büscher, K., Wiggenhauser, H. und W. Wild:
Amplitude sensitive modulation-thermography the new way of moisture measurement in building materi-
als
in: Proceedings of QIRT'98, Technical University of Lodz, Polen, 7.-10. September 1998, Lodz: Technical
University of Lodz (1998)

- 98Gey Geyer, E., Arndt, D., Gründer, K., Roos, A. und H. Wiggenhauser:
Thermographic and shearographic investigations of carbon fibre laminates on concrete surfaces
in: Proceedings of 4th International Workshop on Advanced Infrared Technology and Applications, 15.-16. September 1997, Florenz (1998), Florenz: Fondazione Giorgio Ronchi, Vol. 93 (1998) pp. 297-304
- 98Kae Kääriäinen, H., Rudolph, M. und H. Wiggenhauser:
Moisture measurement in building materials with microwaves
in: VTT Publications 357, Technical Research Centre of Finland, Espoo 1998, 73 Seiten
- 98Kra Krause, M., Müller, W. und H. Wiggenhauser:
Ultrasonic Inspection of Tendon Ducts in Concrete Slabs using 3D-SAFT
in: Less, S. and Ferrari, L. (Eds.); Proceedings of the XXIII. Symposium on Acoustical Imaging, Boston, April 1997, New York and London: Plenum Press Vol. 23 (1997) pp. 433-439
- 98Kra1 Krause, M., Wiggenhauser, H., Müller, W. und V. Schmitz:
NDE of tendon ducts in concrete using 3D-Saft
in: Craue, R. L., Matikas, T. E. (Eds.) Proceedings of MRS Symposium II: Nondestructive Characterization of Materials in Aging Systems, 1. 5. Dezember 1997 in Boston, USA, Warrendale: Materials Research Society Vol. 503 (1998) pp. 237-248
- 98Kra2 Krause, M., Wiggenhauser, H., Müller, W., Kostka, J. und K. Langenberg:
Ultrasonic bridge inspection using 3D-SAFT
in: Fahlstedt, K. (Ed.); Proceedings of the CIB World Building Congress, Symposium A, Gävle, Schweden, 7.-12. June 1998, Gävle: KTH Built Environment (1998) pp. A 87
- 98Kri1 Krieger, J., Krause, M. und H. Wiggenhauser:
Tests and assessments of NDT methods for concrete bridges
in: Medlock, R. D. and Laffrey, D. C. (Eds.); Structural Materials Technology III, Bellingham: Proceedings of SPIE, Vol. 3400 (1998) pp. 258-269
- 98Mai1 Maierhofer, C., Leopold, S. und H. Wiggenhauser:
Investigation of the influence of moisture and salt content on the dielectric properties of brick materials using radar
in: Proceedings of the 7th International Conference on Ground Penetrating Radar in Lawrence, USA, Radar Systems and Remote Sensing Laboratory, Vol. 2 (1998) pp. 477-484
- 98Mai5 Maierhofer, C., Krause, M. und H. Wiggenhauser:
Non-destructive investigation of sluices using radar and ultrasonic impulse echo
in: NDT&E International, Vol. 31 (1998) 6, pp. 421-427
- 98Wig2 Wiggenhauser, H., Krause, M. und G. Wilsch:
Modern Laser Applications for NDT of Concrete Structures
in: Srivastava, N. K. (Ed.) (Structural Engineers World Congress, San Francisco, 20.-23. Juli 1998 Proceedings on CD, Oxford: Elsevier Science Ltd., 1998 Paper T176-6
- 98Wig3 Wiggenhauser, H., Schaurich, D. und G. Wilsch:
LIBS for Non-Destructive Testing of Element Distributions on Surfaces
in: NDT&E International, Vol. 31 (1998) 4, pp. 307-313
- 98Wil Wild, W., Büscher, K. und H. Wiggenhauser:
Amplitude sensitive modulation-thermography to measure moisture in building materials
in: Snell, J. R. and Wurzbach, R. N. (Eds.); Proceedings of Thermosense XX, Orlando, 14.-16. April 1998, Bellingham: Proceedings of SPIE, Vol. 3361 (1998) pp. 156-162
- 99Col Colla, C., Milman, B., Wöstmann, J., Mielentz, F., Henschen, J. und H. Wiggenhauser:
Combined NDT for system assurance in railway construction: Impact-Echo, Ultrasonic and Radar techniques
in: DGZfP (Hrsg.); Fachtagung Bauwerksdiagnose - Praktische Anwendungen Zerstörungsfreier Prüfungen, 21.-22. Januar 1999 in München, DGZfP-Berichtsband 66-CD (1999) Poster 5

- 99Coll Colla, C., Schneider, G., Wöstmann, J. und H. Wiggenhauser:
Automated Impact-Echo: 2 and 3-D Imaging of Concrete Elements
in: DGZfP (Hrsg.); Fachtagung Bauwerksdiagnose - Praktische Anwendungen Zerstörungsfreier Prüfungen, 21.-22. Januar 1999 in München, DGZfP-Berichtsband 66-CD (1999) Poster 22
- 99Wol1 Wolter, B., Dobmann, G., Maierhofer, C. und H. Wiggenhauser:
Non-destructive methods for moisture measuring
in: Proceedings of 8th Conference Structural Faults and Repair 1999, London, 13-15 July 1999

This Page Intentionally Left Blank

NON-DESTRUCTIVE TESTING IN THE UK

J H BUNGEY

*Department of Civil Engineering, University of Liverpool
Liverpool, L69 3GO, United Kingdom*

ABSTRACT

A large range of non-destructive testing techniques are employed for a wide variety of applications within Civil Engineering. Whilst the majority of these applications may be regarded as structural, they also include site surveying and highways problems. Testing may be used during planning and construction phases, but the majority of applications are concerned with troubleshooting, maintenance and repair. The current situation in the United Kingdom is reviewed with reference to some recent developments and research programmes.

KEYWORDS

Non-destructive, Testing, Civil Engineering, Structures, Radar, Thermography, Ultrasonics, Dynamic Response.

INTRODUCTION

Specialist high risk areas such as nuclear and offshore structures, and gas and oil pipelines, make extensive use of Non-Destructive Testing of metallic components during manufacture and construction as part of quality assurance procedures as well as during routine maintenance inspections to detect cracking and corrosion. Radiography and ultrasonics are most widely used for checking of welds, although eddy current and magnetic methods are also available. Alternating current field measurement techniques permit non-contacting crack detection and sizing in welded joints both in air and underwater.

The focus of this paper concentrates on mainstream civil engineering activities, where the extent of N.D.T. usage varies considerably. Examples include assessment of ground conditions and piled foundations, location of buried or hidden features, and appraisal of highway or airfield pavements, sewers, and structures of steel, timber, masonry or concrete. Recent developments and the broad scope of current usage in these areas will be outlined, together with relevant research known to be recently completed or in progress. Insitu testing of masonry and concrete structures are particular areas of interest within the U.K. at the current time, together with

pipeline detection and assessment of filled, derelict or contaminated land.

ASSESSMENT OF GROUND CONDITIONS AND LOCATION OF BURIED FEATURES

Sub-surface radar has been used for many years in geophysical surveying along with sonic pulse testing, to detect buried changes in rock strata. There has recently been a surge of interest in the use of scanning pulsed radar systems with frequencies up to 500MHz applied to a much wider range of circumstances. These include the location of:

- variations in thickness of compacted soil layers
- contaminated land, including pipeline leakage
- poor compaction or voids below ground slabs
- buried water courses or wet zones
- buried caverns, tunnels, tanks or foundations
- buried pipelines, ducts or services

At least two major British organisations have developed their own specialised radar equipment, in competition with that already commercially available from the U.S.A. and elsewhere. Computerised signal processing and enhancement techniques have been developed with colour displays which can be filtered and amplified to assist interpretation of results and identification of features of interest. Such packages are readily available commercially, whilst some companies have developed their own software to meet their particular requirements.

Infra-red thermography is another valuable and widely used technique, frequently using helicopter surveys for investigation of landfill sites, tips and contaminated land [1]. Particular features which can be identified include methane generation and/or escape, leachate escape, sub-surface fires and pollution of watercourses. Surveying from the air enables significant areas to be covered cost-effectively, and permits the development of integrated monitoring programmes. The technique can also locate gas leaking from pipework or shallow land drains.

Other insitu tests which are in routine use for assessment of localised soils parameters are radiometric measurement of density, and measurement of moisture content by microwave absorption techniques. These are both used during highway and dam construction, for testing soils and rolled concrete. Combined equipment is available permitting either surface zone backscatter measurements or direct readings with the aid of a drilled hole up to 300mm deep. Three recent developments include:

1. A self-driving pressuremeter which will measure existing horizontal stress, shear modulus, and strength of soils and weak rock in relatively undisturbed situations since no predrilled hole is required.
2. A swinging hammer impact apparatus for testing subgrades and pavement foundations. Analysis of the signal from an accelerometer in the hammer head can yield an apparent modulus of the material. When fully developed it is hoped that this will be an alternative to more tedious soils testing methods which often require sample extraction.
3. A hand-held portable impact tester (working on similar principles) to monitor compaction performance in trench reinstatement after pipe or cable laying.

TESTING OF HIGHWAY AND AIRFIELD PAVEMENTS

A wide range of dynamic tests have been in use for many years to assist condition assessment of bituminous pavements. These include vehicle towed bump integrators, beam deflectographs and deflectometers which measure elastic surface response to a known load [2]. There are also localised tests for surface regularity, texture and skid resistance. Of particular interest is a high speed laser based non-contacting system for measuring longitudinal surface roughness, with computer based data storage.

Surface scanning radar is being increasingly used for condition surveys of highway pavements, and considerable success is being reported from comparative applications to both bituminous and concrete pavements when used in conjunction with a limited number of trial boreholes or excavations. Data storage and handling is a major problem, and computerised systems are essential in conjunction with vehicle mounted operation which may be at speeds up to 70km/h and involve multiple antenna arrays. Applications include detection of variations in thickness of pavement slab and surfacing layers, as well as underslab voids or deterioration of foundation layers. This has also been extended to location of cracks in concrete pavements [3].

Dynamic response systems have also been developed for testing pavement slabs in which an accelerometer is used to obtain a frequency response function resulting from impact with an instrumented hammer at a grid of predetermined test points. Results are processed to develop mode shapes and natural frequencies for concrete slabs, which can be used to locate cracking and non-uniform support conditions [4]. Practical application has been limited, but research in this, and other non-destructive approaches to assessment of structural maintenance requirements of pavements continues.

TESTING STRUCTURES

It is in this area that many recent developments have been concentrated, largely resulting from an increased need to examine modern concrete structures which are experiencing deterioration and older masonry structures which are still in service. The latter range from historic buildings to bridges carrying loads far in excess of those anticipated in design. Maintenance inspection of the structural condition of masonry and concrete lined sewers and tunnels is included in this category of testing.

OVERALL STRUCTURAL INTEGRITY

Dynamic response testing, involving either cyclic vibration or single impulse loading, has grown in popularity and reported applications range from steel and masonry bridges to precast concrete large panel multi-storey buildings. For masonry bridges, single impact loading may be used to assess arch integrity, spandrel wall condition and backfill stiffness [5]. The approach has also been applied to masonry sewers. Response is measured by accelerometers located at key positions and signal processing permits modal analysis and development of a dynamic signature for a structure. This may be related on a comparative basis to structural integrity and performance, and may be particularly useful for monitoring changes with time or following repairs. A range of similar methods are also commercially available for testing piles which are widely used and well established for routine use during construction.

Long term monitoring of structures, including glued segmentally constructed prestressed concrete bridges, by means of strain gauges has been performed in some instances both to assess performance and enhance design data concerning secondary effects. Optical fibres are increasingly being used for this purpose and there is interest in the development of 'smart structures'. Laser interferometry techniques for remote monitoring of dynamic performance of structures and elements have also been developed at the Building Research Establishment.

The identification of river bed scour around bridge piers is another area in which radar has been successfully used [6] offering advantages over sonar which cannot detect backfilled holes. The nuclear industry has specific problems associated with the inspection of thick concrete elements, often heavily reinforced with a steel liner, and accessible from one face only. These present particular challenges which are currently being addressed, with considerable interest in the use of tomographic methods.

Interest in structural integrity in the UK is considerable, and a major national Structural Integrity and Damage Assessment (SIDA) network has recently been established to bring together engineers from a range of different disciplines.

LOCALISED INTEGRITY

Localised cracking, delamination, or voids are identified by a range of established techniques which includes ultrasonics, pulse-echo, thermography and radar. The use of Acoustic Emission methods for masonry and concrete is also under investigation and these are being actively pursued for steel bridges [7]. Most practical ultrasonic applications are based on through transmission, although a 'thickness gauge' for concrete has been developed requiring access to only surface. Several theoretical and experimental studies of ultrasonic wave propagation in concrete, timber and masonry have been undertaken as well as the development of improved transducers for reflected wave studies on concrete. Multiple transducer equipment for tomographic studies is now available. Research to improve transducer design for ultrasonic weld testing, has also been undertaken whilst laser coupled ultrasonic wave generation, and signal processing of pulse attenuation measurements in concrete has been investigated but not yet developed beyond the laboratory [8].

The need to identify inadequate grouting of post-tensioned construction, and consequent corrosion of steel tendons, has led to work on guided wave ultrasonics seeking to direct a signal along the length of a tendon as well as the establishment of a 'Spongeometer' pressure test for use during construction. This latter test now forms part of routine acceptance testing and will identify the presence of voids in freshly grouted ducts.

Simple, hand-held equipment to quantify pulse echo results associated with surface tapping has not been widely accepted but may nevertheless be useful in a comparative role. Commercially available Impact Echo techniques have similarly not, as yet, become widely used. Portable impact equipment has however been developed for the commonly recurring problem of soundness assessment of sand/cement floor screeds, and this is in widespread use. Infra-red thermography has continued to grow in popularity for a wide range of applications, including location of voids, dampness and poor thermal insulation as well as confirming integrity of finishes and location of services within a variety of structures [9]. The application of thermal pulse video systems to concrete has also been examined. Radiography, which is well-established

in testing metallic structures, is used for checking the standard of grouting in prestressing ducts, but is slow in operation and suffers from practical difficulties including the need for extensive safety precautions. Recently available equipment however has reduced exposure times and safety distances with real time imaging capacity.

Radar has attracted considerable interest for its ability to locate and comparatively assess construction features ranging from poor compaction, voids, reinforcing bars, and cracking. Resolution is improved as the frequency increases and 1GHz is typically used for concrete or masonry elements up to about 400mm thickness. Applications also include identification of unknown construction features (e.g. nature of bridge beams, masonry piers, masonry/concrete wall thicknesses), and location of hidden leakage zones (e.g. in bridge decks). Whilst the potential of this technique is recognised as being considerable it does have limitations, especially where small or complex features located close to the surface are being examined. Major research programmes have been undertaken to study applications to both masonry and concrete, much of this work being under the auspices of a recently completed BRITE-EURAM European Project [10].

Work has included a study of basic materials dielectric properties to aid interpretation, coupled with physical testing of laboratory specimens and on-site testing. Partners from Germany, Italy and Norway have been involved with UK organisations in this project which has also incorporated studies of antenna characteristics and development of a specialised high frequency radar system, numerical modelling, and neural networks. Results have been published in a number of technical papers and research is continuing at present in many of these areas.

Electromagnetic covermeters are widely used to locate the position and depth of embedded reinforcing steel in concrete and there have been significant improvements in equipment in recent years, whilst non-calibrated eddy-current devices are used to locate wall-ties in masonry construction. Some apparatus may be used to estimate bar size, and automatic logging facilities are available. An approach for accurately locating and assessing the structural condition of embedded dowels or reinforcing bars has also been examined based on measurement with flux gate magnetometers of the residual magnetic field of the bars.

MATERIALS PROPERTIES

Developments of insitu testing techniques for this purpose have largely been confined to structural concrete. Three main areas may be identified:

Strength

Ultrasonic pulse velocity and rebound hammer measurements are well established techniques for comparative strength assessment. Partially destructive surface zone strength measurement techniques have recently become more firmly established, especially pull-out and pull-off methods for which considerable research and development has been undertaken. Pull-out testing can be used on concrete with cube strengths up to about 140N/mm² both during and after construction. Interest in this technique for early age testing and later age strength prediction has been stimulated by work on the 'European Concrete Building Project' at

Cardington in the U.K. related to fast-track construction methods. Pull-off testing with partial coring is increasingly used for checking bond integrity of patch repairs.

Monitoring strength development during construction by maturity measurements or temperature matched curing has also been the subject of research, but industrial usage has generally been limited to a few specialised circumstances (e.g. cooling towers).

Permeability

Permeability is recognised as being the principal factor influencing durability and much attention has recently been concentrated in this area. The only British Standard test for use on in-place concrete is the long established Initial Surface Absorption Test (ISAT) which was revised in 1997 as BS 1881 Part 208. This is sometimes used as part of specifications for 'prestige' structures when high durability is required. A range of other methods are available, some of which are essentially pressurised versions of the ISAT, such as the commercially available 'CLAM' and 'AUTOCLAM'. Other methods involve testing within a small surface drilled hole, such as the 'Figg' air and water tests which have been combined in the form of the commercially available 'Poroscope'. Recent research has focused on member conditioning and the effects of insitu moisture content upon interpretation of such tests.

All the insitu permeability tests suffer from the problem of dependency upon the (unknown) insitu moisture content existing in the concrete. This limits quality classification to very broad bands. The moisture content is not easy to assess accurately, and development of a reliable and simple quantitative method of surface zone moisture measurement must be considered a high priority. Currently available methods require a drilled hole and are relatively slow, although a chilled-mirror Relative Humidity meter is particularly useful. Laboratory work on Nuclear Magnetic Resonance (NMR) testing [11] has not yet extended to site.

Abrasion Resistance

A simple, mechanical accelerated wear rotating plate apparatus has been developed which is particularly valuable for assessing the quality of floors to industrial warehouses. It has also been shown that the Initial Surface Absorption Test is sensitive to abrasion resistance and may provide a useful basis of classification.

Materials Condition

Whilst not strictly assessing materials properties, it may be of interest to note that a method (based on localised strain-gauging and coring) has been developed to permit the insitu measurement of stress within existing concrete structures. A 'stiffness damage' test has also been developed for use on cores to assess the condition of concrete which, for example, has been subject to extreme temperature cycling.

Causes and Extent of Deterioration

Causes of deterioration of a concrete matrix can only be fully identified by a combination of chemical and microscopic analysis. Nevertheless, there is scope for comparative testing by ultrasonic methods to assess the extent and degree of deterioration insitu. This has been applied extensively to High Alumina Cement Concrete and also to Alkali-Silica reaction damage.

The principal cause of deterioration of structural concrete is that resulting from reinforcing steel corrosion. Major developments have taken place in the use of both half-cell potential and resistivity methods. In both cases extensive research has examined theoretical and practical factors (including carbonation layering, element dimensions, reinforcing steel, temperature and moisture conditions) which affect measurements. Portable non-damaging equipment has been developed, incorporating computerised data storage and processing facilities. These methods, especially half-cell potential, are widely used on site to locate zones of high corrosion risk with great success. Recent research has focused on linear polarisation techniques in the effort to accurately measure insitu corrosion rates. Further techniques to detect localised corrosion in reinforcing bars based on a magnetic flux exclusion approach and high frequency ultrasonics are also being studied.

DOCUMENTATION

Most techniques identified in this paper are described in detail elsewhere by the Author [12], whilst the principal established methods are covered by British Standards. Standards relevant to concrete were updated some years ago and extended to take account of developments in equipment and improved understanding of interpretative procedures. BS 1881 part 201 'Guide to the use of NDT for hardened concrete' was first published in 1986 and outlines a total of 23 different methods, as well as giving guidance on test selection and planning. BS 1881 part 207 'Near-to-surface strength tests for concrete' was published in 1992 and BS 1881 part 130 on Temperature Matched Curving in 1996. A wide range of European Standards are also at various stages of development. The Concrete Society has published authoritative reports on core and permeability testing as well as analysis of hardened concrete and use of Radar [3]. A major programme to update the core testing report is nearing completion. C.I.R.I.A. has also published substantial documents on Pull-Off testing [13] and on Testing Concrete in Structures [14] which reviews available equipment and suppliers.

PHILOSOPHY OF TESTING

With the exception of specialised situations identified previously, routine use of non-destructive testing during construction is limited by the reluctance of industrial companies to accept the additional costs and time involved, despite potential long term performance benefits. Efforts are in hand, especially in the concrete industry, to move towards performance based specifications, but progress is slow. The majority of current applications and developments of non-destructive testing within civil engineering are thus directed towards on-site trouble-shooting related to appraisal, maintenance and repair, or the development of marginal sites.

Testing is frequently only used following observation of faults or deterioration, although incorporation into routine maintenance inspections of major structures and highways is

increasing. Many engineers are increasingly interested in lifetime prediction, based upon the results of insitu testing and monitoring [15] and this provides the justification for current research programmes.

CONCLUSIONS

Use of N.D.T. for quality control during construction is not extensive, apart from a limited number of specialist areas. Principal applications are thus primarily of a trouble-shooting nature. Recent developments have tended to concentrate principally on aspects of integrity and durability rather than materials properties, and it is in these areas that research continues. More extensive usage of many test approaches is hampered by the difficulties of correlation between measured value and desired property or feature, which has led to scepticism amongst some engineers. Nevertheless, there has been significant growth of awareness of the potential scope and capabilities of N.D.T. within the civil engineering industry, and usage of some methods has expanded rapidly. The principal scope for significant future expansion lies during construction, although research into the use of knowledge based systems in conjunction with non-destructive maintenance testing is underway. Education and training, supported by authoritative documentation, hold the key to a successful future for N.D.T. [11]

REFERENCES

1. Titman, D.J. (1998). In: *Proceedings of Int. Conf. on Polluted and Marginal Land 98*, pp 425-428, M.C. Forde (Ed.), Eng. Technics Press, Edinburgh.
2. Pooh, P.S.H., Sha'at, A.A. and Ferguson, J.D. (1992). *Brit. J.N.D.T.*, 34, 2, 61.
3. Concrete Society (1997). *Guidance on Radar Testing of Concrete*, Tech. Rep. 48, Concrete Society, Slough.
4. MaCavitt, N., Forde, M.C., Armstrong, D.M. and Sibbald, A. (1991). *Brit. J.N.D.T.*, 33, 11, 557.
5. Bensalem, A., Fairfield, C.A. and Sibbald, A. (1998). *Insight - Brit. J.N.D.T.*, 40,2,107.
6. Millard, S.G., Bungey, J.H., Thomas, C., Soutsos, M.N., Shaw, M.R. and Patterson, A., (1998). *NDT & E International*, 31, 4.
7. Carter, D.C. and Holford, K.M. (1998). *Insight - Brit. J.N.D.T.*, 40, 2, 112.
8. Tasker, C.G., Milne, J.M. and Smith, R.L. (1990). *Brit. J.N.D.T.*, 32, 7, 355.
9. Titman, D.J. (1999). In: *Proceedings of Int. Conf. on Structural Faults and Repair 99*, M.C. Forde (Ed.), Eng. Technics Press, Edinburgh.
10. Bungey, J.H. (1997). In: *Proceedings of Int. Conf. on NDT in Civil Engineering*, pp 335-339, J.H. Bungey (Ed.), Brit. Inst. NDT, Northampton.

11. Bungey, J.H. (1997). In: *Proceedings of Int. Conf. on NDT in Civil Engineering*, J.H. Bungey (Ed.), pp69-76, Brit. Inst. N.D.T., Northampton.
12. Bungey, J.H. and Millard, S.G. (1996). *Testing of Concrete in Structures*, Chapman and Hall, London.
13. McLeish, A. (1992). *Standard tests for Repair Materials and Coatings - Pull-Off Testing*, Tech. Note 139, CIRIA, London.
14. Bungey, J.H. (1992). *Testing Concrete in Structures - A Guide to Available Equipment*, Tech. Note 143, CIRIA, London.
15. Long, A.E., Basheer, P.A.M. and Rankin, G.B. (1997). In: *Proceedings of Int. Conf. on NDT in Civil Engineering*, J.H. Bungey (Ed.), pp9-30, Brit. Inst. N.D.T., Northampton.

This Page Intentionally Left Blank

HIGH-RESOLUTION GEOPHYSICAL METHODS AS NDT FOR CIVIL ENGINEERING APPLICATIONS

TORU TAKAHASHI

Tsukuba Technical Research and Development Center, OYO Corporation
43 Miyukigaoka, Tsukuba, Ibaraki 305-0841, Japan.

ABSTRACT

In Japan, geophysical methods have been mainly employed for civil engineering applications. In civil engineering applications, exploration targets vary in a wide range and very high resolution in exploration is required. To meet these requirements, various high-resolution geophysical methods have been developed in this decade. In the seismic method, tomographic analysis is applied to seismic refraction data to obtain higher resolution and more reliable subsurface image. High frequency portable vibrator source has been developed for shallow to very shallow high-resolution seismic reflection. In the electrical method, measurement and analysis using high dense electrode configuration has been employed for obtaining detailed subsurface resistivity image. An electrical measurement system using non contact type electrodes has been developed for a more cost-effective survey. GPR (Ground Penetrating Radar) is one of the most commonly used geophysical methods. Because of very high-resolution (less than several tens of cm) and very easy-to-use method, GPR has been used very frequently for detection of near surface cavities, buried pipes and unexploded objects and defects in a concrete. Micro-gravity survey which can delineate very shallow density anomaly has been developed very recently and applied to detection of shallow subsurface cavities and to characterization of an active fault. In the future, geological and geotechnical interpretation techniques of geophysical exploration results are necessary to be developed for making geophysical methods much more practically useful.

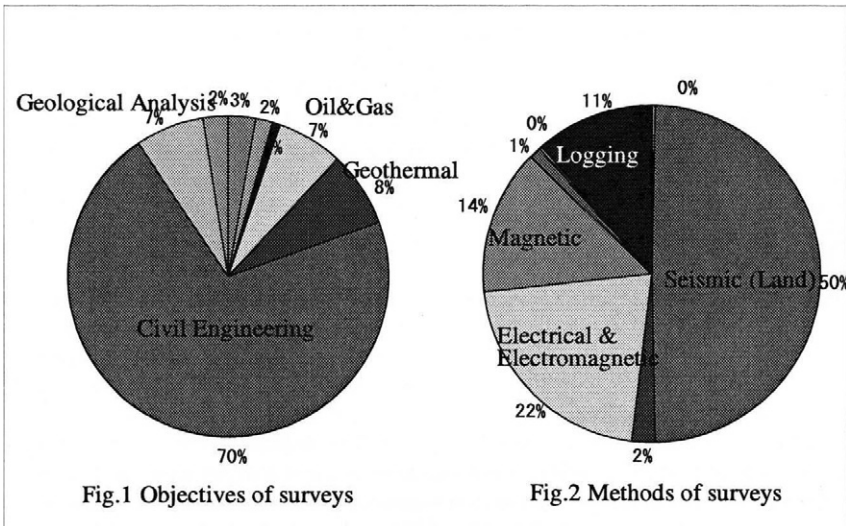
KEYWORDS

Geophysical method, civil engineering applications, shallow subsurface, high-resolution.

INTRODUCTION

In site characterization for civil engineering applications in Japan, drilling at a specific location is first conducted for obtaining geological information of the site and then laboratory tests using drilling cores and in situ mechanical and/or hydrogeological tests are conducted in case that physical and/or hydrogeological properties of the ground are required. However such information obtained at a drilling location is only the information at a specific point in the site. If more areal geological and structural information of the site is required, much more drillings in the site must be conducted, which results in much more cost. In that case, geophysical exploration can be used to interpolate and extrapolate geological and structural information obtained at the drilling points between and/or around boreholes. In addition, geophysical exploration should be used to determine the optimum locations of drilling points for making the investigation more cost-effective.

Figures 1 and 2 show the present status of utilization of geophysical methods in Japan [1]. Figure 1 shows the objectives of geophysical exploration which was used in one year of 1994 in Japan. Main feature of the statistics is that 70% of the total objectives are occupied by those for civil



engineering applications. In Japan, exploration for natural resources such as oil, gas and minerals occupies only a very small portion. Figure 2 is the statistics of geophysical methods which were employed in one year of 1994 in Japan. This diagram shows that the seismic method occupies around a half of the total numbers. The electrical and electromagnetic method is the second. In Japan, magnetic method is mostly employed for detection of buried metal pipes and unexploded objectives like bombs. Velocity logging, especially S-wave logging is almost always conducted in the investigation for an earthquake resistant design of a high-rise building. Therefore these methods occupy a relatively large portion.

Conventionally geophysical exploration has been mainly used for site characterization before the construction of tunnels, dams and large plants like nuclear power plants. However recently utilization of geophysical methods for diagnostics of existing constructions, environmental assessment and solutions and disaster prevention has been rapidly increasing.

In the civil engineering applications, exploration target depth is usually very shallow, which is at most 100m. However the resolution for the exploration target required is very severe, which is often less than 1m. Therefore high-resolution geophysical methods are required in civil engineering applications. On the other hand, the method used should be cost effective, because the budget of the investigation for the project is usually limited. The author's group has therefore tried to develop high-resolution and cost-effective geophysical methods for civil engineering applications in this decade. This paper introduces these newly developed high-resolution methods together with several field examples which can demonstrate the usefulness of these methods.

SEISMIC METHOD

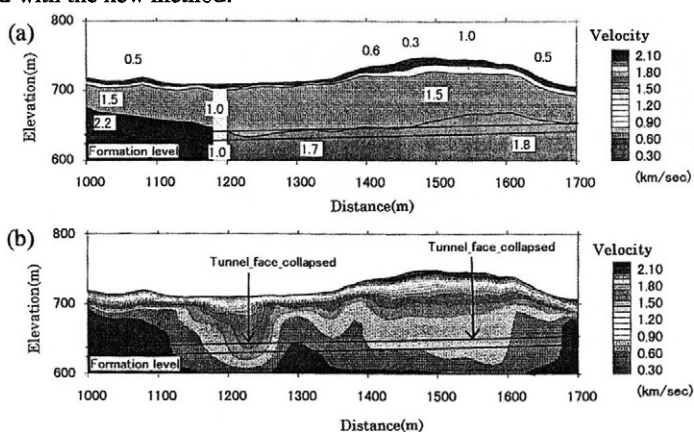
The seismic method is the exploration method which uses various attributes such as traveltimes and amplitude of seismic waves artificially generated to estimate elastic properties of the ground. Through the estimated elastic property distribution, subsurface geological structure can be

inferred. The seismic method can be classified into several methods based on the wave type and observation geometry used in the measurement. The seismic refraction and reflection methods are most commonly used methods. The seismic refraction method makes use of the seismic wave, so called the refracted wave, which is artificially generated on the ground surface and refracts back to receivers on the surface, in order to determine seismic velocity structure of the ground. The seismic reflection method uses the seismic wave, so called the reflected wave, due to the surface seismic source which reflects back to surface receivers from subsurface layer boundaries, in order to determine subsurface geological layering and seismic velocity structure. In the following sections, newly developed seismic refraction and reflection methods are described.

High-resolution Seismic Refraction Method

In the conventional seismic refraction method, seismic refraction data have been acquired and analyzed assuming that the underground consists of almost horizontal layers. Therefore the method can not be applied to the site which has complicated subsurface structure. The newly developed seismic refraction method, called as the high-resolution seismic refraction method, can exclude this horizontal layering assumption by modeling the ground as a grid-based velocity model through which tomographic inversion algorithm can be applied [2]. The main features of the method are as follows; 1) the earth is modeled as a grid-based velocity model, that means this method allows vertical and lateral heterogeneity, 2) the final velocity model is obtained by using tomographic inversion with a ray-tracing method, 3) completely automatic analysis can be done, 4) quality check of the data and the final result can be done by using a quick ray-tracing method.

Figure 3 demonstrates the performance of the new method as compared to the conventional method. In this example, the seismic refraction method is applied to tunnel route investigation. In Japan, P-wave velocities obtained with the seismic refraction method are used for design of the support of the tunnel. During excavation, at two locations indicated in the figure, tunnel faces were collapsed. The velocity profile obtained with the conventional method (upper figure) does not clearly show indications for the collapses. On the other hand, the velocity profile obtained with the new method (lower figure) clearly shows the indications for collapses as low velocity zones on the tunnel formation. The new method can employ the data acquired in a borehole as well as on the ground surface to determine more accurate velocity profile in a complex subsurface structure. Figure 4 shows the comparison of velocity profiles for conventional and new methods. Including the borehole data, high velocity thin lava layer is delineated in the velocity profile obtained with the new method.



Comparison of seismic refraction images of (a) conventional and (b) new methods.

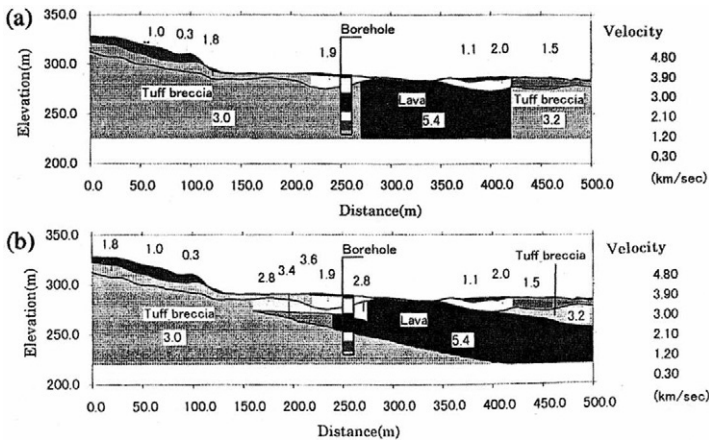


Fig. 4 Comparison of seismic refraction images (a) without and (b) with borehole data.

High-resolution Shallow Seismic Reflection Method

For obtaining high-resolution seismic reflection image, high frequency seismic source is required. We have therefore developed portable P-wave and S-wave electromagnetic vibrators which can generate seismic energy with the frequency of higher than 1 KHz on the surface [3,4]. These vibrators can compensate high frequency energy loss of the seismic waves during propagating in the earth by enhancing high frequency energy in generation.

Figure 5 shows an example of the seismic reflection profile using P-wave portable vibrator on a reclaimed ground near the seashore. The exploration objective in this survey was to delineate subsurface lithological features. The profile clearly shows lithological boundaries between fill, alluvial silty clay, diluvial clayey silt and a bed rock, which are indicated with symbols A, B and C, respectively.

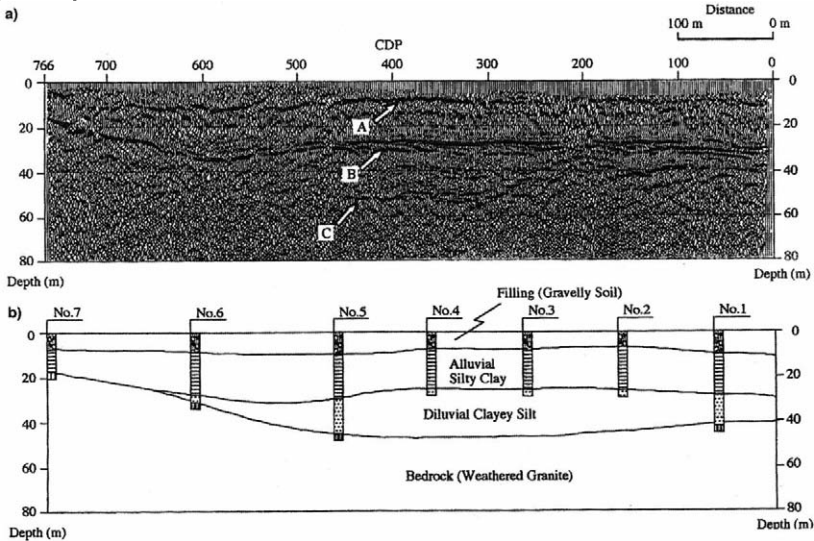


Fig.5 Shallow seismic reflection image using a P-wave portable vibrator.

An example of S-wave portable vibrator reflection profile is shown in Figure 6. The purpose of this survey was to locate the active fault and to describe the deformation of sediments around the fault due to faulting. In this figure, geological interpretation of the profile is also presented. This very high-resolution seismic profile whose resolution is less than 50cm clearly shows the fault location and deformation of the Quaternary sediments in both sides of the fault.

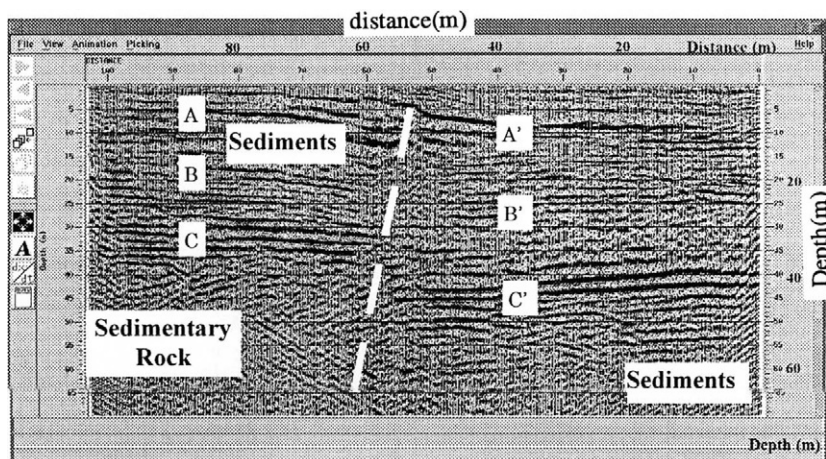


Fig.6 Shallow seismic reflection image using a S-wave portable vibrator.

ELECTRICAL METHOD

There are many kinds of electrical methods. Among them, the direct current (DC) electrical method has long been used mainly for exploration of mineral resources and ground water. In this decade, the method has been aggressively used for civil engineering applications in Japan. In this method, electrical potential data generated with artificial current through electrodes on the ground surface are analyzed to obtain subsurface resistivity distribution. Resistivity is related to various parameters of the ground such as water content, porosity, mineral composition and grain size. Therefore resistivity distribution obtained with the electrical survey allows us to estimate these subsurface parameters which can be used for civil engineering purposes.

Resistivity Image Profiling

The Resistivity Image Profiling [5] is one of the DC electrical exploration methods. In this method, many electrodes are laid out along a measurement line on the ground surface to generate current and measure electrical potential data with any combination of electrodes. The observed electrical potential data are analyzed to obtain subsurface resistivity model using many kinds of inversion techniques.

Figure 7 shows an example of a resistivity image profile which was conducted for tunnel route investigation [6]. Along this tunnel route, there were many fracture zones due to faulting. These fracture zone might cause ground water eruption during excavation. In the investigation before excavation, electrical exploration was conducted to define the location of fracture zones and ground water. In the resistivity profile, low resistivity zone can be interpreted as water saturated fractured and/or altered zones which are potential zones of groundwater eruption.

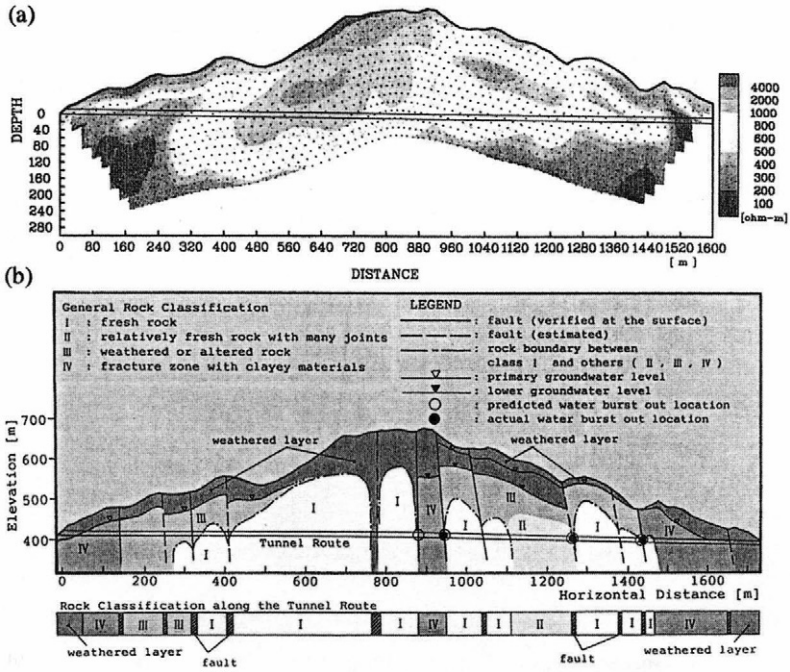


Fig.7 Resistivity image profile for a tunnel route investigation, (a) resistivity image profile, (b) geological interpretation of the profile.

IP (Induced Polarization) Image Profiling

The resistivity image profiling can provide only resistivity of the ground. Induced polarization method, another electrical exploration method, can provide another physical property, chargeability, in addition to resistivity. In this method, not only the electrical potential but also the decay response of the potential after shutting off the current are measured for obtaining two properties above. Chargeability is a property of the material such as an electrical capacitance, which is known to vary with mineral composition, clay content of the soil and so on. Figure 8 shows an example of the resistivity and chargeability distribution obtained with the IP image profiling, which was applied to characterization of an active fault [7]. At the fault plane, there was fault gauge (clay) which was detected as a low resistivity and high chargeability zone in the profiles.

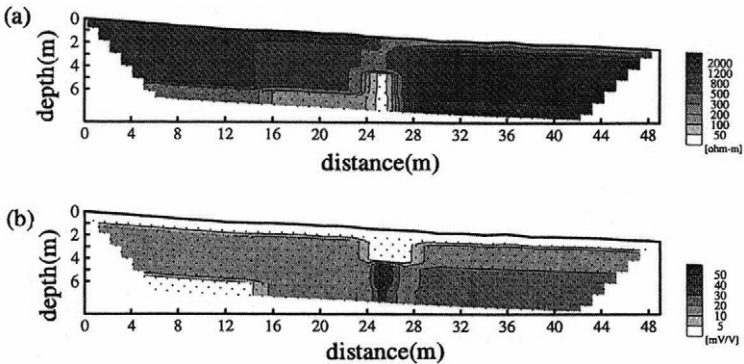


Fig.8 IP image profile at an active fault, (a) resistivity image, (b) chargeability image.

Rapid resistivity image profiling system using multi-channel capacitive electrodes

In civil engineering applications, quick and cost-effective survey is often required. In the usual electrical exploration method as mentioned above, many electrodes should be set up on the ground surface. This time consuming procedure prevents a rapid survey. The author's group has developed a new electrode which does not need direct contact with the ground. The principle of the new electrode called as a capacitive electrode is shown in Figure 9 [8]. Using the system with multi-channel capacitive electrodes, very shallow (up to 6m) resistivity image profile can be obtained within a reasonable time even for a very long profile such as a profile for investigation of a river embankment. The profile as shown in Figure 10 is such an example.

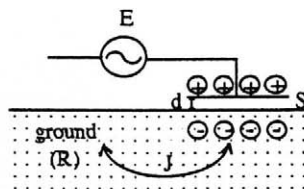


Fig.9 Principle of a capacitive electrode.

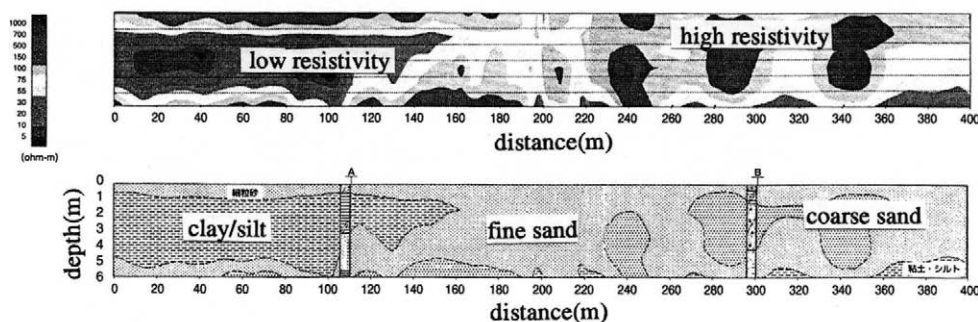


Fig.10 Resistivity image obtained with the rapid resistivity image profiling.

GROUND PENETRATING RADAR

Ground penetrating radar (GPR) is one of the electromagnetic methods which makes use of propagation of the electromagnetic (EM) wave to probe the ground. In a GPR survey, EM reflected waves are used to delineate a geological boundary and buried materials in the ground. As the wave length of the electromagnetic wave is very short (usually several tens of cm) in the ground, very high resolution exploration can be conducted. Penetration of the EM wave into the earth, on the other hand, is very limited. Therefore GPR is usually employed for very shallow exploration (up to around 3m) for detecting buried pipes, cavities in the ground and/or for detecting defects in the concrete.

Figure 11 shows an example of GPR survey for detection of buried pipes under the road. There are three pipes detected in this example. GPR has been widely used for detection of defects in the concrete and cavities behind the concrete on the tunnel wall. Figure 12 shows an example of detection of a cavity behind the lining concrete of a road tunnel. A cavity as well as many steel

supports behind the concrete are detected as diffractions of EM waves. GPR surveys are also widely used in archeological applications mainly for detecting ancient residential traces. Such an example is shown in Figure 13. In this case, GPR profile shows several clear reflections which correspond to a trace of an ancient house and soil boundaries [9].

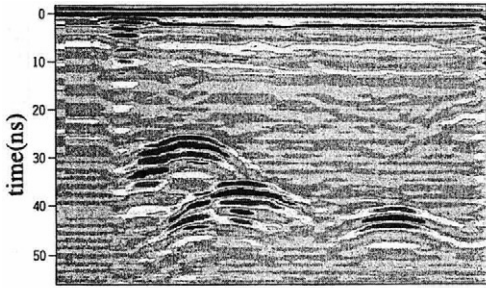


Fig.11 An example of GPR profile in which three buried pipes are detected.

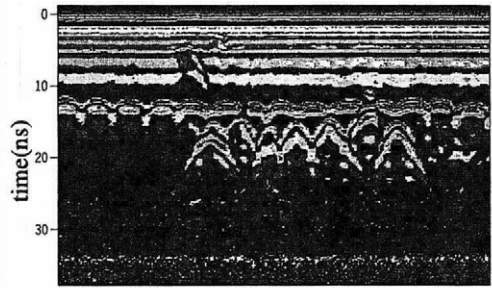


Fig.12 An example of GPR profile in which cavity and steel supports behind the concrete are detected.

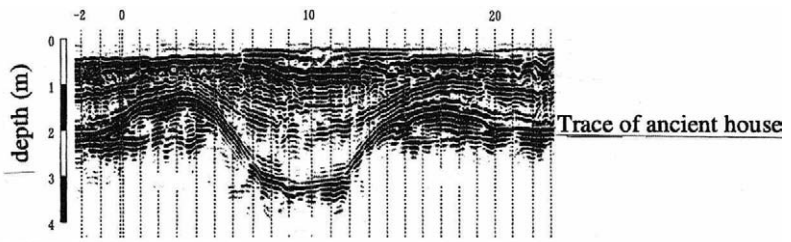
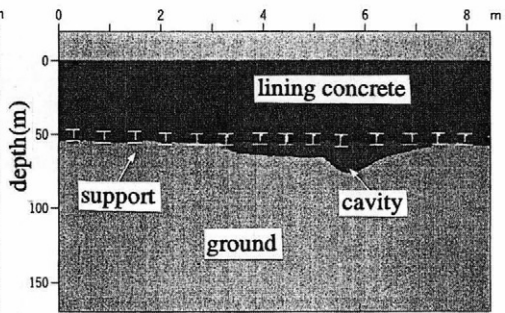
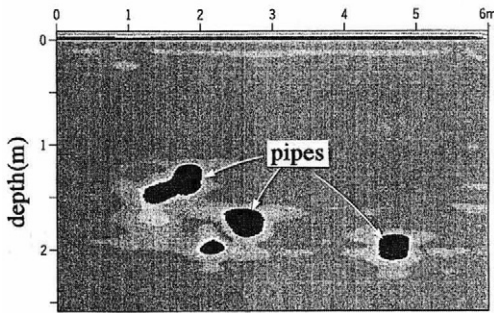


Fig.13 An example of GPR profile applied to archeological deposit detection.

GRAVITY METHOD

Gravity method is a passive survey method unlike the methods mentioned above, which means that no artificial source is used in exploration. Gravity method has been conventionally used for delineating large scale subsurface structure like a several tens to hundreds of km wide sedimentary basin. However recently very easy-to-use and very accurate gravimeter has been developed. The new gravimeter makes gravity exploration much easier than before and provides us with enough accuracy for shallow exploration. Using the new generation gravimeter, the author's group has tried to develop so called micro-gravity exploration technique for civil engineering applications. In civil engineering applications, gravity method has been mainly employed for detection of various scale of cavities or voids in the ground, for characterization of an active fault and for delineation of a bed rock for earthquake resistant design. Figure 14 shows an example of gravity survey for characterization of an active fault [10]. The Nojima earthquake fault which caused the Hyogo-ken Nanbu earthquake in 1995 was clearly detected in both shallow and very shallow explorations.

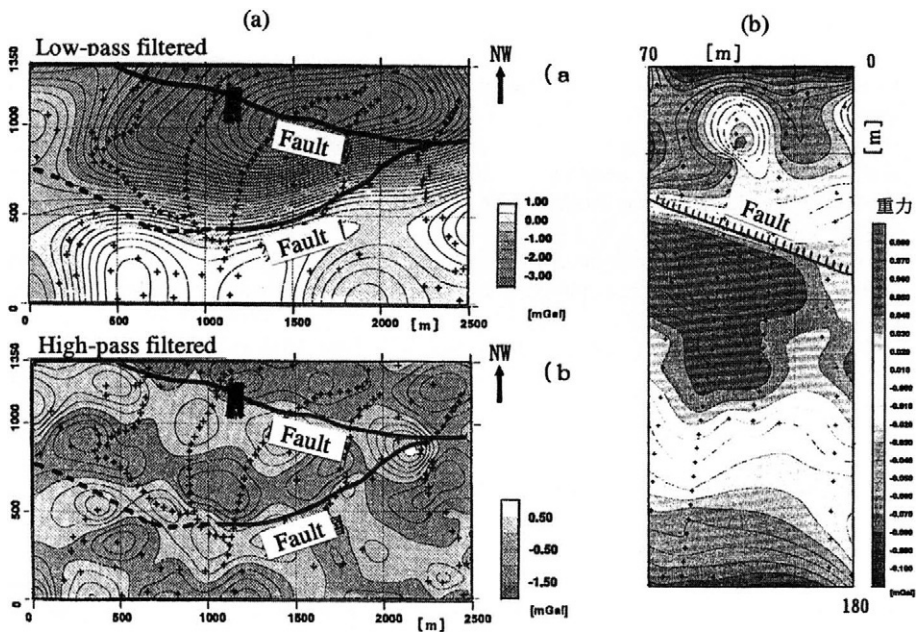


Fig.14 Gravity anomaly maps detecting an active fault location (a) in shallow exploration and (b) very shallow exploration.

CONCLUSIONS

In civil engineering applications in Japan, geophysical exploration methods, especially seismic refraction and electrical methods have long been used for design for various kinds of constructions and for ground water investigations. Recently demand for geophysical methods as non destructive testing methods for the ground has been rapidly increasing in applications for diagnostics of existing constructions, environmental assessment and solutions and disaster prevention. In civil engineering applications, there are many kinds of exploration targets and very high resolution is required in exploration. To meet these requirements, we have developed many kinds of geophysical methods which can provide high-resolution subsurface images. Field examples shown in this paper demonstrate that newly developed high-resolution geophysical methods can be feasible for civil engineering applications. In the future, geological and geotechnical interpretation techniques of the results of geophysical exploration should be developed for making geophysical methods more practically useful in civil engineering applications.

REFERENCES

1. Geological Survey of Japan (1996): Geophysical activity in 1994, Summary in geophysical activities in Japan for 1994.
2. Hayashi K. and Takahashi T. (1997) : High-resolution seismic refraction survey using surface and borehole data for site characterization of rocks, ISRM Symposium, NYRocks'97, Proceedings of International Workshop on Application of Geophysics to Rock Engineering, 17-24.
3. Ghose, R., Nijhof, V., Brouwer, J., Matsunbara, Y., Kaida, Y. and Takahashi, T.(1998): Shallow to very shallow, high-resolution reflection seismic using a portable vibrator system, *Geophysics*, 63, 1295-1309.
4. Nobuoka, D., Kaida, Y., Brouwer, J and Nijhof, V. (1999): High-resolution shallow seismic reflection using a portable S-wave vibrator, Expanded Abstracts, 61 EAGE Meeting, Helsinki, 4-43.
5. Shima, H.(1990): two-dimensional automatic resistivity inversion technique using alpha centers, *Geophysics*, 55, 682-694.
6. Shima, H. (1992): A practical 2D automatic resistivity analysis for pole-pole- array data - analysis algorithm and applications of " Resistivity Image Profiling", BUTSURITANSA (Geophysical Exploration), 45,204-223 (in Japanese).
7. Iseki, S. and Shima, H. (1997): Development of IP Image profiling -Two-dimensional inversion of resistivity and chargeability data-, BUTSURITANSA (Geophysical exploration), 50,275-284 (in Japanese).
8. Kobayashi T., Texier, B. and Shima H.(1996): Field evaluation of a fast resistivity imaging system using multi-channel capacitive electrodes, Expanded Abstracts, 58 EAGE Meeting, Amsterdam, M009.
9. Tohge, M.(1998): GPR applications, BUTSURITANSA HANDBOOK, 1231 (in Japanese).
10. Nozaki, K.(1997): The latest microgravity survey and its applications, OYO Technical Report, No.19, 35-60 (in Japanese).

EXPERIMENTAL RESEARCH FOR ESTIMATING ERECTION STRESS OF STEEL BRIDGE USING MAGNETIC ANISOTROPY SENSOR

Y.SAKAI

*Production Engineering Lab., Tsu Research Center, NKK Corporation
1, Kumozukokan-Cho, Tsu-City, Mie-Pref., 514-0393, Japan*

N.TAMURA

*Technology Center of Metropolitan Expressway
3-10-11, Toranomon, Minato-Ku, Tokyo, 105-0001, Japan*

ABSTRACT

Estimates of the stress level in the loaded condition are valuable for the safety assessment of steel bridges. We developed a unique instrument that can measure the stress using a magnetic anisotropy sensor and applied this method to a steel bridge. In this paper, we introduce this new system, which can easily measure the dead load stress of the steel bridge without contact or destructive measures. The experimental results verified close agreement between the results of this system and strain gauges and demonstrated the usefulness of this system for safety assessments of steel bridges.

KEYWORDS

Stress measurement, safety assessment, magnetic anisotropy, magneto-strictive effect

INTRODUCTION

Estimates of the stress level in the loaded condition are valuable for the safety assessment of steel bridges. The strain gauge method is the most popular stress measurement technique. However this method requires destructive measures to relieve stress, so it is undesirable for steel structures that are in service. Thus, we have been interested in a unique stress measuring method based on the magneto-strictive effect and developed instruments and application systems[1].

In this paper, we introduce the result of a model experiment to examine the possibility of applying this method to steel structures. We then introduce the newly-developed "*Magnetic*

Stress Measuring System for Steel Bridges" and present the results of on-site experiments using this system for a steel bridge under construction.

PRINCIPLE OF MAGNETIC STRESS MEASUREMENT

When stress exists in a ferromagnetic material, the magnetic permeability changes. This phenomenon is called the magneto-strictive effect [2]. Figure 1 shows the principle of stress measurement by the magnetic method. In this case, the magnetic permeability in the direction of tensile stress, " μ_x ", is slightly increased compared to " μ_y " in the orthogonal direction, which causes an anisotropic magnetic field.

In the magnetic method, the stress level and stress direction are measured using a magnetic anisotropy sensor [3]. The sensor is assembled with two cores, an excitation core and a detector core. Each core is a wound coil. The excitation coil is connected to a power supply that supplies alternating current. The detection coil is connected to a specialized voltmeter.

When the sensor is placed over the object to be measured, most of the magnetic flux emitted from E1 of the sensor travels directly to E2. However, some travels along the path indicated by the arrows because the magnetic permeability between E1 and D1 is larger than between E1 and D2. Thus, magnetic flux is induced in the detection core, resulting in a current and voltage.

The voltage V is expressed by the following equation (1)

$$V = M_0 \cdot (\mu_x - \mu_y) \quad (1)$$

Where:

M_0 : Constant determined by excitation condition, magnetic characteristics, etc.

μ_x : Magnetic permeability in the direction of X-axis

μ_y : Magnetic permeability in the direction of Y-axis

Anisotropy " $\mu_x - \mu_y$ " of the magnetic permeability is proportional to the stress difference " $\sigma_x - \sigma_y$ ", so equation (1) can be written as equation (2).

$$V = M_1 \cdot (\sigma_x - \sigma_y) \quad (2)$$

Where:

M_1 : Constant determined by excitation condition, magnetic characteristics, etc.

σ_x : Stress in the direction of X-axis

σ_y : Stress in the direction of Y-axis

Accordingly, once the proportionality constant " M_1 " (magnetic sensitivity) is calibrated, the stress difference can be estimated by the output voltage of the sensor. Moreover, the direction of principal stress can be determined from the output voltage by rotating the sensor on the surface of the object because the direction of maximum output voltage is the direction of maximum principal stress " σ_1 ", and the direction of minimum output voltage is the direction of minimum principal stress " σ_2 ".

Advantages of this method include:

- (1) Measurements can be made without contacting or damaging the object.
- (2) Measurements are possible over anti-corrosion coatings.
- (3) Operation is quick and easy.
- (4) Equipment is small and lightweight.

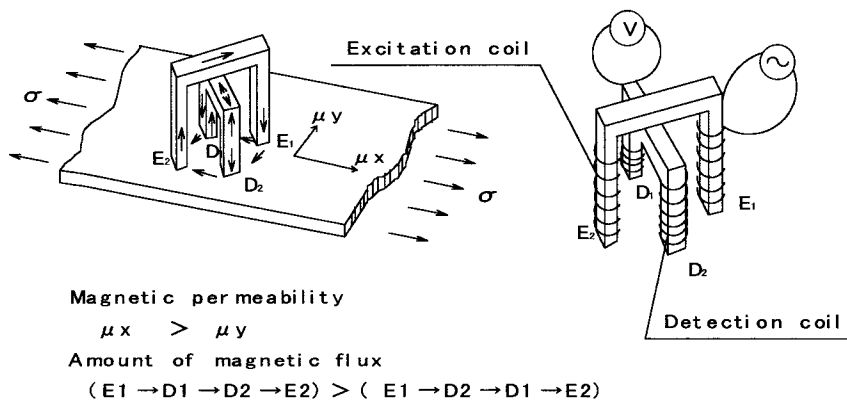


Fig.1. Principle of magnetic stress measurement using magnetic anisotropy sensor

MODEL EXPERIMENT

Experimental method

The magnetic method has several advantages, although some problems were anticipated in its application to steel bridges because of their complexity. So, we conducted a model experiment to confirm the applicability of this method. The model simulates a twin plate girder bridge that is built up by welding. The model was loaded under three point bending, and the stress on

the surface of the web and flange were measured at several locations by the magnetic and strain gauge methods. Figure2 shows an illustration of the experiment, and Fig.3 shows an example of the stress measurement points.

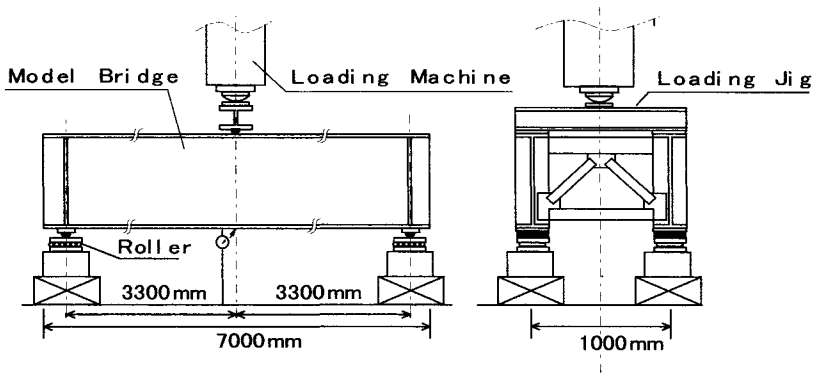


Fig.2 Illustration of model experiment

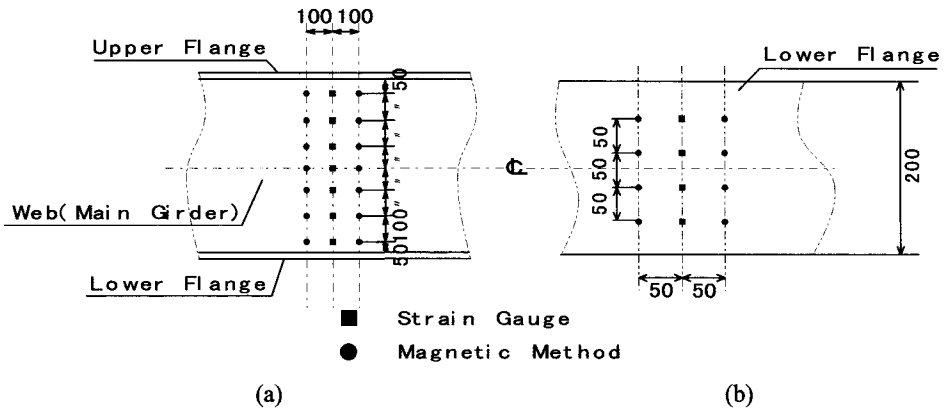


Fig.3 Illustration of stress measuring points: (a) for web plate; (b) for flange plate

Experimental Results

Figure4 shows an example of the experimental results. These are plotted by the principal stress difference " $\sigma_1 - \sigma_2$ " in the direction of maximum principal stress " σ_1 ". The measured data from the magnetic method was converted using magnetic sensitivity calibrated

in another test. The magnetic results show a stress level of nearly 100MPa even in the no-loaded condition because of the residual stress of welding. The stress difference and the direction of the maximum principal stress changes with increasing load, although this is not clear from Fig.4. Figure5 shows the results of subtracting the loaded condition from the not-loaded condition (subtracting Fig.4 (b) from Fig.4 (a)). The close relationship between the results of the magnetic method and those of the strain gauge method are very clear from the result.

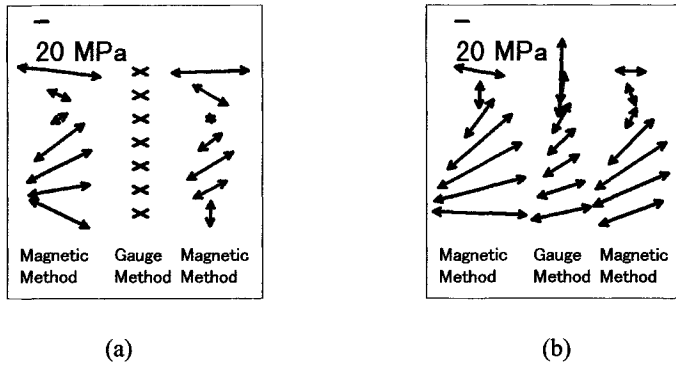


Fig.4 Distribution of stress difference " $\sigma_1 - \sigma_2$ "
: (a) no loaded condition; (b) loaded condition

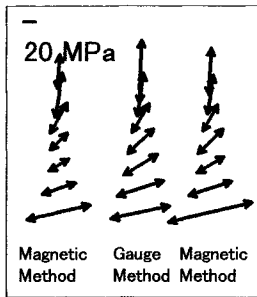


Fig.5 Distribution of stress difference " $\sigma_1 - \sigma_2$ " after subtracting

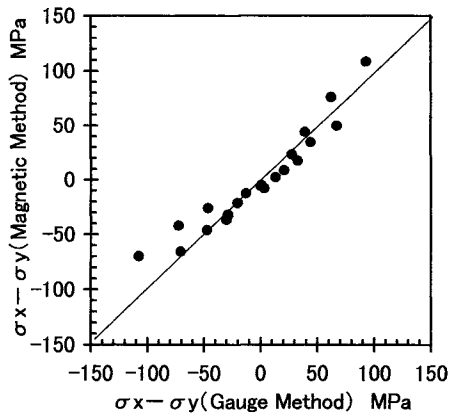


Fig.6 Relationship between magnetic method and strain gauge method

The following conclusions were drawn from the experimental results.

- (1) There is high level residual stress caused by welding that can exceed 100MPa.
- (2) The difference in stress and the direction of the principal stress change by increasing the load, even in the parts with a high level of residual stress
- (3) Subtracting the data under load from the initial data without load provides a close correlation between the magnetic method and strain gauge method.
- (4) The deviation of results in both methods is about 10MPa .

ON-SITE EXPERIMENT

Experimental Method

The model experiment demonstrated the usefulness of the magnetic method, even for a complex structure like a steel bridge. Thus, we carried out further studies using a real structure on site. The structure is a steel bridge for a viaduct constructed by the *Metropolitan Expressway Public Corporation* in Yokohama-City. The viaduct consists of four box girders. We set many measuring points on the lower flange and web of these girders and determined the measured sections by considering the distribution of bending moment in the bridge.

We also researched the residual stress from shop assembly. However in this paper, we estimated the dead load stress by subtracting the data for erection on site, which included the weight of steel girders, a concrete slab and scaffoldings, from the residual stress data after completion of assembly in the shop. We also set strain gauges on girder "G2" to verify the result of the magnetic method. The number of measuring points by the magnetic method was 300 and by strain gauge was 42.

Figure7 shows an overview of the experimental object and the sections measured. In this experiment, we used the newly-developed measuring system "*Magnetic Stress Measuring System for Steel Bridge*" that can easily collect extensive stress data on site. A portable computer controls the overall system, so measurement data can be analyzed into the stress difference and direction of principal stress, correcting the magnetic sensitivity for the distance between the sensor and the object being measured. Figure8 shows a view of the system, and Fig.9 shows measurements being taken on site.

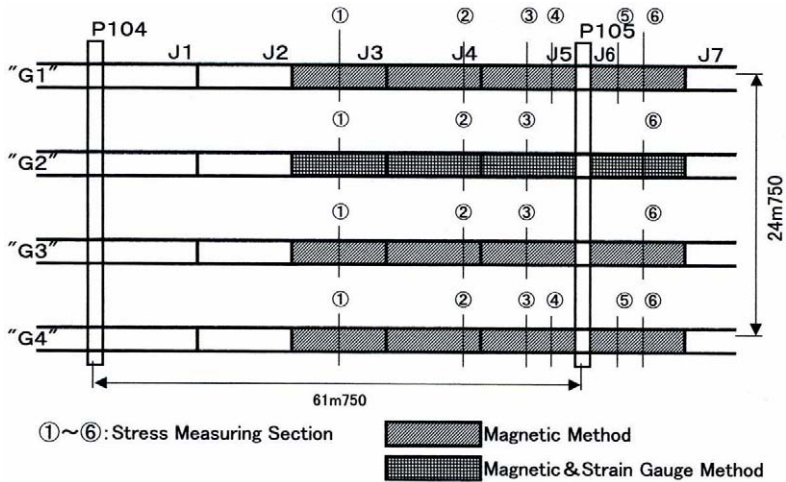


Fig.7 An overview illustration of experimental object and measuring sections

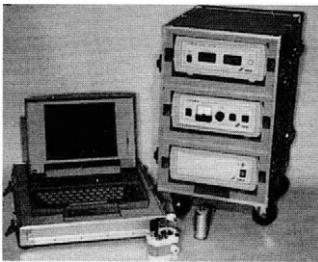


Fig.8 An appearance of the system

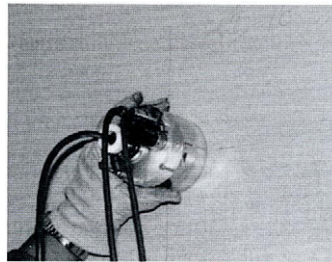


Fig.9 An appearance of measuring

Experimental Results

As an example, Fig.10 shows results of the strain gauge method, and Fig.11 shows results of the magnetic method. These are plotted as the stress difference " $\sigma_1 - \sigma_2$ " in the direction of maximum principle stress " σ_1 ". From these charts, it is clear that the distribution of stress on the flange is quite uniform, and the direction is nearly longitudinal. The distribution of stress on the web indicates that there is a bending moment in the girder. The distribution of stress measured by the magnetic method is almost same as that measured by the strain gauge method.

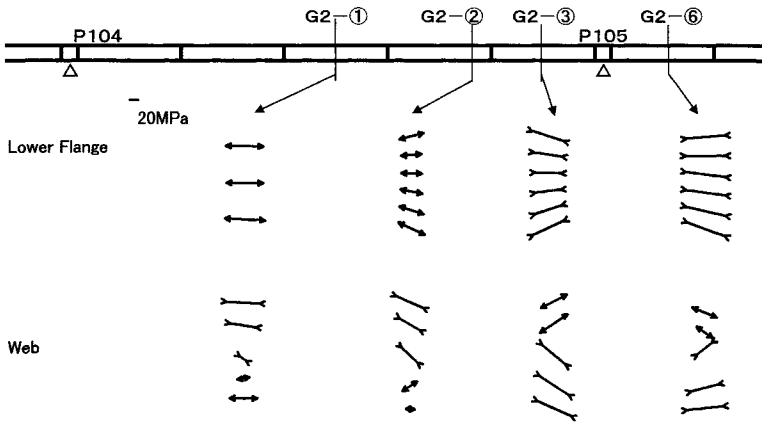


Fig.10 Distribution of stress difference " $\sigma_1 - \sigma_2$ " measured by strain gauge method

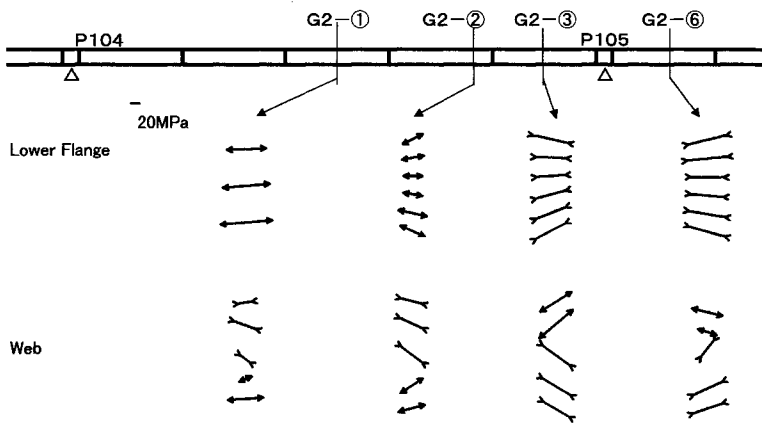


Fig.11 Distribution of stress difference " $\sigma_1 - \sigma_2$ " measured by magnetic method

Figure12 shows the relationship between the stress levels measured by the strain gauge and magnetic methods. The figure clearly shows close correspondence. Figure13 shows the relationship between the stress level measured by strain gauge method and the calculated stress. Figure14 shows the relationship between the calculated stress and that measured by the magnetic method. Table1 shows a statistical analysis of the deviation between the X and Y values in Fig.12, Fig.13, and Fig.14. The statistics indicate that the relationship in the two independent groups of data can be expressed by the following equation (3).

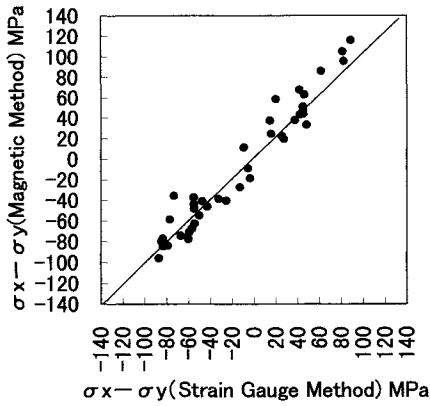


Fig.12 Relationship of the stress level between strain gauge method and magnetic method

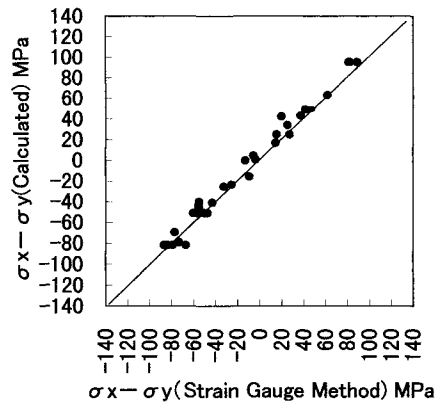


Fig.13 Relationship of the stress level between strain gauge method and calculated value

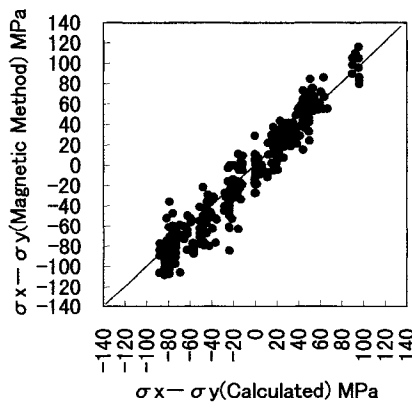


Fig.14 Relationship of the stress level between calculated value and magnetic method

Table1. Statistical analysis of deviation between X and Y value

	Case (1)	Case (2)	Case (3)	Case (1) +Case (2)
Average	-4.4	-4.8	3.4	-9.2
Standard Deviation	15.0	6.5	15.2	16.3

Notes: $\sqrt{15.0^2 + 6.5^2} = 16.3$

$$\begin{aligned}\overline{X}_a + \overline{X}_b &= \overline{X}_c \\ S_a^2 + S_b^2 &= S_c^2\end{aligned}\tag{3}$$

Where :

\overline{X} : Average value, S : Standard deviation value

CONCLUSIONS

This is a first study in applying the magnetic method for estimating the stress in steel bridges. We obtained several useful conclusions.

- (1) The level and the direction of stress measured by the magnetic method closely correspond to the results of the strain gauge method.
- (2) The level of stress measured by the magnetic method appears to be nearly correct because of the close correspondence to the calculated results.
- (3) In the magnetic method, we could measure the stress over anti-corrosion coatings with a thickness of over 500 μ m.
- (4) In the magnetic method, we could measure the stress very easily and quickly, the required time to measure taking less than one minute.
- (5) The magnetic method is very useful for safety assessments of steel bridges for long term maintenance.

ACKNOWLEDGEMENTS

The authors gratefully acknowledge the cooperation of the *Metropolitan Expressway Public Corporation*, and authors also gratefully acknowledge the support of the constructors.

REFERENCES

1. Sakai, Y. et al. (1991). *Development of Stress Level Meter Using Magnetic Anisotropy Sensor*, In: *Proceedings of 23rd Symposium on Stress • Strain Measurements*, JSNDI, pp.132-137
2. Kashiwaya, K. et al. (1985). *Stress Measurement using a Magnetic Anisotropy Sensor with Help of Alternating Current Demagnetization*, JSNDI, Vol.34, pp.201-207
3. Abuku, S. et al. (1986). *Measurement of Welding Residual Stress Distribution by Mean of Magnetic Probe*, JSNDI, Vol.35, pp.805-810

INVERSION OF BOREHOLE MAGNETIC SURVEY DATA FOR ESTIMATING THE DEPTH OF PILE

Y H Cha and J H Suh

*School of Urban, Civil & Geosystem Engineering, Engineering College
Seoul National University, Sillim-dong San 56-1, Kwanak-gu
Seoul, 151-742 Republic of Korea*

ABSTRACT

Forward modeling and inversion algorithms for borehole magnetic data were developed to estimate the depth of a pile. The conventional forward modeling scheme for surface geometry was modified to calculate three components of magnetic induction in borehole geometry. The adaptive simulated annealing algorithm was adopted to relax ill-posedness of conventional inversion scheme for borehole magnetic data. By applying the developed forward modeling and the inversion schemes to synthetic data, it is verified that magnetic anomalies are accurately calculated and the depth of a pile is effectively resolved. In addition, this inversion algorithm gives reasonable results for more practical data including random noise, effects of adjacent pile, or surface structure. Therefore some criteria for field survey was obtained. Finally, the applicability for field data was shown through inverting real data successfully.

KEYWORDS

Pile, forward modeling, borehole magnetic survey, inversion, simulated annealing, depth estimation.

INTRODUCTION

Estimating the depth of a pile in subsurface structures is very important to investigation of construction site and maintenance investigation of structures. There exist some methods for this purpose such as the parallel seismic method, the borehole electromagnetics, the borehole magnetic gradient method and so on. The parallel seismic method uses the contrast of velocity between concrete and ground. For good estimation of the depth of a pile, source energy must reach the bottom of a pile. But this condition is not always satisfied with respect to the structural shape of a pile. Other methods could not provide satisfactory information about the depth of a pile because of difficulties of data acquisition and interpretation.

Over the past few decades a considerable number of studies have been made on the application of the magnetic survey, widely used in mineral exploration, to engineering and environment problems and it is known that the magnetic exploration is effective in detecting metallic objects. The followings are good examples: detection of buried drums in saddy soil [1], locating abandoned oil and gas wells [2], locating underground storage tanks [3] and so on.

For reasons already stated, borehole magnetic survey was used for estimating the depth of a pile in subsurface structures, and modeling and inversion algorithms were developed. The developed algorithm was applied to several synthetic data and field survey data.

NUMERICAL METHODOLOGIES

Forward modeling

The forward modeling of magnetic field has been studied by Bhattacharyya [4], Talwani [5], Barnett [6], Kunaratnam [7] and so on. Because the main objective body of this study is the pile in subsurface structures, the method of Bhattacharyya [4] that corresponds to the purpose of this study was used. It was modified to calculate 3-component magnetic anomalies due to prism-shaped bodies with arbitrary polarization at any position. Through this forward modeling algorithm, magnetic anomalies for a prism at surface and borehole were calculated with variation of a prism's length (Figure 1). In Figure 1, magnetic anomalies at borehole show significant changes with respect to a prism's length but magnetic anomalies at surface do not. So it can be deduced that borehole magnetic survey is more effective than surface magnetic survey for estimating the depth of prism-shaped body.

Inversion

It is well known that inversion result of magnetic data is not unique. So, the objective function (RMS error) used in inversion was calculated about some parameters and local minima were found. For the reason of non-uniqueness, simulated annealing among global optimization techniques was used as inversion scheme in this study, which have been actively applied to geophysical inverse problem. Global optimization techniques have some merit as below. They need not partial derivative information, are independent of initial model and can restrict the range of inversion parameters. Dittmer et al. [8] successfully applied the simulated annealing algorithm to inversion of magnetic data. ASA (Adaptive Simulated Annealing, Ingber [9]) among simulated annealing algorithms was used in this study.

RESULTS AND DISCUSSION

It is difficult to measure x and y component of magnetic field accurately, because a borehole magnetometer rotates horizontally. So, only vertical magnetic field was used for examination of the applicability of borehole magnetic survey for the depth of pile in this study.

The developed inversion algorithm was applied to one prism model (Figure 2 (a)). The solid line in Figure 2 (b) indicates the magnetic anomalies due to one prism model and the dashed line indicates the magnetic anomalies including 10% random noise. Figure 2 shows that the depth of a prism can be roughly estimated from the point (the arrow in Figure 2 (b)) in the

curve of vertical magnetic anomalies. Table 1 and Table 2 illustrate inversion results about each data. X , y , width, z_1 and z_2 in Table 1 and Table 2 were illustrated in Figure 2 (a). Error indicates the percent error of the length of a prism between model and inversion result. They illustrate that the depth of a prism was accurately estimated.

Table 1. Inversion results of synthetic data for one prism model.

	model	inversion result
x(m)	- 0.01	- 0.010
y(m)	3	3.000
width(m)	0.02	0.020
z_1 (m)	6	6.000
z_2 (m)	10	9.999
error(%)		0.011

Table 2. Inversion results of synthetic data for one prism model including various random noise.

random noise(%)	z_1 (m)	Z_2 (m)	error(%)
model	6	10	
5	6.072	9.946	3.164
10	6.089	10.105	4.861
30	6.344	10.051	9.883

From the inversion results in Table 1 and 2, it was verified that the depth of a prism could be estimated within 10% length error about the data including 30% random noise through borehole magnetic data by the developed inversion algorithm.

A pile is made up of many reinforcing rods and concrete, so it was tested whether a pile can be assumed as a prism by comparing magnetic anomalies for the models in Figure 3 (a) and (b). Figure 3 (a) illustrates a pile that is made up of nine reinforcing rods and Figure 3 (b) illustrates the simplification of it. The magnetic anomalies for each model are shown in Figure 3 (c) as solid and dashed line and they are almost same. The followings are the inversion results about data for the model in Figure 3 (a): $z_1 = 5.997$ (m) and $z_2 = 9.996$ (m). Through these results, it was deduced that a pile that is made up of many reinforcing bars can be assumed as a prism.

If structures at surface, another piles and so on are located adjacent the objective pile, these adjacent bodies may affect inversion results. To check the effects by these adjacent bodies, the vertical magnetic data for the models in Figure 4 (a) and Figure 5 (a) were calculated and are shown in Figure 4 (b) and Figure 5 (b). In Figure 4, vertical magnetic anomalies show significant changes. So, these effects must be considered in inversion algorithm. In the case of ignoring the adjacent pile for the model in Figure 4, the inversion result of z_2 is 5.672(m). In the case of considering, the inversion result of z_2 is 6.008 (m). Comparing these results, accurate depth of a target pile could be obtained when the adjacent pile was considered. In Figure 5, vertical magnetic anomalies show significant changes near the surface but show little changes about the bottom of a pile. Because data near the bottom of a pile is important for estimating the depth of a pile, it can be deduced that structures at surface give little effects on

inversion results.

The developed inversion algorithm was applied to field survey data (Figure 6). Vertical borehole magnetic data was obtained in Jan. 1998, using KBHMAG-1 developed by KIGAM (Korea Institute of Geology, Mining & Materials) and Subsurface Information Technologies Inc. and the target of survey is the depth of a pile in a bridge pier. They contain 75 vertical magnetic field samples. Figure 6 (a) shows a schematic diagram of borehole magnetic survey for the pile in a bridge pier. Figure 6 (b) shows the field survey data (solid line) and reconstructed magnetic anomaly data after inversion (dashed line). The reconstructed data was well matched with the field survey data especially below 10m, where the bottom of a pile is expected to exist. The inversion result of z_2 is 10.9 (m). It was verified that the developed algorithm in this study could be applied to field survey data.

CONCLUSIONS

Through the developed forward modeling, the applicability of borehole magnetic survey for estimating the depth of a pile was verified and an inversion algorithm using global optimization technique was developed. The developed inversion algorithm was tested with synthetic magnetic data. Through these tests, it was verified that the developed inversion algorithm can provide the depth of a pile within 10% error about data including 30% random noise. It was deduced that a pile, which is made up of reinforcing bars, can be assumed as a prism. The field applicability of the developed algorithm was verified by field survey data.

ACKNOWLEDGEMENTS

The authors would like to thank the "Subsurface Information Technologies Inc." for giving opportunity to use borehole magnetic survey data.

REFERENCES

1. Tyagi, S., Lord, A. E., Jr., and Koerner, R. M. (1983) *J. Hazardour Materials* 8, 11.
2. Johnston, K. H., Carroll, H. B., Heemstra, R. J., and Armstrong, F. E. (1973). U.S. Dept. of the Interior, Bureau of Mines Inf. Circ. 8578.
3. MacLean, H.D., Dickerson, J.W., Hasbrouck, J.C., and Cotter, E.T. (1991). In: *Proceedings of Symposium of the Application of Geophysics to Engineering and Environmental Problems*, pp. 323-341, SEMEG.
4. Bhattacharyya, B. K. (1964) *Geophysics* 29, 517.
5. Talwani, Manik (1965) *Geophysics* 30, 797.
6. Barnett, C. T. (1976) *Geophysics* 41, 1353.
7. Kunaratnam, K. (1981) *Geophys. Prosp.* 29, 883.
8. Dittmer, J. K. and Szymanski, J. E. (1995) *Geophys. Prosp.* 43, 397.
9. Ingber, L. (1993) Adaptive Simulated Annealing(ASA): [ftp.alumni.caltech.edu:pub/ingber/ASA.zip], McLean, VA, Lester Ingber Research.

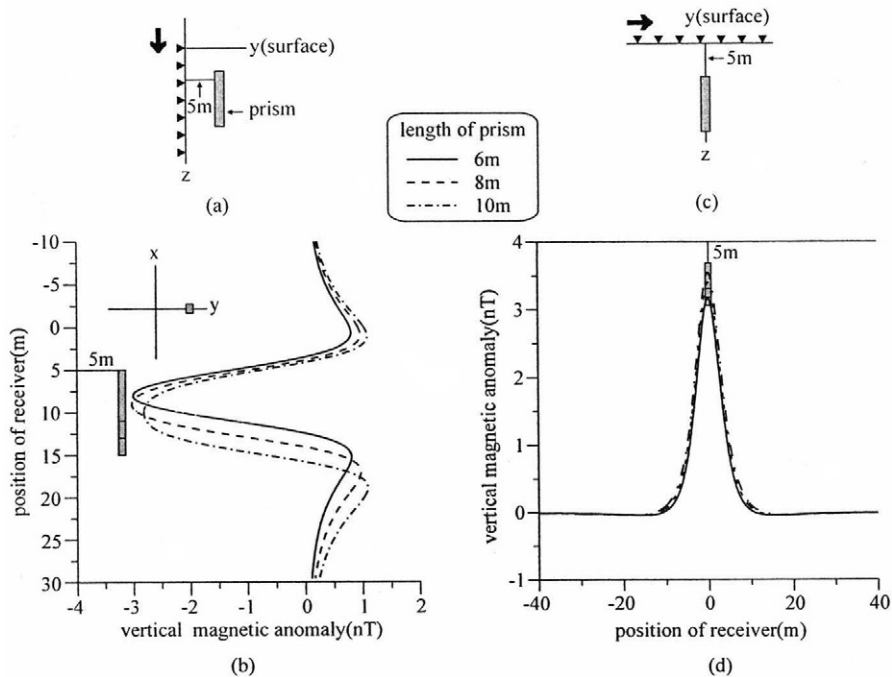


Fig. 1. Vertical magnetic anomalies in borehole survey with variation of a prism's length. Total earth magnetic field is 49500(nT) and the inclination and the declination of earth magnetic field are 53(degree) and 5(degree), respectively. The inclination and the declination of magnetization are equal to that of the earth magnetic field. (a) configuration of borehole magnetic survey (b) vertical magnetic anomalies for (a) (c) configuration of surface magnetic survey (d) vertical magnetic anomalies for (c)

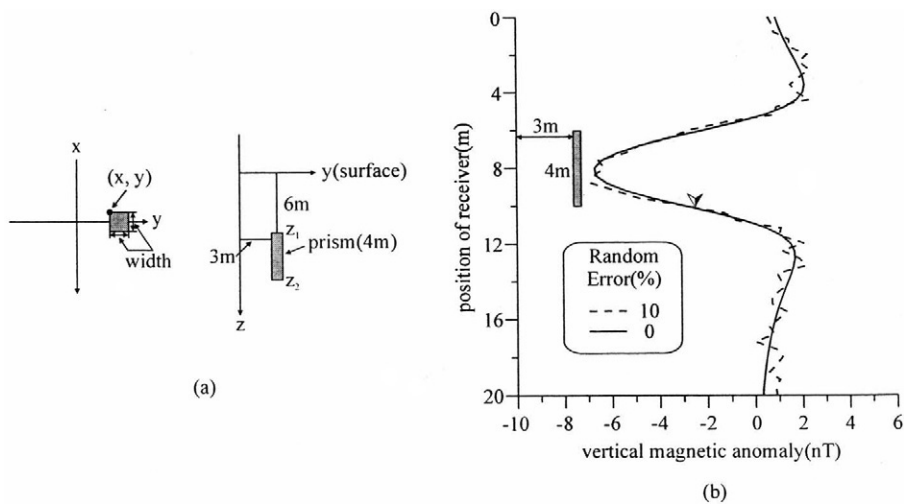


Fig. 2. Vertical magnetic anomalies (b) without and with 10% random noise for one prism model in (a)

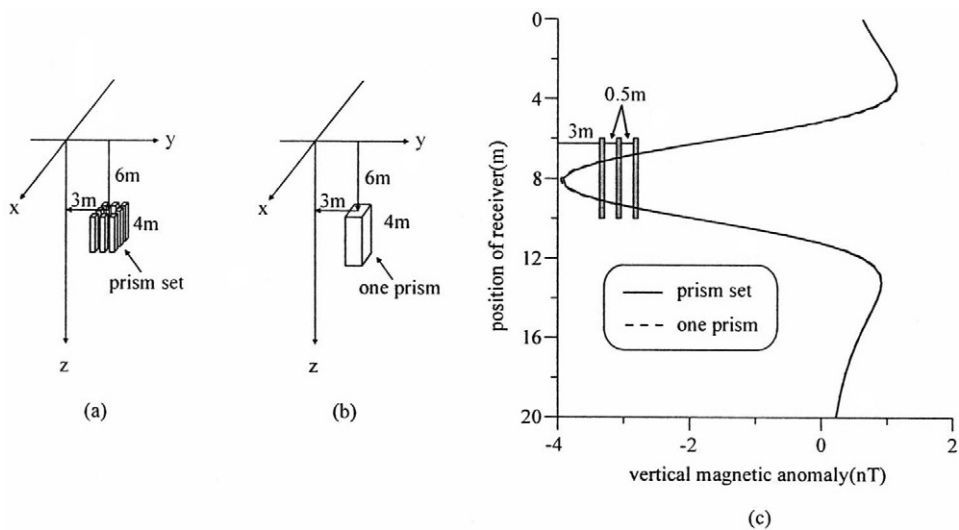


Fig. 3. Comparison of the vertical magnetic anomalies of one prism(a) with that of set of nine small prisms(b).

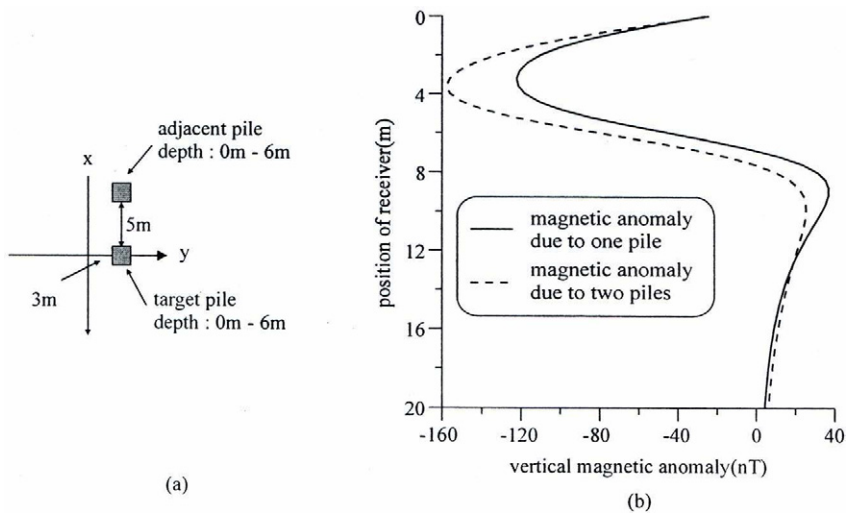


Fig. 4. Comparison of the magnetic anomalies of one pile with that of two piles. (a) plan view of a target pile with an adjacent pile (b) vertical magnetic anomalies of two models

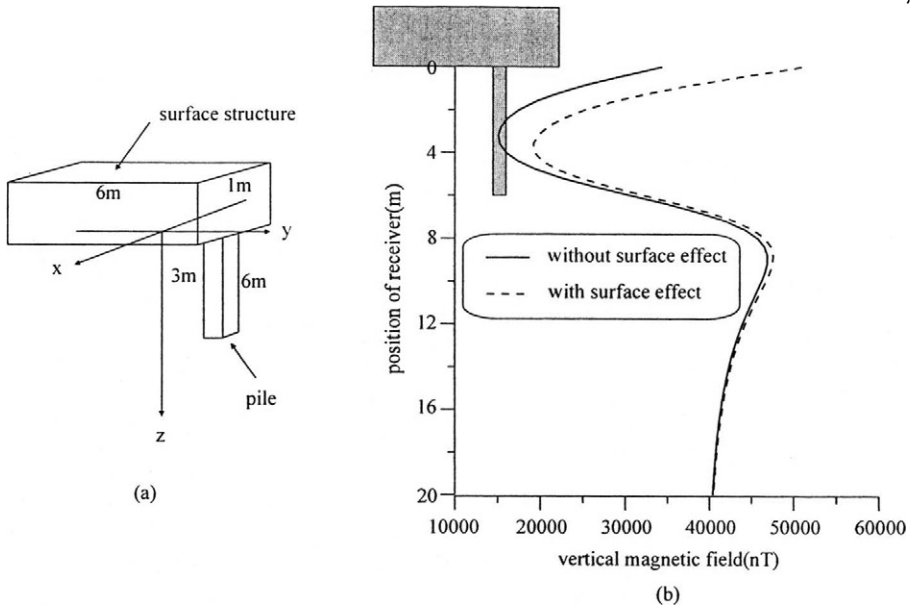


Fig. 5. Effect of surface structure on the magnetic anomalies for a subsurface pile.
 (a) geometry of model
 (b) vertical magnetic anomalies

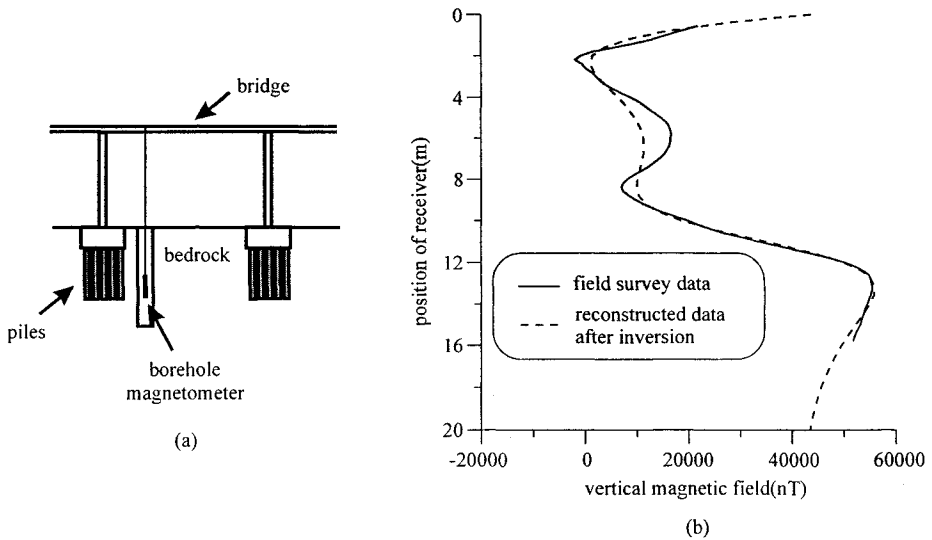


Fig. 6. Comparison of field survey data and reconstructed data after inversion.
 (a) a schematic diagram of boerhole magnetic survey
 (b) field survey data and reconstructed data after inversion

This Page Intentionally Left Blank

APPLICATION OF THE DIELECTRIC MEASUREMENT FOR NON-DESTRUCTIVE TEST OF MORTAR

S. Yagihara, N. Shinyashiki, Y. Hayashi, and M. Asano
*Department of Physics, School of Science, Tokai University
Hiratsuka, Kanagawa 259-1292, JAPAN*

M. Shiotsubo
*Measuring Engineering Division, Komatsu Engineering Corporation
Kawasaki, Kanagawa 210-0818, JAPAN*

Y. Kato and T. Uomoto
*Institute of Industrial Science, University of Tokyo
7-22-1, Roppongi, Minatoku, Tokyo, 106-8558, JAPAN*

M. Arino, T. Tokunaga, K. Noto, S. Tsuda, and W. Kimura
*Tokyo Development Society for Non-Destructive Testing in Road Structures
DEC CO. LTD. 7-2-8 Ueno, Taito-ku, Tokyo 110-0005 JAPAN*

ABSTRACT

Two kinds of dielectric relaxation measurements were performed to study the water structure and the compressive strength of cement paste and mortar. Dielectric relaxation spectra obtained for cement paste and mortar show that the relaxation time of the process due to the orientation of structured water clearly depends on the curing time. The free water content obtained from the dielectric relaxation measurement represents the porosity of mortar cured in water. The compressive strength was expressed by the dielectric constant obtained from the measurement. These results suggest that the dielectric method is applicable to non- or less-destructive test for concrete structures.

KEYWORDS

Dielectric relaxation, time domain reflectometry (TDR), hydration, free water, structured water, porosity, compressive strength, calcium silicate hydrate (C-S-H), cement

INTRODUCTION

A consolidation process of cement developed by hydration is explained by the fact that the gel-

like matrix of calcium silicate hydrate (C-S-H) interpenetrates the region between the adjacent cement grains [1, 2]. The structure of C-S-H gel has been studied by X-ray analysis [1], transmission electron microscopy [3, 4], dielectric spectroscopy [5], and nuclear magnetic resonance [6]. However, it is difficult to observe directly the water behavior in the cement paste by these conventional methods.

Developments on the microwave dielectric measurement techniques via time domain reflectometry (TDR) have made it possible to observe water structures in moist materials [7], such as water/alcohol mixtures [8], water/oligomer mixtures [9], water/polymer mixtures [10], polymer gel [11], emulsion [12], and skin [13]. Molecular clusters in the pure water exhibit a dielectric relaxation process around 18GHz at 25°C [14]. Generally, in the case of mixtures, water molecules behave rotational diffusions with small solute molecules, or large solute molecules hinder water molecules as expected from the free volume theory. These interactions affect the relaxation time of the relaxation process due to free water and bring about its concentration dependency. This kind of water is called free water.

Recently, we applied the TDR measuring system for the hydration process of portland cement paste [15], and found a high frequency relaxation process due to the orientation of free water around 10GHz. The relaxation strength decreased rapidly as the curing time increased during the first three days. The free water is taken into C-S-H and is transformed to structured water. The lower frequency relaxation process due to the orientation of structured water in C-S-H was observed at 1M-100MHz [15, 7]. The similar behavior of water was observed for biopolymers, such as DNA [16], Collagen [17], and globular proteins [18]. Water molecules are bound to the surface of these biopolymers via hydrogen bonding and form the network structure. This water called bound water is observed around 100MHz. However, the peak frequency of dielectric loss curve for cement paste continues to shift to the lower frequency during the curing process. Then the time dependency of the curing process should be confirmed more precisely for a long period.

There have been some empirical expressions to evaluate the strength of concrete. Lyse [19] suggested that the compressive strength of concrete, σ , is related to the cement:water ratio of the cement paste as

$$\sigma = A_L \frac{C_w}{W_w} + B_L, \quad (1)$$

where C_w and W_w are weights of cement powder and water in the concrete, and A_L and B_L are constants determined from experimental results. More general expression was also proposed by Talbot [20] as

$$\sigma = A_T \frac{C_V}{W_V} + B_T, \quad (2)$$

where C_V is the volume of cement, W_V is the volume of void filled up by air and free water in the concrete, and A_T and B_T are constants determined from experimental results. It is expected that the compressive strength of concrete can be evaluated from the total pore space:cement ratio.

In this work, we performed wide frequency dielectric measurements using TDR measuring

system (100k-10GHz) and LCR meter (20-1MHz) to conform the hydration process of specimens of cement paste and mortal. We also performed TDR measurements for mortal which had been cured in water to evaluate the free water amount corresponding to the total pore space, and compared results with the compressive strength obtained from the mechanical measurements.

EXPERIMENTAL

Sample preparation

Three samples of cement paste and mortal with different curing times were used for dielectric measurements. The portland cement was obtained from Chichibu-Onoda Cement Co. (Tokyo, Japan). Distilled water was added to the cement at a water:cement ratio of 0.4(grams of water/grams of cement). This sample is used as cement paste with the curing time of 33days. Two samples of mortal were prepared respectively with the ratio of 1:2:0.65 for cement, sand, and distilled water. Details of these samples are listed in Table I.

Table I. Samples used for dielectric measurements on the curing time dependency.

sample	curing time	cement	sand	sand:cement (g/g)	water:cement (g/g)
cement paste	33days	portland cement	-	-	0.40
mortal	8 months	portland cement (3.16g/cm ³)	200 μ -300 μ m ϕ (2.60 g/cm ³)	2.0	0.65
mortal	4 years	rapid hardening portland cement	< 1mm ϕ	2.0	0.65

Six samples of mortal with different water:cement ratio between 35% and 60% were prepared. The portland cement was obtained from Taiheiyo Cement Co. (Tokyo, Japan). Details of the preparation are listed in Table II. Samples were removed from the cast (4cm \times 4cm \times 16cm) and had been cured in the water at room temperature until dielectric measurements. The particle size of sand used here is 0.15mm-5mm.

Table II. Samples used for dielectric measurements on the water:cement ratio dependency. The density of portland cement was 3.16g/cm³. The fineness modulus and the density of sand is 3.19 and 2.60 g/cm³.

water:cement (g/g)	sand:cement (g/g)	C (g)	W (g)	S (g)
0.35	2.5	921	322	2303
0.40	2.5	894	358	2235
0.45	2.5	868	391	2170
0.50	2.5	844	422	2051
0.55	2.5	821	451	2051
0.60	2.5	799	479	1997

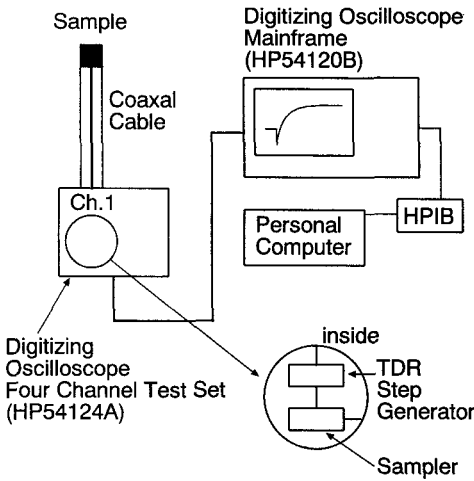


Fig. 1. Block diagram of TDR measuring system.

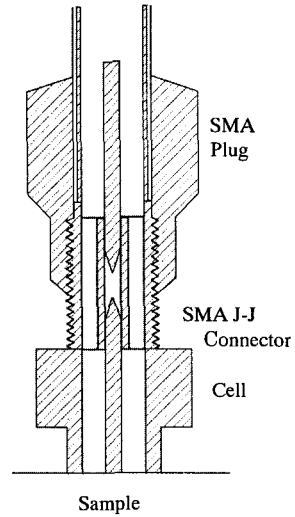


Fig. 2. Scheme of the flat-end probe.

Dielectric Measurements

Dielectric relaxation measurements were performed by the TDR measuring system (mainframe: HP54121A+B, Hewlett-Packard) in the frequency range of 100k-20GHz and the LCR meter (HP4284A, Hewlett-Packard) between 20 and 1MHz.

A block diagram of the TDR system is shown in Fig. 1. An incident pulse with the rise time of 35ps is generated by a pulse generator and passes through a 50ohm coaxial line. The pulse is reflected from the top of the line, where a flat-end probe is attached. A scheme of the cell is shown in Fig. 2. A flat-end probe with the outer conductor diameter 5.0mm was employed. The electric length was 0.31mm. The flat end of the probe was attached on the surface of the sample. Pulses reflected by the unknown sample and the standard sample are respectively digitized and saved. Dielectric relaxation spectra are analyzed using the Fourier Transform. Details on procedures of analyses to obtain the dielectric relaxation spectra were shown in the previous paper [15]. The surface of the sample was polished to prepare the better contact with the probe.

A three-terminal cell with the parallel-plate condenser and the guard ring was made for LCR meter measurements. The sample with 2mm thickness used for this electrode was cut out from the original mortar block.

RESULTS AND DISCUSSION

Dielectric spectra in the curing process

Figure 3 shows the curing time dependency of dielectric spectra. Dielectric dispersion and

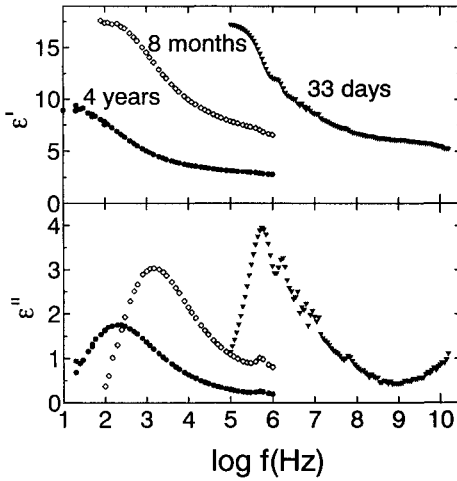


Fig. 3. Curing time dependency of dielectric spectra for the cement paste with various curing time.

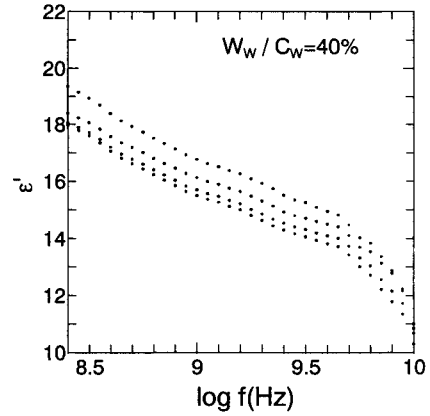


Fig. 4. Dielectric relaxation spectra for mortar cured in the water after the preparation at water:cement ratio of 40%.

absorption curves observed by the TDR system for the cement paste in 33 days after curing at room temperature clearly show at least two relaxation processes. The higher frequency relaxation process for which the maximum loss obtained above 10GHz is due to the orientation of free water. Structured water taken into C-S-H is observed as the lower frequency process observed around 1MHz. Furthermore, it seems possible to discriminate the middle frequency process as shown in the previous paper [15] around 100MHz which is corresponding to bound water observed for biopolymers. Thus the complex dielectric constant is described by [21]

$$\varepsilon^*(\omega) - \varepsilon = \frac{\Delta\varepsilon_l}{(1 + j\omega\tau_l)^{\alpha_l}} + \frac{\Delta\varepsilon_m}{1 + (j\omega\tau_m)^{\beta_m}} + \frac{\Delta\varepsilon_h}{1 + (j\omega\tau_h)^{\beta_h}}, \quad (3)$$

where ε_∞ is the high frequency limit of the dielectric constant, $\Delta\varepsilon$ the relaxation strength, and τ the relaxation time. Shape parameters α and β describe the relaxation time distribution. Subscripts, l , m , and h denote the low, middle, and high frequency processes, respectively.

Dielectric dispersion and absorption curves were also observed in LCR meter measurements for mortals in 8 months and in 4 years after curing at room temperature. The peak frequency of dielectric loss for structured water was found to shift to the lower frequency side still in 4 years after curing. We don't analyze precise relaxation parameters in the present paper. However it can be clearly concluded that the present result suggests a possibility to evaluate the compressive strength and the aging of concrete from dielectric properties.

Dielectric relaxation spectra and compressive strength

Figure 4 shows four dielectric relaxation spectra for mortar cured in water after setting at water:cement ratio of 40% in 14days. We averaged 32 spectra for each spectrum. The fluctuation reflects the inhomogeneous distribution of sand on the surface and water existing

between the flat-end of the probe and the rough surface of mortar. Figure 4 means that averaging of 32 different measurements for each sample is enough for the present purpose. Error bars shown in following figures indicate the fluctuation estimated.

Figures 3 and 4 indicate that the frequency, 1GHz, is just the middle between the high and the middle frequency processes. Then the dielectric constant at 1GHz, ϵ'_{1GHz} , is expressed as

$$\epsilon'_{1GHz} = \epsilon_{\infty} + \Delta\epsilon_h. \quad (4)$$

If the water structure of free water in mortar is the same as that of pure water, the relaxation strength, $\Delta\epsilon_h$, is expressed as

$$\Delta\epsilon_h = \frac{c_f}{c_w} \Delta\epsilon_w, \quad (5)$$

where c_f (in unit of g/cm^3) is the amount of free water per unit volume, c_w ($\approx 1g/cm^3$) is the density of pure water, and $\Delta\epsilon_w$ (≈ 73) is the relaxation strength of pure water. Substituting Eq. (5) in Eq. (4), we obtain

$$\epsilon'_{1GHz} = \epsilon_{\infty} + \frac{c_f}{c_w} \Delta\epsilon_w. \quad (6)$$

The ϵ'_{1GHz} value can be a measure of free water amount.

It is considered that the water amount filling up pores in mortar corresponds to the water:cement ratio, W_w/C_w , since the larger ratio induced the larger total volume of pore space in mortar. In this case, following Talbot's idea, the compressive strength reasonably depends on the dielectric property. Then we tentatively describe the dielectric constant as

$$\frac{1}{\epsilon'_{1GHz}} = A_1 \frac{C_w}{W_w} + B_1, \quad (7)$$

where A_1 and B_1 are constant. Figure 5 shows the cement:water ratio dependency of the reciprocal of the dielectric constant, ϵ'_{1GHz} . The straight line obtained from the least square method suggests that values of A_1 and B_1 are 4.6×10^{-3} and 4.8×10^{-2} . The correlation coefficient is 0.89.

Plot of compressive strength measured in 28days after the preparation against cement:water ratio is shown in Fig. 6. Equation (1) represents the straight line shown in Fig. 6. The values of A_L and B_L were 24 and 9.5, respectively. The

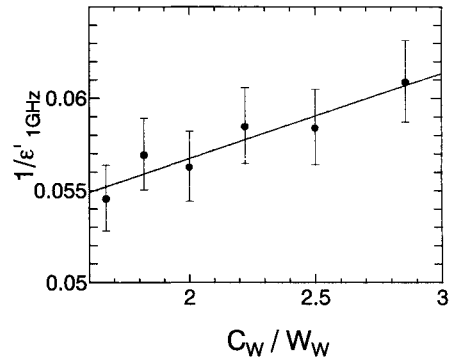


Fig. 5 The cement:water ratio dependency on the reciprocal of dielectric constant ϵ'_{1GHz} .

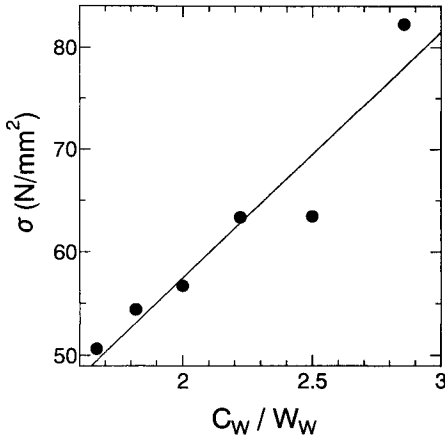


Fig. 6. Plot of compressive strength against the cement:water ratio.

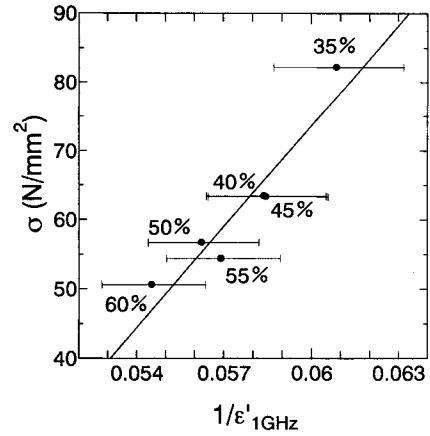


Fig. 7. Plot of compressive strength against the reciprocal of the dielectric constant, ϵ'_{1GHz} .

correlation coefficient was 0.91. This value means that Eq. (7) was satisfied enough in the present range of the cement:water ratio.

The cement:water ratio is obtained from Eq. (7) as

$$\frac{C_w}{W_w} = \frac{1}{A_1} \left(\frac{1}{\epsilon'_{1GHz}} - B_1 \right). \quad (8)$$

Substituting Eq. (8) in Eq. (1), the compressive strength is written as

$$\sigma = \frac{A_L}{A_1} \left(\frac{1}{\epsilon'_{1GHz}} - B_1 \right) + B_L. \quad (9)$$

Eq. (9) suggests that we can obtain the compressive strength from the dielectric measurement for unknown samples. The relationship between the compressive strength and the dielectric constant is simply expressed as

$$\sigma = \frac{A}{\epsilon'_{1GHz}} + B. \quad (10)$$

Figure 7 shows plot of compressive strength against the reciprocal of ϵ'_{1GHz} . The straight line obtained from the least square method gives values of A and B as 4.9×10^3 and -2.2×10^2 , respectively. The correlation coefficient is 0.90. This value of the correlation coefficient is quite better than those obtained from conventional non-destructive test, for example, by the Schmidt concrete testhammer (0.719), or by the ultrasonic measurement (0.457). Therefore dielectric measurements can be one of the most effective candidates in non- or less-destructive test for concrete.

CONCLUSION

Dielectric relaxation spectra obtained for cement paste and mortar show that the relaxation time of the relaxation process due to the orientation of structured water clearly depends on the curing time. Furthermore compressive strength of mortar cured in water depends on the porosity determined from dielectric measurements on free water. These results of dielectric measurements suggest that those dielectric methods are applicable to non- or less-destructive test for concrete.

REFERENCES

1. Taylor, H. F. W. (1990) In: *Cement Chemistry*, Thomas Telford Publishing, London, pp113-156.
2. Double, D. D. and Hellawell, A. (1977) *Sci. Am.*, 237, 82.
3. Double, D. D. and Hellawell, A. (1976) *Nature*, 261, 486.
4. Viehland, D., Li, J., Yuan, L., and Xu, Z. (1996) *J. Am. Ceram. Soc.* 79,1731.
5. Hilhorst, M. A. (1998) In: Dielectric Characterisation of Soil, Doctoral thesis.
6. Ishida, H., Okada, Y., and Mitsuda, T. (1992) *J. Am. Ceram. Soc.* 75, 359.
7. Yagihara, S., Hayashi, Y., Miyairi, H., Shinyashiki, N., Kita, R., Dobashi, T., and Shiotsubo, M. (1999). In: *Proceedings of Third Workshop on Electromagnetic Wave Interaction with Water and Moist Substances*, pp. 107-111 (1999).
8. Mashimo, S., Minura, N., Umehara, T., Yagihara, S., and Higasi, K. (1992) *J. Chem. Phys.*, 96 6358.
9. Shinyashiki, N., Sudo, S., Abe, W., and Yagihara, S. (1998) *J. Chem. Phys.* 109, 9843.
10. Shinyashiki, N., Yagihara, S., Arita, I., and Mashimo, S. (1998) *J. Phys. Chem. B*, 102, 3249.
11. Shinyashiki, N., Sakai, T., Yamada, G., and Yagihara, S. (1999) *Progress in Colloid and Polymer Science*, in press.
12. Miyairi, H., Shinyashiki, N., and Yagihara, S. (1997) *Reports on Progress of Polymer Physics in Japan*, 40, 621.
13. Naito, S., Hoshi, M., and Yagihara, S. (1998) *Biochim. Biophys. Acta* 1381, 293.
14. Barthel, J., Bachhuber, K., Buchner, R., and Hetzenauer, H. (1990) *Chem. Phys. Lett.* 165, 369.
15. Miura, N., Shinyashiki, N., Yagihara, S., and Shiotsubo, M. (1998) *J. Am. Ceram. Soc.* 81, 213.
16. Umehara, T., Kuwabara, S., Mashimo, S. and Yagihara, S. (1990) *Biopolymers*, 30, 649.
17. Shinyashiki, N., Asaka, N., Mashimo, S., Yagihara, S., and Sasaki, N. (1990) *Biopolymers*, 29, 1185.
18. Miura, N., Hayashi, Y., Shinyashiki, N., and Mashimo, S. (1995) *Biopolymers*, 36, 9.
19. Lyse, I. (1925) *Proc. ASTM* 32-II.
20. Talbot, A. N. (1921) *Proc. ASTM*.
21. Hill, N. E., Vaughan, W. E., Price, A. E., and Davies, M. (1969) In: *Dielectric properties and Molecular Behaviors*, Van Nostrand Reinhold, London.

HIGHLY ACCURATE LOW FREQUENCY ELASTIC WAVE MEASUREMENT USING MAGNETOSTRICTIVE DEVICES

Shinichi Hattori(*), Takashi Shimada(*), Ryouzuke Taniguchi(*),
and Kanji Matsuhashi(**)

*Mitsubishi Electric Corporation
Electromagnetic Stress & Sonic Control Systems Engineering Section
Industrial & Environmental Engineering Center
Mitsubishi Electric Corporation
6-14 Maruo-machi, Nagasaki, Nagasaki, Japan

**Matsuhashi Techno Research Co.,LTD
9-14 Motoujina-cho Minami-ku, Hiroshima, Hiroshima, Japan

KEYWORDS

Nondestructive testing, elastic wave measurement, magnetostriction, concrete.

ABSTRACT

Much interest has been focused on testing technology for structural architectures since Hanshin-Awaji earthquake. The elastic wave method with hammering has been applied for these tests so far. However, less stability of hammering and its response make it difficult to detect deterioration and crack accurately. The other ultrasonic method with piezoelectric device also has its limit in the inhomogeneous materials because the ultrasonic wave attenuates rapidly in them. A low frequency measurement in frequency domain will be a solution to this, though it has been thought to be difficult because it requires large dimension of oscillator.

A metal magnetostrictive material, whose magnetostrictive driving force is large, was employed and processed. The material has almost same level of Young's modulus with steel. Utilizing its strength we apply additional compression stress on the device to enhance oscillating efficiency extraordinary, which enabled to generate wide bandwidth of elastic wave even in low frequency in small size. Accordingly, it has become possible to measure the structures with continuous elastic wave or pulse by controlling its frequency and power.

To these days tunnels, piles, and roads have been measured and tested successfully by this new method, which is expected to be applied for various types of structures and materials.

1. INTRODUCTION

Conventionally for nondestructive testing of concrete structures, hammering and ultra sonic methods using elastic wave have been used frequently to date.

The hammering method is one that an operator hammers the surface of the concrete and senses the response of it by his ears and/or transducers, such as microphones or pickups, to analyze and evaluate defects. While these methods are convenient, portable, and easy operational, the property of the elastic waves obtained depends considerably on his experience or technique he carries, and it is still required to employ a trigger mechanism if he wants to drive hammer quantitatively[1].

On the other hand, ultra sonic wave is a method that drives over several hundreds of kHz pulsive waves onto the surface of the concrete structure, and detects the delay of propagation to measure distance to the reflection events. Generally acoustic velocities of the concrete material locate around 4000 m/s, then the wavelength of these elastic waves are several cm or less, almost same size with the aggregates in concrete. Consequently, they suffer dispersion and scattering at aggregates, and it results in difficulty to penetrate deep in the structure and to discriminate internal defects.

Although it will be an answer to use elastic waves less than several hundreds of Hz to avoid the affect from aggregates, custom piezo electric devices can not produce such a low frequency elastic wave efficiently.

2. LOW FREQUENCY OF ELASTIC WAVE MEASUREMENT

As reviewed above, higher frequency acoustic wave has its constraint in propagation in inhomogeneous matrixes. Inversely, lower frequency wave penetrates deep with less scattering and attenuation, because interaction between aggregates and long wavelength is not so critical.

For evaluating civil constructions, it is essential for a tool to be able to measure large scale of structure. In addition to generating low frequency wave, there are two more issues to complete the mission. These are effective injection of energy and the detection of it. Although low frequency extremes in less attenuation, measuring of large scaled construction requires appropriate energy to return from the target. Thus the key issues to measure them are summarized as follows.

- A) Generation of low frequency acoustic energy efficiently and freely
- B) Effective injection of acoustic energy into the target
- C) Detection of low frequency acoustic energy efficiently

4. A NEW METHOD USING MAGNETOSTRICTIVE DEVICE

4.1 Magnetostrictive Device

For solving the issues above, we have introduced a magnetostrictive device which had been developed for low frequency transmitter. The device stretches and produces strain accordingly with the intensity of the applied magnetic field. Inversely, it changes its internal magnetic field, when it receives stress from outside. The first phenomenon comes from Joule effect, and second one from Villari effect.

The device can be well controlled at lower frequency according to the Joule effect[2].

The material we have employed is a polycrystallized magnetostrictive metal, named as Permendur[3] (alloys of iron-cobalt with Vanadium). We are using a specially processed material for our devices. The strain of it is approximately $\epsilon = 120 \times 10^{-6}$, almost three (3) or four (4) times larger than custom magnetostrictive material. The Young's modulus of it is as the same level with the steel.

The device is so strong enough to be compressed with heavy mechanical weight that it can be used even in quite high stress and shock. Using this property, the magnetostrictive device for the receiver is built in its outer casing in a quite high stressed structure, which enhanced receiving sensitivity almost ten (10) times greater than that without it. A laminated layer of thin metal structure is also employed to avoid eddy loss in the device. This extended performance in higher frequency domain to almost tens of kHz. Fig.1 shows the outline of the oscillator and receiver.

4.2 Control Scheme of EMH System

Fig.2 shows the control block diagram of the developed system. The system consists of magnetic oscillator/receiver, named as EMH (Electro Magnetic Hammer), and its control system.

The system has the following control modes. These are:

- A) Impulse drive control
- B) Frequency sweep drive control

The first one is a kind of impact hammer using EMH. Accurately controlled acoustic pulse is emitted into the object in this mode. The mode is useful when we need time domain response.

The second mode is a frequency sweep of the sinusoidal wave, which sweeps its frequency from the lower one to the higher one. We use mainly from 1 kHz to 10/or 20kHz in range. After receiving the raw data in time domain, FFT starts to transform the data into frequency domain. Thus, we get a spectrum of amplitude vs. frequency. The response signals carry the information of target structures or vibration modes determined from acoustic velocity. We can estimate the depth or internal structure by analyzing them. The characterized peaks in the spectrum show that there are reflections come from. These are

cracks, separation, and voids /or vacancy.

The system also has a current control scheme for keeping the output level constant. This contributes to quantize the response quite well. In fact we can memorize the change of the levels at the same point in different time accurately. This shows the possibility to detect and prospect the growth of the defects precisely, such as crack growth in concrete.

4.3 Property of EMH System

A property of the new EMH system was evaluated comparing with hammer. Fig.3 shows waveform and the frequency response of EMH and the hammer. In this case a concrete block with $600mm \times 600mm \times 200mm$ was measured as a target model.

The hammering curve shows strong and low frequency dominant property less than 6 kHz. Though a frequency peak which stands for the thickness of the model was expected to appear near 10 kHz assuming the velocity of the concrete is 4000m/s, we can not find it because the property does not cover this band well.

Conversely, the property curves of EMH shows that its response extends to higher frequency near to 20 kHz. As a result we can see a peak at about 9.6 kHz to show the thickness. The difference of EMH from hammering resides in comparably higher frequency property, where EMH shows wider and flat sensitivity than hammering.

It is one of outstanding tendencies that recent constructions consist of complicated structure, and often contains internal defects due to its structure. The property of EMH discussed above has its advantage in measuring comparably complex matrixes which contains defects inside.

The other point of the system is repeatability of measurement. Using the frequency sweep control of EMH, we evaluated repeatability as Tab.1. The table shows the data when the system measured the floor. In this evaluation the measurement was done 10 times, and the deviation of the amplitude was 0.035mV, where the average of the amplitude is 2.5 mV. Also the deviation of the peak frequency is 2.1 Hz, while the average frequency is 7403 Hz. So it can be said that considerable level of repeatability was achieved by the EMH system.

Tab.1 Stability of Measurement

	Average	Deviation	Deviation/Average	N
Amplitude[mV]	2.5	0.035	1.400%	10
Peak Frequency[Hz]	7403	2.1	0.028%	

5. PRINCIPLE OF THE METHOD

The method mainly uses reflection occurring on the interface where different acoustic impedance meet. Fig.4 shows the schematic block diagram of measuring scheme. Acoustic

signal flows as described in the Fig.4.

As is stated above recent constructions have complicated structure, and are often difficult to access from both ends. This requires measurement from one side or from the surface. In case of hammering impact shock generates surface wave on it which interferes with the receiving signal from reflectors. For this problem frequency sweep method here suffers no interference from this. This figure shows the case of measurement from the surface only. The receiver is placed adjacent to the oscillator.

When the reflection occurs at the distance L , then the delay time of propagation is given as $\Delta t = 2 * L / v$, then, the peak frequency is given by $f = 1 / \Delta t$. Thus we obtain,

$$f = \frac{v}{2 \times L} \quad (\text{Eq.1})$$

The dominant frequency, which appears as peak, gives the acoustic velocity when the depth is already known. On the other hand it shows depth when the acoustic velocity is already given. In the case when the reflections occur inside the concrete by the existence of defects, then we acknowledge the location of them by the same equation.

6. TESTING AND DATA EVALUATION

6.1 Evaluation of the method

Here, we are going to show some data from case studies.

To evaluate performance of the method, we constructed a large concrete structure seen in Fig.5. The model is a kind of wall structure, which is 3000mm(W) x 2500mm(H) x 730mm(D) in dimension. No steel is reinforced.

To confirm the reliability of measurement we measured the velocities in different directions, the first one was in width, and the other one was in depth. The velocities were determined by propagation times triggered by pulse drive.

The EMH oscillator and receiver were placed on both side (right and left) of the wall. The acoustic signal was injected into the wall along with the traverse line. The waveform received by the EMH receiver is shown in Fig.6- (b). The delay time of wave propagation was $740 \mu s$. Then the velocity is calculated by the Eq.1 as below using the width of it is 3000mm.

$$v = \frac{3000[\text{mm}]}{740[\mu\text{s}]} = 4054[\text{m/s}]$$

When the acoustic signal was injected into the wall along with the depth of 730mm, the delay time of signal propagation was measured as $180 \mu s$ shown in Fig.6- (a).

$$v = 730[\text{mm}] / 180[\mu\text{s}] = 4055[\text{m/s}]$$

The calculated data from both measurements meet in quite high accuracy.

Next, using this velocity, we confirmed validity of sweep response. Both of the EMH oscillator and receiver were placed on the front surface. The frequency was swept from 1 kHz to 10 kHz. The peak of elementary frequency seen in Fig.7 is 2.70kHz. From the Eq.1, the depth of the wall is calculated as follows.

$$D = 4055[\text{m/s}] / 2 \times 2.70[\text{kHz}] = 751[\text{mm}]$$

The difference between the calculated depth and the real one is evaluated to be 21mm, approximately 3% accuracy.

6.2 Measurement of Road Tunnel

Fig.8 shows the data of a road tunnel measured at the surface of the concrete liner. The peak of elementary frequency was 5.20 kHz. Assuming the velocity of concrete is 4000m/s, we got the depth of it as 385mm, where the designed thickness was 400mm.

7. DISCUSSIONS

The method is also under evaluation in other constructions. Generally wide and deep plane structure spreads propagating energy so wide and the response levels comes to low. Nevertheless it is true, EMH permits pressed measurement of the heads on the target due to its stiffness. We are expecting this will bring itself in deeper measurement available. We are accounting the range of it will extend to around 4 m even in flat structure.

In the real application it is often the case that the structures were not completed as designed. If we have only access from one side, such as the case from the surface only, then we need to know both of the location of internal reflections and the velocity inside. In most cases the velocities of the concrete are assumed to be approximately 4000 m/s, and it's enough for many applications. For precise application to measure both of them simultaneously, we are now trying to employ multi sensory system. Though the system works in low frequency, we are estimating to establish resolution well using amplitude and phase information combining mutually with them.

8. CONCLUSION

Thus we have concluded as follows:

- A) A newly developed low-frequency, frequency-sweep method (EMH system) has realized highly accurate measurement of concrete structure.
- B) A metal crystallized magnetostrictive oscillator and receiver show higher controllability in low frequency and proved its high performance for measuring large concrete construction.
- C) EMH system has enabled to realize stable and high repeatability in measuring, which has brought about capability to measure time dependent changes in object structures.

Using a magnetostrictive devices and its frequency sweep measurement, a possibility to inspect large concrete construction has been opened. As reviewed in this paper, not only in a wall, floor, tunnel or other structures, but the system will also be applied in more complicated structures and will find its usefulness in more applications. We are now trying to establish a well organized sensory system to inspect wide area in a time. We expect the method will contribute the inspection technology greatly soon.

REFERENCES

1. Nagamatsu, A. (1993) In: *Introduction to Modal Analysis*. Corona Publishing Co., Ltd., Tokyo.
2. Kikuchi, Y. (1959) In: *Magnetostriction Vibration and its Application to Ultrasonics*. Corona Publishing Co., Ltd., Tokyo.
3. Bozorth, R. M. (1951) In: *Ferromagnetism*, D. Van Nostrand C., Inc., New York.

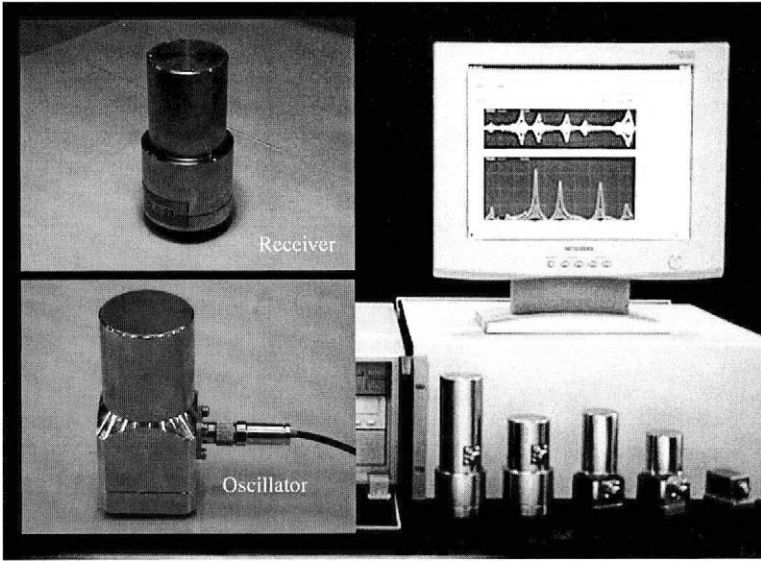


Fig.1 Magnetostrictive oscillator and receiver

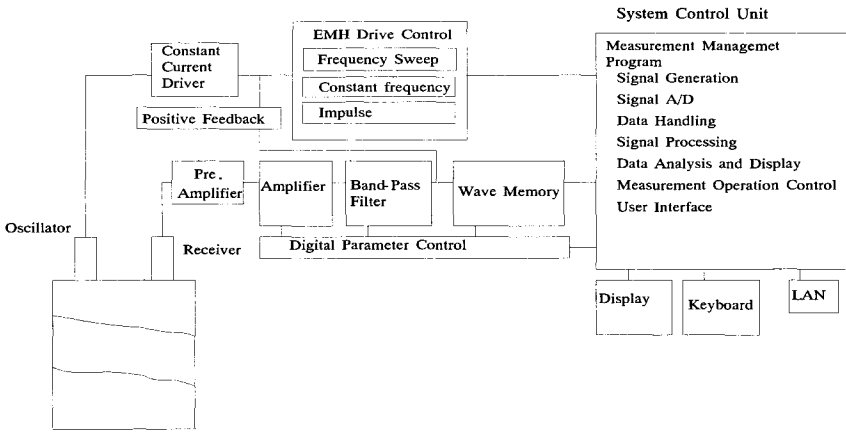
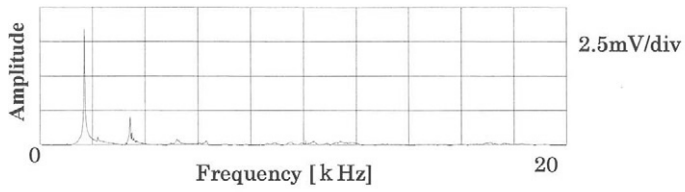
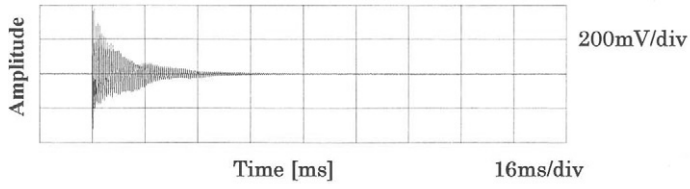
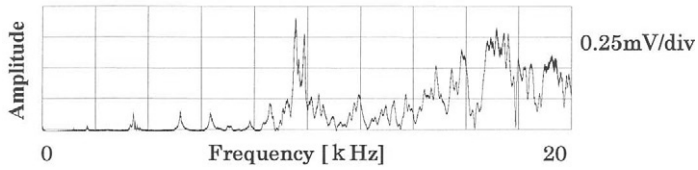
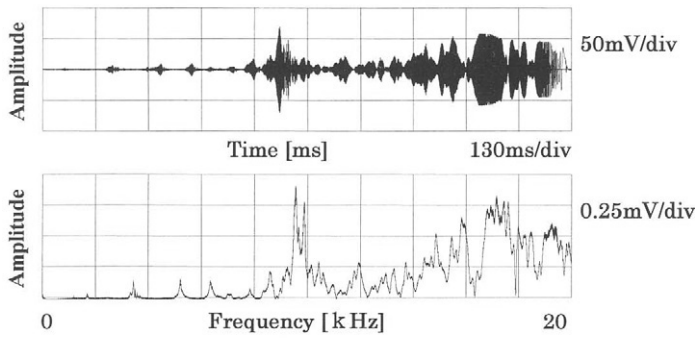


Fig.2 Control block diagram of the EMH system



(a) Response of hammering



(b) Response of EMH

Fig.3 Frequency response of EMH system and Hammering

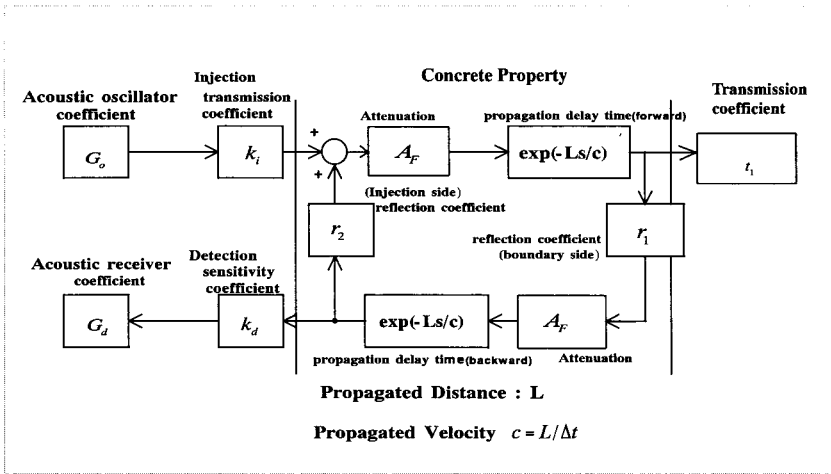


Fig.4 Schematic block diagram of measuring scheme

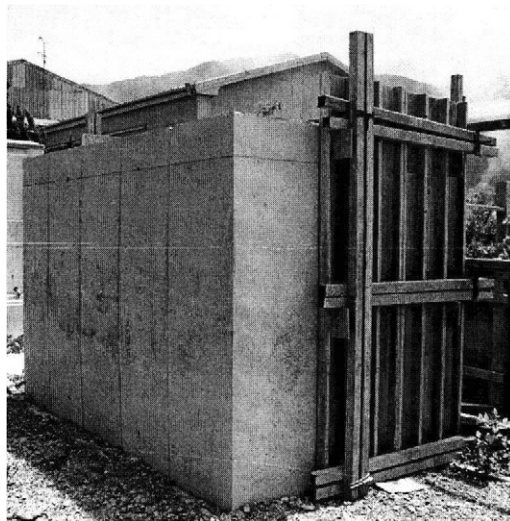


Fig.5 Outline of Large Concrete Model

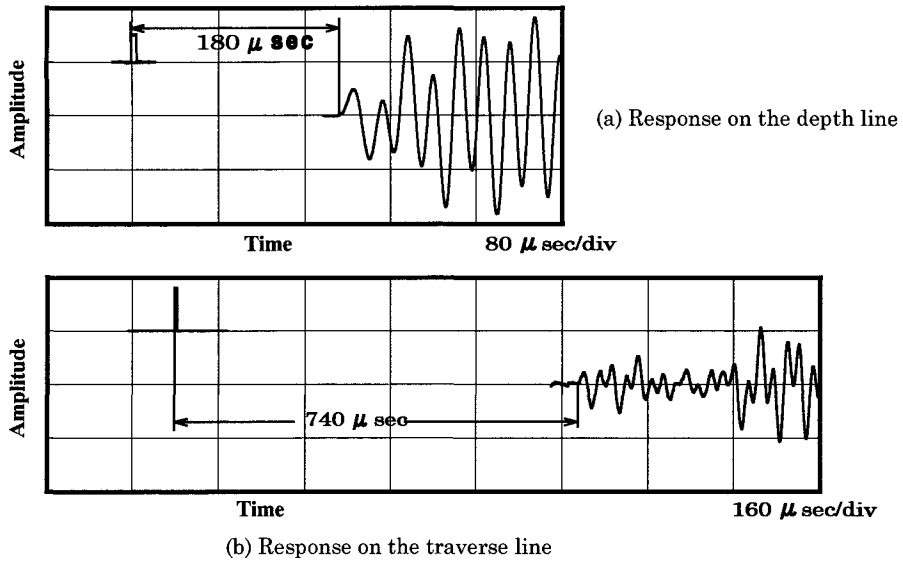


Fig.6 Response of pulse propagation (Large Concrete Model)

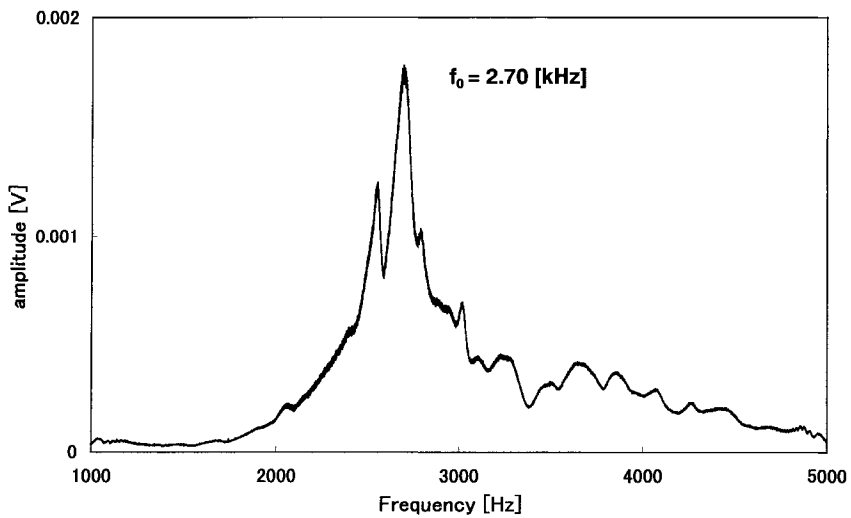


Fig.7 Spectrum of frequency sweep (Large Concrete Model)

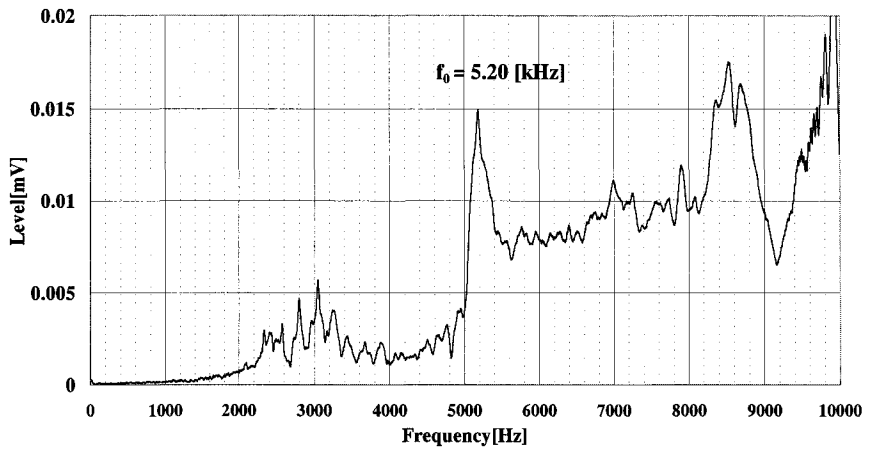


Fig.8 Measurement of the road tunnel liner

NON-DESTRUCTIVE LOCALISATION OF PRESTRESSING STEEL FRACTURES IN POST-TENSIONED CONCRETE

B. HILLEMEIER H. SCHEEL
Technische Universität Berlin
Institut für Bauingenieurwesen
Fachgebiet Baustoffkunde und Baustoffprüfung
Germany

ABSTRACT

The paper deals with the remanent magnetism method (RM-method), a non-destructive method that allows to identify unsafe prestressed structures by localising fractures of the prestressing steel. The method identifies fractures of single wires even in post-tensioned tendons. The magnetic field of externally magnetised tendons, measured at the concrete surface, is used. The parameters which determine the characteristic fracture signal have been studied. The knowledge of these parameters allows to draw conclusions from the characteristic fracture signal to the degree of damage or the number of fractures in a cross-sectional area. The method has been successfully applied on full size units [1].

KEYWORDS

Magnetic Method, leakage field, prestressed concrete, prestressing steel, steel fracture, bridges

THE PHENOMENON AND THE CAUSES OF STEEL FRACTURES

The reasons for the fractures of prestressing steel bars that led to collapses of prestressed concrete girders are of different nature:

- All types of prestressing steels are at risk to fracture if corrosive media penetrate to the prestressing steel wires. This happens, if e.g. the sealings of bridge decks are not watertight and chlorides depassivate the prestressing steel wires or if the grouting of tendons is insufficient and water can penetrate the wires. Sometimes grouting mortars, which were used in the past, got on behalf of frost resistance high contents of chlorides. In this case, a penetration of moisture may start the corrosion process.
- Many heat-treated prestressing steels are so sensitive concerning stress-induced corrosion that steel fractures had been found even if the wires had been embedded in alkaline mortar in high quality grouted ducts. The most probable reason for these fractures is, that the corrosion already started before the grouting works were executed. The transportation and storekeeping of the steel between production and placement in the ducts could have been one decisive factor. Last results turned out that probably a too long period between placement in the ducts and grouting work is the main reason for the fractures of the prestressing steel wires.

In almost any case there were no visible signs at the concrete surface for the fractures of the prestressing wires. The failure of prestressed concrete members often happens abruptly.

THE DETECTION OF FRACTURES OF PRESTRESSING STEEL

The Different Methods

Until now three possibilities exist to detect fractures of prestressing steel wires, these are:

1. Visual inspection after the opening of the concrete
2. Application of the X-ray-method
3. Application of the Remanent-Magnetism-Method

Visual Inspection

The main disadvantage of the visual inspection after the opening of the concrete is the limitation to a local inspection zone. A further disadvantage lies in the fact that after the metal sheathing has been opened only a part of the surface of the wires in the outer layer with three or four wires of a strand containing 16 up to 48 wires can be inspected visually.

After this destructive examination the building is in need of repair. The repair could be the starting point for a corrosive attack.

The X-Ray-Method

The X-ray-method was supposed to be appropriate to locate fractures in prestressing steel wires. The method requires a detectable fracture width. The fracture is not detectable with the X-ray-method, if it is screened by other steel wires. Other steel wires must not cover the fracture. As concrete is a shielding material against x-rays, the method needs high x-ray-energy, long exposure time and focussing to small areas.

The Remanent-Magnetism-Method

The magnetic method is coping with the mentioned difficulties. Ducts can be tested almost along their whole length. The characteristic magnetic leakage field is not screened by other wires or by the metal sheathing. The magnetic leakage field occurs even if the fracture width tends towards zero.

Important results of the laboratory work and experiences of the examinations of full size units are presented in the following. More details are reported in the research report [2], the proceedings of the international symposium 'Non-Destructive Testing in Civil Engineering Berlin 1995' [3], [4] and in the doctor thesis 'Spannstahlbruchortung an Spannbetonbauteilen mit nachträglichem Verbund unter Ausnutzung des Remanenzmagnetismus' [5].

THE PHYSICAL PRINCIPLE

The magnetic field resulting from a magnetised tendon or a magnetised steel wire is comparable to the magnetic field of a bar magnet. In the region of a fracture a magnetic dipole-distribution is forming and accordingly a magnetic leakage field in the surrounding. The transverse component, measured at the concrete surface is shown in Fig. 1. The characteristic leakage field allows to draw the conclusion to one or more fractures of a prestressing steel wire (Fig. 1).

Transverse component of the magnetic flux density

Fig. 1. At the concrete surface a characteristic magnetic signal is measurable, which indicates the location of the fracture. The transverse component of the magnetic flux density is shown schematically.

THE TECHNIQUE OF MAGNETISATION

Necessity of Magnetisation

In order to draw unequivocal conclusions from the magnetic flux density measured at the concrete surface to potential fractures, the first step to be taken is the magnetisation of the prestressing steel up to a magnetic state where all irreversible magnetisation processes are completed. This is indispensable in order to extinguish the unknown magnetic history of the steel. Without this magnetisation the measured magnetic signals could be caused by various former magnetisations (e.g. transport with lifting magnets).

The magnetisation of the tendons is performed from the concrete surface with an electromagnet. A remanent magnetisation of the tendons is achieved up to a concrete cover of 300 mm.

To magnetise the prestressing steel bars before they are built in order to measure the magnetic flux density later without repeated magnetisation does not lead to satisfactory results because the magnetisation is destroyed partially and locally variable by the mechanical impacts during the building process. This can result in signals like fracture signals in absence of a fracture or to a demagnetised steel in the surrounding of a fracture, so that no fracture signal would appear.

Suppression of the Disturbing Signals

Different magnetic material properties of the mild reinforcement and of the prestressing steel lead to different degrees of magnetisation after the multistage magnetisation procedure has been performed. While the magnetisation of prestressing steel is increased by the magnetisation procedure up to remanence (the maximum residual magnetisation), the magnetisation of the mild reinforcement decreases to small values. The disturbing signals caused by the mild reinforcement are suppressed in this way. Mild reinforcement is a magnetic soft material compared to prestressing steel. Even small external fields change the sign (or the direction) of their magnetisation while the magnetisation of the tendon is not influenced considerably. These properties are taken as an advantage of the magnetisation technique. They

allow to create various magnetic states which exclusively differ in the sign of the magnetisation of the mild reinforcement. Signals caused by the prestressing steel can clearly be distinguished from the signals caused by the mild reinforcement by comparison of the measurement data that represent these particular states.

THE FRACTURE SIGNAL

The Peak-Peak-Amplitude

The magnetised tendon has a magnetic field similar to that of a bar magnet. Fractures of single prestressing wires out of a bundle of wires inside the metal sheathing are detectable by characteristic leakage fields.

Fig. 2 shows the transverse component (relative to the direction of the steel wire) of the remanent magnetic field. At the location of a fracture the measurement curve of the transverse component shows a turning point.

As a measure for the strength of a fracture signal the peak-peak-amplitude of the transverse component of the leakage field is used (Fig. 2).

Influences on the Fracture Signal

In order to locate the position of steel fractures in tendons and to evaluate the extent of damage, various influences have to be considered, e.g.

- concrete cover of the prestressing steel wires,
- area of the prestressing steel wires,
- number of prestressing steel wires in the tendon,
- number of fractures in one cross-section of a tendon,
- bonding between the prestressing steel wires and the grouting mortar (fracture width),
- disturbing signals caused by ferromagnetic built-in units especially mild reinforcement,
- magnetic and magnetoelastic material properties of the type of prestressing steel.

Most of the experiments, of which the results are being presented next, were performed with tendons consisting of 16 heat-treated prestressing wires (type: Sigmastahl), round ribbed, diameter: 7.2 mm. To simulate fractures the steel wires were cut, flat ground and glued. Hall generators were used as sensors for the magnetic flux density.

Quantification of the Influences

The peak-peak-amplitude of the transverse component of the leakage field (Fig. 2) for a certain tendon depends on

- the number of fractures in one cross-section,
- the concrete cover,
- the fracture width (distance between the fracture surfaces),
- the degree of prestressing.

Fig. 3 shows the peak-peak-amplitude A_{pp} of the fracture signal as a function of the number of fractures in one cross-section and the concrete cover in a remanent magnetised tendon of 16 steel wires. The fracture surfaces were in contact.

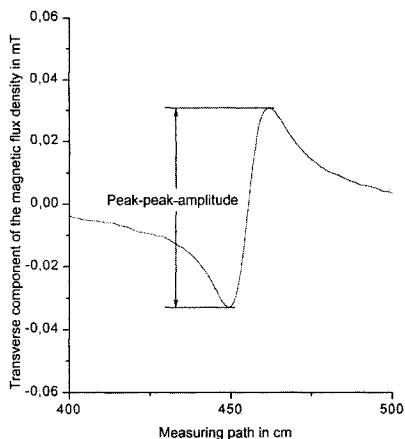


Fig. 2. The peak-peak-amplitude of the transverse component as a measure for the strength of the leakage field.

Mathematical formulas for the peak-peak-amplitude as a function of the concrete cover (Fig. 3), the number of fractures (Fig. 3) and the fracture width (Fig. 4) are given in former publications, e.g. [5,6].

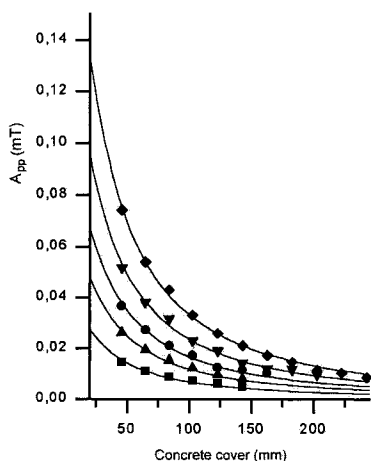


Fig. 3. Peak-peak-amplitude of the transverse component of the leakage field as a function of the distance to the tendon (with 16 prestressing steel wires) for different numbers of fractures in one cross-section. The fracture surfaces were in direct contact. The fractures were located in the bundle opposite to the concrete surface. (◆: 5 broken steel wires; ▼: 4 broken steel wires; ●: 3 broken steel wires; ▲: 2 broken steel wires, ■: 1 broken steel wire).

Figure 4 shows the influence of the fracture width on the peak-peak-amplitude. The data points are results of calculated fracture signals [5]. The calculation is based on the measured divergence of the magnetisation of the prestressing steel wire in the vicinity of a fracture. The most important fact is that the peak-peak-amplitude does not tend towards zero if the fracture width does. The distortion of the structure is sufficient to cause the leakage field. That

means that even partial fractures are detectable. The fracture width depends on the effective bond length, which in turn depends on the bonding between the prestressing steel and the grouting mortar and also on the friction between the steel wires. A fracture width of about 1 mm is a realistic mean value. On the other hand fractures that were not visible, that means, the fracture surfaces were in contact, had been found too.

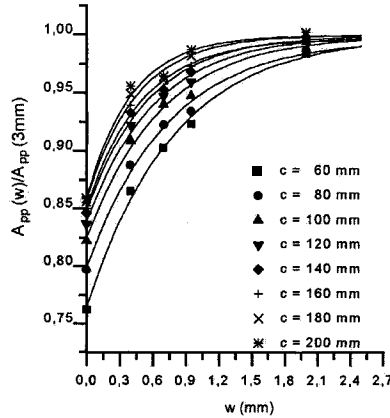


Fig. 4. Relative peak-peak-amplitude of the transverse component of the leakage field as a function of the fracture width w for different concrete covers c .

The physical reason that the peak-peak-amplitude does not tend to zero with a zero fracture width and the reason for the relative weak decrease of the amplitude with increasing concrete cover c ($A_{pp}(c) \propto c^{-1.75}$) is that a fracture causes a distribution of 'magnetic charges' which are dropping exponentially with increasing distance from the location of a fracture. These 'magnetic charges' are not exclusively located on the fracture surfaces. The distribution of the magnetic charges also effects that the influence of the fracture width on the peak-peak-amplitude decreases with increasing concrete cover (Fig. 4) [5].

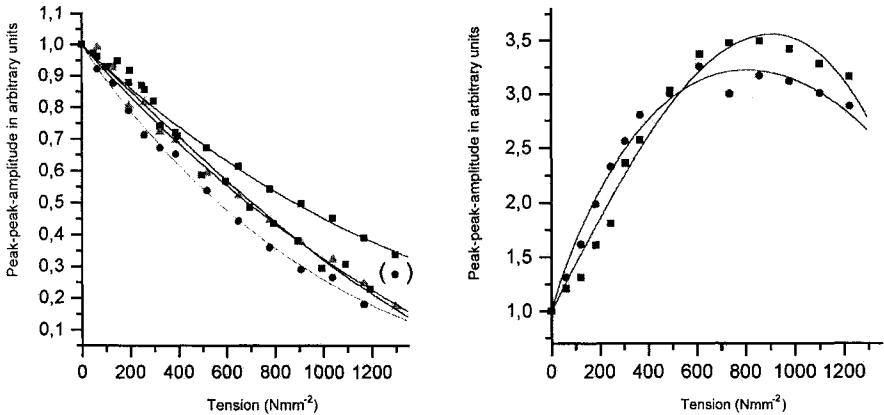


Fig. 5. The peak-peak-amplitude of the leakage field is strongly influence by tensional stress. In the case of cold-drawn steel (left) it decreases with increasing stress. Each line belong to a single steel sample. In the case of heat-treated steel (right) it increases with increasing stress. Each line belong to a single steel sample.

The peak-peak-amplitude is strongly influenced by the degree of prestressing. The remanence of cold-drawn steel and heat-treated steel is almost the same if they are not stressed, but the remanence of cold-drawn steel decreases with increasing degree of prestressing (Fig. 5 left) while the remanence of heat-treated steel increases. The peak-peak-amplitude of prestressed heat-treated steel is up to three times higher compared to the unstressed state (Fig. 5 right). The value for cold-drawn steel decreases up to one third in the prestressed state.

NUMERICAL OPERATIONS TO SUPPRESS THE DISTURBING SIGNALS

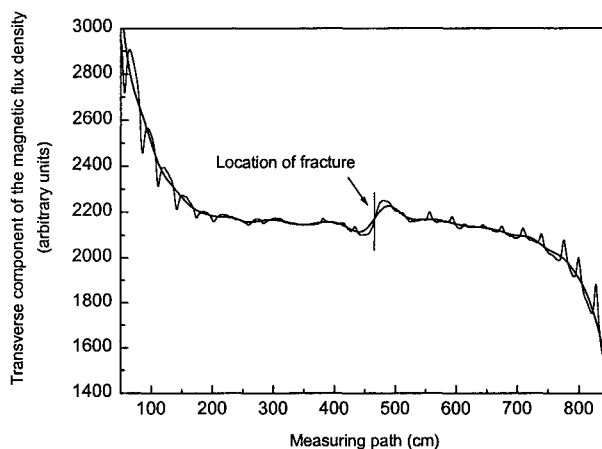


Fig. 6. Effect of FFT filter smoothing. The measurement curve shows small peaks caused by the residual magnetisation of stirrups. The smoothed curve shows the significant fracture signal, but the stirrup peaks are filtered out.

The disturbing signals caused by the mild reinforcement and other ferromagnetic built-in units are strongly suppressed by the applied magnetisation procedure. Besides that there are still remaining disturbing signals. To diminish these signals and to separate them from fracture signals, the following data processing can be applied:

- Simple addition of two measurement data arrays:
Two arrays with the magnetic flux density data of the system in different magnetic states, in which the residual magnetisations of the mild reinforcement have different signs, but not the residual magnetisations of the prestressing steel wires, are added. The signals caused by all kinds of mild reinforcement decrease, whereas the signals caused by the prestressing steel increase.
- Fast Fourier Transformation (FFT) filter smoothing (Fig. 6):
The signals with a small width compared to the width of a fracture signal are filtered out. FFT filter smoothing suppresses signals caused by transverse reinforcement (e.g. by stirrups), if their distances do not vary too much. It also filters the signals of ferromagnetic built-in units with a small width compared with the width of the fracture signal, e.g. nails, binding wires etc.. Noise with a frequency $\nu > 5 \text{ s}^{-1}$ (depending on the measurement speed) is also filtered out. Fig. 6 shows a measurement curve and the resulting FFT filter smoothed curve.
- Deconvolution of the (smoothed) curve with fracture signals.
- Calculation of the cross correlation function of the (smoothed) curve and fracture signals.

APPLICATIONS ON FULL SIZE UNITS

The method has been applied on full size units. The installed measurement device is shown in Fig. 7 under a girder for inspection. This device is used to inspect tendons from the underside of structure elements.

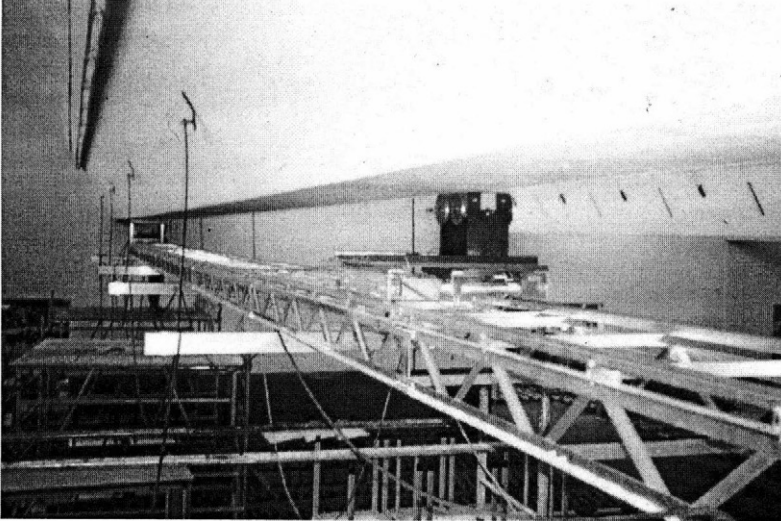


Fig. 7. The measurement device under a girder for inspection.

The examination of tendons can also be performed from the lateral surface (Fig. 8 left) or from the upper side (Fig. 8 right). Girders of bridges, fabrication halls, indoor pools, tendons of bridge slabs and tangential tendons of oil tanks have been inspected. Some concrete members had fractures others had not. Even in the same building some tendons had several fractures while others were completely intact.

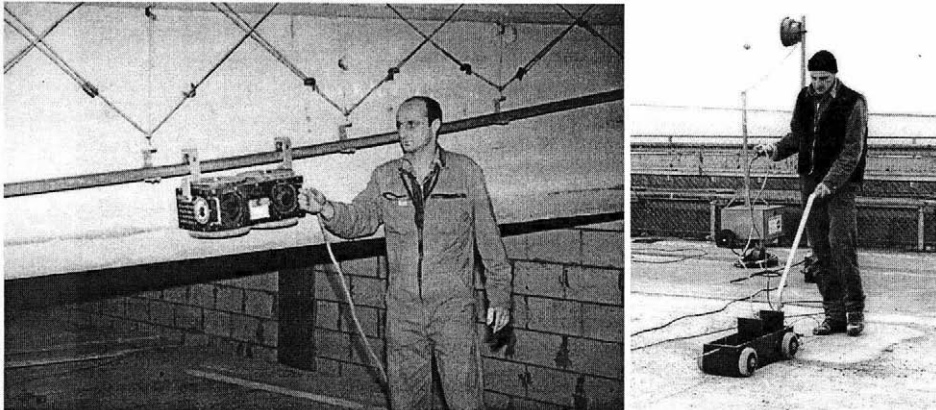


Fig. 8. Left: Measurement from the side surface of a girder. The magnet is suspended mobile on a flexible support system to follow the trace of the tendon inspected in the girder. Right: Magnetisation and measurement from the upper surface.

One of the latest applications of the methods was the examination of post-tensioned girders in factory halls built in the fifties in Germany. By chance a completely corroded tendon was found in one of the girders, when installation works were carried out. A chemical analysis of the grouting mortar resulted in a chloride content higher than 0,5 up to 3,9 percent related to the mass of cement. A typical difficulty in the examination of girders in a factory hall lies in the accessibility. Different attachments, like conveyor systems, crane ways and pipes complicate the examination works (Fig. 9).

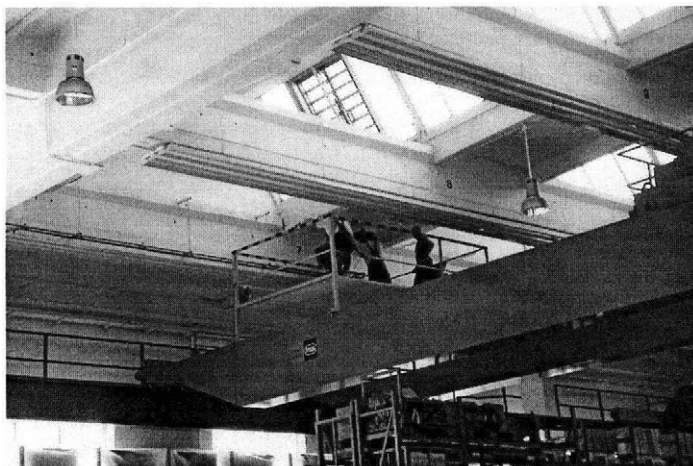


Fig. 9. The accessibility to the girders in this factory halls is complicated by crane ways and pipes.

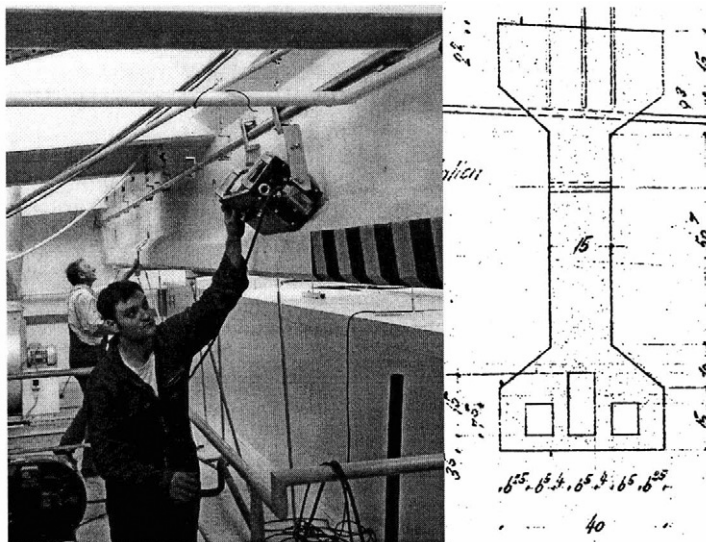


Fig. 10. The measurements could not be performed from the underside but from the slope of the bottom chord after the auxiliary construction had been modified (photo on the left). Each outer tendon had been checked together with the medium tendon in one working step (sketch on the right).

Some of the attachments had to be removed, but the most problems were avoided by performing the measurements not from the underside but from the slope of the bottom chord (Fig. 10 left) after the auxiliary construction had been modified. Each outer tendon could be checked together with the medium tendon in one working step (Fig. 10 right). The required large spot check could be realised. One of the examined girders was at risk to collapse. It could be supported for stabilisation. About 40 % of the other girders had single fractures of prestressing steel wires. The structural stability of these girders is still ensured. They will be examined again after two years to get more information about the damage process.

OUTLOOK

Especially in prestressed bridge slabs prestressing steel wires of transverse tendons are broken relatively often. The reason for the fractures is chloride induced corrosion. It is planned to increase the measurement speed by magnetising the tendons in one step using an appropriate large mobile magnet and by scanning the magnetic flux density on the entire surface of the bridge deck. A research project at the Technische Universität Berlin to develop the appropriated devices is supported by the building authorities of Berlin and carried out.

REFERENCES

1. Scheel, H., (1999), *Bauwerkeinsatz des Remanenzmagnetismus-Verfahrens: Spanndrahtbruchortung in Spanngliedern einer Fahrbahnplatte der Autobahnbrücke bei Michelsrombach*, <http://www.dgzfp.de/bauwerk.html>, Plakat 16
2. Hillemeier, B.; Scheel, H., (1996), *Ortung von Spannstahlbrüchen in metallischen Hüllrohren*, Abschlußbericht zum Forschungsauftrag des Deutschen Instituts für Bautechnik AZ.: IV 1-5-672/92, Berlin
3. Scheel, H.; Hillemeier, B., (1995), *The Capacity of the Remanent Magnetism Method to Detect Fractures of Steel in Tendons Embedded in Prestressed Concrete* in the Proceedings Vol. 1 of the International Symposium Non-Destructive Testing in Civil Engineering (NDT-CE). Ed. by G. Schickert, H. Wiggenhauser, Deutsche Gesellschaft für zerstörungsfreie Prüfung e. V., p. 211 - 218
4. Hillemeier, B., (1995), *Assessment of Structural Stability of Prestressed Concrete by Non-Destructive Detection of Steel Fractures* in the Proceedings Vol. 1 of the International Symposium Non-Destructive Testing in Civil Engineering (NDT-CE). Ed. by G. Schickert, H. Wiggenhauser, Deutsche Gesellschaft für zerstörungsfreie Prüfung e. V., p. 23 - 29
5. Scheel, H., (1997), *Spannstahlbruchortung an Spannbetonbauteilen mit nachträglichem Verbund unter Ausnutzung des Remanenzmagnetismus*, Dissertation, Technische Universität Berlin
6. Scheel, H., (1999), *Magnetic Detection of Prestressing Steel Fractures in Prestressed Concrete*, Structural Faults + Repair - 99, London

MEASUREMENT OF AXIAL-STRESS IN HIGH-TENSION BOLTS BY ACOUSTOELASTIC VELOCITY-RATIO METHOD

H. TODA

Department of Opto-Mechatronics, Wakayama University

Y. GO and K. YOKOYAMA

Sakai Iron Works Co., Ltd.

O. YOSIKAWA and T. YAWATA

Osaka Institute of Technology and Sosei Consulting Co., Ltd.

ABSTRACT

An acoustoelastic velocity-ratio method for estimating an axial-stress in high-tension bolts was studied to check adaptability in a field measurement. An acoustoelastic velocity-ratio constant was almost constant for some bolts forged by various factories and was independent of bolt temperature. Although a velocity-ratio was slightly dependent on both production factory and bolt temperature, this dependence was smaller than those by other acoustoelasticity methods were. These facts indicate the effectiveness of the present method for nondestructive bolt axial-stress measurement without demanding any preparatory checking at an initial stress-free state.

KEYWORDS

Acoustoelastic velocity-ratio method, acoustoelasticity, bolt axial-stress, bolt axial-force.

INTRODUCTION

High tension bolts take an important roll in civil engineering and are mainly applied up to 95% in amount for field construction of steel bridges. In fastening work high-tension bolts are fastened and adjusted their axial-forces by using a torque wrench. It is very important to control fastening force, because bolt loosening is caused by insufficient fastening, or because bolt neck breaking is caused by too tight fastening. Accident such as bolt neck breaking is improved by exchanging F13T bolts for F10T bolts.

In periodic inspection, bolt fitness is usually checked by hammering test. This checking is insufficient and impossible to obtain a bolt axial-force (*i.e.* residual force, or residual stress). Some studies of the bolt axial-stress measurement were done by using acoustoelasticity technique [1-7]. The acoustoelasticity stress analysis is based on the phenomenon that ultrasonic wave velocity changes with stress-state in medium.

In bolt axial-force measurement equipment on the market, longitudinal ultrasonic waves

traversing along an axis are usually applied, and transit time in a round trip is measured. A change in the transit time is measured and then the axial-force is calculated by using an acoustoelasticity constant. However the transit time at a stress-free state is not constant due to both variations of bolt length and of material heterogeneity. Therefore, in the measurement it is claimed to measure in advance a transit time at a stress-free state. Furthermore, ultrasonic wave velocity changes depending on medium temperature, then the reliability of measurement declines unless the bolt temperature can be checked.

In the present paper, an acoustoelastic velocity-ratio method for the estimation of bolt axial-force was studied to overcome these difficulties. [8] We checked the feasibility test to measure bolt axial-force without knowing the transit time at a stress-free state and bolt temperature as well.

Also in order to check its adaptability in a field measurement, we prepared some various bolts made of different factories and some of them were kept unfinished on both surfaces of top and bottom.

ACOUSTOELASTIC VELOCITY-RATIO METHOD

When being fastened, a bolt is elongated. According to this elongation, the transit time of ultrasonic wave traversing along an axis of bolt increases. Furthermore, as wave velocity decreases in proportion to the applied tensile stress due to an acoustoelasticity effect, the transit time increases again in addition to the one by elongation effect. The increment of transit time by acoustoelasticity effect is dominant and becomes from 3 to 4 times the one by the elongation effect. From a point of view large change in transit time, the acoustoelasticity method seems to be advantageous.

The transit time in each bolt varies widely according to both the scatters of bolt length and material heterogeneity. Therefore, it is difficult to evaluate bolt axial-force from only once in-situ measurement using conventional acoustoelasticity method without knowing transit time at stress-free state.

We proposed in previously a new method named acoustoelastic velocity-ratio method, which makes possible to evaluate bolt axial-force by once in-situ measurement. The principle of the acoustoelastic velocity-ratio method is as follows.

In this method, both longitudinal- and shear-waves are used. Each wave is transmitted from a top surface of a bolt head. As each wave propagates just the same path length along axis of the bolt, the transit time-ratio calculated from two transit times just corresponds to the velocity-ratio, which is independent of scatter of bolt length.

Acoustoelastic velocity-ratio law is given by eq.1.

$$R = \frac{V_i}{V_s} = R_0 + C_r \beta \frac{N}{A_e} \quad (1)$$

$$C_r = R_0(K_s - K_l)$$

Where, R is velocity-ratio and R_0 is velocity-ratio at stress-free state. N is bolt axial-force. β is an effective ratio of loaded length. This is defined as the ratio of stretched part length (L_0) to

Table 1. Factories and treatments of Bolt specimens

No.	Steelmaker of raw material	Factory of bolt forging	Treatment of end surfaces
No.1	A	a	Unfinished
No.2	B	b	Unfinished
No.3	C	c	Unfinished
No.4	D	d	Unfinished
No.5	E	e	Unfinished
No.6	A	a	Finished
No.7	A	a	Plated with zinc (thickness $70 \mu\text{m}$)
No.8	A	a	Coated with paint (thickness $250 \mu\text{m}$)

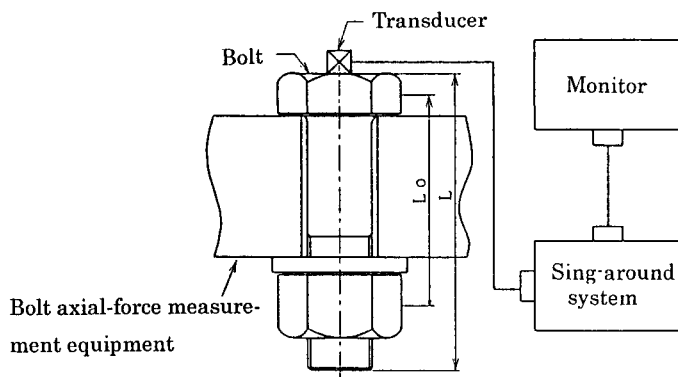


Fig.1 Block diagram of measurement system

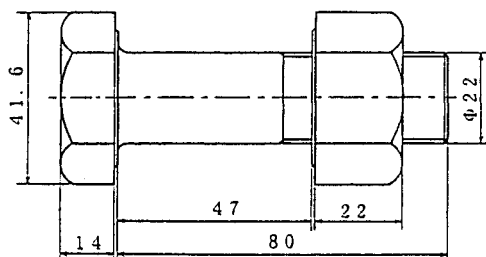


Fig.2 High-tension Bolt

total bolt length (L). V_L and V_S are longitudinal- and shear-wave velocities, respectively. K_L and K_S are longitudinal- and shear-wave acoustoelasticity constants, respectively. C_R is acoustoelastic velocity-ratio constant. A_e is the cross section area of the bolt.

As directly measurements of each wave velocity are difficult, each transit time are measured. Transit times of longitudinal- and shear-wave velocities are related to each wave velocity by eqs.(2) and (3), respectively.

$$T_L = \frac{2L_0 \left(1 + \frac{N}{A_e \cdot E} \right)}{V_{L_0} \left(1 - \frac{K_L \cdot N}{A_e} \right)} + \frac{2(L - L_0)}{V_{L_0}} \quad (2)$$

$$T_S = \frac{2L_0 \left(1 + \frac{N}{A_e \cdot E} \right)}{V_{S_0} \left(1 - \frac{K_S \cdot N}{A_e} \right)} + \frac{2(L - L_0)}{V_{S_0}} \quad (3)$$

Where, T_L and T_S are transit times of longitudinal- and shear-waves, respectively. E is Young's modulus of bolt material. V_{L_0} and V_{S_0} are longitudinal- and shear-wave velocities at stress-free state, respectively.

In eqs.(2) and (3), the first- and second-terms are transit times in stretched region and in stress-free region, respectively. Using eqs.(2) and (3), eq.(1) can be transformed as eq.(4).

$$R_r = \frac{T_S}{T_L} \doteq R_0 + \beta R_0 (K_S - K_L) \frac{N}{A_e} \quad (4)$$

Where, R_r is transit time-ratio defined as ratio T_L/T_S .

From eqs. (1) and (4), an acoustoelastic velocity-ratio law can be given by eq.(5).

$$R_r \doteq R = R_0 + C_R \beta \frac{N}{A_e} \quad (5)$$

An acoustoelastic velocity-ratio at stress-free state (R_0) is not affected by scatter of bolt length, but affected by material, shape, factory, and temperature of bolt. Therefore, both validity and adaptability of this method heavily depend on the magnitude of scatter of R_0 .

EXPERIMENTAL TECHNIQUE

Method of measurement. Block diagram of the method of measurement is shown in Fig.1. A high-tension bolt was settled in bolt axial-force measurement equipment. This equipment was used to compare our estimated forces with real forces. Longitudinal- and shear-type transducers were used. Transmission and receiving of ultrasonic waves are done by a single probe technique.

Frequency and size of each transducer are 5 MHz and 0.5 inch diameter, respectively. The

transducer was attached to the top surface of the bolt head by couplant of base ingredient of Araldite adhesive, and it was pressed about 20 N force against the surface by a spring. Transit time measurement was done using the sing-around method. In transit time measurement, the first echo from a bottom of bolt was selected and was gated in a circuit. To check an influence of bolt temperature, experiments were done in a room with temperature adjustable facility.

It is practical sense that velocity measurement of a bolt is difficult and low precise, because a traversing path is much longer than a lateral distance, and further the lateral wall is zigzag surface, which makes strong back-scattering and disturbs the echo. However, in this experiment, measurements were rather stable and repeatable.

Bolt specimens. We prepared eight bolts of types F10T and M22. Each bolt was forged by different factories using material rods drawn by different steelmakers (see Table 1). Shape and dimensions of the bolt are shown in Fig.2. Thickness of the flange put between bolt head and nut was 47mm. Then, an effective ratio of loaded length was calculated as $\beta=0.69$. In this calculation, We proposed that stress distribution is triangular along the axis in the area of both the head and the part of axis covered with the nut.

In order to check effects of the end surface condition on measurement, we prepared bolts with various kinds of end surface. Their end surfaces were unfinished, finished, plated with zinc, or coated with paint. In each bolt, there was a carved seal on a top surface of bolt head. Position of carved seal was at the periphery of top surface in almost all the bolts, but was just at a center of top surface in only No.5 bolt.

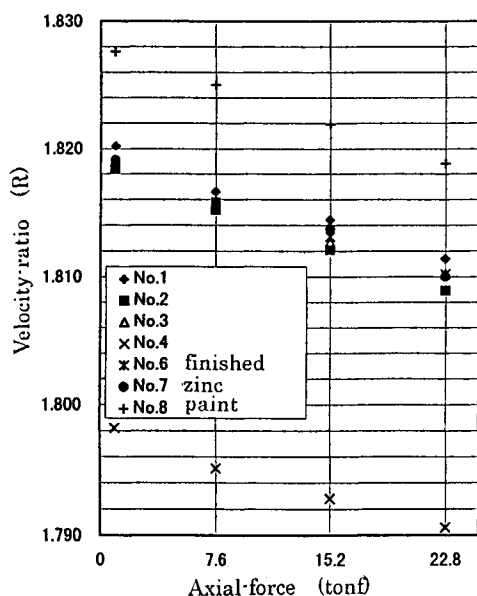


Fig.3 Velocity-ratio versus axial-force (Temperature 25°C)

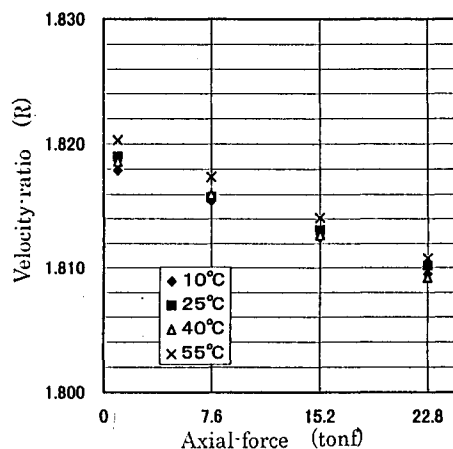


Fig.4 Temperature dependence of relation between velocity-ratio and axial-force

EXPERIMENTAL RESULTS

For No.5 bolt, experiment could not be executed, because a center carved seal interrupted transmission of ultrasonic. We show the experimental results obtained for other seven bolts. Figure 3 shows the relations between the velocity-ratio and the applied axial-force. These data were obtained at a constant temperature of 25-deg.C. In all bolts, velocity-ratio varied almost linearly with the applied axial-force, and their gradients were coincident with each other. The acoustoelastic velocity-ratio constant was within $(4.2 \pm 0.1) \times 10^{-4} \text{ tonf}^{-1}$. Only result for bolt No.4 were separately from ones for the other bolts. No.4 bolt has a concave surface at bottom and this data separation seems to be caused by irregular reflection at the concavity.

For No.8 bolt with coat of paint of 250- μ m thickness, echo signals were a little smaller than ones for other bolts, and data were a little separately from ones for the other bolts. For other five bolts except No.4 and No.8, velocity-ratios at stress-free state almost converged into a value and scatter of them was within ± 0.0013 . This magnitude of the scatter corresponds to a estimation error $\pm 3 \text{ tonf}$ (30 kN).

Next, we checked an influence of bolt temperature. Experimental results obtained at various temperatures are shown in Fig.4. This experiment was done using bolt No.6 with finished both ends. Experimental temperature was changed from 10- to 55-deg.C.

Figure 4 shows that the acoustoelastic velocity-ratio at stress-free state changed a little, but that acoustoelastic velocity-ratio constant was almost kept constant. Both longitudinal- and shear-wave acoustoelasticity constants were also independent of temperature.

It is well known that acoustoelasticity constants of waves propagating perpendicularly to an applied stress direction are dependent on specimen temperature. [9] Therefore, using these waves, stress measurements were difficult for the specimen of unknown temperature. However, in the bolt axial-force measurement, it becomes easy to estimate stress, even though the bolt temperature is unknown.

Figure 4 also shows that acoustoelastic velocity-ratio increases only 0.002 against temperature rise of 45-deg.C. Even when bolt temperature is mistaken by an error of 10-deg.C, the error of estimation of bolt axial-force becomes smaller than 1.2 tonf (12 kN). This estimation error becomes one third of those by conventional acoustoelastic methods.

CONCLUDING REMARKS

To check the adaptability of the acoustoelastic velocity-ratio method to nondestructive measurement of bolt axial-force, we did experiments using eight bolts, which were forged at various factories and ends of which were treated with various conditions. Experiments were done at the various temperature changed for a range of 45-deg.C.

Conclusions are as follows.

(1) The velocity-ratio at stress-free state converged into a narrow range for bolts forged at a same factory, and it was little affected by surface conditions at both ends of the bolts. Our experimental data are few in amount, it is concluded that the acoustoelastic velocity-ratio method can be applied to measure bolt axial-force by only once in-situ measurement without demanding a measurement of the velocity-ratio at stress-free state before hand. Bolt axial-force

can be measured within an error as small as 3 tonf (30 kN).

(2) When bolt temperature was changed, the acoustoelastic velocity-ratio at stress-free state changed a little, but the acoustoelastic velocity-ratio constant was almost kept constant. Using the acoustoelastic velocity-ratio method, the bolt axial-force can be measured within an error less than 1.2 tonf (12 kN), even when bolt temperature is mistaken by an error of 10 °C.

REFERENCES

1. Sakai, Makino and Toriyama, (1977) JSME, 43, 366, pp.723-729 (in Japanese).
2. Yamamoto, S. and Mogi, (1979) J. of JSME, 82, 731, pp.1166-1168 (in Japanese).
3. J.S.Heyman ,(1977)Experimental Mechanics.17,pp.183-186.
4. S.G.Joshi and R.G.Pathare, (1984)Ultrasonics,22,pp.270-275.
5. Okada, K. (1989) Acoustoelasticity meeting, JSNDI, No.34, pp.58-61 (in Japanese).
6. Fukuoka, H., Toda, Yaegawa, Uehira, Yamagata, Siomoda, Ito and Hasinori, (1990) Acousoelasticity meeting, JSNDI, No.54, pp.39-43 (in Japanese).
7. Mori, Takekosi, Yagisawa, Ohyabu and Nakamura (1980) JSME, A47, 413,pp.102-106(in Japanese).
8. Uryu, S., Toda, H.and Fukuoka, H. (1992) Acoustoelasticity meeting, JSNDI, No.83, pp.36-40 (in Japanese).
9. Kobori, O. and Iwasimizu, Y. (1988) JSME, 54, 498, pp.245-250 (in Japanese).

This Page Intentionally Left Blank

FATIGUE CRACK PROPAGATION MONITORING IN STEEL STRUCTURES WITH INTELLIGENT SYSTEMS

MUHAMMAD S. RAHMAN, TOSHIYUKI OSHIMA, SHUICHI MIKAMI,
TOMOYUKI YAMAZAKI and NAOYUKI TAKADA

*Department of Civil Engineering, Kitami Institute of Technology,
165 Koen-cho, Kitami, Hokkaido, 090-8507, Japan*

ABSTRACT

Fatigue crack occurrence in steel structure is a common phenomenon that causes several catastrophic failures in past decades. In this research nondestructive testing (NDT) is adopted as diagnostic tool to analyze and evaluate fatigue crack in several laboratory specimens that may apply for real bridge structures and its components. It is shown that ultrasonic scanning images and reflection waves from assumed damaged portion give precise information of the defect. Several tests under laboratory condition were performed for accuracy improvement of the system. Fatigue crack developed by input repeated loading to steel specimen and crack elongation were measured by ultrasonic scanning images. Crack propagation, load level, strain variation also monitored with fiber optic sensor and conventional electrical strain gages until specimen's failure. Some results are compared with numerical analysis and sensor output under loaded condition. Long term remote monitoring, applicability of smart sensor for structural integrity and fatigue crack propagation assessment by using intelligent monitoring system are shown in this paper.

KEYWORDS

Fatigue crack propagation, ultrasonic testing, fiber optic sensor, wireless, remote monitoring

INTRODUCTION

Fatigue crack is the most common one that causes damage to structure and impairs its service life. To achieve proper functioning of structures accurate diagnostic method and efficient monitoring system is essential for maintenance and management of civil structures. A number of researches did in the fracture mechanics field to evaluate fatigue crack propagation [1,2,3]. Many techniques of NDE (Nondestructive Evaluation) currently available to diagnose fatigue crack in steel components may have several advantages and disadvantages. Without proper diagnosis accurate condition assessment of the structure is not possible. Structural health monitoring should be considered within the realm of condition assessment [4]. Some diagnostic criteria for structural monitoring and evaluation are discussed by Raphael and Smith

[5]. Those depend upon some logistics and conditions, economic feasibility and applicability to the real structure.

Two types of laboratory specimen considered in this study. One is conjugate with cross rib welded at transverse rib of J-type web opening (scallop) and a deck plate as floor beam on it. Scallops are subjected to both shear and bending moment. The crosswise ribs on the deck plate are subjected to alternating axial stress range of a large magnitude. Other one is V-notched specimen for which maximum stress concentrates at notch tip area. So it is worth to calculate stress distribution and monitoring of strain change around scallop and notch tip area.

Recently sensor technology and smart structures emerges in the field of civil engineering. So it becomes time demanding to explore the opportunity of accurate defect diagnosis by intelligent monitoring systems using smart tools. Crack may occur in structural steel due to various conditions during fabrication and harsh environmental effects. Sometime it is difficult to arrest crack but information is required for precaution to avoid loss of valuable lives and costly structural retrofit. For this purpose monitoring is essential, so that we can alert for preparation to replace or strengthen the existing structure. Fiber optic sensor offers a number of advantages with respect to electrical sensors and will open up the opportunity for many new systems to be developed in smart technology. A number of real scale structure involved with sensing technology to measure crack is reported in USA and Canada [6,7]. The lightweight, wide band width and small size of fiber sensors are strongly complemented by their strong immunity to electromagnetic interference and huge data transmitting capability make its position stronger as a tool for structures integrity monitoring. Here by applying these sensors as an integrated part

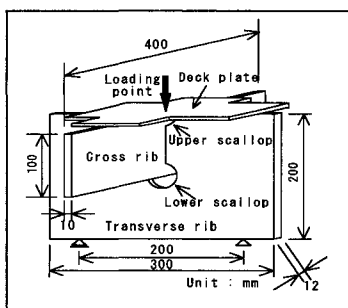


Fig.1 Specimen geometry (crosswise rib)

Table.1 V-notched specimen details

Sp No	Notch Angle α	Slit Width S (mm)	Notch Depth d (mm)	Notch Tip Radius ρ (mm)	Thickness (mm)
1-2	45°	2	42.414	0.125	25
2-1	45°	1	41.201	0.110	25
2-2	45°	1	41.201	0.110	25
3-1	60°	2	41.732	0.150	25
3-2	60°	2	41.732	0.150	25
7-2	45°	2	42.414	0.125	20
8-2	60°	2	41.732	0.150	20

of structure that will measure internal deformation due to load and environment during service are verified on trial basis. In our previous experiments crack propagation in invisible part of structure monitored by ultrasonic testing. From ultrasonic scanning images, it was clear that crack tip elongated at higher loading cycles and strong reflection gradually appeared from crack propagated zone [8]. Some of our results are very promising to apply the diagnostic technique for monitoring of practical structures.

EXPERIMENTAL WORK

Test Specimens

Crosswise Ribs. Test specimen of SS400 steel crosswise rib with geometric dimension is shown in Fig.1. The crossing point of transverse and cross rib with J-type web opening

(scallop) is connected by fillet welding of thickness 7mm. A deck plate welded on the crosswise rib and scallop which makes the specimen as a model of the real structure.

V-notched Y-shape Specimen. A number of compact tensile fatigue test specimens loaded for crack propagation monitoring and evaluation. The Y-shaped V-notched specimen is shown in Fig.2. Specimens are of about same thickness, size, and shape except notch angle and slit width variation. Specimen details with dimension are shown in Table.1.

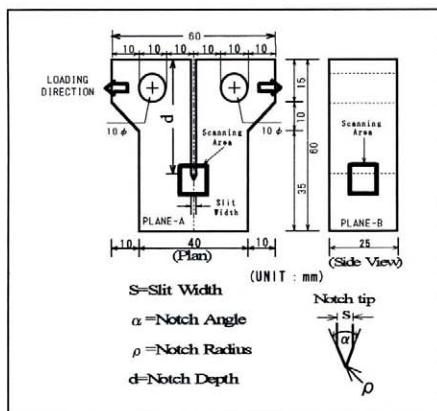


Fig.2 Fatigue test specimen (V-notched)

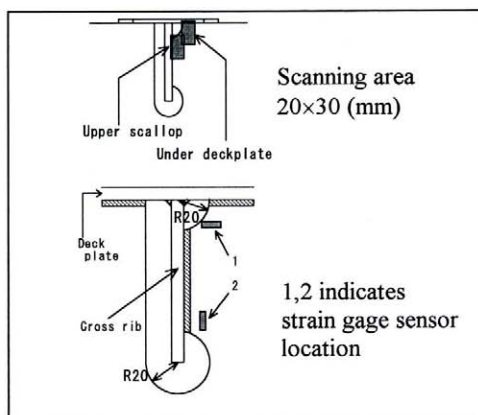


Fig.3 Scanning area and sensor location

Fatigue Loading

Fatigue loadings performed with hydraulic equipment of servo-pulsor unit that subjected the specimens to compressive and tensile repeated loading. The equipment is capable of maximum 200KN controlled by stroke and displacement. For crosswise rib, repeated compressive load range of 160KN~1KN (max-min) applied with loading frequency 10Hz. During loading maximum and minimum strain measured for 10 seconds of 200Hz frequency after 2.5×10^4 cycles loading interval. For strain monitoring data measured at same loading amplitude of frequency 5Hz. Tensile sinusoidal wave cyclic loading performed under constant load range of 5.0KN~1.0KN with frequency of 10Hz for crack development and propagation in V-notched specimen. During strain monitoring data recorded at lower loading frequency of 1Hz and 2Hz. It is observed that for sinusoidal loading strain response for optical sensor is clear at lower loading frequency. Due to repeated tensile loading notch tip opens and closes according to loading speed. After crack initiates the crack tip permanently opens and elongation of crack length happens which is sensed by attached sensor.

Ultrasonic Scanning

Ultrasonic scanning performed under water with a piezo-electric transducer of 10 Hz frequency, 80mm focal length and 9.52 mm diameter all over the experiment. Ultrasonic waves emitted from transducer are reflected from the specimen interior received as electric signals and amplified by ultrasonic receiver. Water used here as couplant to improve energy transfer. Automatic scanning control system has scanning range (mm) of 500(W) \times 500(L) \times 250(D), scanning pitch of 0.005~9.95 mm and 10~150 mm/sec scanning speed. C-scan image generates from echo amplitude and time of flight data on a 2-D coordinate and is a collection

of A-scan that plots time versus echo amplitude data. During scanning the echo height and time of flight data stored in memories corresponding to positions of transducer at predetermined intervals. The sampling gate is set to receive first boundary and bottom echo of the reflection echo. It shows the location of defects, but in the simplest form it does not show their depth.

For crosswise rib specimen angle beam scanning performed. The refraction angle is the key parameter for angle beam inspection, which is a function of the material properties and the incident angle. Incident angle was 18.9° so that under water refracted angle became 45° . Scanning image measured area of 20×30 (mm) with pitch of 0.1mm after predetermined loading cycles. For V-notched specimen image data measured at transducer normal position of area 10×10 (mm) around notch tip.

Strain Measurement with Attached Sensor

Good bonding is necessary for measurement accuracy. Proper cautions were taken during sensor instrumentation to the specimen. For crosswise rib the sensors attached close to scallops (web openings) as shown in Fig.3. For V-notched specimen fiber optic sensor (FOS) and strain gage sensor (SGS) attached 3 mm far for notch tip on both side at same position opposite to

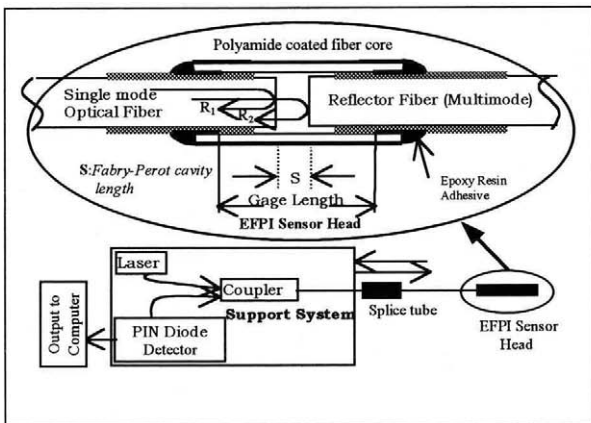


Fig.4 AFSS system and FOS head

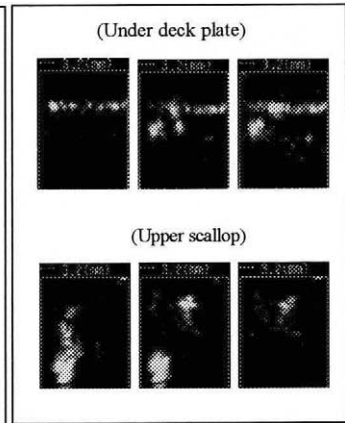


Fig.5 C-scan images

each other side. For electrical strain gages output of metal resistance changes with external effects amplified and converts data by A/D converter to strain output as microstrain. For fiber optic sensor the sensor system employs a broadband light-emitting diode (LED) as the optical source. A single mode fiber ($\lambda = 1300 \text{ nm}$) is used as the input/output fiber and a multimode fiber used as reflector. An air gap is formed that acts as a low-finesse Fabry-Perot cavity. Light is sent down the input/output optical fiber to the sensor head where it is modulated by the Fabry-Perot cavity inside the EFPI (Absolute Fabry-Perot Support System). As the test material is strained the silica tube and hence the air gap changes in length which causes a change in phase difference between the reference reflection and the sensing reflection [9]. This change in the intensity of light and spectral properties that is monitored by a coupler. A simple algorithm is used to determine the Fabry-Perot cavity length, s , from the optical signal returned from the EFPI sensor head. The absolute measurement system can measure within range 30 to 300 micrometer, 10% strain range, 1 microstrain resolution and maximum 5Hz refresh rate. For electrical strain gages strain output is directly recorded as microstrain and for FOS measured

absolute displacement data converted to strain data as microstrain. When the crack proceeds close to sensors sensing zone significant strain variation is observed.

RESULTS

C-scan Image Analysis

C-scan image is obtained by synchronizing flaw or discontinuity signals as the transducer is moved across the selected area of the specimen. C-scan images for varying loading cycles are shown in Fig.5 and Fig.6. A cracked portions which has a lower density and refractive index

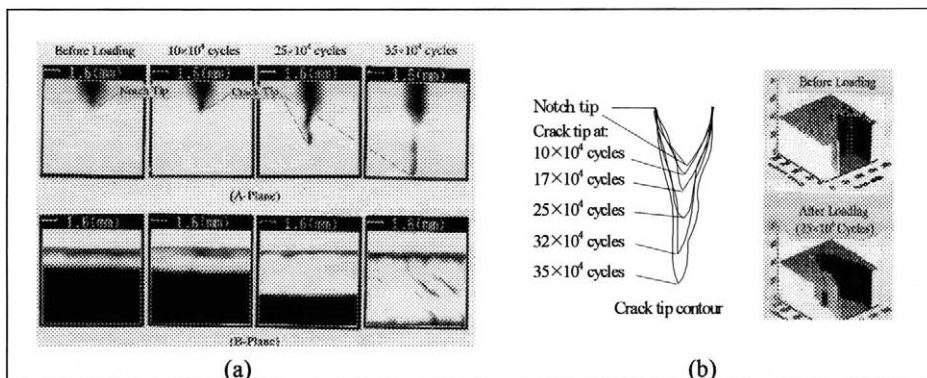


Fig.6 Scanning images from notch tip area of V-notched specimen: (a) C-scan images of A- and B-plane; (b) crack tip contour with 3-D image display of crack tip.

from the surrounding material. In these C-scan images color is directly proportional to the flaw amplitude compared to given amplitude within a certain range. For black and white images, echo amplitude data areas where echo amplitude is high with short time of flight are displayed in white and areas where echo amplitude is low with long time of flight are displayed in black. In the Fig.5 scan image of under deck plate illustrates that at initial loading stages reflection waves returned from deck plate plane. At higher loading cycles strong reflection echoes gradually observed from cracked plane. From upper scallop scanning image reflection echoes attenuated and scattered in other directions after crack propagated. From Fig.6 (a) crack tip clearly propagated for higher loading cycles is clearly observed. The trace of crack propagation as well as propagation direction is confirmed from C-scan images. Crack tip contour and 3-D image are shown in Fig.6 (b). 3-D images here are two-dimensional array of pixels displayed by 200x200 (mm) size of 8 bit per pixel is obtained from P-V Wave graphic software analysis.

Crack Growth Analysis from C-scan Images of Notched Specimen

Conventional formulas and theories of fracture mechanics are applied for calculation. Crack length measured from C-scan images verses loading cycles plotted as damage accumulation curves are shown in Fig.7 (a). The crack opening, crack closure and crack growth behavior are discussed in detail by Yamada et al. [10,11]. Constant amplitude loading of stress ratio $R = 0.2$ was keep constant in our experiment. At initial stage notch tip opens and closes according to loading frequency. When the sufficient number of cycles experienced crack nucleates but still tip may closes. After certain ranges of plane stress developed causes the fatigue crack to

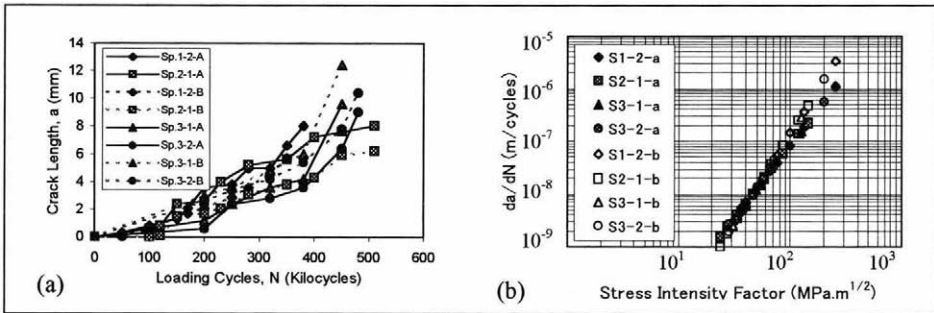


Fig.7 Fracture parameters: (a) damage curves; (b) ΔK factor versus crack growth rate.

change into increasing shear. Crack growth rate as a function of stress intensity range is shown in Fig.7 (b). Notch tip elongation is always observed in the beginning as after 5×10^4 cycles and with further cycling it would propagate rapidly as stress concentration rises towards the plastic zone leading to its final collapse. The crack growth behavior is very similar for the specimens considered. More experiment with a number of specimens is needed to establish and improve accuracy of the measurement technique.

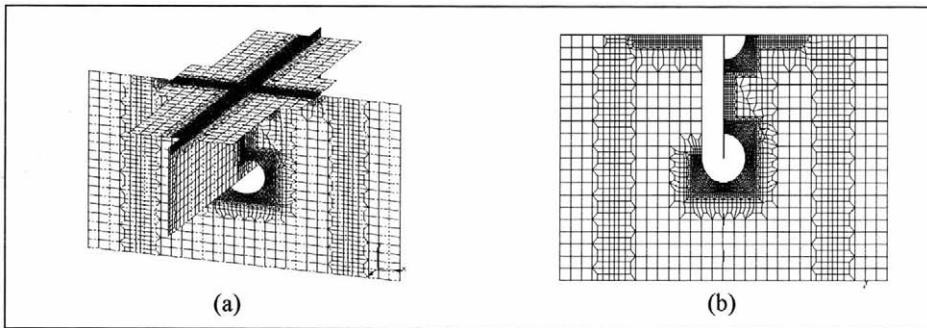


Fig.8 FEM model for crosswise rib: (a) total specimen; (b) scallop area details.

NUMERICAL STRAIN CALCULATION FOR CROSSWISE RIBS

The finite-element model of the crosswise rib accomplished by using MENTAT program of MARC analytic tool is shown in Fig.8. 4-nodes bilinear thick shell type elements used for analysis. The finite element model has 7857 elements with 7966 nodes. The whole specimen model is shown in Fig.8 (a). Size of the elements around scallop area has been progressively reduced to get more accurate trace of strain variation. Enlarged portion of the J-type scallop is

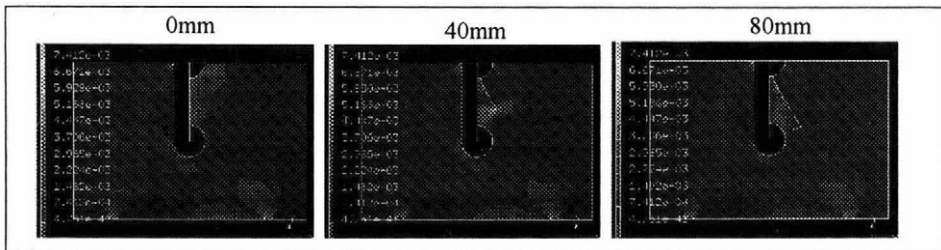


Fig.9 Strain variation due to crack elongation

illustrated in Fig 8 (b). Here elasto-plastic analysis considering monotonic stress-strain curve and not changing material properties of model elements near severe stress variation area. Boundary condition considered as fixed displacement at nodes of supports. Static loading of 16320 kg (160KN) as surface load applied at loading point that is equal to actual loading during experiment. The modulus of elasticity, yield stress and Poisson’s ratio are taken into computations as 210Gpa, 250Mpa and 0.30 respectively. In the Fig.9 strain variation due to static loading with crack length elongation around scallop areas are illustrated. From the color scale it is observed that higher strain value distributed around scallop area. Calculations done for crack shape in FEM model of crack length 0mm, 40mm and 80mm with same boundary conditions. Due to crack growth and elongation complex strain distribution occurs for changes in remaining area. Average strains are measured by stain gages. Results of maximum principal total strains are plotted to crack lengths are shown in Fig.12 (b). It is noted that a greater percentage of the specimens strained volume remains elastic. The finite element method, however, would need a different analytical tool to account for the elastic-plastic response of repeated loading.

MONITORING SYSTEM DETAILS

NDE techniques can be considered within the framework of structural diagnosis and monitoring. The accuracy of the diagnosis depends upon the resolution of the measurement system. Layout and detail components of our monitoring system are shown in Fig.10. There are essentially four main components for this condition based monitoring system that includes

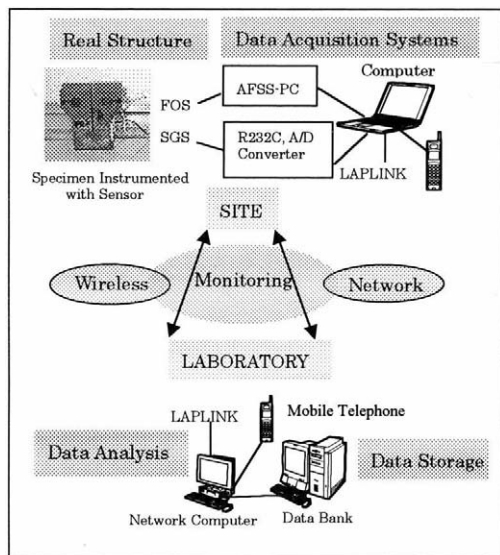


Fig. 10 Layout of monitoring system

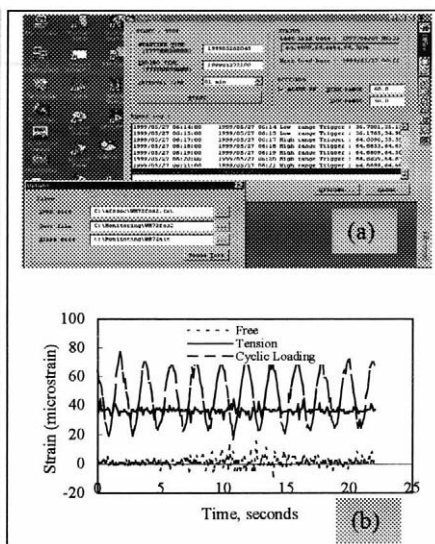


Fig. 11 (a) Windows display during monitoring, (b) strain responses (SGS).

sensors, data acquisition unit, data converter and data transmission unit [12]. An Absolute Fabry-Perot Support System (AFSS) used for data acquisition from fiber optic sensor. For strain gages we developed signal conditioner for RS232C serial data interface with A/D converter. LabView program is used to display in Windows environment for data measurement, display and recording. Monitoring software LabAssist can load file of data acquisition units and can automatically save measured data from mentioned starting time to

ending time. It has a convenient interval time setting capability that can set between 1 minute to 24 hour. Within this interval time three data can be record as data at interval time and minimum-maximum data during interval. It can also give alarm message when data exceeds the given limit or any abnormal change if occurs. Windows display of LabAssist and strain responses for loading conditions are shown in Fig.11 (a) and (b) respectively. Data file can be download to see previous data and control the computer from site to laboratory or laboratory to site by remote control software LAPLINK. A wireless modem mobile DP Card used with mobile telephone for download data from anywhere. DoPa service can transmit data at speed of 28.8Kbps. The mobile telephone has the operating frequency of 800MHz. DoPa modem card has the access to Internet provider for automatic data transfer.

STRAIN SENSING FOR REMOTE MONITORING

For Crosswise Rib

After clear confirmation of crack propagation from C-scan images strain monitoring starts after 255×10^4 loading cycles. The loading amplitude was same as 160KN ~ 1KN of frequency 5Hz. 3 strain gages attached at the locations shown in Fig.12 (a). The location choosing criteria considered from FEM analysis. Maximum and minimum strain data measured for 1 minute

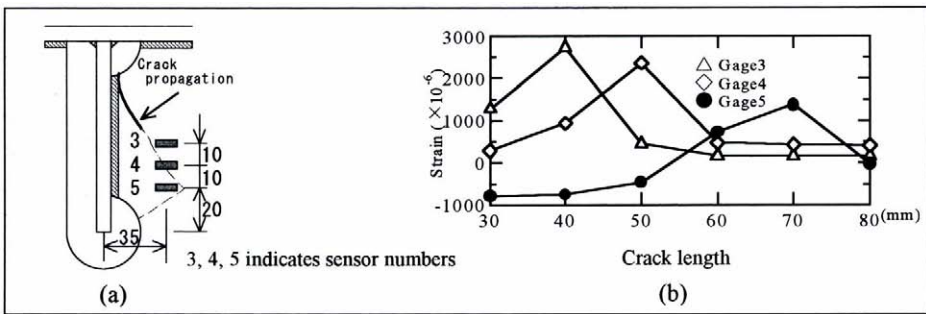


Fig.12 Strain measurement for crosswise rib: (a) sensor locations; (b) FEM results.

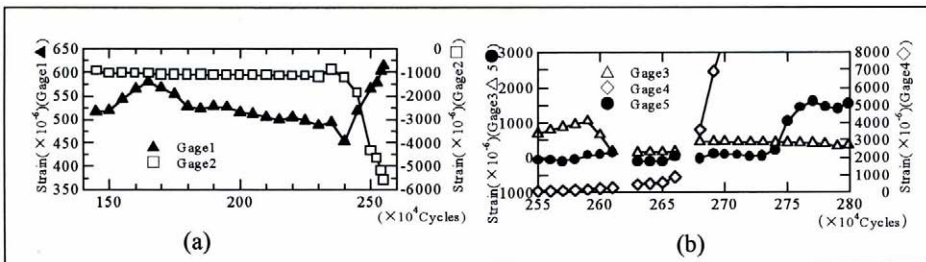


Fig.13 Measured strain data for crosswise rib: (a) strain measurement for 0~ 255×10^4 loading cycles; (b) monitored strain data during 255×10^4 ~ 280×10^4 loading cycles.

Interval till 280×10^4 loading cycles. From FEM model strain distribution measured from three sensor locations plotted to elongated crack length is shown in Fig.12 (b). Measured strain verses loading cycles are illustrated in Fig.13. It is observed that after 266×10^4 cycles irregular strain response occurred that can verified from FEM strain distribution. No data represents is due to interruption or measurement failure during monitoring. After 280×10^4 loading cycles

Gage4 failed and crack from two scallop area crossed each other and caused the specimen to complete failure. From numerical calculation as crack propagates stress concentration also varies according to crack length elongates. Sensor location could be chosen from numerical calculation and thus design for less sensor attachment will be possible.

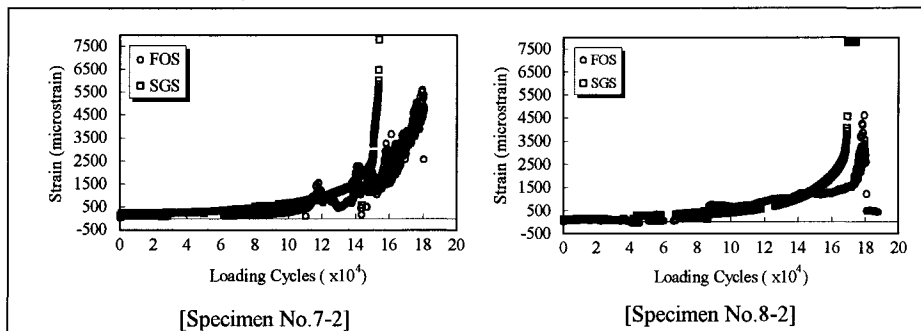


Fig. 14 Strain monitoring for V-notched specimen

For V-notched Specimen

Crack tip/notch tip expands and contracts in order to loading frequency, then sensor senses this fluctuation and average data represents as strain reading of the loading cycles. Monitoring status can be verified downloading by remote control software LAPLINK from laboratory to site. When the crack proceeds close to sensors sensing zone strain variation is observed. Comparison of measured strain for FOS and SGS are shown in Fig. 14. Sometimes negative or compressive strain is observed which is may be due to strain response for bond performance between sensor and specimen or crack tip deformation nature. Interval time for measurement was 2 minutes and applied loading frequency of 2Hz. After 14×10^4 cycles we set interval time of 1min and loading frequency of 1Hz for more detail strain data at near or end of fatigue life of the specimen. It is observed in Fig. 14 that strain reading gradually increased due to load increasing with time. The specimens were loaded for continuous monitoring for more than 100 hours though SGS failed to data measurement after around 15.2×10^4 cycles loading. It is noted that both sensors showed regular performance below 1600 microstrain. Notch tip elongation started at the very beginning of around 6×10^4 cycles and is clearly visualized (from C-scan image) after exceeding 10×10^4 cycles when strain reading is about 1300 microstrain. The difference of maximum-minimum strain increases as crack proceeds. Though the protection-coating bond of the sensor absorbs some portions of actual strain. The fiber optic sensor showed lower value of strain than strain gage sensors but it varied only within 5-10%. Sometimes error occurred during measurement of showing abnormal strain reading due to program error and data could not measured for file access error in Hardware. Crack clearly visualized with naked eye after 15×10^4 cycles for Specimen No. 7-2 and 17.8×10^4 cycles for Specimen No. 8-2. Before that both sensor showed unexpected abnormal strain data or failed to measurement. However the strain data is very similar at transition zone for both sensors even varying frequency of loading.

CONCLUSION

Ultrasonic testing performed with strain sensing for diagnosis and monitoring on laboratory specimens. From the damage accumulation curves and C-scan images it is clear that crack tip

propagated due to increased loading cycles. Sharp crack tip and rough crack surface affects in the energy transmission of transducer and C-scan images. Images are amplified and are obtained from varying focal positions, so it may differ in accuracy for actual crack propagation length. Material constants considered from reference journals for fatigue crack growth calculations. Proper bonding affected on the durability of sensor and measured data. In the fiber optic sensor measurement the sensors survived after loading and vibration that proves its durability in adverse situation. Crack propagation and strain variation depends upon load amplitude and frequency of loading.

Applicability of strain sensing technique and current motivations of NDE methods to diagnose fatigue crack for structural health monitoring have been verified in this paper. Ultrasonic testing performed on laboratory specimens that can be used for defect detection on real structures. New diagnostic tool for crack detection and evaluation verified in this research. Specifically we simultaneously monitored applied loads, crack tip propagation length, wave shape change and strain variation for accuracy improvement of ultrasonic testing. Before practical implementation numerical model is helpful to locate critical sections and locations. Taking these criteria into account the long-term use of fiber optic sensor as integrated measuring device for remote online monitoring via wireless, early damage assessment will be possible for aging structures.

Acknowledgements

This research work was supported by Grant-in-Aid for Scientific Research, Ministry of Education (MONBUSHO), Japan, to whom the authors wishes to express their sincere appreciation.

REFERENCES

1. Kavatura, M. and Shukla, A. (1998) *J. of Applied Mechanics*, Vol. 65, ASME, 293.
2. Chiang, M.M and Chai, H. (1998) *Int. J. Solids Structures*, Vol.35, No. 9-10, 799.
3. Miki, C., Sakano, M., and Murakoshi, J. (1988) *Str. Eng./Earthquake Eng.*, Vol.5, No.2, JSCE, 31.
4. Aktan, A. E., Farhey, N. D., Brown, D. L., Dalal, V., Helmicki, A.J., Hunt, V. J. and Shelly, S.J. (1996) *J. of Infrastructure Systems*, Vol.2, No3, ASCE, 108.
5. Rapheal, B. and Smith, I. (1998) *Artificial Intelligence in Structural Engineering*, Computer Science, LNAI 1454, Springer, Heidelberg, 308.
6. Rizkala, S., Shehata, E., Abdelrahman, A. and Tadors, G. (1998) *Concrete International*, ACI, 35.
7. Prine, D. W., An Overview of Remote Monitoring, *ASNT Spring Conference*, March 1997, Texas, USA.
8. Oshima, T., Mikami, S., Yamazaki, T., Rahman, M. S., and Taira, S (1997) *J. of Construction Steel*, Vol.5, pp. 295-302.
9. Claus, R. O., Gunther, M. F., Wang, A. and Murphy, K. A. (1992) *Smart Mat. and Struct.*, 1, 237.
10. Yamada, K., Cao, Q., Okuhara, Y. and Cheng, X (1998) *J. Struct. Mech. Earthquake Eng.*, JSCE, No598/I-44, 37.
11. Paris, P and Erdogan, F. (1963) *Transactions of the ASME*, 528.
12. Rahman, M. S., Oshima, T., Mikami, S., Yamazaki, T. and Tamba, I. (1999). In: *Structural Health Monitoring – 2000*, pp. 484-494, Chang F.K. (Eds). Technomic Publishing, USA.

NON - DESTRUCTIVE TESTING BEING ESSENTIAL PART OF THE SAFETY ASSESSMENT OF STEEL BRIDGES

K. BRANDES, J. HERTER and R. HELMERICH
Federal Institute for Materials Research and Testing (BAM)
Laboratory for Structural Safety
D - 12205 Berlin, Germany

ABSTRACT

Preservation of old structures for further use generally require a sound diagnosis of the present condition state. Together, the margins of safety of load carrying structures like bridges have to be verified. Taking into account some damage caused by decades of being in service. The big number of steel bridges having been installed about 100 years ago when the transportation systems were rapidly developed, which are subjects of doubts about their safety caused an extensive R&D project dealing with all safety-related methods of investigation. As a result, a big step forward has been reached concerning the rating procedure for old steel bridges including non-destructive testing methods.

KEYWORDS

Steel bridges, riveted bridges, remaining fatigue life, fatigue resistance, non-destructive testing, radiographic inspection, model identification

INTRODUCTION

Steel bridges were widely used during the rapid development of railway networks around the world. Up to now, many of them are still in service. Some of them are really benchmarks of ingenious bridge engineering like the Firth of Forth bridge in Scotland from 1889. Also road bridges were made of steel at that time. Steel structures suffer from corrosion and from heavy loading repeated frequently and causing fatigue sometimes damage to structural members.

The state of corrosion of steel structures can easily be recognised by visual inspection. However, fatigue damage is often hidden inside the structure which is assembled of many thin steel plates, fig. 1.

Simplifying the real problem, fatigue damage means the initiation and growing of small cracks by many stress reversals up to a critical crack length which causes the failure of the respective structural member. The initiation and growing of a crack is a function of the level of stressing. Therefore, the real stressing of structural members have to be evaluated not only by advanced calculation, but by measurement, together, which generates a validation of the structural modeling for calculation.

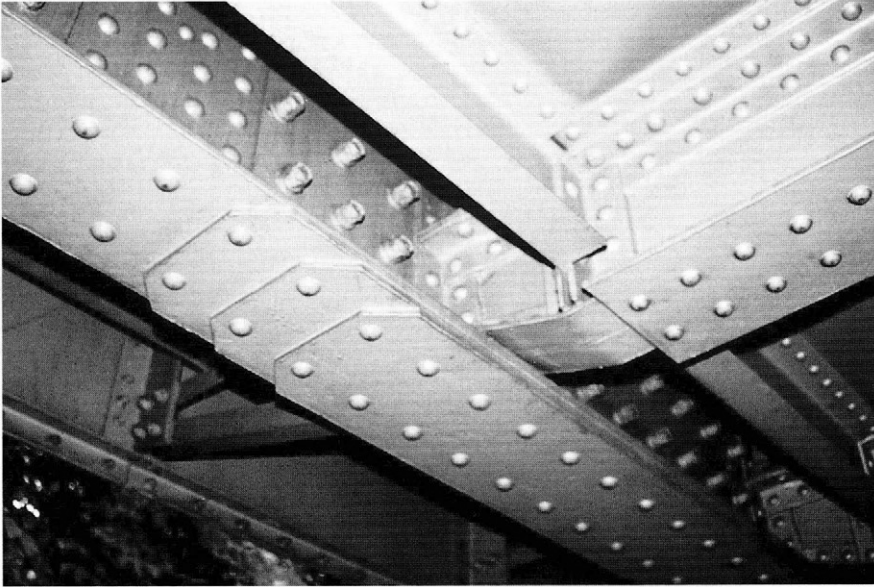


Fig. 1. Typical detail of riveted steel bridges where a crack in a covered plate is invisible

When dealing with an old steel bridge structure, we have to suspect that there are some cracks and we have to search for them because they might be dangerous to the structure. There are numerous methods of detecting cracks in steel structural elements like Ultrasonic Inspection or Magnetic Particle Inspection which can be applied successfully in many cases (not for wrought iron !).

Concerning riveted steel bridges, cracks very often grow in steel plates covered by other ones, fig. 1. Under these circumstances, easy detection is impossible. Only radiographic evaluation can help, however, it is rather doubtful whether a small crack in a steel plate covered by other plates and by heads of rivets can really be detected. In a series of large scale tests on real old steel bridges, we confirmed the effectiveness of a radiographic inspection on that type of structures.

PROBLEM

Corrosion is the one harm to steel bridges, fatigue the other one. Corrosion on the one hand is easy to detect, however, on the other hand, damage by fatigue stressing is often invisible. In principle, it is possible to have a look inside the structure by radiographic inspection (Gamma-ray radiography). However, in reality, it is impossible to inspect all the relevant structural elements of a big bridge, fig. 2.

There is the new approach (new to bridges !) of fracture mechanics dealing with the "life of cracks", real ones or, most frequently, hypothetical ones. This approach is new in the field of structural engineering and deviates from the "design thinking", however, contributes to the safety assessment of existing steel structures.



Fig. 2. Viaduct of the Berlin Underground railway system

Looking at the design procedure for bridges, there are S-N-curves (Stress range - Number of cycles - curves) available representing the resistance of structural members with typical constructional details to stress reversals, fig. 3. The number of stress reversals (stress cycles) amounts to many millions in a life of a railway bridge. The stress range of the cycles is different, however, the tests on structural member specimens have been performed on one-step-tests with only one amplitude which had been applied until fracture in the respective test after a big number of stress cycles. To find a correlation between the test results (S-N-curves) and the real stressing of a structural element necessitates the implementation of a "damage accumulation hypothesis" which is the so-called Palmgren-Miner rule [1]

$$D = \sum_i n_i / N_i \quad (1)$$

with the number of cycles n_i on that level which is related to N_i in the S-N-curve. D should become 1, however, there is a certain scatter which results from the scatter in the physical reality.

There is a similar rule for the propagation of a crack under stress cycles (Paris equation),

$$da / dN = C [\text{sqrt}(\pi \times a) \times \Delta\sigma \times f(a)] \exp(m) \quad (2)$$

with physical constants C and m ; da / dN means the extension of the crack of the length a with each stress cycle which is about (1 / 1 million) or less, fig. 4.

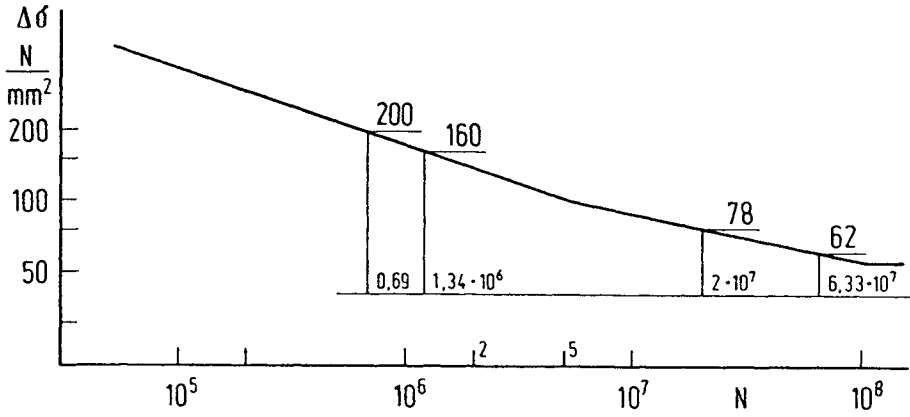


Fig. 3. S - N - curves for typical details of steel bridges according to European Codes

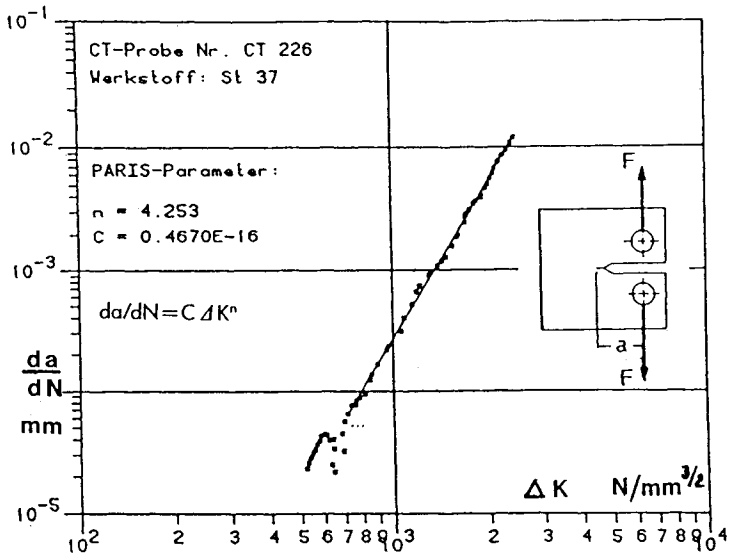


Fig. 4. Relationship between crack propagation da/dN and the stressing of a typical specimen (Paris equation)

It can be recognised from the equations that the accurate knowledge of the stress level is essential when rating steel bridges under heavy loading. Therefore, in most of the cases, the real stressing has to be evaluated by measurement and by validating the structural model for calculation according to the measured results.

After that procedure, we have a reliable idea about the stressing of any structural element and can identify those parts of the structure which are really endangered to cracking. For these parts only, a searching for cracks and a radiographic inspection is reasonable.

However, the question arises what is the resolution of the radiographic inspection when searching for a hidden crack in a plate covered by other ones or by rivet heads ?

DEVELOPMENT OF ADAPTED RADIOGRAPHIC INSPECTION

When being confronted with problems of detecting covered cracks, a lot of questions arises: How large will a crack become before it is detectable reliably ? What about the old steel material with the coarse internal structure ? How is the surface of a crack - is it rough and because of that only detectable when becoming very large ? Will be the angle of the crack perpendicular to the surface ? Do all cracks really start from rivet holes as experience up to now teaches ?

How to answer all these questions faultlessly and reliably ? The only way was to load real old structures until the occurrence of cracks, because we can not wait for the failure of some bridges under service conditions.

During several years, there were loaded cyclically dismantled large bridge structures on about that level they had been loaded by traffic before, fig. 5.

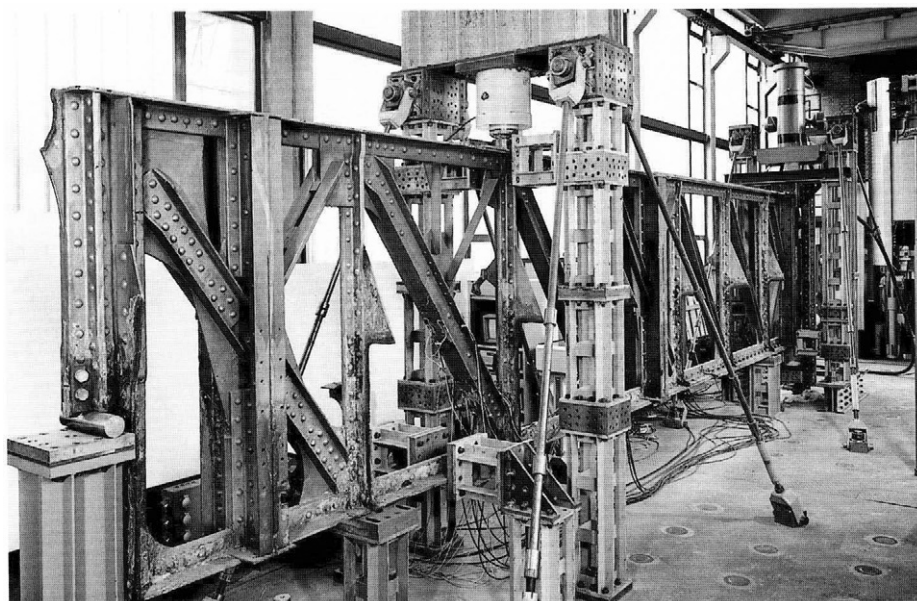


Fig. 5. Truss girder of the Berlin Underground railway which had been dismantled and has been loaded cyclically in the testing hall

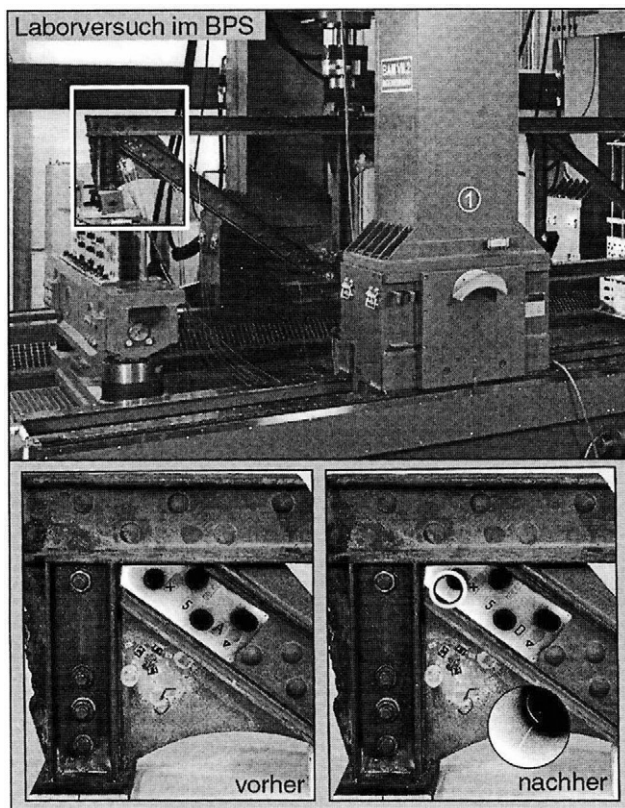


Fig. 6. Equipment for radiographic inspection applied in the testing hall of BAM on a dismantled truss girder. Above: Part of the testing arrangement. Below: Photographic trick shots with films of radiographic inspection fastened to the bridge taken before the test and after a crack had occurred.

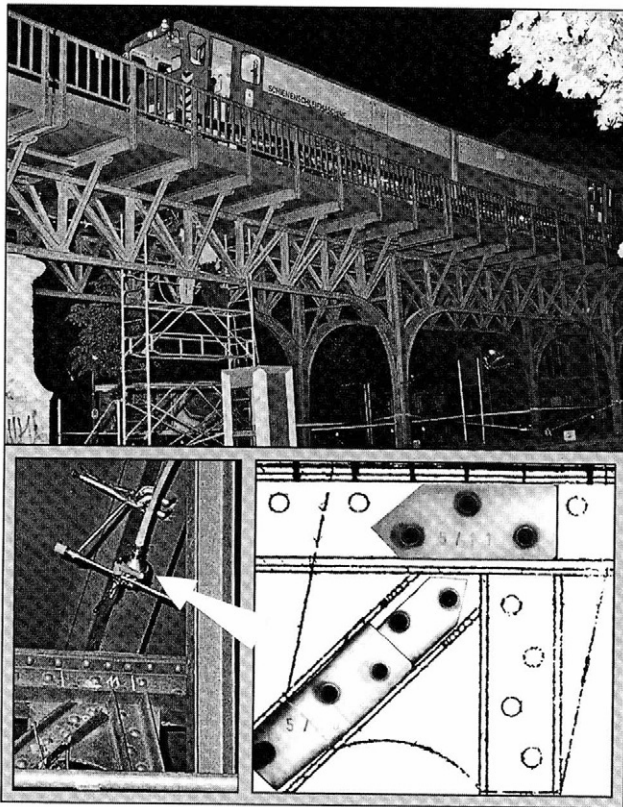
All the time, the long term tests were accompanied by measurement and, occasionally, by radiographic inspection, fig. 6. After detecting a crack, we removed the rivets and investigated the crack comparing its appearance with the result of the radiographic inspection result, fig. 8. There is needed some more investigation, however, the application for bridges being subject of rating is under way.

PRACTICAL APPLICATION

During the last about ten years, we investigated a large series of old bridges, and only once, we included radiographic inspection in 1999. This was a viaduct of the Berlin Underground railway system, fig. 7. It was necessary because we knew from tests on similar structures that the connecting plates ("gusset plates") were the weakest elements in terms of fatigue resistance. At the end of a complicated procedure of rating, we applied radiographic inspection to about 40 gusset plates of more than 300, to some of them with more than only one exposure. Each exposure needs about 15 to 25 minutes. Only in one of the nodes, cracks were identified.

When recouring to fracture mechanics for evaluating the propagation of a crack, it was possible to refer to the real length of the crack as had been identified from the radiographic inspection. Otherwise, we had to refer to some assumption about crack length which is often to large and misleading to a very short "remaining fatigue life".

SUMMARY



After several years of development of advanced rating procedures for old riveted steel bridges, a comprehensive procedure has been established comprising different methods of investigation crowned by radiographic inspection as a logical consequence of a fracture mechanics approach to fatigue resistance of structural members and whole bridges. The procedure, just now, has been approved by practical application.

Fig. 7. Radiographic inspection at a viaduct of the Berlin Underground railway system by night in 1999. The radiographic source is indicated on the photograph below left, the films of the three exposures are arranged below right

REFERENCES

1. Geissler, K. and Brandes, K.. Bauingenieur 71 (1996), pp 541-553
2. Helmerich, R., Brandes, K., and Herter, J. : Int. Ass. Bridge and Structural Engineering (IABSE) Workshop "Evaluation of Steel and Composite Bridges", Lausanne, 1997, IABSE Reports Vol. 76 (1997), pp 191- 200

This Page Intentionally Left Blank

DETECTION OF STRUCTURAL DAMAGE BY AMBIENT VIBRATION MEASUREMENT USING LASER DOPPLER VIBROMETER

Kiyoyuki Kaito, Masato Abe, Yozo Fujino and Hidenori Yoda
*Department of Civil Engineering, The University of Tokyo
Hongo 7-3-1, Bunkyo-ku, Tokyo, 113-8656, Japan*

ABSTRACT

In order to detect local damage in structures using vibration measurement, identification of high order vibration modes is needed. However, in civil structures, the difficulties of measuring spatial vibration and disturbance decrease the identification accuracy of higher modes. Laser Doppler Vibrometer can be applied to reliably measure vibration characteristics of spatially large civil structures under microscopic vibration such as ambient vibration. In this study, non-stationary and random components in measured ambient vibration are eliminated by sweeping the area of interested and stacking the time histories recorded repeatedly. In this way, mode shapes can be identified with high accuracy by assuming the ambient vibration as a stationary process even without the knowledge of input excitation. Then, the measured modal frequencies and mode shapes after damage and measured data before damage are compared to inversely solve the location and extent of stiffness change which will indicate the degree of damage in the structure. The method is demonstrated by experiments of plate vibration with additional mass which simulates local stiffness degradation.

KEYWORDS

Laser Doppler Vibrometer, Ambient Vibration, Spatial Vibration Measurement, Mode Shape, Damage Detection

INTRODUCTION

The establishment of appropriate maintenance method for enormous infrastructures in Japan is an urgent problem [1]. Especially, the maintenance method, which is possible to detect damage based on quantitative data and hand down final judgments objectively, is expected [2].

The change of modal frequencies and mode shapes is considered as one of the indexes that can evaluate damage quantitatively [3, 4]. Particularly, mode shape possesses the possibility of detection of initial damage, because it is changed sensitively for local damage. However it is difficult to identify mode shape of large infrastructures by following reasons.

Spatial vibration measurement is needed. Therefore, current measurement technique using an

accelerometer, which is one of the attachment type devices, causes lack of measurement points and decrease of accuracy. On the other side, mode shape has to be identified without knowledge of input excitation such as wind force, traffic load and ground motion due to the difficulties in measurement [5]. Considering above things, objectives of this paper are,

1. The establishment of spatial vibration measurement method using Laser Doppler Vibrometer
2. The construction of accurate identification method for higher mode shapes without knowledge of input excitation
3. The suggestion of local damage detection method based on change of mode shape

First of all, the spatial vibration measurement system is constructed by automatically controlling irradiation angle of laser beam of Laser Doppler Vibrometer. Next, measured vibration results are processed by spatial and temporal averaging. By these processes, non-stationary and random components in measured ambient vibration are eliminated, and stationary component is extracted. Then mode shape is identified by assuming the ambient vibration as a stationary process. Finally, with respect to damage detection, the change of mass and stiffness by damage is quantified. To be concrete, measured mode shapes before damage are added the change of mass and stiffness virtually, and the mass and the stiffness are inversely calculated by minimizing the error between solved mode shapes and measured ones after damage. Especially, the damage detection method that is able to directly use measured vibration results is suggested to decrease the error caused by idealizing material characteristics. Further, to investigate the validity of above methods, experimental verification for each method is demonstrated.

IDENTIFICATION OF MODE SHAPE BY SPATIAL VIBRATION MEASUREMENT

Laser Doppler Vibrometer

Laser Doppler Vibrometer (LDV) is an optical measurement device that is able to detect velocity of moving objective using the difference of frequencies between irradiation and reflection laser (Fig.1). The features are shown as following, and concrete characteristics are shown in Table.1.

At first, LDV is able to measure vibration by non-contact method. There is no surface processing such as attachment of reflection tape. Second, it possesses extremely high resolution, and capable to measure in wide frequency range. Therefore, it is able to accurately measure until high frequency vibration component of the spatially large civil structures, which are difficult to set sensors, under ambient vibration. Third, LDV can measure spatially many points by controlling irradiation angle of laser beam by rotating two reflection mirrors in the sensor head.

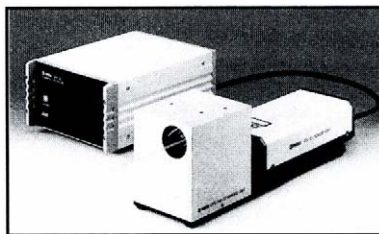


Fig.1. Laser Doppler Vibrometer

Table 1. Characteristics of LDV

Laser type	He-Ne Laser
Wave length	633nm
Laser output / class	2mw / 3A
Possible measurement distance	100m
Resolution	0.5 μ m/sec
Measurement frequency range	0 ~ 35kHz
Laser irradiation Range	-15 ~ 15 $^{\circ}$

Spatial Vibration Measurement using LDV

Spatial vibration measurement system that is able to measure vibration at designated points in selected range is constructed by controlling irradiation angle of laser beam automatically (Fig.2) [6, 7].

In identification of mode shape, measured vibration results are needed high accuracy as a matter of course. However speckle noise, which is circled in Fig.3, is often contained in recorded time history, when optical measurement device is used. Minute response spectrum can not be measured by containing much speckle noise, which causes the decrease of identification accuracy. Therefore the decrease countermeasures of speckle noise are carried out by both hardware and software side.

The content of speckle noise is entirely different by microscopic change of irradiation point of laser beam. So, changing the irradiation angle per 0.01 degree around the first measurement point each repetitive measurement, concentrated contain of speckle noise for a particularly point is prevented.

Next, the standard deviation of the measured vibration results is calculated, and the response that has constant time larger than the standard deviation is considered as speckle noise. Then, in the case that contained less than five speckle noise in one measured vibration results, the extraordinary values are re-calculated by the front and the rear data, and in the case that contained more than five speckle noise, the measured vibration results were eliminated when the averaging of the spectrum was carried out.

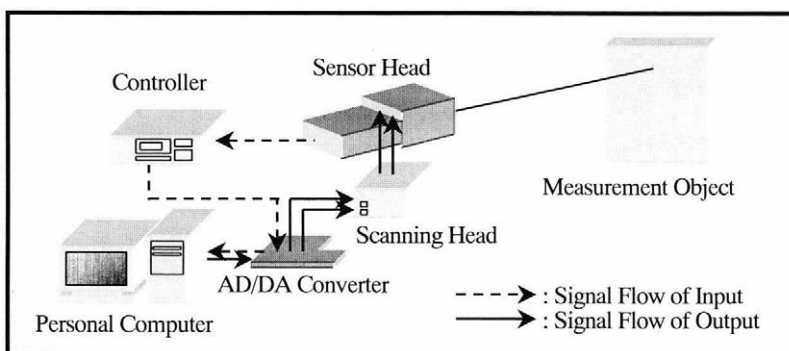


Fig.2. Spatial vibration measurement system

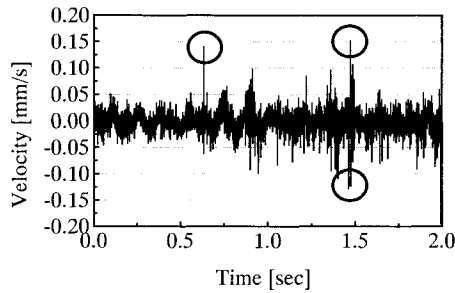


Fig.3. Speckle noise

Identification Method of Mode Shape without Knowledge of Input Excitation

The measured vibration results using LDV can not be measured all points at the same time. Furthermore ambient vibration that is used as input is random vibration, which possesses non-stationary, so usually mode shapes can not be identified. Then following averaging methods are carried out.

At first, the effect of non-stationary in measured ambient vibration is dispersed by getting shorter of the measurement time for one point and sweeping the area of interested. Next, temporary averaging that random components is stacked the time histories recorded repeatedly is carried out. In these way, stationary vibration components are extracted from ambient vibration without knowledge of input excitation, and then mode shape is identified by counting peak amplitudes of spectrum.

Experimental Verification

The identification of mode shape for a steel plate ($385 \times 300 \times 2$ [mm]), which was fixed at one side, was demonstrated experimentally.

With respect to measurement condition, measurement points were arranged as 20 points along vertical direction and 15 points along horizontal direction, and total 300 points were set. Measurement time was 2048[sec] per point considering the step size of frequency and the length of measurement time. Sampling frequency was decided as 2000[Hz] from objective modal frequency. Then, the measured vibration results were recorded into the a personal computer through an AD converter. On the other hand, the change of measurement point was controlled by the personal computer through a DA converter. In this measurement, the maximum irradiation angle was 4 degrees.

Based on this measurement condition, measured velocity amplitude spectrum was averaged by 300 times repetitive measurement. The 5 times standard deviation per each measured vibration result was employed to judge speckle noise.

Fig.4 shows the comparison of averaged velocity amplitude spectrums between 1 and 300 times repetitive measurement. From this figure, noise level was suppressed by the averaging process, and the peak of high frequency vibration component was stuck out clearly.

The identified 6th and 14th mode shapes, which were changed in repetitive number [10,100,300], and theoretical analysis results of the plate by Rayleigh-Ritz method [8] are shown in Fig.5. The mode

shapes were normalized that maximum value became 1, and the absolute values were plotted. It is clear that the identified mode shapes are closely to the theoretical results, as the number of repetitive measurement is increased. Therefore it can be considered that non-stationary and random component in measured ambient vibration are eliminated by 300 times repetitive measurement. Table.2 shows the comparison between identified modal frequencies and theoretical ones. From this table, 10 mode shapes until 16th mode were identified in this vibration measurement.

Moreover, in Fig.4, many peaks except for vibration components are stuck out. These are caused by vibration component of LDV, electric noise and so on. For example, these peaks are extracted and plotted in Fig.6. This shape is not obviously different from mode shape of the plate. Therefore mode shapes and the other noise components can be distinguished visually using this proposed method.

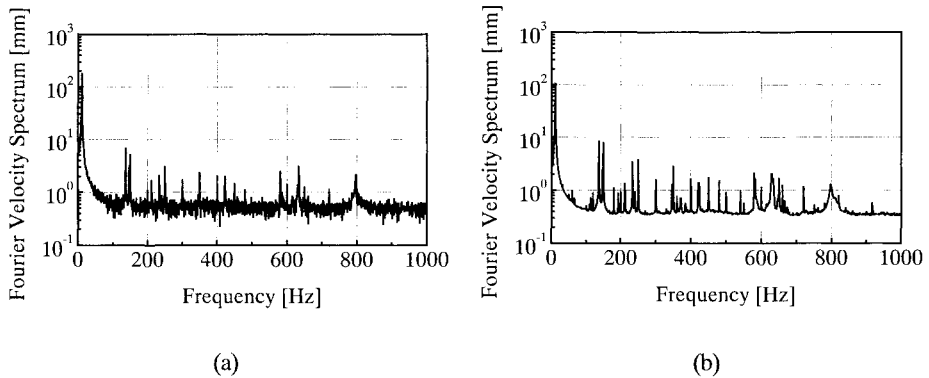


Fig.4. Comparison of averaged velocity amplitude spectrum: Repetitive number (a) 1; (b) 300

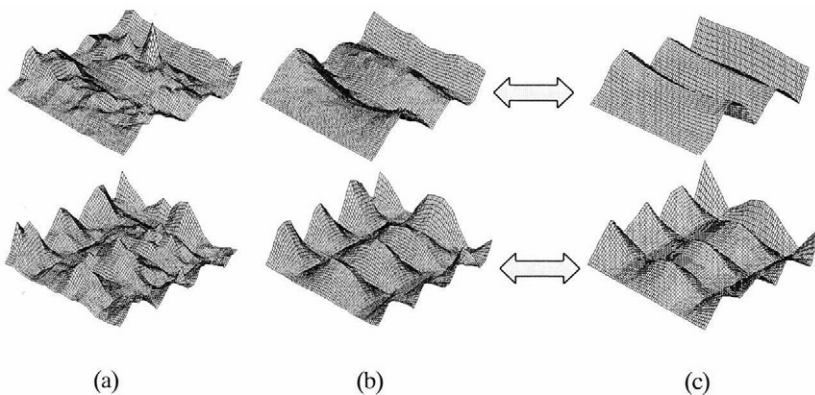


Fig.5. Comparison of identified mode shapes and theoretical ones: (a) Repetitive number: 1; (b) Repetitive number: 300; (c) Theoretical mode shapes (6th mode; above, 14th mode; below)

Table 2. Identified Modal Frequencies

Mode order	Theoretical Value [Hz]	Identified Value [Hz]
1	12.07	10.74
2	34.18	—
3	76.01	66.41
4	121.0	112.8
5	135.0	137.2
6	212.7	192.4
7	234.5	233.9
8	260.9	—
9	336.7	—
10	391.6	384.8
11	417.7	371.1
12	432.5	—
13	465.6	—
14	599.5	580.1
15	606.0	—
16	686.4	666.5

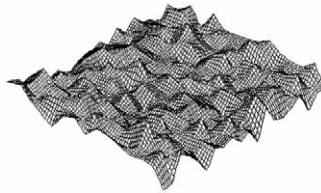


Fig.6. Vibration shape due to noise

DAMAGE DETECTION BASED ON THE CHANGE OF MODE SHAPE

Identification Method of Change of Mass and Stiffness Caused by Damage

The effect of structural damage comes out as the change of mass and stiffness of structures. So the quantitative knowledge of mass and stiffness decrease is needed to evaluate damage degradation. Hence, the damage detection method based on the change of mode shape before/after damage is suggested. The merit of this method is that information of material characteristics, geometrical shape and boundary condition is not needed if modal frequencies, mode shapes before/after damage and mass density are obtained. That is, the damage detection can be carried out by identified modal frequencies and mode shapes before/after damage using the spatial vibration measurement method, if mass density is obtained. The theoretical procedure is shown as follow.

At first, it is considered that negative mass and stiffness are added to the objective structure by damage. Considering that the structure before damage, additional mass and stiffness are separated, total kinetic

energy : T and potential energy : V are shown in the following equation [9].

$$T = \frac{1}{2} \sum_{i=1}^N M_i \dot{q}_i^2 + \frac{1}{2} \sum_{j=1}^J m_j \dot{u}_j^2 \quad (1)$$

$$V = \frac{1}{2} \sum_{i=1}^N K_i q_i^2 + \frac{1}{2} \sum_{j=1}^J k_j u_j^2 = \frac{1}{2} \sum_{i=1}^N \omega_i^2 M_i q_i^2 + \frac{1}{2} \sum_{j=1}^J k_j u_j^2 \quad (2)$$

In these equations, i is mode order, N is total mode number. M_i, K_i, ω_i and q_i show modal mass, modal stiffness, modal frequency and modal displacement of i th mode, respectively. On the other side, j is the number of additional mass and stiffness, J is total number of those. m_j, k_j and u_j show j th additional mass, stiffness and the displacement at point j respectively. Further \dot{q}, \dot{u} means first derivative of q and u with respect to time. However, the amount of J numbers of restrict conditions, which are shown as following equation, have to be considered at each additional location j of mass and stiffness.

$$\sum_{i=1}^N \Phi_i(j) q_i - u_j = 0 \quad (j = 1, \dots, J) \quad (3)$$

Hence, $\Phi_i(j)$ is i th mode shape before damage at point j . Considering the restrict conditions of Equation(3), Lagrange function is given by next equation.

$$L = T - V + \sum_{j=1}^J \lambda_j \left\{ \sum_{i=1}^N \Phi_i(j) q_i - u_j \right\} \quad (4)$$

λ_j is Lagrange's unknown parameter. By Lagrange's motion equation,

$$\frac{\partial}{\partial t} \left(\frac{\partial L}{\partial \dot{q}_i} \right) - \frac{\partial L}{\partial q_i} = 0 \quad (5)$$

is given, then the following two equations were obtained by expanding Equation(5) with respect to u_j , the same as q_i .

$$M_i \ddot{q}_i + \omega_i^2 M_i q_i - \sum_{j=1}^J \lambda_j \Phi_i(j) = 0 \quad (6)$$

$$m_j \ddot{u}_j + k_j u_j + \lambda_j = 0 \quad (7)$$

Hence, $q_i = \bar{q}_i e^{i\omega t}$, $u_j = \bar{u}_j e^{i\omega t}$, $\lambda_j = \bar{\lambda}_j e^{i\omega t}$ are substituted into Equations(5),(6),(7),

$$-\omega^2 M_i \bar{q}_i + \omega_i^2 M_i \bar{q}_i - \sum_{j=1}^J \bar{\lambda}_j \Phi_i(j) = 0 \quad (8)$$

$$-\omega^2 m_j \bar{z}_j + k_j \bar{z}_j + \bar{\lambda}_j = 0 \quad (9)$$

$$\sum_{i=1}^N \Phi_i(j) \bar{q}_i - \bar{z}_j = 0 \quad (10)$$

were given. Next equations are derived as z is eliminated by solving equations given by Equations(8),(9),(10).

$$\left[\omega_i^2 M_i \bar{q}_i - \sum_{j=1}^J k_j \sum_{i=1}^N \{ \Phi_i(j) \bar{q}_i \} \Phi_i(j) \right] - \omega^2 \left[M_i \bar{q}_i + \sum_{j=1}^J m_j \sum_{i=1}^N \{ \Phi_i(j) \bar{q}_i \} \Phi_i(j) \right] = 0 \quad (11)$$

Therefore, the calculation of modal frequencies and mode shapes of the structure after damage is come back solving eigen problem given by following equation [10].

$$\left[\mathbf{A} - \omega^d \mathbf{B} \right] \nu = \{0\} \quad (12)$$

\mathbf{A} and \mathbf{B} are matrices($N \times N$), the components for each matrix are shown by following Equations(13), (14). And ω^d is equal to ω , ν is the N order vector $\{\bar{q}_1 \cdots \bar{q}_N\}^T$.

$$A_{mn} = \delta_{mn} \omega_m^2 M_m + \sum_{j=1}^J k_j \Phi_m(j) \Phi_n(j) \quad (13)$$

$$B_{mn} = \delta_{mn} M_m + \sum_{j=1}^J m_j \Phi_m(j) \Phi_n(j) \quad (m = 1, \dots, N, n = 1, \dots, N) \quad (14)$$

In the above equations, δ is the Dirac's delta function. Therefore, i th modal frequency after damage is given by ω_i^d , mode shapes Φ_i^d after damage is obtained by

$$\Phi_i^d = \sum_{j=1}^N v_{ij} \Phi_j \quad (15)$$

So, unknown parameters, which were needed to calculate mode shape after damage, are only additional mass, stiffness and location, if the distributed mass of structures and mode shapes before damage are obtained.

m_j and k_j are identified by minimizing the following evaluation function(16), that is the difference between the mode shape : Ψ and modal frequency : ϖ after damage measured by spatial vibration measurement and ones obtained analytically is minimized.

$$E = \sum_{i=1}^N \left[\sum_{k=1}^P \left\{ \frac{\Psi_i(k) - \Phi_i^d(k)}{\Phi_i^d(k)} \right\}^2 + \left\{ \frac{\varpi_i - \omega_i^d}{\omega_i^d} \right\}^2 \right] \quad (16)$$

P is the total number of measurement points.

Identification Experiment of Additional Mass

The experiment to identify location and size of damage was demonstrated by adding a mass to the plate used in the previous section. A magnet was employed as an additional mass. The additional location and size are shown in Fig.7(a). The spatial vibration measurement were carried out both plates before/after adding mass, the additional location and size were identified by the suggested method. In this case, k_j in Equation(13) could be ignored, because identification object was only the change of mass. In the same figure, identification result is shown. However it is able to verify little error with respect to both location and size. Especially, identification result about additional mass size was obtained as 300[g], for exact value was 376[g]. This reason was caused by that non-symmetry mode shapes before additional mass could not be measured. Therefore, it was considered the mode shapes after additional mass as before condition, another mass, which possesses different mass size, was added. The identification result are shown in Fig.7(b), it is able to verify that identification accuracy of additional location and size are increasing.

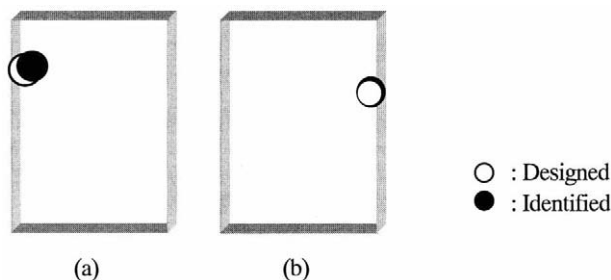


Fig.7. Identification results: (a) case1(designed: 376[g], identified: 300[g]);
 (b) case2(designed: 118[g], identified: 150[g])

CONCLUSIONS

1. Spatial vibration measurement method was constructed by controlling automatically irradiation angle of laser beam of LDV.
2. Identification method of high order mode shapes was constructed without knowledge of excitation by eliminating non-stationary and random component measured ambient vibration with repetitive vibration measurement.
3. Damage detection method that was possible to identify local damage directly using only spatial vibration measurement results was suggested.

REFERENCES

1. Nishikawa, K. (1997) : A Concept of Minimized Maintenance Bridge, *Bridge & Base*, Vol.31, No.8, pp.64-72 (in Japanese)
2. Abe, M. (1998) : Structural Monitoring of Civil Structures using Vibration Measurement –Current Practice and Future–, *LNAI 1454 Artificial Intelligence in Structural Engineering*, pp.1-18
3. Salawu, O.S. (1997) : Detection of Structural Damage through Changes in Frequency : A Review, *Engineering Structures*, Vol.19, No.9, pp.718-723
4. Doebling, S.W., Farrar, C.R., Prime, M.B., Shevitz, D.W. (1996) : Damage Identification and Health Monitoring of Structural and Mechanical Systems from Changes in Their Vibration Characteristics : A Literature Review, *LA-13070-MS*
5. Farrar, C.R., Duffey, T.A., Cornwell, P.J., Dowbling, S.W. (1999) : Excitation Methods for Bridge Structures, *Proceedings of 17 International Modal Analysis Conference*, pp.1056-1062
6. Kaito, K., Abe, M., Fujino, Y. and Yoda, H. (1999) : Measurement of Mode Shape using Laser Doppler Vibrometer and Application to the Damage Detection, *Proceedings of 2nd Structural Diagnosis Symposium*, pp.157-162 (in Japanese)
7. Yoda, H., Abe, M., Fujino, Y. and Kaito, K. (1999) : Experimental Modal Analysis using Laser Doppler Vibrometer, *Proceedings of 54th Annual Conference of JSCE* (in Japanese)
8. Leissa, A.W. (1969) : Vibration of Plates, *NASA Special Publication SP-160*
9. Dowell, E.H. (1979) : On Some General Properties of Combined Dynamics Systems, *ASME Journal of Applied Mechanics*, Vol.46, pp.206-209
10. Kaito, K., Abe, M., Fujino, Y. and Tariq, M.T.A. (1999) : Performance Evaluation of a Base-Isolated Bridge using Complex Modal Analysis, *Proceedings of 17 International Modal Analysis Conference*, pp.1749-1755

This Page Intentionally Left Blank

RADAR AND SEISMIC TOMOGRAPHIES ON GYPSUM PILLARS

X. DÉROBERT, O. ABRAHAM

Department of survey and soil mechanics, Central Laboratory of Bridges and Roads,
44340 Bouguenais, France

ABSTRACT

A combination of ground penetrating radar and seismic tomographies has been done in a gypsum quarry in western Europe. The objective was to localize the main cracks, and the damaged areas inside pillars which presents some indication of stress limits.

The GPR tomography has been designed, from classical profiles with GPR processes and an home made imaging processing software for PC. The seismic tomography is obtained from travel time measurements, which are inverted by a SIRT technique in order to give a map of seismic velocities.

The two techniques are compared on different pillars, by presenting the similarity and the complementary aspects revealed by the tomographies. Indeed, the seismic tomography gives a map of velocities, related to the state of the internal stress of the pillar, and the radar data localize the main fractures.

KEYWORDS

Ground Penetrating Radar, Seismic, Data processing, tomography, Imaging, Fractures, Damaged zones.

INTRODUCTION

A gypsum quarry in western Europe has revealed stability problems which require local reinforcement. For this purpose, a non destructive technique (NDT) campaign has been carried out. The objective herein was to localize the weathered areas inside these pillars, which correspond to high levels of stress, along with the main cracks. Two complementary techniques were employed : seismic tomography and radar investigation.

Ground penetrating radar (GPR) is a very useful technique for carrying out geological NDT, which detects dielectric contrasts at the boundary planes by the reflection of electromagnetic (em) pulses measurements. In general, the rock's dielectric attenuation is very low, thereby suggesting several meters of radar investigation [1,2]. Although this technique is quick and easy to use, its major limitation lies in its inability to yield information on the state of stress in the structure.

For this reason, a secondary aim of seismic tomography is to produce a map of objects' internal mechanical properties in a non invasive fashion. By measuring the travel times of the compression wave between source and receiver points around the object, it is possible to calculate a map of the compression wave velocity. In the case of an *a priori* homogeneous

material, the appearance of a zone of lower velocity indicates that the material has weathered locally.

RADAR INVESTIGATION

The GPR system is a SIR-10A, manufactured by GSSI, and is associated with a 500 MHz shielded antenna. The range has been selected in order to ensure rising the backs of the pillars. We took measurements (4 GPR profiles) at a height corresponding to the minimum section of the pillar at which point the horizontal seismic tomography was conducted (Fig. 1).

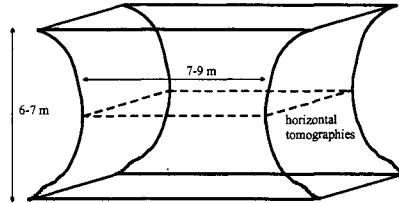


Fig. 1. Shape of a pillar under test.

Successive GPR processing steps have been employed in order to localize cracks and damaged zones from the different sides. After a vertical high-pass filter (over 250 MHz) on the profiles, the first step consisted of normalizing the surface. Afterwards, frequency bandpass filters were applied in order to remove all noise. The next step involved the use of a time migration to focus the electromagnetic energy and establish a relation between time and distance; these measurements take into account the possibility of errors due to the 3D shape of the pillar. Following this step, we concluded with the Hilbert transform in order to present the reflected energy (Fig. 2).

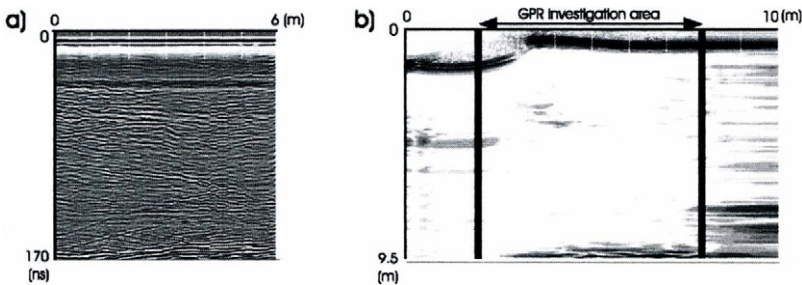


Fig. 2. Processing applied to GPR data. a) Untreated data; b) GPR data after the Hilbert transform.

This last GPR processing step then provides the basis for the radar imaging. Since these profiles were already migrated and surface normalized, the four maps can be superimposed in order to represent the pillar by a radar image. The dark plots are then added, thus increasing the darkness, with the assumption that the result is correlated with a high damage level. This last step is accomplished by means of an image processing software for PCs called "PICTURE", which has been designed and developed at the LCPC laboratory by J.M. Moliard (see Fig. 3).

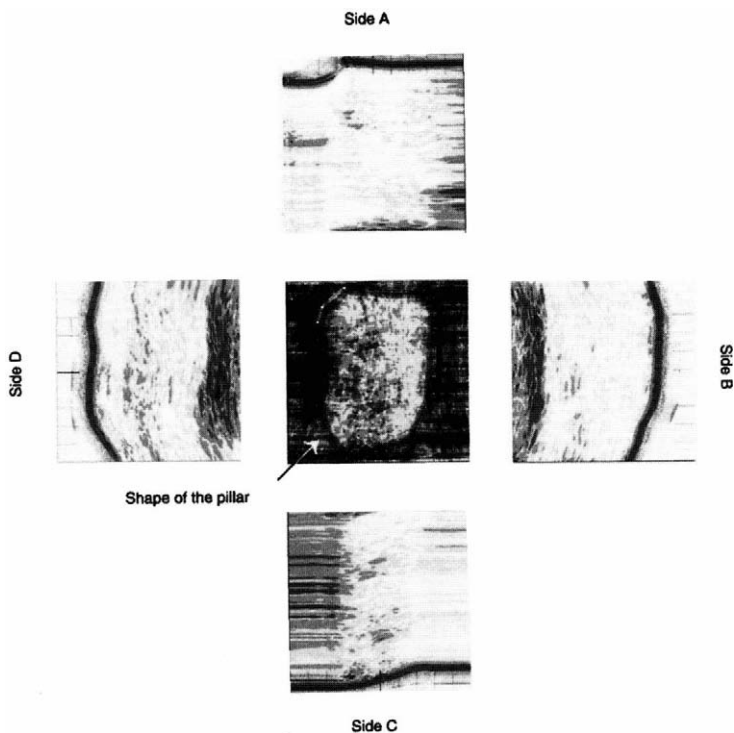


Fig. 3. Radar tomography by image processing.

The borders of the pillars are drawn over the radar tomographies in order to localize the damaged areas, to avoid taking into account the gray values beyond the pillars, and to allow paying special attention to those areas located very close to the borders. We consider that the dark plots have been correctly added, due firstly to the fact that the surface normalization gets corrected by the half-wavelength of the radar pulse, and secondly because visual investigation showed only vertical, or sub-vertical, external cracks on the pillars (no 3D migration corrections needed).

SEISMIC TOMOGRAPHIC INVESTIGATION

Even though the geometry of a pillar is essentially 3D, we carried out our measurements in 2D. As the major zone of interest is around the pillar's smallest section, where are located the highest stressed zones, the seismic velocities are also highest, keeping the ray paths in the horizontal plane.

We located 9 equidistant source/receiver points on each side. Afterwards, a surveyor provided us with all of the NGF (French geographic standards) coordinate points. A Krenz data-acquisition system of transitory signals (the TRC 4000 and TRC 4011 model), with sampling frequencies of up to 1 MHz on 10 channels (10 bits), was used to collect and store the seismic signals on a microcomputer. The arrival times and the coordinates were then fed into the RAI-

2D algorithm for inversion. The tomography algorithm used in this paper, RAI-2D, was developed by the LCPC laboratory [3]. RAI-2D has been inspired by the SIRT method [4].

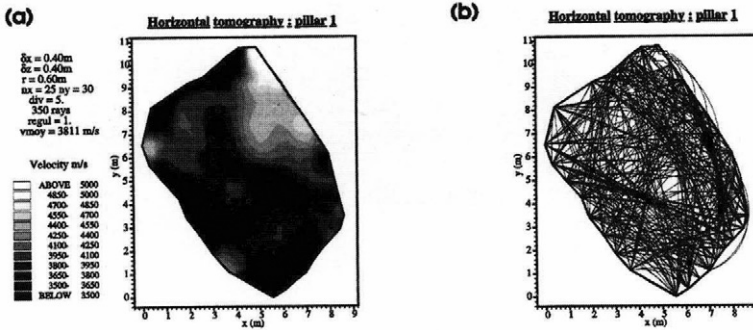


Fig . 4. a) Seismic tomography on pillar 1. b) Ray curve density.

The seismic tomography reveals a large damaged zone inside the section extending downwards (see Fig. 4a). The rays tend to travel around this damaged area. Apart from a small zone in the upper right-hand part, the pillar is quite damaged. Its mean velocity (3,811 m/s) is well below the average velocity of mechanically sound pillars at this level (around 4,500 m/s).

COMPARISON AND INTERPRETATION

As previously discussed, these two geophysical techniques provide complementary information. The first classical means of combination therefore is to superimpose the cracks detected by GPR onto the seismic tomography displaying the velocities. But the major problem concerns the human factor on the cracks' pointing. So, the automatic GPR imaging process avoids any interpretation error due to arbitrary choice : an absence of cracks signifies a homogeneous area.

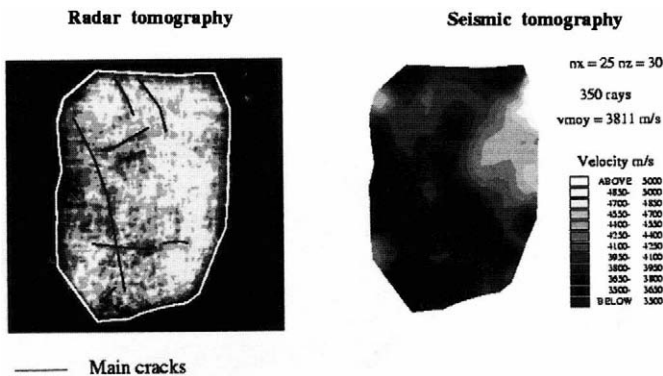


Fig. 5. Radar and seismic imaging on pillar 1.

Figure 5 presents both tomographies simultaneously for Pillar 1. GPR imaging is carried out to focus the presentation not only on the cracks but also on the diffracting areas. However, we must take into account the em energy resulting from the main cracks, which can locally increase the apparent em damage level. For this reason, it is useful to include the information from the presentation of the cracks into the radar imaging.

Similarly, the damage zones are localized by low seismic velocities (plotted in dark). Pillar 1 therefore appears to be a good example of a non-homogeneous pillar, in which most of the damaged zones are detected either by GPR or by seismic imaging. Both the left and center parts of the pillar display lower seismic velocities and higher densities of em reflected energy at the same locations.

CONCLUSION

This work has been conducted in order to compare two kinds of tomographies, using electromagnetic and seismic waves, as well as to propose to geologists a radar imaging technique for quarry pillars.

Seismic tomography presents the tremendous advantage of providing direct information on the soundness of surveyed structures or pillars. The main limitations herein stem from the impossibility of detecting major cracks in a homogeneous material, and the overall cost implied.

GPR has been proposed as a complementary technique. This paper has thus presented an automatic processing technique which enables constructing a damage-related radar image that can support the superimposed drawing of main cracks. GPR profiles are filtered, surface normalized, migrated, Hilbert transformed and, at last, added in order to present an image of the reflected energy.

Comparative experiments have been performed on some pillars; results suggest some strong analogies. This observation will have to be confirmed under other test conditions and on other materials in order to accurately determine the limitations of this analogy.

ACKNOWLEDGEMENTS

The authors wish to thank J.M. Moliard, from the LCPC - Image Processing Section, for his kind help and high-performance imaging software "PICTURE", which facilitated the last radar processing sequence.

REFERENCES

- [1] Stevens K. M. , Lodha G. S. , Hollowaay A. L. , Soonawala N. M. (1995) In: *J. appl. geophys.* 33, n° 1-3, pp. 125-141.
- [2] Grandjean G., Gourry C. (1996) In: *J. appl. Geophys.* 36, n° 1, pp. 19-30.
- [3] Côte Ph. (1988) Doctoral thesis, J. Fourier University, Grenoble, France.
- [4] Gilbert P. (1972) In: *J. Theor. Biol.*, pp. 105-117.

This Page Intentionally Left Blank

INVESTIGATION ON SEVERAL NON-DESTRUCTIVE INSPECTION METHODS ABOUT STRENGTH DEGRADATION OF REINFORCED CONCRETE BEAM

T.TOMOKIYO

*Technology Center of Metropolitan Expressway
3-10-11, Toranomon, Minato-Ku, Tokyo, 105-0001, Japan*

T.HIKICHI and K.HIDA

*Chiyoda Engineering Consultants Co., Ltd., Tokyo, Japan
3-3-7, Iidabashi, Chiyoda-Ku, Tokyo, 102-0072, Japan*

T.UOMOTO

*Center for Collaborative Research, The University of Tokyo
7-22-1, Roppongi, Minato-Ku, Tokyo, 106-8558, Japan*

ABSTRACT

In order to investigate applicability of non-destructive inspection to evaluate the strength degradation of reinforced concrete structures, static and dynamic load test were carried out with reinforced concrete beam specimens. Throughout the fatigue test, from the initial stage until the destruction stage, measurements were carried out by Acoustic Emission, Ultrasonic and Impact Acoustic method, and the crack was recorded with a digital still camera. It has been investigated whether the measured data and data recorded by strain gauges affixed to the reinforcement can be used as indicator of strength degradation of concrete beam.

KEYWORDS

Reinforced concrete beam, acoustic emission, ultrasonic, impact acoustic, digital still camera

INTRODUCTION

Various non-destructive inspection techniques such as the ultrasonic method, infrared methods and impact acoustic method are proposed to detect the flaws and damages in the concrete structures. However, each non-destructive inspection is studied individually, and studies on relations between those non-destructive tests are very few.

In this study, reinforced concrete beam specimens were tested under static and dynamic loading and some non-destructive inspections were executed in the degrading process of the beam. The measurement results of each non-destructive inspection were compared, and applicability of

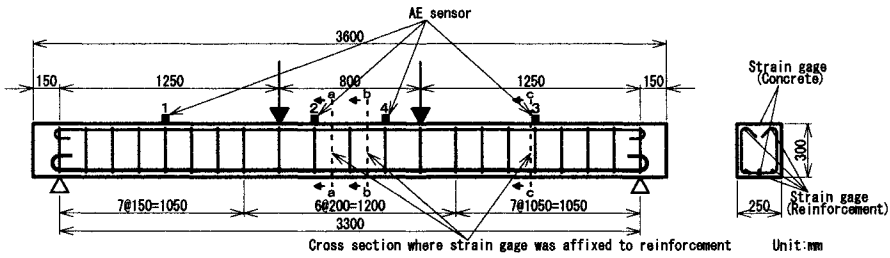


Fig.1. Specimen of reinforced concrete beam

Table 1. Mixture proportion of concrete

W/C (%)	s/a (%)	Unit weight(kg/m ³)				G _{max} (mm)	Chemical admixture (m/C=100kg)	Air entraining agent (C×%)	Slump (cm)	Air content (%)
		W	C	S	G					
65	48.5	165	254	888	970	20	250	0.004	8.5	4.6

Table 2. Properties of concrete

Compressive strength (MPa)	Static modulus of elasticity (GPa)	Dynamic modulus of elasticity (GPa)
37.4	24.6	31.4

Table 3. Properties of reinforcement

	Yield point (MPa)	Tensile strength (MPa)
D10(upper)	377	569
D16(lower)	358	514

each non-destructive inspection technique was examined.

EXPERIMENTS

Test specimen

Fig.1 shows a schematic representation of load tests. Dimensions of specimen are 3600mm in length, 300mm in height and 250mm in width. Mixing of concrete and the material properties of beam specimen are shown in Table 1, 2 and 3.

Test Load

Beam specimens were loaded statically and dynamically. The beam has clear span of 3300 mm and subjected to two points load shearing span of 1250 mm with electric oil pressure servo type loading machine. Strain gages were affixed to the embedded reinforcing bars and concrete surface, and the deflection of the beam was measured by laser displacement gauge at the mid-span of the beam (Fig.1).

Table 4. Static loading pattern

Step	Load (kN)
1	0 → 20 → 0
2	0 → 40 → 0
3	0 → 60 → 0
4	0 → 80 → 0
5	0 → 90

Table 5. Dynamic loading pattern

Step	Cycle
1	0 → 25,000
2	→ 50,000
3	→ 400,000
4	→ 450,000
5	→ 478,000

Static load test

Static test was carried out with load applied in increments of 20 kN and unloaded in each step as shown in Table 4.

Dynamic load test

In dynamic test, load was applied at frequency of 0.8 Hz with maximum load of 50kN and minimum load of 5kN. In dynamic test, non-destructive test data were recorded between each load step under unloaded condition (Table 5).

INVESTIGATION METHOD

Digital still camera

In taking a picture by the digital still camera, it was set to magnification of taken pictures became the angle of view of the width of 60 cm on the specimen, and took a picture of the crack which occurred in the specimen were taken. Afterwards, effects of misinterpretation and aberration according to the lens and flap and magnification when taking a picture were corrected. This was synthesized in the panorama, and the panorama image of the entire specimen was made. Cracks of specimen were traced on this panorama image using personal computer and the crack chart was made.

Acoustic Emission method

Four AE sensors were installed on the specimen as shown in Fig.1, and AE generated by loading was measured. The AE sensor analyzed the parameter of the AE event by the AE analysis system with a sensor built-in the preamp of 50 kHz resonance frequency and 20 dB amplification factor.

Ultrasonic method

By installing the transmitting and receiving sensor on both ends of the specimen, test data were recorded under unloaded condition in both static and dynamic load tests.

Impact Acoustic method

Impact Acoustic data were measured with the microphone at an end of specimen applying impact by hammer at another end of the specimen. Test data were recorded under unloaded condition.

EXPERIMENTAL RESULTS

Static load test

Measurement of displacement and strain. The results of measuring the displacement of the specimen and the strain of the tensile reinforcement in a-a cross section are respectively shown in Fig.2 and 3. From Fig.2, there was a phenomenon in which the load did not increase in the 80kN loading stage, and at Fig.3, it was judged that the specimen yielded at this time, because the strain of the reinforcement rapidly increased in this loading.

Digital still camera. As Example, the image recorded by the digital camera of which the cracks were traced is shown in Fig.4. Cracks were first generated in the loading of 20 kN along the stirrup. And though they grew with the loading of 40 kN and 60 kN in the length direction, the cross-direction growth was hardly confirmed. It was confirmed that the width of the crack opened to about 0.06 - 0.1 mm in the loading. However, since the crack closed and the width

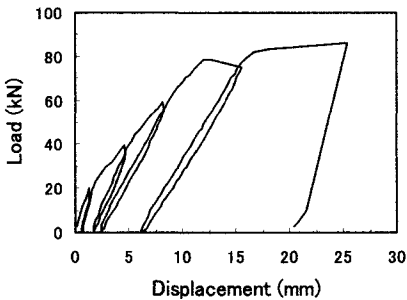


Fig.2. Relationship between load and displacement

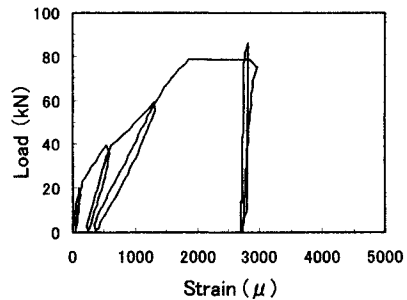


Fig.3. Relationship between load and strain of reinforcement

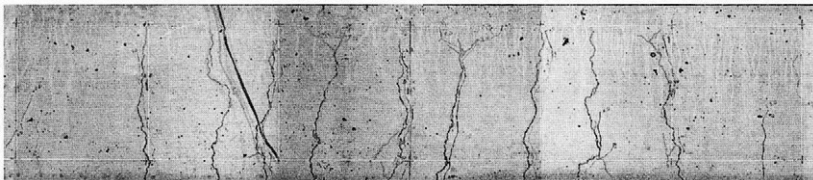


Fig.4. The image of which cracks were traced (after failure)

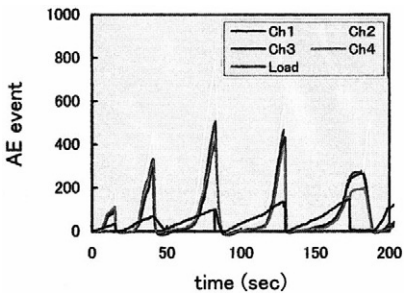


Fig. 5. Relationship between AE event and loading time

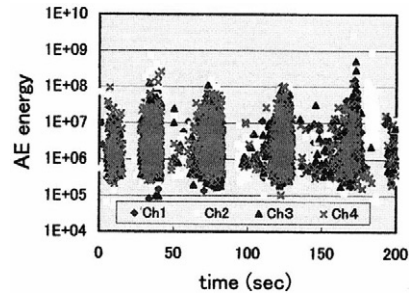


Fig. 6. Relationship between AE energy and loading time

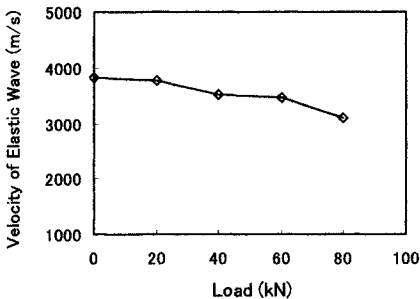


Fig. 7. Relationship between velocity of elastic wave and load

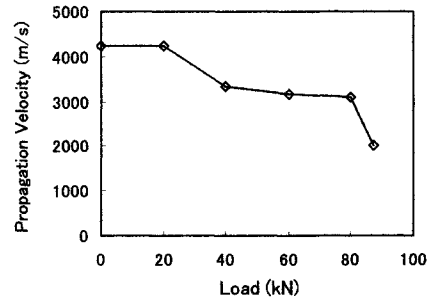


Fig. 8. Relationship between propagation velocity and load

became about 0.01 - 0.04 mm in unloaded condition, it was not possible to confirm the crack in the image recorded that time.

Acoustic Emission method. The relationship between AE event number and testing time is shown in Fig. 5, and the relationship between AE energy and testing time in Fig. 6. It was remarkable to generate AE at sensor Ch2 installed near the a-a cross section in which the specimen was finally broken. Especially, it was proven that number of generation of AE event number in the loading of 60kN was large. In this experiment, there was the Kaiser-effect to the 60 kN loading stage, and there was no the Kaiser-effect after the 80 kN loading. From this fact, it seemed to generate large damage near the a-a cross section, when it put on 60 kN load.

Impact Acoustic method. The relationship between velocity of elastic wave and applied load is shown in Fig. 7. Though velocity of elastic wave lowered with the increase of the loading, it was not possible to catch the sign of the destruction without observing the rapid change of velocity of elastic wave in the 80 kN loading near the destruction. It was not possible to measure velocity of elastic wave after the destruction.

Ultrasonic method. The result of measuring the propagation velocity of ultrasonic wave in axial direction of the specimen is shown in Fig.8. In the 20 kN loading, there was hardly the change on the propagation velocity. And, there was the rapid lowering of the propagation velocity in the 40 kN loading, and it tended to gradually lower to the destruction afterwards.

Consideration. Fig.9 shows the result obtained by Impact Acoustic method and Ultrasonic method as a lowering rate (value of how to lower for the initial value). In the 80 kN loading near the destruction, lowering rate by Impact Acoustic was about 19 %, and by Ultrasonic method about 27 %. In the loading process, too, the different tendency was shown that the lowering rate by Ultrasonic method rapidly increased in the 40 kN loading, while it by Impact Acoustic method gradually increased. Though, in AE method, it seemed to generate large damage in the 60 kN loading, there is the change at 40 kN in Ultrasonic method. Therefore, the time, in which measured value changes with the increase in the damage, seems to be different in each test method.

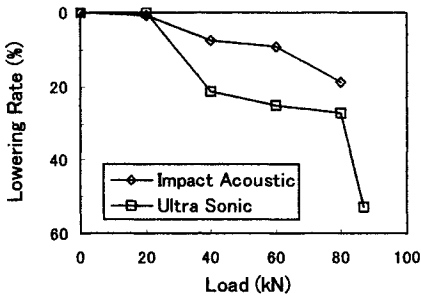


Fig.9. Transition of lowering late by Impact Acoustic and Ultrasonic

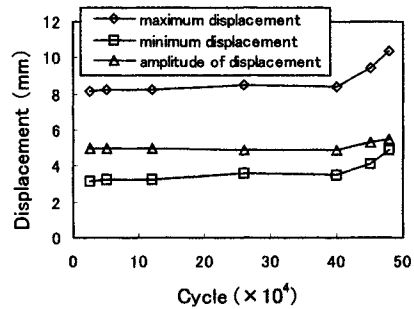


Fig.10. Relationship between displacement and loading cycle

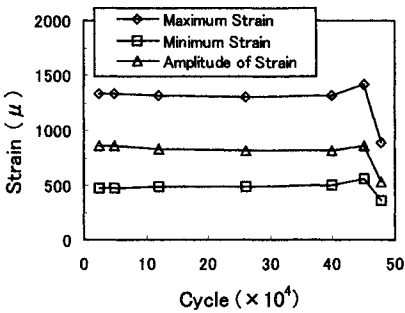


Fig.11. (1) Relationship between strain of reinforcement (left) and cycle

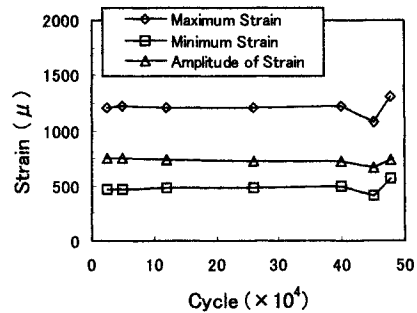


Fig.11. (2) Relationship between strain of reinforcement (right) and cycle

Dynamic load test

Measurement of displacement and strain. The relationship between dynamic displacement of the specimen and cycle of the loading is shown in Fig.10. At about 480,000 cycles, a tensile reinforcement broke in the part in which the crack was arose near the b-b cross section, and the specimen was broken. Though the displacement increased to 400,000 cycles a little, it was almost fixedly about 8.3 mm and it was about 30 % high value further than in static loading test. However, it began to increase after 400,000 cycles, and the displacement increased further than it in the static loading at about 60 % (about 10 mm).

The result of measuring strain of the tensile reinforcement (left and right side) in the a-a cross section are shown in Fig.11 (1) and (2). The strain of the reinforcement was also almost fixed to 400,000 cycles as well as the displacement. And, there was the change of the strain of the reinforcement after 400,000 cycles in which the displacement began to increase. This tended to be similar even in the b-b cross section.

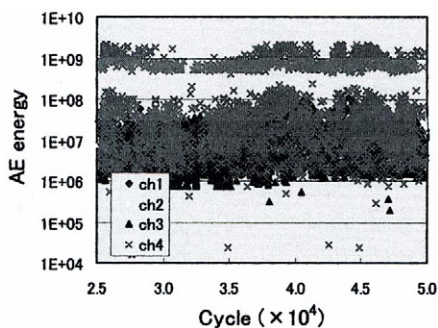


Fig.12. Relationship between AE energy and cycle (25,000 – 50,000)

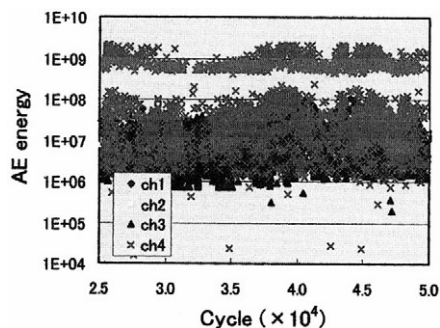


Fig.13. Relationship between AE energy and cycle (450,000 - failure)

Acoustic Emission method. The relationship between AE energy and loading cycle from 25,000 cycles to 50,000 is shown in Fig.12, and from 450,000 cycles to the destruction in Fig.13. Since the initial stage, there was the generation of AE of large energy at the Ch4 installed near the b-b cross section, and there was generally the increase of the energy after 450,000 cycles.

Impact Acoustic and Ultrasonic method. As well as the static loading test, the relationship between lowering rate by Impact Acoustic and Ultrasonic method and cycle is shown in Fig.14. Though velocity of elastic wave by Impact Acoustic lowered a little in the effect of generated crack in the loading initial stage, it was almost fixed to 400,000 cycles, and it rapidly lowered at 450,000 cycles near the destruction. The tendency though was shown that the propagation velocity gradually lowered in the first half of the loading, it was almost fixed after middle stage, and there was no change even after 450,000 cycles.

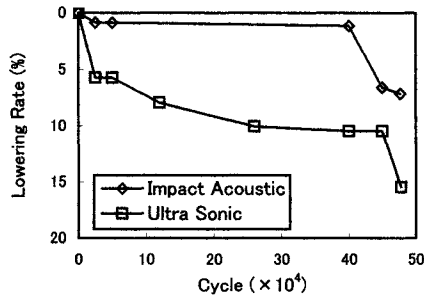


Fig.14. Transition of lowering late by Impact Acoustic and Ultrasonic

ANALYTICAL RESULTLS

Test results of displacement of beam specimen and strain of reinforcing bars were compared with FEM analysis (TNO DIANA) using plane strain smeared crack elements and embedded reinforcement elements. Fig.15 shows the results of static load test and numerical analysis concerning the relationship between displacement and applied load. Good agreement between test and analysis has been verified.

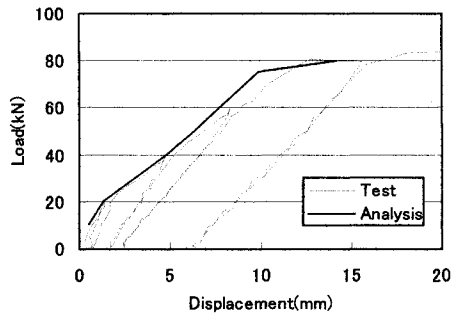


Fig.15. Beam mid span displacemnet

Fig.16 shows strain distribution of cross section at applied load of 20 kN and 40 kN, respectively. Location of neutral axis in cross section moves up to beam top surface as load increases. Although alteration of section performance expects changes in measuring results, data which denote alteration of section performance was hardly identified from the test.

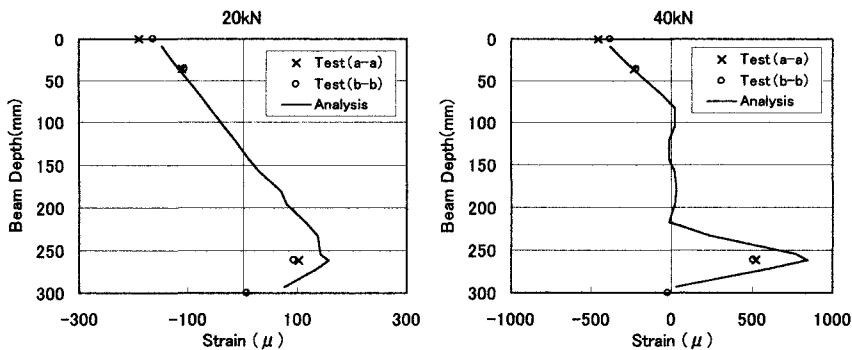


Fig.16. Strain distribution of cross section

Fig.17 shows the relationship between applied load and stiffness of beam $K = \frac{\Delta P}{\Delta \delta}$ (ΔP : load increment, $\Delta \delta$: displacement increment) .

Damage of beam seemed to progress at load of 60 kN from the fact that the value of K decreased at that point, though degradation of K was not confirmed from analysis result. This seemed to be a specific phenomenon of the beam uses for this test from the fact that the K value increased again at next load step. And large AE energy measured at this load step seemed to respond the decrease of K or progress of damage of beam specimen. At applied load of 20kN, most test results showed some changes from the initial data. Changes in data at applied load of 40 kN was detected only by ultrasonic method measurement.

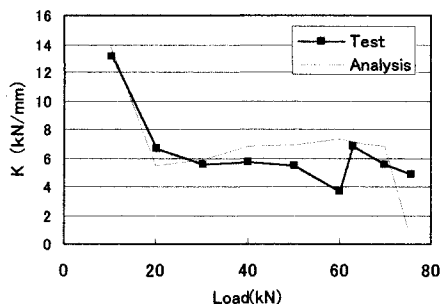


Fig.17 Relationship between applied load and K

CONCLUSIONS

In this experiment, by the degree of the damage of the specimen, the timing in which the change of the measured value of each non-destructive inspection appears was different. It is considered that this is because the condition (condition, effect) of the member subject which affects measured value of each inspection differs.

ACKNOWLEDGEMENTS

The experiment is a part of the program of Institute of Industrial Science Committee of Non-Destructive Evaluation for Concrete Structures, and the cooperation of the committee members is gratefully acknowledged.

ADVANCED NDT OF REINFORCED CONCRETE MEMBERS BY ULTRASONICS AND ACOUSTIC EMISSION

Uchida, M., Ohtsu, M., and Okamoto, T.
Taiheiyo Cement Co. Ltd. Central Research Lab., Kiyosumi
Kiyosumi 1-2-23, Koutou-ku, Tokyo 135-8410, Japan

ABSTRACT

Advanced nondestructive testing (NDT) is investigated to obtain practical and quantitative information on cracks in reinforced concrete (RC) members by using ultrasonic testing (UT) and acoustic emission (AE) methods. The UT method is well-known as a method for evaluating the crack depth, while the AE method can detect the cracking process. In cases where the UT method is applied to RC members, it is found that arrival times are affected by the presence of reinforcement and the configuration of crack surfaces. Thus, specimens with surface opening cracks which were created artificially and with flexural cracks which were induced by flexural load were tested. Empirical relations were determined to compensate these effects.

In order to distinguish the growth of tensile and shear cracks, AE events were measured in concrete members under flexural and shear loading. The cracks were classified from AE parameters. On an RC pier of a bridge in which cracks were observed in situ, AE observation was conducted under live loading. Then it is confirmed that these AE parameters can give quantitative information on cracking in the pier.

KEYWORDS

NDT, ultrasonics, acoustic emission, concrete members, crack depth, type of crack

INTRODUCTION

A variety of concrete structures were built in a rush to establish infrastructure during the period of rapid economic growth in Japan. With the maturity of the society and the revelation of various environmental problems, maintenance of these existing concrete structures has turned out to be an important problem, requiring urgent development of simple techniques to evaluate the structural integrity of concrete [1].

The current study first investigates the effects of the presence of reinforcement and the width of cracks in the measurement of ultrasonic testing (UT) on the depths of cracks in reinforced concrete (RC) structures. Next, acoustic emission (AE) method is investigated as a means to

evaluate cracking processes. A simple technique is developed to identify crack types utilizing the characteristics of AE waves generated while tensile and shear cracks develop inside concrete. The evaluation technique is finally applied to an existing concrete pier.

CRACK INVESTIGATION BY ULTRASONICS

Experiment

It has been previously pointed out that the UT method may not accurately estimate the depth of surface cracks in RC structures when elastic waves are affected by the presence of reinforcement or the width of cracks [2].

In the current study, a crack depth estimation technique based on the difference in longitudinal (P) wave propagation is investigated to empirically understand how the accuracy of crack investigation is affected by various conditions including the presence of reinforcement and the width of cracks. The conditions of the UT measurement are schematically shown in Fig.1. The crack depth is determined from Eq.1.

$$d = \frac{L}{2} \sqrt{\left(\frac{T_c}{T_0}\right)^2 - 1} \quad (\text{Eq. 1})$$

where d: crack depth, L: distance between the transmitting and receiving sensors, T_c : P wave propagation time through the crack, and T_0 : P wave propagation time through intact area.

A two-sensor technique was employed for the measurement [3]. Ultrasonic waves were generated by a pulse generator with a rise time of 20 ns and a maximum voltage of about 300 V. These waves were detected by two types of AE sensors, R1.5 (15 kHz resonant) and R6 (60 kHz resonant), amplified by 40 dB, and recorded by a waveform measurement system as shown in Fig. 2.

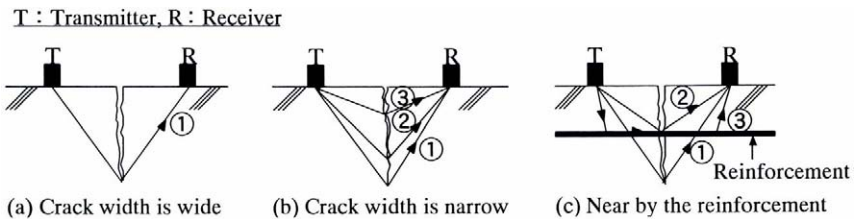


Fig.1 Traveling path of ultrasonics

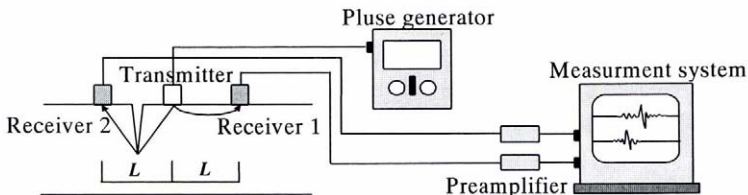


Fig.2 Sensors location and measurement system

Model specimens

Two types of specimens were prepared. One with an artificial crack introduced by inserting a 0.3 mm thick steel plate during concrete casting is shown in Fig.3 . The other with a flexural crack caused by bending is shown in Fig.4. All specimen were made of ready-mixed concrete with a 28-day compressive strength of 30 MPa, a slump of 15 cm and a maximum aggregate size of 20 mm.

In the specimen of the flexural crack, a notch was first made at the center of the specimen to induce cracking. The specimens with two different thickness, 150 mm and 200 mm, were prepared.

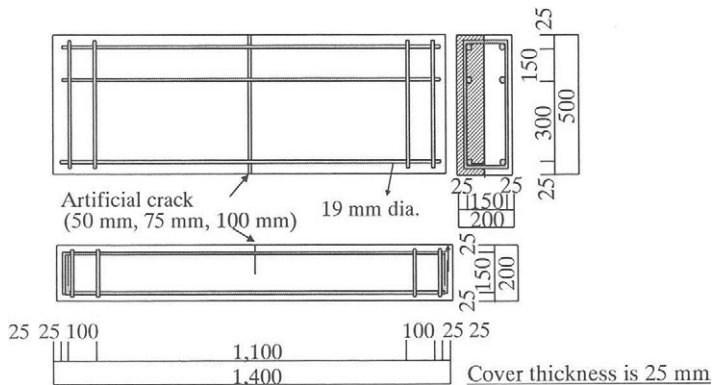


Fig.3 Specimen of artificial opening-crack

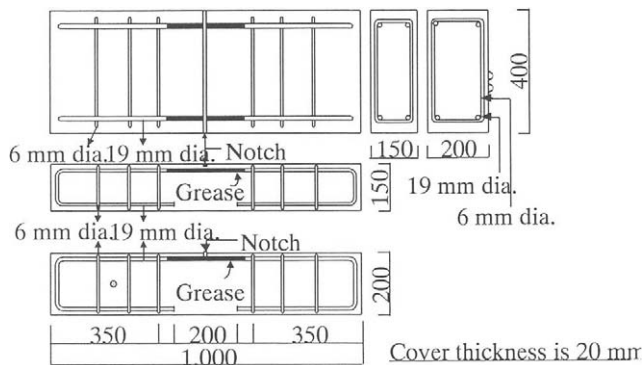
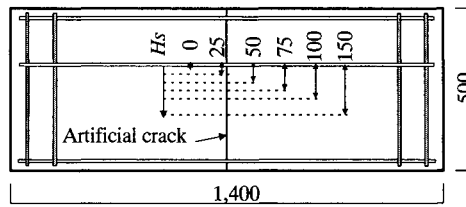


Fig.4 Specimen of flexural cracking

Effects of reinforcement on the estimation of crack depth

The RC specimens of artificial cracks were tested. As shown in Fig.5, the horizontal distance (H_s) from the sensors to the reinforcement varied from 0 to 150 mm. Measurements were carried out with two types of AE sensors, R1.5 and R6, at three different distances (L) from the transmitter to each receiver, namely 150, 200 and 300 mm.



H_s : Horizontal distance between sensors and reinforcement (mm)

Fig.5 Sensor locations on the specimen of artificial opening-crack (mm)

Figure 6 shows the experimental results. The estimated values matched the actual values when the distance (H_s) from the sensors to the reinforcement was almost equal to or larger than the crack depth. The average of the estimated values measured right above the reinforcement (distance to the reinforcement: 0 mm) was about 25 mm, which was equal to the cover thickness over the reinforcement. The differences in sensor type or in sensor distance (150, 200 and 300 mm) resulted in no major differences.

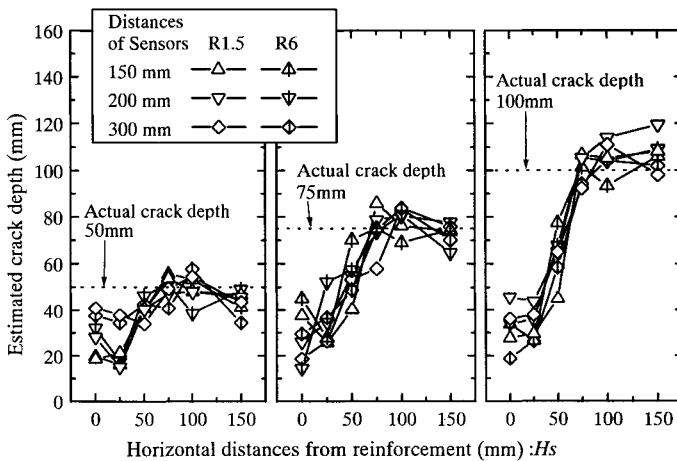


Fig.6 Effect of reinforcement location on the estimation of crack depth

To study these findings theoretically, two paths were assumed for P wave propagation as shown in Fig. 7, and the shortest lengths were used for individual paths. Ultrasonic waves are diffracted at the tip of a crack (depth: d_c) in Fig. 7 (a), while the waves are reflected at the reinforcement on the crack surface (depth: d_s) in Fig. 7 (b). Therefore, the measurement is formulated ,

$$d_m = \text{Min}(d_c, d_s)$$

$$d_s = \sqrt{H_s^2 + H_c^2} \quad (\text{Eq. 2})$$

where d_m : model analysis depth value, d_s : analytical depth value from an ultrasonic wave reflected at the reinforcement, d_c : analytical depth value from an ultrasonic wave diffracted at

the tip of the crack, H_c : cover thickness, and H_s : horizontal distance from the sensors to the reinforcement.

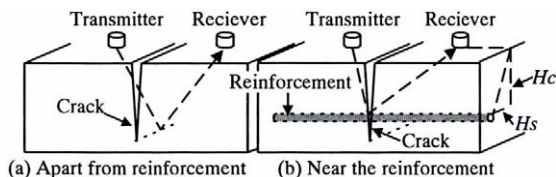


Fig.7 Model of reflected waves on the crack

The depths analyzed is in good agreement with the estimated values as shown in Fig. 8. The results from this model successfully explains the changes in the estimated values due to the presence of reinforcement. This model, when applied to existing structures, could provide the conditions for crack depth estimation on reinforcement location and cover thickness. Any estimated values smaller than d_s in Eq. 2 can be free from the effect of the presence of reinforcement.

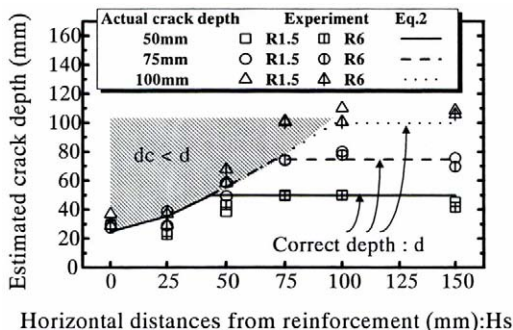


Fig.8 Estimated crack depth in the experiments and relations of d_c and d

Effects of the crack width on the estimation of crack depth

The width of the surface crack was changed from 0.1 mm to 0.5 mm by applying a load to the specimen as shown in Fig. 9. The averaged value on the sides of each specimen was used as the actual crack depth. From the results, it was found that the larger the crack width on the concrete surface, the better agreement between the actual crack depths and the measured was observed. Since this tendency was thought to be related with the angle at which the crack opens (crack opening angle), the relationship between the crack opening angle ($\theta \approx$ crack width/crack depth) and the accuracy ratio (estimated value/actual value) was examined.

Figure 10 shows the results, where a unique relationship is found between the crack opening angle and the accuracy ratio, irrespective of the crack depth. This is probably because the configuration of crack surfaces is dominated by the crack opening angle, rather than by the surface crack width. Within the range tested in the current experiment, the crack depth can be estimated without the effect of the crack surface configuration when the crack opening angle

exceeds 0.0015 rad.

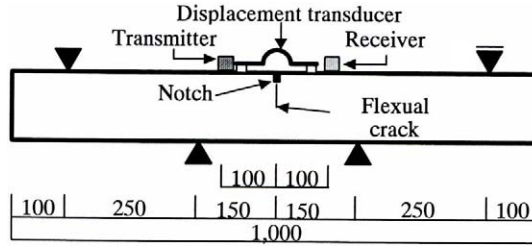


Fig.9 Test method and transducer location (mm)

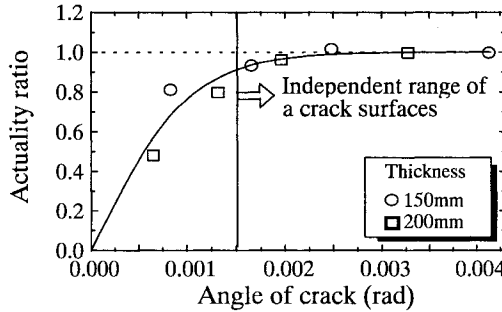


Fig.10 Angle of crack and relative ratio

IDENTIFICATION OF CRACK TYPES BY AE METHOD

Experiment

Cracks in concrete structures are classified largely into two types: tensile cracks and shear cracks. In order to take appropriate repair or strengthening measures, precise identification of the prominent characteristics of each crack is in demand. Therefore, concrete specimens were tested under a single flexural load and a double shear load, and then the analog parameters of the AE waves indicated in Fig.11 were analyzed [4].

AE measurement

AE sensors were attached to specimens with adhesive tape, using silicone grease as the couplant. AE waves were recorded by the AE measurement system after being amplified by 40 dB. Three types of sensors with different resonance frequencies (R3: 30 kHz resonant; R6: 60 kHz resonant; and R15: 150 kHz resonant) were used to check the influence of the sensor type on estimation results. The threshold level for AE measurement was set to 45 dB so that environmental noise was eliminated. The measuring system was essentially the same as given in Fig.2.

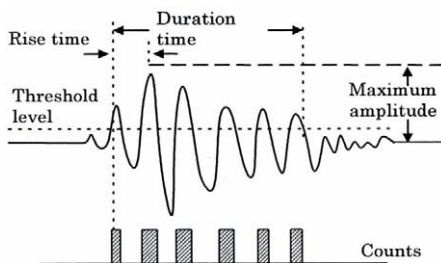


Fig.11 Elastic waveform analogue parameters

Testing method

Single flexural loading was carried out in accordance with JIS A 1106 [5], and double shear loading was in accordance with the JCI-SF6 [6], respectively. Three specimens were prepared for each condition. Figure 12 shows the sensor locations and loading method. Cracking positions were controlled by making a notch of about 10 mm in length at the center on the bottom of the flexural loading specimens and at the right below one of the shear planes on the bottom of the double shear loading specimens.

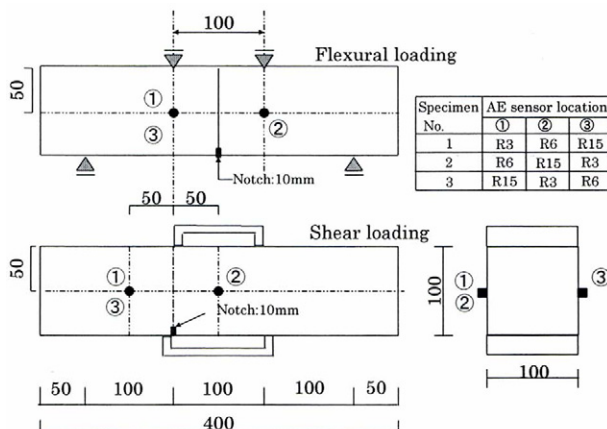


Fig.12 Test method and sensor location

Cracking conditions and AE parameters

Figure 13 shows typical AE waveforms and frequency spectra obtained during the single flexural loading and the double shear loading as classifying into a tensile crack and a shear crack [7]. Typical AE waves under the single flexural load and of tensile cracking contain high frequency components higher than 200 kHz. Under the double shear load, shear cracking was prominent, of which waves contain almost no peaks in the same frequency range and the longer rise time. These two patterns were analyzed using the RA value (rise time/maximum amplitude) and the average frequency (counts/duration). These AE parameters are illustrated in Fig. 11. The rise time was divided by the maximum amplitude as RA value. The average

frequency is widely used as the value representing the frequency characteristics of measured AE waves [8].

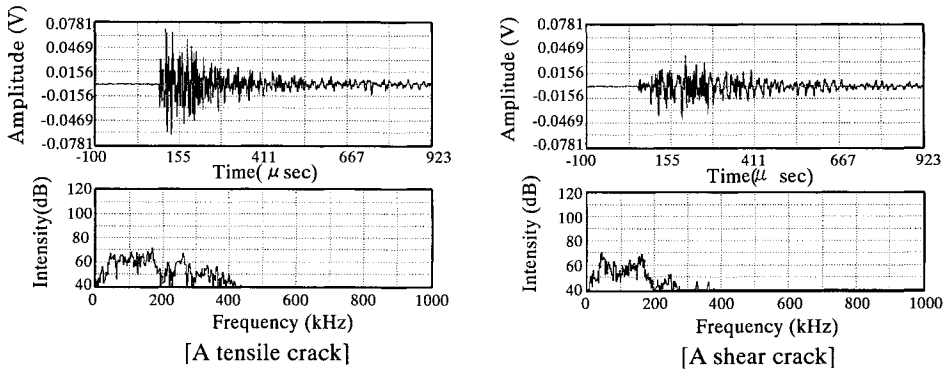


Fig.13 Typical AE waveforms and frequency spectra

To obtain more distinct feature on tensile cracking and shear cracking, the parameters of 100 AE events in the flexural specimens detected prior to the maximum load and of 100 AE events in the double shear specimens after the maximum load were analyzed. Figure 14 shows the averaged values of the parameters under different conditions. It is found that AE waves observed under flexural load where tensile cracking was thought to be prominent have the smaller RA values and the larger average frequencies, irrespective of the sensor type.

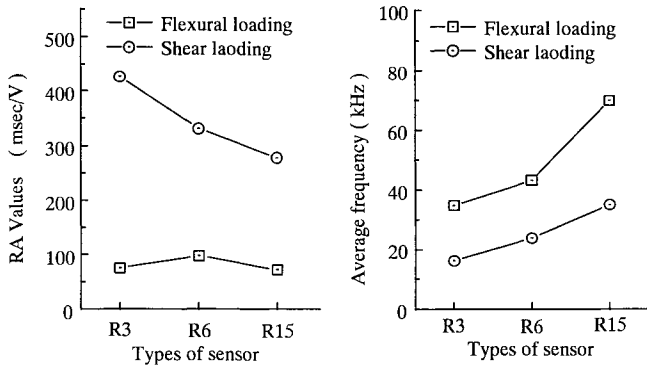


Fig.14 Relationship between crack pattern and AE parameter values

Application to an existing RC structure

The evaluation technique by AE method was applied to an existing concrete pier where cracking had been actually observed. The tested structure was an RC pier of a bridge of a cylindrical shape 2 m in diameter and 5 m in height, as shown in Fig.15, two longitudinal cracks were observed on the surface of the pier symmetrically with respect to the center of the section. The width of the cracks was 20 mm at the top and about 5 mm at the bottom.

AE sensors (R6) were attached along the crack in a line longitudinally from the top of the pier as shown in Fig. 15. AE events generated at the crack due to traveling vehicles were recorded by the AE measurement system for two hours. The threshold level for measurement was set to 50 dB to eliminate environmental noise. RA values and average frequencies of the AE waves measured on the pier are shown together with the results of the laboratory experiment in Fig. 16.

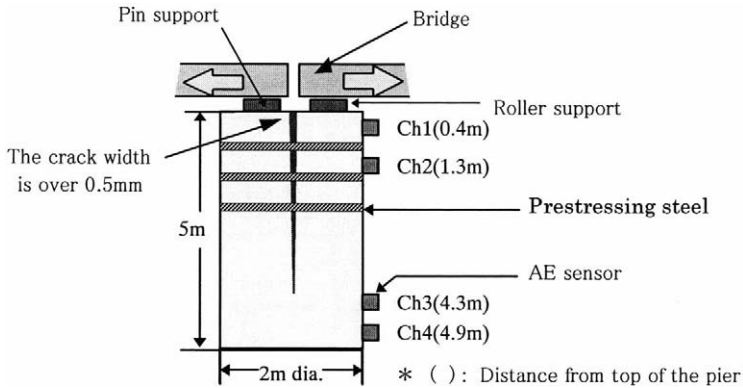


Fig.15 RC Pier of a bridge and test set-up

AE waves detected by ch.1 and ch.2 placed in the upper part of the pier had larger RA values and smaller average frequencies, which could be classified as the shear type. AE waves detected by ch.3 and ch.4 near the tip of the crack had smaller RA values and larger average frequencies, which was characteristic of the tensile type.

These results imply that tensile cracking is in progress at the tip of the crack due to the repair using the inadequate prestressing bars. While AE occurred still in the upper part. This is because the crack confined by the prestressing bars results in generating displacement under live load.

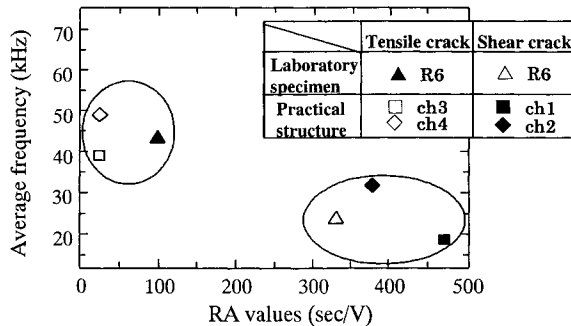


Fig.16 AE parameter values under live loading

CONCLUSION

- (1) The range where the presence of reinforcement affects crack depth estimation was obtained quantitatively in UT. Based on information of the cover thickness and the reinforcement location, if an estimated crack depth is smaller than the estimation limit (d_s) determined from the minimum horizontal distance (H_s) and the cover thickness (H_c), the value estimated is confirmed to be not affected by the presence of reinforcement.
- (2) The range where the configuration of crack surfaces affects crack depth estimation was obtained quantitatively in UT. Based on the surface crack width (w), if an estimated crack depth is smaller than $w/0.0015$, the value estimated is confirmed to be not affected by the crack configuration.
- (3) Larger RA values (rise time/maximum amplitude) among the AE parameters imply growth of cracking where the shear type is prominent. Larger average frequency values (counts/duration) among the AE parameters imply growth of cracking where the tensile type is prominent. The crack evaluation technique based on these AE parameters was applied to an existing RC structure. Thus, the types of cracks in progress were identified successfully.

Consequently, the combined technique of UT and AE methods with a common measurement system was found to be promising for evaluation of cracks in RC structures.

REFERENCES

1. H. Watanabe and K. Kawano : Diagnosis Techniques for Effective Maintenance of Concrete Structures, Concrete Journal, Vol.33, No.9, pp.19-28, 1995
2. M. Ohtsu, M. Shigeishi and Y. Sakata: Non-destructive Evaluation of Defect in Concrete by Quantitative Acoustic Emission and Ultrasonics, Ultrasonics, Vol. 36, pp. 187-195, 1998
3. Y. Lin, T. Liou C. Hsiao: Influences of Reinforcing Bars on Crack Depth Measurement by Stress Waves", ACI Material Journal, Vol.95, No.4, pp.407-418, 1998
4. M. Ohtsu: The history and development of acoustic emission in concrete engineering, Magazine of Concrete Research, Vol.48, No.177, pp.321-330,1996 Dec.
5. JIS A 1106: Method of Test for Flexural Strength of Concrete, Japanese Industrial Standard, 1999
6. JCI-SF6: Method of Tests for Shear Strength of Fiber Reinforced Concrete, JCI Standard for Test Methods of Fiber Reinforced Concrete, pp57-59, 1984
7. M. Ohtsu, M. Uchida, D. Mori, T. Okamoto and Y. Murakami: Structural Integrity Evaluation of Reinforced Concrete Construction by Acoustic Emission Method, JSNDI Proceedings of National Conference on Acoustic Emission, pp. 221-226, 1997
8. M. Iwanami, T. Kamada, S. Nagataki: Application of Acoustic Emission Technique for Crack Monitoring in RC Beams, JCA Proceedings of Cement & Concrete No. 51, 1997

APPLICATION OF VARIOUS NON-DESTRUCTIVE INSPECTION FOR EXISTING REINFORCED CONCRETE STRUCTURES

Taketo UOMOTO

*Center for Collaborative Research, University of Tokyo
7-22-1, Roppongi, Minato-Ku, Tokyo, 106-8558, Japan*

Shuji TOMIZAWA

*Metropolitan Expressway Public Corporation
1-4-1, Kasumigaseki Chiyoda-Ku, Tokyo, 100-8930, Japan*

Hiromasa TANAKA

*Central Japan Railway Company
3-1-17, Nihonbashi, Chuo-Ku, Tokyo, 103-0027, Japan*

ABSTRACT

Many different kinds of non-destructive inspection (NDI) methods have been developed to investigate existing concrete structures, such as sonic, ultrasonic, acoustic emission, radar, X-rays, thermography, natural potentials, etc.. However, it seems that the use of these different methods jointly has not been done so often to obtain more reliable evaluation. In this paper, several non-destructive inspection methods were carried out to evaluate existing reinforced concrete bridges in service for both cars and trains. The results show that combination of different NDI methods can evaluate existing structures in more reliable manner than single NDI.

KEYWORDS:

Non-destructive inspection, combination of NDI, reinforced concrete bridges, evaluation

INTRODUCTION

Various NDI techniques have been developed throughout the world to detect defects of existing concrete structures. These individual inspection methods are especially important to evaluate the service life of the structures. However, since all NDI methods have advantages and

disadvantages, the combined application of several inspection methods may offer the data which can not be obtained by a single inspection method.

In this paper, various non-destructive inspection (NDI) methods were carried out to existing reinforced concrete slabs, beams and columns in service bridges in order to obtain basic data, and applicability of combined NDI method.

INSPECTION OUTLINE

The inspections were carried out on the reinforced concrete slab of a road bridge and a railway bridge. About 28 years and 35 years have passed since construction, respectively.

In case of the road bridge, after about 8 years of use, vertical girders were added for the reinforcement of the slab. In this viaduct, two panels, partitioned by main girders and horizontal beams, panel A and B which are connected in the bridge axial direction were chosen and inspected.

Appearance of each panel are respectively shown in Fig.1 and 2, and bar arrangement of the slab is shown in Fig.3. The panel A has a portion where free lime appeared on the surface, and it has been evaluated by the visual inspection: "though it must be repaired, the urgent repair is not needed". In case of the panel B, it has been evaluated: "degree of damage must be recorded", and the damage of the panel A is greater than that of the panel B. Acoustic emission, thermography, impact acoustic, radar, natural potentials, and photography by digital still camera were carried out for the panels.

In case of railway bridge, the bridge was used without any additional reinforcements after use. The same inspections were performed on a reinforced concrete slab, beams and a column as in the case of the road bridge as shown in Fig.5. Although several cracks can be observed, the viaduct is evaluated by visual inspection as "degree of damage must be recorded".

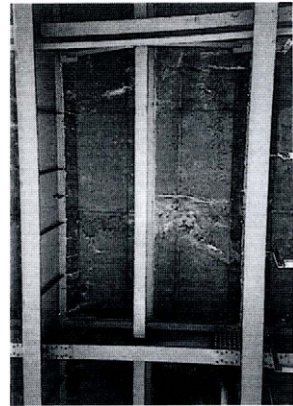


Fig.1. Panel A

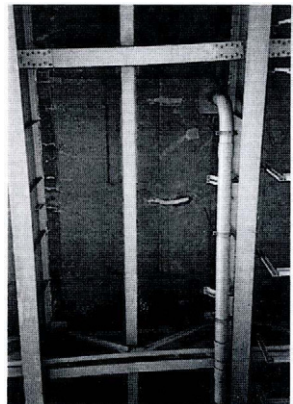


Fig.2. Panel B

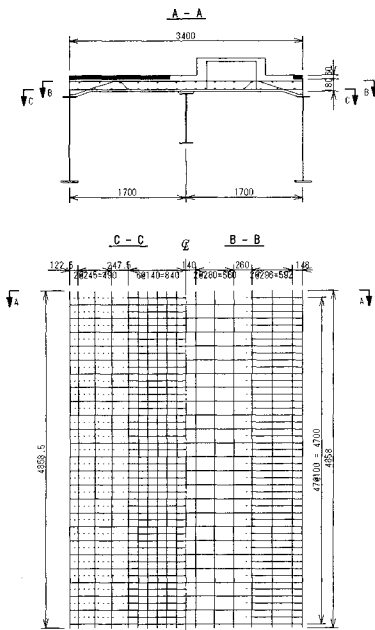


Fig.3. Bar arrangement of Road Bridge slab

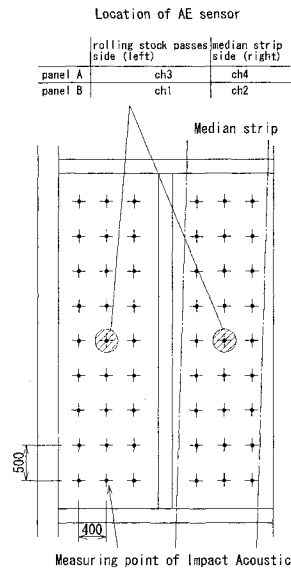


Fig.4. Location of AE sensor and measuring point of Impact Acoustic

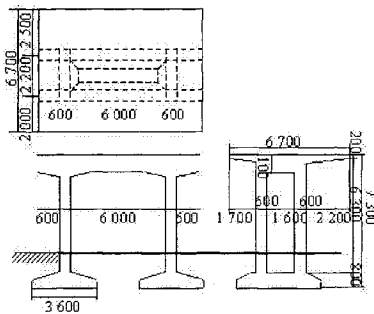


Fig.5. Arrangement of Railway Bridge

INSPECTION METHOD

Digital Still Camera Inspection

The surface of one panel was divided into several parts. These parts were individually recorded with the digital still camera (1,300,00 pixels) from under the viaduct. And then, the image of the whole panel was made by connecting them.

Acoustic Emission Measurement

In case of the road bridge, two sensors on one panel, sum total of 4 pieces, were installed on the surface of the slab. The sensor Ch1, 3 (the odd number channel) were installed in rolling stock passage side, and Ch2, 4 (the even number channel) in the median strip side (Fig.4). Measurement was carried out for about 2 hours.

Thermography

In case of the road bridge, it was recorded by thermography installed in just under of the panel (about 8m heights to the slab) every one hour in the whole day and night (24 times).

Impact Acoustic Measurement

In case of road bridge, the measuring points were set grating-like of 400 mm by 500 mm, as is shown in Fig.4. The points were struck with impulse hammer and the stroke sounds were recorded by a microphone and a recorder installed near the points.

Natural Potential Measurement

The natural potential measurement was carried out on the surface of slabs on 200mm by 200mm grating-like measuring points.

Radar Inspection

The radar inspection was performed on slabs, beams and columns to inspect both degradation and bar arrangement using 1GHz wave radar system.

RESULTS AND DISCUSSION

1. Road Bridge

Acoustic Emission measurement

AE hit number and AE energy value of each channel detected during all measurement periods are shown in Fig.5, and 6, respectively. AE hit number detected by sensor Ch1, 3 and 4 were almost equal, but the value by Ch2 was larger than others for about 15% (Fig.6). AE energy detected by Ch1 and 3 measured in the rolling stock passage side showed the values over 10 times to the values by Ch2 and 4 measured in the median strip side (Fig.7). Although the detected AE seemed to be originated mainly from the live load, the value of Ch3 installed in the panel A is larger than that of Ch3 in the panel B. The difference may be originated from the difference of the damage of each panel. (The damage of panel A is larger than that of that B.)

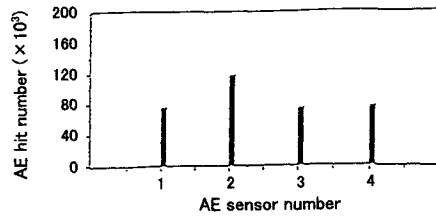


Fig.6. AE hit amount of each channel

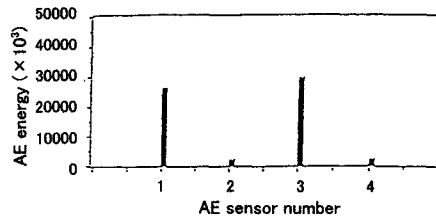


Fig.7. AE energy amount of each channel

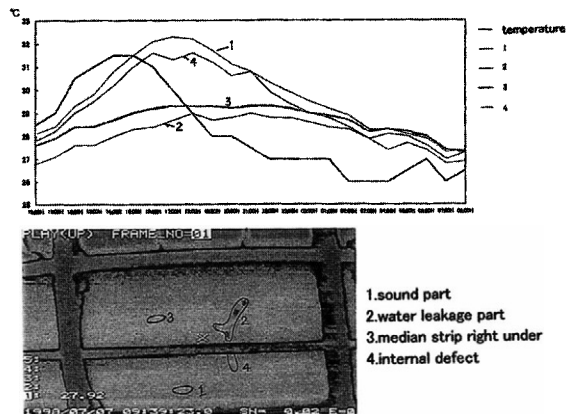


Fig.8. Aging variation of temperature of concrete slab

Thermography measurement

In Thermography measurement, the following four parts were recognized: “1:Sound portion”, “2:Water leakage portion”, “3:Underneath the median strip“ and “4:Portion supposed to have internal defects“. The variations of the temperature at different measuring times are shown in Fig.8. And the aging variations of infrared image of the whole panel A are shown in Fig.9 ① - ⑥. From these figures, the low-temperature region was obtained where free lime was observed. The portion 4 in Fig.8, which could not be detected by visual inspection, has lower temperature than the surrounding portions, as can be seen in Fig.9 ⑤ and ⑥. In addition, the

temperature gradient between sound portion and this portion was about 1 degree at the maximum (Fig.8).

Impact Acoustic measurement

The waveforms of impact acoustic measured in the panel A and B are shown in Fig.10. The undulate amplitude value of the panel A was larger than that of the panel B, and low frequency wave is contained in case of panel A.

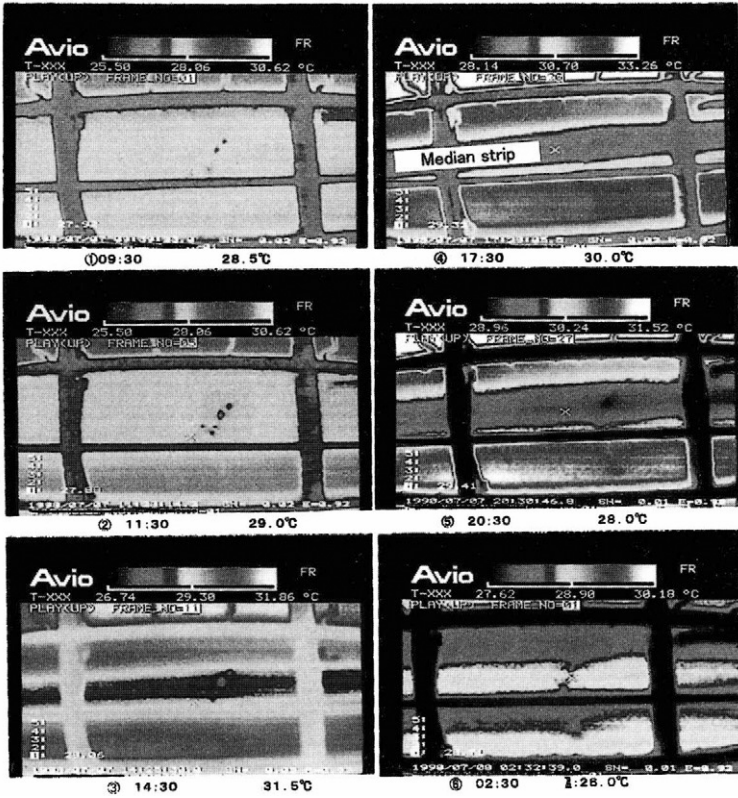


Fig.9. Aging variation of infrared image

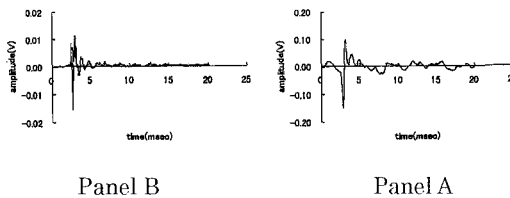


Fig.10. Waveform of the stroke sound

Generally, amplitude of a slab which is damaged by fatigue load increases, since the rigidity of the slab reduces. Amplitude ratio, the ratio between amplitude value of impulse hammer and that of stroke sound obtained by measurement, is shown as contour diagram in Fig.11. Since the amplitude ratio of the panel A was larger than that of the panel B, the damage of the panel A seems to be larger.

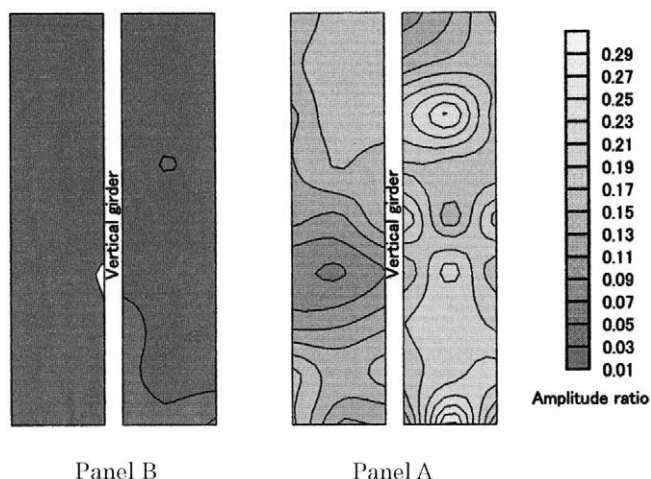


Fig. 11. Contour diagram of amplitude ratio of stroke sound

Examination of superimposed image

The superposition of the image of the measurement result of panel A was examined.

Fig.12 shows the superimposed image recorded by the digital still camera (original image), the image tracing the crack by personal computer (crack image) and the bar arrangement drawing investigated by the radar. Fig.13 shows the superimposed crack image and infrared image on the original image. Similarly, Fig. 14 shows the superimposed crack image and contour diagram made from natural potential measurement and Fig.15 shows the superimposed crack

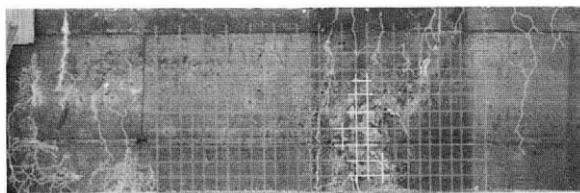


Fig.12. Superimposed image of original, crack and bar arrangement

image and contour diagram of impact acoustic ratio. In the crack image, the crack over 0.1mm was traced. Comparatively wide cracks were observed in the portion where free lime was observed.

In Fig.12, looking at the bar arrangement, the portion with whitish straight lines indicates the measured radar results were slightly out of order compared to other portions. It was estimated that there must be some defects around the portion and water has been accumulated in this portion.

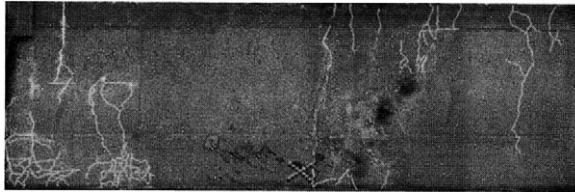


Fig. 13. Superimposed image of original, crack and infrared image

From Fig.13, the low-temperature portion measured by thermography was close to the portion where crack width was wide and free lime was leaching. In Fig. 14, since the portion with low values of the natural potentials were close to the portions where crack width is wide and free lime was leaching, it is estimated that corrosion of the reinforcement may occur.

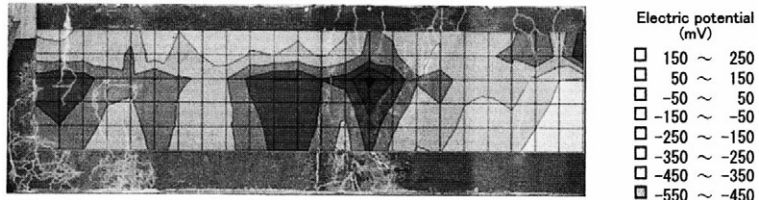


Fig. 14. Superimposed image of original, crack and natural potential

Looking at Fig.15, the superimposed image with impact acoustic ratio does not fit well with the distribution of cracks nor free lime leaching portions. Since there is a good correlation between amplitude ratio and internal defects, the portions with high values of amplitude ratio

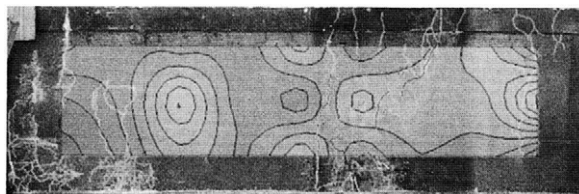


Fig. 15. Superimposed image of original, crack and impact acoustic

may contain internal defects.

2. Railway Bridge

Examination of superimposed image

The superimposed images of the measured result of slab and beams were examined.

Fig. 16 shows the superimposed image of the slab recorded by the digital still camera (original image), the image tracing the crack by personal computer (crack image) and the bar arrangement drawing investigated by the radar. Fig.17 shows the superimposed image of the beam with cracks and bar arrangement. In the crack image, the cracks over 0.1mm width were traced.

Both figures shows that most of the cracks are flexural cracks, but there are also some cracks which may be caused by some other causes such as shrinkage, etc.. Although natural potential measurements is not indicated in the figures, the values were large and it seems that there is no corrosion of the steel bars. Considering these results, it can be said that the deterioration degree of the inspected railway is much smaller. compared to the road bridge mentioned above.

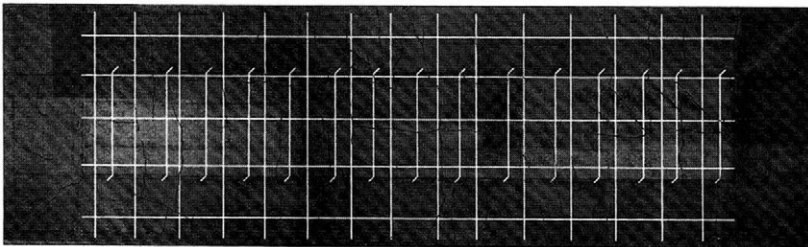


Fig. 16. Superimpose image of the Slab with crack and bar arrangement

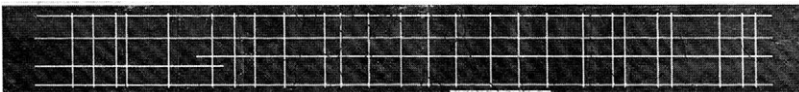


Fig.17. Superimpose image of the Beam with crack and bar arrangement

CONCLUSIONS

It is necessary to inspect concrete structures not only by the visual inspection but also by using NDI technique to evaluate the structure. As shown in this paper, visual inspection can not offer enough information on internal defects, such as internal voids and corrosion of the reinforcement, etc.

In this paper, various non-destructive inspections were carried out for reinforced concrete slab, beam and columns of a road bridge and railway bridge. Although individual inspection method gives important information, combination of several NDI results may offer further detailed information. By utilizing superimposed images mentioned in this paper, it may be helpful for civil engineers to find out not only the deteriorated portion but also the cause of the deterioration. This enables the engineers to carry out reliable evaluation of existing concrete structures.

ACKNOWLEDGEMENTS

The inspection is performed as a part of the program of IIS Committee of Non-Destructive Evaluation for Concrete Structures, and the cooperation of the committee members is greatly acknowledged. The authors would like to send their sincere thanks to Mr. T. Tomokiyo and Mr. M. Yoshizawa for arranging all the works in the site inspection.

REFERENCES

1. IIS Committee Report: Non-Destructive Evaluation for Concrete Structures, IIS, University of Tokyo, 1999 (in Japanese)
2. S. YUYAMA, Z.W. LI et al: Evaluation of Fatigue Damage in Reinforced Concrete Slab by Acoustic Emission, *Journal of Materials, Concrete Structures and Pavements*, No.627/V-44, pp.251-259, JSCE, 1999.8., ISSN 0289-7806 (in Japanese)
3. T. TOMOKIYO and T. UOMOTO: A Study on Applicability of Various Non-Destructive Testing Methods for Reinforced Concrete Slab in Service Road Bridge, "SEISAN-KENKYU" *Monthly Journal of Institute of Industrial Science, University of Tokyo*, Vol. 51, No. 11, pp.57-60, 1999.11., ISSN 0037-105X (in Japanese)

INVESTIGATION OF THE DRYING PROCESS OF MOIST BUILDING MATERIALS BY MEANS OF HEAT FLUX DENSITY MEASUREMENTS

H. ROGASS and U. FISCHER

*Brandenburg Technical University Cottbus, Department of Applied Physics,
PF 101344, D-03013 Cottbus, Germany*

ABSTRACT

The drying process of moist building materials is connected with a demand of desorption enthalpy for the evaporation of the moisture. In most cases the corresponding amount of heat flows through the surfaces into the moist material. The relation $g = q_{\text{lat}}/r_{\text{pc}}$ (r_{pc} : specific desorption enthalpy of water, in Ws/kg) between the desorption rate g (in $\text{kg}\cdot\text{m}^{-2}\cdot\text{s}^{-1}$) and the needed heat flux density q_{lat} (in W/m^2) exists for a one-dimensional geometry as well as for a given temperature. Under non-uniform thermal boundary conditions the heat flux density must be substituted by the net amount Δq of all participating fluxes. The total moisture loss can be calculated by integration of the heat flux densities over the time.

The expression given before is the basis for a non-destructive investigation of the moisture decrease by help of heat flux measurements. For this purpose heat flux meters are to fix onto the surfaces of the building material.

The described method has been tested successfully for different materials (brick, porous concrete, concrete) as well as boundary conditions (steady-state, transient field). The results are in a good correspondence with simultaneous gravimetric measurements.

KEYWORDS

Drying process, heat flux density measurements, moist building materials, desorption enthalpy.

INTRODUCTION

The estimation of the drying state of building materials or building components is important for subsequent construction processes as well as for the assessment of the building climate. Various moisture measurement methods are common in civil engineering. Many of them require a partial destruction of the building material (e.g. NMR, gamma-ray or gravimetric methods) or at least a drilling hole (e.g. microwaves, needle probes, lithium chloride-sensors, capacitive sensors or chemical methods). However in many cases a non-destructive measurement is desirable.

The described moisture-measuring method by means of heat flux sensors combines the advantage of being a non-destructive method with a continuous moisture monitoring. It is the aim of this paper to give a proof of the method for various practical cases with different boundary conditions and materials.

MODEL OF THE HEAT AND MOISTURE TRANSPORT

The drying process of construction materials is connected with different heat and moisture transport processes. In this paper two main cases of boundary conditions are represented. The first case is the drying under non-isothermal boundaries in an one-dimensional geometry. A practical example is the drying of an external wall with different temperatures on the surfaces. The second case is the drying under isothermal boundaries, for instance a construction material indoor.

In the first non-isothermal one-dimensional case the following heat transport processes occur. The main amount is heat transport due to heat conduction of the moist material:

$$q_c = \lambda(u) \frac{\partial \vartheta}{\partial x} \quad (1)$$

with

- q_c - heat flux density, W/m^2
- λ - thermal conductivity of dry material and sorptive bounded water, $W/(m \cdot K)$
- u - moisture content, m^3/m^3
- ϑ - temperature.

Additional heat transport is caused by moisture transport. The capillary fluid water transport gives following heat flux density:

$$q_f = c_w \rho_w a_w \frac{\partial u}{\partial x} \Delta \vartheta \quad (2)$$

with

- c_w - specific heat capacity of water, $Ws/(kg \cdot K)$
- ρ_w - mass density of water, kg/m^3
- a_w - moisture diffusivity, m^2/s .

Under real circumstances this heat transport amount is less than one percent and therefore negligible. The heat flux density due to water vapour diffusion is:

$$q_{Diff} = c_{p,v} \frac{D_v}{\mu R_v T} \cdot \frac{\partial p_v}{\partial x} \Delta \vartheta \quad (3)$$

with

- $c_{p,v}$ - specific heat capacity of water vapour, $Ws/(kg \cdot K)$
- D_v - diffusion coefficient of water vapour within air, m^2/s
- μ - water vapour diffusion resistance coefficient
- R_v - gas constant of water vapour, $J/(kg \cdot K)$
- p_v - partial pressure of water vapour, Pa.

This amount is far less than one percent of the overall heat conduction too. Finally a latent heat flux density is to take into account:

$$q_{lat} = r_{pc} \cdot g \quad (4)$$

with

- r_{pc} - specific phase change (desorption) enthalpy of water, Ws/kg
- g - mass flux density of desorbed water, $kg/(m^2 \cdot s)$.

In formula (4) q_{lat} is the heat flux demand for the desorption of water during the drying process and corresponds therefore with the actual moisture loss of the construction material. This allows to measure the drying process by heat flux measurements pointed out in the next chapter.

Contrary to the non-isothermal case for the isothermal state only the latent heat according to formula (4) is to consider.

MEASURING TECHNIQUE

A heat flux transducer consists of many thermocouples within a thin (about 1.5 mm) plate of epoxy resin. Typical sizes of the area of the plate are circles of 33mm diameter or rectangles of $3 \times 10 \text{ cm}^2$ to $25 \times 25 \text{ cm}^2$. The bigger the temperature difference between the transducer surfaces the bigger is the heat flux density across the transducer. Therefore the heat flux transducer gives a thermo voltage proportional to the heat flux:

$$q = c \cdot U \quad (5)$$

with

- c - calibration factor $\text{W}/(\text{m}^2 \cdot \text{mV})$
- U - thermo voltage (mV).

The calibration factor is about $80 \text{ W}/(\text{m}^2 \cdot \text{mV})$ for the 33mm diameter transducer and about $10 \text{ W}/(\text{m}^2 \cdot \text{mV})$ for the $12 \times 12 \text{ cm}^2$ transducer. Using formulas (4) and (5) and assuming $r_{pc} = 2454 \text{ kJ/kg}$ (20°C), $c = 80 \text{ W}/(\text{m}^2 \cdot \text{mV})$ and a resolution of the voltmeter of $\Delta U = 0.1 \mu\text{V}$ one gets an estimation of the heat flux transducer resolution Δg for the mass flux density of desorbed water:

$$\Delta g = \frac{c \cdot \Delta U}{r_{pc}} \approx 3.3 \cdot 10^{-6} \frac{\text{g}}{\text{m}^2 \cdot \text{s}} \approx 0.29 \frac{\text{g}}{\text{m}^2 \cdot \text{d}} \quad (6)$$

This mass flux density resolution is far more less than one percent of the mass flux densities of real drying processes (see following chapters) and therefore rather precise.

The heat flux transducers are applicated onto the surface of the moist test material with acryl adhesive. Different types of measurements are suited to different boundary conditions.

In the case of non-isothermal and one-dimensional conditions of a drying wall on both surfaces a heat flux transducer is to adhered. The transducer on the warm side gives the heat flux densities due to heat conduction (according to (1)), moisture conduction (according to (2) and (3)) and the latent heat flux density due to desorption of water within the wall (according to (4)). The transducer on the cold side only measures the first three contributions. Therefore the latent heat flux density q_{lat} is the difference between the warm side and the cold side heat flux density.

Under isothermal conditions the application of only one transducer on the surface is sufficient, because all entering heat flux is consumed by water desorption in this case.

An important question to clear up is the influence of the heat flux transducer on the drying process itself as the transducer represents a water vapour diffusion barrier. Indeed in a first short time period of the test the heat flux transducer is not able to measure the latent heat flux density if the moisture content of the material is in the over-hygroscopic humidity range. In this range the evaporation of water and therefore the phase change heat demand mainly occurs at the material surfaces. The transducer is able to measure the latent heat flux density reliable if the desorption and therefore the heat sink moves to deeper material layers [1]. The time period after getting sufficient precise measurement results depends on the transducers area, the initial moisture content of the material and the material itself. For quantitative values of this time period caused by the "cover effect" of the transducer see the measurement examples in the next chapters.

MEASUREMENTS

Brick

Difference climate. A first validation of the method was performed on a small scale non-plastered brick wall with an area of 0.6 m x 0.5 m and a thickness of 7.1 cm. This wall was built up into an indoor climate chamber with definite climate boundary conditions with a temperature of 25°C and a relative air humidity of 29 % rh on one side and 5°C and 80 % rh on the other side. The wall edges were isolated with polystyrene foam. The heat flux density as well as the temperature were measured on both wall sides. It was possible to determine the actual moisture content by means of weighing a special prepared detachable brick of the wall. The measurement results are shown in fig. 1 and 2.

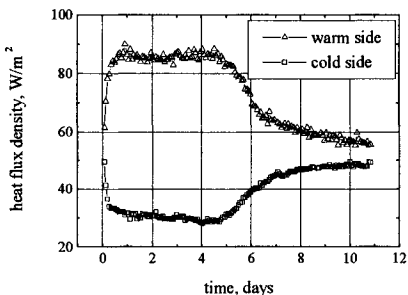


Fig. 1. Heat flux densities – brick wall

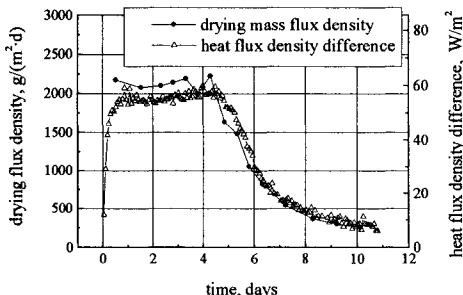


Fig. 2. Heat flux difference and mass flux density – brick wall

The entering heat flux density (see fig. 1: warm side) is determined by the two phase drying process [1]. The escaping cold side heat flux density corresponds to this behaviour. It is increasing with the decreasing demand of desorption enthalpy during the second drying phase. Both curves converge to a common value, representing the end stage of the drying process. According to the explanations before the difference between the heat flux densities on the warm and cold side corresponds to the heat demand due to drying. Figure 2 illustrates this good coincidence. A numerical integration of the heat flux density difference curve and using formula (4) yields a mass loss of 0.229 kg for the detachable brick during the test time. The overall mass loss for this brick by weighing was 0.248 kg. These results confirm the possibility to measure the drying process by heat flux measurements in this non-isothermal and one-dimensional case. Furthermore one gets the specific phased change (desorption) enthalpy of water r_{pc} with formula (4) by plotting the mass flux density against the heat flux density difference (see fig. 3). The obtained value of $r_{pc}=2.170 \cdot 10^6$ Ws/kg is about 10 % less than the theoretical value. The main reason for this error were deviations from the ideal one-dimensional geometry. In this case also heat fluxes from the wall edges enter the test wall. These fluxes were not recorded by the heat flux transducers on the surfaces.

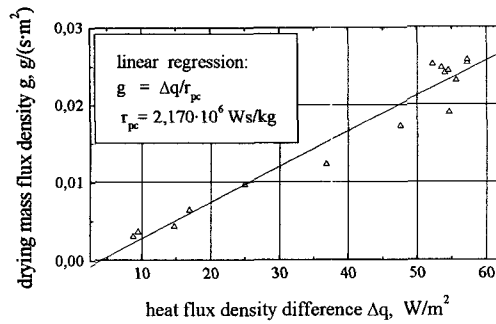


Fig. 3. Mass flux density against heat flux density yields the specific phased change enthalpy

Isothermal conditions. With the same material the drying test under indoor isothermal boundaries was performed. The test brick had a size of 24 cm x 11.5 cm x 7.1 cm and was surrounded also with polystyrene foam too on the smaller edges for a good thermal insulation. The residual moisture exchanging areas of 24 cm x 11.5 cm were exposed to 21°C. The results are visible in fig. 4. Because of the fact, that the test conditions are not ideal one-dimensional, the heat flux transducers detect a heat amount smaller than necessary for the evaporation of the mass lost. It is however possible to distinguish the two drying phases and to evaluate the drying process qualitative.

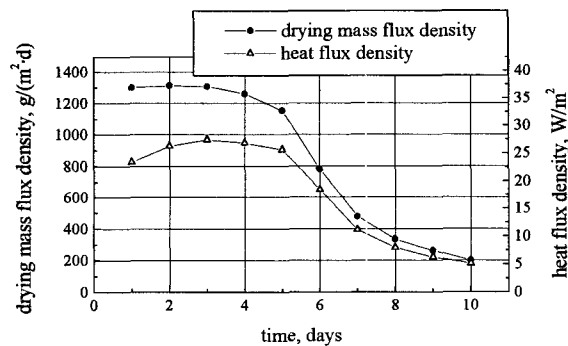


Fig. 4 Brick- isothermal conditions

Porous concrete

The next two examples describe measurements on porous concrete. First there are a test on a porous concrete wall with plaster within a difference test chamber. The second test with this material was performed on a single brick, exposed to natural climate.

Difference climate. A whole porous concrete wall was built up into a difference climate test chamber. The test wall had an area of $2.3 \times 2.3 \text{ m}^2$, a thickness of 15 cm and an initial moisture content of 18 vol%. It was plastered on both sides. One side of this wall was exposed to a temperature of 7°C and a relative humidity of air of 80 %, the other hand side to 25°C and 50 % rh. The heat flux densities were measured on both the warm and the cold surface. To minimize the “cover effect” small $3 \times 10 \text{ cm}^2$ heat flux transducers were used. Eventually the moisture content of the wall was determined during the whole drying process of the wall by weighing a detachable drawer. This drawer was representative as it consisted of the same material layers as the wall. The test lasted 11 months. The measuring results of the heat flux transducers are shown in fig. 4.

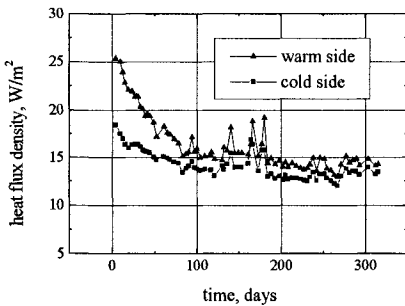


Fig. 5. Heat flux densities - porous concrete wall

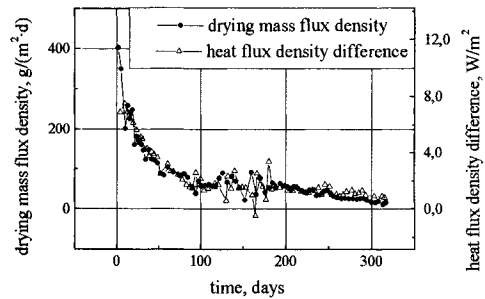


Fig. 6. Heat flux difference and mass flux density – porous concrete wall

As explained in the chapter *measuring technique* the warm side heat flux density initially exceeded the cold side flux. The latent heat due to the drying process within the wall is again the reason for this phenomenon. This latent heat is only detectable by the warm side heat flux sensor. Therefore the signal difference between the warm and cold side heat flux transducer gives the latent heat. Zero difference indicates the final stage of the drying process. Furthermore a decay of the cold side transducers signal curve in fig. 5 is apparent. This behaviour is according to formula (1) because the thermal conductivity $\lambda(u)$ decreases with decreasing material moisture content u [1]. Therefore the decay ceased at the end of the drying process. This instant relates to the zero signal difference of the heat flux transducers.

Figure 6 shows the difference of the heat flux densities along with the mass flux density due to drying. It is obvious, that already about 20 days after the test start the difference heat flux density corresponds with the latent heat flux density and the drying mass flux density respectively.

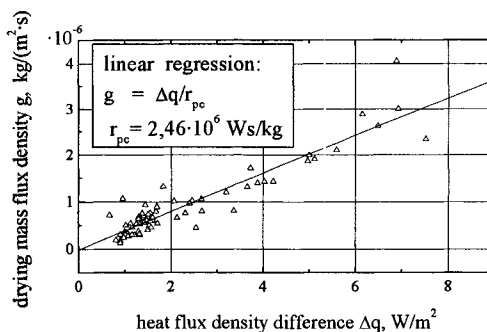


Fig. 7. Mass flux density against heat flux density yields the specific phase change enthalpy.

The plot of the drying mass flux density g against the heat flux density difference Δq (see fig. 7) is another good proof of the reliability of the measurement method under the actual conditions. According to formula (4) the reciprocal slope is the specific phase change enthalpy r_{pc} . Due to the better one-dimensional conditions in relation to the case of chapter *brick*, the value of $r_{pc}=2460$ kJ/kg is in a very good coincidence with the theoretical value of 2454 kJ/kg (20°C).

Natural climate. Yet another drying test was performed on porous concrete under the influence of real climate. It was intended to examine, whether the good results of the test chamber measurements are transferable with sufficient precision to a real drying process of a building material. The porous concrete test brick had a size of 0.22 m x 0.17 m x 0.16 m and was exposed to natural climate from may until august. To prevent repeated wetting the brick was protected from rain by a roof. The measurement results are shown in fig. 8.

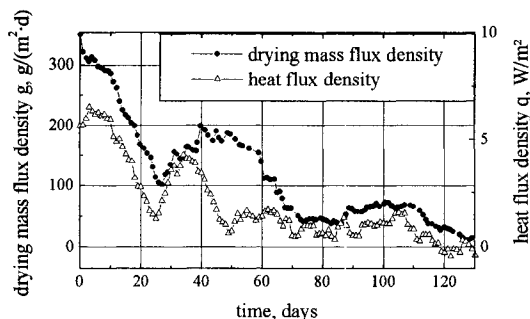


Fig. 8. Drying of porous concrete under natural climate

Also under natural climate it is apparent, that the heat flux density measurement results follow the drying tendency in principal. However the real heat flux density values are less than the heat flux density required for the gravimetrically measured drying mass flux density. This behaviour arises from the heat flux transducers property to be very sensitive to deviations from the ideal one-dimensional hygro-thermal field in this real case. The integral mass determination

by weighing is independent from this deviations however. According to this fact, the heat flux transducer responds faster to fluctuations of the climate boundary conditions. Therefore it is not meaningful in this test to compare momentary values of heat and mass flux density.

Brick with plaster

Changes in the capillary structure of the building materials or altered exchange conditions on the surfaces are essentially modifying the dynamics of the drying process. Then the distinction of two drying phases like visible in fig. 1 and fig. 2 is often impossible. In the case of unplastered brick already the shape of the heat flux density curve gives sufficient information on the current drying phase whereas in the case of plastered or rather salt containing brick this information lacks. Bear in mind, that the plastered brick case is also connected with some hydration heat in the very early drying phase. Therefore the heat flux density measurement values in this time period might be to small if the plaster layer is considerable thick (2 - 3 cm).

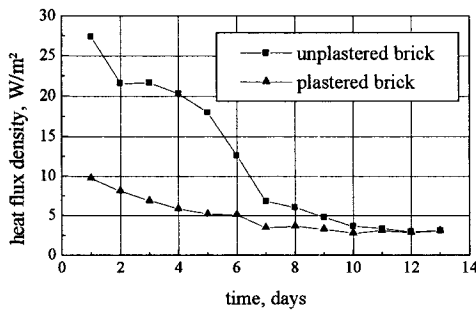


Fig. 9 . Heat flux densities – plastered and unplastered brick

Figure 9 shows the heat reception while a drying up of a plastered (plaster thickness 1 cm) moist brick in comparison to a brick of the same geometry but without plaster. The brick sizes are similar to the test case of chapter *brick*. The small heat fluxes entering the plaster indicate a distinct slower drying process. A seeping flow of water through the capillaries as characteristic for the so called 1. drying phase is apparently impeded.

Building materials with salt content

A brick (size and test conditions see also chapter *brick*) wetted with a salt solution (35g NaCl, 5g Na₂SO₄ and 15g NaNO₃ in 1 litre H₂O) shows a similar behaviour like the plastered brick explained in the previous chapter. The reason for the diminished drying velocity is but another. Due to the salt content the water vapour saturation pressure is reduced within the brick. Therefore the water vapour pressure gradient to the ambient air and consequently the water vapour flux decreases. Consequently this lower water vapour partial pressure is responsible for the diminished heat flux density of the salt brick in comparison to the saltless brick under the same test conditions (see fig.10). In addition to this reason the block of capillaries by salt crystals can cause a slower drying [3].

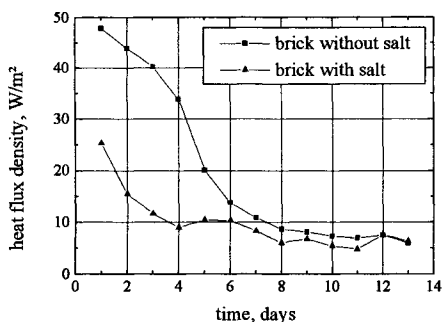


Fig. 10. Heat flux densities - salt containing brick and saltless brick

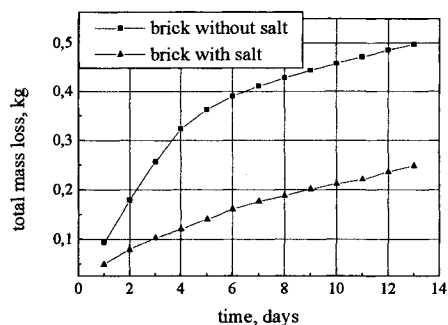


Fig. 11. Total mass loss - salt containing brick and saltless brick

Concrete

In the case of fresh concrete or gypsum for an estimation of the drying state it is not sufficient to take into account only the heat flux entering the material from the ambient air. In addition to this energy also the hydration heat produced within the material is to consider for the energy balance. The latter amount is divided into two parts. One part evades through the material surfaces, whereas the other part is consumed by the drying process already since the test begin. In fig. 12 this is noticeable on an example of fresh concrete with heat flux transducers on the surfaces.

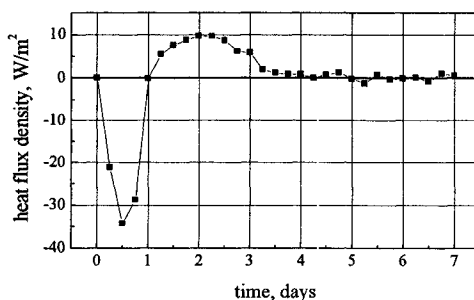


Fig. 12. Heat flux density - concrete

This concrete sample during the first day delivers heat to the surroundings (negative values in fig. 12) and subsequent heat flux due to drying enters the concrete (positive values in fig. 12). The begin of the drying process already in an early period is proved by the total energy balance. In the present case an estimated hydration heat of about 132 kJ was produced and from the 2nd until the 7th test day 71.7 kJ were accepted by the sample from the surroundings. Consequently a total heat of 203.7 kJ was available. Initially a part of 79.8 kJ of this amount was delivered to the environment. The residual part of 123.9 kJ would be sufficient to

evaporate 0.051 kg water at 20°C. A gravimetrically measurement yields an evaporated mass of 0.062 kg. This result confirms the deliberations with respect to the precision of the value of the hydration heat in this case.

CONCLUSIONS

The introduced test method for the evaluation of the drying process of building materials and components was proved on several test examples with different materials and boundary conditions. If there are good one-dimensional and isothermal test conditions formula (4) holds and one gets a satisfying correspondence between the desorption rate of water and the needed heat flux density. Under non-isothermal boundary conditions the net amount of desorption heat of all participating heat fluxes is to take into account for the calculations. Then a quantitative estimation of the drying behaviour is also possible.

The method has a high sensibility. This feature enables to evaluate drying processes in the range of over-hygroscopic moisture content down to the moisture equilibrium.

In the case of deviations from the ideal one-dimensional geometry the measured heat flux is often less than the theoretical demand due to the water desorption. However one gets qualitative information about the drying state and dynamics.

The utilization of the method is not limited to homogeneous materials. It provides also an evaluation of the drying progress in the case of multilayer systems, salt containing bricks or under hydration conditions.

REFERENCES

1. Rogass, H., Fischer, U., Rudtsch, S. (1997). *Bauphysik* 5, 150.
2. Krischer, O., Kast, W. (1992). *Die wissenschaftlichen Grundlagen der Trocknungstechnik*. Springer Verlag, Berlin.
3. Künzel, H. (1991). *Bautenschutz und Bausanierung* 4, 63.

A MICROWAVE-SENSOR FOR MONITORING THE MOISTURE CONTENT OF CONCRETE

B. Jannsen and A. F. Jacob
 Institut für Hochfrequenztechnik
 Technische Universität Braunschweig
 D-38023 Braunschweig, Germany

ABSTRACT:

The adaptive modeling of chemical attack for the prediction of durability and for the quality control of concrete structures requires the assessment of the moisture content. A sensor is presented to determine the permittivity which is related to the moisture content. The simple and compact sensor requires a microwave reflection measurement. It consists of a coaxial/circular waveguide discontinuity, where the circular waveguide is filled with the unknown material. From the measured reflection coefficient of the discontinuity the dielectric constant of the material can be extracted by means of a full wave analysis. This procedure was validated by determining the known dielectric constants of Teflon and 1-propanol. To monitor the moisture content of concrete the sensor is filled with a porous material that is in contact with the surrounding concrete. For calibration the permittivity is determined under different specified moisture contents.

KEYWORDS: moisture, microwave, permittivity, measurement, concrete.

INTRODUCTION

The assessment of the moisture content is required for the adaptive modeling of the chemical attack on concrete. This is essential for the prediction of the durability and for the quality control of concrete structures [1]. A waveguide-sensor with coaxial excitation was designed to determine the permittivity which, in turn, is related to the moisture content. Based on a numerical description of the coaxial/circular waveguide discontinuity a model of the sensor was developed. For practical moisture determination the correspondence between permittivity and moisture must be established. First results of a practical measurement on a test-building under natural weathering conditions are presented.

THE SENSOR

The absorption of water affects a characteristic electrical property of a material, namely the permittivity ($\epsilon_r = \epsilon_r' - j\epsilon_r''$). This parameter can easily be determined at microwaves, either in transmission or reflection measurements. Resonant sensors offer an increased sensibility at the expense of bandwidth [2]. In order to obtain a maximum of information (bandwidth) and for simplicity a reflection-type sensor was chosen here. It is based on a circular waveguide of small enough diameter for operation below cutoff in the considered frequency range (Fig. 1). One end is left open so that the porous filling (test-material) is in contact with

the moist surrounding material to be characterized. The waveguide has to be sufficiently long to prevent microwave leakage through the open end, a possible source of measurement errors.

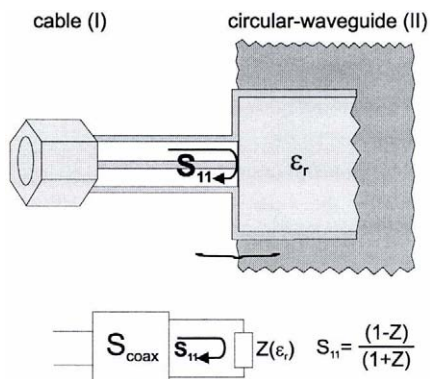


Figure 1: Model of the sensor

The other end is connected to a standard coaxial line for the measurement of the reflection coefficient S_{11} .

The sensor performance relies crucially on the choice of a suitable test-material. For a high sensitivity the permittivity must strongly depend on the moisture content [2]. Therefore, porous materials, particularly like cement or concrete, are well qualified. But also porous ceramics or polymers are imaginable. In any case the relation between the moisture in the test-material and the moisture in the concrete under investigation must be specified. This can be achieved by measurements or with suitable models [1].

ANALYSIS

To determine the relation between the reflection coefficient S_{11} and the material parameter ϵ_r , the discontinuity between the coaxial line and the circular waveguide was analyzed using a mode-matching approach [3]. The eigenmodes in both guides are assumed to be terminated with their characteristic impedance. Because of the coaxial arrangement of the sensor only a part of the whole mode spectrum can be excited [4]. This greatly simplifies the analysis. At

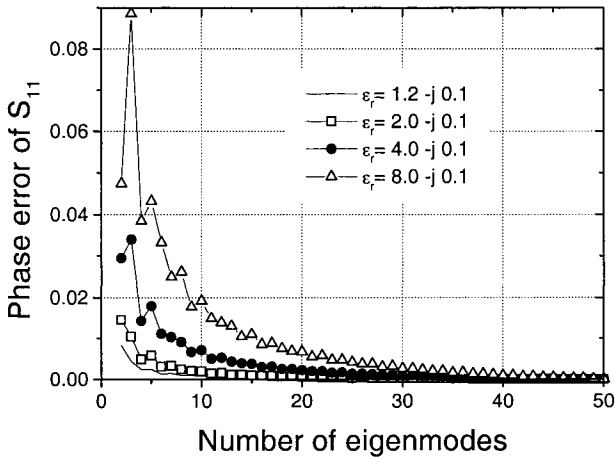


Figure 2

some distance of the discontinuity the evanescent higher order modes on the coaxial line are sufficiently attenuated so that only the fundamental mode needs be considered. Hence, the discontinuity can be described by a (normalized) impedance Z which is a function of the permittivity of the test material. Spurious reflections and losses of the coax or the connector are included in the scattering matrix S_{coax} , which can be determined from a calibration with three known terminations (e.g. a short, air and a liquid).

The infinite set of eigenmodes needed for an exact description of the discontinuity has to be truncated in practice. This results in a numerical error. The convergence is illustrated in Figure 2 which shows the phase error (absolute value) of the reflection coefficient versus the number of modes for different values of ϵ_r ' at 5 GHz. The following parameters were used for the coax: radius of the center conductor = 1.5 mm, radius of the outer conductor = 3.5 mm, $\epsilon_r = 2.03 - j0.0004$. The radius of the circular waveguide was 3.5 mm. The value of S_{11} obtained with 50 eigenmodes was taken as reference. For more than 30 eigenmodes the calculated phase error is smaller than the uncertainty of commercially available measurement instruments. The convergence is better for smaller ϵ_r' , ϵ_r'' , and radius of the circular waveguide. The magnitude of S_{11} behaves in a similar way [5].

EXTRACTION OF THE PERMITTIVITY

The permittivity is obtained numerically by comparing the theoretical value of S_{11} with the

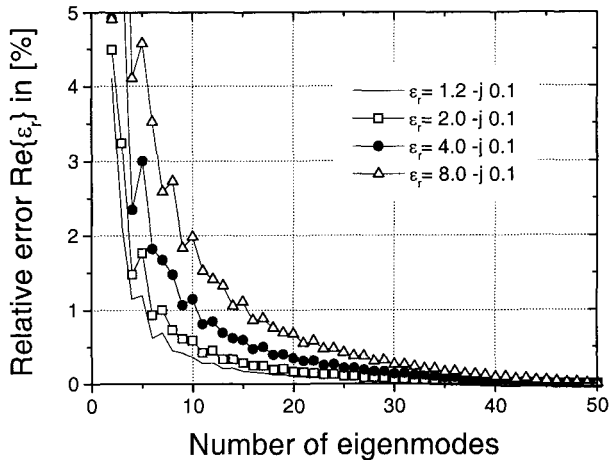


Figure 3

measured one. Figure 3 shows, as a typical result, the convergence of ϵ_r' for the same data as in Figure 2. A synthetic reflection coefficient obtained from the analysis with 50 eigenmodes was taken as the “measured” value. An inspection of the results shows the expected behavior. The convergence of the imaginary part, not shown here, is very similar. A detailed numerical investigation of the sensitivity using statistically altered input data shows that the algorithm is stable against disturbances that remain on the order of typical measurement errors. The uncertainty increases with ϵ_r' and the radius of the waveguide [5].

CONSTRUCTION OF THE SENSOR

Two types of sensors were used. The first one (test-sensor) consists of a commercially available APC7/SMA precision connector. The SMA-part is replaced by a circular waveguide (radius: 7 mm). Because of the precise manufacturing, losses and reflections within the connector can be neglected; a calibration is therefore not required. A detailed report on its properties can be found in [5]. For practical applications the construction of the sensor was modified. A semi-rigid cable (0.250”) provided with a connector at one end and a circular-waveguide at the other a simple, cheap and variable sensor (prototype) was realized (Fig. 4). Due to the larger losses and reflections of this structure a calibration is now necessary. Three standards, for instance a short, an open and a load (such as a well-known liquid) are needed for this purpose. The properties of this sensor will be discussed in the following.

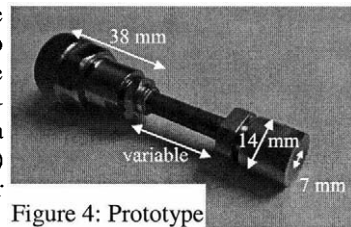


Figure 4: Prototype

VERIFICATION

The measurements of the reflection coefficient were done with a vector network analyzer in the frequency range 30 kHz - 6 GHz (HP8753D) and 1 GHz - 17 GHz (HP8510C). To verify the validity of the model, the functionality of the sensor and the accuracy of the extraction algorithm well known materials (TEFLON, various liquids) were characterized. To this end the circular waveguide was filled with the material to be characterized. Figure 5 depicts the extracted permittivity of TEFLON. The real part shows a very good agreement with the value known from literature ($\epsilon_r=2.03-j 0.0004$). The very small imaginary part is more uncertain.

This is a typical feature of non-resonant sensors in general and of reflection-type ones in particular. In the case of higher losses, as for instance in concrete, the sensor operates well. This is demonstrated in Figure 6, which compares the permittivity extracted from a measurement on 1-propanol with the theoretical prediction according to the Debye-model [2]. For calibra-

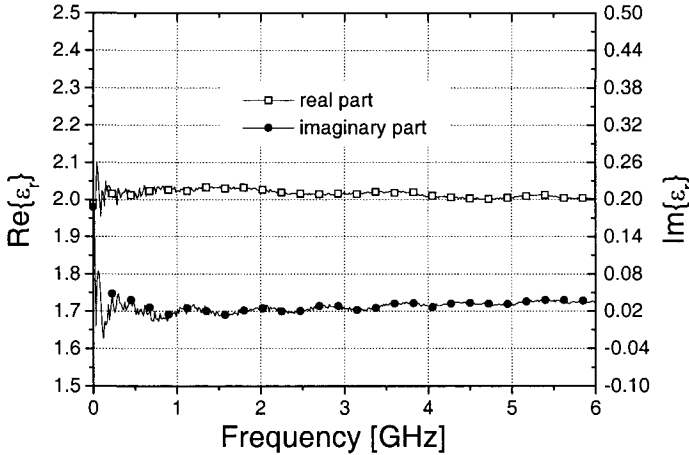


Figure 6

tion the waveguide was filled with air, acetone and methanol, here. These and numerous other experiments show that a material with $\epsilon_r'' > 0.1$ can be characterized with sufficient accuracy using this sensor. Therefore this sensor should be suited for moisture measurements in concrete.

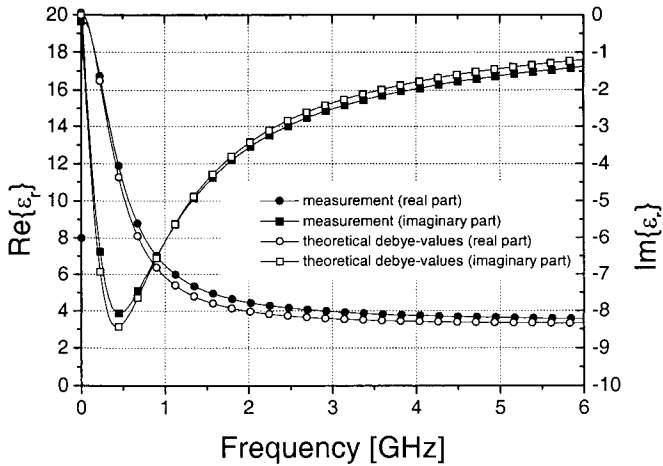


Figure 5

MEASUREMENT RESULTS

For optimum moisture transport the sensor should be filled with a test-material that is identical to the surrounding material. This could lead to the following problems: Large aggregates in the concrete could result in non-reproducible inhomogeneities, which cannot be taken into account by the model and would therefore falsify the measurements. Hence, there are some requirements on the test-material:

- sensitivity to moisture,
- long-term stability,
- homogeneity.

In the following the study of two different test-materials will be presented. The measurements were performed with the test-sensor and no calibration was used.

Cement: The first test-material was a cement (CEM I 32.5 R, w/z=0.4). The measurement results for five similar samples are presented in Figure 7. The relation between the relative

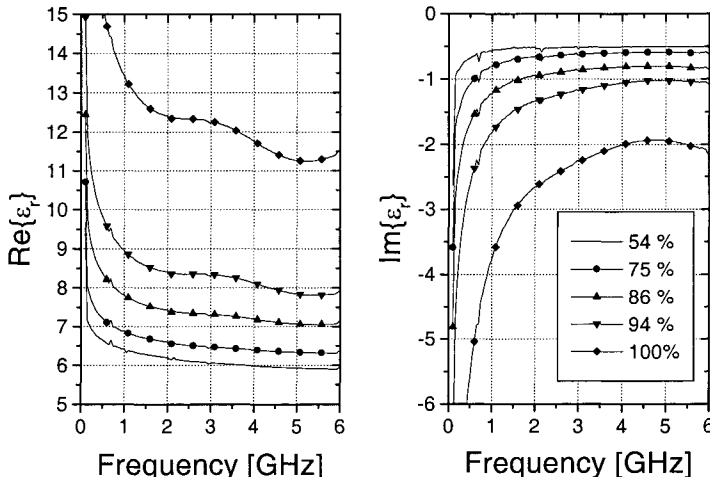
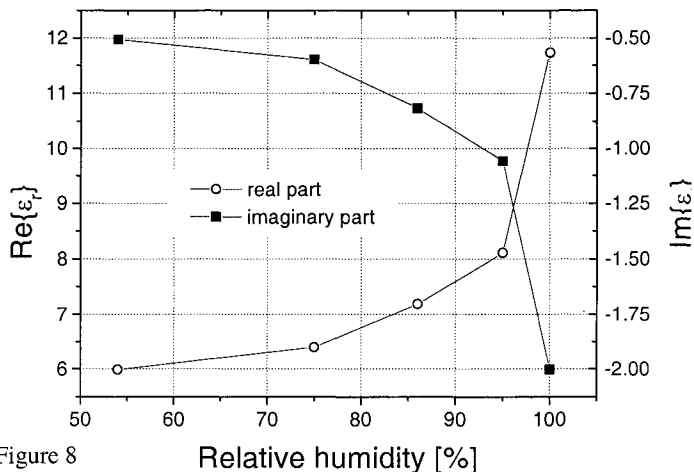


Figure 7 humidity at 25°C and the permittivity follows from a calibration procedure: Different saturated aqueous solutions of inorganic salts were used to define constant relative humidity levels in air tight boxes and the permittivity of probes placed in these boxes were specified [6]. When stating the relative humidity level the temperature dependence must be taken into account. Although in the experiment reported here the stationary condition was not fully reached

the moisture dependence of both the real and the imaginary part is obvious. This broadband measurement provides a large degree of redundancy which decreases measurement uncertainty. The curves in Figure 8 were extracted from these results and show the increase of the sensitivity with relative humidity at 4 GHz.



Ceramic: A porous ceramic test-material was investigated next because of its good mechanical and chemical properties, its reproducibility and its homogeneity. However, sensors equipped with this kind of ceramic showed only little sensitivity for a relative humidity under 90%. A strong effect on the permittivity can only be seen when soaking the ceramic (Figure 9). In this experiment the material was placed a fairly long time in distilled water. To quantify the relative moisture content under these conditions gravimetric measurements are needed.

In the following only the permittivity of the sample was monitored during the drying process.

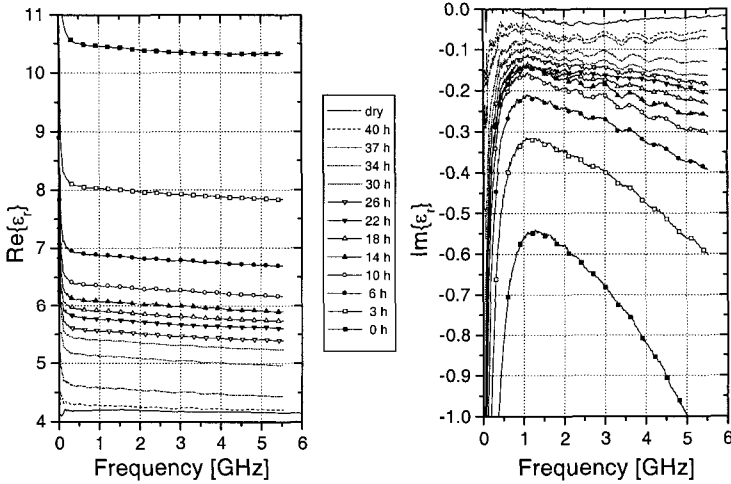


Figure 9

A clear decrease (increase) of ϵ_r' (ϵ_r'') with time can be observed. The plot of ϵ_r'' hints at a resonance above 6 GHz. This was confirmed by another measurement over a wider frequency range (Figure 10). For an optimum sensitivity this sensor should be operated on the slope of the resonance, i.e. around 5-6 GHz in this case. To improve the sensitivity of this sensor experiments with ceramics of different porosity are planned.

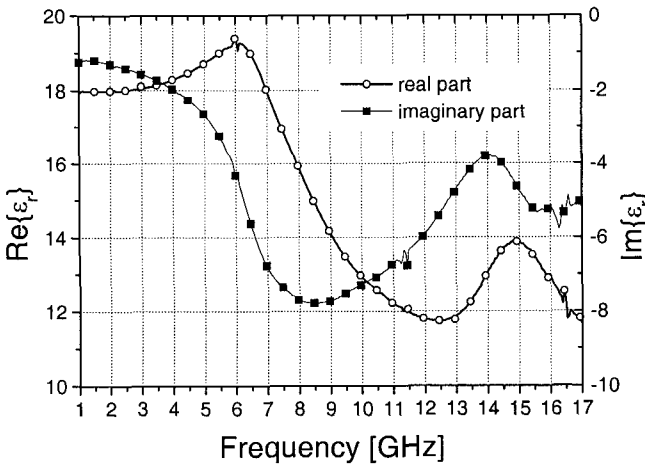


Figure 8

APPLICATION

Figure 11 shows two sensors mounted in a prestressed test-building, which is exposed to the natural environment (humidity, temperature, etc.). The sensors are filled with cement as a test-material and placed with their tip 2 cm beneath the surface. The first measurement was made two days after construction. Figure 12 shows a typical result. The real part of the permittivity and accordingly the moisture content decreases with time during the first few weeks (drying process). The different peaks in the diagram (e.g.

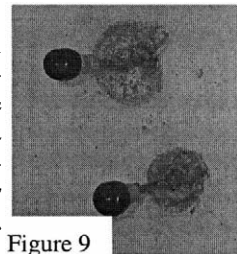


Figure 9

after 70 days) correspond to measurements done after strong rainfalls (humidification). The other sensor mounted in the test-building behaves in the same way.

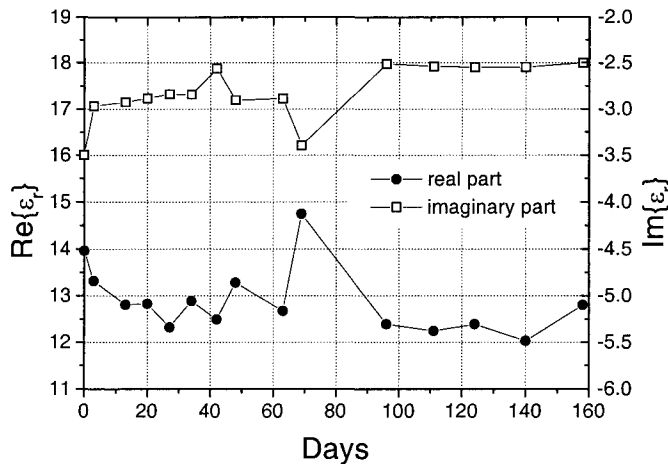


Figure 10

CONCLUSION AND OUTLOOK

The presented results show the qualification of the presented sensor in determining the moisture content of concrete. With the determination of the permittivity a sensor independent parameter can be calculated and the comparability with other sensors is simplified. For practical operation and to improve the sensibility, accuracy and reproducibility additional experiments with emphasis on

- the temperature dependence,
- additional test-materials,
- and gravimetric measurements of the relative moisture content

are needed.

REFERENCES

1. F. Schmidt-Döhl, *Ein Modell zur Berechnung von kombinierten chemischen Reaktions- und Transportprozessen und seine Anwendung auf die Korrosion mineralischer Baustoffe*. PhD Thesis, Technical University Braunschweig, 1996.
2. K. Kupfer: *Materialfeuchtemessung*, Renningen-Malmsheim: Expert-Verlag, 1997
3. G. Busse, A.F. Jacob, Lossy Chiral Slabs in Circular Waveguides. *Inst. Elect. Eng. Proc.. Microwave, Antennas, Propagat.*, vol. 143, no. 1, pp. 51-56, 1996.
4. N. Marcuvitz: *Waveguide Handbook*. New York, Toronto, London: McGraw-Hill Book Company, inc., 1951.
5. B.Jannsen, A.F. Jacob, Ein Mikrowellensensor zur in-situ-Messung von Feuchte in Beton, in Proceedings 10. Feuchtetag, Berlin, 1999.
6. L. Greenspan, *Humidity Fixed Points of Binary Saturated Aqueous Solutions*, Journal of Research of the National Bureau of Standards, vol. 81A, no. 1, 1977.

AUTHOR(S): Institut für Hochfrequenztechnik, Technische Universität Braunschweig, Schleinitzstr. 23a, D-38106 Braunschweig, Germany, Phone Int +49-531-391-2020, Fax Int +49-531-391-2045, E-mail: b.jannsen@tu-bs.de, a.jacob@tu-bs.de

This Page Intentionally Left Blank

MOISTURE MEASUREMENTS IN BUILDING MATERIALS WITH MICROWAVES

Hannu Kääriäinen, Michael Rudolph^{*}, Dieter Schaurich^{*}, Kauko Tulla
and Herbert Wiggenhauser^{*}

VTT Technical Research Centre of Finland
Building Technology
BAM Bundesanstalt für Materialforschung und -prüfung^{*}
Abteilung VII Bauwerkssicherheit

ABSTRACT

In order to assess the condition and evaluate the reliability of buildings and structures, it is essential to establish the moisture condition of structural elements of the building. NDT-methods are increasingly being used for such moisture measurements because they do not cause any damage to the building under investigation. Microwave transmission is one of the NDT-methods that has been in use for several years.

The equipment used in this research has been developed at BAM over the last few years. The method requires two parallel boreholes in the specimen in which two microwave antennae can be moved. The moisture content in the material can be calculated from the microwave intensity transmitted between the two boreholes. Moisture profiles along the boreholes can be obtained by moving the antennae in steps along the length of the boreholes and taking measurements at each step.

The microwave frequencies used in the laboratory measurements ranged from 8 to 16,5 GHz in steps of 0,5 GHz. The diameters of the antennae were between 7 and 9 mm, and of the boreholes between 8 and 12 mm. The moisture content measured by the microwave technique was verified by the moisture content determined by weighing.

The microwave method produced measurement uncertainties between 0 and 2 % by volume for all the materials studied in this report. In some measurements and materials the differences were so small that they could be neglected. The accuracy of the results can be improved by eliminating some of the uncertainty factors. Special parameters for the quality of the material and the aggregate size were introduced in the moisture calculations. When these factors were determined for each material, it was possible to obtain comparable results for the microwave and weighing measurements.

KEYWORDS

Construction materials, moisture transport, moisture meter, microwaves, concrete, sand, wood.

INTRODUCTION

Moisture measurements in buildings must be applicable to many different kinds of building materials. A building element may be composed of different materials, and different moisture levels may exist. Only in a few cases destructive methods can be applied. In most cases non-destructive or quasi-non-destructive testing methods should be preferred.

The most common and most accurate method is the drying method, where specimens are removed from the investigated construction and dried in an oven.

Microwave moisture measuring method has shown early good results with materials such as brick, mortar or sandstone. Only two boreholes with a diameter of 8 or 12 mm are required, and the method can therefore be considered a quasi-non-destructive-testing method. The depth of the moisture measurement depends only on the length of the antennae and the boreholes in the construction. The moisture is measured between the two boreholes along their length and therefore the measurement can be made through different layers.

In Finland, constructions made of composites of different thin layers are much more common than massive constructions. The materials investigated in this report are concrete, sand, wood and their composite constructions.

THE MICROWAVE TRANSMISSION METHOD

The basic principle

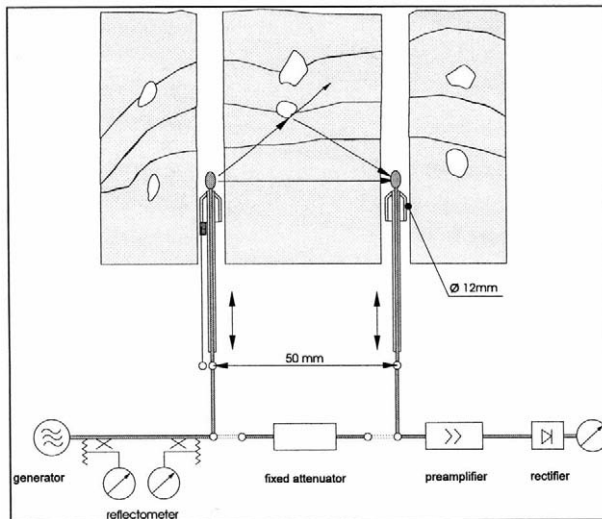


Figure 1. Arrangement of the antennae in the material and the microwave circuits //.

Moisture measurement with microwaves is based on the propagation of electromagnetic waves in the material. These waves pass through the material between two antennae, a transmitter and

a receiver. Moisture absorbs part of this energy transmitted between the antennae. The moisture content can then be calculated from this energy loss according to a model with a numerical data analysis programme.

Low moisture levels

There are some additional measurement uncertainties for low moisture contents, e.g. change in the bond structure of the water molecules to the matrix and the scattering of the microwaves due to inhomogeneities.

The shape of the function describing the attenuation of microwaves in relation to the moisture content shows two linear ranges (see Figure 2). Even material like brick that seems to have no aggregates attenuate the microwaves at zero moisture level and high frequencies. This influence of small aggregates brick and sandstone has not yet been included in the model. The attenuation depends on the size and distribution of the aggregates.

The first segment AB with a lower inclination corresponds to water physically bound to the interior surfaces of the pores. Therefore, the segment AB depends on the pore size distribution in the material. The segment BC represents liquid water in the pores. The dielectric properties of water bound to the interior surfaces and of free water are different. Point B describes the water content where the bonding of additional water molecules changes. For material with small interior surfaces, point B is found at values of about 1,5 vol-% (gravel). For material with larger inner surfaces (e.g., quartz sand), it can be as high as 8 vol-%. Clay and silica gel have much higher values. The functions shown in reference /6/ give only a qualitative picture of the behaviour of different building materials.

When measurements are performed at low moisture levels, the kind of material should be known, so that the scattering parameters and point B can be corrected accordingly.

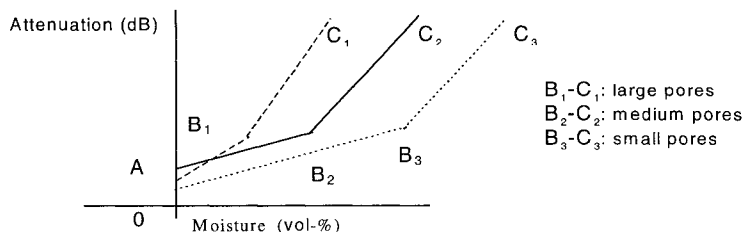


Figure 2. Principle of attenuation in relation to moisture content /1/.

- 0A - attenuation due to scattering on aggregates
- AB - attenuation due to physically bound water
- BC - attenuation due to free water

Measurement and calculation of moisture in inhomogeneous materials.

Microwave moisture measurements in inhomogeneous materials involve some difficulties as:

- the internal structure of the materials to be examined produces scattering effects;
- some materials contain only a very small amount of water. The absolute measurement uncertainty should therefore not exceed $\pm 1,5$ vol-%;

- the reinforcement may cause deflections or interferences of the microwaves.

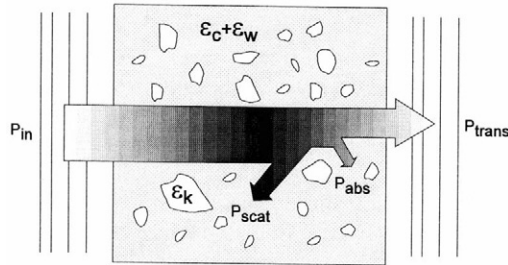


Figure 3. Transmission of microwaves through a concrete specimen. The dielectric constant of the aggregates is ϵ_k , of the cement, ϵ_c and of water, ϵ_w .

The dielectric constants change and cause reflections at the interfaces between the cement matrix and the aggregates. Each aggregate produces scattering with its maximum scattering cross section at its resonance frequency /2, 3, 4/.

The scattering caused by an aggregate with a diameter a depends on the wavelength λ . There are three classes of scattering ranges /5/:

- class I: $0 \ll a \ll \lambda/30$ no scattering
 - class II: $\lambda/30 \ll a \ll \lambda/8$ scattering according to RAYLEIGH's law
 - class III: $\lambda/8 \ll a$ scattering according to MIE's law,
- a and λ in millimeters.

The energy losses occur even in dry material. Microwave measurements generally show higher moisture contents compared with those obtained by drying and weighing. This is due to the imaginary part of the dielectric constants for building materials. The function for the dielectric constant in the presence of scatterers may have the following form:

$$\epsilon_s = a \cdot c_1 \cdot f^{c_2} \quad (1)$$

Scattering is proportional to the aggregate size a . The relationship between the frequency range and the extent of scattering is mainly given by the f^4 law of the Rayleigh-scattering /1/, which means $c_2 = 4$. Because there are always some Mie-scatters, a small frequency dependence remains. The value c_1 is only weakly influenced by the frequency.

The values for c_1 and c_2 are calculated from the measurement of the dry specimen. The dielectric constant ϵ_s was introduced in the data analysis programme as a frequency-dependent term. The moisture content of a dry concrete specimen was measured and calculated, and verified by weighing. In the data analysis, the coefficients c_1 and c_2 were varied until the calculation showed zero moisture content for the dry specimen. Of course, this method is also subject to other uncertainties in the measurement process. Table 1 shows the constant values c_1 and c_2 for some specimens in the formula (1).

Table 1. Constant values of some specimens in the formula (1)

Fequency (GHz)	$C_2 = 4$		
	C_1		
	VTT01	VTT02	VTT03
8,5	$1,00 \times 10^{-3}$	$6,23 \times 10^{-6}$	$1,16 \times 10^{-5}$
10	$3,61 \times 10^{-6}$	$3,80 \times 10^{-6}$	$3,99 \times 10^{-6}$
11,5	$2,11 \times 10^{-6}$	$1,89 \times 10^{-6}$	$2,35 \times 10^{-6}$
15,5	$5,05 \times 10^{-7}$	$1,95 \times 10^{-7}$	$3,43 \times 10^{-7}$

LABORATORY TESTS

Specimens

The following materials were used in the laboratory tests:

- eight concrete specimens (max. aggregate size 12 mm)
- four concrete specimens (max. aggregate size 8 mm)
- two wood specimens (glue-laminated pine)
- sand (max. aggregate size 4 mm, standardized sand)

One composite specimen made from the above-mentioned materials were measured.

Test programme

A series of measurements was made at different moisture levels. The initial test was done after exposing the specimens to normal indoor room climate for a longer period of time. The concrete specimens were then dried in an oven at 103-105 °C, and the wood material at 65 °C. weeks, with the process slowing down considerably at the end of the drying period.

After the measurement the dried specimens were submerged in water.

The microwave frequencies used ranged from 8 to 16,5 GHz in steps of 0,5 GHz. Since only six different frequencies could be used during one measurement scan, three subsequent sweeps had to be made to collect data at all the frequencies.

RESULTS OF LABORATORY TESTS

General

The moisture contents of the specimens were calculated from the central part of the measurement path. In the data analysis, the values measured at a distance of 20 mm from the surface were discarded because of the disturbing effects of the interface. The results obtained in this area are not reliable enough. The constants c_1 and c_2 (see eq. 1) derived from data of the specimen VTT02 were mostly used for the moisture calculations of concrete.

Concrete specimens

In figures 4 to 5, the moisture values determined by the microwave technique (M-mw) are plotted against those measured by weighing (M-grav). The line represents the points where both values are identical.

Specimens VTT01-VTT08. The results of the moisture measurements of specimens VTT01-VTT08 are plotted in figure 4, where the microwave results are plotted against those measured by weighing. The two methods give similar results, but the microwave values tend to be higher at low moisture levels and lower at higher ones. The absolute differences between the values obtained by both methods are between -2,0 and 3,8 vol-%.

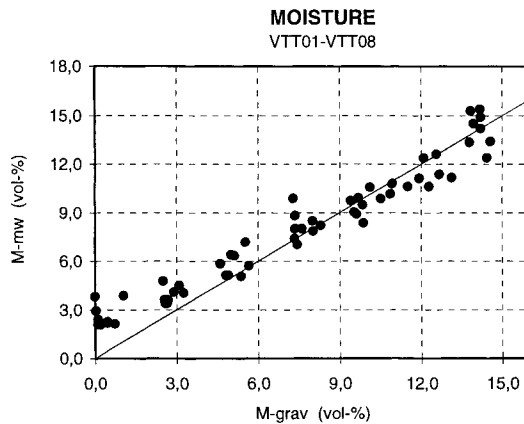


Figure 4. Moisture measurements in the specimens VTT01-VTT08. The moisture varied between 0,0 and 14,6 vol-% measured by weighing.

Specimens VTT09-VTT12. The specimens VTT09-VTT12 were thinner than VTT01-VTT08, and made of concrete with a maximum aggregate size of 8 mm. The results are again comparable with two exceptions for specimen VTT09: the microwave values of 14,7 and 16,4 vol-% contrast with values of 10,08 and 12,13 vol-% obtained by weighing. A possible explanation could be the presence of cracks in the specimen and the use of the "scattering coefficients" of VTT02 adjusted for the correct aggregate size. The microwave method produced higher values than those obtained by weighing.

In the specimen VTT12, boreholes with a diameter of 8 mm were drilled with an impact drilling machine. This drilling method produced breakouts at the opposite surface.

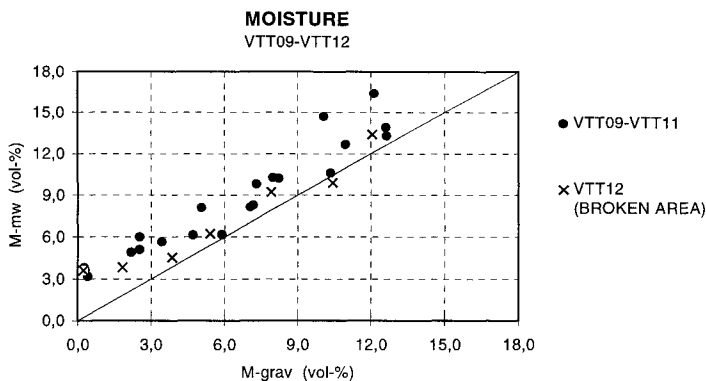


Figure 5. Moisture measurements in the specimens VTT09-VTT12. The moisture varied between 0,2-12,7 vol-% measured by weighing.

Sand and gravel

The moisture values in sand were calculated using the same parameters as for the concrete specimens. The microwave measurements in concrete gave higher values when the concrete was dry and lower values when it contained more water. The differences were similar to those for sand, but when the sand was very wet the microwave method again gave higher values than the weighing method.

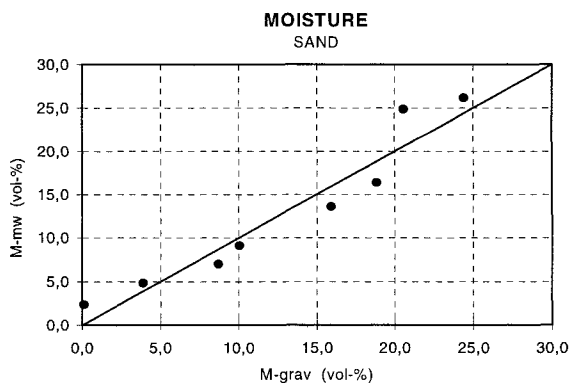


Figure 6. Moisture measurements in standardized sand, maximum aggregate size 4 mm. The moisture varied between 0,1-24,4 vol-% measured by weighing.

Wood

The differences between the microwave and the gravimetric methods were very small in the moisture range below 18 vol-%. In wet specimens the microwave method produced smaller moisture values than the gravimetric ones.

The directions of the annual rings had no influence on the moisture values determined by the microwave method. Also, some small cracks appeared in the wood specimens during the drying process. These kinds of cracks are very typical in solid wood material. Presently, the influence of the cracks on the moisture results is not completely understood.

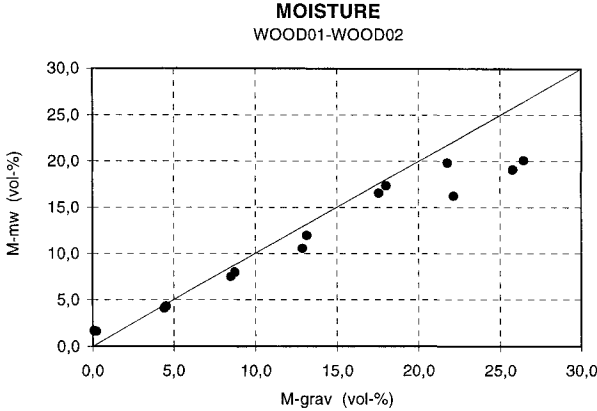


Figure 7. Moisture measurements in two different glue-laminated pine specimens. The cross section of the specimens was 99 x 99 mm². The moisture varied between 0,1-26,5 vol-% measured by weighing.

Composed structures

The composite specimen represents a typical floor construction used in Finland, mostly in small houses. This kind of floor system consists of layers of different materials with different thicknesses. The effect of the interfaces between the different materials is the same as in tests of separate materials. Small air gaps were located on both sides of the insulation material, figure 8.

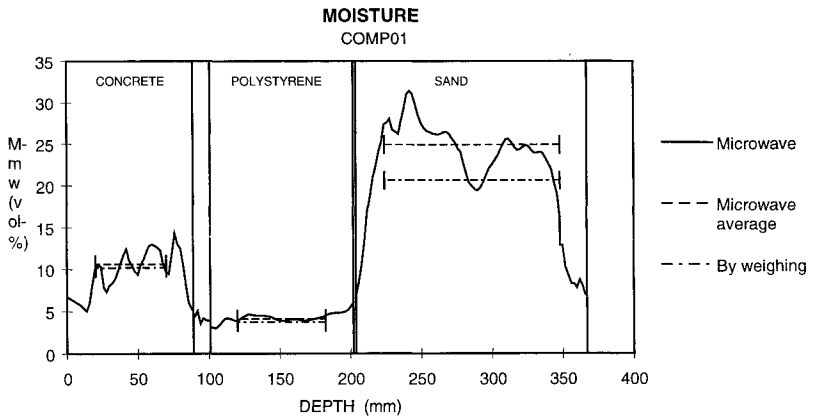


Figure 8. Moisture measurements in a composed structure of concrete, polystyrene insulation and standard sand.

CONCLUSIONS

The microwave technique has been applied to historical buildings made of brick and sandstone for several years, already. In this paper also the applicability of this method to concrete, sand and wood was tested. In addition, the moisture content in composite specimens made of the above-mentioned materials was measured.

Special formulae were developed for calculating the moisture content of materials containing specific aggregates. Two constants were introduced to allow for the influence of the scattering of electromagnetic waves at the aggregates. These formulae were used for concrete and sand, which are not homogeneous - in contrast to sandstone and brick - which are considered to be homogeneous with regard to electromagnetic wave propagation in the given frequency range.

The differences between the measured moisture values are much smaller, when ε'' (the imaginary part of the dielectric constant) is a function of the microwave frequency and the aggregate size distribution in the specimen. Two contents c_1 and c_2 for each material must be introduced to achieve a better accuracy. In these measurements only one set of constants, derived from specimen VTT02, was used.

In order to improve the accuracy of the measurement results, it is essential to determine accurate data for the parameters c_1 and c_2 describing the amplitude of scattering in inhomogeneous materials.

At low moisture levels the microwave measurements still produce slightly higher moisture contents than those obtained by weighing, whereas the values determined at higher moisture levels tend to be lower than those determined gravimetrically. In very wet sand, however, the microwave results were higher.

REFERENCES

- 1 *Kääriäinen, H., Rudolph, M., Schaurich, D. and Wiggenhauser, H.*: Moisture measurements in building materials with microwaves, VTT, publications 357, Espoo, Finland, 1998
- 2 *Stratton, J. A.*: Electromagnetic Theory, McGraw, New York 1941
- 3 *Paletta, F. and Ricca A. M.*: Concrete moisture evaluation by microwaves, Alta Frequenza, Vol. LV (1986) 4, S. 255-264
- 4 *Kupfer, K. und Morgeneier, K.-D.*: Grundlagenuntersuchungen zur Feuchtemessung von Zuschlagstoffen nach dem Mikrowellenverfahren, Betontechnik 2 (1988), S. 57-58
- 5 *Göller, A.*: Mikrowellenfeuchtemessung unter Einbeziehung wichtiger Materialparameter - ein verbessertes Konzept der Signalauswertung, Dissertation A, Technische Universität Ilmenau, Ilmenau 1992
- 6 *Schmidt, J.*: Untersuchungen zur Einsatzmöglichkeit der Mikrowellenmeßtechnik zur zerstörungsfreien und berührungsfreien Erfassung von Wasseranlagerungs- und Hydratationsprozessen an Baustoffen, Dissertation (A), Ingenieurhochschule Cottbus, Cottbus 1986

This Page Intentionally Left Blank

MEASUREMENT OF THE MOISTURE AND SALT CONTENT OF BUILDING MATERIALS

W. LESCHNIK and U. SCHLEMM

*Building Physics and Materials Science Section, Technical University of Hamburg-Harburg,
D-21071 Hamburg, Germany*

Phone/Fax: ++49-40-42878-3744/2905, E-Mail: leschnik@tu-harburg.de

ABSTRACT

For measuring the moisture content in building materials and components a reliable, non- or less-destructive moisture meter for repeated measuring is demanded. For developing such a moisture meter, a dielectric measuring method seemed to be most suitable. A systematic investigation into the dielectric properties of building materials proved, that at microwave frequencies there is a good correlation between the real part of the complex relative permittivity and the moisture content. Based on these results a microwave method and a prototype of a measuring instrument for measuring the moisture content of building materials were developed and tested in laboratory and in situ as well. As the imaginary part of the complex relative permittivity depends on the moisture and salt content of the material, the measuring method was expanded for measuring not only the moisture content of the probe but also the salt content.

KEYWORDS

Microwave measurement, moisture content, salt content, building materials

OBJECTIVES

In Europe, many damages in buildings are caused by moisture, penetrating into components, for example through leaks of the foundation or the facade of a building. The damaging effect of moisture is increased by salt, which is solved by the water and transported to the surface of the components. The moisture can evaporate, the salt however remains at the drying areas. Because of the hygroscopic behaviour of most salts further damages are nearly unavoidable. To find out the reason and the extent of a damage and to determine a measure for repair, measurements of the moisture and salt content are necessary.

For precise measuring of the moisture content of building material and components only classic destructive methods are disposable. Samples of building materials have to be taken out destructively, and the moisture content is determined accurately by applying the oven-drying method in laboratory or less accurately by chemical methods like the Calcium-Carbide method in situ. A continuous observation of the moisture content is impossible. The salt content of building material can only be determined by laboratory analysis.

For a long time scientists have been trying to develop a method for non- or less-destructive measuring of the moisture content of building materials. Up to now, no reliable measuring instrument is available for this purpose.

Table 1
Properties of an ideal moisture meter

Measurement
<ul style="list-style-type: none"> • Non-destructive or less-destructive • Independent of structural parameters of the sample • Independent of solved salts in the sample • Continuous and repeatable at the same position • Determining the moisture profile • Save in view of injuring radiation

Table 2
Possibly suitable measuring methods for developing an ideal moisture meter

Measuring methods
<ul style="list-style-type: none"> • Thermometric • Hygrometric • Nuclear • Nuclear Magnetic Resonance • Electric, radio frequencies • Electric, microwave frequencies

In Table 1 the demands are shown which a moisture meter for application in civil engineering should meet. The methods which in principle may be suitable for this purpose are shown in Table 2. Comparing the advantages and disadvantages of the different techniques it resulted, that an electrical method seemed to be most suitable for developing a moisture meter meeting the requirements shown in Table 1 [1]. This paper reports on investigations which were carried out by the author, his collaborators and the partners in co-operation¹⁾²⁾³⁾ to develop a moisture meter by evaluating electric parameters. Furthermore, a method for in-situ and less-destructive measuring of the salt content of building materials will be presented.

DIELECTRIC PROPERTIES OF BUILDING MATERIALS

According to MAXWELL'S theory the electromagnetic properties a dielectric material can be expressed by the complex relative permittivity $\epsilon(\omega) = \epsilon' - j\epsilon''$. In this relation ϵ' is the dielectric constant, ϵ'' the loss factor and ω the angle frequency. For dry building materials $\epsilon'=3...6$ and $\epsilon''\approx 0$ are found, for pure water up to frequencies of some GHz $\epsilon'\approx 80$ and $\epsilon''\neq 0$. Measuring at wet building materials, both parameters, the dielectric constant and the loss factor as well, can be used to measure the moisture content of the materials. However, there was only fragmentary knowledge of the dependence of the dielectric parameters on the structural, mechanical and chemical properties of the building materials. Therefore a detailed investigation into the di-

References

- 1) Research project of the Deutsche Forschungsgemeinschaft, No. LE 765/1 and LE 765/2 «Diagnostik und Sanierung», partly in co-operation with Prof. Dr. Venzmer, Technical University Wismar, final report 1995 (in German)
- 2) Research project of the Stiftung Volkswagenwerk, No. I/67 193 «Kontinuierliche und zerstörungsfreie Feuchte-meßverfahren mit Mikrowellen», in co-operation with Prof. Dr. Knöchel, Prof. Dr. Kammeyer and Prof. Dr. Eggers, Technical University of Hamburg-Harburg, final report (1996) (in German)
- 3) Research project of the Deutsche Forschungsgemeinschaft, No. LE 765/3-1 and LE 765/3-2 «Entwicklung eines Feuchte- und Salzmessers», final report (1999) (in German)

electric properties of building materials was made in the frequency range from 50 Hz to 4.000 MHz [2][3]. Samples were made of different sorts of brick, sandstone, sand-lime brick, lime mortar and cement mortar. The moisture and salt content of the samples were systematically varied and determined absolutely by classic methods. By means of a network analyser different electric signals were measured and the complex permittivity was calculated. The measuring arrangement depended on the frequency range. At frequencies up to 1 MHz a modified capacitor was used, at frequencies from 1 MHz to 1.000 MHz a dilated co-axial guiding and at frequencies above 1.000 MHz wave guides were applied. Evaluating the measurements it results, that different frequency ranges have to be distinguished.

Frequencies below about 100 MHz

At frequencies below 100 MHz a precise measurement of the moisture content is impossible. At low frequencies contact and dielectric transition problems are dominating. In general a separation of the influence of water and salt on the dielectric parameters is impossible, as the permittivity depends in the same way on the moisture content as on the salt content of the probe.

Frequencies between about 100 MHz and 1.000 MHz

At frequencies above 100 MHz the dielectric constant and the loss factor depend in different ways on the moisture content and the salt content of the probe. Thus, the influence of water and salt on the dielectric parameter can be separated by measuring the real and the imaginary part of the permittivity.

Frequencies between about 1.000 MHz and 4.000 MHz

At frequencies above 1.000 MHz the influence of the salt content on the real part of the permittivity becomes very low. Regarding the ISM-Band, e. g. at a frequency of 2.450 MHz, the moisture content of building material can be determined, independent of the salt content, by measuring the real part of the permittivity only. The imaginary part of the permittivity however is still depending on the moisture and salt content of the material and can be used to determine the salt content.

It results, that a moisture measurement at building materials can be realised at Microwave frequencies of about 2.450 MHz by determining the dielectric constant. Regarding the dielectric loss, also a determination of the salt content is possible.

THE MICROWAVE SENSOR SYSTEM FOR MOISTURE MEASUREMENTS

A first application of microwave methods for measuring the moisture content of structural elements was realised by WATSON in the sixties [4]. He used two horn antennas, measuring the transmission loss of a wall. Since that time microwave technique and microwave components have changed a lot. Especially the progress of the commercial satellite transmission and TV accelerated the development of very efficient, small and nevertheless cheap microwave components.

To achieve the aims mentioned above, especially to determine the moisture profile of components, a sensor is necessary penetrating into the building material. The displacement of the sensor enables the detection of the moisture content depending on the depth of the component. In general, it is possible to «look» from outside into the building component by applying the Time-Domain-Reflectometry. However, usual inhomogeneities inside the component cause

wave reflection and diffraction, so a distinguished analysis of the reflected signal is nearly impossible.

Suitable is a measuring system that requires two parallel bore holes, each for the transmission and the receiving aerial. A laboratory measuring system based on two-borehole-method was developed by WIGGENHAUSER et. al. [5]. More comfortable in application is a system, which requires only one bore hole for one aerial, while the other aerial is positioned in front of the building component. A measuring system using this method was developed by the co-operation partners (see footnote, page 2 of this paper) and is schematically shown in Fig. 1. A plane microwave field (frequency about 2.450 MHz) is radiated by a patch antenna into the building material. The electric field is detected by a small dipole antenna within one bore-hole of 16 mm diameter. The detected signal is analysed by a network-analyser. The electric circuits (oscillator, network-analyser etc.) and the mechanic parts (step motor for moving the antenna) of the measuring system are controlled by a Personal Computer [2][6][7].

The dielectric constant ϵ' cannot be measured directly but calculated via the wave propagation constant γ . It can be shown that the wave propagation constant can be calculated by differentiating the electric field intensity twice and relating this to the original electric field intensity. By applying mathematical methods such as signal processing the problem of the differentiation could be solved [8].

Comparing the results of the dielectric measurements to moisture measurements with the classical oven-drying method, a linear equation was found empirically to calculate the moisture content off the real part the permittivity, the dielectric constant ϵ' . It resulted, that there is no difference in the dielectric behaviour of most mineral, capillary porous building materials like sandstone, brick, lime-brick and lime mortar, except those which have a cement bond like cement mortar and concrete and also except those which don't have capillary porous structure like sand and soil. So, for cement bound materials, for sand and for soil different equations are valid [9].

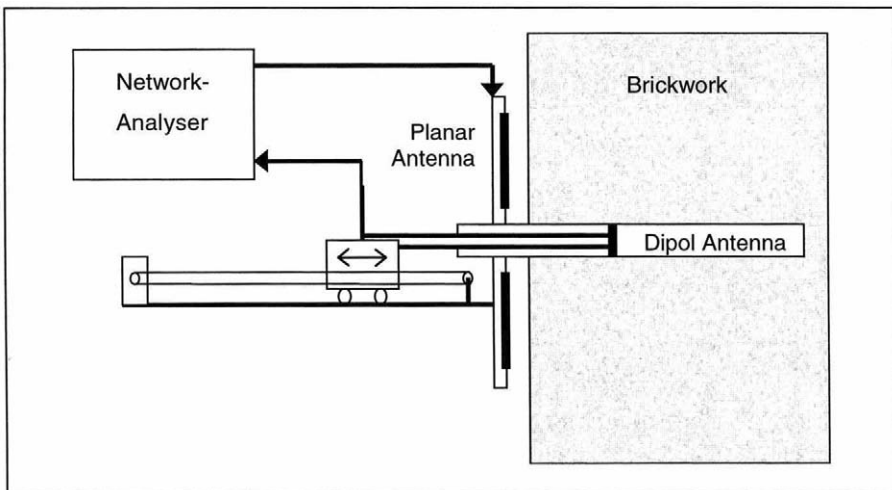


Fig. 1. Schematic drawing of the system for measuring the moisture content of building material

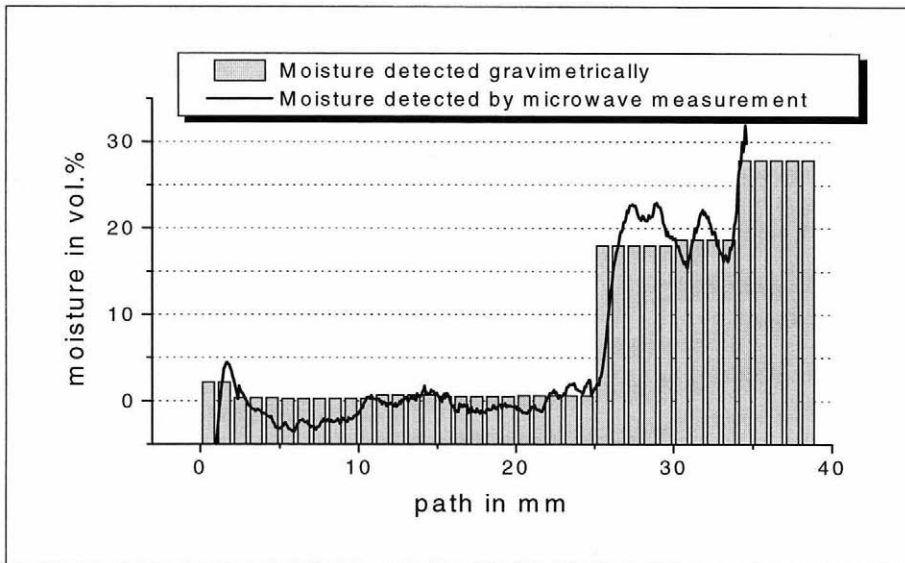


Fig. 2. Moisture measurement at a brick wall of an old building in Hamburg after an exposure to driving rain (from the right hand side). Dielectric measurement at 2.450 MHz in comparison to classical oven drying method.

The measuring system was tested in laboratory and in situ as well. At first the quality of the applied algorithms was tested and improved by measuring at plates of PVC. Then, under laboratory conditions, moisture profile measurements were carried out at samples of sand-lime bricks with different moisture content. Last not least a lot of outdoor measurements were made.

In Fig. 2 the results of moisture profile measurements at brick wall of an old building are shown. The wall had been exposed to driving rain from the right hand side for some time. The microwave measurements are compared to samples analysed by the classic oven-drying method, and a good accordance is given. It can be concluded, that the developed measuring system is suitable for determining the moisture content and moisture profiles of building materials and structural elements.

THE MICROWAVE SENSOR SYSTEM FOR SALT MEASUREMENT

The Microwave Sensor System, which had been developed for measuring the moisture content of building materials can also be used to measure the salt content. The investigation into the dielectric properties of building materials had proved, that at a frequency of about 2.450 MHz (i) the real part of the complex relative permittivity is correlated with the moisture content of the specimen and is fairly independent of the salt content of the material, and (ii) that there is a relation between the imaginary part of the complex relative permittivity and the moisture *and* salt content of the material. Thus it is possible at least to determine the moisture content *and* the salt content of the specimen as well by calculating the real and the imaginary part of the permittivity. Investigations have shown, that in fact a separation of different salt contents is

possible by analysing both parts of the complex permittivity [3]. These results were confirmed by an investigation of MAIERHOFER et. al. [9].

Comparing the results of the dielectric measurements to salt measurements with the classical laboratory method, an equation was found empirically to calculate the salt content off the imaginary part of the permittivity, considering also the real part. These investigations were carried out up to now only for mineral, capillary porous building materials like sandstone, brick, lime-brick and lime mortar which show the same dielectric behaviour.

In Fig. 3 a profile measurements of the salt content at a wall of lime-sand bricks built inside the laboratory is shown. The wall had been exposed to a salt solution from the right hand side for 20 hours and than rested for about 4 days. The results of the dielectric measurements are compared to the results of a classical photometric salt analysis. The peak of the dielectric determined salt content at a depth of 190-200 mm is caused by wave scattering and will be discussed lateron.

It is to notice, that a salt determination is only possible at a presence of water. A dry salt has got approximately the same dielectric properties like a dry building material, so a separation of its influence is not possible.

SOME MORE MEASUREMENTS

The measuring setup enables to measure the moisture and salt content in dependence of the depth of component. The measurement can be repeated at the same position.

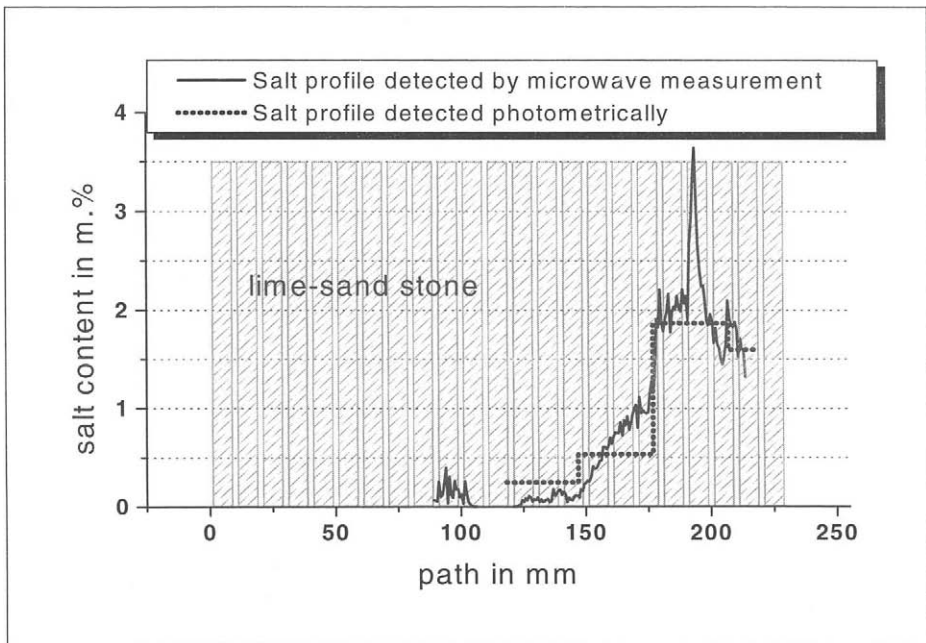


Fig. 3 Profile measurements of the salt content at a wall of lime-sand bricks. Dielectric measurements in comparison to classical photometric salt analysis.

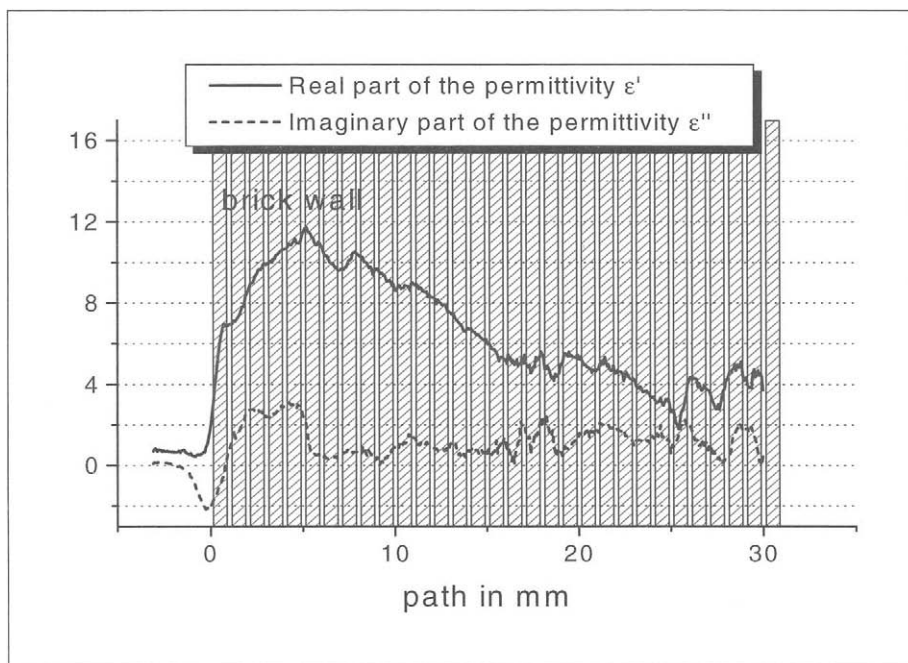


Fig. 4. Dielectric measurements at an old, not water-tight brick wall after exposure to driving rain. The real part of the permittivity indicates the water content, the imaginary part the salt content.

In Fig. 4 dielectric measurements at an old, not water-tight brick wall are shown. Driving rain had found its way (from the left hand side) into the component, obviously solving some salts. The water began to move through the capillaries to the dry side (right hand side). After the rain, the wall began to dry at the wet side (see real part of the permittivity), leaving behind the salt (see imaginary part of the permittivity). However, for a qualified diagnostics some more measurements are necessary.

In Fig. 5 the drying process of porous concrete is shown. The first measurement was made, after a probe of porous concrete had sucked water from the right hand side for 2½ hours. Then the probe could dry under room conditions, and the measurements were repeated 4 times, for the last time after 32 days. Though porous concrete has got a different porous structure than other mineral building materials, the drying process can be observed very well.

LIMITS OF THE PROCEDURE

To calculate the permittivity of a component, plane wave propagating perpendicular to the planar antenna and a reflected wave with opposite direction are assumed. At inhomogeneities like hollow spaces or solid stones a three-dimensional wave scattering is possible. As these scat-

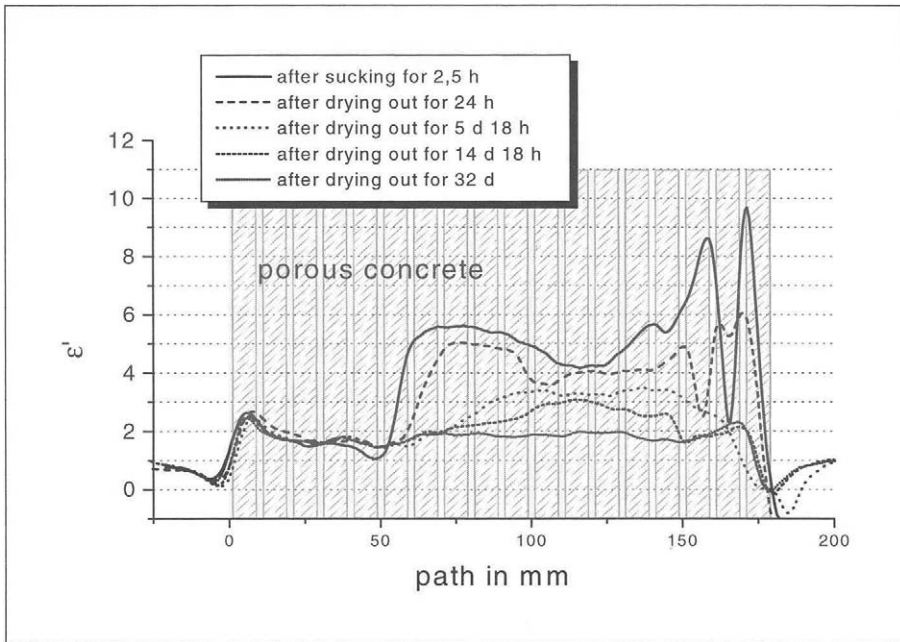


Fig. 5. Dielectric measurements at porous concrete, observing a drying process. The real part of the permittivity indicates the water content. After having sucked water for 2½ hours (from the right hand side), the probe could dry under room conditions. Measurements were made at five different times.

tered waves cannot be simulated by the one-dimensional system, the calculation of the permittivity becomes faulty.

As the procedure to calculate the permittivity deals with a error estimation, it is possible in general to indicate and to eliminate single measured points of the profiles which obviously show an error. Furthermore, the Microwave Sensor System was improved by a rotating antenna. Another paper of the authors to be presented at this conference deals with this subject. [10]

If there is a high moisture content, a high attenuation of the microwave signal will result and the measurement of the moisture content inside a wall may be difficult at a depth of more than about 25-30 cm. However, to protect the staff from injuring radiation the Microwave output power of about 100 mW cannot be increased without limits.

The moisture content can be calculated off the measured dielectric data from a saturated state down to a moisture content of 0 Vol.-%. Salts however can only be measured when solved in water. Dry salts behave like a dry building material and cannot be separated from this. That means, that a measurement of the salt content is only possible in the presence of water. Practically, for the determination of the salt content of building materials a moisture content of about 4-5 Vol.-% is necessary. Taking this fact into account, it results that building diagnostics and

control will not be possible without classical salt determination by laboratory methods. However, the Microwave Sensor System is well suitable to observe a drying and desalination process after a redevelopment.

SUMMARY

A new Microwave Sensor System for measuring the moisture and salt content in building material and structural elements has been developed. Tests in laboratory and in situ as well confirm that this system is suitable for this application.

All demands on an «ideal» moisture meter, shown in Table 1, could be achieved. The measuring system has been evaluated for measuring the content of solved salt as well. Further advantages of the developed Microwave Sensor System are, that no physical contact between antennas and building material is necessary and that the application of microwaves at the public frequency of 2.450 MHz does not require a permission or special admission.

Daring an outlook, it can be expected that applying small and cheap microwave components of the satellite communication technique, it will be possible in the near future to develop a small and comparably cheap moisture and salt meter.

ACKNOWLEDGEMENT

The author wants to give thanks to the Deutsche Forschungsgemeinschaft and the Stiftung Volkswagenwerk, who supported this research by grants (see also footnote on second page).

REFERENCES

1. W. Leschnik: Moisture measurement at building materials. Between yesterday and tomorrow (in German). *Proceedings of: 10. Feuchttag*, Berlin, Germany (1999).
2. C. Hauenschild: Investigation on the dielectric properties of mineral building materials for the development of moisture measurement procedures (in German). *Doctor Thesis*, Technical University of Hamburg Harburg, Germany (1999), being printed.
3. W. Leschnik and U. Schlemm: Investigation on the dielectric properties of mineral building materials at 2.450 MHz, depending on water and salt content (in German). *Proceedings of: 10. Feuchttag*, Berlin, Germany (1999).
4. A. Watson: The non-destructive measurement of water content by microwave absorption. *C.I.B. No. 3* (1960), Pp. 15-16.
5. M. Rudolf and H. Wiggerhauser: Measurement of moisture profiles in walls (in German). *Proceeding of: 8. Feuchttag*, Berlin, Germany (1993).
6. F. Menke, R. Knöchel, T. Boltze, C. Hauenschild and W. Leschnik: Moisture measurement in walls using microwaves. *Proceedings of: MTT*, Orlando, USA, (1999).

7. W. Leschnik, C. Hauenschild, R. Knöchel, F. Menke, T. Boltze: A Microwave Moisture Sensor for building components. *Int. Symposium on Non-Destructive Testing in Civil Engineering*, Berlin, Germany (1995).
8. T. Boltze, C. Hauenschild, K.-D. Kammeyer and W. Leschnik: Robust estimation algorithm for the determination of moisture profiles with microwaves. *Proceedings of: 8. Feuchtetag '95*, Berlin, Germany (1995).
9. U. Schlemm, W. Leschnik: Influence of inhomogeneities on the microwave measurement of moisture- and salt-content of building materials (in German). *Proceedings of: 5. Internationales Kolloquium 'MSR '99'-Werkstoffwissenschaften und Bauinstandsetzen*, Esslingen, Germany (1999).
9. Ch. Maierhofer, S. Leipold, G. Wilsch, J. Wöstmann, H. Wiggenhauser: Application of Pulse Radar and Laser Induced Breakdown Spectroscopy to investigate the influence of salts on the dielectric properties of porous building materials (in German). *Proceedings of: 9. Feuchtetag '97*, Berlin, Germany (1997).
10. U. Schlemm and W. Leschnik: A new Microwave Sensor System for moisture and salt content measurements at building materials to reduce disturbances by inhomogeneities. *Proceedings of: 5. Int. Symposium on Non-Destructive Testing in Civil Engineering*, Tokyo, Japan (2000).

A NEW MICROWAVE SENSOR SYSTEM FOR MOISTURE AND SALT CONTENT MEASUREMENTS AT BUILDING MATERIALS TO REDUCE DISTURBANCES BY INHOMOGENEITIES

U. Schlemm, W. Leschnik
Building Physics and Material Science Section
Technical University of Hamburg-Harburg

ABSTRACT

A developed Microwave Sensor System makes it possible to measure moisture and salt profiles of building materials and components by using a two-antenna system.

Inhomogeneities like hollow spaces can cause a scattering of the wave and disturb the measured profiles that way. The influence of inhomogeneities on the dielectric measurements was investigated by measuring several inhomogeneous components. By use of the unmodified Microwave Sensor System, hardly disturbed profiles were measured at several kinds of bricks, that contained hollow cavities. At other inhomogeneous samples, like sand with artificially added scattering centres and brickwork, only partially disturbed profiles were measured.

To reduce the influence of inhomogeneities, the measuring setup was improved, developing a special antenna system. By using a turnable system of transmitting and receiving antenna the position of the radiation lobe and the polarisation of the wave can be varied. The intensities of the disturbances caused by the scattering centres is related to these two parameters. A minimisation of the disturbance's intensities can be realised by the development of special evaluation algorithms.

Improvements of the measurements achieved by this antenna system will be presented.

KEYWORDS

Microwave Sensor System, turnable antenna system, scattering phenomena.

THE MICROWAVE SENSOR SYSTEM

A Microwave Sensor System working at a frequency of 2,45 GHz for the repeatable measurement of moisture profiles at components was developed within the scope of a co-operation project, financed by the foundation of the Volkswagen Company [1], [2]. Further investigations has shown, that the device can also be used for the measurement of salt profiles in components at the same time [3], [4].

A microstrip patch antenna transmits an approximately plane wave into the component. The receiver is a short dipole antenna, that is moved into a borehole of 16 mm diameter by a step-motor.

By use of a network analyser, the local attenuation and the phase shift of the wave are measured. The data-acquisition and the step-motor are controlled by a computer. The data is used to calculate the real part ϵ' and the imaginary part ϵ'' of the local dielectric constant numerically.

Investigations in dielectric properties of mineral building materials had proved, that the real part ϵ' of the dielectric constant at 2,45 GHz is quite independent of the salt content. Therefore, a moisture measurement can be realised by determination of ϵ' . A linear relation between real part ϵ' and the material's moisture content could be found, that is applicable for a great

variety of building materials. The imaginary part ϵ'' of the dielectric constant at 2,45 GHz is still dependent on moisture- and salt-content. By additional determination of ϵ'' , the salt content can be measured [5].

The evaluation algorithm of the measurement deals with an estimation of errors of the calculated profile points. Faulted sectors of the profile can be recognised that way [6].

MEASUREMENTS AT INHOMOGENEOUS MATERIALS

Inhomogeneities like hollow spaces can cause a scattering of the approximately plane wave. The resulting multipath propagation cannot be simulated by the evaluation algorithm, and disturbances of the measured profiles can occur. For that reasons, first measurements of dielectric profiles had been made at homogenous building materials. The influence of inhomogeneities on the dielectric measurements was investigated later, using inhomogeneous materials like sand and soil with artificially added scattering centres and concrete [7]. Further measurements were made at brickwork containing inhomogeneities and at bricks with hollow cavities.

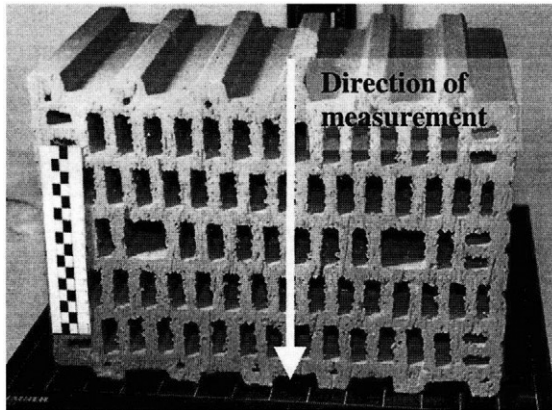


Figure 1: Structure of a porous brick

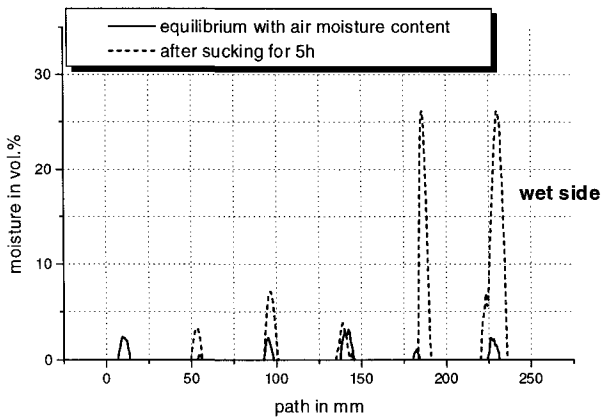


Figure 2: Measured moisture profiles

Profiles were measured at the porous brick, that can be seen in Figure 1. It shows the structure of the brick's cavities and the direction of the profile measurements. The brick has got a thickness of 230 mm. Figure 2 shows moisture profiles, that were measured with the Microwave Sensor System. The first one was detected, when the stone's moisture content was in equilibrium with the air's moisture content. The second profile was measured after the stone had been sucking in water for 5 hours. The profiles are strictly related to the structure of the stone (Figure 1). Comparing these results to gravimetrically determined moisture profiles, a good correspondence results.

Thus it is possible to measure dielectric profiles in these inhomogeneous bricks with the unmodified Microwave Sensor System.

Another example for successful measurements at inhomogeneous materials can be given for lime-sand-bricks with hollow cavities. The structure of these stones and the direction of the measurements can be seen in Figure 3. The bricks have got a thickness of 180 mm at the location of the measurement.

An example for the measurement of dielectric profiles can be seen in Figure 4.

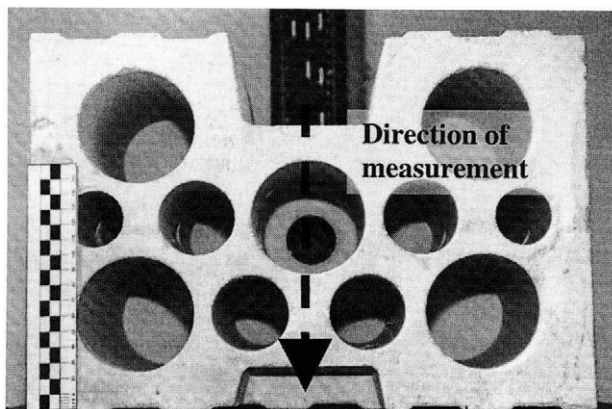


Figure 3: Structure of a lime-sand brick with hollow cavities

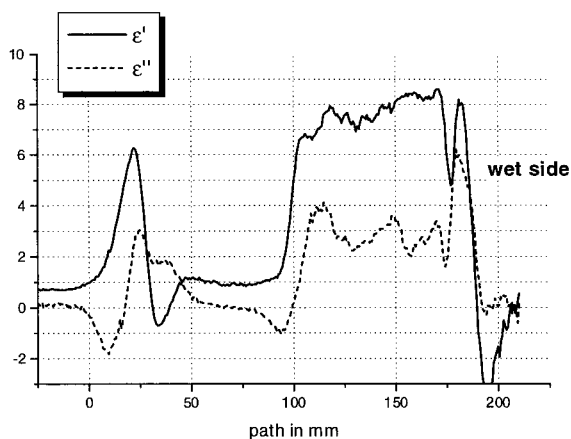


Figure 4: Dielectric profiles in lime-sand-brick with hollow cavities

The brick had been sucking in a saline solution for 19 hours. After that there was a period of 2 days of redistribution of the salt- and moisture-profiles. The saline solution contained 17g HCl, 31,5g Na_2SO_4 and 7g NaNO_3 per litre of water. The profiles are strictly related to the stone's structure (Figure 3). The material section on the left, that has got a thickness of 20 mm, seems to be reduced due to damages done to the brick when boring the hole. Furthermore, the profiles show the hollow cavity of 80 mm thickness and the material on the right hand side with thickness of 80 mm, that contains the main part of moisture and salt, because the brick had been sucking from that side.

The dielectric profiles can be used to calculate salt- and moisture-profiles by use of relations, that had already been documented [4], [8]. The calculated profiles can be seen in Figure 5.

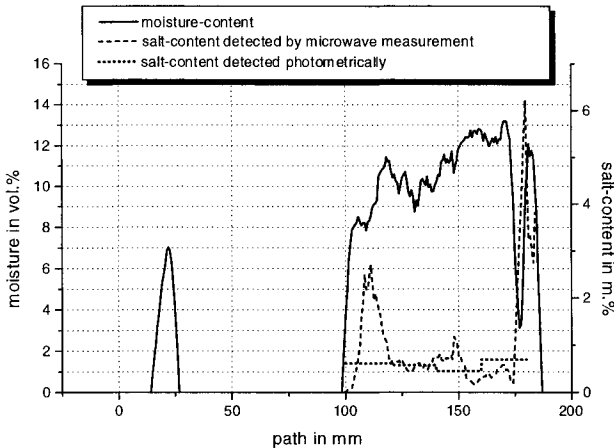


Figure 5: Salt- and moisture-profiles

As expected, the part of the stone, that had been sucking, contains the highest moisture content. The calculated salt profile is nearly homogenous in the inner part of this section and the amount is rising at its surfaces, the zones of evaporation. In Figure 5, the salt-profile determined by photometry can be seen. To detect this profile, the collected boremeal in steps of 20 mm was analysed. The salt content in the inner material shows good correspondence of the two profiles. The amount of the photometrically determined profile doesn't rise near the surfaces. The steps of 20 mm could be too big to detect an accumulation of salt at the surfaces.

After showing successful measurements at inhomogeneous components with the unmodified Microwave Sensor System, two examples of measurements shall be given, that contain errors due to scattering phenomena. The first example was measured at sand, that had a moisture-content of 4,1 m.%. The moisture content had been homogenised by mixing the sand, the material was put into special boxes made of PVC. These boxes contain three tubes made of PVC with a diameter of 16 mm, that cross the box rectangularly and pass through holes in the sidewalls. During a measurement, the receiving dipole is moved through these tubes. Hollow tubes made of PVC with a diameter of 16 mm and with a length of 120 mm were put into the sand perpendicular to the direction of the measurement to act as scattering centres. Figure 6 shows a measured profile of the real part ϵ' of the dielectric constant, that is proportional to the moisture content. In the middle of the profile, a disturbance can be seen, that is induced by one of the scattering centres in the sand. In this case, it is impossible to measure an undisturbed profile with the unmodified Microwave Sensor System.

The second example is a profile-measurement made at a brickwork of lime-sand bricks, that was put together without mortar. Due to the alternating orientation of the bricks, the brick-

work contains gaps filled with air between parallel stones. A side view of the brickwork's structure can be seen in Figure 7a. Figure 7b shows measured profiles of the real part ϵ' of the dielectric constant, measured at dry brickwork and at the same brickwork containing moisture. While the profile measured at dry brickwork is widely undisturbed, the profile of the wet brickwork contains disturbances in the region of the second brick.

The detected profiles of these two measurements at inhomogeneous components are partially disturbed. The disturbed regions can be recognised by the evaluation algorithm. A measurement of salt- and moisture-content failed in these regions.

In those cases, the unmodified Microwave Sensor System can only detect incomplete profiles. A measurement with improved quality can be realised by modification of the transmitting antenna. The turnable antenna system, that is introduced in the following chapter, is an example for a modified system.

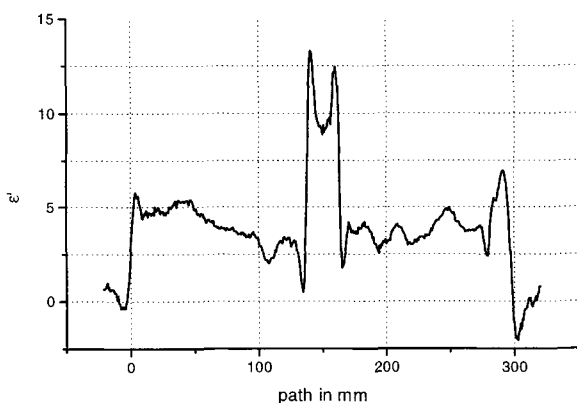


Figure 6: Measurement at sand containing tubes made of PVC as scattering centres

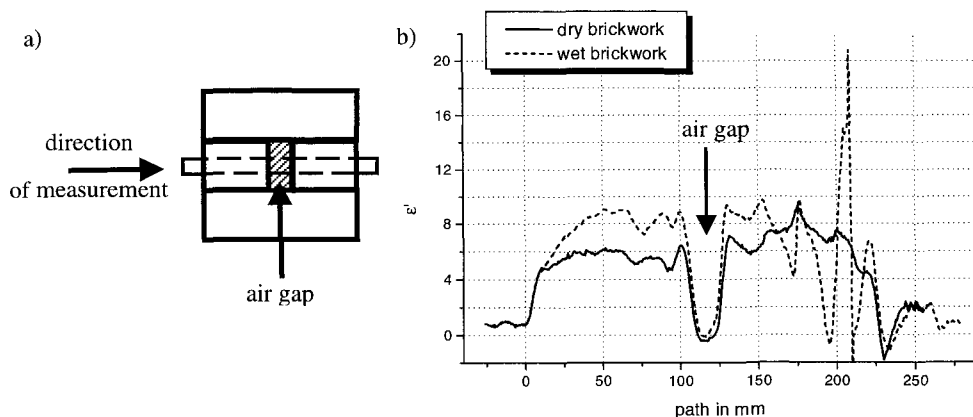


Figure 7a): Side view of the brickwork made of lime-sand bricks

Figure 7b): Dielectric profiles of the dry and the wet brickwork

THE TURNABLE ANTENNA SYSTEM

The measuring setup can be improved to reduce the influence of inhomogeneities. A special antenna system was developed, that enables the variation of several parameters of transmission. An antenna system with a displaceable radiation lobe was first introduced by MENKE and KNÖCHEL [9], a system of turnable transmitter and receiver was proposed by HAUENSCHILD [10].

By using a turnable system of transmitting and receiving antenna the position of the radiation lobe and the polarisation of the wave can be varied. The intensities of the disturbances caused by the scattering centres is related to these two parameters. The influence of the scattering centres on the received signal depends on its location. This influence also varies when the radiation lobe is displaced. By variation of the wave's polarisation, the influence of anisotropic scattering centres can be varied.

The front view of the developed turnable antenna system can be seen in Figure 8. The transmitting 4-patch antenna can be seen, the receiving dipole is located in the middle of the system. The antenna is turnable in steps of 30° , so each profile is measured up to 12 times under variation of the parameters of transmission.

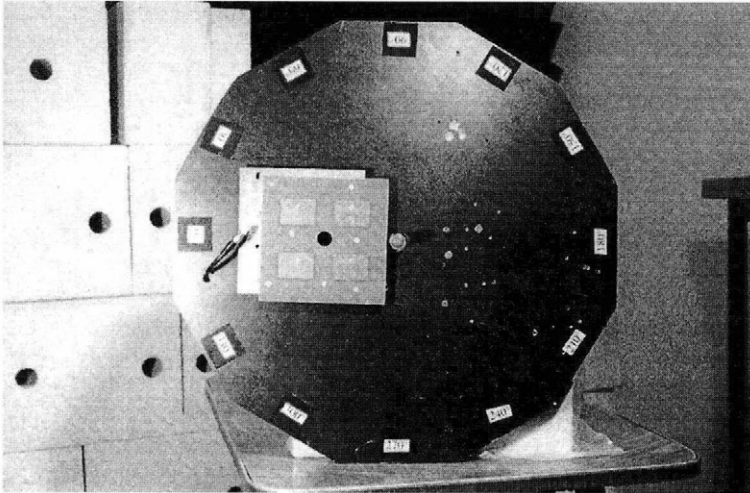


Figure 8: Turnable antenna system, front view.

The influence of the scattering inhomogeneities varies for these different profiles. A minimisation of the disturbance's intensities can be realised by the development of special evaluation algorithms. These algorithms can use the estimation of errors of the calculated profile points, that is part of the evaluation algorithm of the unmodified Microwave Sensor System. Two different ways of evaluation have been tested already [11]. The result of the first one is the profile with the lowest amount of the integral over the error estimation of the whole profile. The result of the second one is a profile, that is composed of single points of the 12 measured profiles, that have got the lowest error estimation under variation of the parameters of transmission. Though these algorithms are not optimised yet, an improvement of the characteristics of the measurement is obvious. The improvement of the algorithms for the turnable antenna system is subject of investigations presently.

MEASUREMENTS WITH THE TURNABLE ANTENNA SYSTEM

To demonstrate the improvements achieved by using the turnable antenna system, the measurements made at sand and brickwork, which are shown in Figures 6 and 7, were repeated by use of the new system.

Figure 9 shows the measurement at sand with embedded tubes of PVC.

The resulting profile is hardly disturbed, the disturbance in the middle of the profile (Figure 6) could be completely eliminated. The profile's slight fluctuations are resulting from fluctuations of density and moisture inside the sample.

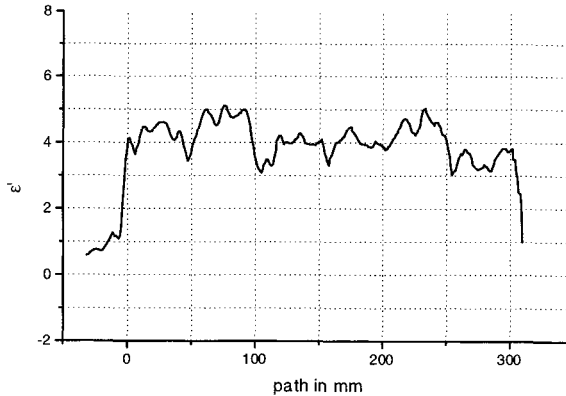


Figure 9: Dielectric profiles measured at sand with embedded tubes (to compare with Figure 6)

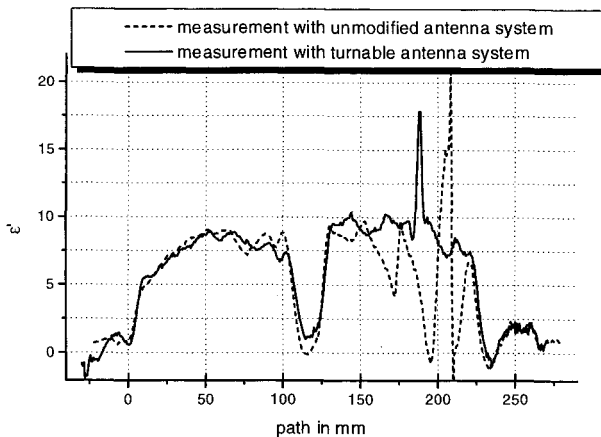


Figure 10: Dielectric profiles measured at brickwork with unmodified antenna and turnable antenna system (to compare with Figure 7)

The profile measured with the turnable antenna system is much better than the one that resulted from measurement with the unmodified system. There's only one small distortion in a depth of about 190 mm.

In both cases it was possible to suppress distortions caused by scattering phenomena by use of the turnable antenna system, though only simple evaluation algorithms were applied. Better algorithms have to be developed. The antenna system itself can be modified to obtain a maximum of efficiency.

CONCLUSIONS

The developed Microwave Sensor System enables the measurement of moisture and salt profiles of building materials and components.

Though inhomogeneities like hollow spaces can cause a scattering of the wave and disturb the measured profiles, it is possible to measure profiles in inhomogeneous components with the unmodified system. In case of porous bricks with hollow cavities and in lime-sand-bricks with hollow cavities, we are able to present hardly disturbed profiles. At other inhomogeneous components like sand with embedded tubes and a brickwork made of lime-sand-brick, the resulting profiles content local disturbances, which admittedly can be recognised by the estimation of errors of the evaluation algorithm. At disturbed profile-locations, no detection of salt- and moisture-content is possible.

The measuring setup has been improved to reduce the influence of inhomogeneities. A special antenna system was developed. By using a turnable system of transmitting and receiving antenna the position of the radiation lobe and the wave's polarisation can be varied. The intensities of the disturbances caused by the scattering centres is related to these two parameters. Though only simple evaluation algorithms were applied, the characteristics of the profile measurement was improved significantly. So undisturbed measurements at the same samples were possible, that led to partially disturbed profiles when using the unmodified system.

By further investigations, the evaluation algorithms and the construction of the antenna itself shall be improved.

LITERATURE

- [1] F. Menke, R. Knöchel, Th. Boltze, C. Hauenschild, W. Leschnik: Moisture Measurement in Walls using Microwaves. IEEE-MTT-S, Orlando/USA (1995), Proceedings.
- [2] W. Leschnik, C. Hauenschild, R. Knöchel, F. Menke, T. Boltze: A Microwave Moisture Sensor for Building Components. International Symposium on Non-Destructive Testing in Civil Engineering, Berlin (1995), Proceedings.
- [3] W. Leschnik, U.Schlemm: Measurement of the Moisture and Salt Content of Building Materials with Microwaves, International Symposium on Non-Destructive Testing in Civil Engineering, Tokyo (2000), Proceedings (will be published).
- [4] W. Leschnik and U. Schlemm: Measurement of the Moisture and Salt Content of Building Materials. III. Workshop on Electromagnetic Wave Interaction with Water and Moist Substances, Athens/GA, USA (April, 1999), Proceedings .

- [5] W. Leschnik, U. Schlemm: Dielektrische Untersuchung mineralischer Baustoffe in Abhängigkeit von Feuchte- und Salzgehalt bei 2,45 GHz, 10. Feuchtetag, Tagungsbericht, Berlin 1999
- [6] T. Boltze, C. Hauenschild, K.D. Kammeyer, W. Leschnik: Robust Estimation Algorithms for the Determination of Moisture Profiles with Microwaves, Feuchtetag '95, Berlin, (1995), Tagungsbericht.
- [7] U. Schlemm, W. Leschnik: Einfluß von Inhomogenitäten auf die Messung von Feuchte- und Salzgehalt von Baustoffen mit Mikrowellen, 5. Internationales Kolloquium 'MSR '99'-Werkstoffwissenschaften und Bauinstandsetzen-, Esslingen (99) – erscheint demnächst-
- [8] W. Leschnik, C. Hauenschild: Feuchtemessung an Bauteilen. Schlußbericht zum Projekt der Stiftung Volkswagenwerk Nr. I/67 193 'Kontinuierliche und zerstörungsfreie Feuchtemeßverfahren mit Mikrowellen', TU Hamburg-Harburg (1996)
- [9] F. Menke, R. Knöchel: Mikrowellen-Feuchtemeßsystem mit verringerter Empfindlichkeit gegenüber Störungen durch Materialinhomogenitäten, 9. Feuchtetag, Tagungsbericht, Weimar 1997
- [10] C. Hauenschild: Untersuchung der dielektrischen Eigenschaften mineralischer Baustoffe für die Entwicklung von Feuchtemeßverfahren, Dissertation, TU Hamburg-Harburg 1999,-erscheint demnächst-
- [11] U. Schlemm, W. Leschnik: Drehbares Antennensystem zur Unterdrückung von Störungen bei der Messung des Salz- und Feuchtegehaltes von Bauteilen bei 2,45 GHz, 10. Feuchtetag, Tagungsbericht, Berlin (1999)

This Page Intentionally Left Blank

NDT FOR ASSESSING CONCRETE STRENGTH

ALMIR P. FERREIRA (1) and PROTASIO F. CASTRO (2)

(1) *MSc. Eng. Civil, Universidade Federal Fluminense, Rua Passo da Pátria, 156, CEP 24210-240, Niterói, RJ, Brasil, e-mail: almir_ferreira@zipmail.com.br.*

(2) *PhD, Professor Titular de Tecnologia das Construções, Curso de Pós-Graduação em Engenharia Civil, UFF, Rua Passo da Pátria, 156, CEP 24210-240, Niterói, RJ, Brasil, Pesquisador do CNPq, e-mail: pcastro@civil.uff.br.*

ABSTRACT

It is already widely accepted that quality control is a part of the production process and that high-quality products require a high level of quality control. The estimation of concrete strength in building Portland Cement Concrete pavement by Non Destructive Tests (NDT) is of considerable interest to engineers. Several national and international standards recognize the various NDT methods as suitable. Basically, most test methods measure some others properties of concrete than its mechanical strength. However, the evaluation of insitu concrete strength is carried out by means of an established correlation of these properties with strength. Therefore, the reliability of assessing the concrete strength primarily depends upon the precision of the established calibration

In the non destructive tests used to determine the compressive strength of concrete, the relationship between the NDT measured result, mechanical or physical, and the strength is generally not unique. This arises from the diversity in the existing relations between the measured characteristic and the factors making up concrete strength, among others: cement contents, type of aggregates, bond between cement: paste and aggregates and water cement ratio.

In order to improve the significance of the NDT \times Concrete Strength correlation the coarse aggregate strength may be introduced as an independent variable. Another way of improving the concrete strength estimation consists in combining two different non destructive testes.

The aim of the present is to check the validity of pulloff, pin penetration and ultrasonic pulse velocity for assessing concrete strength, that are widely used in quality control system. The NDT are compared on basis of sensitivity of measurements and scatter of results. The advantage deriving from the aggregate strength used as a variable is also examined.

An extensive series of tests was carried out to obtain a correlation of the NDT results with compressive strength. Nine concrete mixes for each three different coarse aggregate strength, of 19 mm max. size, were tested.

KEYWORDS

Concrete; NDT; pulloff test; penetration test; UPV.

INTRODUCTION

The reliability on the standard compressive test came as result of experience gained in extensive development work conducted during the last 100 years throughout the world.

However, concrete placed in a structures to pavement has different compaction and curing conditions to concrete tested using the standard compressive test. Hence, the standard compressive test reflects a strength potential but not necessary the in situ strength.

Nondestructive tests (NDT) , such as pulse velocity, pin penetration and pulloff, provide indirect data that can be empirically related to compressive strength by calibration with strength measurements from a number of cast specimens.

NDT measurement technique has been used for more than two decades for concrete quality evaluation and assessing concrete compressive strength. During this period, the advantages of its use and the factors influencing the test results have been widely reported. According to Castro [1] age, mix proportion, water/cement ratio, cement type, aggregate type have an influence on the pulses velocity test results and its relationship to concrete compressive strength.

Using different concrete mixes, but with the same materials Castro [2] showed a comparison between NDT trough their relationship with compressive strength of cast cylinder specimens and concrete strength by extracted cores.

Structural inspection to repair or reinforce structures is probably the main application for combine NDT. Measurement of NDT at points on a regular grid on the surface of concrete structures provides a reliable method for assessing the homogeneity of the concrete as shown by Ludwig and Castro [3].

An experimental program, consisting of nine series of mixes, was carried out. The variable assessed were: (1) concrete strength at different mix proportion with a range of 15 to 40 MPa to duplicate strengths found in practice; and (2) coarse aggregate of different crushing strength. The effect of these parameters on the relation between compressive strength by cast specimens and the nondestructive tests results was measured.

PURPOSE OF THE INVESTIGATION AND EXPERIMENTAL PROGRAM

In most of the development of nondestructive test methods for concrete attempts have been made to correlate the measurement with concrete compressive strength measured on standardized test specimens under standard conditions of mechanical loading. This approach has often been linked to an assumption that compressive strength test results are of primary importance and represent a basic standard by which nondestructive tests may be judged. One results of this has been that limited confidence has emerged among engineers in the NDT results, since they are always correlated with standard compressive strength test results and the regression curves are disturbed by the influence of a large number of factors which are encountered in practice.

Portland cement (CP-II F40), complying with the ABNT - NBR 11578 / 91 [4], and natural sand were used in all mixes. Crushed coarse aggregate of three different origins were used in the research work. They were named after their crushed strength (kN) 95, 120 and 180. Nine series of mixes was carried out for each coarse aggregate origin. The aim of the mixes set was to minimize: (1) the internal variables, keeping the same materials but the coarse aggregate; (2) the external variables, keeping the same workability

Therefore the mixes set used have the same: (1) Portland cement; (2) sand / aggregate ratio; (3) coarse aggregate maximum size of 19 mm; (4) and admixture proportion. The mixes used for the test series are shown in Table 1.

TEST RESULTS AND ANALYSIS

All test results were adopted as the mean of three individual test results, apart from compressive strength by cylinders which were mean of two. Also, all test results are 56 days of age, hence test date. NDT were carried out on prismatic specimens, as shown in Fig. 1.

The development of the pulloff test device is described in Miranda [5]. The pulloff test is a partial non destructive test. The steel plate of 75 mm diameter is fixed to the concrete surface by epoxy. Applying an axial pulloff force to the bolt by means of a torque wrench and bearing system results in a vertical force on the plate, which eventually leads to the fracture of the concrete.

The penetration test was introduced in Brazil by Pontes Vieira [6]. Thus, pin penetration tests were carried out according to the Brazilian tradition: smooth 55 mm long pin of 6.4 mm diameter and a short cartridge 22, medium powder potential. Test results were measured by using a caliber and referred to millimeter.

UPV (54 kHz) measurements by direct transmission arrangement were used in the present research program.

Table 1. Mix characteristics and test results

Mix ID	Mix Proportion	W/C Ratio	CACs* (kN)	Fc** (MPa)	Prismatic Specimens (230x230x340 mm)		
					Pulloff (N.m)	UPV (km/s)	Pin*** (mm)
1/95	1 : 2.53 : 3.53	0.60	95	18.7	14.7	3.41	14.8
2/95	1 : 2.42 : 3.64	0.60		26.3	16.3	3.71	19.0
6/95	1 : 1.58 : 2.67	0.42		28.7	18.2	4.00	25.7
7/95	1 : 1.41 : 2.50	0.42		32.6	23.3	4.12	26.6
8/95	1 : 1.24 : 2.35	0.39		38.2	22.3	4.09	29.4
9/95	1 : 1.17 : 2.21	0.37		31.8	23.2	4.07	27.9
2/120	1 : 2.42 : 3.64	0.60	120	26.8	16.3	4.14	23.0
3/120	1 : 2.20 : 3.14	0.54		24.1	11.7	4.12	25.0
4/120	1 : 1.95 : 2.97	0.49		29.3	17.0	4.15	27.2
5/120	1 : 1.75 : 2.75	0.45		26.3	17.8	4.15	24.6
7/120	1 : 1.41 : 2.50	0.42		40.2	24.5	4.22	23.1
8/120	1 : 1.24 : 2.35	0.39		40.6	22.3	4.25	25.7
9/120	1 : 1.17 : 2.21	0.37	28.2	18.2	4.07	25.1	
1/180	1 : 2.53 : 3.53	0.60	180	29.5	20.7	4.22	23.7
2/180	1 : 2.42 : 3.64	0.60		35.3	14.5	4.29	33.9
3/180	1 : 2.20 : 3.14	0.54		24.7	14.8	4.19	28.2
4/180	1 : 1.95 : 2.97	0.49		32.8	18.3	4.28	30.8
5/180	1 : 1.75 : 2.75	0.45		34.5	14.5	4.30	28.7
6/180	1 : 1.58 : 2.67	0.42		34.8	22.0	4.36	24.5
7/180	1 : 1.41 : 2.50	0.42		41.9	19.7	4.30	35.5
8/180	1 : 1.24 : 2.35	0.39		26.3	19.7	4.39	26.7

Notes:

- *Coarse Aggregate Crushed Strength; **Compressive Strength from Cylindrical Specimens (150x300mm) at testing date; *** Exposed Length.
- Outlier mixes due to test results: 3/95, 4/95, 5/95, 1/120, 6/120 and 9/180.

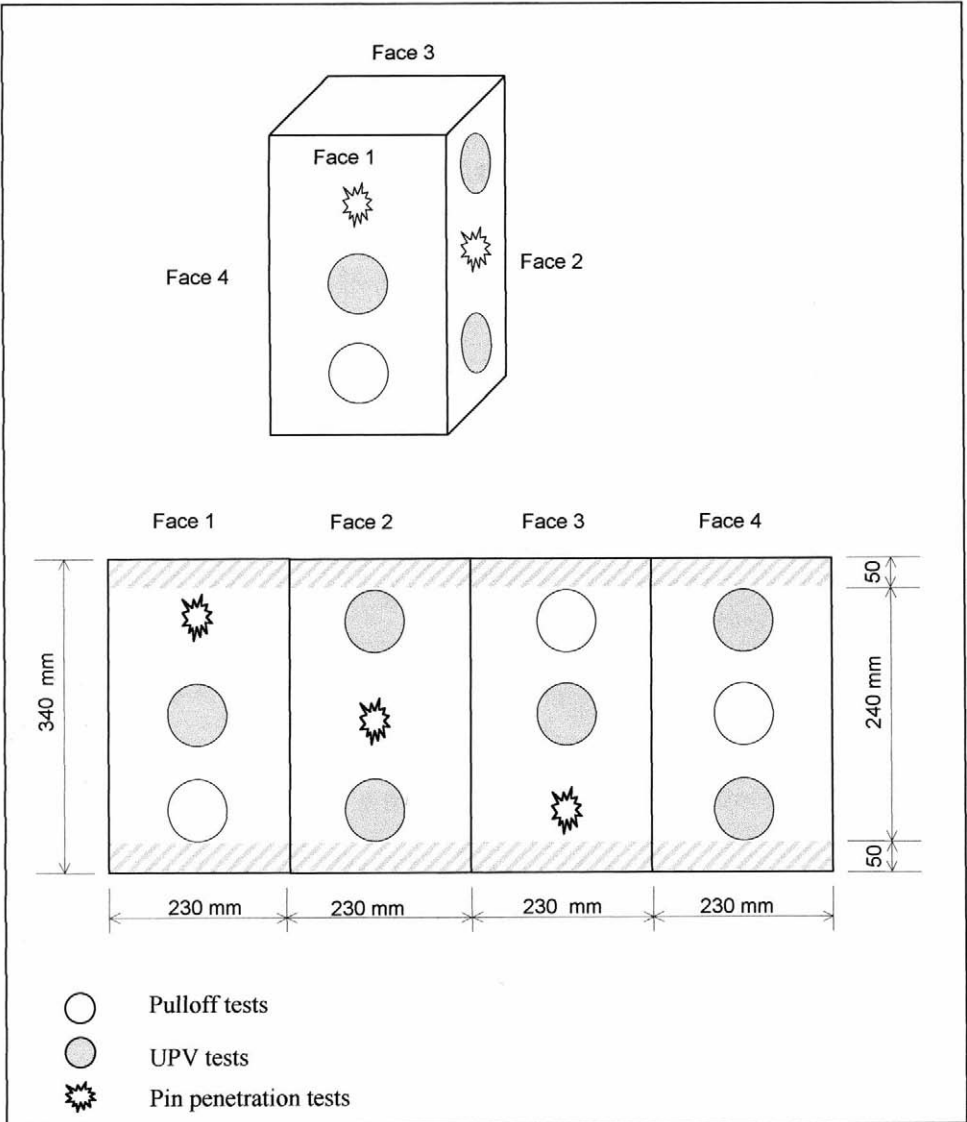


Fig. 1. Prismatic specimens: NDT location.

The tests results of the present investigation were previously analyzed to figure out which were the outlier results for each test. Whenever a mix proportion has more than two outlier results from different non destructive tests, all NDT results for that mixes were excluded. Therefore, the analysis and conclusions are based on tests results, shown in Table 1, obtained in the present research, which are limited by the number of mixes materials and procedure employed.

The number of test used to develop the models is small. However, statistical test were carried out. The first test was to verify whether the NDT results and compressive test result fitted to a Gauss Distribution. The Henry straight line test shows all test fitted to Gauss Distribution.

Just as a frequency distribution can be described diagrammatically by a frequency polygon, so can a cumulative frequency distribution be represented by a curve called ogive. The ogive curves for the experimental test results are shown in Fig. 2. The pulloff test results produced an ogive close to the concrete compressive test results. Actually the mechanical measurement of the two tests results can be assumed as the main support for that close behavior. Note that pulloff test measure the tensile strength of the concrete.

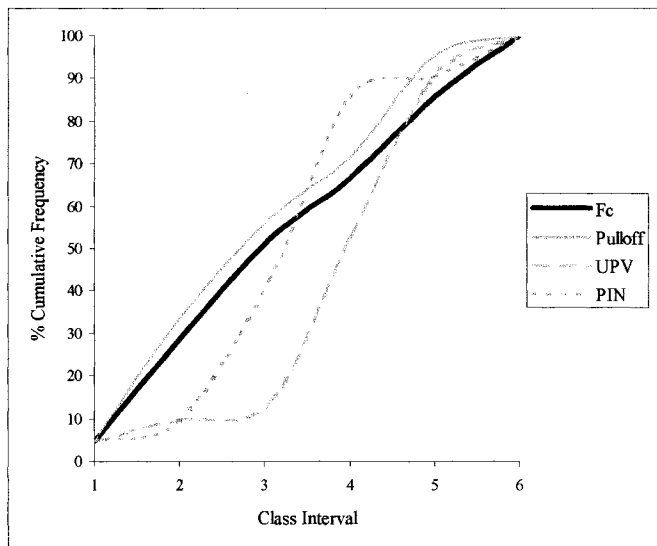


Fig. 2. Ogive for the test results of the experimental program.

UPV and pin penetration test results produced an ogive significantly different from the compressive strength test results. This statement is supported by hypothesis test carried out to ogive area at 5% risk. The effect of the coarse aggregate crushed strength on the pin test result can be assumed as a parameter for that behavior. The density of the coarse aggregate can be related to the crush strength. Therefore, the effect of the coarse aggregate origin is assume to explain the UPV ogive behavior.

Regression analysis is an useful tool to evaluate the relationship between concrete tests. Statistical parameter are first used to evaluate the fit of the chosen regression curve. However, when comparing models obtained for different test types, the regression curves parameters should be carefully used. Table 2 shows regression models, correlation coefficient and standard errors obtained for the experimental program. Fig. 3, 4, and 5 show one independent variable models. Assuming coarse aggregate crushed strength as a second independent variable, models shown in Table 2 can be plotted as presented in Figure 6.

Table 2. Regression models

NDT	CACS (kN)	Regression Curves	Correlation Coefficient	Standard Error
Pulloff Test	95	$fc = 1.101 B^{1.100}$	$R^2 = 0.792$	3.660
	120	$fc = 13.005 e^{0.046B}$	$R^2 = 0.856$	3.021
	180	$fc = 1.763 B$	$R^2 = 0.694$	5.934
	All results	$fc = 0.049 B^2 - 0.776 B + 27.849$	$R^2 = 0.379$	4.961
	All with C	$fc = 1.346 B^{0.667} C^{0.242}$	$R^2 = 0.466$	4.559
UPV	95	$fc = 0.435 V^{3.083}$	$R^2 = 0.896$	2.936
	120	$fc = 94.644 V - 362.647$	$R^2 = 0.705$	4.018
	180	$fc = 0.437 V^{2.948}$	$R^2 = 0.069$	5.804
	All results	$fc = 1.304 V^{2.222}$	$R^2 = 0.394$	5.138
	All with C	$fc = 1.415 V^{3.070} C^{-0.263}$	$R^2 = 0.463$	4.734
Pin Penetration Test	95	$fc = 1.825 P^{0.876}$	$R^2 = 0.910$	2.486
	120	$fc = 0.674 P + 10.112$	$R^2 = 0.257$	1.994
	180	$fc = 0.819 P + 8.713$	$R^2 = 0.386$	4.689
	All results	$fc = 12.782e^{0.032 P}$	$R^2 = 0.635$	3.493
	All with C	$fc = 3.876 P^{0.771} C^{-0.091}$	$R^2 = 0.437$	4.790

Note: fc – Concrete Strength; B – Pulloff Test Results; V – UPV Test Results; P – Pin Penetration Test Results; C – Coarse Aggregate Strength

The tests in this research measure different properties of the concrete and the results were correlated with compressive strength. The standard errors of these correlation is the statistical parameter used as basis of comparison between tests: it has the units of MPa.

Although the correlation coefficient shows the extend to which the non-destructive test results and the compressive strengths are related, the effectiveness of compressive strength evaluation cannot be obtained from this parameter. The residuals standard deviation is the measure of the accuracy in evaluating the compressive strength hence the measure of the model's effectiveness.

Gross model violations, when present, are often exposed by an appropriate graph of the residual. When the model is correct, the standard residuals tend to fall between 2 and -2 and are randomly distributed about zero. The standardized residuals were plotted as the ordinate against the model value. The normal pattern fits into two parallel straight lines. The figures patterns means that the variance of the observations may be increasing with the magnitude of compressive strength or the test results.

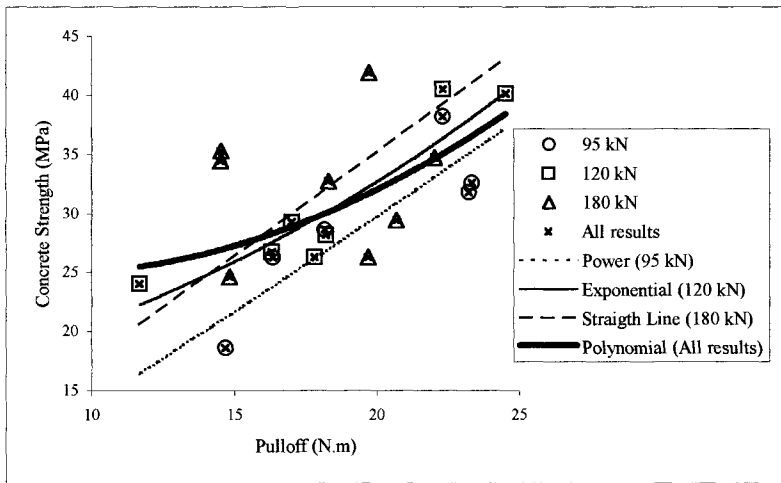


Fig. 3. Pulloff: one independent variable regression models.

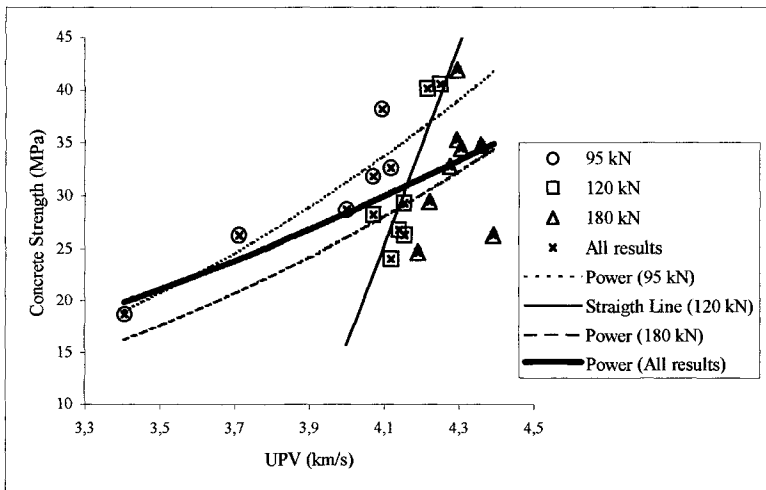


Fig. 4. UPV: one independent variable regression models.

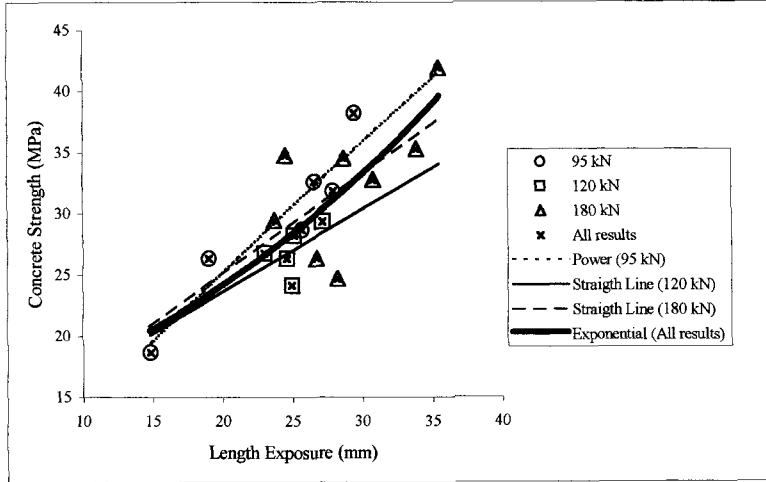


Fig. 5. Pin : one independent variable regression models.

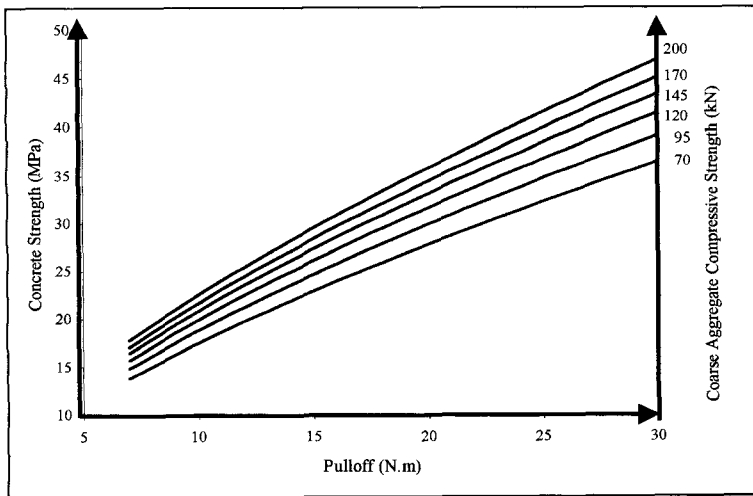


Fig. 6. Pulloff regression model: coarse aggregate crushed strength as second independent variable.

CONCLUSIONS

The main aim of this research was to analyze the effect of crushed coarse aggregate on NDT relationship to concrete compressive strength. The approach for assessing that effect was to introduce aggregate crushed strength as an independent variable to the correlation models. A laboratory program was developed using data collected from different mixes and three coarse aggregate of different origin. A set of variables (age, aggregate grading and size, curing procedure, etc) considered to influence the NDT – compressive strength relationship was excluded.

The procedure used for analyzing data included one variable statistic and regression analysis by least squares method. An analysis of residual variation was undertaken to evaluate the effect of the aggregate origin on the tests relationship.

The present NDT test results confirms that a crushed strength effect is present, i. e., coarse aggregate crushed strength has an influence on NDT - concrete strength relationship.

REFERENCES

1. Castro, P. F.(1985). *An Expandable Sleeve Test for Assessing Concrete Strength*. PhD Thesis. University College London, England.
2. Castro, P. F. (1987). *Concrete Strength – Comparison Between Non-Destructive Tests*. Fourth International Conference on Durability of Building Materials & Components, pp. 885-890. Singapore.
3. Ludwig Filho, U. and Castro, P. F. (1991). *A Homogeneidade do Concreto na Estrutura de Edifícios*. XXV Jornadas Sul-Americanas de Engenharia Estrutural, Porto Alegre, pp. 221-231.
4. Associação Brasileira de Normas Técnicas – NBR 11578/91. *Cimento Portland composto*.
5. Miranda, H. C.(1990). *Equipamento Portátil para Ensaio de Aderência*. 97 pp. MSc. Thesis – Fluminense Federal University, Niterói - RJ, Brasil.
6. Pontes Vieira, D.(1978). *Método Brasileiro de Penetração de Pinos*. – XIX Jornadas Sul-americanas de Engenharia Estrutural, Santiago, Chile.

This Page Intentionally Left Blank

NEW TEST METHOD FOR PULLOUT STRENGTH FOR THE HARDEND CONCRETE USING POST SETTLED PULLBOLT

M. Arazoe*1, Y. Ito*1 and F. Katsuki*2

**1 Dept. of Civil Engineering, Research Center, Satokogyo Co., Ltd.
47-3, Sanda, Atsugi city, Kanagawa, 243-0211, Japan*

**2 Dept. of Civil Engineering, Shibaura Institute of Technology
3-9-4, Shibaura, Minato-ku, Tokyo, 108-8548, Japan*

ABSTRACT

Pullout test, which is classified one of non-destructive testing methods, has been investigated to estimate the strength of concrete [1]. Many types of pullout test method are developed to examine the concrete structures. In the case that the pullout test is applied, it is required that test surface is smooth and plane, and that the pullbolt is pulled straightly in the bolt shaft. But it is difficult to set the equipment appropriately to the existing aged structures that usually have rough and deteriorated surface. A new pullout testing method, which a shallow round groove is cut to install the bearing ring in, is developed to apply such structures. Some experiments were took place to examine the applicability of the proposed method. As a result, good results were obtained even in the rough concrete surface condition.

KEYWORDS

Pullout test, Compressive strength, Shotcrete, Variation, Roughness of the surface

INTRODUCTION

It is very important to estimate the strength of concrete when the performance and durability of the existing structure is evaluated. The Schmidt Hammer test [2] is the most famous and the simplest method to estimate the compressive strength of concrete, but the deterioration of the concrete surface, that is usually observed in the aged structure, influences on the obtained results seriously.

Pullout test is another method for estimating the strength of concrete. The principle of the method is that the force required to pull a bolt embedded in the concrete has a correlation with concrete strength. So, many types of pullout test method have been developed to examine the

strength of existing structures. Comparing with the Schmidt Hammer test, it is more certain method as in-situ test because it is not influenced by the surface condition and the results are obtained by breaking the inside of the concrete.

In spite of this, it is not popular in Japan. One of the reasons why it is not spread widely in Japan seems that it takes more time and the cost is higher than the Schmidt Hammer test. The other reason seems that it is difficult to apply this method to the existing aged structures, for example,

- 1) Although the test surface of the structure must be smooth and plane, the aged structures usually have rough, dirty and deteriorated concrete surface.
- 2) It is necessary to pull the pullbolt straightly in the bolt shaft, so that the pullbolt must be perpendicular to the wall, but it is difficult to set it accurately.

A new test method is developed to solve these problems and to estimate compressive strength of concrete more correctly. The uniqueness of this method is that a shallow round groove is cut to install the bearing ring. By using the groove, bearing ring is able to be set perpendicular to the pullbolt certainly, and the roughness or the deterioration of the test surface is canceled in the proposed method. In this work, some basic experiments were carried out to clarify the applicability of this method to the test specimens including the shotcrete specimen which has very rough surface.

TEST PROCEDURE

In this method, the pullbolt, of which the diameter of the bottom is extended by hammering, is used. Figure 1 shows the form of the pullbolt.

The test is carried out as follows:

- (1) Drill a hole in the concrete and clean out it.
- (2) Extend the bottom of the hole with the length of more than 8cm by the undercutter and clean the hole again.
- (3) Insert and hammer the pullbolt, then the bottom of the pullbolt expands and the pullbolt is fixed in the concrete.
- (4) Attach the shaft to the top of the pullbolt, and cut the shallow circular groove with the diameter of 10cm by the core drill until the base of the drill touches the tip of the shaft. Here, it is possible to keep the distance 7cm from the bottom of the groove to the head of the pullbolt.
- (5) Put the bearing ring around the pullbolt and insert it in the groove. Then bearing ring is certainly set perpendicular to the axis of the pullbolt regardless of the concrete surface condition. Replace the shaft with the pull rod and mount the hydraulic ram on the bearing

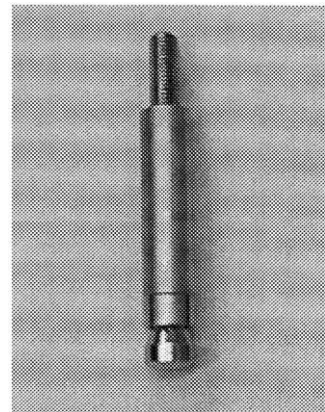


Fig.1 The shape of pullbolt

ring and connect it to the pull rod.

(6) Load at a uniform rate until pullout rupture occurs.

(7) Record the maximum value of the force and check the form of pullout cone.

The procedure is shown in Fig.2

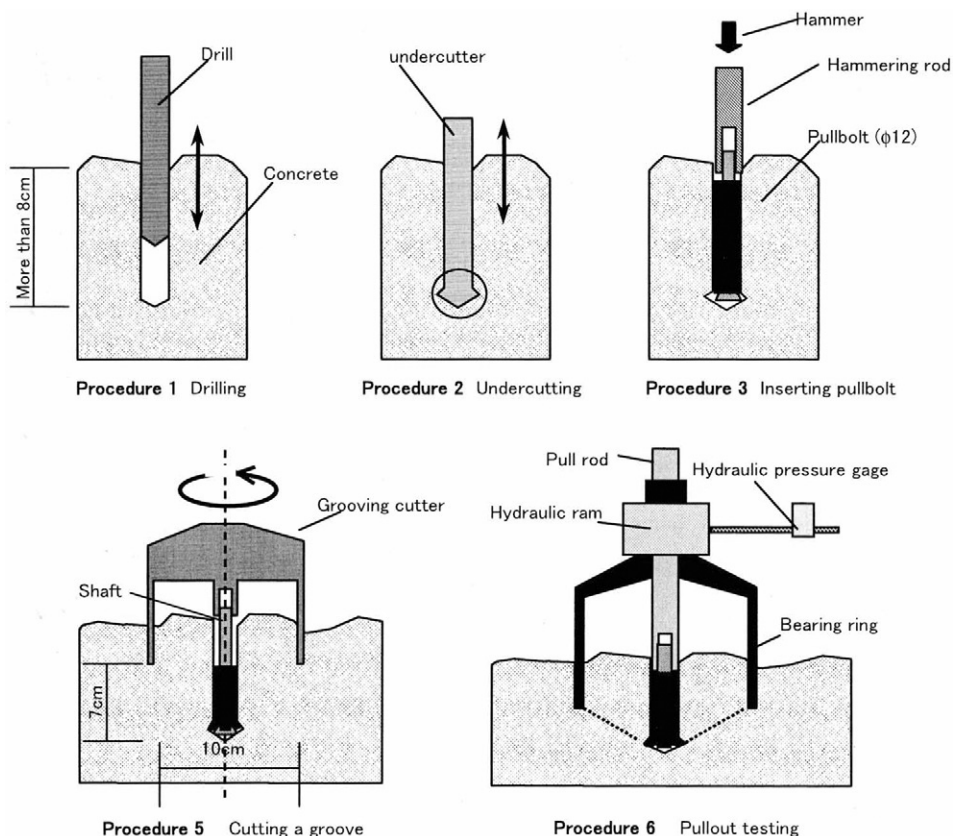


Fig.2 Procedure of proposed method

EXPERIMENTS

The pullout force is influenced mainly by the shear strength of concrete [3]. However, the coarse aggregates randomly exist in the shear fracture zone around the pullout cone and they may influence on the pullout force. Therefore, the problem of the variation of pullout forces exists in the pullout test.

An experiment was took place firstly in order to clarify the variation of the pullout forces. Table 1 shows the mix proportion of the specimen which has 20mm size coarse aggregates.

Table1. Mix proportion of specimens

Gmax (mm)	Slump (cm)	Air (%)	W/C (%)	s/a (%)	W (kg/m ³)	C (kg/m ³)	S.A (kg/m ³)	C.A (kg/m ³)	AE (kg/m ³)
20	18±2.5	4.5±1.5	53	46.6	175	331	835	956	2.98

s/a = Sand aggregate ratio

Pullout test was carried out 54 times in one specimen at the age of 3 days and the variation of pullout forces was evaluated statistically. Typical shape of the cone pulled out is conical which is shown in Fig.3. The cumulative frequency ratio of the pullout forces is described in Fig.4. Normal probability distribution curve, which was calculated from the average of the pullout force 61.4kN and standard deviation 5.6kN, is also shown in this figure. Comparing the distribution of pullout forces with normal probability distribution curve, it is clear that they almost agree with each other.

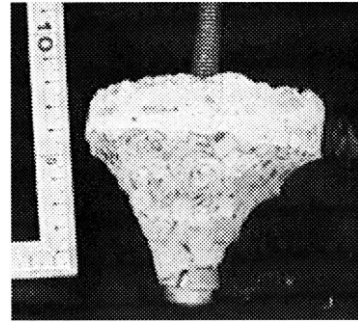


Fig.3 Typical shape of the cone

It means that the variation of pullout forces distributes normally.

Using these data, a more statistical analysis was carried out to determine the number of times of testing at one specimen. The t-distribution gives us information about the relation between the average of sampling data and the population. Regarding the distribution of 54 data as the distribution of the population, the average and the standard deviation of the data can be used in the analysis.

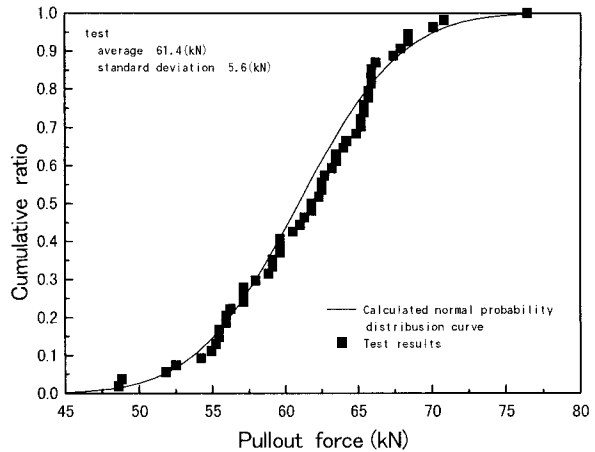


Fig.4 Variation of pullout forces

Fig.5 shows the t-distribution of the obtained data. The distributions of the average when the sampling number is 2 to 5 are shown in this figure. This figure indicates that accuracy increases with the number of sampling, but the accuracy is not so improved when the sampling number increases. Table 2 shows the 95% confidence interval of each sampling number. In the case that the number of sampling is 3, it seems to be better that 95% of averaged

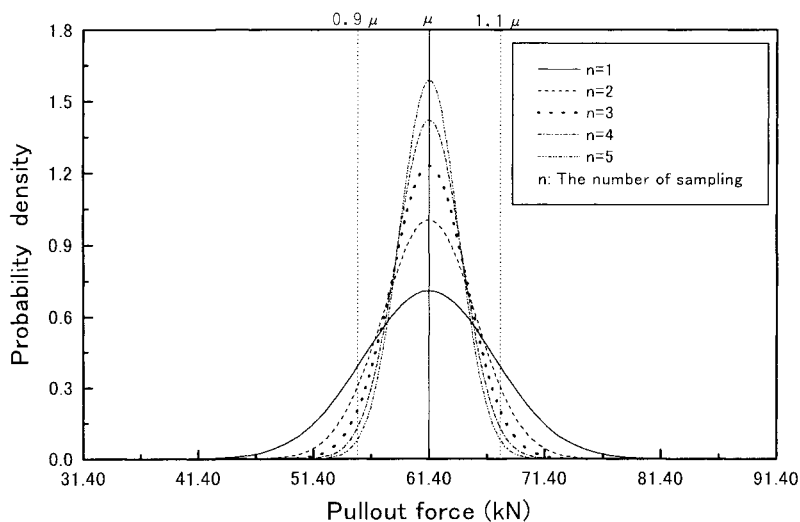


Fig.5 T-distribution of pullout forces

data are in the range of 90% to 110% of the average of population.

IN the next experiment, a shotcrete specimen was produced to evaluate the applicability of the method to the concrete with rough surface. Mix proportion is shown in Table 3 and production process is shown in Fig.5. The shotcrete specimen has considerably rough surface with no treatments. Pullout forces are compared with compressive strength estimated by the standard pullout test [JSCE-G561] at the

age of 3 hours and 24 hours and standard compressive test [JIS A 1108] at the age of 7 days. Test results shown in Fig.6 which shows the quite linear relationship between pullout forces and compressive strength. It explains that the proposed method can also estimate concrete strength.

Table 2 95% confidence interval of averaged pullout force

The number of sampling	95% confidence interval
1	50.1 ~ 71.6 (kN)
2	53.4 ~ 69.3 (kN)
3	54.9 ~ 67.9 (kN)
4	55.7 ~ 67.0 (kN)
5	56.3 ~ 66.4 (kN)
90 ~ 110% of the average of the population	55.2 ~ 67.6 (kN)

Table 3 Mix proportion of Shotcrete

Gmax (mm)	W/C (%)	s/a (%)	W (kg/m ³)	C (kg/m ³)	S.A (kg/m ³)	C.A (kg/m ³)
13	50	59	205	410	990	719
13	56.9	60	205	360	1031	719

s/a = Sand aggregate ratio

CONCLUSION

It has been clarified that the proposed pullout test is able to apply to rough surfaces and the compressive strength can be estimated from the pull force. It is also clarified that the pullout test at one time on one specimen should be done three times in order to obtain the range from 90% to 110% of the mean value of the population. As there are various types of degraded surface conditions such as freezing and thawing, it is necessary to apply the proposed method to many structures.

ACKNOWLEDGEMENTS

We thank Mr.Kitayama and Mr.Fujigasaki who carried out the experiments carefully and also thank Miyanaga Co., Ltd. for the offer of the equipment used in the experiments.

REFERENCES

1. Ronald L.Dilly, Dan G.Zollinger.(1998).*ACI Materials Journal*. pp.304-319.
2. K.Gaede,E.Schmidt.(1957).*Deutschen Ausschusses fur Stahlbeton*. Heft 158
3. W.F.Chen.(1982).*Plasticity in Reinforced Concrete*. McGraw-Hill Int.Book.Co.Ltd.
4. K.Takahashi,et al.(1975).*The Theory of Statistics*. Kyoritu.Publication Co.,Ltd.

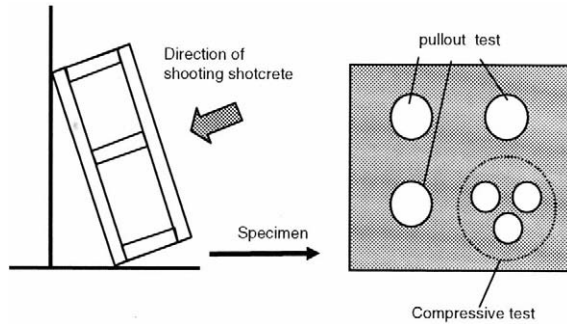


Fig.6 Shotcrete specimen

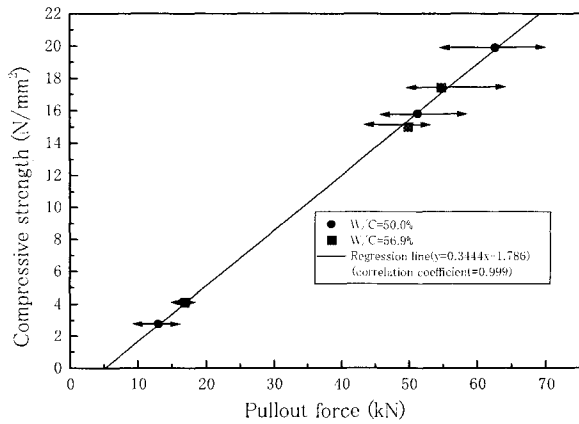


Fig.7 Relationship between Pullout force and Compressive strength of shotcrete

Evaluation of the Strength Characteristics of Building Materials

Dr. Shkolnik, I.E.¹; Dr. Aktan H.M.¹; Dr. Wu H.C.¹; Dr. Russell D.A.²

Introduction

The possibility to predetermine the strength of building materials such as concrete at different strain rates and cyclic loading is studied. The purpose of the study is to evaluate the toughness of infrastructure in service. Therefore, particular emphasis is placed on describing the methods of nondestructively evaluating the strength of concrete at static loading and its dynamic strength from results of static loading. The NDE methods that are explored in this article are nonlinear stress wave techniques at ultrasonic frequencies. Other stress wave techniques such as, the Pulse-Echo utilizing frequencies within sonic range shows significant promise.

Physical Basis

One approach to solving this problem is based on by making allowance for the kinetic nature of fracture. Kinetic nature of fracture postulates that the failure of building materials (metals, glasses, polymers, composites, etc.) under loading is not a critical event but rather is the result of a process of nucleation, accumulation, and the development of damage elements. At the atomic-molecular level, this process is controlled by events of breaking of interatomic bonds by thermal fluctuation. New diagnostic methods are based also on the fact that the nonlinearity of deformation of concrete is an integral microstructure-sensible parameter, which characterizes their behavior up to the point of failure at static and dynamic loading [1,2,3].

The presence of non-linear dependence between stress and deformation has been derived from basic provisions of modern theory of solid bodies and is stipulated by the nature of interatomic forces. Different flaws in structure (dislocations, micropores, microcrevices) have a significant influence and predetermine the non-linearity of deformation diagrams. From the point of view of non-linear ultrasonic diagnostics of materials, the most important condition is that within a wide range of strain (10^{-6} - 10^{-3}) the relation between stress (σ) and strain (ε) is described by one equation [4]:

$$\sigma = E_0 \varepsilon - b \varepsilon^2 \quad (1)$$

where, E_0 : Young's modulus, b : parameter of non-linearity deformation (b/E_0 - the relative value of the parameter of non-linearity deformation).

From (1) it follows that the strength is defined as:

$$R = \frac{E_0^2}{4b} \quad (2)$$

and the coefficient ' b ' given below characterizes the change of elastic property at loading:

$$b = \frac{(E_0 - E)}{2\varepsilon} \quad (3)$$

¹ Wayne State University, Detroit, MI 48202, USA

² Kettering University, Flint, MI 48504, USA

or

$$\frac{b}{E_o} \approx \frac{\Delta E}{\Delta \sigma} = E_o - E$$

One can see from (2) and (3), strength increases with reduction of, the non-linearity parameter, coefficient 'b'.

The thermofluctuation theory, based on the view of lattice anharmonicity and overwork of intermolecular connections, and the non-linearity of deformation leads to the following dependence between strength at dynamic (R_d), cyclic (R_c) and quasi-static (R_s) loading for concrete [3]:

$$\frac{R_d}{R_s} = K_1 = 1 + 0.0906 \log \left(\frac{\varepsilon_d}{\varepsilon_s} \right) \quad (4)$$

$$\frac{R_c}{R_s} = K_2 = 0.914 + 0.0060 \log f - 0.0906 \log N \quad (5)$$

where ε_s , ε_d - strain rates at quasi-static and dynamic loading, f - loading frequency, and N - number of loading cycles.

Equations (4,5) are well established for many traditional materials. However, based on the thermofluctuation theory and non-linearity of deformation, this fact requires experimental verification for concrete and other composite materials (graphite/epoxy, carbon/epoxy, glass-fiber reinforced, etc.).

Comparison with Experimental Results

In order to estimate the dynamic strength from the results of quasi-static tests, the dynamic coefficient K_1 and cyclic coefficient K_2 given in equations 4 and 5, were calculated for concrete corresponding to tensile, compressive and flexural failure modes.

Table 1 contains comparison of K_1 with the experimental results of many investigators compiled in reference (5) for tensile strength of concrete. The comparisons shown in Table 1 are between the following equation for dynamic coefficient K_1 , which is based on these experimental results given in reference (5) and theoretical expression for K_1 shown in equation 4:

$$K_1 = 1.770 + 0.2190 \log \varepsilon_d + 0.0154 (\log \varepsilon_d)^2 \quad (6)$$

In describing the dynamic strength the strain rate ratio was varied by an order of seven, and the quasi-static strain rate that appears in equation 4 was $5 \cdot 10^{-7}$ 1/s

Table 1 shows that the relative error between the experimental expression (6) and theoretical expression (4) (in this case $K_1 = 1.570 + 0.0906 \log \varepsilon_d$) did not exceed 11%.

Table 2 shows the experimental values of K_1 for the compressive strength of plain and steel fiber reinforced concretes [6]. The values of K_1 calculated using equation (4) are: $K_1 = 1.1812$ for $\varepsilon_d = 10000 \mu/s$, $\varepsilon_s = 100 \mu/s$; $K_1 = 1.2244$ for $\varepsilon_d = 30000 \mu/s$, $\varepsilon_s = 100 \mu/s$ (μ - microstrain).

One can see from Table 2 that the experimental values of compressive strength were less than the average value calculated from Eq. (4) and the relative error did not exceed 17%.

Thus, the results presented in Tables 1 and 2 show that the dynamic strength of concrete under tensile, and compressive loading can be determined if its static strength and the parameter of non-linear deformation is known.

Table 1. Dynamic Coefficient K_1 for Tensile Strength of Concrete

Strain rate, (1/s)	K_1 Ref[4]	K_1 Ref[6]	Relative error, (%)
(1)	(2)	(3)	(4)
10^{-7}	0.94	0.99	+5.0
10^{-6}	1.03	1.01	-2.0
10^{-5}	1.12	1.06	-6.0
10^{-4}	1.21	1.14	-6.0
10^{-3}	1.30	1.25	-4.0
10^{-2}	1.39	1.39	0.0
10^{-1}	1.48	1.57	+6.0
10^0	1.57	1.77	+11.0

Table 2. Dynamic Coefficient K_1 for Compressive Strength of Concrete

	K_1			
	$\varepsilon_d=10000$		$\varepsilon_d=30000$	
	(m/s)	%	(m/s)	%
(1)	(2)	(3)	(4)	(5)
Mix 1-control	1.130	-4.4	1.240	1.3
Mix 1-A	1.015	-16.4	0.991*	-
Mix 1-B	1.077	-9.7	1.074	-14.0
Mix 1-C	1.071	-10.3	1.092	-12.0
Mix 2-A	1.070	-10.4	1.106	-10.7
Mix 2-B	1.056	-12.0	1.157	-5.8
Mix 3-C	1.143	-3.3	1.105	-10.8
Mix 3-A	1.220*	-	1.315*	-
Mix 3-B	1.100	-7.4	1.070	-14.4
Mortar	0.095*	-	1.083	-13.1
Mix 4-A	1.055	-12.0	1.123	-9.0

Note: * excluded with reliability 95%.

In Tables 3 and 4 the values of K_2 obtained from equation 5 are compared with experimental results for cyclic loading that are presented in references [7,8]. As follows from column 1 of Tables 3 and 4, the average value of the first coefficient in experimental expressions of K_2 equals to 1.1346 and the average value of the coefficient of $\log N$ equals to 0.0810.

Table 3. Equations of K_2 for Compressive Strength of Concrete

Compressive loading			
K_2	K_2	Frequency	The value of
Experiment	Equation (5)	(min^{-1})	$\rho = \sigma_m / \sigma_M$
(1)	(2)	(3)	(4)
0.997-0.0623logN	1.158-0.0906logN	500	0.075
0.974-0.0580logN	1.158-0.0906logN	500	0.150
1.250-0.0278logN	1.158-0.0906logN	500	0.850
1.036-0.0286logN	1.158-0.0906logN	500	0.925
1.155-0.0945logN	1.186-0.0906logN	1000	0
1.160-0.0900logN	1.166-0.0906logN	600	0
1.039-0.0680logN	1.129-0.0906logN	240	0.100

Table 4. Equations for Cyclic Coefficient K_2

Tensile loading			
K_2	K_2	Frequency	The value of
Experiment	Equation (5)	(min^{-1})	$\rho = \sigma_m / \sigma_M$
(1)	(2)	(3)	(4)
0.626-0.0188logN	1.158-0.0906logN	500	0.040
1.568-0.1520logN	1.158-0.0906logN	500	0.015
1.136-0.1100logN	1.158-0.0906logN	500	0.330
1.151-0.0681logN	1.158-0.0906logN	500	0.500
0.965-0.0350logN	1.158-0.0906logN	500	0.700
Flexural loading			
1.157-0.1012logN	1.185-0.0906logN	1000	0.100
1.000-0.0560logN	1.185-0.0906logN	1000	0.180
2.225-0.3360logN	1.158-0.0906logN	500	0.150
0.930-0.0400logN	1.158-0.0906logN	500	0.250
0.920-0.0300logN	1.515-0.0906logN	420	0.500

The experimental relations for K_1 shown in the first column of Tables 3 and 4 compare very well with the theoretical relation shown in second column obtained by substituting the cycle characteristics (ρ) and load frequencies given in third and fourth columns.

In recent years fiber reinforced concrete has become increasingly popular for use in structures subjected to severe environmental loads and conditions. Therefore, it is very important to know if it is possible to use the theoretical relation presented in equation 5 for fiber concrete mixtures. The relations given in Table 5 evaluated using the experimental data from reference [9] are compared to the relation evaluated from equation 5 by substituting a frequency of 1Hz, given below:

$$K_2 = 1.075 - 0.0906 \log N \quad (8)$$

Table 5. Experimental equations for Cyclic Coefficient K_2 for Concrete under Compressive Loading

Plain concrete			
A	B	C	D
1.073-0.1172LogN	1.094-0.0983LogN	1.069-0.0876LogN	1.070-0.1173LogN
Steel fiber (SF) reinforced concrete			
0.25%SF	0.50%SF	0.75%SF	1%SF
1.141-0.1241LogN	1.147-0.1223LogN	1.085-0.1137LogN	1.158-0.1121LogN
Polypropylene fiber (PF) reinforced concrete			
0.25% PF	0.50% PF	0.75% PF *	1% PF
1.043-0.0799LogN	1.045-0.0950LogN	1.199-0.2409LogN	1.1040-0.0757LogN

* -are excluded with reliability of 99%. A, B, C, D are different concrete mix proportions

A statistical analysis of the coefficients of the experimental relation showed that with reliability of 99% the first coefficient in the experimental expressions is (1.0881± 0.06) and the coefficient of logN is (0.1039± 0.0242). These values show excellent correlation with the coefficients for K_2 in equation 8.

Based on their experimental results Hsu and Su [10] presented equation 9 describing the cyclic coefficient. Table 6 contains the comparison of K_2 from equations 8 and 9.

$$K_2 = \frac{1.17 - 0.13 \log N}{[1 + (0.32 \log N)^5]^{12}} - 0.033 \log N \quad (9)$$

Table 6. Cyclic coefficients K_2 for concrete

LogN	K_2 Ref[9]	K_2 Ref [8]	Relative error (%)
0	1.170	1.074	+8.0
1	1.007	0.980	+2.2
2	0.849	0.893	-5.0
3	0.724	0.803	-11.0
4	0.652	0.712	-9.3
5	0.606	0.621	-2.6
6	0.568	0.531	+6.0
7	0.534	0.440	+17.5

These equations compare well when considering the relative error between the two equations for

various number of cycles that is shown in Table 6 didn't exceed 17.5%.

A number of cases for different kinds of concrete, different kind of stress, different investigators in different countries) compared in Tables 1 through 6 clearly demonstrate that the strength of concretes at different strain rates and cyclic loading may be predicted from the results of static tests.

Ultrasonic Stress Wave Techniques for Evaluating K_1

It is logical to suppose that non-linearity of deformation reflecting a reaction of structure to external force, may be measured under very low load levels by increasing the measurement accuracy. Based on this premise three ultrasonic methods of measuring deformation non-linearity parameters were developed: spectral, phase and frequency [2].

The spectral method is based on measuring the oscillation amplitude of the double frequency-the second harmonic-which appears in material with "local nonlinearities" (e.g. micropores, microcrevices). An ultrasonic wave of known frequency, $f=50\text{KHz}$, was applied across a sample. The energy wasted by scattering when the wave "stumbles" upon inner defects is proportional the energy spend on forming the second harmonic, $f=100\text{KHz}$. Consequently, in the amount of energy lost, observed by the decrease in amplitude of the input wave output of the input wave indicates the level of quadratic dependence of the given specimen. The ratio of the second harmonic to the first one was within a few fraction to one percent in signal passing through concrete (Fig. 1).

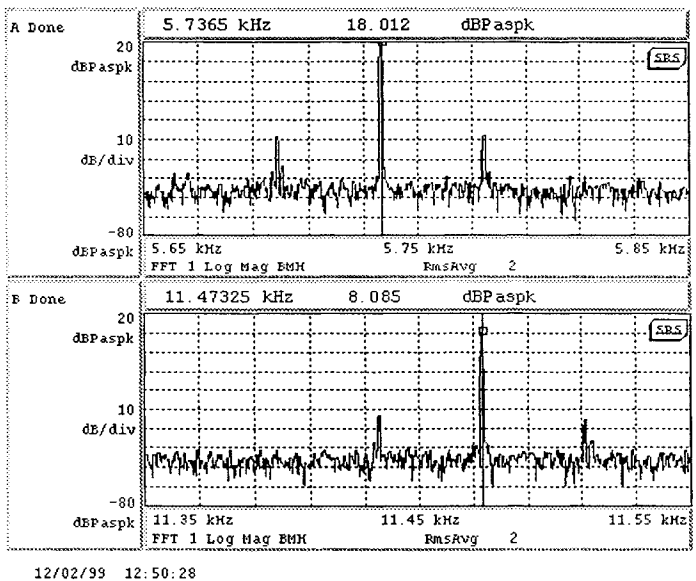


Figure 1. Spectral Analysis Showing Amplitudes of the 1st and 2nd Harmonics

In phase method the non-linear parameter is determined from the phase change in a specimen due to changes in the speed of propagation at different amplitudes of excitation. The experiment consisted of driving an ultrasonic emitter at 50KHz with two voltage levels, 10v and 100v (non-linear distortion in the driver was small), on several concrete specimens. In each test the phase of the response relative to the driver

signal was measured, and the phase difference, φ , for the two levels was found. The phase method and equipment enabled us to solve a problem of testing concrete strength for high grades (more than 50MPa) [2]. It was found that the following relationship between strength and non-linear parameter: $R_s = 66.5 - 6.84 \varphi$, the main quadratic error of the definition of strength didn't exceed 10% in the investigated range satisfying the practical requirements (Fig. 2)

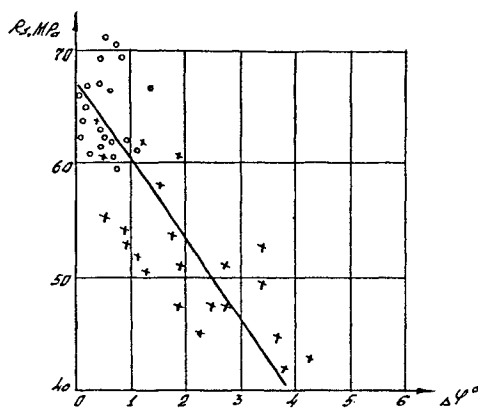


Figure 2. Dependence 'phase shift ($\Delta\varphi$) – strength (R_s)' for concrete 10-cm cubes: x-age of concrete-3 days, 0-age of concrete-28 days. [3]

In the frequency method, the non-linear parameter is determined from the resonant frequency shift in a specimen due to an increase in the acoustic excitation amplitude. For cylindrical steel bars (length 450 mm, and diameter 10 mm) the relative change in resonant frequency shift was about decimal fraction of percent due to increase in the excitation amplitude by five times. When the excitation amplitude was doubled the relative change in resonant frequency shift was: for brick between 0.1%-2%, and for concrete samples with dimensions 40 by 40 by 160 mm between 0.5%- 1% (Fig. 3). Physical bases of this method also allow the use of impact-echo method for predicting the strength characteristic of concrete in situ by measuring the shift of resonant frequency with an increase in the amplitude of impact loading.

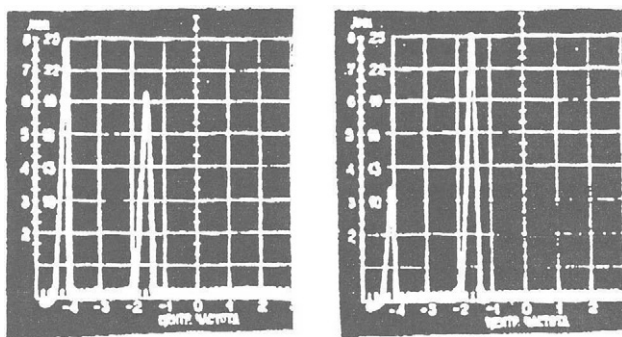


Figure 3. Spectrograms of acoustic oscillations, (a) cement-sand solution (b) concrete [1]

Summary and Conclusions

A method for predicting the dynamic strength of concrete is presented. The laws of dynamic fracture of concrete correspond to the general kinetic ideas about fracture as a process of accumulation of damage and are governed by thermofluctuational and breaking of interatomic bonds due to overstress. The parameters of non-linear deformation reflect the response of structure of external forces at static loading and may also be used to predict the behavior of concrete at different strain rates and cyclic loading. The model suggests a simple way to predict the dynamic characteristics from the results of static tests.

The basic understanding of knowledge on nonlinearity, and improvements in technology providing better measurement resolutions lead to new practical applications in determining properties of building materials. The methodology presented here is such a use of ultrasonic methods for the prediction of the strength characteristics of materials utilizing the fundamentals non-linear behavior and the influence of insignificant stresses, created by the stress wave.

New ultrasonic methods presented here are easy to implement, do not require special and expensive equipment that are required for cyclic and dynamic tests. The ultrasonic methods discussed here also demonstrate the possibilities to improve existing methods of NDT.

References

1. Shkolnik, I.E. Estimation and prediction strength of solids on the basis of calculation of non-linearity of deformation diagram. Proceedings of USSR Academy of Science. Mechanics of Solid. 3: p. 189. 1980.
2. Shkolnik, I.E. Non-destructive testing of concretes: new aspects. *J. Nondestr. Test. Eval.*, Vol. 10, pp. 351-358. 1993.
3. Shkolnik, I.E. Evaluation of Dynamic Strength of Concrete from Results of Static Tests. *Journal of Engineering Mechanics*. Vol. 122, No. 12, December, pp. 1133-1138. 1996.
4. *Encyclopedia of Physics*, Volume VIa/1, Editor C. Trusdell. 1973
5. Soroushian, P., Ki-Bong, C., and Gung, F. Tensile strength of concrete at different strain rates. *Mat. Res. Soc. Symp. Proc.*, Vol.64, 87-92, 1986.
6. Otter, D., and Naaman, A. E., Steel fiber reinforced concrete under static and cyclic compressive loading. 3rd RILEM Symp. on Developments in Fiber Reinforced Cement and Concrete. 1986.
7. Antrim, and McLoughlin, Y. F. Fatigue study of air entrained concrete. *J. Am. Concrete Inst.*, 30(11), 1173-1178, 1959.
8. Shkolnik, I. E. Diagnostics of concrete quality: new aspects. Technoproect, Moskow, 1993.
9. Paskova, T., and Meyer, C. Damage of plain and reinforced concrete under low-cycle fatigue load. *Tech. Rep.*, Columbia Univ., Department of Civil Engineering Mechanics. New-York, N.Y. 1994.
10. Su, E.C.M. Biaxial compression fatigue of concrete, PhD dissertation, Univ. of Houston, Houston, Tex. 1987.

A PROPOSAL OF CONTROL METHOD ON SHOTCRETE STRENGTH BY PIN PENETRATION TEST USING AIR PRESSURE

K. IWAKI and A. HIRAMA

Technological Research Institute, Tobishima Corporation,
5472 Kimagase, Sekiyado-machi, Chiba 270-0222, Japan

K. MITANI and S. KAISE

Research Institute, Japan Highway Public Corporation
1-4-1 Tadao, Machida-City, Tokyo 194-8508, Japan

K. NAKAGAWA

Department of Civil Engineering, Yamaguchi University,
Tokiwadai, Ube-City, Yamaguchi 755-8611, Japan

ABSTRACT

Shotcrete is recognized as a significant support element in NATM because of its quick strength development. It is necessary to investigate the real strength development of shotcrete at surface of tunnel lining for safety's sake and designing support structure. Conventionally, however, the strength testing methods are almost destructive methods using specimens. Therefore, a new pin penetration test using air pressure is proposed as a simple in-situ test. At first, pins are driven on the surface of shotcrete by an ordinary pneumatic nailer. Then, compressive strength of shotcrete is estimated from the pin penetration depth. In this study, the applicability of this method was verified through laboratory and field tests. There are close relationships between the pin penetration depth and the compressive strength in the range from 1 to 30 N/mm². Therefore, it is found that the newly proposed testing method is effective for estimating the shotcrete strength. In addition, the merits of in-situ testing method serve the purpose of proposing a new control method on shotcrete strength.

KEYWORDS

compressive strength, in-situ test, pin penetration test, pneumatic nailer, shotcrete

INTRODUCTION

One of required functions of shotcrete for mountain tunnels constructed by the new Austrian tunneling method (NATM) is its mechanical role as a support structure after application. Qualities contributing to this role include strength-developing properties in terms of compressive strength, bond strength, stiffness and so forth. Strength development up to the age

of 24 hours is much more important for shotcrete than for concrete placed in formwork. In order to rationalize support structures and ensure safety during tunneling, there have been demands for adequate assessment of ground, a higher strength of shotcrete and reinforcing with fibers. Establishment of an efficient method of evaluating early strength of shotcrete is anticipated as well.

In this study, authors applied a “pin penetration testing method using a pneumatic nailer” (pneumatic pin penetration method) on the evaluation of early strength development of shotcrete as a simple in-situ test method. Laboratory and field tests were then conducted to verify the applicability of this method. A control method of shotcrete strength was also developed making the most of this in-situ test method.

THE RANGE OF EARLY SHOTCRETE STRENGTH TO BE CONTROLLED

The tunneling cycle requires shotcrete to develop sufficient strength for withstanding the mechanical and explosive vibrations resulting from subsequent rock-bolting of the span and excavation of the next span. These operations are normally carried out within a few hours after shotcreting. The compressive strength to withstand the vibration of blasting is empirically known to be from 0.5 to 1.0 N/mm² [1].

From the aspect of the ground-supporting function, the strength of shotcrete to resist the ground pressure at the age from 1 to 2 days is important in the early strength range [1]. Recently, high-strength shotcrete that develops a compressive strength of over 20 N/mm² at 1 day have been put into practical use for the purpose of rationalizing support structures.

Accordingly, the ranges of early shotcrete strength to be controlled are considered to be between a few hours and 2 days in age and between 1 and 25 N/mm² in compressive strength.

CONVENTIONAL TEST METHODS

Generally, indirect test methods have been adopted for the early strength of shotcrete. This is because it is difficult for shotcrete to be made into cylindrical specimens as those normally used for compressive strength control and the early strength of shotcrete is insufficient for drilling cores. Moreover, direct compression tests require a compression test machine, which is not suitable for field use.

It is true that indirect test methods can lead to a lower accuracy than direct methods. However, early strength of shotcrete is known to vary relatively widely depending on such factors as accelerator dosage. Simple and indirect methods, which may be less accurate, are therefore preferable for this kind of testing in which quick judgement is paramount.

Generally employed methods are introduced below with their characteristics described:

Pull-out method

The “pull-out test” is the most widely used method standardized in the JSCE (Japan Society of Civil Engineers) Standard and the JH (Japan Highway Public Corporation) Standard. In this method, concrete is sprayed onto forms or ground on which draw bolts are attached beforehand. The draw bolts embedded in the sprayed concrete are then pulled out together with truncated cone specimens, and the compressive strength of the concrete is estimated using its shear strength calculated from the pull-out force. Shotcreting on forms is mostly employed rather than on the ground for convenience. And the relevant strength range is from 1 to 30 N/mm². The shortcomings of this method are as follows:

- 1) Strength of concrete sprayed on forms does not directly represent the strength of shotcrete applied to the ground.
- 2) When using forms, molding and conveyance of specimens require substantial labor.
- 3) When testing directly on the ground, the area around the bolt ought to be finished smoothly after shotcreting. This is not suitable for shotcrete, which quickly develops strength.

Austrian guidelines

The Austrian Concrete Society established Guideline on Shotcrete, in which test methods are specified in detail. The “penetration needle method” and “bolt driving method” specified in this guideline for strength testing within the age of 24 hours are explained as follows:

Penetration needle method. In this method, a needle is penetrated to a specified depth (15 mm) using a proctor penetrometer according to ASTM C 403. The force required for this operation is measured and converted to compressive strength. Either a flat-tipped needle (dia. 9 mm) or a pointed tipped needle (dia. 3 mm) is used depending on the strength. The compressive strength range estimated by this method is from 0.1 to 1.0 N/mm².

Bolt driving method. In this method, a bolt screw is driven into shotcrete with a constant driving force, and pulled out immediately. The compressive strength of the shotcrete is estimated from the ratio of the pull-out force to the penetration depth. This method covers a compressive strength range of from 2 to 12 N/mm².

Windsor probe method

Though the Windsor probe test (ASTM C 803) is not usually applied on early strength of shotcrete, it is applied as a simple in-situ method for testing concrete strength. In this method, a probe is driven into concrete with a specified penetrating force, and the concrete strength is estimated from the penetration depth. An explosive of an adjusted amount produces the specified kinetic energy for penetration. This method provides a relatively high estimation range from 10 to 40 N/mm². Whereas mortar strength determines the compressive strength of concrete, type and hardness of coarse aggregate are said to affect the penetration depth by this method, as the probe penetrates through mortar and coarse aggregate.

Problems of conventional test methods

The Windsor probe test is difficult to apply to daily operations, as the use of explosives is

strictly regulated in Japan [2]. Also, the applicable range of each conventional method is shown in Fig. 1. The pull-out method is currently the only method available that covers the range from 1 to 25 N/mm² required for early strength control of shotcrete. A simple in-situ test method to replace this is anticipated.

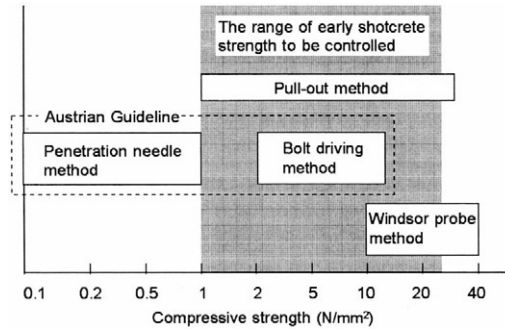


Fig. 1 Applicable range of each conventional method.

PNEUMATIC PIN PENETRATION TEST

Test procedure

Shotcrete is proportioned to contain less coarse aggregate than conventionally placed concrete, and the maximum aggregate size is relatively small at 15 mm. While the strength has not fully developed, the coarse aggregate is not fully confined by mortar. It is therefore unlikely that coarse aggregate inhibits the penetration of pins into shotcrete at early ages. Therefore, methods using penetration resistance as an index, such as the Windsor probe method, are considered to be effective in estimating early strength of shotcrete. However, the Windsor probe method requires official permission for using explosives. Moreover, it can involve a risk of injury during testing, and requires a skilled testing operator familiar with explosives to adjust the penetrating force by the powder amount.

The authors propose a pneumatic pin penetration test, in which air pressure provides the energy required for driving pins. As shown in Fig. 2, pins are driven into shotcrete using an ordinary pneumatic nailer. The concrete strength is estimated by the pin penetration depth. This method is characterized by the constant penetrating force easily obtained from an ordinary pneumatic nailer and the ability to adjust the penetrating force by varying the air pressure.

Equipment specifications

The air pressure is basically set at 1.47 MPa (15.0 kgf/cm²) in consideration of the equipment specification and the driving reaction. In order to enable the testing operator to easily check the air pressure, a digital manometer is attached at the connection between the equipment and air hose. The pins are shown in Fig. 2. Pins A and B have different diameters, leading to different resistance values when they penetrate into concrete. The use of these two sizes can widen the

range of strength estimation. The qualities of pins including material, strength and surface finish conform to JIS A 5529 (Pins and studs for powder actuated tool). The pin penetration depth is measured with a depth meter attached to a dedicated jig.

The pin-driving capability of pneumatic nailers has been elucidated based on penetration tests into polyethylene. The following have been confirmed:

The stability of the penetrating force. The pneumatic nailer used in this study provides a constant penetrating force, with the standard deviation of penetration depth into a homogeneous material being 0.8 mm.

The effect of penetrating direction. The penetrating energy of the pneumatic nailer is large enough to eliminate the effect of gravity on the penetrating force. Therefore, tests can be conducted at any point on tunnel walls.

The relationship between the air pressure and the penetrating force. The pin penetration depth is proportional to the air pressure at a ratio of approximately 38 mm/MPa. In the controllable air pressure range of ± 0.01 MPa, the penetration depth by the pneumatic nailer varies by only ± 0.4 mm.

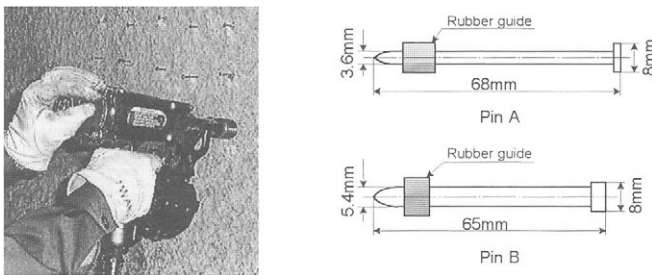


Fig. 2 State of pneumatic pin penetration test and specification of pins.

VERIFICATION OF APPLICABILITY TO SHOTCRETE STRENGTH EVALUATION

Laboratory and field tests were conducted to verify the applicability of this method to early strength evaluation of shotcrete. The pull-out test was employed to determine the strength development, as it is a standard method for early strength testing and capable of measuring the shotcrete strength from immediately after application. The changes in the penetration depth were measured, while the strength developed, to elucidate the relationship between the penetration depth by the proposed method and the compressive strength estimated by the pull-out method. The relationship between the pin penetration depth and the uni-axial compressive strength of cylindrical specimens was then determined from the relationship between the uni-axial compressive strength of cylindrical specimens and the compressive strength estimated by the pull-out test simultaneously conducted in the laboratory.

Mix proportions for experiment

In order to elucidate the effects of the diversifying mix proportions of shotcrete on the pin penetration depth of this method, tests were conducted with various parameters: normal/high-strength proportions, presence/absence of steel fiber reinforcement, maximum aggregate size, etc. When selecting the proportions, those normally used and those expected to be used in the future were taken into account. Table 1 gives the mix proportions selected for the laboratory and field tests.

Table 1 Mix proportions for experiment (laboratory tests and field tests) .

Mixture No.	Mixture type	Fiber content (vol%)	Maximum size of aggregate (mm)	Slump (cm)	W/C (%)	Cement (kg/m ³)	Water (kg/m ³)	Fine aggregate (kg/m ³)	Coarse aggregate (kg/m ³)
Laboratory tests									
P-10	Plain	—	10	10.0	47.5	392	186	807	874
P-15	Plain	—	15	18.0	44.0	455	200	903	756
F-0.50	Fiber reinforced	0.50	15	18.0	44.0	478	210	1030	567
F-0.75	Fiber reinforced	0.75	15	18.0	44.0	500	220	1074	471
F-1.0-1	Fiber reinforced	1.00	15	18.0	44.0	512	225	1053	461
F-1.0-2	Fiber reinforced	1.00	10	18.0	45.0	450	203	1114	481
Field tests									
N-10	Normal strength	—	10	8.0	56.8	380	216	1126	610
N-15	Normal strength	—	15	8.0	57.5	360	207	1036	700
H-10-1	High strength	—	10	18.0	45.0	450	203	1040	603
H-10-2	High strength	—	10	18.0	45.0	450	203	1035	610
H-15	High strength	—	15	18.0	45.0	450	203	991	673
F-10-1	Fiber reinforced	0.75	10	18.0	45.0	467	210	1146	498
F-10-2	Fiber reinforced	0.75	10	18.0	45.0	450	203	1076	546
F-10-3	Fiber reinforced	1.0	10	18.0	45.0	450	203	1114	481

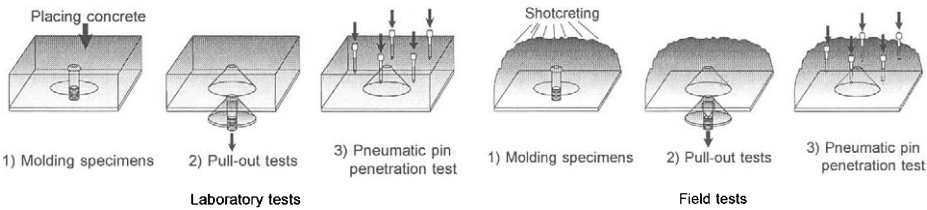


Fig. 3 Test procedure (laboratory tests and field tests) .

Test procedure

In the laboratory tests, specimens were prepared by placing concrete in forms for pull-out testing with attached side frames as shown in Fig. 3. Pull-out tests were conducted on these specimens, followed by pneumatic pin penetration tests on the same specimens. Eq. 1 was used for estimating compressive strength by the pull-out method in accordance with the JH Standard. Uni-axial compression tests were also conducted on cylindrical specimens 100 mm in diameter and 200 mm in length at the same ages.

$$\sigma = 4\tau \tag{1}$$

where σ = compressive strength (N/mm²)
 τ = shear strength (N/mm²)

In the field tests, specimens were prepared by shotcreting onto forms for pull-out testing as shown in Fig. 3, and then subjected to pull-out tests and pneumatic pin penetration tests as in the laboratory. Pins were driven on uneven shotcrete surfaces to simulate in-situ testing.

Results and discussion

Compressive strength estimated by pull-out method. The relationships between the uni-axial compressive strength of cylinders and the compressive strength estimated by simultaneous pull-out tests are shown in Fig. 4. The strength estimated by pull-out tests tends to be higher in the range below 18 N/mm², whereas it tends to be lower in the higher strength range. This relationship is approximated by Eq. 2 in the uni-axial compressive strength range of up to 33 N/mm², with the coefficient of correlation being 0.96.

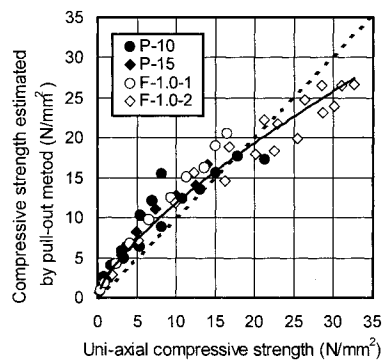


Fig. 4 Relationship between the uni-axial compressive strength and the compressive strength estimated by pull-out method.

$$F_p = 2.297 F_c^{0.71} \quad (2)$$

where F_p = compressive strength estimated by the pull-out method (N/mm²)
 F_c = uni-axial compressive strength (N/mm²)

Results of pneumatic pin penetration tests. The relationships between the pin penetration depth and the compressive strength estimated by pull-out test are shown in Fig. 5.

In the laboratory test with the larger diameter Pin B, no appreciable effect of proportioning parameters, such as fiber content and maximum aggregate size, is observed. The penetration depth of Pin B sensitively changes from 55 to 35 mm responding to the increase in the estimated strength from 5 to 7 N/mm². In the strength ranges above and below this range, the penetration depth decreases more moderately. The relationship between the penetration depth and the compressive strength estimated by the pull-out method of all mix proportions is approximated to a curve of 3rd degree equation. The coefficient of correlation is as high as 0.95. In the strength range of over 15 N/mm², the pin penetration depth remains around 20 mm, showing no appreciable reduction.

In the laboratory test of the smaller diameter Pin A using only one mix proportion, the penetration depth decreases more linearly than that of Pin B as the compressive strength increased from 3 to 25 N/mm². No sensitive changes as with Pin B are observed. This relationship using Pin A is also approximated to a curve of 3rd degree equation similarly to Pin B, with the coefficient of correlation being around 0.94.

In the field tests, the decreasing tendencies of the penetration depth are evident with both pin types as the strength developed. Despite of shotcreting on uneven surfaces, the results nearly coincide with the approximate curves obtained from the laboratory tests. The curve of Pin A agrees particularly well, as the same mix proportion is used both in the laboratory and in the field. With Pin B, the curve agrees well in the penetration depth range of over 27 mm (in the strength range of less than 12 N/mm²).

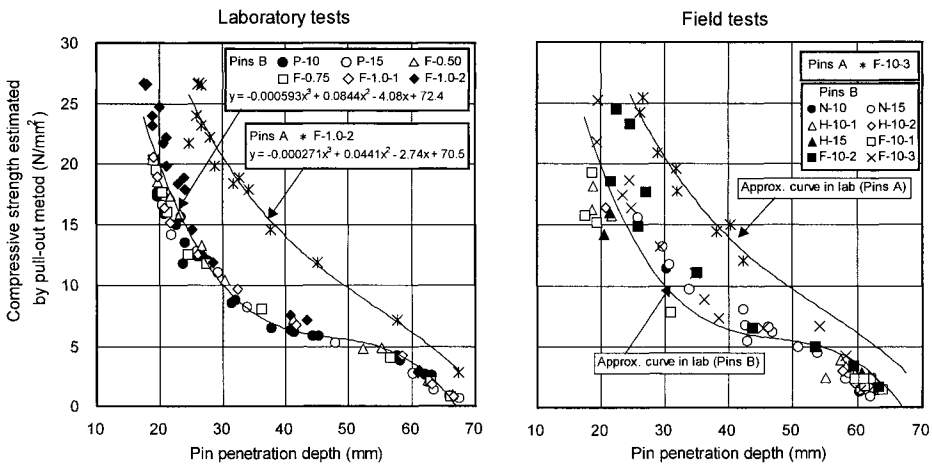


Fig. 5 Relationships between the pin penetration depth and the estimated compressive strength (laboratory tests and field tests) .

Discussion. Being uneven, shotcrete surfaces have to be finished smooth before testing by such methods as the Schmidt hammer test, in which the surface hardness is measured [3]. By the proposed test method, however, the relationship between the pin penetration depth and the estimated compressive strength obtained from laboratory tests was reproduced by field tests in which the pins were driven into uneven shotcrete surfaces. This suggests the applicability of this method to strength evaluation of shotcrete.

As for the ranges of strength estimation, Pin B, which is sensitive to strength changes, is effective for the low-strength range up to 12 N/mm² in terms of compressive strength estimated by the pull-out method. Pin A is effective for a higher strength range of 12 to 25 N/mm² estimated by the pull-out method.

The relationship using estimated compressive strength shown in Fig. 5 is modified to a relationship using uni-axial compressive strength by Eq. (2), which is the relationship between

uni-axial compressive strength and estimated compressive strength. This is then approximated to curves of 3rd degree equation as shown in Fig. 6. A compressive strength of 12 N/mm² estimated by the pull-out method corresponds to a uni-axial compressive strength of 10 N/mm².

These results have proved that a wide range of compressive strength can be evaluated by the proposed method by using pins with different diameters for different strength ranges. In other words, early strength of up to the age a few hours can be estimated using Pin B, whereas Pin A can be used for a higher compressive strength range, such as 1-day strength.

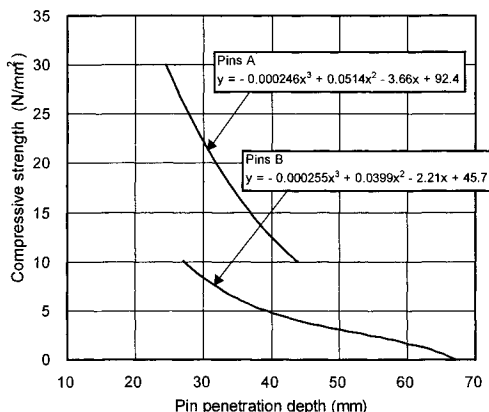


Fig.6 Modified relationships between the pin penetration depth and the compressive strength.

PROPOSAL FOR A STRENGTH CONTROL METHOD

Evaluation of support structure by In-situ Tests. Conventional control using specimens, such as the pull-out method, has a shortcoming of being unable to assure the strength of concrete actually sprayed onto the ground. The application of the proposed method enables in-situ tests and easily grasping the strength of shotcrete applied to the ground.

Strength control by tests at short intervals. By the application of the proposed method, which is simpler than conventional methods, tests can be conducted more frequently as required, and the strength development at any age can be grasped more easily. In order to ensure safety of tunneling, a rational method can be realized by establishing the required strength development of shotcrete in consideration of the time of tunnel excavation cycles and selecting mix proportions meeting the strength requirements.

Evaluation of nonuniformity of support structure. The dosage of accelerator, which determines the early strength development of shotcrete, is not necessarily constant, as it is normally adjusted by the operator taking into account the state of rebound and the ground condition, such as water inflow. The variation of accelerator dosage results in nonuniform strength development of concrete sprayed to tunnel walls, posing problems for the evaluation of shotcrete as a support structure. The proposed method enables the evaluation of concrete

strength at any point including the crown and walls. The nonuniformity evaluation of shotcrete, therefore, becomes possible, contributing to the improvement of safety and quality of support structures.

CONCLUSIONS

The authors investigated and verified the applicability of a pneumatic pin penetration method on strength control of shotcrete. The following findings were obtained:

- 1) The ordinary pneumatic nailer employed in the pneumatic pin penetration test exhibits constant penetrating force not affected by the pin direction. This will provide a high accuracy of strength evaluation and make possible in-situ testing of concrete sprayed onto tunnel walls.
- 2) The applicability of this method was investigated by laboratory and field tests. The laboratory tests revealed that the relationship between the pin penetration depth and the estimated compressive strength could be approximated to curves of 3rd degree equation with a high coefficient of correlation. The field tests led to results that nearly agree with the approximate curves obtained from the laboratory tests, suggesting the applicability of this method as a test method for early strength of shotcrete.
- 3) Proportioning parameters were selected in consideration of the proportions currently employed and those expected in the future. In this study, these parameters produced no appreciable effects on the pin penetration depth.
- 4) By using Pins A and B having different diameters, a wide range of compressive strength from 1 to 30 N/mm² can be evaluated by this method. In other words, this method covers the entire range of early shotcrete strength to be controlled.
- 5) By making the most of this method as a simple in-situ test method, a strength control method can be proposed. This will enable the evaluation of strength development required by tunneling cycles and nonuniformity of shotcrete as a support structure.
- 6) In this study, proportioning parameters were selected in consideration of mix proportions that are generally employed and those expected to be used in the future. Separate investigation may therefore be necessary for special proportioning parameters, which are not included in this study, such as sprayed mortar.

REFERENCE

1. Tazawa, Y. (1996). Dr. Eng. Thesis, Tokyo Metropolitan University, Japan (in Japanese).
2. Uomoto, T., Kato, K., Hirono, S. (1990). In: *Non-destructive inspection of Concrete Structure*, pp. 18-19, K. Kobayashi (Ed.), Morikita, Tokyo (in Japanese).
3. Katase, T., Tanimoto, C., Ishikura, M. (1984). In: *Tunnels and Underground Vol. 15*, pp.91-98, N. Yamamoto (Ed.), JTA, Tokyo (in Japanese).

EVALUATION OF CONCRETE IN STRUCTURES WITH SMALL CORE SPECIMEN

Y. KASAI, N. YUASA and M. KUNIMOTO

Dept. of Architecture and Architectural Eng., College of Industrial Technology,
Nihon University, Japan

1-2-1 Izumi-cho, Narashino-shi, Chiba-ken, 275-8575, Japan

T. MANO

Japan Testing Center for Construction Materials

5-21-20 Inari-cho, Soka-shi, Saitama-ken, 340-0003, Japan

ABSTRACT

Methods of soundness test for concrete in structures by small core specimen have been proposed in many papers this paper deals with a boring method of small core specimen from structure, compressive strength test method and physical properties test of small core specimen etc. As a result, an evaluation test methods of concrete in structures with small core specimens is discussed.

KEY WORDS

Small cores specimen, Concrete in structure, Boring method of concrete core, Compressive strength test, Density test, Water absorption test.

INTRODUCTION

Many papers have been made to evaluate the soundness of concrete in structures with small core specimens of 20~50 mm in diameter.

These test methods possess following features compared to the method using core of 100~150 mm in diameter.

Advantages

- Reduction of the damage to structures.
- There are little restrictions in the selection of the test spots.
- Increase the number of test pieces.
- Ease of repair and low repair cost.

Disadvantages

- Special attention to the sampling (boring) spots.
- Small core specimens have a tendency of lack of homogeneity.
- The test results have a large variation, this defect could be solved by increasing number of specimens.

To solve the above-mentioned disadvantages, it is required to establish a "Standard method of test for small core specimen" e. g. boring core specimen and evaluation method of homogeneity etc.

In this paper, referencing the past literatures, a tentative method is presented regarding to the boring method of small core specimen, compressive strength test and other physical properties tests with small core specimen.

BORING METHOD OF SMALL DIAMETER CORE SPECIMEN

When boring core specimens, deterioration factors such as high temperature and excessive vibration should be avoided. Method of boring small specimens is as follows.

(1) Rotation speed of core bit and boring speed

The quality of core is affected by the rotation speed and boring speed of core drill. A systematic experimental research was done by Hiraga et al. [1] already on the effect of number of rotation per minute (e.g. rotation speed of core bit) and boring speed of specimen on the compressive strength of ϕ 100~200 mm core specimen. As a result, the following boring conditions are recommended, the speed of bit (number of rotations per minute \times length of circumference) about 600 m/min, boring speed of specimen 7.5 cm/min, maximum cutting torque 1.8 kg·m. Although the small specimen has longer circumference relative to the sectional area of specimen than ordinary specimen, hence the small specimen is influenced largely by boring rather than ordinary specimen.

In case of ϕ 50 mm specimen, speed of circumferences of drill will be 94-157 m/min, and to spread this test method to engineers a appropriate boring method of specimen will be needed that is to make boring speed slower and to decrease torque.

In the recent report [2], there are no significant differences in the strength of each small core specimens, when the number of rotation of core drill: 600, 1100, 1300 r.p.m. and boring speed are 3, 1.5, 1 cm/min.

From the results mentioned above, the number of rotation of drill 600-1000 r.p.m. and boring speed of 2 cm/min are recommended for boring the small core specimen..

(2) Diameter of core specimen

After the JIS 1107 (Method of obtaining and testing core and sawed beams of concrete), the diameter of core specimen should be three times larger than the maximum size of coarse aggregate, and not to be less than two times.

However, in another test, the following the cases are pointed out. In the estimation of cement concrete in concrete, the diameter of core specimen has been recommended to be 1.5 times larger than the maximum size of coarse aggregate [3, 4]. For the compressive strength test, the ratios of the diameter of core specimen to the maximum size of 20 mm coarse aggregate of 0.9 to 1.2 times [2, 5, 6] and 1.25 to 1.65 times [6] were examined in the several papers.

From these papers, the difference of compressive strength according to the diameter of specimen are available, though the concrete strength in structure can be estimated by increasing the number of specimens and applying correction factor. Although the more investigation is needed to the influence of diameter of core specimen to the compressive strength. Commercial size of core bit is 25, 29, 32, 40 and 52 mm in diameter, so actual the diameter of core will be 20, 23, 29, 34 and 46 mm because they are reduced diameters by the trickiness of bit.

(3) Age of sampling specimens

T. HIRAGA et al. [1] reported when the core specimen is bored after the age 28 day. There recognize few difference in the strength of concrete between the core specimen and the ordinary specimen, though sampled more younger age, the strength of core specimen is a few smaller than that of ordinary concrete specimen.

In the JIS A 1107, the boring age of core specimen is prescribed be after 14 day or more. Above mentioned paper [1], the boring age of specimen of lightweight aggregate concrete needs 14 day or more, and the ordinary concrete needs 28 day or more. In general, estimation of strength of concrete in structure should be done after the age of 28 day or more.

(4) Boring spot of specimens

When specimens are taken from horizontal members, e.g. floor slab and beam, the affects of bleeding is small. However from a vertical member, e.g. wall and column, the specimen is affected by bleeding, so when boring specimen from vertical member, it is better to boring from three spots, upper spot, middle spot and lower spot.

Fig.1 is the authors result, it is based on the relationship between the pore-size distribution of concrete and the compressive strength [8, 9]. The near-surface concrete has less strength than that of inner concrete, because the former is dried earlier than the latter.

Miura and et al. tested the hardness of mortar part of small concrete core specimen with a specific needle and converted it into the compressive strength as shown in Fig.2, which shows the damage of freeze and thaw effects on concrete [10].

The test result of the difference in compressive strength according to the placing direction of concrete is very few, so more tests are needed.

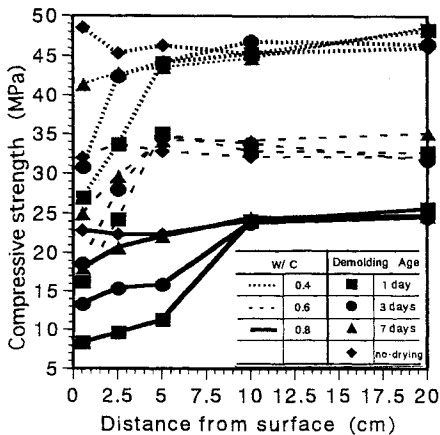


Fig. 1 Distribution of compressive strength estimated by porosity of concrete

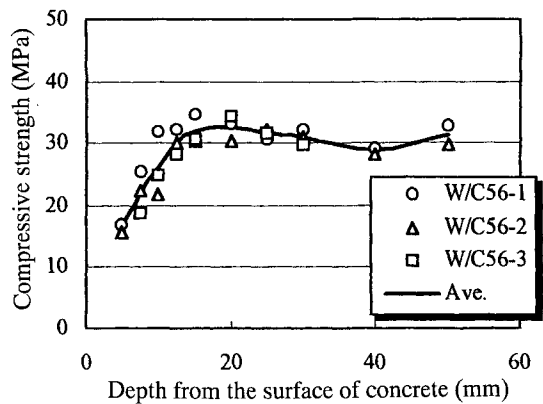


Fig. 2 Distribution of compressive strength of concrete after 180 cycles of freezing and thawing test

STRENGTH TEST OF CONCRETE IN STRUCTURES WITH SMALL CORE SPECIMEN

There are many sort of strength of test for the concrete in structures, compressive, tensile and so on. We will discuss the compressive strength test as the most important.

(1) Relation between the compressive strength of small core specimen and that of ordinary sized ($\phi 100 \times 200$ mm) core specimen

After the test of Tanigawa et al., strength of the small core specimen is a little larger than that of the ordinary sized core specimen ($\phi 100 \times 200$ mm). To make the strength difference of both size clear, the strength difference is better than the strength ratio (refer to Fig.3 [5]).

The author's recent tests indicate that the strength of small core specimens bored at the age of 28 day shows smaller strength than that of ordinary core specimen (Fig.4).

(2) Shape and size of specimen.

How should be the size of diameter of core specimen? From the results mentioned in references [4, 5, 6, 7], diameter of specimen 30 mm or so can be recommended. The length of specimen may be recommended to be twice as much as the diameter. For ordinary size specimen, when the ratio of

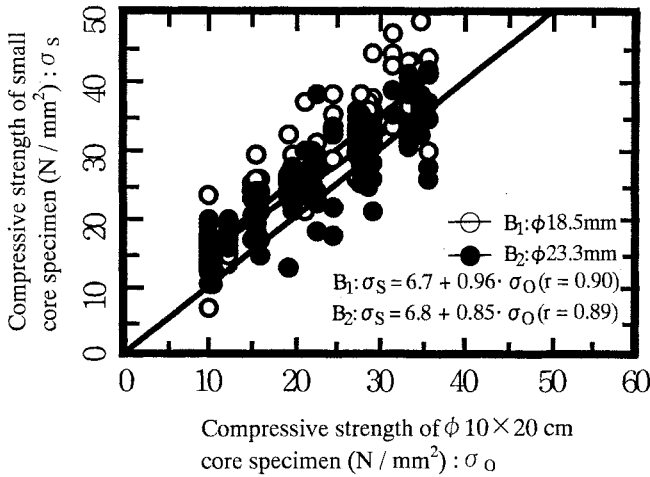


Fig. 3 Relation between the strength small core specimen and that of $\phi 10 \times 20$ cm core specimen

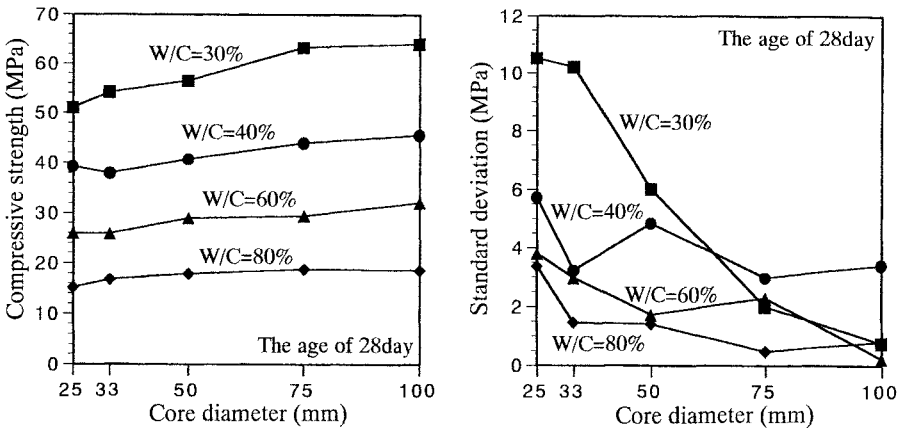


Fig. 4 Relations between the core diameter and compressive strength corresponding to water-cement ratio

height per diameter is varied, the correction factor is shown in Table 1 as designated in JIS A 1107. But, there are no particular correction factors for the small core specimen.

(3) Number of specimens

Wakabayashi and Tanigawa reported that the appropriate number of specimens are 3 or 4 at one spot [5], and the author's results implied a need of more pieces, for fear of breaking at boring and polishing of end plane and for improvement of confidence of compressive strength. The proper number of specimen will be investigated considering an engineering factors.

(4) Treatment of ends

There are several treatment methods for the ends e.g. no-treatment, polishing, capping (sulfur, gypsum and metal) and un-bond capping, the polishing and sulfur capping were tested.

Fig.5 and Fig.6 show the relation between the ends treatment and the average of compressive strength and variance of them by the authors [7].

Table 1 The ratio of height per diameter of ordinary sized-specimen (JIS A 1107)

Ratio of height per diameter h/d	Correction factor
2.00	1.00
1.75	0.98
1.50	0.96
1.25	0.93
1.00	0.89

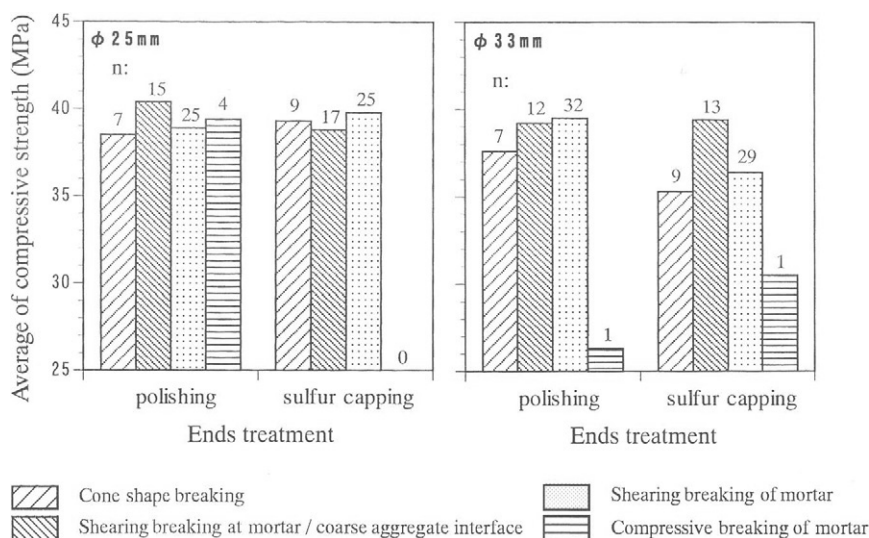


Fig. 5 Relations between the ends treatment and the breaking pattern and the average of compressive strength

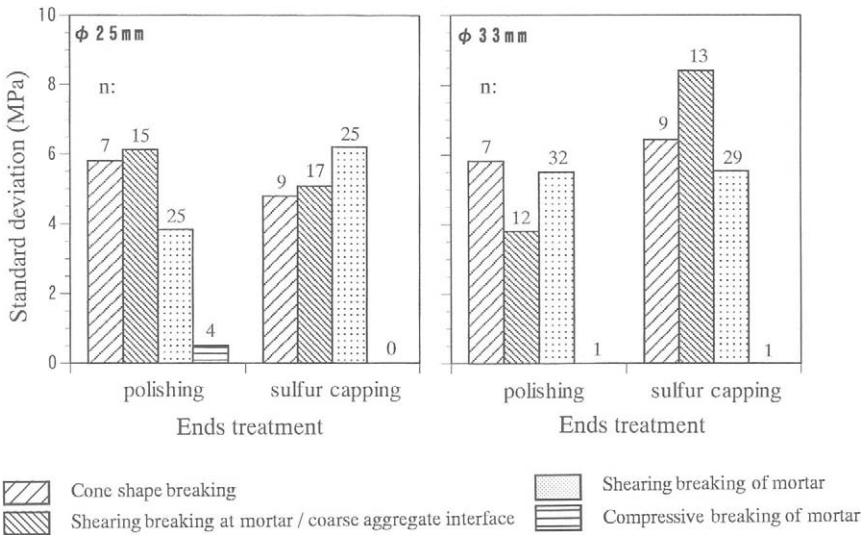


Fig. 6 Relations between the ends treatment and the breaking pattern and the standard deviation

In case of sulfur capping with 33 mm in diameter, the average strength is small about 2.0 MPa and variance is large, reason is not clear, the ends treatment should farther be investigated.

The ends should be perpendicular to the axial direction of specimen, as close as possible, but when the angle a little inclined, a correction factor may be necessary.

(5) Moisture content of core specimen at testing

It is widely known that the compressive strength becomes smaller when the specimen contains much moisture. In JIS A 1107, concrete specimens kept in water for 40 to 48 hours before test to control moisture content. For the small core specimen, the time of immersion in water will be shorter, but the time to reach equilibrium of moisture should be investigated.

(6) Loading method of compressive strength

Study on the following items has not always been made sufficiently

- Specification of spherical load bearing
- Loading control method (loading ratio control type or deformation control type)
- Loading speed

More investigation of the loading method for the small core specimen is needed.

(7) Breaking pattern of specimen

Tanigawa et al. classified the breaking pattern of small core specimen. Fig.7 shows the authors' results, Breaking pattern are classifies into ① Cone shape breaking, ② Shearing breaking of mortar, ③ Shearing breaking at mortar / coarse aggregate interface, ④ Compressive breaking of mortar. More investigation needed.

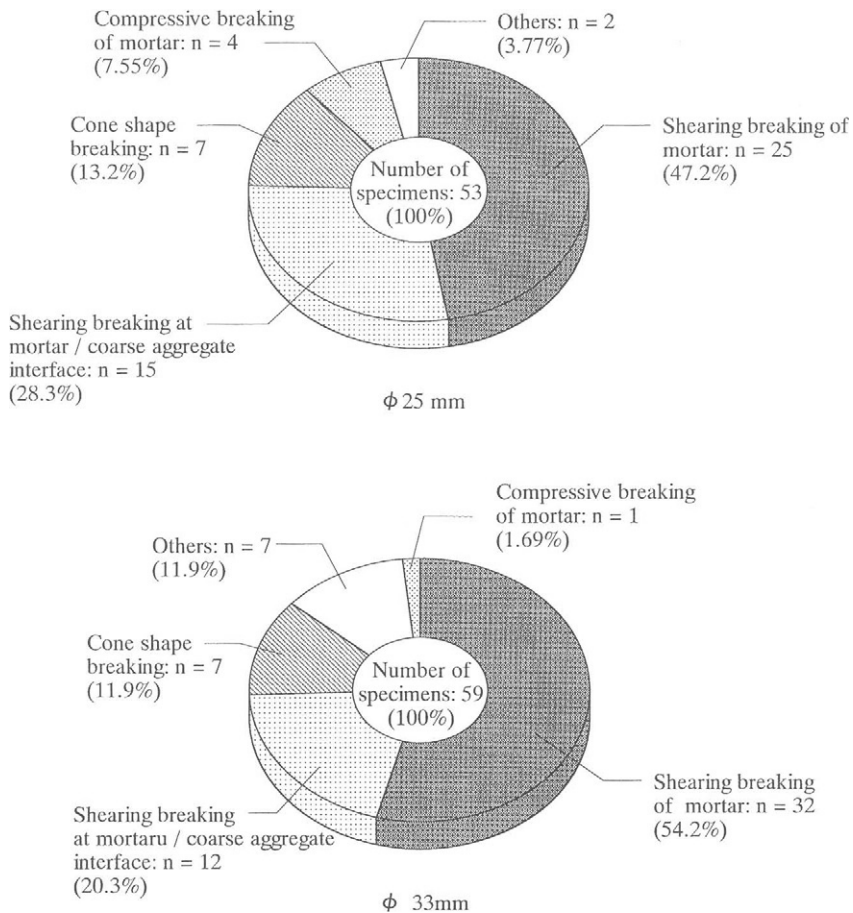


Fig. 7 Classification of breaking pattern and those occurrence ratio (Ends treatment polishing)

PHYSICAL TEST OF SMALL CORE SPECIMEN

The small core specimen has a tendency to vary the composition in each specimen by specimen. In the compressive strength test, distribution of coarse aggregate in a specimen affects the results significantly. Before preliminary tests, the physical tests should be done to evaluate the homogeneity of specimen.

(1) Density test

The density test may be done according to JIS A 1100 (Method of Test for Specific Gravity and Absorption of Coarse Aggregate). After the core specimen is immersed in water for 24 hours, the volume of the specimen can be measured by the Archimedes's methods. The saturated surface-dry density and dry density are then calculated by dry and saturated surface dry masse / volume of specimen.

In case of lightweight aggregate concrete, density (in wet condition) is varies according to the duration of immersion in water. As far as, the homogeneity of specimen is evaluated, even lightweight concrete can be tested in the same way applied to the ordinary concrete.

(2) Absorption test

The absorption can be tested according to JIS A 1110. When the drying temperature is too high, the bound water will be released and hair-clacks will be occurred, so the drying temperature shall be the range from 40 to 60°C, and drying duration should be determined by preliminary tests, it will be shorter because the size is very small.

The drying temperature and drying time should be determined according to the purpose of the subsequent test.

(3) Moisture content

It is possible to evaluate the homogeneity of core specimens by the moisture content immediately after boring.

In general, a core specimen with high amount of mortar shows high moisture content. When coarse aggregate is rich in a specimen, the moisture content becomes smaller.

(4) Distribution of coarse aggregate

When the composition of aggregate and that of cement are almost the same, the variation of the results of chemical analysis may be small, but the strength is much affected by position and distribution of coarse aggregate.

When a large size coarse aggregate is appeared at the side of a core specimen, the strength much influenced and decreased usually.

The distribution of coarse aggregate can be transferred to a tracing paper or firm [11]. Then the area of coarse aggregate can be determined with an image processing or so. From the ratio of area of aggregate, it will be evaluated a few characters of core specimen. The evaluation method of distribution of coarse aggregate needs more investigation.

(5) Appearance ratio of coarse aggregate and the maximum size of aggregate

The distribution of coarse aggregate affects the breaking pattern and strength, so the appearance ratio of coarse aggregate (ratio of the coarse aggregate length intersected by a test line) will be applicable as specified in JIS A 5411 (Pre-cast terrazzo).

In case of core specimen, a base line is set to a center of appearance of maximum aggregate in the axial direction and the six or eight lines are settled in equal distance on circumference of core side

and measure the length of coarse aggregate on the lines are calculated.

$$Ag = \frac{\Sigma(Ag_1, Ag_2, \dots Ag_8)}{(6 \text{ or } 8) \cdot h} \quad (1)$$

h: length of specimen

The appearance ratio of coarse aggregate (Ag) is can be given by follow.

Measurement of appearance ratio of coarse aggregate can not only evaluate the homogeneity of each specimen, but confirm the ratio of the maximum size of aggregate to the diameter of core.

OTHER TEST OF CONCRETE WITH SMALL CORE SPECIMEN

(1) Estimation test of mixture proportion

An estimation test of mixture proportion of concrete with small core specimen was presented by the authors [3]. The influence of core size and number of specimens are already studied.

(2) Chloride content test

The chloride content is tested with small core specimens in site will be done conveniently. The paper is presented in this symposium [12].

(3) Neutralization depth test

Neutralization depth test is usually done with small core specimen. Recently NDI established NDIS 3419-1999 (Method of test for neutralization depth of concrete with drilling powder). This paper is also presented in this symposium [13].

CLOSING REMARKS

The several test method with the small core specimens are refined with the past papers, there are many items to be investigate for the development of method of small core specimen. If the test using the small core specimen is once established, it can be a convenient and almost nondestructive test for concrete in structures.

REFERENCES

1. Hiraga, T., Kurabayashi, K., Aramaki, T. and Kemi, T. (1977). The Study about the Penetration Factors of Diamond Core Bit and Its Effect on the Concrete Strength, The Annual Technical Paper of the CAJ, pp.403-407.
2. Terada, K., Tanigawa, Y., Nakagome., A. and Sahara, H. (1998). Experimental Study on Estimation for Strength of Concrete in Structure with Small Size Cores (Part 1: Compressive Strength of Small Size Cores Sampled from Standard Cylinder Specimens), Annual Scientific Paper of TOKAI Chapter of the AIJ, pp.93-96.
3. Nakata, Y., Kasai, Y., Matsui, I. and Yuasa, N. (1994). Test Method for Cement Content of Hardened Concrete – An establishment of test method by sodium gluconate –, J. Struct. Constr. Eng., AIJ, No.460, pp.1-10.

4. Nakata, Y., Kasai, Y., Yokoyama, S. and Nishiyama, N. (1997). Effect of the Diameter of Concrete Core Samples on the Measurement of Unit Cement Content, *Journal of JSNDI*, Vol.46, No.7, pp.511-519.
5. Nakagome, A., Tanigawa, Y., Terada, K. and Sahara, H. (1998). Experimental Study on Estimation for Strength of Concrete in Structure with Small Size Cores (Part 2: Compressive Strength of Small Size Cores Sampled from Concrete Block Specimens), *Annual Scientific Paper of TOKAI Chapter of the AIJ*, pp.97-100.
6. Wakabayashi, S., Tanigawa, Y., Terada, K., Nakagome, A. and Sahara, H. (1998). Experimental Study on Estimation for Strength of Concrete in Structure with Small Size Cores (Part 3: Compressive Strength of Small Size Cores Sampled from Mortar Specimens and Concrete in Structure), *Annual Scientific Paper of TOKAI Chapter of the AIJ*, pp.101-104.
7. Kunimoto, M., Kasai, Y., Matsui, I. and Yuasa, N. (1999). Testing Method for Compressive Strength of Structural Concrete with Small Size Cores, *AIJ*, pp.709-710.
8. Yuasa, N., Kasai, Y. and Matsui, I. (1999). Inhomogeneous Distribution of Moisture Content and Porosity in Concrete, *Creating with Concrete, Concrete durability and repair technology*, pp.93-101.
9. Yuasa, N., Kasai, Y. and Matsui, I. (2000). Inhomogeneous distribution of compressive Strength from the Surface layer to Internal Parts of Concrete In Structure, *CANMET/ACI/JCI, Fifth International Conference on Durability of Concrete* (in press).
10. Miura, T., Iwaki, I. and Itabayashi, H. (1999). Study on Evaluating Deterioration of Concrete Structure using Needle Penetration Test, *Japan Society of Civil Engineers*, No.620, V-43, 1999.5, pp.245-255.
11. Kakimoto, N. (1996). Study on Characteristics of Hardened Concrete by Measurement of Core Texture, *JCA Proceedings of Cement & Concrete*, No.50, pp.428-433.
12. Yuasa, N. and Kasai, Yoshio. (2000). A Rapid Field Testing Method for Chloride Ion Content in Concrete Using Drilling Powder, *The 5th International Symposium on Non-Destructive Testing in Civil Engineering 2000*.
13. Kasai, Y., Yuasa, N., Mano, T. and Kunimoto, M. (2000). Evaluation of Concrete in Structure with Small Core Specimen, *The 5th International Symposium on Non-Destructive Testing in Civil Engineering 2000*.
14. John G.L. Munday and Ravindra K. Dhir (1984). Assessment of situ concrete quality by core testing, *CANMET/ACI, International Conference on In Situ / Non-Destructive Testing of Concrete*, SP-82-19, pp.393-410.

When we completely made this paper, John G.L. et al.'s paper is find out, this paper is very useful for core test over 50 mm in diameter, so we introduce the paper [14].

QUANTITATIVE DIAGNOSIS OF REINFORCED CONCRETE STRUCTURES BY AE-SIGMA ANALYSIS

M SHIGEISHI[†], D YUKAWA[‡] and M OHTSU[†]

[†] *Department of Civil Engineering and Architecture, Kumamoto University,
2-39-1 Kurokami, Kumamoto 860-8555, Japan*

[‡] *Miyazaki Public Works Office, Miyazaki Prefectural Government,
1-9-10 Tachibana-dori-higashi, Miyazaki 880-0805, Japan*

ABSTRACT

The waveform analysis of acoustic emission (AE), SIGMA (Simplified Green's functions for Moment tensor Analysis) is applied to estimated damaged reinforced concrete (RC) members due to corrosion. AE waves are detected from RC members under cyclic loading. The reinforcing bars of RC members are corroded by an accelerated corrosion test. Crack locations and orientations are determined by SIGMA. To remove the noise from AE waves and to pick up the first motions automatically, the auto-regressive (AR) model is studied. Further, an applicability of the wavelet transform is investigated.

KEYWORDS

Acoustic emission, reinforced concrete, corrosion, crack, waveform analysis, moment tensor, noise reduction, auto-regressive model, wavelet

INTRODUCTION

The phenomenon of acoustic emission (AE) is the propagation of elastic waves generated from a source, which is a micro motion caused by rapid dislocation of mass in an elastic material. The most typical AE source is the release of internal energy due to propagation of an existing crack. In addition, contact of the faces and friction at the existing crack surfaces are regarded as sources of AE. Thus, AE behaviour, activity and waveforms contain data on source mechanisms and the conditions of the medium during propagation. Accordingly, it is expected that the existence and degree of damage can be evaluated using AE measurement and analysis.

The AE technique enables real-time and comprehensive monitoring of structures without interfering with their service. In addition, the behaviour of structure can be observed under dynamic loading. In view of these advantages, the AE technique has been actively developed to diagnose condition and behaviour in the field of civil engineering [1].

In this study, AE activity in reinforced concrete (RC) beams, some undamaged and some damaged by electrolytic corrosion, were subjected to repeated-static bending and monitored. The experimental application of moment tensor analysis was attempted on these real AE waveforms to identify and classify the micro cracks occurring in the cyclic-dynamic bending tests of the RC beams. The result showed the onset of damage with the progress of fatigue quite clearly. Moreover, to remove the noise from AE waves and to pick up the first motions automatically, the auto-regressive (AR) model is studied. An applicability of the wavelet transform is also investigated.

RC MEMBER BENDING TEST DETAILS

RC Beam Specimens

The configuration of test specimens is shown in Figure 1. These were designed to bear 44.1 kN static bending in the tests. The specimen had a square section of 100 mm and a length of 400 mm. Type A contained a single deformed steel bar, type D10, which had a diameter of 10 mm approximately. A normal steel bar of 10 mm diameter was embedded in the Type B specimen. Each bar was arranged at a covering depth of 20 mm. Air entrained concrete was used and the compressive strength of concrete aged 28 days was 31.4 MPa.

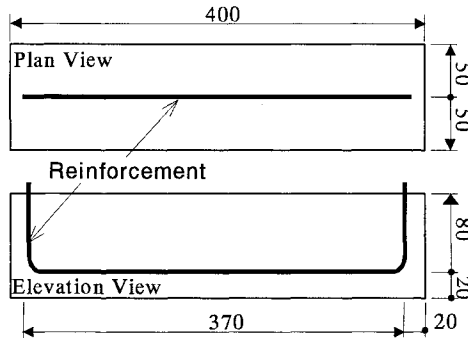


Fig. 1. Configuration of RC beam specimen

A damaged RC beam specimen (Type A') was created using a galvanic corrosion by introducing a 30 mV direct current for 6 days. This electrolytic corrosion of the reinforcement in the Type A' beam caused a crack at the center of the bottom surface in parallel with the reinforcement direction.

Bending Test and AE Measurement

The experimental set-up of the four-pointed bending test is shown in Figure 2. For comparison the AE activities between the non-damaged (Type A) and damaged (Type A'), loading and unloading was statically repeated five times whilst increasing the peak load to 10, 20, 30, 40 kN and then yield.

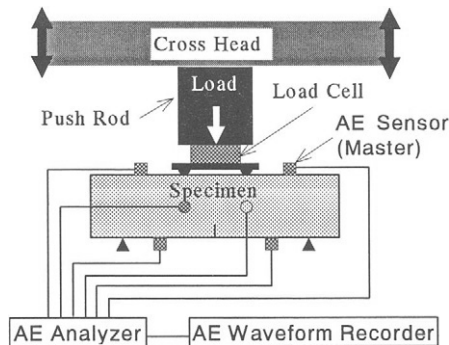


Fig. 2. Experimental set-up of bending test

For the observation of the fatigue process under bending, cyclic-dynamic loading from 0.98 kN to 22.05 kN was automatically applied one hundred times to another Type A (deformed reinforcement) and Type B (normal round reinforcement) beam. The loading speed of the ram was set to 10 mm/s.

AE BEHAVIOUR OF RC BEAM UNDER BENDING

Figure 3 shows the relationship between cumulative number of AE events and bending load in a non-damaged RC beam (Type A), together with the load-displacement curve. Figure 4 like Figure 3 shows the AE and displacement behaviour under bending in a damaged RC beam (Type A'), which has corroded.

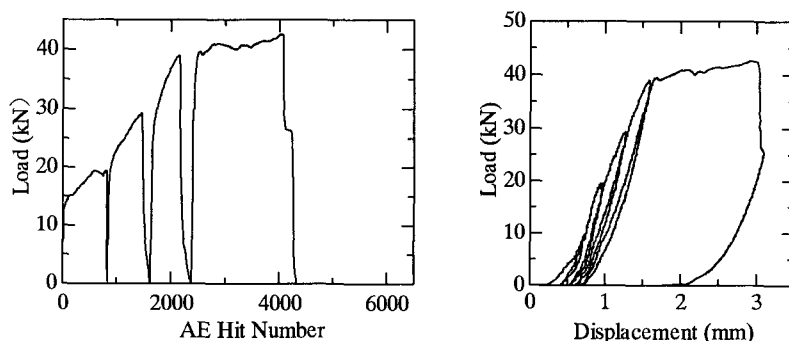


Fig. 3. Displacement (left) and AE (right) behaviour in a non-damaged RC beam

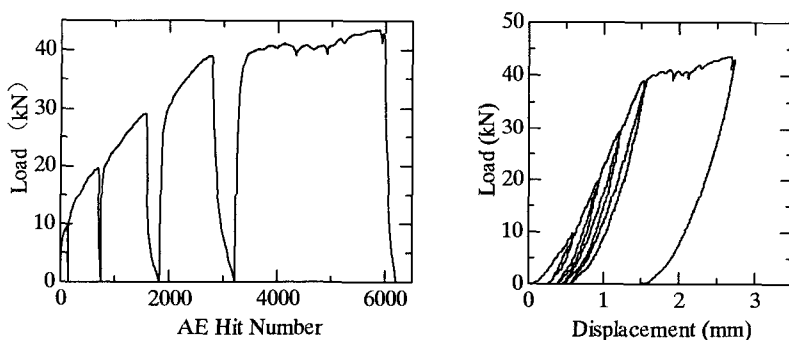


Fig. 4. Displacement (left) and AE (right) behaviour in a damaged RC beam

There is no significant difference in yield load and bending stiffness except for early tangent modulus until second time loading between Type A and Type A'. The difference in displacement between these two emerged in early AE behaviour. In the case of Type A, even if first loading was applied up to 10 kN and removed, the AE event was hardly recognized. The occurrence of the AE was noted over 10 kN load at the second bending. Otherwise, in the case of Type A', AE events increased as the load increased.

FATIGUE PROCESS OBSERVATION USING AE SOURCE INVERSION

AE-SiGMA Analysis Procedure

The AE wave is emitted in a variety of radiations patterns [2] depending upon micro cracking at its location. To identify the AE source kinematics [3], that is location and crack-type, an AE inversion method of quantitative AE waveform analysis was proposed [4].

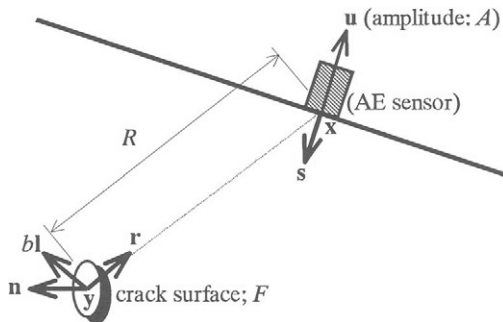


Fig. 5. Micro crack model and AE observation

Crack kinematics at the point \$\mathbf{y}\$ is modelled using the crack motion vector \$\mathbf{b}(\mathbf{y}, t)\$ and the unit vector \$\mathbf{n}\$ normal to the crack surface \$F\$ as shown in Fig. 5. The vector \$\mathbf{b}\$ is known as Burgers vector and represented as \$b(\mathbf{y})\mathbf{l}S(t)\$, where \$b(\mathbf{y})\$ is the magnitude of crack displacement, \$\mathbf{l}\$ is the direction unit vector of crack motion, and \$S(t)\$ is the source time function of cracking. The integration on the crack surface \$F\$ is expressed using the second-tensor \$\mathbf{m}\$ on the crack kinematics, which is moment tensor:

$$\int_F C_{pqkl} [b(\mathbf{y})\mathbf{l}_k S(t)] n_i dS = [C_{pqkl} l_k n_i] \Delta V S(t) = m_{pq} S(t), \tag{1}$$

where \$C_{pqkl}\$ is the tensor of elastic constants and \$\Delta V\$ is the crack volume which is product of the magnitude \$b(\mathbf{y})\$ and the crack area \$\Delta F\$ or \$\Delta V = b(\mathbf{y}) \cdot \Delta F\$.

In an isotropic material, the moment tensor is derived,

$$m_{pq} = [C_{pqkl} l_k n_i] \Delta V = [\lambda l_k n_k \delta_{pq} + \mu l_p n_q + \mu l_q n_p] \Delta V, \tag{2}$$

where \$\lambda\$ and \$\mu\$ are Lamé constants, and \$\delta\$ is Kronecker’s delta symbol.

Referring to the generalised theory [3] of AE based on the elasto-dynamic field on the boundary element method (BEM), the elastic displacement \$\mathbf{u}(\mathbf{x}, t)\$ due to the crack motion \$\mathbf{b}(\mathbf{y}, t)\$ represents AE wave,

$$u_i(\mathbf{x}, t) = G_{ip,q}(\mathbf{x}, \mathbf{y}, t) m_{pq} * S(t). \tag{3}$$

Moreover, the amplitude $A(\mathbf{x})$ of the first P-wave portion at observation point \mathbf{x} in the far field is simply represented,

$$A(\mathbf{x}) = C_s \text{Ref}(\mathbf{s}, \mathbf{r}) \gamma_p m_{pq} \gamma_q / R, \quad (4)$$

where C_s is coefficient containing the relative sensor sensitivity calibration. R is the distance between the source and the sensor. $\text{Ref}(\mathbf{s}, \mathbf{r})$ is the reflection coefficient associated with the sensor sensitivity directions \mathbf{s} and direction of wave incidence \mathbf{r} from the source. When the source location and the amplitudes of the first motion are known, the independent six components of the moment tensor can be determined by solving the simultaneous equations of Equation (4) at each observation point.

Applying eigenvalue analysis to the determined moment tensor, the crack kinematics can be obtained. A quantitative classification of the crack types into shear mode, tensile mode and mixed mode is developed. The eigenvalues of the moment tensor are decomposed into a shear component X , a deviatoric component (CLVD) Y , and a hydrostatic component Z [5]. Three eigenvalues are normalised and uniquely decomposed into three ratios X , Y , and Z ,

$$\begin{aligned} \text{(the maximum eigenvalue } e_2 / \text{the maximum } e_1) \quad 1.0 &= X + Y + Z, \\ \text{the intermediate eigenvalue } e_2 / \text{the maximum } e_1 &= 0 - 0.5Y + Z, \\ \text{the minimum eigenvalue } e_3 / \text{the maximum } e_1 &= -X - 0.5Y + Z. \end{aligned} \quad (5)$$

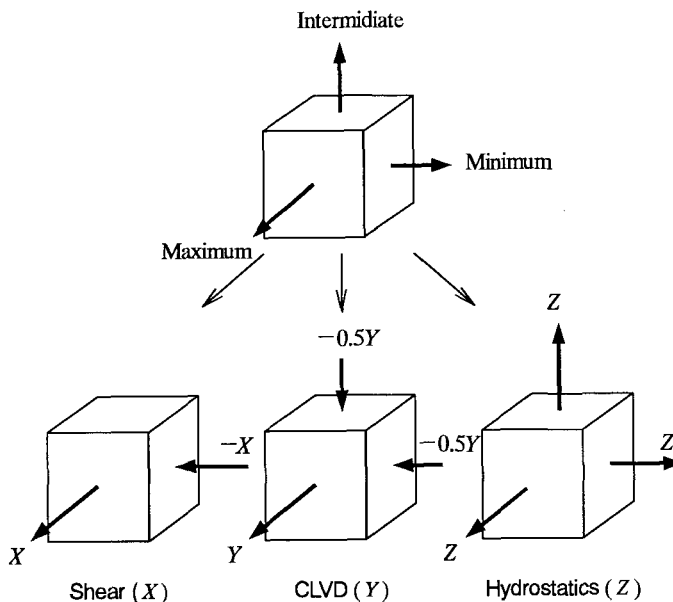


Fig. 6. Eigenvalue decomposition of the moment tensor

From the unit eigenvectors $\mathbf{e}_1 = \mathbf{l} + \mathbf{n}$, $\mathbf{e}_2 = \mathbf{l} \times \mathbf{n}$ and $\mathbf{e}_3 = \mathbf{l} - \mathbf{n}$ corresponding to three eigenvectors, the vectors \mathbf{l} and \mathbf{n} can be recovered from the following relations,

$$\begin{aligned} \mathbf{l} &= \sqrt{2 + 2l_k n_k} \cdot \mathbf{e}_1 + \sqrt{2 - 2l_k n_k} \cdot \mathbf{e}_3, \\ \mathbf{n} &= \sqrt{2 + 2l_k n_k} \cdot \mathbf{e}_1 - \sqrt{2 - 2l_k n_k} \cdot \mathbf{e}_3. \end{aligned} \tag{6}$$

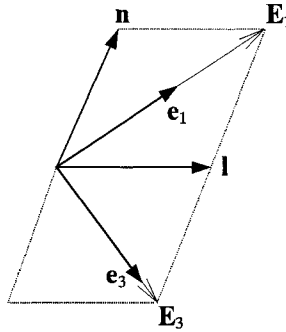


Fig. 7. Crack orientations and eigen vectors of moment tensor

AE Source Inversion on Fatigue Tests of RC Beam

Figure 8 shows the implications of AE source locations and crack types in a concrete beam reinforced by a single deformed steel bar (Type A) under cyclic loading. Figure 9 shows the results in a RC beam reinforced by a normal bar (Type B). In these figures, the arrow symbols (\leftrightarrow) indicate the micro-cracks resulting from tensile motion and its tensile directions. Otherwise, the cross symbols (\times) indicate the micro shear cracking. Propagation of the visible cracks on the surface are also showed by the dotted lines in these figures.

In the case of Type A, micro-cracks are generated by compressive stress at the upper part at the 15th loading. Some micro-cracks created near the reinforcement indicate either the loss of bond or the slipping off. Most micro-cracks are generated along the visible cracks after the 15th loading. In the case of Type B, before the 16th loading, the propagation of the visible cracks is hardly observed. However, some of micro-cracks are scattered across a wide area from the visible cracks. This means that the fracture process zone is spreading out gradually. At the final stage, the area, where the micro-cracks are generated, spreads out further. Thus, it was found that the shape of the deformed bar contributed significantly in preventing damage.

From the above results, the difference in the damage processes resulting from the shape of reinforcement is clearly observed. In Beam type A, the visible cracks propagate only a little and a few micro-cracks are produced at the tip of the notch. In contrast, the visible cracks in Type B grow and almost reach the top of the specimen. The micro-cracks have a wide distribution around the visible cracks. Thus it was confirmed that Type B was already severely damaged at this early stage.

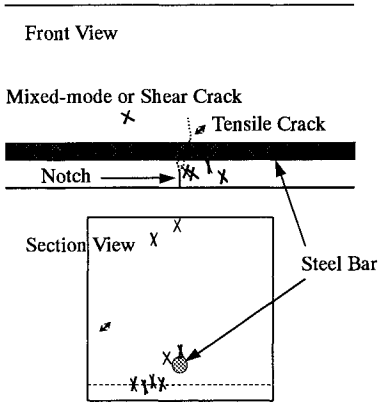


Figure 8a Results of Type A at 1st loading

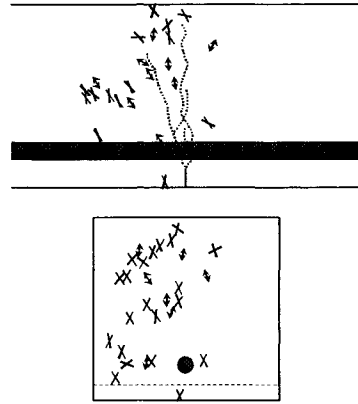


Figure 9a Results of Type B at 1st loading

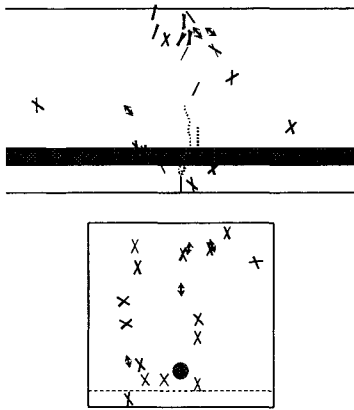


Figure 8b Results of Type A at 15th loading

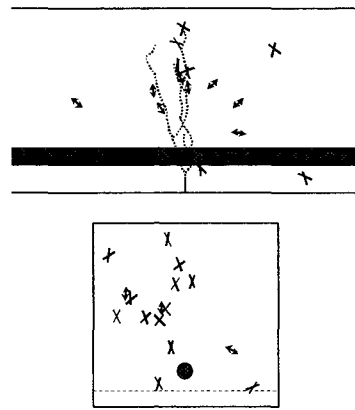


Figure 9b Results of Type B at 15th loading

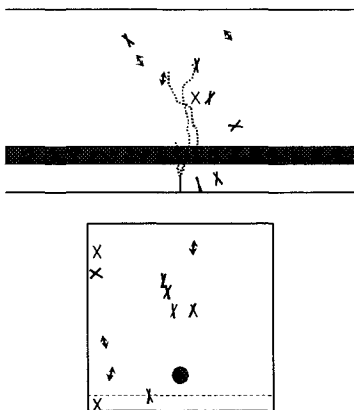


Figure 8c Results of Type A at 100th loading

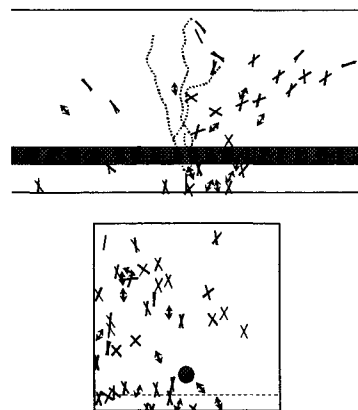


Figure 9c Results of Type B at 100th loading

AE SIGNAL PROCESSING FOR AE-SIGMA ANALYSIS

Noise Reduction by Numerical Calculation

In precise AE waveform analysis, practical problems on noise and start point of true signal must be discussed incessantly. Figure 10 shows the typical waveform data contains nose and AE signal that was recorded in the testing. In also AE-SiGMA, it is necessary and important to pick up the arrival point of AE signal from the record.

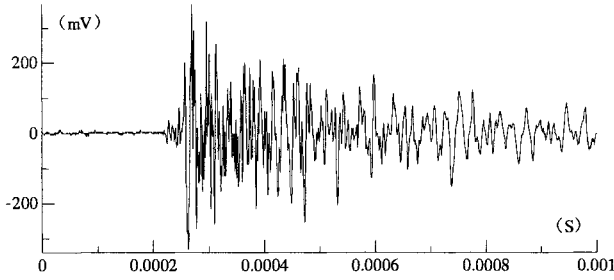


Fig. 10. Example of AE signal record

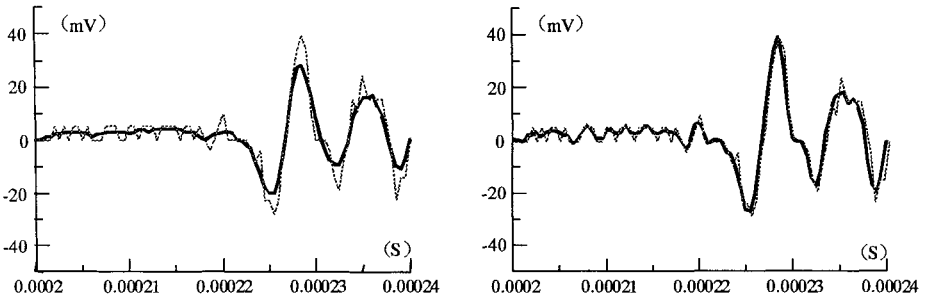


Fig. 11. Smoothing by method of moving averages (left) and polynomial approximation (right)

Figure 11 shows the initial part of original waveform (gray line) and the results of noise reduction using the method of moving averages (left) and polynomial approximation (right) setting the number of smoothing points as 5. In case of the method of moving averages, the noise is almost reduced and the arrival point of AE signal can be identified. However, strong waveform distortion is recognised. In contrast, the polynomial approximation inhibits the waveform distortion but the nose reduction effect is decreased down slightly.

Application of AR Model to Signal Detection

Assuming the signal data is in stationary state before and after the arrival of AE signal, a dividing method of time series data using auto-regressive (AR) model. Fitting the AR model to a time series data: $x_1, x_2, \dots, x_i, \dots, x_{n-1}, x_n$; an arbitrary term x_{i+1} is expressed as follow by the backward date: $x_1, x_2, \dots, x_{i-1}, x_i$;

$$x_i = a_1x_i + a_2x_{i-1} + \dots + a_{i-1}x_2 + a_i x_1 + \varepsilon_i. \tag{7}$$

Here, the regressive process order is i . $a_1, a_2, \dots, a_{i-1}, a_i$ are regressive coefficients and ε_i is the distraction term on a normal distribution base on average value 0. Akaike's Information Criteria (AIC) [6] can be used as a goodness-of-fit index of AE model. When the regressive order is i , AIC value is defined as

$$AIC = n (\log \sigma^2 + \log 2\pi + 1) + 2(i + 2), \quad (8)$$

where σ^2 is the error variance on fitting of AR model to the data, n is the number of data. When the AIC value approaches to minimum, it is regarded as that the AR model fits at most goodness. To detect the AE signal arrival point from the record, an AR model application is considered. First, divide the waveform data: $x_1, x_2, \dots, x_k, \dots, x_{n-1}, x_n$; to two parts: x_1, x_2, \dots, x_k and $x_{k+1}, x_{k+2}, \dots, x_n$; at a proper point k . Next, calculate a goodness-of-fit index defined as

$$AIC_1 + AIC_2 = k \log \sigma_1^2 + (n - k) \log \sigma_2^2 + n (\log 2\pi + 1) + 2(n + 4), \quad (9)$$

where σ_1^2 and σ_2^2 are the error variance at the backward part and the forward part respectively. Subsequently, seek the point where the value of the equation (9) minimises varying the divide point to $k+1$ (or $k-1$).

Application of Discrete Wavelet Analysis

Nowadays, wavelet analysis [7] extremely becomes popular in engineering field. A (mother-) 'wavelet' is a short-term waveform as a unit for sampling from a continuous waveform data. In this study, a mother wavelet corresponding to B-spline function of 4-rank, which is shown in the figure 12, is used and the discrete wavelet transformation is carried out. The discrete wavelet transformation of a function $f(x)$ using a mother wavelet function $\psi(x)$ and inverse are defined as follows.

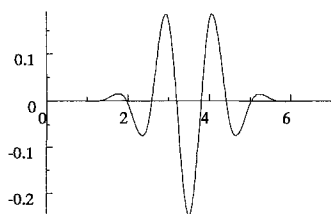


Fig. 12. A mother wavelet (4-ranked B-spline)

$$d_k^{(j)} = 2^j \int_{-\infty}^{\infty} \overline{\psi(2^j x - k)} f(x) dx \quad (10)$$

$$f(x) \sim \sum_j \sum_k d_k^{(j)} \psi(2^j x - k) \quad (11)$$

The results of wavelet transformation are shown in the figure 13. From the result on $j = -5$, AE signal arrival point is clearly noted as an abnormality. Further, the results on $j = -1$ and $j = -2$ show the noise components of original waveform. From these results, wavelet analysis shares the advantage of possible to reduce the noise and detect the AE signal arrival simultaneously.

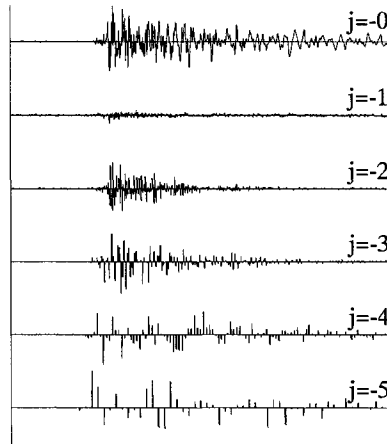


Fig. 13. Result of wavelet analysis

CONCLUSIONS

AE measurement experiments and analysis were performed under controlled laboratory. AE activity in undamaged and electrolytic corrosion damaged RC beams was observed under repeated bending. Different AE behaviour was noted between them. In order to monitor the fatigue process, moment tensor analysis was performed in the RC beams under the cyclic-dynamic bending. The result clearly showed the clustering and distribution of micro cracks depending upon the progress of fatigue. The influence of deformed bar against the fatigue was confirmed. To remove the noise from AE waves and to pick up the first motions automatically, the auto-regressive (AR) model is studied. In case of the method of moving averages, the noise is almost reduced and strong waveform distortion is recognised. In contrast, the polynomial approximation inhibits the waveform distortion but the noise reduction effect is decreased down. For detecting of AE signal arrival, an incremental calculation to seek arrival point using Akaike's Information Criteria based on AR modelling is considered. Further, an applicability of the wavelet transform is investigated for noise reduction and AE signal arrival detection.

REFERENCES

1. Ohtsu, M. (1995) The History and Development of Acoustic Emission in Concrete Engineering. In: *Concrete Library of the Japan Society for Civil Engineers*, **25**.
2. Ohtsu, M. and Ono, K. (1984). In: *Journal of Acoustic Emission* **3**, 1, pp. 124-133.
3. Ohtsu, M. (1987). In: *Material Evaluation* **45**, 9, pp. 1070-1075.
4. Ohtsu, M. and Shigeishi, M. (1991). In: *Magazine of Concrete Res.* **43**, 155, pp. 127-134.
5. Knopoff, L. and Randall, M. J. (1970). In: *Journal of Geophysical Res.* **75**, pp. 4975-4963.
6. Kitagawa, G. and Akaike, H. (1978). In: *Annual Report of the Inst. of the Statistics and Mathematics*, **30**, B, pp. 351- 363.
7. Newland, E. D. (1993) *An Introduction to Random Vibrations, Spectral and Wavelet Analysis*, 3rd Edition, Addison Wesley Longman.

EVALUATION OF FATIGUE DAMAGE IN REINFORCED CONCRETE SLAB BY ACOUSTIC EMISSION

S. YUYAMA and Z-W. LI

Nippon Physical Acoustics Ltd.

8F Okamoto LK Bldg., 2-17-10, Higashi, Shibuya-ku, Tokyo 150-0011 Japan

M. YOSHIZAWA and T. TOMOKIYO

Technology Center of Metropolitan Expressway

3-10-11, Toranomon, Minato-ku, Tokyo 105-0001 Japan

T. UOMOTO

Center for Collaborative Research, University of Tokyo

7-22-1, Roppongi, Minato-ku, Tokyo 106-0032 Japan

ABSTRACT

Applicability of acoustic emission (AE) technique for evaluation of fatigue damage in reinforced concrete (RC) slabs under cyclic loadings is studied in both laboratory and a structure in service. The fundamental test performed in laboratory shows that cracking process can be practically monitored by the measurement of AE signals. Analysis of relationship between loading phase and AE activity indicates that the final stages of the fracture process can be evaluated by detecting AE signals generated near the minimum loading phase. Comparison of the result from the structure and that from the laboratory specimen demonstrates that AE energy can be an effective parameter for evaluation of fatigue damage in RC slabs in service.

KEYWORDS

Acoustic emission, non-destructive evaluation, fatigue loading, reinforced concrete slab

INTRODUCTION

In recent years the deterioration and cracking of concrete structures such as bridges and buildings has been a significant problem. Proper techniques for the inspection of damaged structures are important in making rational decisions regarding rehabilitation, repair or replacement. Thus, the development of techniques to evaluate degradation of concrete

structures in long-term service has been one of the most important issues for an effective maintenance program.

Acoustic emission (AE) is a term named for elastic waves generated by sudden changes which occur locally in materials due to deformation, cracking, transformation and so forth. At present, this term is used as an inspection technique for non-destructive evaluation. Since AE is very sensitive to the initiation and the growth of cracks in the materials and structures, it has been widely utilized for materials studies in laboratory. In concrete engineering, the applicability has been intensively studied in both materials [1] and structures [2 - 5].

In the present study, AE is monitored from the initial loading to the final failure under fatigue loadings in a laboratory test using a model reinforced concrete (RC) slab. AE monitoring is also carried out in a structure (RC slabs) under active loads due to traffic in service. Applicability of AE technique for evaluation of fatigue damage is discussed by comparing the results obtained from the structure and those from the laboratory test.

TEST PROCEDURE

Laboratory test

Reinforced concrete slabs shown in Fig. 1 were prepared for model tests in laboratory. Dimensions of the specimens are 2,000 mm in width, 1,500 mm in length and 160 mm in center thickness, respectively. Mix proportion and mechanical properties of the concrete are given in Table 1. The specimens were subjected to sine-wave compressive cyclic loadings at the center with a frequency of 0.7 Hz by a servo-type fatigue machine. The tests were performed under seven different conditions.

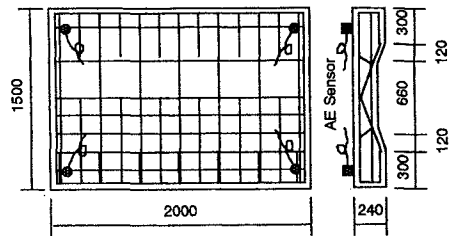


Fig. 1 RC model slab for laboratory test.

The result obtained in the case where water was filled on the top side of the specimen is reported in this paper. The maximum load of the cyclic loadings was increased from 150 kN to 200 kN, 225 kN, 250 kN, and 270 kN in a step-wise manner. Photo 1 demonstrates how the test was performed.

Table 1 Mix proportion and mechanical properties of the concrete.

W/C (%)	s/a (%)	Weight of Unit Volume (kg/m ³)				Maximum Size (mm)	Slump (cm)	Air Content (%)	Compressive Strength (MPa)	Static Modulus of Elasticity (GPa)	Dynamic Modulus of Elasticity (GPa)
		W	C	S	G						
64.0	48.5	165	258	892	972	25	7.5	4.5	39.3	27.5	34.3

Structure

AE measurement was conducted in two RC slabs (A and B) which had been in service for about 27 years. Figure 2 schematically illustrates the structure and the location of AE sensors. The dimensions of the slabs are 4.8 m in length, 3.4 m in width and 180 mm in thickness. Asphalt pavement of 60 mm in thickness is placed on the surface of the slabs. A median strip covers almost half part of the upper side of the slabs. AE signals were monitored continuously for two hours under active fatigue loads in service.

AE instrumentation

PAC MISTRAS 4 channel AE system was used for the test. AE signals detected by PAC R6I (60 kHz resonant) integral-type sensors were input into the MISTRAS system for digital signal processing. AE features such as hit, count, energy and amplitude were extracted and waveform analysis as well as frequency analysis was performed in necessary cases. Four AE sensors were attached to the specimen at each corner in laboratory test as shown in Fig. 1, while two sensors were attached to each slab in service as indicated in Fig. 2.

RESULTS

Laboratory test

Cracking process and AE behavior. Shown in Fig. 3 is a relationship between number of loading cycles and crack density defined as crack length per 1 square meter. Four stages are clearly observed in the cracking process. Stage I corresponds to the region in N

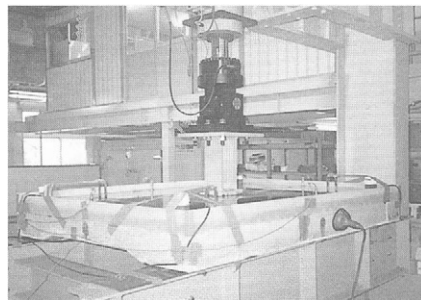


Photo 1 The test setup.

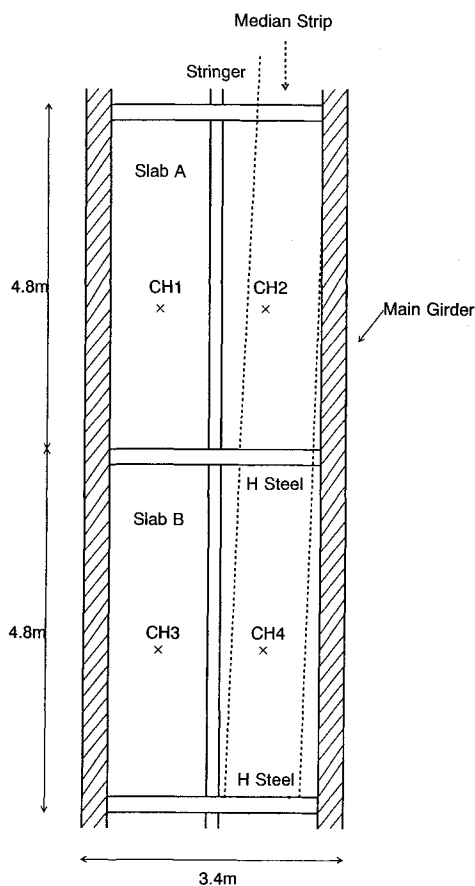


Fig. 2 Schematic illustration of the tested structure.

(number of loading cycles) = $0 - 10^5$, where early cracks initiate and grow very rapidly. Stage II corresponds to the region in $N = 10^5 - 4.0 \times 10^5$, where no significant crack growth is observed, showing a stable state. Stage III corresponds to the region in $N = 4.0 - 7.9 \times 10^5$, where the crack density increases almost linearly at a constant rate. Stage IV gives the region after $N = 7.9 \times 10^5$, where the crack density increases rapidly to the final failure.

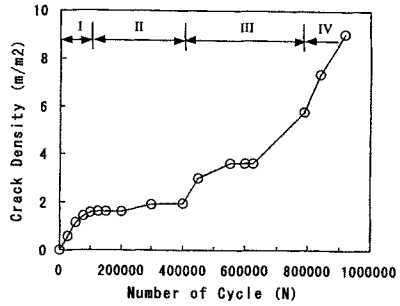


Fig. 3 Relationship between number of cycles and crack density.

Shown in Fig. 4 are histories of AE hit rate, amplitude and the maximum load as a function of number of loading cycles. High AE activity is observed in the early time of Stage I due to the initiation of early cracks. However, it diminishes rapidly and then increases again as the crack density increases. In stage II, the activity slowly increases showing some instability, while it becomes stable in Stage III. In Stage IV, it starts to increase rapidly from $N = 8.8 \times 10^5$, i.e. just before the final failure ($N = 9.17 \times 10^5$). It is thus shown that the process of the final failure (the transition from Stage III to Stage IV) under fatigue loadings can be predicted and evaluated by monitoring AE signals. The initiation of the final failure corresponds to the time when the AE activity increases rapidly from the stable state in Stage IV.

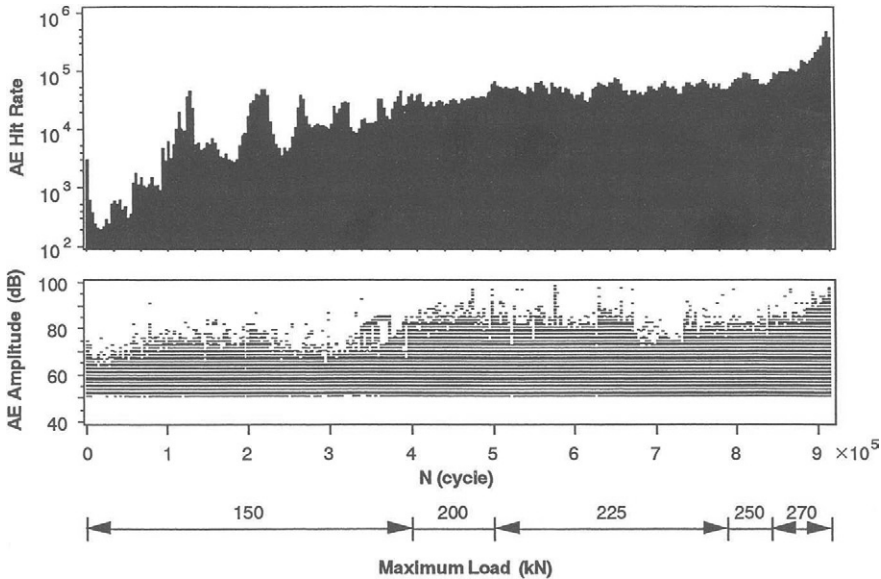


Fig. 4 Histories of AE hit rate, amplitude and the maximum load.

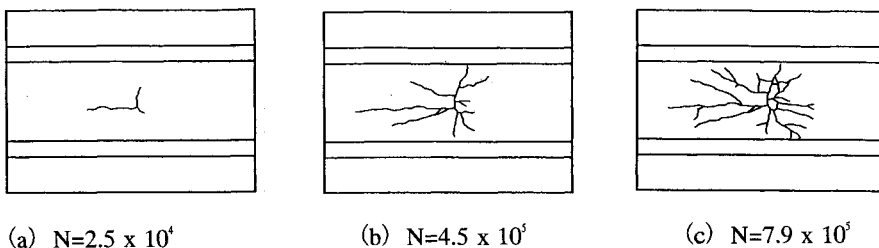


Fig. 5 Visual observations of surface cracks.

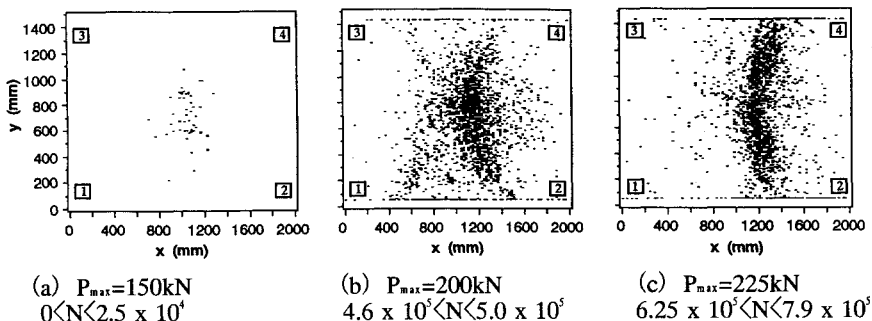


Fig. 6 AE source location.

AE source location. The results of visual observation of the surface cracks at $N = 2.5 \times 10^4$, 4.5×10^5 and 7.9×10^5 are given in (a), (b) and (c) of Fig. 5, respectively. The results of AE source location obtained during $0 - 2.5 \times 10^4$, $4.6 - 5.0 \times 10^5$ and $6.25 - 7.9 \times 10^5$ are exhibited in Fig. 6. Comparison of Fig. 5 and Fig. 6 shows that the locations of the surface cracks roughly correspond to the area covered by AE event locations. Therefore, cracking area can be roughly evaluated by AE source location analysis.

Relationship between loading phase and AE activity. Numerous studies have been made of relationship between cracking process and AE behavior in metallic and composite materials [6, 7]. Figure 7 schematically illustrates relationship between loading phase and AE activity,

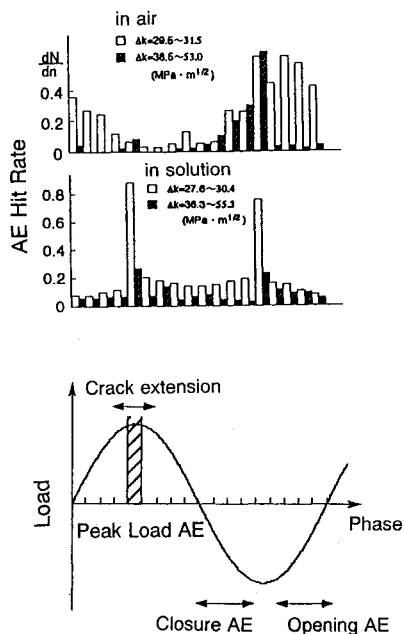


Fig. 7 Relationship between loading phase and AE activity.

obtained from these results. It has been reported that the AE activity detected near the maximum load is mainly due to main crack extension and called Peak Load AE. Meanwhile the AE activities observed during unloading and re-loading are considered to be from mechanical sources such as frictions due to closure and opening of the crack faces and called Closure and Opening AE, respectively.

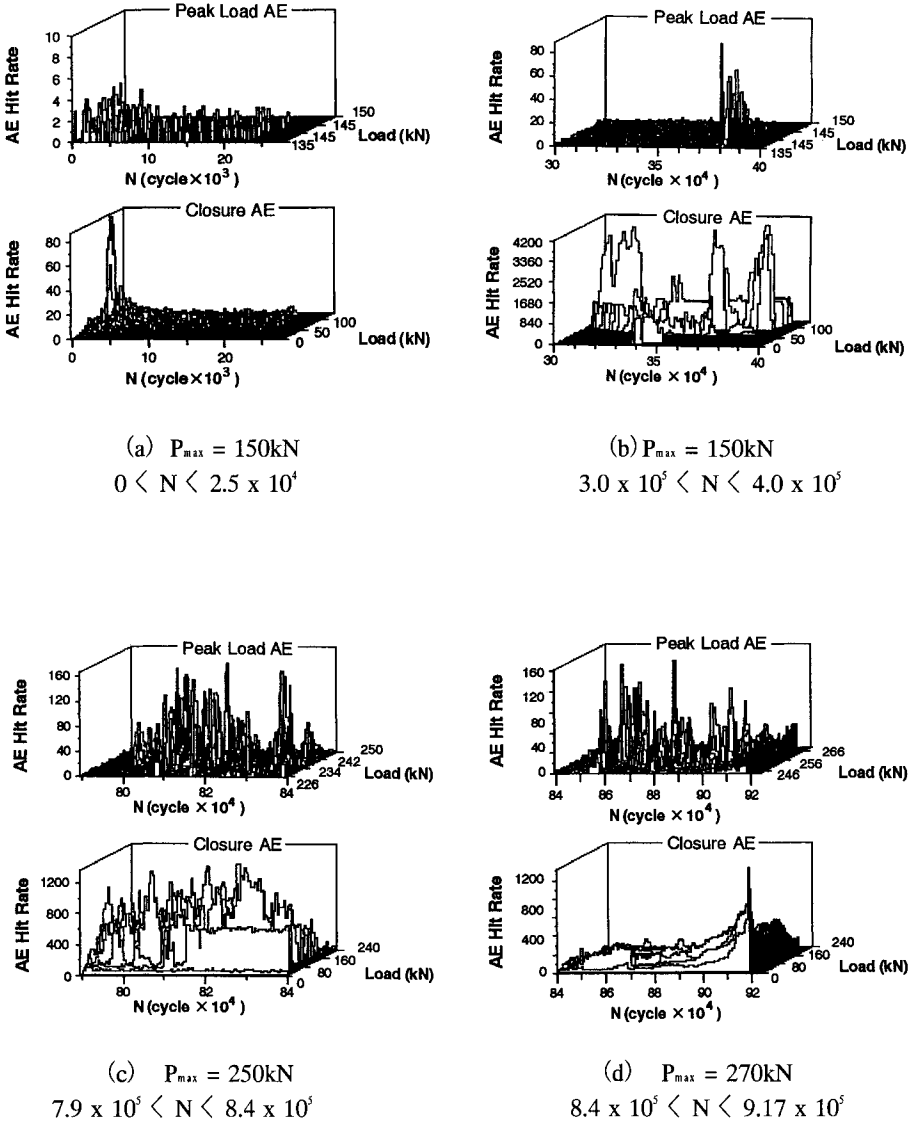


Fig. 8 Relationship between loading phase and AE activity.

Relationship between loading phase and AE activity has not been studied in RC specimens so far. In the present research, this relationship has been intensively studied by using the method applied to metallic materials. Experimental results obtained in this work are given in Fig. 8. Here Peak load AE is defined as the AE signals detected in the loading phase above 90% of the maximum load, while all the signals detected in the other phase are defined as closure AE.

Figure 8 (a) demonstrates the results obtained during the loading cycle $N = 0 - 2.5 \times 10^4$ (Stage I). It is seen that Peak Load AE is mostly detected in the early time of Stage I, while its activity decreases after this. This is because the crack density increases rapidly in the early time due to the micro-crack initiation but the crack extension rate starts to slow down after this. Accordingly, it is quite obvious that the Peak Load AE has a strong correlation with the crack extension in the RC slab under the fatigue loads. The AE source in this case should be attributed to the main crack extension.

The results obtained during the loading cycle $N = 3.0 - 4.0 \times 10^5$ (Stage II) are given in Fig. 8 (b). The activity of Peak Load AE is quite low in this stage. Some activities are observed only during $N = 3.8 - 3.9 \times 10^5$. This implies that the Peak Load AE is due to crack extension and the low activity corresponds to the fact that no significant crack growth was visually observed in Stage II. However, closure AE gives high activity all through the stage in the loading phase above 50 kN. Mechanical sources such as closure or opening of the cracks should contribute to this high activity.

Figure 8 (c) gives the results obtained during $N = 7.9 - 8.4 \times 10^5$ (from the end of Stage III to Stage IV). More Peak Load AE is observed as the crack density increases significantly during the transition from Stage III to Stage IV. However, the number of the detected closure AE signals are almost one order of magnitude greater than that of the Peak Load AE. This is because large number of closure AE is generated by mechanical frictions due to opening and closure of the existing cracks in the slab during loadings and unloadings.

Shown in Fig. 8 (d) are the results for $N = 8.4 - 9.17 \times 10^5$ (Stage IV to the final failure). The most distinct fact seen here is that the activity of closure AE increases very rapidly at low load levels as the cracking process approaches to the final failure. This is because many AE signals due to mechanical causes were detected since many cracks already existed in the specimen at this stage. This result suggests that the process of the final failure can be practically monitored by detecting the closure AE observed near the minimum load.

AE monitoring in a structure

AE hit increased almost linearly as a function of time during continuous monitoring for two hours in CH1. The same tendency was observed in CH2, CH3 and CH4 sensors. Other

AE features such as energy and count gave the same kind of history. Therefore, it is thought that there was no significant change in active loads due to traffic during the monitoring and AE measurement was carried out under a stable condition.

Figure 9 indicates cumulative number of AE hits (a) and AE energy (b). The number of detected hit is almost the same in CH 1, 3 and 4 (about 8×10^7) but it is about 50 percent greater in CH2. In contrast, AE energy exhibits about 10^6 in CH2 and CH4, while 2.6×10^7 and 3.0×10^7 are detected in CH1 and CH3, respectively. Thus more than one order of magnitude larger AE energy is seen in CH1 and CH3 than in CH2 and CH4.

This is because CH1 and CH3 sensors detected AE signals generated by active loads due to the traffic since the sensors were attached under the traffic lane. However, AE signals due to indirect causes such as vibration of the structure were thought to be detected in CH2 and CH4 because the median strip was on the area where the sensors were attached.

Comparison of AE energy in CH1 attached to Slab A and that in CH3 attached to Slab B indicates that it is about 15% greater in CH3 than in CH1 although AE measurement was made under the same traffic condition. Visual observations of crack density found that the damage level of Slab A corresponds to mid Stage I shown in Fig. 3, while that of Slab B corresponds to late Stage I. Accordingly, the difference of the detected AE energy between CH1 and CH3 should be attributed to the difference of damage levels between the slabs.

DISCUSSION

In the laboratory test, AE was monitored from the initial loading to the final failure. However, it should be very difficult to carry out continuous monitoring of structures in service. Figure 10 indicates history of AE hits detected during 100 loading cycles at every 10^4 cycles. The shape of the AE hit rate history shown in Fig. 4 is in good agreement with the result given in Fig. 10. Therefore, it is good enough to perform periodic AE monitoring for evaluation of damage levels in structures instead of performing continuous monitoring.

Shown in Fig. 11 is AE energy detected during 100 loading cycles at every 10^4 cycles in the laboratory test. The four stages of the cracking process resulted from the visual

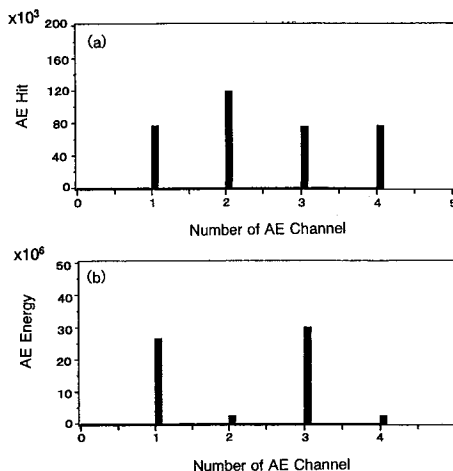


Fig. 9 Cumulative number of AE hits (a) and AE energy (b).

observations are also indicated for reference. As described before, the results of the AE measurement from the slabs in service under the active loads showed that the AE energy in Slab B is 15% greater than that in slab A under the same loading (traffic) condition. This is because Slab B has greater damage than Slab A, confirmed by the visual observations. In Fig. 11, it is seen that high AE energy is detected particularly at the very early time in Stage I. However, the energy decreases immediately and then increases continuously almost at a constant rate as the damage progresses. The visual observations of the cracking process showed that the damage level of Slab A corresponds to mid Stage I indicated in Fig. 11, while that of Slab B corresponds to late Stage I. Therefore, it should be possible to evaluate damage levels of slabs in service by measuring AE energy periodically under active loads due to traffic.

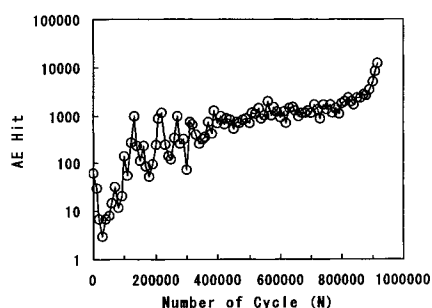


Fig.10 History of AE hits detected during 100 loading cycles.

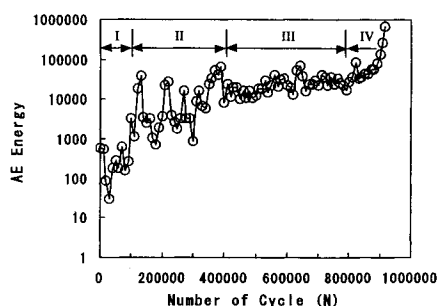


Fig.11 History of AE energy detected during 100 loading cycles.

CONCLUSIONS

In the present study, AE was monitored from the initial loading to the final failure in a model RC slab under fatigue loads in laboratory. AE monitoring was also carried out for two hours in RC slabs in service under active loads due to traffic. From these results, the following conclusions can be drawn :

- (1) Comparison of crack density history and AE activity history showed that cracking process under fatigue loadings can be predicted and evaluated by monitoring AE signals.
- (2) Comparison between visual observations of cracking process and AE source location analysis indicated that damage area due to the cracking can be roughly identified by the AE source location.
- (3) The analysis of the relationship between loading phase and AE activity found that the AE signals detected near the maximum load have strong correlation with crack extension. It was also shown that the cracking process to the final failure can be practically monitored by detecting AE signals emanated near the minimum load.
- (4) AE monitoring for two hours in the RC slabs under active loads due to traffic

confirmed that the detected AE energy is about 15% greater in the slab with greater damage than the one with less damage.

- (5) It was demonstrated that fatigue process of structures in service can be practically evaluated by periodic AE monitoring.
- (6) Comparison of AE activities detected in a structure and in laboratory test showed that damage levels of RC slabs under active loads in service can be evaluated by monitoring AE energy.

REFERENCES

- [1] Yuyama, S., Okamoto, T., Shigeishi, M., and Ohtsu, M. (1995) Quantitative evaluation and visualization of cracking process in reinforced concrete by a moment tensor analysis of acoustic emission, *Mater. Eval.*, **53**, pp. 751-756.
- [2] Yuyama, S., Okamoto, T., and Nagataki, S. (1994) Acoustic emission evaluation of structural integrity in repaired reinforced concrete beams, *Mater. Eval.*, **52**, pp. 86-90.
- [3] Yuyama, S., Okamoto, T., Shigeishi, M., and Ohtsu, M. (1995) Acoustic emission generated in corners of reinforced concrete rigid frame under cyclic loading, *Mater. Eval.*, **53**, pp. 409-412.
- [4] Minemura, O., Sakata, N., Yuyama, S., Okamoto, T., and Maruyama, K. (1998) Acoustic emission evaluation of an arch dam during construction cooling and grouting, *Construc. Build. Mater.*, **12**, pp. 385-392.
- [5] Yuyama, S., Li, Z-W., Ito, Y., and Arazoe, M. (1999) Quantitative analysis of fracture process in RC column foundation by moment tensor analysis of acoustic emission, *Construc. Build. Mater.*, **12**, pp. 87- 97.
- [6] Yuyama, S., Kishi, T., and Hisamatsu, Y. (1984) Fundamental aspects of AE monitoring on corrosion fatigue process in austenitic stainless steel, *J. Mater. Ener. Syst., Am. Soc. Met.*, **5**, No.4, pp. 212-221.
- [7] Yuyama, S., Kishi, T., and Hisamatsu, Y. (1984) Effect of environment, mechanical conditions, and materials characteristics on AE behavior during corrosion fatigue processes of an anstenific stainless steel, *Nucl. Eng. Des.*, **81**, No.2, pp. 345-355.

QUANTITATIVE EVALUATION OF FRACTURE PROCESSES IN CONCRETE BY THE USE OF IMPROVED b -VALUE

T. SHIOTANI

*Technological Research Institute, Tobishima Corporation,
5472 Kimagase, Sekiyado-machi, Chiba 270-0222, Japan*

S. YUYAMA and Z. W. LI

Nippon Physical Acoustics LTD.,

8F Okamoto LK Bldg., 2-17-10, Higashi, Shibuya-ku, Tokyo 150-0011, Japan

M. OHTSU

*Department of Civil Engineering and Architecture, Kumamoto University,
2-39-1 Kurogami, Kumamoto-City, Kumamoto 860-8555, Japan*

ABSTRACT

In the present study, fracture processes were investigated quantitatively in four different kinds of concrete specimens by applying improved b -value (Ib -value) analysis. It is observed that the variation of the Ib -value well corresponds to fracture process of specimen during each loading stage, independent of dimension, shape and reinforcement of the specimen. The results of the Ib -value analysis are in good agreement with those obtained from the moment tensor analysis. It was found that in case that the moment tensor analysis may not be applicable, the fracture process of the specimen can be evaluated by applying the Ib -value analysis. It is shown that the Ib -value analysis is a very useful method for quantitative evaluation of the fracture process.

KEYWORDS

Acoustic emission, b -value, concrete, fracture process, structural integrity

INTRODUCTION

In recent years, it has been recognized that concrete structures deteriorate under various service environments. Especially, during the 1995 great Hanshin earthquake, many reinforced concrete (RC) structures were severely damaged due to strong ground motions. With this as a start, it is strongly expected to establish a non-destructive inspection method with which the deterioration of concrete structures can be evaluated quantitatively in the early stages.

Acoustic emission (AE) is a term used for elastic waves generated by sudden changes which occur locally in materials due to deformation, cracking, transformation and so forth. At present, this term is used as an inspection technique for non-destructive evaluation. Since AE is very effective to monitor the initiation and the growth of cracks in materials and structures, it has been widely utilized for materials evaluation in laboratory. In concrete engineering, the applicability has been intensively studied in both materials [1] and structures [2-5].

To analyze AE data acquired, parameter analysis is widely and frequently employed, which analyzes AE activities based on the measurement of such AE parameters as hit, count, energy, amplitude and so on. Among these parameters, in particular, the AE peak-amplitude is considered to be closely related to the magnitude of fracture. For this reason, many researchers have studied b -value and m -value determined from a negative gradient of the peak-amplitude distribution. Recently, in order to apply the b -value analysis for fracture evaluation of slope failure, a calculating method of the b -value has been improved by using statistical values of amplitude distribution [6,7].

In this paper, four different kinds of concrete specimens are evaluated by applying the above mentioned improved b -value (Ib -value) analysis. Comparison was made for the results obtained from both the Ib -value analysis and the moment tensor analysis [8].

ANALYSIS

AE peak-amplitude distribution, b -value and improved b -value

Concept of the b -value. The b -value is a parameter defined by Gutenberg and Richter. It is calculated from the earthquake magnitude: M and its frequency: $n(M)$. The total number: $N(M)$, calculated from magnitude greater than M , is given by,

$$N(M) = \int_M^{\infty} n(M) dM \quad (1)$$

Because the frequency distribution $n(M)$ obeys the exponential distribution, the following equation is obtained,

$$\log N(M) = A - bM \quad (2)$$

in which A and b are constants. Because the magnitude, M , is defined by the logarithm of amplitude, then Eq.2 becomes,

$$\log N(a) = A - b \log a \quad (3)$$

where a is the peak-amplitude in decibel.

The coefficient b in Eq.3 is well known as the b -value. The b -value is given as a gradient of linear descending branch of cumulative frequency distribution. In the process where micro-fracture occurs superior to macro-fracture, the b -value tends to increase. While in the process where macro-fracture is superior to micro-fracture, the b -value tends to decrease.

Improved b -value. The b -value is given by a negative gradient of the amplitude distribution corresponding to a straight line. However, in most cases, AE amplitude distributions do not express one straight line. Different ranges of amplitudes may give different lines. Thus, it is necessary to search for the amplitude range which can stand for one straight line. Although appropriate ranges of amplitude might be determined by advance studies, AE waves practically detected are affected by conditions of sensor coupling, existence of unexpected cracks and so forth. As a result, derived amplitude may not be distributed in an expected amplitude range. Then in order to determine the amplitude range, the following method was proposed [6,7].

The amplitude range is obtained from mean value of the distribution (μ) and standard deviation (σ). It was reported that in the amplitude range from $\mu - \sigma$ to $\mu + \sigma$, the amplitude distribution can be represented by one straight line [6]. Then the formula for improved b -value is given as follows:

$$Ib = \frac{\log N(\mu - \alpha_1 \sigma) - \log N(\mu + \alpha_2 \sigma)}{(\alpha_1 + \alpha_2) \sigma} \quad (4)$$

where Ib is the improved b -value, α_1 is a coefficient which determines lower value of amplitude and α_2 is a coefficient which determines fracture level. In the present study, $\alpha_1 = 0$ and $\alpha_2 = 1$ were adapted.

Sampling number of amplitude data used for Ib -value calculation. To determine the proper number of sampling data necessary for calculating μ and σ , correlation coefficient between the logarithmic cumulative frequency and AE amplitude is given in Fig. 1. It is shown that in all the different specimens, the relations between the logarithmic cumulative frequency and AE amplitude give a straight line when the number of sampling data becomes larger than 50. Moreover, in laboratory and field model slope failure tests, Shiotani and his group [6] have shown that AE amplitude data with samples from 50 to 100 gives reasonable result. Hence, in this study AE amplitude data consisting of 50 samples are used to calculate the Ib -value.

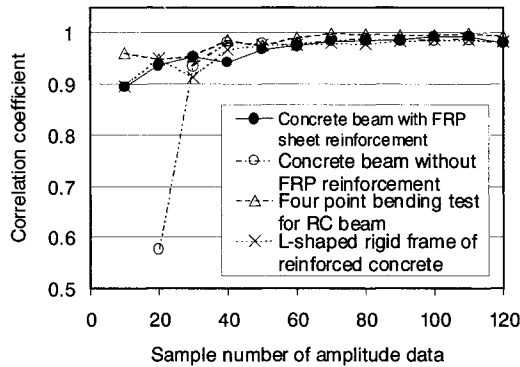


Fig. 1. Correlation between the logarithmic cumulative frequency and AE amplitude.

Moment tensor analysis [8]

Moment tensor analysis using a SiGMA (Simplified Green's function for Moment tensor Analysis) code is a method developed for quantitative AE waveform analysis based on the measurement of very first P-wave arrivals. Quantitative information on AE sources is analyzed by applying theoretical treatment to the waveform sets recorded from a multi-channel transient recorder with more than six sensors. The procedure can give quantitative information on three-dimensional location of cracks, crack types, crack orientation and direction of crack motion. It has been shown that the moment tensor analysis is very effective to analyze fracture processes of concrete members.

In this paper, results of the moment tensor analysis are compared with those obtained from *Ib*-value analysis.

SPECIMEN AND TEST METHOD

Cyclic flexure test of reinforced concrete beam

A four-point flexure test was conducted as shown in Fig. 2. Locations of six AE sensors (S1~S6) are also given in the figure. A reinforcing bar of 19mm in diameter was inserted below the center of the specimen. The specimen was loaded and unloaded cyclically in five stages. At the first and the second stage, the maximum load was 49kN. In the other three stages, it was increased in a step-wise manner.

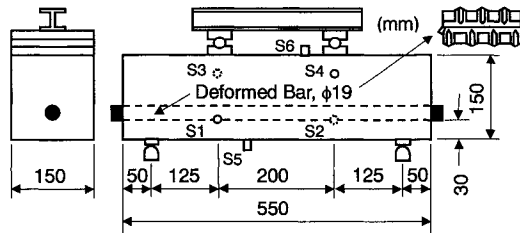


Fig. 2. Reinforced concrete specimen in flexural test and AE sensor locations.

L-shaped rigid frame

A sketch of an L-shaped RC rigid frame and arrangement of reinforcements are illustrated in the left side of Fig. 3. Tensile force was applied to expand a corner of the L-shape model and six AE sensors were attached as shown in right side of Fig. 3. In the experiment, cyclic loading was applied to the specimen in a step-wise manner.

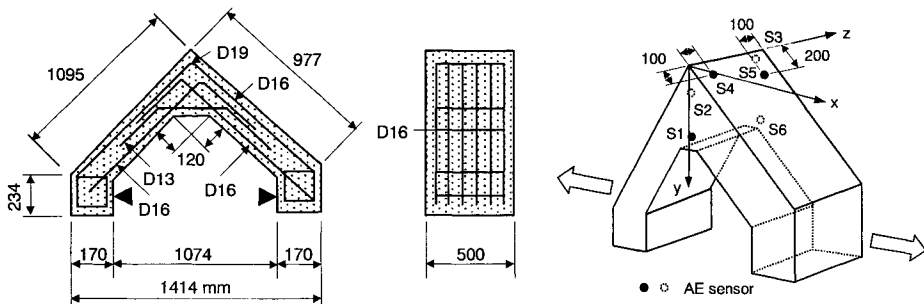
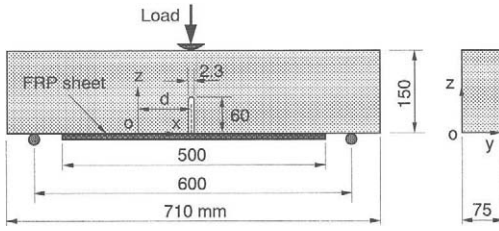


Fig. 3. Sketch and AE sensor locations for the cyclic loading test of "L" shaped rigid frame.

Center notched concrete beams with and without FRP sheet reinforcement

Center notched concrete beams with and without FRP sheet reinforcement were subjected to three-point flexure load. Figure 4 gives a sketch of the specimen. The coordinates system and sensor locations are also shown in the figure. In the FRP reinforced specimen, one ply of CFRP sheet was bonded on the bottom corresponding to the tensile zone.



x-y-z: AE sensor coordinations
 d=100mm for specimen without reinforced FRP sheet
 d=10mm for specimen with reinforced FRP sheet

CH	without FRP sheet			with FRP sheet		
	x	y	z	x	y	z
1	0	55	0	180	8	0
2	200	20	0	30	75	10
3	0	20	150	0	0	140
4	200	55	150	110	38	150
5	50	75	130	160	75	120
6	150	0	130	110	0	30

Fig. 4. Details of three-point flexure tests for concrete specimen with a center notch.

RESULTS AND DISCUSSIONS

To apply the moment tensor analysis, six sensors were used for AE measurement. In this paper due to the page limitation, typical results of the *Ib*-value analysis from one channel data will be reported in each experiment.

Cyclic flexure test in reinforced concrete beam

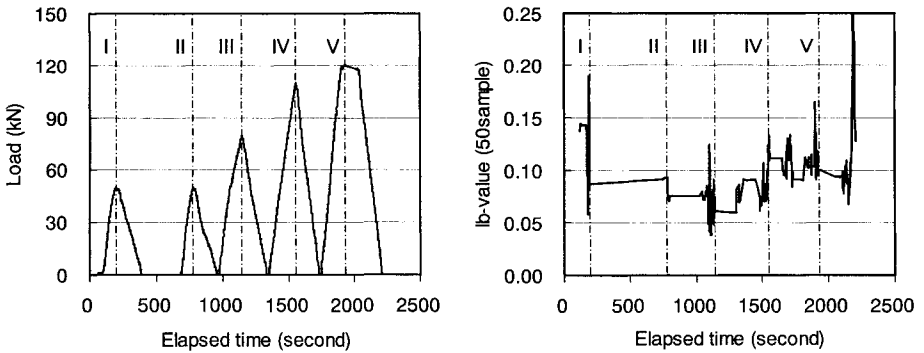


Fig. 5. Results of cyclic flexure test in reinforced concrete beam (left: loading history; right: result of *Ib*-value analysis).

In this experiment, results of the *Ib*-value analysis are explained with regard to CH5 AE sensor, which is placed below the center of the specimen. Results of *Ib*-value analysis and the loading history are shown in Fig.5. In this figure, the maximum load of each stage is represented by a dotted line. In stage I and stage II, the load was applied up to 49kN and then unloaded. After that, it was increased in a step-wise manner to the final load, 120kN.

In stage I, the Ib -value decreased first and then increased just before the maximum load. This change of the Ib -value is considered to be the initiation of fracture. In stage II, the Ib -value decreased slightly, at the maximum load, however the change is not large. For the stage III, the Ib -value begins to increase at the load a little lower than the maximum load of stage II. The Ib -value increases sharply one and then decreases. In this stage, it is considered that large-scale failure began to take place just after the occurrence of small-scale failure. In stage IV, the change of Ib -value started at a load much lower than the maximum load of stage III. The repeated decrease and increase of Ib -value in this stage is considered to be due to the propagation of large-scale failure and initiation of small-scale failure in the process zone ahead of the main cracks. Finally in stage V, it is observed that the Ib -value begins to increase corresponding to the load over about 50% of the maximum load of the stage IV and then decreases. The moment tensor analysis showed that 8 events, 2 events, 32 events, 25 events and 9 events were detected from stage I to stage V, respectively. Except stage V, stages where the AE events are detected by the moment tensor analysis correspond to the stages in which the Ib -value changed dramatically. In stage V, only 9 events were obtained by the moment tensor analysis, while the Ib -value changed remarkably. To perform the moment tensor analysis, waveform sets consisting of at least six readable waveforms are required. However, at latter periods of fracture there are a lot of cracks generated in the specimen, accordingly, it was very difficult to obtain waveform sets with six effective waveforms. This is the main reason why the moment tensor analysis was not applicable in the later periods of fracture. Unlike the moment tensor analysis, the Ib -value analysis is able to evaluate fracture process occurring in heavily damaged materials. This is because it does not require readable and meaningful waveforms necessary for the theoretical treatment but requires only amplitude information from each AE sensor.

L-shaped rigid frame

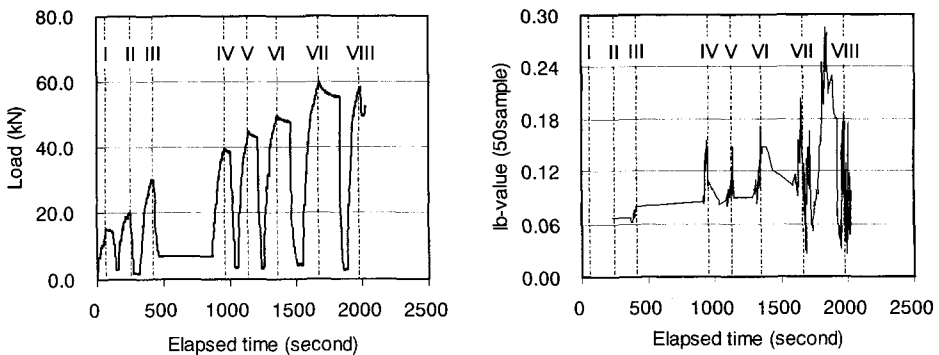


Fig. 6. Results of cyclic loading test in L-shape rigid frame (left: loading history; right: result of Ib -value analysis).

Here, the results from CH1 sensor is given as an example to interpret the Ib -value analysis. As demonstrated in Fig. 6, loading process is divided into eight stages with the increasing step-wise maximum loads. In each stage, the maximum load is marked by a dotted line. Slight change of Ib -value can be observed from stage III. In stage IV, V and VI, the change of Ib -value becomes remarkable. In all of the three stages, the Ib -value shows the same level of variation. In stage VII with the load increase, more remarkable changes of the Ib -value are observed. Up to this stage the Ib -value repeats rises and falls at a region above 0.6. In the last stage, the specimen failed at a load less than the maximum load of stage VII. In this stage, changes of the Ib -value are quite remarkable and it is observed that the Ib -value dramatically falls to the region below 0.6, which implies that the macro-fracture becomes dominant. Meanwhile, among the total 1024 sets of waveforms, only 19 sets were applicable to the moment tensor analysis. To perform moment tensor analysis waveform sets of six readable waveforms are necessary as mentioned before. In this experiment the specimen is relatively large in size and with a quite complicated shape. Therefore, it was difficult to get waveform sets consisting of six readable waveforms. This is the reason why most of the waveform sets data were discarded. On the other hand, by applying the Ib -value analysis it is possible to evaluate the fracture processes of such a structure, since the Ib -value is obtained from the amplitude information for individual AE sensors.

Center notched concrete beams with and without FRP sheet reinforcement

Loading history and test results of the Ib -value analysis for center notched concrete beams reinforced with and without FRP sheet are given in Fig. 7. In this case, the data from CH1 is given as a typical example for the results of Ib -value analysis.

As observed in Fig. 7 (left), in the case of concrete beam without FRP reinforcement, the Ib -value increased first at about 80% of the maximum load. Then at the maximum load, the Ib -value decreases dramatically. The increase may be caused by nonlinear deformation, while the decrease may be due to catastrophic failure. On the other hand, the fracture process of the specimen could be divided into two stages by moment tensor analysis [9]. The first stage was observed until the maximum load. The cracks in this stage occurred only at a narrow area near the notch tip. After the maximum load, as the second stage, cracks grew rapidly upward and the specimen failed right away. The results of Ib -value analysis were in good agreement with the one obtained from the moment tensor analysis.

Regarding the concrete beam reinforced with CFRP sheet, the fracture process can be divided into three stages, demonstrated by the moment tensor analysis. As shown in Fig. 7, the first stage corresponds to the loading level before point A, where cracks are generated only within the area close to the notch tip. This is the same behavior observed in the first stage of the concrete beam without CFRP sheet reinforcement. Therefore, the loading point A can be regarded as functional maximum load of this structure. The second stage (stage II) is

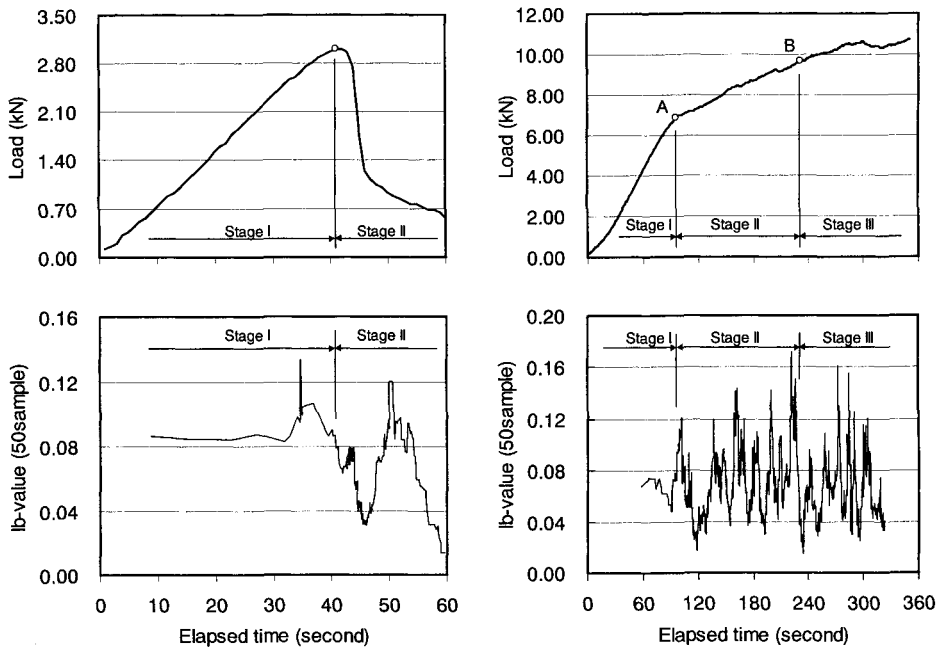


Fig. 7. Loading history and Ib -value analysis results for center notched concrete beams (left: concrete beam without FRP sheet reinforcement; right: concrete beam reinforced with FRP sheet).

determined between loading point A and loading point B, where the main cracks ahead of the notch tip grew rapidly. It was shown by the moment tensor analysis that in this stage, an inclined crack initiates from the bottom of the specimen toward the notch tip and a bottom crack propagates near the interface between the CFRP sheet and the concrete. After loading point B, the third stage is observed, where the propagation of the main crack has completed and only cracks in the bottom of the specimen continued to propagate towards the supports. Therefore, it could be considered that the main crack has reached the upper surface of the specimen in the second stage. Meanwhile it is shown in Fig. 7 that the Ib -value begins to change at about 80% of loading point A in the first stage. After loading point A, the change of the Ib -value becomes remarkable and the same tendency continues all through the second stage. When the load approaches to the point B, the most considerable change of the Ib -value is observed. This remarkable change of the Ib -value is considered to be resulted from the rapid propagation of the main crack to the upper surface of the specimen. Thus, the fracture process can be evaluated by applying the Ib -value analysis.

CONCLUSIONS

Fracture processes in four types of concrete specimens were evaluated by the *Ib*-value analysis. Comparing the results with those obtained from the moment tensor analysis, the followings are concluded:

1. It was shown that the *Ib*-value analysis can evaluate fracture process of concrete specimens with different dimensions, shapes and reinforcement arrangements. Thus, the *Ib*-value is a useful feature to characterize fracture process in concrete structures.
2. It was demonstrated that fracture process can be evaluated by the *Ib*-value analysis when the moment tensor analysis is not applicable due to specimen size and shape.

REFERENCES

1. Yuyama, S., Okamoto, T., Shigeishi, M. and Ohtsu, M. (1995). *Mater Eval* 53, 751.
2. Yuyama, S., Okamoto, T. and Nagataki, S. (1994). *Mater Eval* 52, 86.
3. Yuyama, S., Okamoto, T., Shigeishi, M. and Ohtsu, M. (1995). *Mater Eval* 53, 409.
4. Marukami, Y., Yuyama, S., Shimizu T. and Kouyama, H. (1993). *In: Proceedings of the 9th National AE Conference, JSNDI, pp. 143-150 (in Japanese).*
5. Minemura, O., Sakata, N., Yuyama, S., Okamoto, T. and Maruyama, K. (1998). *Construc Build Mater* 12, 385.
6. Shiotani, T., Fujii, K., Aoki, T. and Amou, K. (1994). *In: Progress in Acoustic Emission VII, JSNDI, T. Kishi, Y. Mori and M. Enoki (Ed.), pp. 529-534.*
7. Shiotani, T. and Ohtsu, M. (1999). *In: AcousticEmission: Standards and Technology Update, ASTM STP 1353, S. J. Vahaviolos (Ed.). American Society for Testing and Materials, West Conshohocken, PA, pp. 156-172.*
8. Ohtsu, M., Okamoto, T. and Yuyama, S. (1998). *ACI Struct J* 95, 87.
9. Li, Z. W., Yuyama, S., Ohsawa, I., Kimpara, I., Kageyama, K. and Yamaguchi, K. (1998). *In: Proceedings of FRAMCOS-3, H. Mihashi and K. Rokugo (Ed.). Aedificatio Publishers, Freiburg, Germany, pp. 1863-1872.*

ULTRASONIC IMAGING OF CONCRETE MEMBERS USING AN ARRAY SYSTEM

M. KRAUSE, F. MIELENTZ, B. MILMAN and H. WIGGENHAUSER

*Department of Buildings Diagnostics; Non-destructive Testing in Civil Engineering,
Federal Institute for Materials Research and Testing
D 12200 Berlin, Germany*

and

W. MÜLLER and V. SCHMITZ

*Fraunhofer Institute for Non-destructive Testing
D 66123 Saarbrücken, Germany*

ABSTRACT

The use of an ultrasonic array system is described, which can be used combined with 3D reconstruction calculations. In this way ultrasonic reflection and backscatter from the inside of concrete members can be imaged and interpreted. The application of the system is demonstrated for two examples: Measuring the concrete cover of utility pipes in a tunnel and the examination of transversal ducts in a bridge plate.

KEYWORDS

Ultrasonic echo, array technique, SAFT (Synthetic Aperture Focusing Technique), tunnels, reinforced concrete, prestressing ducts.

INTRODUCTION

Ultrasonic echo methods are nowadays often used for analyzing the internal structure of concrete members and buildings [1-7]. The enormous progress, which has been achieved in the last decade to overcome the difficulties characteristic of testing concrete is mainly due to the development of new types of broadband transducers operating in the frequency range of 50 to 250 kHz and to the application of the principle of synthetic aperture. The latter means, that ultrasonic measurements are carried out at many points of the surface and are evaluated by means of reconstruction calculations, which show the location and distribution of acoustic reflectors and scatterers in the volume of the concrete member tested.

Briefly summarized, the state of the art is as follows:

Thickness measurement and localization of construction features having a diameter of about 100 mm and larger are feasible aims by means of single A-scan interpretation, when the site conditions are not too difficult. This means, that the maximum aggregate size is 16 mm or less

and the non prestressed reinforcement is not too dense (e.g. mesh size of 150 mm). Additionally the concrete porosity has not to be too excessive [8].

In many cases these conditions are not fulfilled. Concrete with a maximum aggregate size of 32 mm is widely used, the mesh size of the rebars is often 100 mm or less and the rebar diameter is 24 mm or 32 mm. Under these conditions many A-scans must be collected at different points on the surface and reconstruction calculations have to be performed.

This is also important, when ducts in prestressed concrete have to be analyzed. For this aim a scanning laser interferometer can successfully be used to localize injection faults in tendon ducts.

In this contribution, the principle and the application of an ultrasonic array are described. It consists of an ensemble of broadband transducers which are successively used as transmitters and receivers and permit fast data acquisition. Thus large data sets can be collected and reconstruction calculation by means of SAFT (Synthetic Aperture Focusing Technique) is applicable.

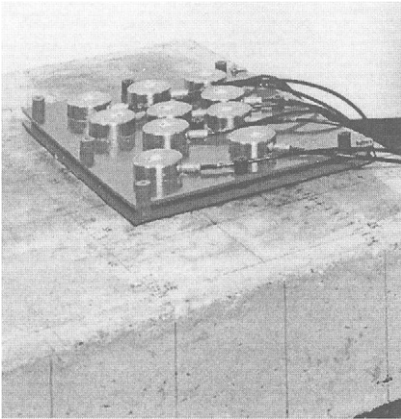


Fig. 1 Array of 10 broadband transducers

The ultrasonic array used for data acquisition consists of an array of ten broadband transducers (diameter 50 mm, frequency range of about 50 to 250 kHz). In most cases the transducers are positioned on the concrete surface using a template, as shown in fig. 1. They are used in a transmit-receive configuration using an electronic multiplexer. The principle of the configuration is shown in fig. 2. In case of transmitter, the pulse amplified to typically 1000 V produced by an arbitrary function generator is sent to the transducer. In the case of receiver, the signal is guided to an oscilloscope/averager, in order to suppress low frequency vibrations and high frequency noise, a band pass filter is used. The measurement and data acquisition is governed by a portable PC. In this way, 45 pairs of transmitting-receiving positions — that means 90 different A-scans — are registered in a short time

and can be used for reconstruction calculations. The equipment can be installed in a van and cables up to 25 meter length are used.

The use of broadband transducers allows to optimize the frequency band for the exciting pulse which is programmed in the function generator. In order to have a good depth resolution, usually frequencies of 150 to 200 kHz are used (corresponding to the wavelength (λ) of 27 mm to 20 mm in concrete with $c_1 = 4000$ m/s). If the attenuation of the waves is too high, lower frequencies can be chosen (80 kHz $\Rightarrow \lambda = 50$ mm).

A typical excitation pulse and the result of the phase-corrected superposition (see below) of 100 A-scans is shown in fig. 3 (left). It is the result of the thickness measurement of a concrete plate made with maximum aggregate size of 32 mm. The (normalized) transmitting pulse and the received pulse (showing a phase shift due to the reflection at the interface concrete/air) can be observed in this figure.

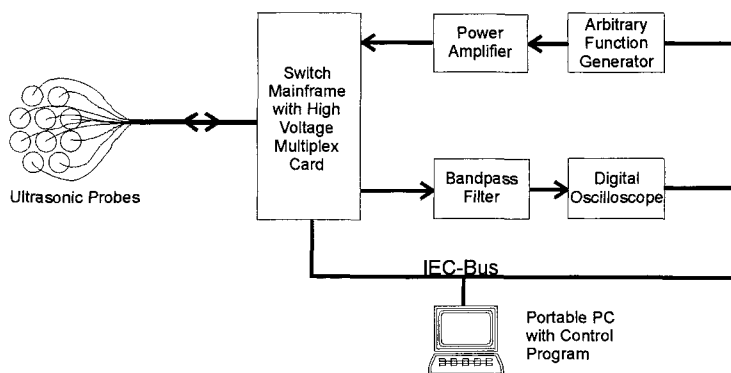


Fig. 2 Principle sketch of the array equipment.

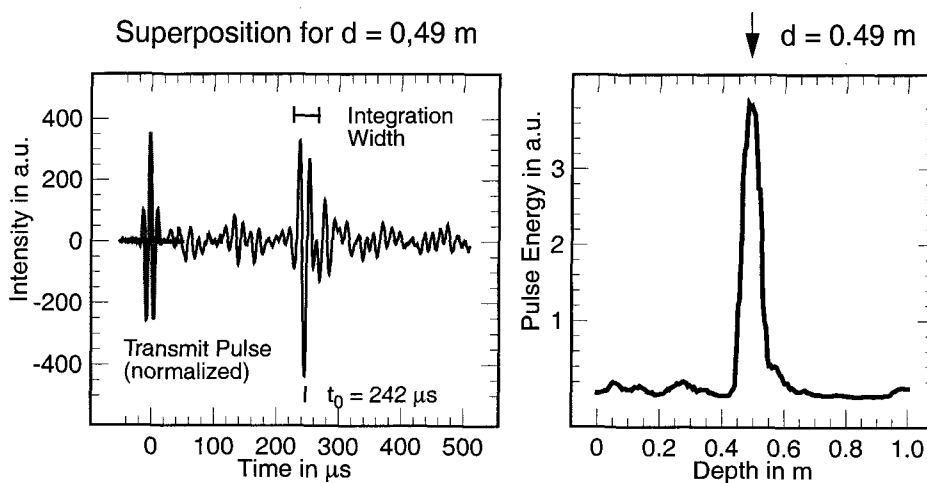


Fig. 3 Measurement of a concrete specimen (0.50 m thick) with a maximum aggregate size of 32 mm. *Left*: Time-of-flight corrected superposition of 100 A-scans. t_0 : expected arrival time of the echo signal. *Right*: pulse energy vs. calculated thickness for the integration interval which is indicated at the left side.

When an imaging of the internal structure of the concrete member is planned, a data set may consist of many different positions of the template. Depending on the desired resolution, the template is moved in steps between 10 mm and 100 mm over the surface. In this way data sets of several thousands of A-scans can be recorded in a relatively short time. The coupling of the transducers to the concrete surface is a difficult point for the ultrasonic measurements. A good coupling of every transducer of the array has to be carefully realized for each location of the template. For horizontal surfaces liquid coupling agents as glycerin or water may have an advantage.

For the ultrasonic non-destructive applications described in this paper, the array technique was used for data acquisition. During earlier examinations of ducts positioned rather deep below the surface, adjacent areas of the surface were scanned by a laser interferometer working as an ultrasonic detector [9]. In this way a continuous scanning of the surface was obtained with only a few locations of transmitting transducers. For the applications discussed in this paper ducts were expected to have a concrete cover of only 80 mm to 120 mm. In this case it seemed to be more convenient to move the whole array over the surface, rather than changing often the location of the ultrasonic sending transducer and readjusting the laser interferometer.

RECONSTRUCTION CALCULATIONS

When the desired resolution for an experimental measurements is not too pretentious, for example for thickness measurement or localization of large construction elements, a time-of-flight corrected superposition of A-scans at one or few positions of the template is performed. It results in the distribution of the reflected energy vs. depth for the volume below the template (usually a surface of 250 mm x 350 mm). This is realized by integrating the square of the ultrasonic intensity during the pulse length. An example is shown in fig. 3 (right) for the thickness measurement of a concrete plate.

When a better resolution of the reconstruction calculation is necessary, for example for the examination of ducts in prestressed concrete members, a three dimensional version of the SAFT method (Synthetic Aperture Focusing Technique) is applied [10]. This evaluation method was already successfully used for analyzing injection and compaction faults during a round robin test [9,11]. Briefly described it is an integration of the time-of-flight surface in the x-y-z-t data field for each voxel of the specimen. It results in a three dimensional representation of the backscatter intensity from the inside of the specimen. To interpret such data fields, projection planes are presented, which are the well known B-scans (ultrasonic intensity along the scan-axis vs. depth; perpendicular to the surface) and C-scans (ultrasonic intensity parallel to the surface in an adjustable depth).

With this method an axial and depth resolution in the order of one wavelength can be achieved.

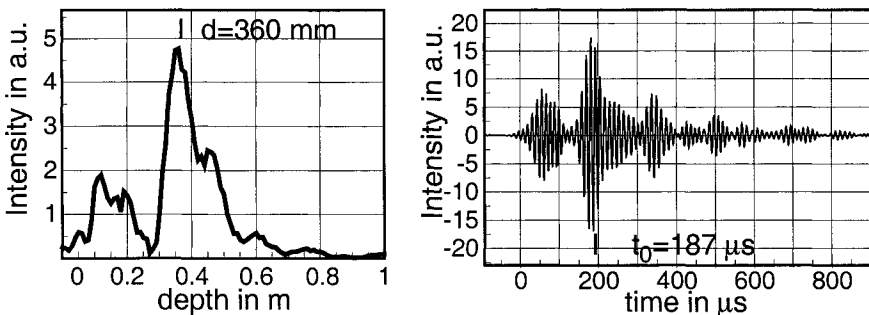


Fig. 4 Result of measuring the concrete cover of a duct for utility installations. *Left:* Reflected ultrasonic energy vs. depth indicating a clear maximum at 360 mm. *Right:* Corresponding time-of-flight corrected superpositions of 90 A-scans for the depth of 360 mm, t_0 : time-of-flight for the reflected pulse for that depth.

EXPERIMENTAL AND RESULTS

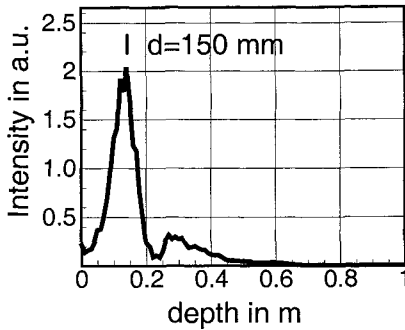


Fig. 5 Reference measurement near the element joint over the bore hole with a known depth.

were placed having the correct depth for the tubes. At this point a reference measurement was performed.

The measurement was strongly influenced by dense non prestressed reinforcement (diameter 28 mm, mesh size about 100 mm). For this reason the reinforcement was first localized using a scanning magnetic device, and the transducers of the array were manually placed between the rebars on the surface. Two different location of the array (180 A-Scans) were used to obtain a data field for the time-of-flight corrected superposition. Figure 4 shows the reflected ultrasonic energy vs. depth indicating a clear maximum at 360 mm. In the range between 100 and 200 mm disturbing reflections caused by the reinforcement are visible. The corresponding time-of-flight corrected superposition for the depth of 350 mm is shown at the right side of fig. 4. The multiple reflections caused by the reinforcement have been suppressed by digital filtering prior to the evaluation.

Figure 5 shows the reference experiment over a core with a known duct cover of 180 mm. The depth measurement (150 mm) is very clear, the error of 30 mm is caused by the fact, that calculations were performed with an estimated velocity and by the overlap with reflections and stray signals from the rebars. The knowledge of the exact ultrasonic velocity was not necessary for the described question, because the measurements had only to estimate, if the ducts were placed about 200 mm (correct position) or 400 mm (wrong position) below the surface. Using the ultrasonic array it could be clearly demonstrated, that the ducts were wrongly placed, deeply below the surface.

Examination of transversal ducts in a bridge plate

Prior to a planned site application on a bridge deck it was to be verified, if transversal ducts can be investigated with the system described combined with 3D-SAFT reconstruction calculations. As mentioned above the ducts to be analyzed had a concrete cover of only 80 mm to 120 mm. In order to test the principal function of the array system and the 3D-SAFT reconstruction, a test specimen with a step in thickness and a steel tube (diameter 40 mm) was constructed (fig. 6) The array was scanned in steps of 30 mm over the surface using glycerin as coupling agent. The B- and C-scans resulting from the 3D-SAFT reconstruction are presented in fig. 7 and fig. 8. In the B-scan the step in the thickness is clearly seen, whereas the tube is not represented in the

In this chapter two examples of the application of the array system and the reconstruction calculation are described.

Measurement of the concrete cover of utility pipes

The task was to localize and measure the depth of ducts for utility installations in the wall of a tunnel. The ducts (diameter 200 mm) that should have been installed at 20 cm depth were instead installed towards the outer side of the wall (at 40 cm depth in a wall thickness of 0.8 m). It became visible at an element joint. At another part of the tunnel the ducts had to be localized in order to know, if the fault continued. At the element joint new holes

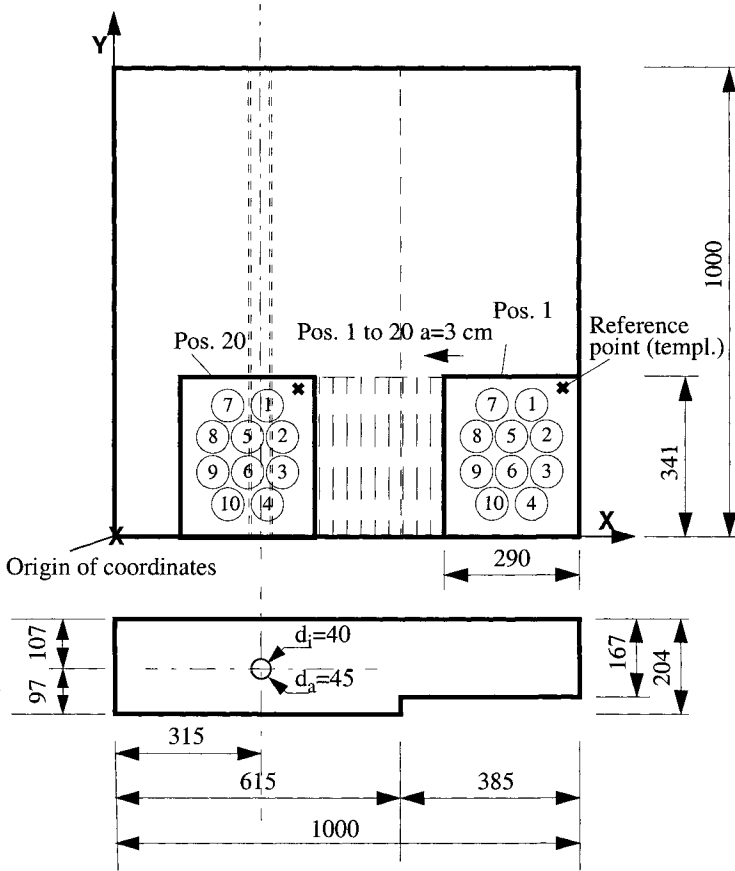


Fig. 6 Test specimen for the application of 3D-SAFT reconstruction.

reconstruction. As expected, at the border of the aperture the intensity is small, because the outer regions of the specimen are not homogeneously irradiated by the ultrasonic waves.

The signals below the surface reflection are partly due to disturbing pulses produced by the transducers and multiple reflections. The C-scan shows that the reconstruction of the back wall is relatively homogeneous indicating that the system can be used for imaging plain surfaces. The variations of about 6 dB are due to the inevitable changes in the coupling conditions. It can be seen that for imaging ducts the aperture in the direction of the ducts has to be larger.

In order to test the system for imaging ducts, a second test specimen was constructed. It contains three ducts having the depth expected at the bridge deck. Figure 9 represents the B-scan of an empty duct (diameter 40 mm, concrete cover: 100 mm). The back wall and the duct are clearly represented. The slight bowing of the duct of about 20 mm towards the center of the specimen corresponds with the real situation in the specimen. The additional signals about 80 mm below the duct and the back wall, respectively, are due to the wave mode conversion from longitudinal to transversal waves. This can be proved by a reconstruction calculation taking into account the corresponding velocities.

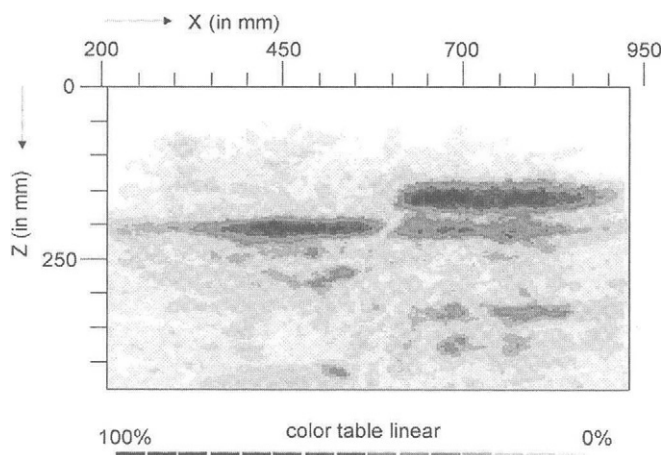


Fig. 7 B-scan from array measurement and SAFT reconstruction of the test specimen shown in fig. 6.

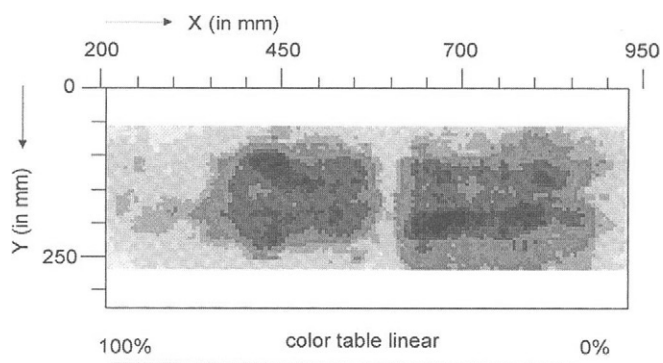


Fig. 8 C-scan from array measurement and SAFT reconstruction of the test specimen shown in fig. 6.

The change in the intensity of ultrasonic reflection from both, the duct and the back wall is evident: Although the measured surface was very smooth, the reason is probably the changing of the coupling conditions. The existence of the clear back wall echo can help in this interpretation. Assuming that the concrete quality does not strongly depend on the location, a normalization to the back wall intensity was performed. The result (fig. 10) shows a relatively constant reflection intensity of the empty duct except in the region around $x = 0.8$ m. Here an anomaly of the concrete quality is assumed which will be examined later.

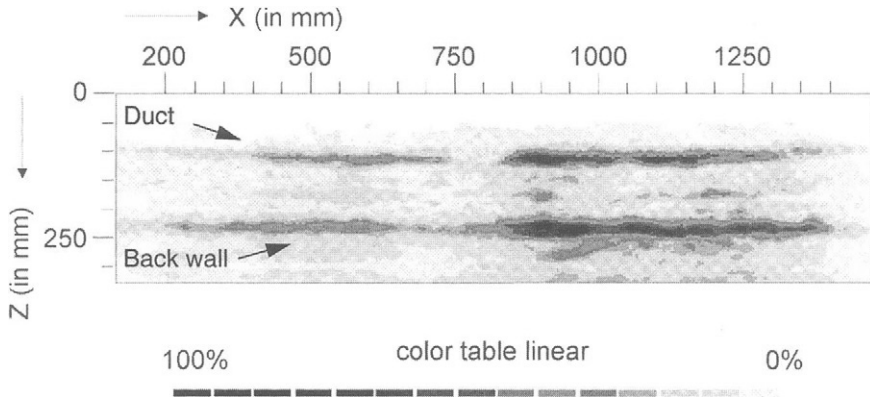


Fig. 9 Imaging of an ungrouted duct in a concrete plate: B-scan from 3D SAFT reconstruction.

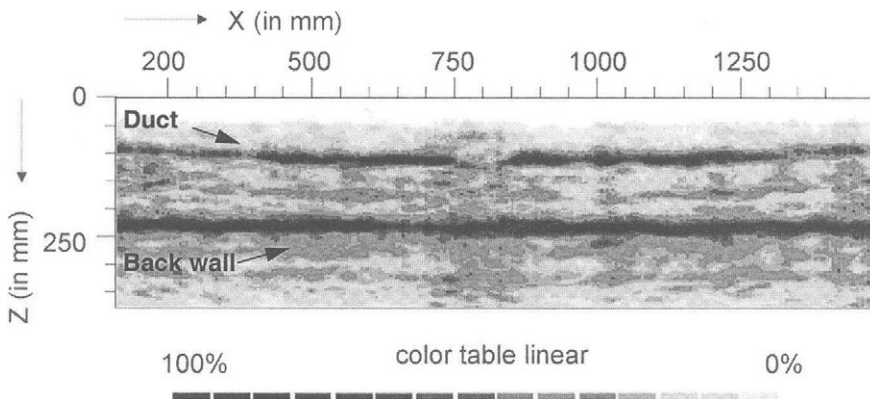


Fig. 10 Imaging of an ungrouted duct in a concrete plate: B-scan from 3D SAFT reconstruction. Same data as fig. 9, the intensity is normalized to the back wall reflection.

SUMMARY AND CONCLUSION

The use of an ultrasonic array system is described, which consists of 10 broadband transducers working each one successively as transmitter and receiver. The practical application of the system on site shows that it is possible to measure the concrete cover of large constructions elements even behind dense reinforcing bars. To do this the data are evaluated by means of time-of-flight corrected superposition.

It is demonstrated, that the array system together with 3D-SAFT reconstruction calculation can be used for the examination of transversal prestressing ducts having a concrete cover of about

100 mm. The change of the coupling conditions can be compensated by a normalization, so that the analysis of grouting and compaction faults in and around the duct can be performed by considering the reflection intensity. The system has already been used on site successfully.

REFERENCES

1. Kroggel, O., Jansohn, R. and M. Ratmann (1995). In: Forde, M. C. (Ed.); *Proceedings of the 6th International Conference on Structural Faults and Repair*, UK, July 1995, Vol.1, pp. 203-208, Engineering Technics Press, London.
2. Schickert, M. (1996). In: *II. Int. Conference on NDT of Concrete in the Infrastructure*, Nashville, Tennessee, 12.-14.06.96, pp. 135-142.
3. Krause, M., Bärmann, R., Frielinghaus, R., Kretzschmar, F., Kroggel, O., Langenberg, K., Maierhofer, C., Müller, W., Neisecke, J., Schickert, M., Schmitz, V., Wiggenhauser, H. and F. Wollbold (1997) *NDT&E International* **30**(4), 195.
4. Wollbold, F. and J. Neisecke (1998). In: *Proceedings ECNDT Conference*, 26-29 May 1998, Copenhagen.
5. Kapphahn, G. and K. Kaschmierzeck (1998). In: *Wissenschaftliche Beiträge der MFPA 1998 Vol 3*, Leipzig.
6. Maierhofer, C., Krause, M. and H. Wiggenhauser (1998) *NDT&E International* **31** (6), 421.
7. Krieger, J., Krause, M. and H. Wiggenhauser (1998). In: Medlock, R. D. and Laffrey, D. C. (Eds.); *Structural Materials Technology III*, pp. 258-269, Proceedings of SPIE, Vol. 3400, Bellingham.
8. Krieger, J., Krause, M. and H. Wiggenhauser (1998). *Erprobung und Bewertung zerstörungsfreier Prüfmethoden für Betonbrücken*. Wirtschaftsverlag NW, Bremerhaven.
9. Krause, M., Müller, W. and H. Wiggenhauser (1997) *Acoustical Imaging* **23**, 433.
10. Schmitz, V., Kröning, M. and K. Langenberg (1996) *Acoustical Imaging* **22**, 735.
11. Krause, M., Wiggenhauser, H., Müller, W., Kostka, J. and K. Langenberg (1998). In: Fahlstedt, K. (Ed.); *Proceedings of the CIB World Building Congress*, Symposium A, pp. A 87 Gävle, Schweden, 7.-12. June 1998, KTH Built Environment, Gävle.

This Page Intentionally Left Blank

INFLUENCE OF AGGREGATES ON ULTRASONIC ELASTIC WAVES PROPAGATION IN CONCRETE

Nobuaki Otsuki*, Mitsuyasu Iwanami**, Shin-ichi Miyazato*, Norio Hara*

* *Faculty of Engineering, Tokyo Institute of Technology, Japan*

** *Port & Harbour Research Institute, Ministry of Transport, Japan*

Abstract:

In this study, the ultrasonic elastic waves propagation (hereafter referred as UEWP) behavior in concrete was investigated through the experimental and theoretical approach, mainly focusing on the influence of aggregates. The experimental factors were the maximum size, the volume percentage, and the acoustical impedance of aggregates. The velocity and the frequency characteristics of the UEWP through concrete were examined. For calculating the scattering of elastic waves by aggregates, Mason's method was adapted.

The main conclusion is "The maximum size of aggregates influences the frequency distribution, however, is not a key factor for the velocity. On the other hand, the volume percentage of aggregate is very influential on both the frequency distribution and the velocity".

Key Words

Concrete, Aggregates, Elastic Waves, Velocity, Frequency, Scattering

INTRODUCTION

In recent years, non-destructive evaluation techniques got to attract attentions. Especially, the technique utilizing the UEWP is very effective. For example, the technique is used to estimate 1) the depth of crack, 2) the compressive strength [1], 3) the material deterioration of concrete, and so on. These purposes can be achieved only if the UEWP in concrete is satisfactory understood. However, a lot of unclear parts are left unanswered. Therefore, it cannot help saying that the evaluation result from the UEWP lacks the trustability.

The the authors considered there were three major factors (1. characteristics of aggregates, 2. matrix properties, and 3. existence of microcracks) and in this paper especially the influence of aggregates on the UEWP is reported.

This investigation is constituted in two parts. In the first part, the authors manufactured specimens with model aggregates to clarify the basic influence of aggregates on the UEWP, and in the second part, the authors confirmed the influence of the aggregates in the actual situations.

EXPERIMENTAL AND THEORETICAL INVESTIGATION WITH MODEL AGGREGATES

In the experimental works, the main factors under consideration were the diameter, the volume percentage and the acoustical impedance of model aggregates. In this study, glass balls and steel balls were used as model aggregates. Also, a theoretical analysis was conducted to verify the experimental results.

Experimental Outline

Specimens.

The specimens were made of the cement paste and model aggregates. The size of the specimens was 100x100x200(mm). The water to cement ratio of the cement paste was 0.30.

The properties of model aggregates are shown as follows.

[Size] The diameters of glass ball were 12, 20, and 30mm, and that of steel balls was 12mm.

[Volume Percentage] The volume percentages of the glass balls were 10, 25, and 35% and that of the steel balls was 25%.

[Acoustical Impedance] The acoustical impedance of the glass balls is $13.1 \times 10^6 \text{ kg/m}^2\text{s}$ (density; 2.5 g/cm^3 , and velocity; 5.60 km/s), and that of steel balls is $46.8 \times 10^6 \text{ kg/m}^2\text{s}$. The range for normal actual aggregates are between $10\text{-}15 \times 10^6 \text{ kg/m}^2\text{s}$. The acoustical impedance of the cement paste is $9.58 \times 10^6 \text{ kg/m}^2\text{s}$. Accordingly, the ratio between the impedance of cement paste, glass balls, and steel balls were 1:1.36:4.89. In the case of investigating the influences of the acoustical impedance on the UEWP, the diameter and the volume percentage were set to be constant as 13mm and 25%, respectively.

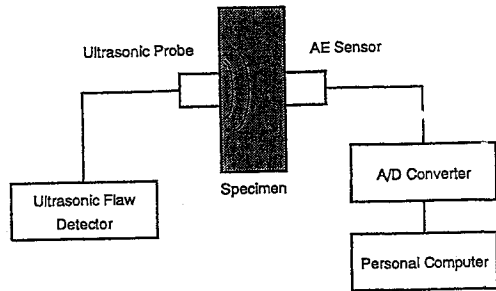


Fig.1 Elastic Waves Measurement System

Outline of UEWP Test. The ultrasonic waves measurement system is shown in Fig.1. A pulse was produced by a wide-range ultrasonic transducer and received by a wide-range AE sensor after propagating through a specimen. The width of the pulse is $0.8 \mu \text{ sec}$, and the input voltage is 65V. The analog data of the received waves was converted to the digital data in a A/D converter with the sampling frequency of 2MHz. Finally, the velocity and the frequency distribution of the elastic waves were calculated and evaluated. The frequency distribution was obtained from the FFT procedure.

The surface of the specimens was grounded and greased, and the moisture condition was controlled to be the saturated surface dry.

The waveform of the transmitted waves through a aluminum plate and its frequency distribution are shown in Fig.2 and Fig.3, respectively. From Fig.3, it was confirmed that the transmitted waves in this study had a very wide frequency distribution of 0-500 kHz.

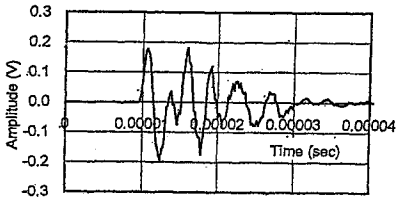


Fig.2 Waveform of Elastic Waves Propagating Through Aluminum

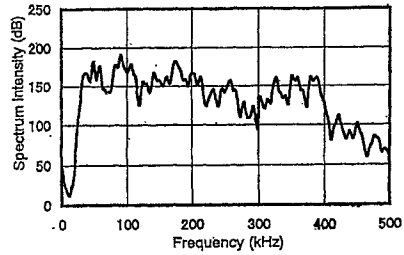


Fig.3 Frequency Distribution of Elastic Waves Propagating Through Aluminum

Experimental Results and Discussions

Influences of Size and Amount of Model Aggregates on Elastic Waves Velocity. In Fig.4, the influence of the diameter, in Fig.5, the influence of the volume percentage, of model aggregates on the velocity are shown respectively. From these figures, the influence of the volume percentage of model aggregates is much larger than the diameter.

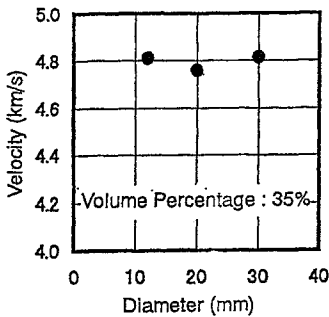


Fig.4 Influence of Diameter on Elastic Waves Velocity

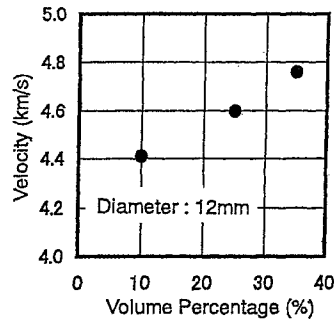


Fig.5 Influence of Volume Percentage on Elastic Waves Velocity

Influences of Size and Amount of Model Aggregates on Frequency Characteristics. In Fig.6, the influence of the diameter, in Fig.7, the influence of the volume percentages, of model aggregates on the frequency distribution are shown respectively. From these figures, the larger the diameter or the volume percentage of model aggregates, the decrease of the high frequency component is getting larger.

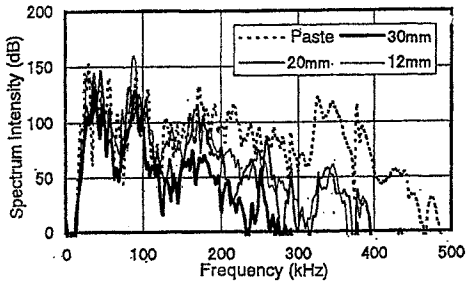


Fig.6 Influence of Diameter on Frequency Distribution

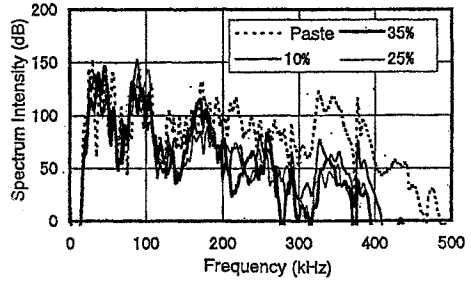


Fig.7 Influence of Volume Percentage on Frequency Distribution

This attenuation is especially clear in the frequency range of 200-400kHz, which is equivalent to the wavelength as much as the model aggregates' diameter. From this fact, the attenuation of the elastic waves is supposed to be due to the scattering of waves by model aggregates. To compare the influences of diameter and volume percentage of model aggregates on the attenuation, an index called "average frequency, Fave" is defined by formula (1).

$$F_{ave} = \frac{\int f \cdot S(f) df}{\int S(f) df} \tag{1}$$

(Note, f : frequency , S(f) : spectrum intensity at f)

This Fave becomes smaller when the high frequency ingredient attenuates. In Fig.8, the influence of the diameter, in Fig.9, the influence of the volume percentage, of model aggregates on this index "Fave" are shown respectively. Comparing these two figures, it is recognized that the influence of the diameter is larger on the frequency characteristics.

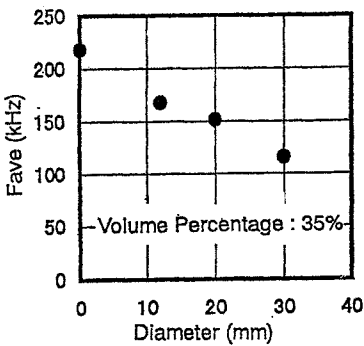


Fig.8 Influence of Diameter on Fave

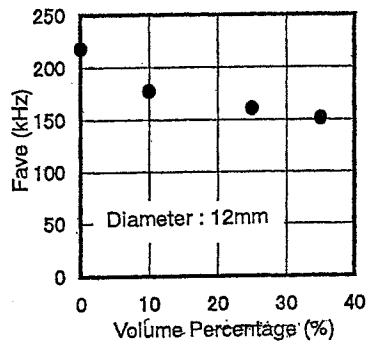


Fig.9 Influence of Volume Percentage on Fave

Influence of Acoustical Impedance (Differences Between Glass Balls and Steel Balls). The elastic waves velocities through the specimens with glass balls and steel balls (in the case the volume percentage is 25%) are 4.42 km/sec and 4.60 km/sec, respectively. Concerning to the attenuation in the high frequency region, the attenuation with steel balls is larger than that of with glass balls. Also, the reason is related to the acoustical impedance.

Theoretical Considerations

Examination about Elastic Waves Velocity. Theoretically, the elastic waves velocity can be calculated in the following formula.

$$V = \sqrt{\frac{E(1-\nu)}{\rho(1+\nu)(1-2\nu)}} \quad (2)$$

(Note, E : elastic modulus, ρ : density, ν : Poisson's ratio)

In this equation, the elastic waves velocity can be obtained from the data set of E, ρ , and ν of the material considered. In the calculations, the specimen used is assumed to be a 2-phase material [2].

Table 1 Values used for Calculation

Materials	Density (g/cm ³)	Velocity (km/s)	Poisson's Ratio
Cement Paste (W/C=0.3)	2.21	4.33	0.242
Glass Balls	2.50	5.60	0.200
Steel Balls	7.86	5.95	0.300
Cement Paste (W/C=0.5)	1.97	3.72	0.265
Aggregates	2.61	5.63	0.200

There are four equations which relates K, K₀, K₁, G, G₀, G₁, E, and

$$\frac{K}{K_0} = 1 + \frac{r}{\frac{3(1-r)K_0}{3K_0 + 4G_0} + \frac{K_0}{K_1 - K_0}} \quad (3)$$

$$\frac{G}{G_0} = 1 + \frac{r}{\frac{6(1-r)(K_0 + 2G_0)}{5(3K_0 + 4G_0)} + \frac{G_0}{G_1 - G_0}} \quad (4)$$

$$K = \frac{E}{3(1-2\nu)} \quad (5)$$

$$G = \frac{E}{2(1+\nu)} \quad (6)$$

(Note, K, G : volume elastic coefficient and stiffness of 2-phase composite material, K₀, G₀ : those of cement paste matrix, K₁, G₁ : those of inclusion, r : volume ratio of inclusion)

So, if the $K_0, K_1, G_0, G_1,$ and r are given, E and ν of the 2-phase composite material can be calculated from equations (3) to (6). To calculate $K_0, K_1, G_0,$ and G_1 for each material (cement paste, glass balls, and steel balls), the longitudinal waves velocity V_p (usually referred as elastic waves velocity V), ρ , and ν should be known. Then, with the formula (7) as shown below, the shear waves velocity (V_s) can be calculated. Then with the values of V_p and V_s , the K and G can be known with equations (8) and (9). Hence, the elastic waves velocity through the specimen with model aggregates can be calculated by the equation (2), by using the values of $V, \rho,$ and ν for each ingredient.

$$V_s = \sqrt{\frac{1-2\nu}{2(1-\nu)}} V_p \tag{7}$$

$$\frac{3K + 4G}{3} = \rho \cdot V_p^2 \tag{8}$$

$$G = \rho \cdot V_s^2 \tag{9}$$

The relationship between the calculated values with this method and measured ones is shown in Fig.10. From this figure, the validity of this theory is confirmed and also the larger influence of the volume percentage on the velocity is confirmed. Consequently, the concrete is considered to be treated as a 2-phase material in which the particles dispersed randomly in a uniform matrix.

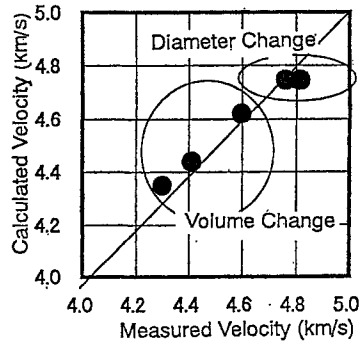


Fig.10 Relationship Between Calculated Elastic Waves Velocity and Measured One

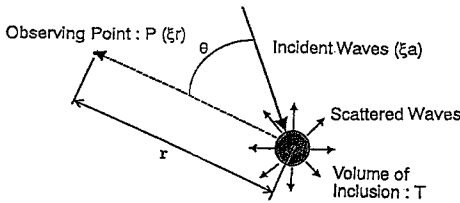


Fig.11 Concept of Scattering of Elastic Waves

Examination about Frequency Characteristics. To investigate the influences of the diameter and the volume percentage on the UEWP through concrete, a model of the scattering of the elastic waves, as shown in Fig.11, was introduced. In this case, the ratio of the amplitude of the scattered waves at P to that of the incident waves, ξ_r / ξ_a , is theoretically given by Rayleigh [3] as shown in the formula (10). In this formula, it is assumed that the matrix is uniform and the wavelength is smaller than the diameter of the inclusion.

$$\frac{\xi_r}{\xi_a} = \frac{\pi T}{r \lambda^2} \left(\frac{K_1 - K_0}{K_0} + \frac{\rho_1 - \rho_0}{\rho_0} \cos \theta \right) \tag{10}$$

(Note, λ :wavelength, ρ_0 : density of matrix, ρ_1 : density of inclusion, K_0 : acoustical impedance of matrix, K_1 : acoustical impedance of inclusion, T : volume of inclusion)

With this formula, the attenuation coefficient of the elastic waves can be given by Mason [4] as shown in the formula (11). In this formula, the effect of multi scattering is neglected and the particles are randomly arranged in a three-dimensional space.

$$\alpha = \frac{2\pi^3 r \cdot T}{\lambda^4} \left(\frac{K_1 - K_0}{K_0} \right)^2 \quad (11)$$

(Note, r : volume ratio of inclusion)

By using this formula, the influences of the diameter, the volume percentage, and the acoustical impedance are calculated and shown in Figs. 12, 13, 14, respectively. From these figures, the influence of the diameter is the largest of the three factors. And, the difference in the frequency distribution due to the acoustical impedance can be explained as follows. The larger the acoustical impedance, the larger the value of K as reference to formula (8) and (9). The larger value of K causes the higher attenuation in the frequency distribution, especially in a higher frequency range, as shown in formula (11).

It can be concluded that the experimental results are well explained by theoretical considerations.

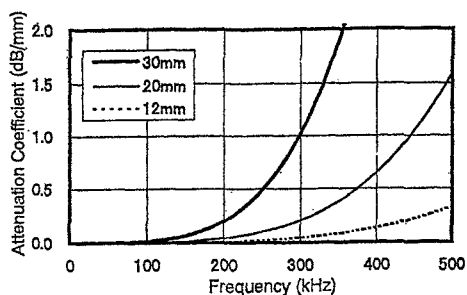


Fig.12 Influence of Diameter on Attenuation Coefficient
(Glass Balls, Volume Percentage: 35%)

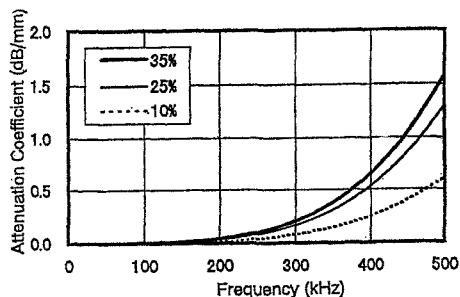


Fig.13 Influence of Volume Percentage on Attenuation Coefficient
(Glass Balls, Diameter: 12mm)

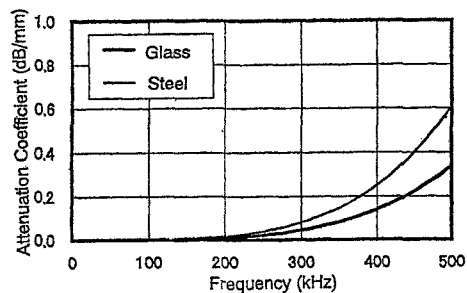


Fig.14 Influence of Acoustical Impedance on Attenuation Rate
(Diameter: 12mm, Volume Percentage: 25%)

INFLUENCE OF ACTUAL AGGREGATES ON ULTRASONIC ELASTIC WAVES PROPAGATION IN CONCRETE

In this chapter, the results with model aggregates will be confirmed through the investigation with actual aggregates.

Examination about Maximum Size of Aggregates

Outline of Specimens. The used specimen was 100×200×200(mm) prism. Three specimens were employed in each testing condition. The mixture proportions of the specimens are No.1 and No.2 in Table 2. The W/C of cement paste was 0.50, and the ordinary Portland cement was used as a binder. River sand and gravel were used as actual aggregates. The maximum sizes of the aggregates were 0.6, 1.2, 2.5, 5, 10, 20(mm).

The volume percentages of aggregates were controlled to be 54% (in the case the maximum size of aggregates was 0.6, 1.2, 2.5, 5 (mm), namely, mortar) and 68% (in the case the maximum size was 10 and 20 (mm), namely, concrete). The specific gravity, the water absorption ratio, and the fineness modulus of the river sand are 2.59, 1.41%, 2.26. Those of the gravel are 2.60, 1.67%, 6.68.

Table 2 Mixture Proportion of Concrete

No.	Slump (cm)	Air (%)	W/C	Va*1 (%)	Unit Weight (kg/m ³)				
					W	C	S	G	Ad
1	-	6±1	0.50	54	258	515	1288	-	-
2	8±2.5	1±1	0.50	68	190	380	783	980	-
3	8±2.5	1±1	0.50	68	190	380	783	984	-
4	8±2.5	1±1	0.50	55	272	544	636	783	2.7*2
5	8±2.5	1±1	0.50	78	127	254	911	1122	2.1*3

*1 Volume percentage of Aggregates *2 Segregation Reducing Agent *3 Superplasticizer

Experimental Results and Discussions. The relationship between the maximum size and the elastic waves velocity is shown in Fig.15. As mentioned above, the volume percentages of mortar and concrete are different, so in this figure, the measured data is separated into two groups. And, the two dotted lines indicate the theoretical waves velocity for each material, calculated as the previous chapter, assuming complete bonding between the matrix and inclusions.

From this figure, little influence of the size of aggregates on the elastic waves velocity can be seen, and there is a tendency that the measured velocity is smaller than the theoretical one, especially the smaller the maximum size. The reason is assumed to be the existence of interfacial transition zones (hereafter referred as ITZ). Since the porosity of ITZ is higher than the bulk of cement paste matrix, the mechanical and physical properties of ITZ is said to be worse. The amount of ITZ can be calculated by formula (12) with the assumption of the thickness of ITZ is 50 μm [5].

$$S = \frac{6}{\rho \cdot d} \quad (12)$$

(Note, S : specific surface area, ρ : density of aggregates, d : diameter of aggregates)

As the maximum size of aggregates becomes smaller, the amount of ITZ becomes larger. The existence of ITZ is one of the reasons why there is a difference between the measured velocity

and the calculated one.

In Fig.16, the relationship between the maximum size of aggregates F_{ave} , is shown. From this figure, it is clear that the larger the maximum size of aggregates, the value of F_{ave} becomes smaller, and this tendency is quite the same clarified with model aggregates.

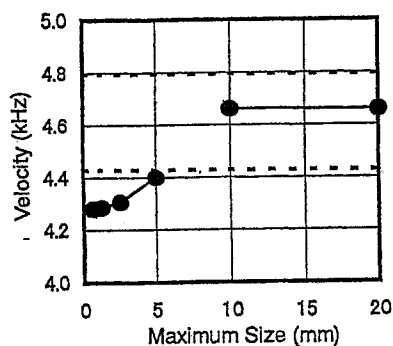


Fig.15 Influence of Maximum Size of Actual Aggregates on Velocity

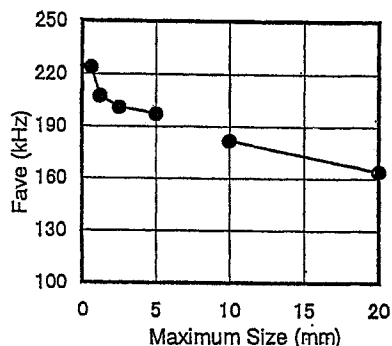


Fig.16 Influence of Maximum Size of Actual Aggregates on F_{ave}

Examination about Volume Percentage of Aggregates

Outline of Specimens. In this section, the volume percentages were selected to be 55%, 68%, and 78% and the influence of this factor was clarified. Then, the W/C was 0.50, and the maximum size of aggregates was 20mm. The shape and dimensions of the specimens was 100×200×200(mm) prism. The mixture proportions are shown in No.3-5 in Table 2, and the material used for mixing were the same as those of the previous section (2).

Experimental Results and Discussions. The relationship between the volume percentage and the elastic waves velocity is shown in Fig.17. It can be seen that the larger the volume percentage, the larger the velocity. The tendency is similar in the case of model aggregates and the theoretical calculations. And, this variation of the velocity is larger than that due to the difference of the maximum size, as mentioned in (1).

The elastic waves frequency distribution in each volume percentage are shown in Fig.18. It can be seen that the reduction of the spectrum intensity in the frequency range greater than 200kHz is recognized clearer as the volume percentage of aggregates becomes larger. This is because the scattering of waves became remarkable with the increase in the amount of aggregates. These results are also the same in the case of model aggregate.

From these results, the volume percentage of aggregate influences the frequency characteristics of the elastic waves propagating through concrete as well as the velocity.

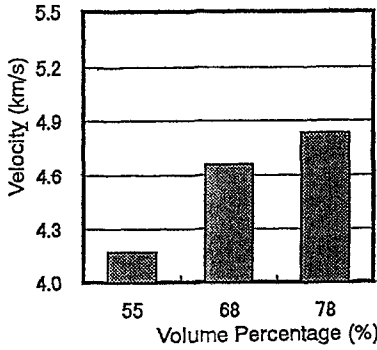


Fig.17 Influence of Volume Percentage of Actual Aggregates on Velocity

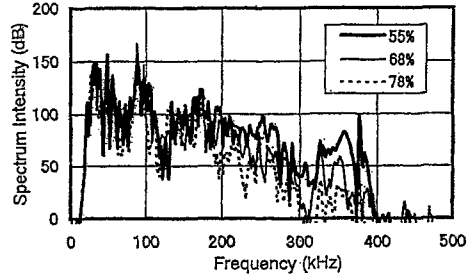


Fig.18 Influence of Volume Percentage of Actual Aggregates on Frequency Distribution

CONCLUSIONS

As results of the investigations with model aggregates and actual aggregates, conclusions are made as follows;

- (1) The maximum size of aggregates is very influential on the frequency characteristics of the UEWP through concrete, especially within the frequencies larger than 200kHz. However, this factor is not influential on the velocity.
- (2) The volume percentage of aggregate is a decisive factor for both the velocity and frequency characteristics of the elastic waves propagating through concrete.
- (3) The results mentioned (1) and (2) are confirmed by theoretical calculations.

REFERENCES

1. British Standards Institution (1986). In: Recommendations for Measurements Velocity of Ultrasonic Pulses in Concrete, BS 1881, Part 203, pp.618-619
2. Weng, G.J. (1984) In: Some Elastic Properties of Reinforced Solids, with Special Reference to Isotropic Ones Containing Spherical Inclusions, International Journal of Engineering Science, Vol.22, pp.845-856
2. Rayleigh, L. (1929) In: The Theory of Sound, Vol.II, p.152
3. Mason, W.P. , and McSkimin, H.J. (1947) In: Attenuation and Scattering of High Frequency Sound Waves in Metals and Glasses, Journal of Acoustical Society of America, Vol.19, No.3, pp.464-473
4. Mindess, S. (1989) In: Interfaces in Concrete, Materials Science of Concrete, pp.163-180

DIFFERENTIAL APPROACH TO ULTRASONIC TESTING OF STRENGTH AND HOMOGENEITY OF CONCRETE

E. NESVIJSKI, T. NESVIJSKI, and A. LORENZI
*Center of Technology, Federal University of Santa Maria
Campus Universitário, Santa Maria, 97110-900, RS, Brazil*

ABSTRACT

In spite of the fact that new technologies and materials are developing in the field of civil engineering, such traditional materials as concrete still secure their important place in infrastructure construction. Bridges, tunnels, dams, highways, offshore structures etc. are the main consumers of concrete. Destructive and nondestructive testing (NDT) methods provide means for quality testing and control of concrete structures. Destructive methods are applied for testing of strength and modules of plasticity and elasticity of standard concrete specimens. Application of NDT methods also requires destructive testing of standard specimens for calibration. The task of testing data transfer from specimens to real structures contains several problems. Ultrasonic testing by differential approach can solve problems connected with identification and classification of properties of concrete in structures. This approach is based on "point by point" surface sounding of cylindrical specimens and real concrete structures. The dry point contact transducers were used for "point by point" ultrasonic testing. The obtained experimental data is considered as stochastic space rows. It gives the opportunity to use modern statistical analysis and elements of artificial intelligence. The described approach allows improving reliability of estimation of strength and homogeneity of concrete.

KEYWORDS

Civil engineering, concrete, nondestructive testing, ultrasonics, strength.

INTRODUCTION

Destructive and nondestructive testing (NDT) methods provide means for quality testing and monitoring of concrete structures. Destructive methods are applied for testing of strength and modules of plasticity and elasticity of standard concrete specimens. Application of NDT methods also requires destructive testing of standard specimens for calibration. Some standard ultrasonic methods are applied for estimation of concrete properties [1]. The standard methodology of ultrasonic application is based on the "integral approach" to ultrasonic testing. That means that ultrasonic pulse is propagating through the body of a concrete specimen evaluating all mechanical properties on cross-section of the testing sample. Practical application of this method is based on traditional ultrasonic equipment using plate surface transducers. As a rules, ultrasonic transducers for concrete applications are low frequency plate surface transducers (25-60 kHz) with considerable diameter of contact plates [2]. These

transducers cause some problems for standard calibration method of testing concrete cylinder specimens.

STANDARD REQUIREMENTS (ASTM) AND CURING STUDY

Standard test method for cylindrical concrete specimens is covered by ASTM C 39-96 Standard [3]. This document regulates size of test specimens, procedure of compressive load testing and contains requirements to the machine design, and its accuracy (1%). Individual diameter of specimens should not differ from any other diameter of the same specimen by more than 2%. The time-table of the standard tolerances is given in the Table 1.

Table 1. Time-Table For Concrete Cylinder Testing

1	2	3	4	5
24 Hours	3 Day	7 Day	28 Day	90 Day
± 0.5 hours or 2.1%	± 2 hours or 2.8%	± 6 hours or 3.6%	± 20 hours or 3.0%	± 2 days or 2.2%

The single operator precision of compression tests of cylinders with size 6 by 12 inches (150 by 300 mm) made from a well-mixed concrete and cured in a laboratory environment and under normal field conditions. The requirements of this standard are very strict and hard to accomplish in practice. There is also influence of human factor, when an operator can contribute to inaccuracy. If it possible to describe these uncertain factors as τ -factor (current errors in-situ) the following formula is used for evaluation of strength of concrete cylinders $R(\tau)$:

$$R(\tau) = \left\{ \left[\frac{P_{MAX}(\tau)}{\pi \cdot D(\tau)^2} \right] + E(\tau) \right\} \quad (1)$$

where $P_{MAX}(\tau)$ - fixed maximum pressure on cylinder (that also has some variations); $D(\tau)$ - diameter of concrete cylinder, $E(\tau) = \sum_{\tau} \varepsilon_{\tau}$ -sum of errors produced by other τ -factors.

Modeling of time related concrete curing could be realized as regression function, for example:

$$R(t, \tau) = \left\{ \left[A \cdot R(\tau) \left(\frac{B}{1 - \ln(t)} \right) \right] + E^*(\tau) \right\} \quad (2)$$

where A, B - experimental coefficients and $E^*(\tau)$ - standard error of fitting regression line. Selection of regression function could be made by minimum dispersion or data variance.

That is why, standard procedure of compressive testing of concrete cylinders for strength estimation should be considered as stochastic model, which requires adequate statistical instruments for analysis.

Though destructive testing of cylindrical concrete specimens is recognized as the main test method for strength estimation of concrete, it has a number of disadvantages: problems connected with inaccuracy of strength estimation described above, economical problems connected with considerable consumption of time, labor, and material resources and energy. But the most important problem is connected with necessity of translation of destructive testing results from specimens to real structures. Special approaches have been searched to make this translation reliable and effective. Differential approach to ultrasonic testing is proposed as a “bridge” between estimation of strength of concrete specimens and structures.

ULTRASONIC TESTING OF CONCRETE CYLINDERS

There are many problems connected with estimation of strength of cylindrical concrete specimens by ultrasonic testing:

- Strength of concrete is not functionally connected with modules of elasticity, but has a regression relation;
- Modules of elasticity calculated on the base of ultrasonic measurement data are dynamic modules and require special coefficients for recalculation to standard static modules of elasticity;
- Estimation of dynamic modules of elasticity by ultrasound require identification of the wave types for correct choice of formula for calculation of modules depending on the wave velocity;
- Measurements of velocity of different wave types require special techniques and apparatus.

Some of the problems are considered below.

Ultrasonic wave propagation on cylinder specimen

In order to keep uniformity of ultrasonic measurements of cylinder specimens and real structures it would be recommended to use surface testing. Different types of surface waves are used for these purposes depending on the location of transducers on the testing surface. In the case of “vertical” surface testing of cylinders Rayleigh and sub-surface longitudinal waves are used [4]. In case of “horizontal” surface testing bulk (longitudinal and shear) waves are used. Usage of ultrasonic velocity values of each pair of waves allows to calculate all effective elastic dynamic modules: E – Young module, G – ahift module, K – volume module, μ, λ – Lamé constants, σ – Poisson ration, l, m, n – modules of the third degree (Murnaghan) [5]. Poisson ratio is calculated as

$$\sigma = \frac{\lambda}{2(\mu + \lambda)} \quad (3)$$

Relation between velocity of longitudinal V_L and shear V_t waves is the following

$$V_L = V_t \cdot \sqrt{\frac{2(1-\sigma)}{1-2\sigma}} \quad (4)$$

Connection between velocity of shear waves V_t , module of elasticity E , Poisson ratio σ , and density ρ of material could be described

$$V_t = \sqrt{\frac{E}{2\rho(1+\sigma)}} \quad (5)$$

Dependency for shear module G

$$G = \frac{E}{2(1+\sigma)} \quad (6)$$

gives solution for velocity of sub-surfaces longitudinal waves [6]

$$V_{ss} \cong [1.425 + 0.299\sigma + 4.092\sigma^2] \cdot \sqrt{\frac{G}{\rho}} \quad (7)$$

Then it is possible to calculate coefficient $k(\sigma)$ connecting velocity of sub-surface V_{ss} and longitudinal V_L waves

$$k(\sigma) = \frac{V_{ss}}{V_L} \quad (8)$$

Calculated values of coefficient $k(\sigma)$ are shown in the Fig. 1.

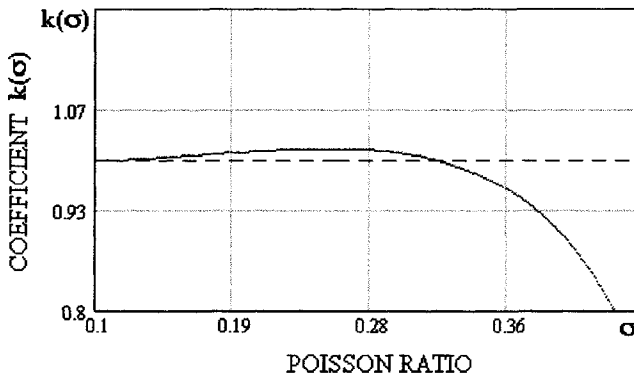


Fig. 1. Calculated values of coefficient $k(\sigma)$.

DPC transducers and differential approach to ultrasonic testing

The DPC transducers are new tools of ultrasonic testing of concrete. Their application have brought new features to the methodology of materials evaluation as they allowed to increase accuracy of ultrasonic data measurements. High repeatability of measurements and point-by-point testing have opened doors for application of differential approach to ultrasonic testing [7].

Differential approach is based on “point by point” surface testing of cylindrical specimens and real concrete structures. The obtained experimental data is considered as stochastic space rows. It gives the opportunity to use modern statistical analysis and elements of artificial

intelligence. The described approach allows improving reliability of estimation of strength and homogeneity of concrete.

Experimental Set-up

Experimental set-up was in accordance with the ASTM C39-96 [3]. Three types of hard concrete were used of planned strength $R(t) = 4.5, 9.0,$ and 12.0 MPa. The schematic of the experimental set-up is given in Fig.2.

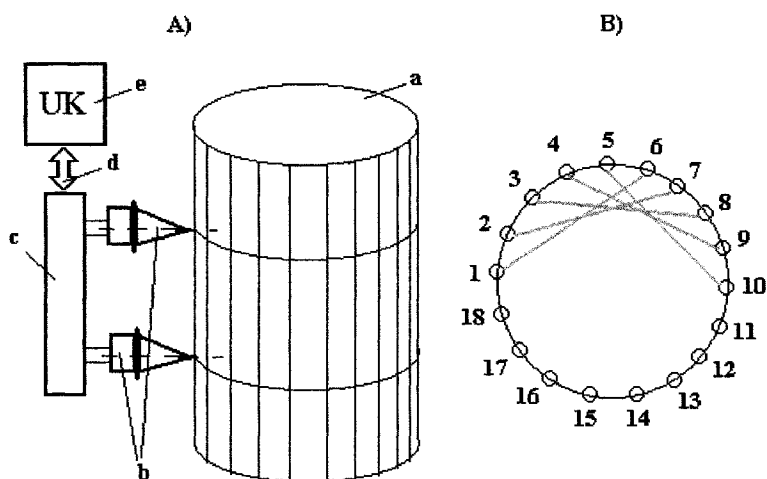


Fig. 2. Experimental set-up for ultrasonic testing of concrete cylindrical specimens.

A) "vertical" testing: a – concrete cylinder; b – the DPC transducers; c – pre-amplifier; d – interface; e – ultrasonic equipment UK-14P. B) Scheme of the "horizontal" testing.

Experimental results

Testing of the cylindrical concrete specimens were carried out using the differential approach that gave the opportunity to receive representative quantity of measurement data. The results of "vertical" testing are presented in the Fig. 3 and the results of "horizontal" testing are presented in the Fig. 4 as histograms of ultrasonic velocity values.

Strength, R (MPa)	4,5 MPa	9,0 MPa	12,0 MPa
Data			
12.08.98 30 days	 Mean(V)=3014,444	 Mean(V)=3309,594	 Mean(V)=3715,278

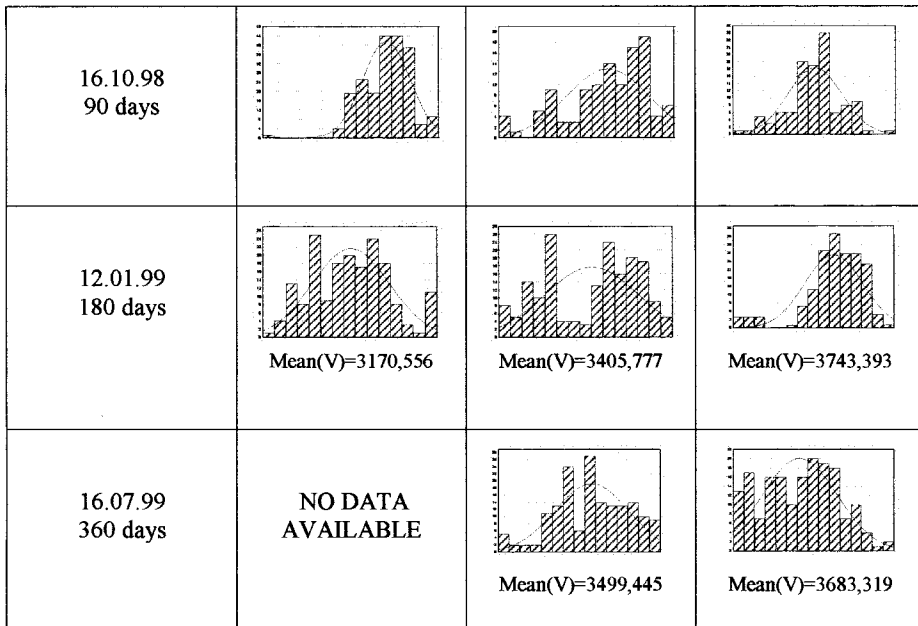
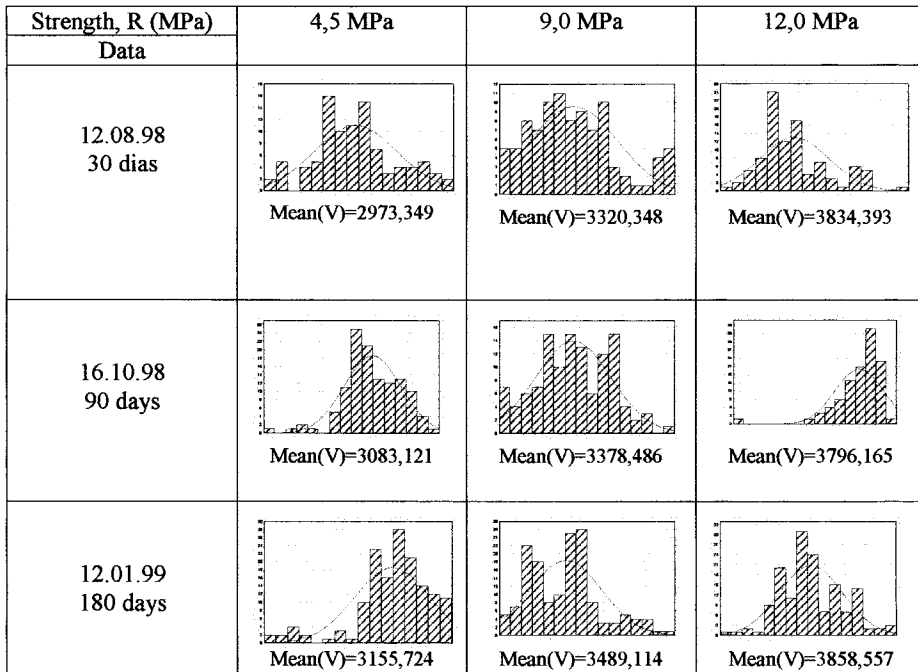


Fig. 3. Histogram of ultrasonic velocity values of “vertical” testing



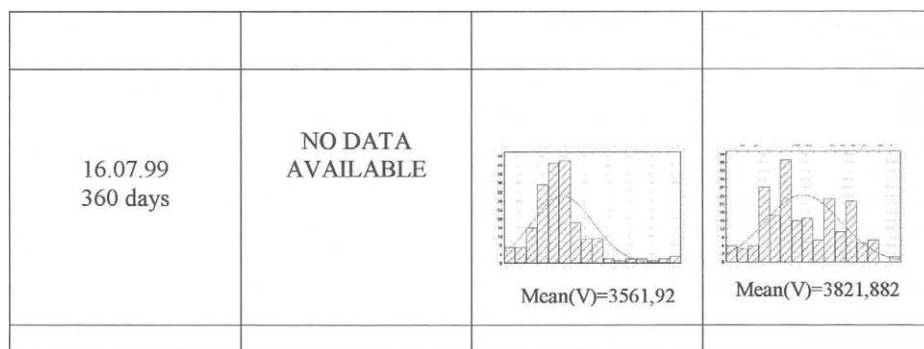


Fig. 4. Histogram of ultrasonic velocity values of “horizontal” testing

Statistical evaluation of coefficient $k(\sigma)$

The obtained experimental data allowed to make statistical evaluation coefficient $k(\sigma)$ equal to relation between statistical means of sub-surface V_{ss} wave velocities (“vertical” testing) and longitudinal V_L wave (“horizontal” testing) velocities as 3-D regression surface is given in the Fig. 5. Curing time t and strength $R(\sigma)$ were used as parameters.

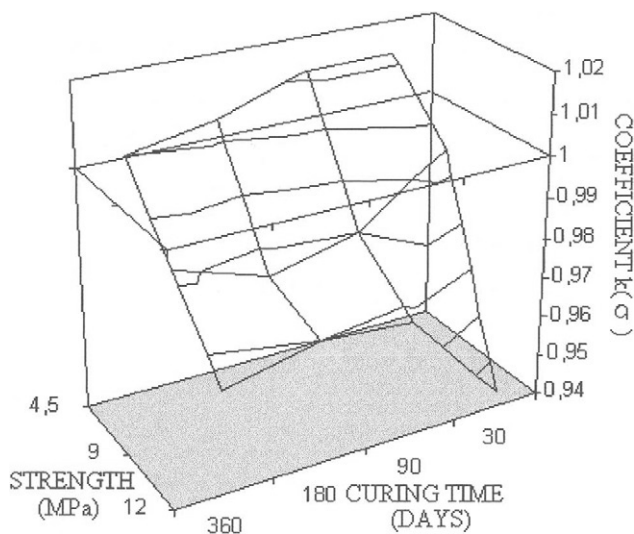


Fig. 5. Evaluation of coefficient $k(\sigma)$ using “vertical” and “horizontal” ultrasonic testing.

CONCLUSIONS

The described research demonstrated a new vision of the problems of the standard strength testing of concrete, where application of ultrasonics could build a bridge between the

laboratory testing data and properties of the material in real structures. A new differential approach is proposed based on utilization of the DPC transducers. The advantages of the new techniques are shown and some problems are analyzed.

Experimental data received on cylindrical concrete specimens bare stochastic character and require special instrumentation for processing. Some statistical parameters, such as mean of velocity of different types of ultrasonic waves give good convergence with theoretical premises.

The proposed approach could serve as a base for creation of a new standard for estimation of strength of cylindrical concrete specimens. This standard could unite destructive and nondestructive concrete testing for practical tasks of civil engineering with improved accuracy of the material strength estimation.

REFERENCES

1. Standard Test Method for Pulse Velocity Through Concrete, ASTM: C597-97, Annual Book of ASTM Standards, Vol. 0402 *Concrete and Aggregates*, 1999.
2. S. Popovics, *Strength and Related Properties of Concrete - A Quantitative Approach*, John Wiley and Sons, New York, 1998.
3. Standard Test Method for Compressive Strength of Cylindrical Concrete Specimens, ASTM: C39-96, Annual Book of ASTM Standards, Vol. 0402 *Concrete and Aggregates*, 1999.
4. Dzenis, V.V., *Application of the Ultrasonic Transducers with Point Contact for the Nondestructive Testing*, "Zinetne", Riga, Latvia, 1987.
5. Frantsevich, I.N., Voronov, F.F., and Bakuta, S.A., *Elastic Constants and Modules of Elasticity of Metals and Non-Metals*, "Naukova Dumka", Kiev, Ukraine, 1982 (in Russian).
6. Nesvijski, E.G., On the Matter of Physical Nature of the So Called Longitudinal Sub-Surface waves, in: *Proceedings of the Seventh International Symposium on Nondestructive Characterization of Materials*, Prague, Czech Republic, June 19-23, 1995.
7. Nesvijski, E.G., On the Problem of Application of the Conic and Exponential Wave Guiding Extensions for Ultrasonic Transducers for Materials Testing, in: *NASTA Technical Bulletin*, Philadelphia, PA, USA, 1997 (ISSN 1079-8498).

**MEASUREMENTS OF THICKNESS AND CRACK DEPTH
IN CONCRETE BY ULTRASONIC METHODS**

TETSUO YAMAGUCHI and TATSUO YAMAGUCHI
Toyoko Elmes Co;Ltd, Tokyo,Japan

ABSTRACT

An ultrasonic reflected-wave method and apparatus developed for the thickness measurement of concrete is presented in this paper. Fourier spectra analysis of received waves is employed to separate low amplitude reflected waves from large amplitude useless direct waves. NDT by this method is also discussed.

Another ultrasonic measurement of crack depth by the diffracted waves which proceeds in the direction of right angle to that of the direct waves at the edge of crack in RC structures is also shown. By setting the direction of two probes in oblique angle to that of bars, disturbing waves diffracted from the bars passing through the cracks, are eliminated and the crack depth is measured.

KEY WORDS

Ultrasonic Measurement, Thickness, FFT analysis, Crack Depth Measurement

INTRODUCTION

It is important to apply the non-destructive testing of thickness as well as internal defects in concrete structures. Principle of an ultrasonic reflected wave method and apparatus developed for the object is discussed in this paper [1]. An improved right angle diffracted wave method by oblique angle set in order to measure the depth of cracks which passing through reinforcing bars is also discussed[2,3,4].

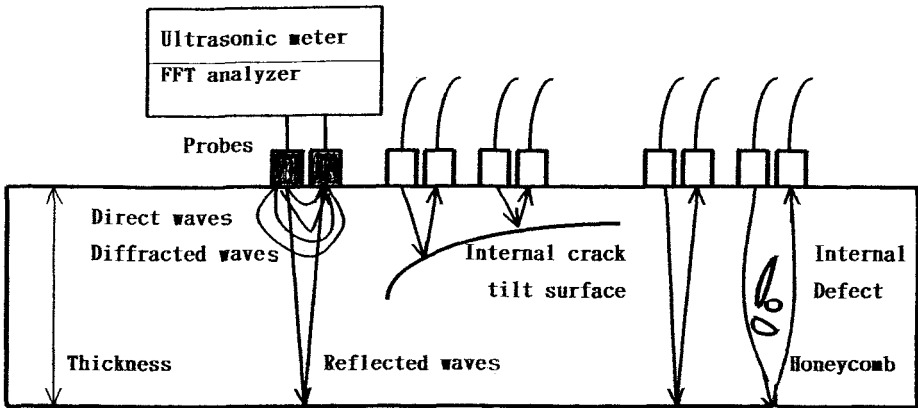


Fig.1 Measurement of thickness and anomalies for a slab

PRINCIPLE OF THICKNESS MEASUREMENT

Thickness measurement of concrete by reflected-wave method is not so easy. The arrangement of the method is shown in Fig. 1. The received direct waves including near by diffracted waves from the transmit probe, are very high amplitude and last for a long time during the arriving times of reflected waves. But the needed reflected waves are very low amplitude. In case of 500mm thick concrete, the amplitude of received waves are only 1/ 100 to 1/ 50 in the direct waves. Fourier spectra analysis of received waves is employed to effectively separate low amplitude reflected signal waves from large amplitude useless direct waves. In this measurement, the thickness d is given by the equation $2d/c=s/1/f$, where c is the pulse velocity, s is the arrival time of reflected-wave. The thickness d is given from the frequency f that is reciprocal of arrival time s .

Heavy damped short pulse probes with wide frequency range, are used to avoid the interference error of waves on the thickness measurement. The thickness is measured by single pulse, but not the resonance frequency of multiple reflection, although FFT analyzer is used. The apparatus can measure the reflection from a tilt surface of internal crack. The existence, extent and degrees of internal defects is measured by this method as illustrated in Fig.1.

MEASURING METHOD OF THICKNESS

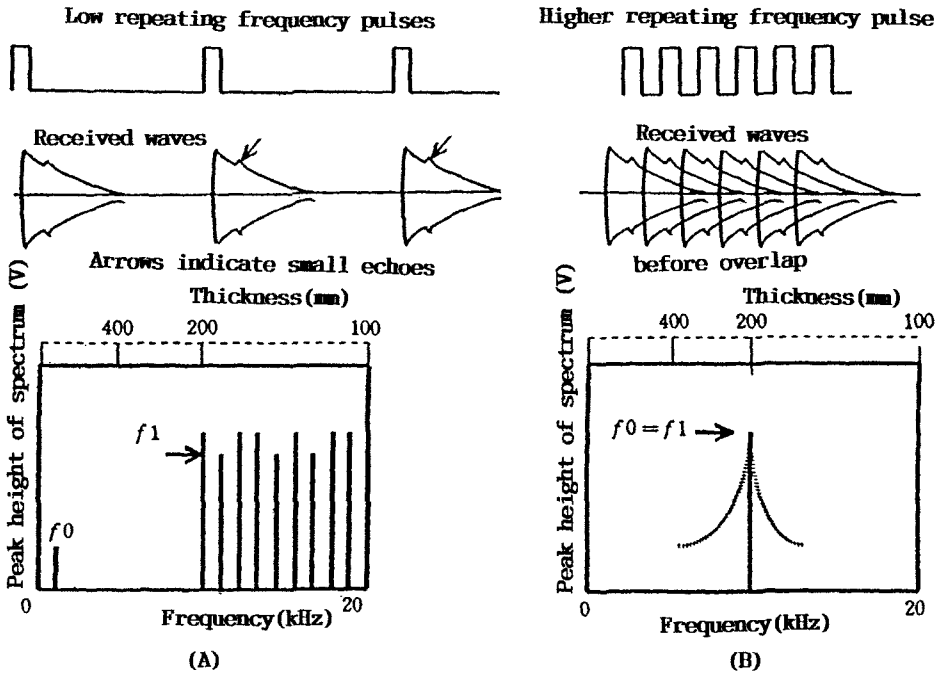


Fig.2 The No.1 and No.2 method of thickness measurement

No.1 Method

Three different types of method are prepared. In the No.1 method, illustrated in Fig.2(A), transmitted pulses are of a low repeating frequencies f_0 such as 1 kHz. All of periodical received waves mostly consisting of useless direct waves, is Fourier analysed as one phenomena. In the figure of spectrum there is no spectrum in the region at low frequencies, and from a frequency of f_1 , many spectra appear to higher frequencies. Among many received waves in a fl at slab measurement, the spectrum of lowest frequency $f_1 = 1/s$ is for the thickness, corresponds to highest "s", because there is no more far distance of reflection than from thickness. The immediately analyzed FFT spectrum of the received waves give approximate values of the thickness. The resolving power of f_1 is not so good as the frequency of thickness $f_1 = 1/s$ is the higher factor of f_0 in Fourier spectra. But the immediate expression of the approximate thickness in FFT analyzer is useful for field measurement.

No.2 Method

In the No.2 method, illustrated in Fig.2(B) , the repeating frequency of pulses are increased so higher as to make the arrival times of reflected waves coincide with the period of the repeated pulses. The method is similar to that of the pulse echoes overlap method in case of the measurement of pulse velocity, in which the received waves are feed backed to the input of sending pulse, although the two probes are set at the opposite side of measuring materials. By increasing the repeating frequency of f_0 in Fig.2(B), a single spectrum corresponds to the repeating frequency, moves toward to higher frequencies and at the frequency $f_0=f_1$, the spectrum indicates the maximum value superposing on the amplitude of reflected waves. Thus, the accurate frequency f_1 to evaluate the thickness is obtained from the maximum spectrum position. Two methods are used together in field for the reliability of the result.

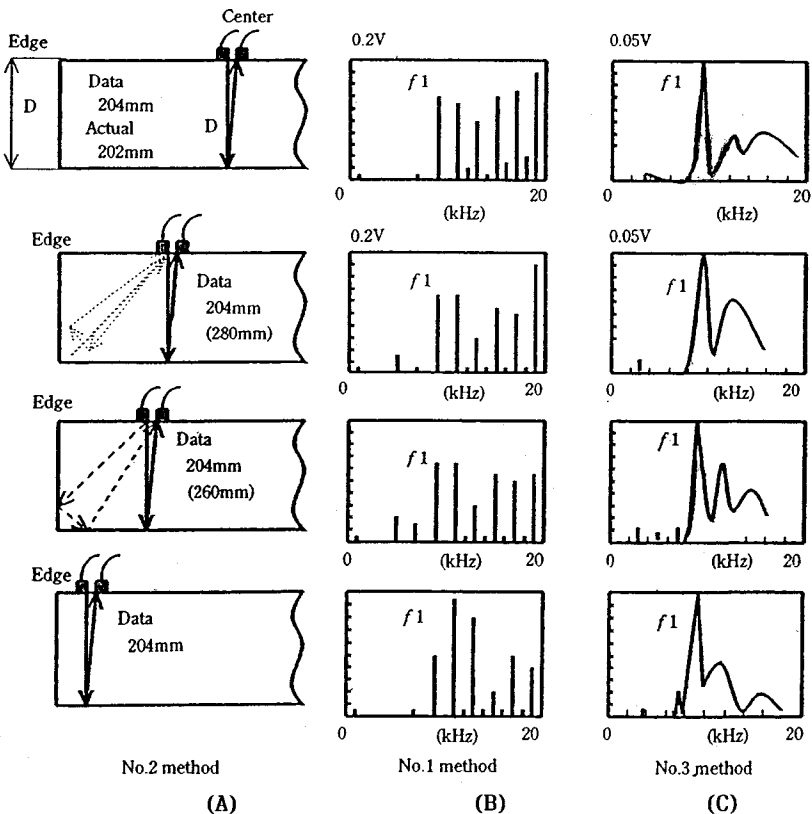


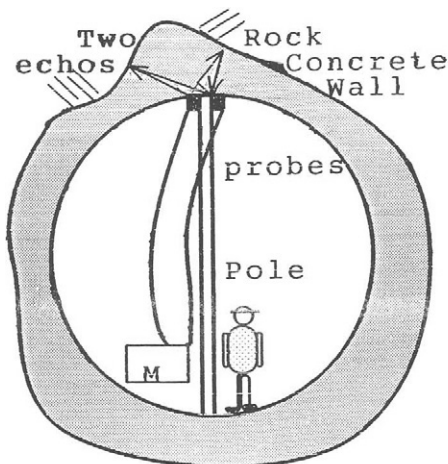
Fig.3 Effect of beam spread on thickness measurement near the edge of a slab

No.3 Method

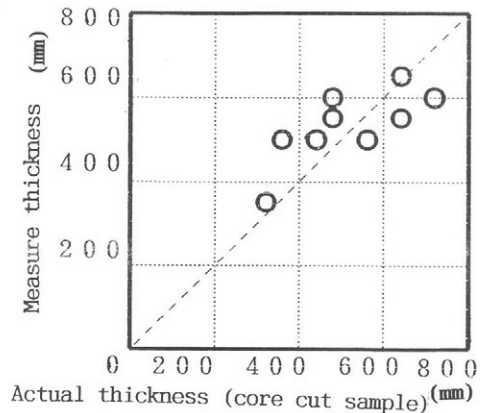
In the No.3 method, summed average spectra of pulses in No.1 method are obtained on FFT display, by changing repeating frequency f_0 . The frequency f_1 to evaluate the thickness is taken from the maximum point of summarized spectrum. Thus the resolving power of f on Fourier spectra in No.1 method is improved by just pushing the scan switch on the instrument. The example is given in Fig.3(C).

EFFECT OF BEAM SPREAD

Sometimes, the phenomena of beam spread effect of pulses appear in this measurement. If the thickness is measured near the edge of a slab as is shown in Fig.3, useless small reflected-waves from the bottom corner is received as well as that from needed bottom surface. The useless waves of lower frequencies than f_1 of thickness, lead to confusion on the thickness measurement. The measured results are shown in Fig.3, comparing with No.1 method. Numericals in Fig.3(A) in parentheses indicate the measured distances by No.2 method which corresponds to the diagonal distance from the probes to the corner. It is advisable to measure at the 50mm position from the edge, rather than at an angle of 45 degrees from the bottom corner.



(A) Tilt wall



(B) Relationship between actual and tested thickness

Fig. 4 Thickness measurement for uneven wall in tunnel

When the thickness is measured at uneven wall on the top of a tunnel in rock, 2-3 peaks of spectrum line were observed as a result of tilt surface of the reflection. The maximum peak was used in this measurement as for thickness. The relationship between actual and tested thickness is shown in Fig. 4. The pulse velocities of core cut samples are used as the velocity c of wall. Owing to the uneven thickness of wall, accuracy of the thickness is about 20%.

Surface of internal tilt cracks originated from sheer stress in a highway slab is detected by moving the position of the probes, as is shown in Fig. 1. Thickness measurement for sloped surface of retaining wall is applied in the same way.

MEASUREMENT OF SLAB AND WALL

Thickness of many construction such as slab, wall, tunnel, pillar, pipe, separation of walls, are measured by the method. The accuracy depends on that of estimated pulse velocity c . Pulse velocity of longitudinal waves on the surface of concrete is measured by changing the probes distances such as from 400 to 1000mm or to 1500mm . The pulse velocity for the concrete in thickness direction is estimated from an idea of the relationship curve between distances of two probes and pulse velocities c . Spectra of thickness measurement on the floor is given in Fig.5.

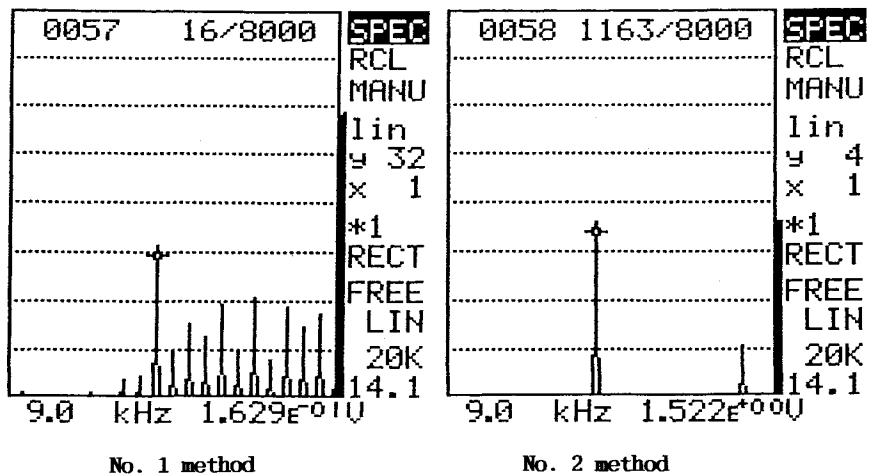


Fig. 5 Spectra of thickness measurement on the floor

MEASUREMENT OF INTERNAL DEFECT

Defects are detected by thickness measurement (Fig. 1). The thicknesses 450-700mm were measured as shown in Fig. 6, at the construction joint of many pillars. Defects were detected as apparently thicker parts than sound parts. The ratio of over 5% of two parts corresponded to defect from cut tests. The defects consisted of finger size hollows around the bars.

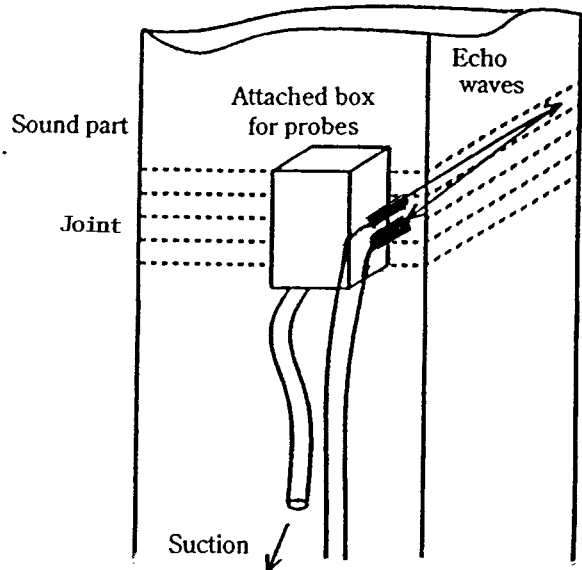


Fig. 6 Defect detection at the joint

MEASUREMENT OF CRACKS ON BACK SURFACE

Using the reflected wave No.1 method, it is possible to detect the invisible deep cracks on the back of wall. The probes are set on the measuring surface separating as shown in Fig.7. Propagation routes of pulses are intercepted by the crack that depth is over 1/2 of wall thickness and the spectrum disappears. Many tests were carried out on the walls under the ground.

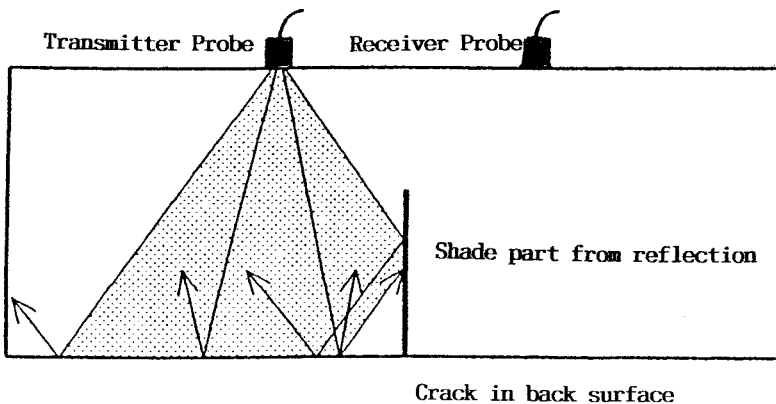


Fig. 7 Detect of back crack by reflected wave method

CRACK DEPTH MEASUREMENT BY OBLIQUE SET OF PROBES

The principle of the measurement of crack depth by diffracted wave in right angle to the direct waves is illustrated in Fig.8. Using the method, measurement of the crack which crossing steel bars, had been studied.

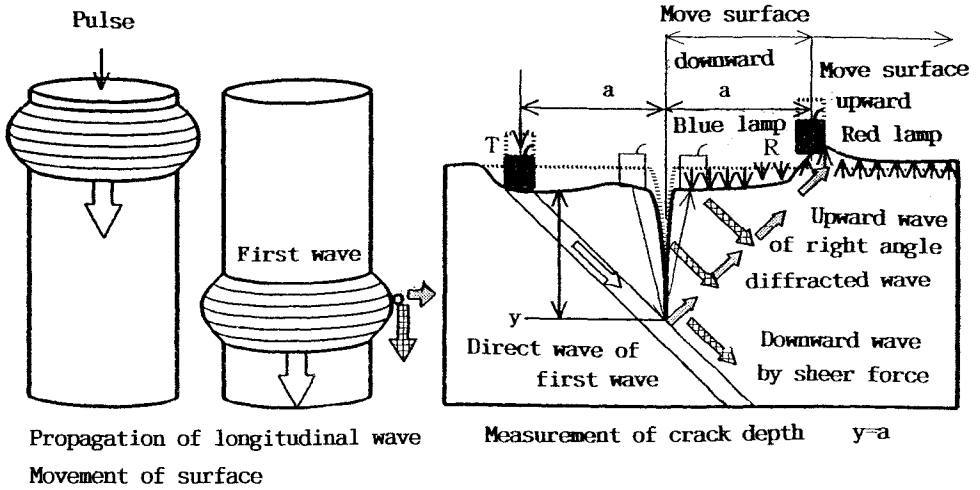
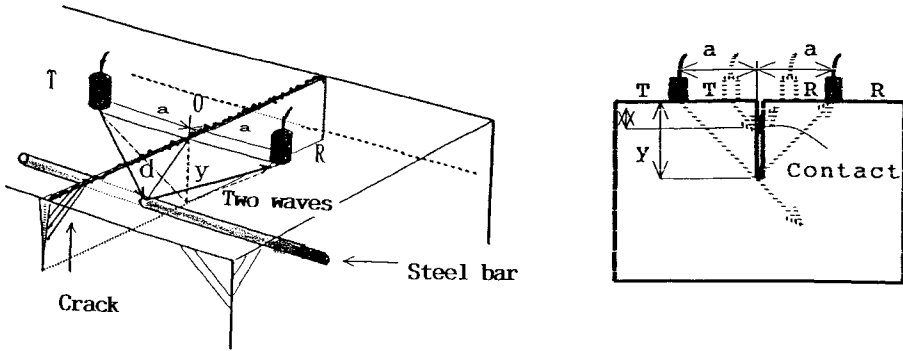


Fig.8 Illustration of the principle of diffracted wave method

In case of parallel set of two probes to the bars, as is shown in Fig.9(A), disturbing waves diffracted from the bar in a solid right angle are received, simultaneously with the needed waves from the bottom edge of the crack. The phenomena are similar to the case of contact in a crack as shown in Fig.9(B). When the contact is measured in the process of increasing the distances of two probes, two depths correspond to contact and crack depth are obtained separately.

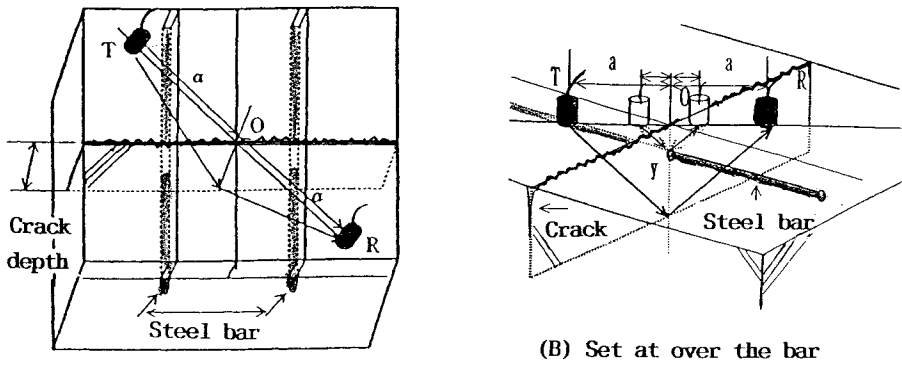
In case of steel bars, in order to separate the two waves from the bar and crack depth, oblique set of probes had been studied using many test blocks including the crack depth of 400mm. By setting the center O of two probes at the middle of two bars as shown in Fig.10(A), the disturbing waves were not detected at all. If the center of two probes O in Fig.10(B) located on the



(A) Parallel set to steel bar

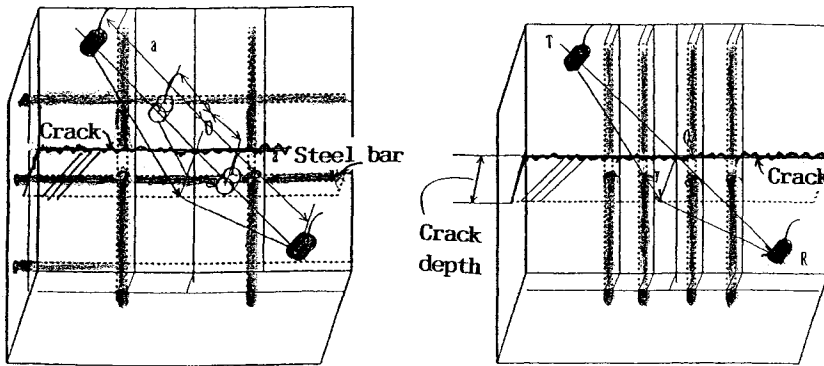
(B) Contact in a crack

Fig. 9 Depth measurement of crack in parallel set of probes



(A) Set at the center of bars

(B) Set at over the bar



(C) Bar existing in a crack

(D) Many parallel bars

Fig. 10 Depth measurement of crack in oblique set of probes

bar, small disturbing waves diffracted from the bar was detected only temporary. By ignoring the temporal waves, the depth was measured from the last diffracted waves.

Natural cracks formed by bending a slab of 250mm thick, 2000 X 4000 mm surface, were measured by this method. Most of the cracks existed in the same surface of reinforcing bars as shown in Fig.10(C), as illustrated a part of the slab. By ignoring the temporal waves, the depths were measured again in this case.

Deep depth of cracks in field, were measured on the vertical surfaces of pillars in section 2000 X4000mm, with many parallel steel bars as shown in Fig.10(D). Probes of 5kHz were used. The temporal diffracted waves from many bars appeared several times before arrival of the last waves for the crack depth. The red and blue lamps system on the apparatus indicating the arrival of diffracted waves were useful for the measurement. The last lighting of red lamp was for the depth. The measured depths were from 300mm to 1500mm. The results were confirmed by drill holes.

Many tests of depth measurement had been carried out by the oblique set of probes in field. Most of the results were seemed to be successful, except for random cracks or filled cracks in the structure.

CONCLUSIONS

It was found that analyzing the received waves was useful for the ultrasonic measurement of thickness by FFT analysis as well as crack depth by wave form detection in non-destructive testing of concrete.

REFERENCES

1. Yamaguchi, T., Marumo, F., Yamaguchi, T. (1996). *Journal of JSNDI*, Volume 45, Number, 9, pp.670-676
2. Yamaguchi, T., Hirono, S., Mizobuchi, T. (1993). *Proceed of International Conference NDT in Liverpool*, Volume 2, pp.519-529
3. Yamaguchi, T., Marumo, F., Yamaguchi, T., Okamura, K. (1996). *Journal of JSNDI*, Volume 45, Number, 10, pp.742-748
4. Yamaguchi, T. (1996). *Journal of JSNDI*, Volume 47, Number, 9, pp.636-642

BASIC STUDY FOR AN ULTRASONIC TESTING METHODS OF PC GROUTING CONDITION

N.SATO

Sankyo Co.,Ltd.

2-12-10 Minami-Ohi,Sinagawa-ku,Tokyo,Japan

ABSTRACT

Prestressed concrete bridges (PC bridges) with long and short spans have been constructed for 40 years in Japan. Management for the arrangements and prestressing of PC cables, and grouting in sheaths has been paid at construction. Nevertheless there were some accidents, for example, destruction of transverse steel rods for PC, unfilled grout in the sheaths which could be checked by cutting. The unfilled grout causes decreasing friction strength between the grout and a steel bar or a wire for PC, weakening the effect of rust protection and destruction with for corrosion due to the water flowing from anchor points to the sheaths. The accidents by the unfilled grout were mainly related to the insufficient management.

The authors have carried out the ultrasonic testing to establish the confirming inspection for grout condition of constructed and constructing bridges to protect destruction of the steel rods for PC.

KEYWORDS

Grouting condition, Maintenance, PC cable, Sheaths, Sound speed, Resonance wave

INTRODUCTION

It is important for management and maintenance to check grouting condition for constructed structures.

The following testings to conform the grouting condition have been used;

- ① X-ray testing
- ② Strike vibration testing
- ③ Fiber scope testing

The X-ray testing has reliance till 40cm width concrete and can clearly conform the grouting condition by a monitor. If the testing is used for long span bridges, it will take much time, and cost and be not practical. The strike vibration testing judges the grouting condition by the differences among natural frequencies and excellent frequency bands due to the filling rates of the grout. The testing has difficulty to get stable results because of the change of striking strength and also needs indoor analysis.

The authors have studied to establish a judging criteria by stable data without complicated indoor analysis and improve the workability.

1. Test piece

Sizes of test pieces, material and number of sheaths are almost same as actual condition.

The outline of the test pieces and the grouting condition of each cables are shown in Fig. 1-1 and Table 1-1 respectively.

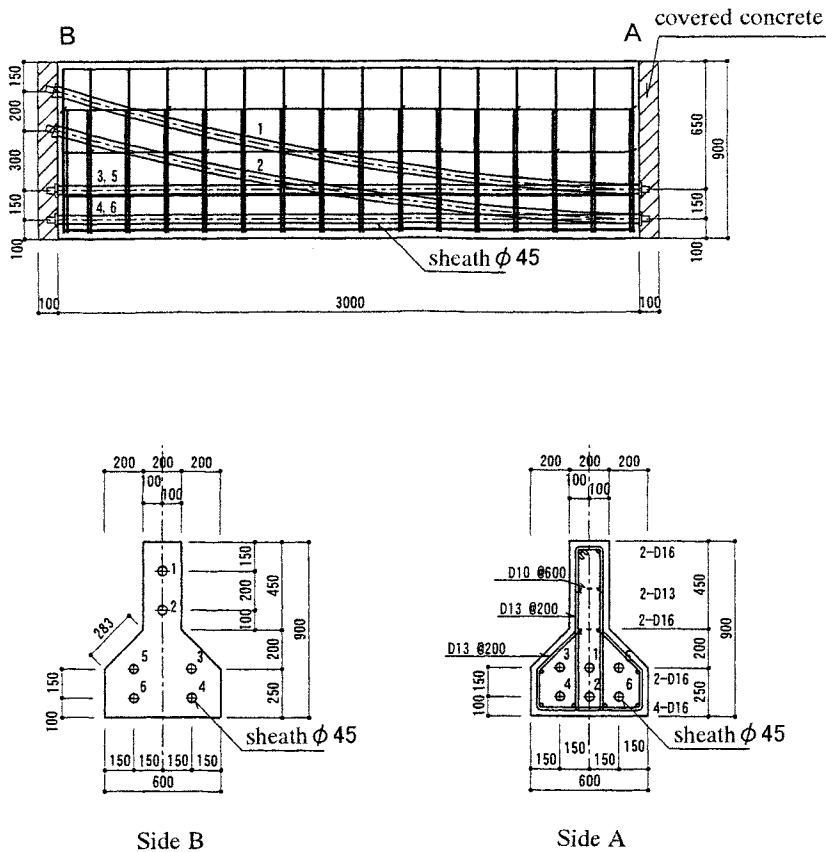


Fig.1-1 The outline of the test piece

Table 1-1. Grouting condition of each cables

Cable No.	Grouting condition(%)	Remarks
1	0	Curved cable
2	100	Curved cable
3	60	Straight cable
4	25	Straight cable
5	50	Straight cable
6	80	Straight cable

2. Equipment

A low-frequency ultrasonic measuring equipment is used. Its characteristics are shown in Table 2-1.

Table 2-1. Characteristics of Ultrasonic equipment

INPUT	Input frequency	1~200KHz
	Input voltage	0~±12V
	Power voltage	0~±0.5V
	Gain	2,3,5,7,10,20,30,40~600
	Sumpling time	0.1 μ s
OUTPUT	Pulse voltage	DC 320V
	Pulse time	5,10,20,50,100,200,500 μ
	Connector	BNC

3. Measurement

The waves are measured the sensors set between the anchor point A and B on different grouting condition cables (Case 1 to 6).The girder has 100mm width and is covered with concrete.

The posting sensor at the anchor point B and the receiving sensor at the A are used for measurement.

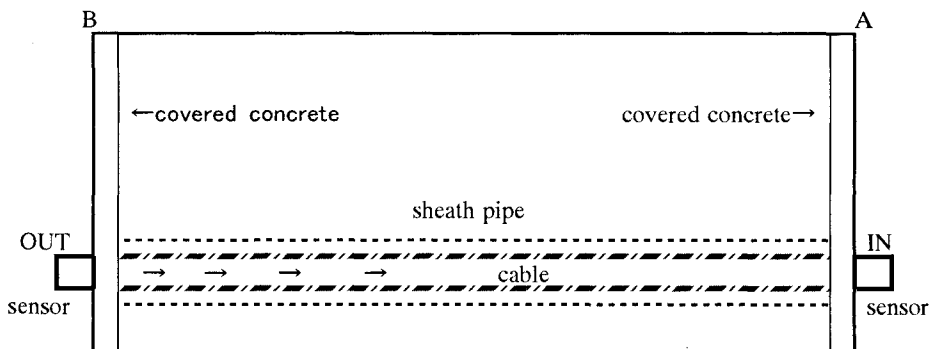


Fig.3-1. Measurement method

4.Result of measurement

The waves have apparent differences due to the filling rates of the grout, the sound speeds and the characteristics.

4-1.Filling rate of grouting and sound speed

Fig.4-1 shows the relationship between the filling rate of grout and the sound speed which are got by the ultrasonic testing to the bridge girder direction.

Transmitting sound speeds of the unfilled grouting cables are almost same as the ones of copper wires and steel rods. The sound speeds are in inverse proportion to the filling rates.The difference of the sound speed between 100% filling rate and 0~50% ones is about 20%.

The deference causes as follows;

The sound speeds are near the propagation speeds of metal as inverse proportion to the filling rates in considering propagation roots of longitudinal resonance waves on the cross section with the diameter 45mm sheath.

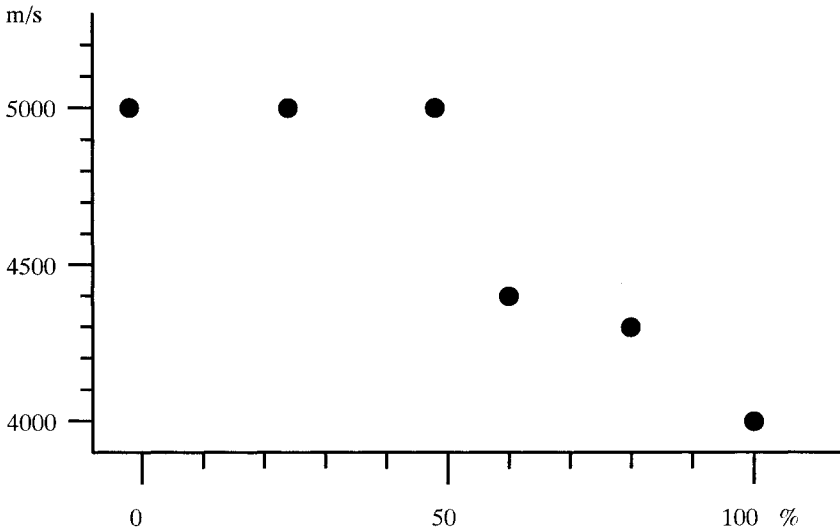
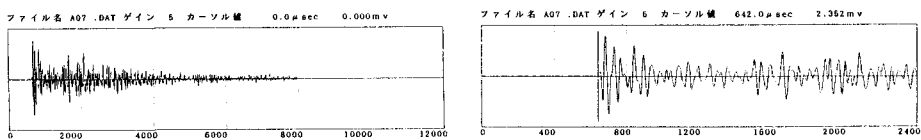


Fig.4-1. Filling rate of grouting and sound speed

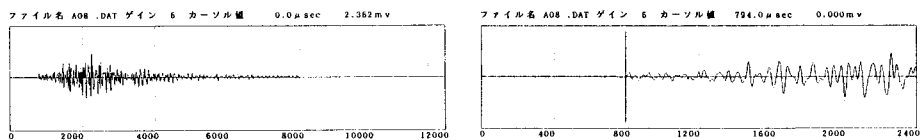
4-2. Filling rate of grout and characteristic of wave

The original ultrasonic waves measured by cable No.1~No.6 are shown in Fig.4-2.

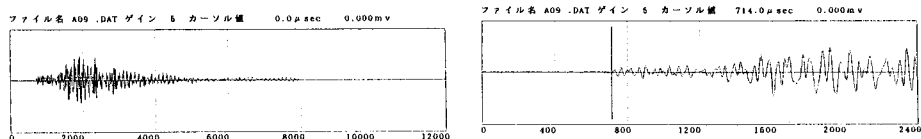
Resonance waves having high amplitude reach after the first wave reached at the cable No.1,4 and 5, which are less than 50% filling rate of the grout.And then the resonance waves converge at the period of about 1300 μ s.On the other hand, The resonance waves appear at 400 μ s later after the direct actual wave reached at the cable No.2,3 and 6, which are more than 60% filling rate of the grouting. The reaching periods of the resonance waves are among 400 to 500 μ s because the natural frequencies of steel wires increase due to stopping thier vibration by grouting.



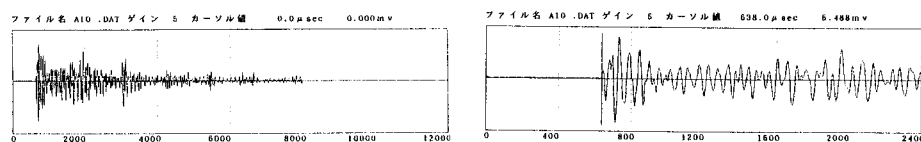
Cable No.1



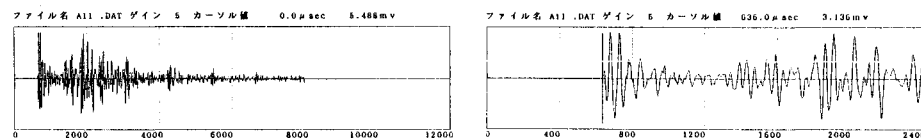
Cable No.2



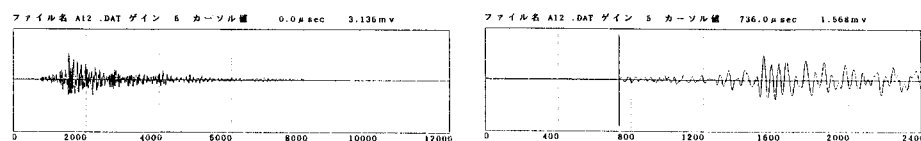
Cable No.3



Cable No.4



Cable No.5



Cable No.6

Fig.4-2. The original ultrasonic wave measured by cable No.1~No.6

5. Conclusion

The sound speeds and characteristics of waves differ according to the filling rates.

The authors can not make clear from the testing how they influence the tension forces of PC, so we continue studying to set a threshold value with many data and practical diagnostic methods by experiments and analysis.

The vibration testing is used for only the transverse steel bars for PC at construction sites because it is same as semi-transplant testing.

As the testing can also make clear the difference on curved cables, it may be also used to check grouting condition of main cables.

Engineers can simultaneously grasp the sound speeds and characteristics of waves by using the compact equipment.

Although testing based on the sound speeds and characteristics of waves had not been presented, if a judgement standard with the ultrasonic testing is established by theorizing in the future, the testing will be expected as the one of the easiest inspection.

Acknowledgement

We especially thank to the institute director Yoshioka and Mr. Ishikawa of Oriental construction Ltd. for providing test pieces and opportunity to experiment.

REFERENCES

1. Yoshizawa M., Uomoto T. (1997) *JCI (Japan Concrete Institute) Vole.19, No.1*
2. Yosizawa M., Uomoto T., Masuda K. *NDT-CE(1997)*

ULTRASONIC NONDESTRUCTIVE TESTING METHOD FOR HEAVY PLATE BUTT WELDS USING LOW FREQUENCY BROADBAND ANGLE PROBE AND SYNTHETIC APERTURE FOCUSING TECHNIQUE

S. WADAKA, M. KOIKE, T. KIMURA, S. KAMEYAMA and Y. MANOME

*Mitsubishi Electric Corporation,
5-1-1 Ofuna, Kamakura, Kanagawa, 247-8501 Japan*

ABSTRACT

An ultrasonic testing method is presented, which uses a low frequency broadband angle probe and the synthetic aperture focusing technique to improve the probability of detection of planar flaws and to provide high resolution. The method presented in this paper, furthermore, uses the mirror region of a test object with regard to the bottom surface of the test object, in addition to the region of the test object itself, as an image reconstruction region. Using the reconstruction region and taking into consideration of wave propagation paths, difference in reconstructed images between volumetric flaws and planar flaws is predicted, and a method for classification of flaw types is proposed based on the difference. The predicted difference in reconstructed images is demonstrated by experiments.

KEYWORDS

Ultrasonic nondestructive testing, Low test frequency, Broadband angle probe, SAFT, Volumetric flaws, Planar flaws

INTRODUCTION

In the conventional ultrasonic testing of welds, the test frequency of 5 MHz has been widely used. However, it has been reported that the lower test frequency, 2 MHz, has the possibility to give better performance in the probability of detection of planar flaws such as cracks [1,2]. However, decreasing the test frequency to 2 MHz increases time duration of ultrasonic pulses and also increases ultrasonic beam divergence, resulting in reduction in range resolution and lateral resolution, respectively.

In this paper, a testing method using a low frequency broadband angle probe and the synthetic aperture focusing technique (SAFT) [3] is presented. The broadband probe gives short time duration of ultrasonic pulses and so improves the range resolution. The synthetic aperture focusing technique provides remarkable improvement in the lateral resolution in reconstructed images. The method presented in this paper uses, furthermore, the mirror region of a test object with regard to the bottom surface of the test object, in addition to the region of the test object itself, as an image reconstruction region. Using this image reconstruction region, and also taking into consideration of wave propagation paths involving reflection at the bottom surface of a test object as well as the direct wave propagation path between an angle probe and a flaw, difference in reconstructed images between volumetric flaws and planar flaws is predicted, and a method for classification of flaw types is proposed based on the prediction. A

new display method named "modified B-scan" is introduced, which is applicable to display of reconstructed images in the image reconstruction region including the mirror region of a test object, and is effective for reduction of the amount of acquisition data for SAFT. The predicted difference between volumetric flaws and planar flaws is demonstrated by experiments using side drilled holes and slits made in thick steel plates as models of volumetric flaws and planar flaws, respectively.

METHOD FOR CLASSIFICATION OF FLAW TYPES

A method for classification of flaw types is proposed. Four wave propagation paths between an angle probe and a flaw [4] is taken into account. In image reconstruction using SAFT, the mirror region of a test object with regard to the bottom surface of the test object is added to the region of the test object itself as an image reconstruction region.

Propagation paths

An angle probe is supposed to be used for both transmission and reception of ultrasonic waves. Figure 1 shows the four wave propagation paths between the angle probe and a flaw. The path I involves only one time reflection at the flaw. The paths II and III involve one time reflection at the flaw and one time reflection at the bottom surface of a test object. The path IV involves one time reflection at the flaw and two times reflection at the bottom surface of the test object. Hereinafter, an echo signal related to the path I is referred to as a direct echo, that related to the paths II and III is referred to as a corner echo, and that related to the path IV is referred to as a double traverse echo, for the sake of simplicity.

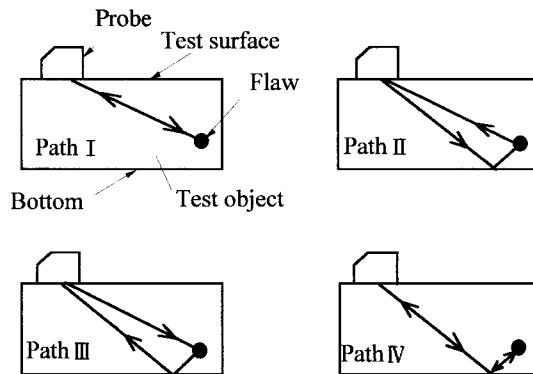


Fig. 1. Wave propagation paths.

Difference in reconstructed images

A volumetric flaw scatters ultrasonic waves in all directions almost uniformly, and so all of the direct echo, the corner echo and the double traverse echo will be detected by the probe. It is supposed hereinafter that image reconstruction using SAFT is done including the mirror region of a test object as described above. Images of the volumetric flaw will be reconstructed by SAFT at three points, as shown in Fig. 2. The images A, B and C in Fig. 2 are reconstructed by the contribution of the direct echo, the corner echo and the double traverse echo, respectively. The intensities of the three images A, B and C will be almost the same. On the other hand, a planar flaw scatters ultrasonic waves in a particular direction strongly. When the

planar flaw is inclined in the reverse direction of the probe as shown in Fig. 3(a), the direct echo will be primarily detected by the probe, and so the intensity of the image A will be dominant. When the planar flaw is inclined toward the probe as shown in Fig. 3(b), the double traverse echo will be primarily detected by the probe, and so the intensity of the image C will be dominant. When the planar flaw is vertical with regard to the bottom surface of the test object, the corner echo will be primarily detected by the probe, and so the intensity of the image B will be dominant. Such difference in the reconstructed images shown in Figs. 2 and 3 will give the information of flaw types and will be able to be used as an index for classification of flaw types. Experimental results demonstrating such difference in reconstructed images will be presented later.

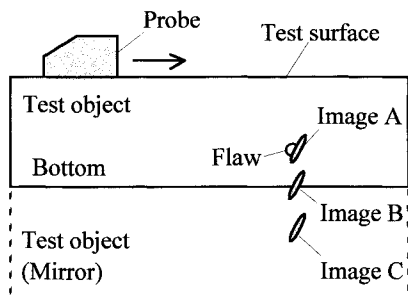


Fig. 2. Prediction of images of a volumetric flaw.

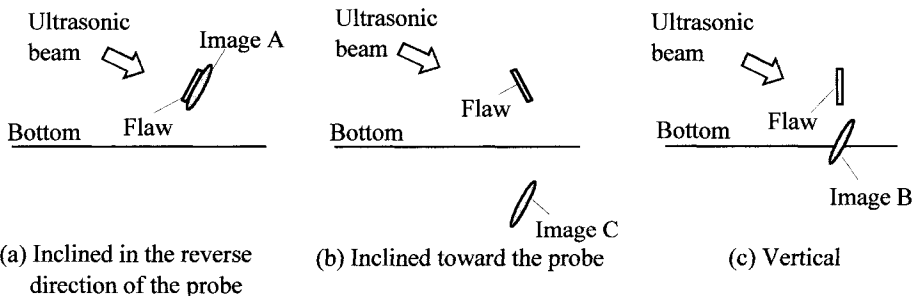


Fig. 3. Prediction of dominant images of planar flaws.

MODIFIED B-SCAN

In order to include the mirror region of a test object in an image reconstruction region and also to optimize the amount of acquisition data for signal processing using SAFT, a new display method named "modified B-scan" is introduced. It will be explained using Fig. 4. Figures 4(a) and (b) show the conventional B-scan display and the modified B-scan display, respectively. Figure 4(c) is the one for explaining Figs. 4(a) and (b). As shown in Fig. 4(c), an angle probe is scanned on the test surface, and flaw echoes are detected at each probe position on the test surface. In the conventional B-scan display shown in Fig. 4(a), the horizontal axis is the time of flight and the vertical axis is the probe position. The flaw echoes appear along an oblique line on the display as shown in Fig. 4(a). In the modified B-scan display shown in Fig. 4(b), the origin of time base is varied depending on the probe position, so that the flaw echoes appear along an almost vertical line, that is, they appear at nearly the same position on the

horizontal axis, regardless of the probe position. In order to achieve this, the origin of the time base is shifted at each probe position by $(Y \sin \theta_f) / V_s$, where Y is the distance shown in Fig. 4(c), θ_f is the angle shown in Fig. 4(c), and V_s is the shear wave velocity in the test object. The distance Y varies depending on the probe position. The angle θ_f is a predetermined one and is chosen to be a fixed value near to the so called angle of refraction of the probe. The displayed area on the modified B-scan display shown in Fig. 4(b) corresponds to the area bounded by the bold rectangle in Fig. 4(c), and the bold line in Fig. 4(b) corresponds to the position of the bottom surface of the test object. The modified B-scan can be used not only to display flaw echoes directly but also to display images reconstructed by SAFT, and it can be seen from Fig. 4(c) that images reconstructed in the mirror region of a test object can be displayed, in addition to images reconstructed in the region of the test object itself. Moreover, the amount of echo data for signal processing using SAFT can be reduced and optimized by acquiring echo data only after the origin of the time base at each probe position, provided that the area of interest is restricted to the area near the bottom surface of a test object.

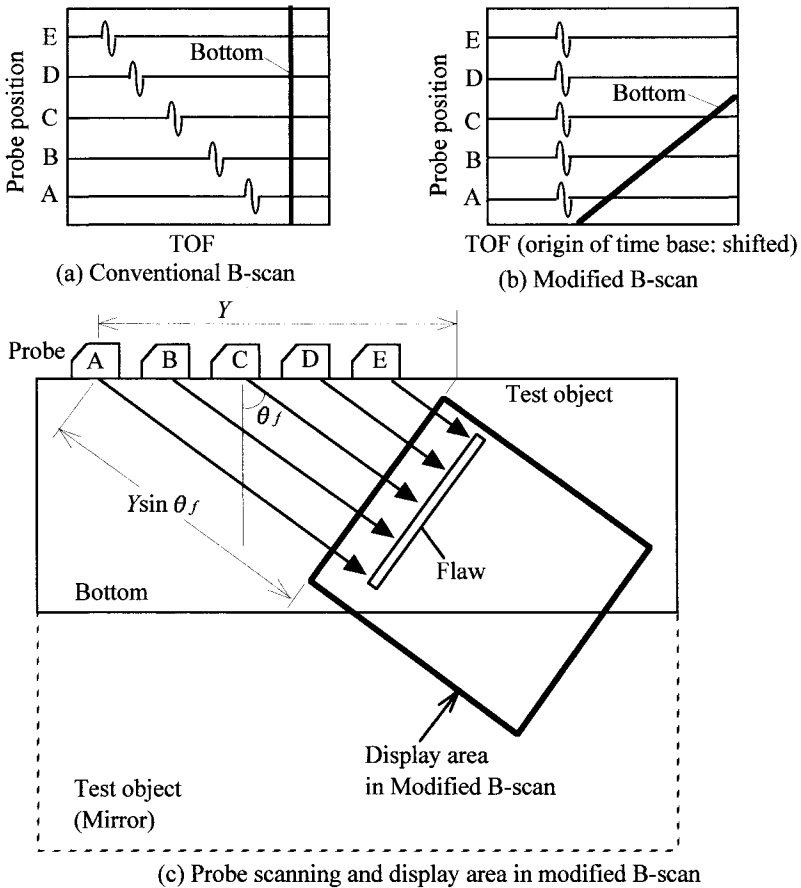
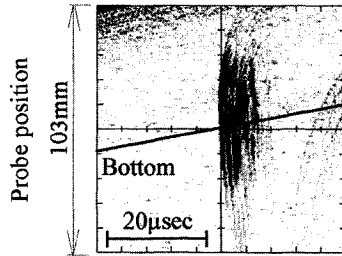


Fig. 4. Modified B-scan.

Figure 5 shows an example of the modified B-scan display. A side drilled hole in a steel plate is used as a model of volumetric flaws. The thickness of the plate is 60 mm, and the hole with the diameter of 2 mm is made at the distance of 7.5 mm above the bottom surface of the plate. An angle probe with the frequency of 2 MHz, described later in detail, is used. The echo signals received by the probe are directly displayed, that is, signal processing using SAFT is not done. It can be seen from Fig. 5 that echo signals appear at nearly the same position on the horizontal axis. The direct echo, the corner echo and the double traverse echo can not be distinguished in Fig. 5, because the lateral resolution is not satisfactory. In order to improve the lateral resolution, signal processing using SAFT is applied in the following.



TOF (origin of time base: shifted)

Fig. 5. An example of modified B-scan.

TIME DELAY USED IN IMAGE RECONSTRUCTION PROCESS

In image reconstruction process using SAFT, time delay between an angle probe and an image reconstruction point is needed. The time delay is given, in this paper, based on the geometrical optics approximation [5]. The expression of the time delay will be explained using Fig. 6. The point O is the center of the transducer, and the aperture size of the transducer is denoted by b . The medium 1 and the medium 2 correspond to a wedge constituting an angle probe and a test object, respectively. The point R is the image reconstruction point. The bold line connecting the points O, T and R is a sound ray. The point T is the saddle point. The angle of incidence of the sound ray passing through the saddle point T is denoted by α , and the corresponding angle of diffraction by θ . The distance between the point O and the point T is denoted by r_{01} , and that between the point T and the point R by r_{02} . The time delay τ between the probe and the image reconstruction point R is given in the far field by

$$\tau = \frac{r_{01}}{V_w} + \frac{r_{02}}{V_s}, \quad (1)$$

where V_w is the longitudinal velocity in the wedge and V_s is the shear wave velocity in the test object. The time delay given by Eq. (1) is used in image reconstruction process using SAFT. In Fig. 6, the angle α_0 is the so called angle of incidence of the probe, and the angle θ_0 is the so called angle of refraction of the probe. The point I is the so called probe index. It should be noted that the angle α is different from the angle α_0 and also that the angle θ is different from the angle θ_0 . The angles α and θ vary depending on the location of the image reconstruction point R.

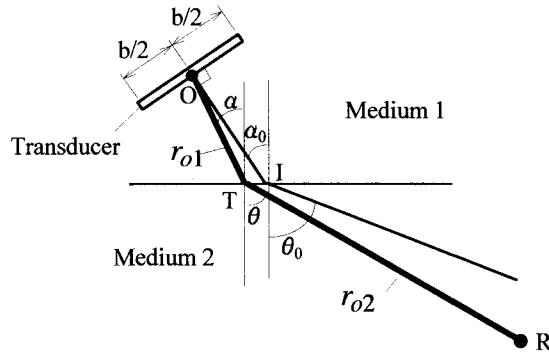


Fig. 6. Geometrical optics approximation.

Signal processing using SAFT is applied to the echo data shown in Fig. 5. Figure 7 shows the reconstructed images. Comparing Fig. 7 with Fig. 5, it can be seen that the lateral resolution is remarkably improved in Fig. 7. The image A contributed by the direct echo, the image B contributed by the corner echo, and the image C contributed by the double traverse echo can be clearly distinguished in Fig. 7.

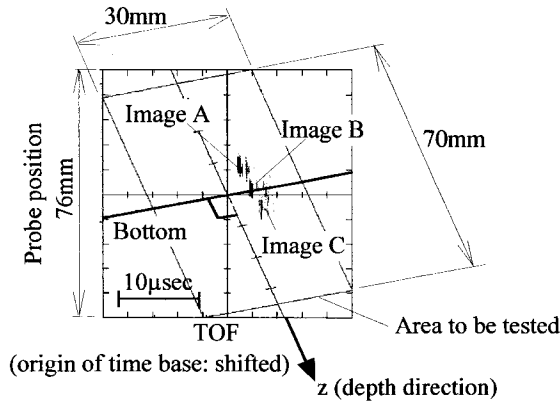


Fig. 7. Images reconstructed by SAFT.

EXPERIMENTS

Experimental set up

The equipment used for experiments consists of an ultrasonic test instrument, an angle probe, a scanning mechanics, and test objects. The pulse compression ultrasonic test instrument UI-1000 [6] is used. The angle probe is fabricated using a wedge made of acryl. The size of the transducer is 12 mm x 20 mm ($b=12$ mm in Fig. 6). The so called angle of incidence α_0 shown in Fig. 6 is set to be 54.6° , and so, the so called angle of refraction θ_0 is about 74° . The distance between the center O of the transducer and the probe index I in Fig. 6 is set to be 20.17 mm. The measured center frequency and the fractional bandwidth of the fabricated probe are 2.1 MHz and 98 %, respectively. The probe is excited by a tone burst signal of one cycle long, generated by the ultrasonic test instrument. The carrier frequency is set to be

2 MHz. The probe is scanned by the scanning mechanics shown in Fig. 8, and echo data are acquired at intervals of 2 mm. Figure 9 shows the test objects. A steel plate with the thickness of 60 mm is used as a model of heavy plates. The side drilled holes shown in Fig. 9(a) and the slits shown in Fig. 9(b) are used as a model of volumetric flaws and that of planar flaws in butt welds, respectively. In Fig. 9(b), δs is the inclination angle of each slit.

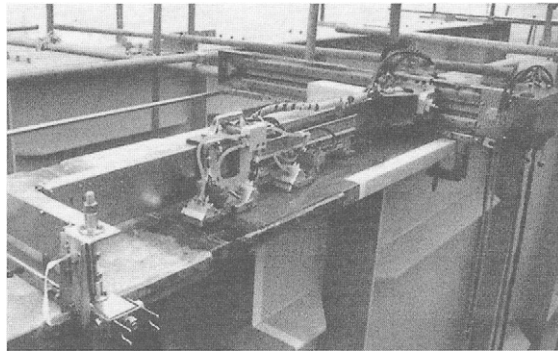


Fig. 8. A photograph of the scanning mechanics.

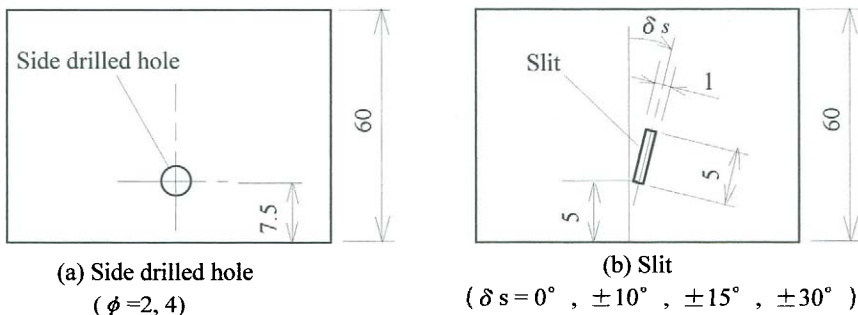


Fig. 9. Test objects.

Experimental results

Reconstructed images of side drilled holes

Figure 10(a) shows the reconstructed images of the side drilled hole with the diameter of 2 mm, and Figure 10(b) shows those of the side drilled hole with the diameter of 4 mm. It can be seen from these figures that all of the image A contributed by the direct echo, the image B contributed by the corner echo, and the image C contributed by the double traverse echo are reconstructed as predicted in Fig. 2 and also that they are distinguished from each other. The positions of the holes are estimated by using the images A, B and C, separately. The estimation error in the depth direction is less than 0.57 mm in the case of the images A, that in the case of the images B is less than 0.43 mm, and that in the case of the images C is less than 0.76 mm.

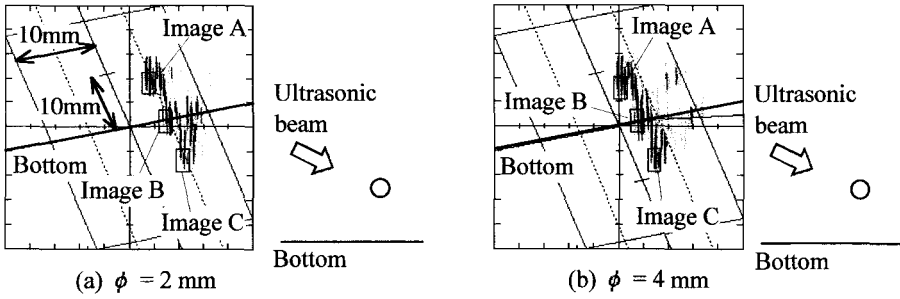


Fig. 10. Reconstructed images of the side drilled holes.

Reconstructed images of inclined slits with $\delta_s > 0$

Figures 11 (a), (b) and (c) show the reconstructed images of the inclined slits with $\delta_s = 10^\circ$, 15° and 30° , respectively. It can be seen from these figures that the image A contributed by the direct echo is reconstructed in all cases as predicted in Fig. 3(a). However, the image B is also reconstructed in the case of $\delta_s = 10^\circ$ as shown in Fig. 11(a). This results from that the corner echo is detected in addition to the direct echo since the slit is near vertical. The image C in Fig. 11(c) is considered to be reconstructed by the double traverse echo reflected from the lower side of the slit, since the slit has the width of 1 mm as shown in Fig. 9(b). The estimation error of the position of the slits is less than 0.78 mm in the case of the images A, and that in the case of the image B in Fig. 11(a) is 0.8 mm.

Reconstructed images of inclined slits with $\delta_s < 0$

Figures 12 (a), (b) and (c) show the reconstructed images of the inclined slits with $\delta_s = -10^\circ$, -15° and -30° , respectively. It can be seen from these figures that the image C contributed by the double traverse echo is reconstructed in all cases as predicted in Fig. 3(b). However, the image B is also reconstructed in the case of $\delta_s = -10^\circ$ as shown in Fig. 12(a). This results from that the corner echo is detected in addition to the double traverse echo since the slit is also near vertical. The image A in Fig. 12(a) is considered to be reconstructed by the direct echo reflected from the upper side of the slit, and the same as for the image A in Fig. 12(c). The estimation error of the position of the slits is less than 2.95 mm in the case of the images C, and that in the case of the image B in Fig. 12 (a) is 0.33 mm.

Reconstructed image of vertical slit

Figure 13 shows the reconstructed image of the vertical slit, that is, $\delta_s = 0^\circ$. It can be seen from this figure that only the image B contributed by the corner echo is reconstructed as predicted in Fig. 3(c). The estimation error of the position of the slit is 0.58 mm.

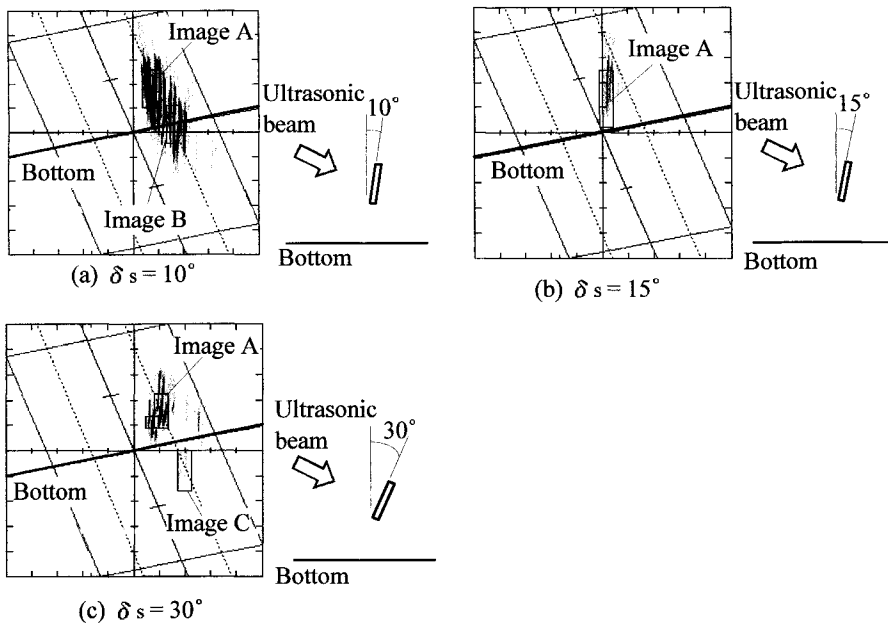


Fig. 11. Reconstructed images of the slits inclined in the reverse direction of the probe.

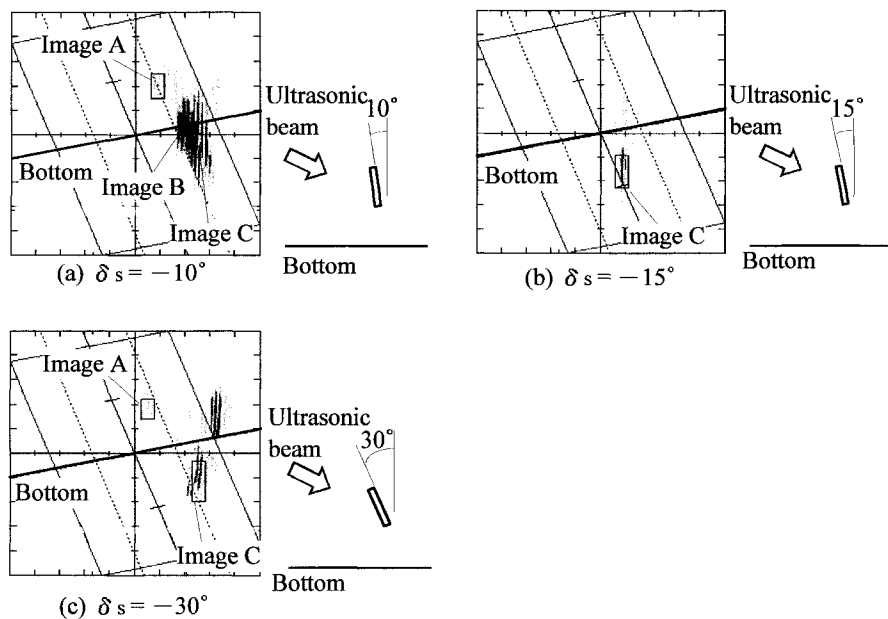


Fig. 12. Reconstructed images of the slits inclined toward the probe.

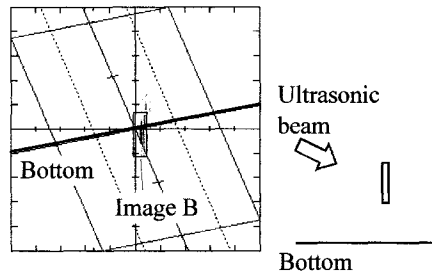


Fig. 13. Reconstructed image of the vertical slit.

CONCLUSIONS

An ultrasonic testing method using a broadband angle probe with the frequency of 2 MHz and SAFT is presented. The method has the potentiality to increase the probability of detection of planar flaws, and also provides high resolution. The method, furthermore, is combined with a new display method named "modified B-scan", which uses the mirror region of a test object in addition to the region of the test object itself as an image reconstruction region. Using this reconstruction region and taking into consideration of wave propagation paths, difference in reconstructed images between volumetric flaws and planar flaws is predicted, and a method for classification of flaw types is proposed based on the difference. The predicted difference in reconstructed images is demonstrated by experiments.

REFERENCES

1. *Chouonpa Tanshou Shiken II 1990 (Ultrasonic Nondestructive Testing II 1990)*, (1990) p. 119, published by The Japanese Society for Non-Destructive Inspection. [In Japanese]
2. *Toriatukai Setsumeisho (Instruction Manual) of Standard Test Block for Ultrasonic Testing, STB-A31(JIS Z 2345)* (1995) p. 1, published by The Japanese Society for Non-Destructive Inspection. [In Japanese]
3. *Nondestructive Testing Handbook, Second Edition, Volume 7, Ultrasonic Testing*, (1991), pp. 300-303, published by the American Society for Nondestructive Testing.
4. Kimura, T., Kameyama, S., Wadaka, S., Manome, Y. and Koike, M. (1998) *The Journal of the Acoustical Society of Japan* 54, 276. [In Japanese]
5. Kimura, T., Kameyama, S., Wadaka, S., Manome, Y. and Koike, M. (1999). In: *Review of Progress in Quantitative Nondestructive Evaluation*, pp. 1123- 1130, D. O. Thompson and D. E. Chimenti (Ed.). Kluwer Academic/Plenum Publishers, New York.
6. Wadaka, S., Nagatsuka, T., Misu, K., Kimura, T., Koike, M. and Ichikawa, H. (1996). In: *Review of Progress in Quantitative Nondestructive Evaluation*, pp. 1779-1786, D. O. Thompson and D. E. Chimenti (Ed.). Kluwer Academic/Plenum Publishers, New York.

SIMULATION FOR ULTRASONIC EVALUATION OF A WELDING DEFECT IN A THICK PLATE

S.HIROSE, K.KIMOTO and C.MIKI

*Department of Civil Engineering, Tokyo Institute of Technology
2-12-1 O-okayama, Meguro-ku, Tokyo 152-8552 Japan*

ABSTRACT

This paper presents a numerical method to simulate ultrasonic wave scattering by a defect in a thick plate. The method is a combined method of a ray method and a boundary element analysis, in which the ray method is used to evaluate a free field without a defect, while the boundary element method is employed to calculate a scattered wave field by a defect. Pulse-echo tests with angle beam probes are simulated numerically and some of the computed results are compared with experimental data in both time and frequency domains.

KEYWORDS

BEM, ray theory, SH-wave, thick plate, ultrasonic testing, welding defect

INTRODUCTION

Recently, steel bridges with small numbers of main girders have been constructed to reduce the construction cost. For the bridges of this kind, steel plates tend to become thicker and the thickness sometimes reaches 5 to 10cm. Therefore, it is necessary to inspect welded joints of thick plates in a nondestructive manner. However, a conventional X-ray test is no longer applicable to thick plates. That is why an ultrasonic testing (UT) is recently given attention as an alternative way to the X-ray method.

Unlike an X-ray, the ultrasound can go deep into a specimen and exhibits eminent wave phenomena such as diffraction or scattering. These are attractive features of the ultrasound. However, the interaction of an ultrasound with defects sometimes makes echo patterns quite complicated. Without knowledge based on a wave propagation theory, complicated echo patterns may cause false acceptance or false rejection of joints being tested. Therefore, to establish a UT system with high reliability, a quantitative testing method based on understandings of a wave propagation theory must be developed.

To achieve this end, many UT simulations have been carried out numerically. A boundary element method (BEM) is one of the most frequently used techniques for this purpose. In the BEM analysis, boundaries of a medium are divided into a finite number of elements. Although discretization is required only over the boundary, computational time becomes unacceptably large if the wave path between transmission and reception points becomes large compared to an incident wave length. From this reason, a more efficient numerical method has to be developed for the UT simulation of a thick plate model.

This paper presents a numerical method to solve reflection and scattering problem in a thick plate. The method developed here is the one that combines a BEM with a ray theory,

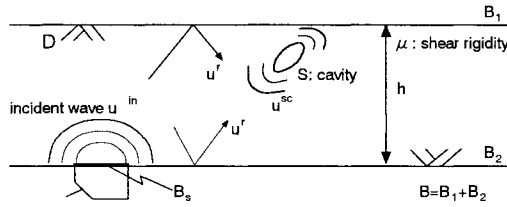


Fig. 1. Two dimensional elastic plate of a laterally infinite extent.

aiming to exploit advantages of each method. An integral equation formulation for the combined method is shown for a 2-D time-harmonic SH-wave. For simplicity, SH-waves are considered here, but the way to combine the two methods is basically the same as for other types of waves such as SV- or P-wave [1]. In the following, two numerical examples which simulate pulse-echo tests are given after an integral equation formulation for the combined method. Then, some of them are compared to experimental data.

FORMULATION

Basic Equations

Let D be a two-dimensional infinite elastic plate of thickness h in which a time-harmonic SH-wave with the wave number k_T propagates. A cavity of an arbitrary shape is assumed to be embedded in D near the upper surface, see Fig.1. It is also assumed that h is sufficiently large compared to the wave length, namely $k_T h \gg 1$. The governing equation of the problem is the well-known Helmholtz equation.

$$\nabla^2 u(\mathbf{x}) + k_T^2 u(\mathbf{x}) = 0 \quad \mathbf{x} \in D. \tag{1}$$

When the incident wave is generated by a given surface traction distributed over a portion of the lower surface (B_S) and the rest of the surface is free from traction, the boundary conditions may be given as follows:

$$t(\mathbf{x}) = \mu \frac{\partial u}{\partial n}(\mathbf{x}) = \begin{cases} \bar{t}(\mathbf{x}) & \mathbf{x} \in B_S \\ 0 & \text{otherwise} \end{cases} \tag{2}$$

where μ is the shear modulus. In the following, the boundary of a cavity, the upper and the lower surfaces of a plate are denoted by S, B_1 and B_2 respectively.

Definition of the wave fields

In scattering problems the total field is usually expressed as a sum of the incident field and the scattered field. In case of scattering in a plate, there also exists the reflected wave from the upper and the lower surfaces. Therefore the total fields can be written as

$$\mathbf{u} = u^{in} + u^r + u^{sc}, \quad t = t^{in} + t^r + t^{sc} \tag{3}$$

where superscripts in, r and sc mean the incident, reflected and scattered fields, respectively. As the incident and reflected fields compose the total wave field in the absence of a defect, the sum of them will be referred to as the free field in the following and denoted by the superscript f .

$$u^f = u^{in} + u^r = u - u^{sc}, \quad t^f = t^{in} + t^r = t - t^{sc}. \tag{4}$$

Combined method of BEM and ray theory

The boundary integral equation for scattered fields can be formulated as[2]:

$$\frac{1}{2}u^{sc}(\mathbf{y}) = \int_{S+B} \{U(\mathbf{x}, \mathbf{y})t^{sc}(\mathbf{x}) - T(\mathbf{x}, \mathbf{y})u^{sc}(\mathbf{x})\}ds_x \quad \mathbf{y} \in S \text{ or } B \quad (5)$$

where $U(\mathbf{x}, \mathbf{y})$ is the fundamental solution for an unbounded medium given by $\frac{i}{4\mu}H_0^{(1)}(k_T r)$, and $T(\mathbf{x}, \mathbf{y}) = \mu \frac{\partial U(\mathbf{x}, \mathbf{y})}{\partial n(\mathbf{x})}$. Here, $H_0^{(1)}$ is the 0th order Hankel function of the first kind and r is the distance between \mathbf{x} and \mathbf{y} .

The scattered waves are mainly distributed in the neighborhood of the cavity. If \mathbf{y} in eq.(5) is on S or B_1 , therefore, the contribution from the scattered field on B_2 to the integral over S and B_1 on the right hand side of eq.(5) may be negligible. Hence neglecting the integration over B_2 , eq.(5) can be written as

$$\frac{1}{2}u^{sc}(\mathbf{y}) = \int_{S+B_1} \{U(\mathbf{x}, \mathbf{y})t^{sc}(\mathbf{x}) - T(\mathbf{x}, \mathbf{y})u^{sc}(\mathbf{x})\}ds_x \quad \mathbf{y} \in S \text{ or } B_1. \quad (6)$$

Substitution of eq.(4) into eq.(6) yields the following integral equation:

$$\begin{aligned} \frac{1}{2}u(\mathbf{y}) - \int_{S+B_1} \{U(\mathbf{x}, \mathbf{y})t(\mathbf{x}) - T(\mathbf{x}, \mathbf{y})u(\mathbf{x})\}ds_x \\ = \frac{1}{2}u^f(\mathbf{y}) - \int_{S+B_1} \{U(\mathbf{x}, \mathbf{y})t^f(\mathbf{x}) - T(\mathbf{x}, \mathbf{y})u^f(\mathbf{x})\}ds_x. \end{aligned} \quad (7)$$

To solve eq.(7), it is necessary to know the free fields on S and B_1 . On the assumption of $k_T h \gg 1$, they can be evaluated by the ray theory, which gives the high frequency (or far field) approximation. Eq.(7) has the integration over the free surface B_1 of an infinite length. In the numerical integration, therefore, the surface B_1 must be truncated at appropriate points.

After solving eq.(7) for the total fields on S and B_1 , the wave fields observed at the receiver are calculated. To this end, the boundary integral equation derived with the aid of the Green's function $G(\mathbf{x}, \mathbf{y})$ for a plate can be used as follows

$$u^{sc}(\mathbf{y}) = \int_S \{G(\mathbf{x}, \mathbf{y})t^{sc}(\mathbf{x}) - H(\mathbf{x}, \mathbf{y})u^{sc}(\mathbf{x})\}ds_x \quad \mathbf{y} \in D \text{ or } B \quad (8)$$

where H is the traction component of G . It's worthy to note that the integrations over B_1 and B_2 disappear from eq.(8) since the traction free boundary conditions on B_1 and B_2 are satisfied by $H(\mathbf{x}, \mathbf{y})$ and $t^{sc}(\mathbf{x})$. Obtaining the rigorous expression of $G(\mathbf{x}, \mathbf{y})$ and $H(\mathbf{x}, \mathbf{y})$ is generally very difficult, but they can be approximated by the ray theory when $r = |\mathbf{x} - \mathbf{y}|$ is large because $G(\mathbf{x}, \mathbf{y})$ and $H(\mathbf{x}, \mathbf{y})$ are nothing short of the displacement and traction of the free field at \mathbf{x} due to a point force at \mathbf{y} .

NUMERICAL EXAMPLES

The combined method proposed in the last section is applied to the numerical simulation of pulse-echo testings to show the applicability and efficiency of our method for various types of defects and probes. Types of probes considered here are angle beam probes with the dominant incident angles α of 90 and 45 degrees. The angle beam probe with the 90-degree incidence produces the strong amplitude along the surface. Therefore, this probe is sometimes called a surface SH wave probe though it doesn't actually generate a surface wave.

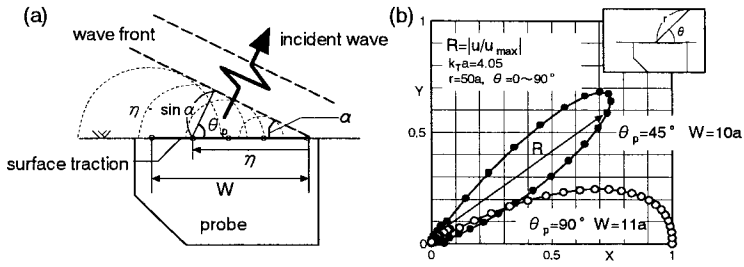


Fig. 2. (a) Numerical model for an angle beam probe and (b) the directivity of incident fields obtained by setting $\theta_p = 45^\circ$ and 90° .

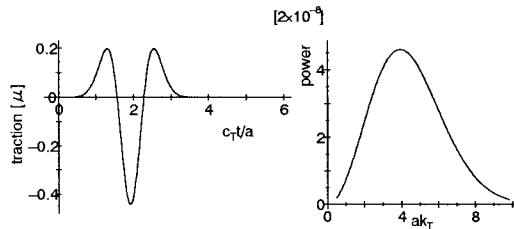


Fig. 3. (a) Time variation of traction and (b) its power spectrum.

Numerical model for an angle beam probe

Neglecting a propagation process inside a probe, the probe is modeled as a distributed traction applied on a contact surface between the probe and the specimen. The directivity of an incident field is emulated by varying the time delay or phase of the traction forces on the contact surface. This technique is in principle the same as the phased array transducer. The time delay of the traction force is determined so as to form a plane wave front as shown in Fig.2(a). In the frequency domain, the time delay is given as a phase shift. Referring to Fig.2(a), the phase at a local coordinate η is advanced by $k_T \eta \sin \alpha$ to have the directivity at the angle $\theta_p = (\pi/2 - \alpha)$. As for the amplitude, a parabolic distribution is assumed expecting that the strongest and no traction forces are excited at the center and the edges of a probe, respectively. Using the abovementioned assumptions, the far field amplitudes of the incident waves are calculated and plotted in the polar coordinate system as shown in Fig.2(b). It clearly shows the maximum amplitudes appear at the expected angles of $\theta_p = 45^\circ$ and 90° .

In order to obtain time domain solutions, the inverse Fourier transform is applied to the frequency domain results. In the numerical examples shown in the sequel, it is supposed that the time variation of the traction is given by the Ricker wavelet as shown in Fig. 3.

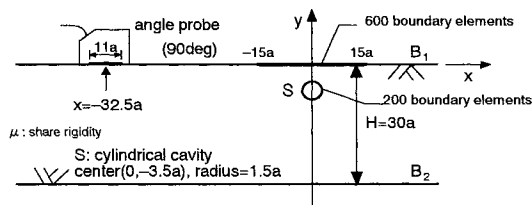


Fig. 4. Numerical model for a pulse-echo test with a surface SH wave probe.

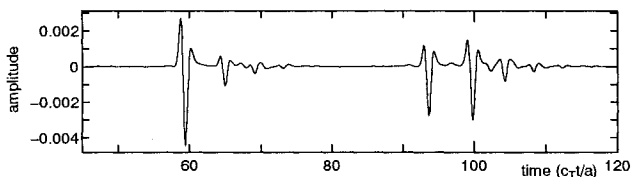


Fig. 5. Time variation of displacement waveform at $(-32.5a, 0)$.

Surface SH wave probe

The numerical model for a pulse-echo test with a surface SH-wave probe is illustrated in Fig. 4. As a simple model of a subsurface defect in a welded joint, a cylindrical cavity of radius $1.5a$ is in an infinite plate of thickness $30a$, where a is a unit length. In Fig.5, the displacement waveform at $x = (-32.5a, 0)$ is shown as a function of the nondimensional time $c_T t/a$. In evaluating the free field appeared in eq.(7), reflections on the upper and lower surfaces are considered up to two times. In Fig.5, three small echoes can be seen after the first arrival of the large echo. These echoes are due to the multiple scattering between the cavity and the upper surface. Although there ought to be more than three echoes, subsequent echoes may be too small to be seen. Noting that the lower surface neglected in the BEM analysis is much far from the cavity than the upper surface is, it can be deduced that the interaction between the cavity and the lower surface does not have a significant effect on the results. The second group of echoes seen after $c_T t/a = 90$ corresponds to the waves which return to a probe after reflected once on the upper or lower surface on the way from or to the cavity. It can be seen that they still have large amplitudes.

45-degree angle beam probe

The second numerical example is a pulse-echo test with a 45-degree angle beam probe. An infinite plate containing a cavity is considered again, but the cavity is located near the bottom surface and its shape is ellipse. The probe is located on the top surface and moved at an interval of $2a$ from $x=-47a$ to $-27a$ to emulate a scanning operation. Fig.7 shows displacement waveforms observed at various probe positions. From this figure, we can easily see which one is the echo from the cavity. The waves whose arrival times are not affected by probe positions are apparently the waves traveling back and forth between top and bottom

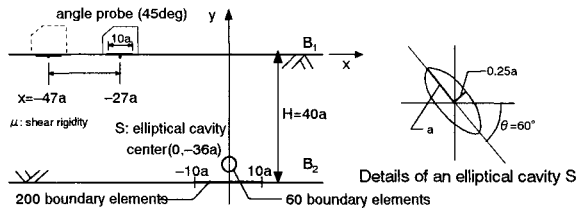


Fig. 6. Numerical model for a pulse-echo test with an 45-degree angle beam probe.

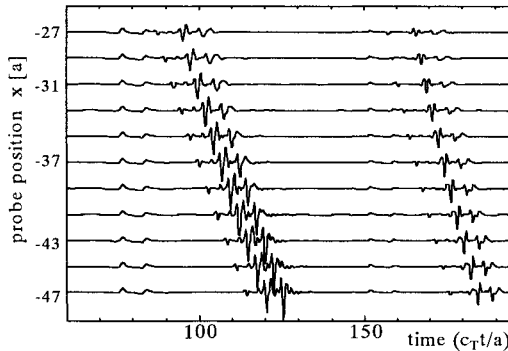


Fig. 7. Time variations of displacement waveforms calculated for various probe positions.

surfaces. The waves that change their time of flight are of course the echoes from the cavity. There are two groups of waves from cavity. The first bigger ones are the waves which directly go to and come back from a cavity with no reflection on the plate surfaces. On the other hand, the second echoes are the backscattered waves which are reflected once on the upper or lower surfaces while propagating between the probe and the cavity.

If an ordinary numerical simulation like FEM or BEM is applied to the same problem, the calculation for the whole region including a probe and a scatterer is required for each probe position. In the combined method, on the other hand, the wave propagation process between a probe and a scatterer is evaluated by the ray theory and only the scattering process in the local area is analyzed by the BEM. Therefore both ray theory and BEM in the combined method require little additional computational time even in the calculation for various probe positions. Hence the combined method may have great advantage when numerous simulation data are necessary in an imaging technique or a reconstruction of a defect in a thick plate.

COMPARISON WITH EXPERIMENTAL RESULTS

Numerical solutions calculated by the combined method are compared with the experimental results of a pulse-echo test using a surface SH-wave probe. Since echoes from natural welding defects such as lack-of-fusion or blowhole are quite complex and difficult for quantitative comparison with numerical analysis, an aluminum test block with an artificial cylindrical cavity is used for the pulse-echo measurement as shown in Fig.8. Two types of aluminum blocks are prepared with a cylindrical cavity at the depth $d = 3.5\text{mm}$ or $d = 6.5\text{mm}$. The surface SH-wave probe used here has a central frequency of 5MHz. During the measurement a probe is kept fixed at the position indicated in the figure. A corner echo is also measured by setting the probe at the distance of 25mm away from the rectangular corner point.

Power spectra

Fig.9 shows the power spectra of the measured waveform data. However, the power spectra can not be directly compared with the numerical solutions, because experimental data are affected by the unknown characteristics of transducers and other measurement equipments. In order to eliminate undesirable effects, the experimental signals have to be pre-processed using a reference signal.

Using the linear system theory in the frequency domain, the whole pulse-echo system may be represented as

$$O(\mathbf{x}, \omega) = B(\omega)E_r(\omega)D(\mathbf{x}, \omega)E_t(\omega)I(\omega) \quad (9)$$

where $O(\mathbf{x}, \omega)$ and $I(\omega)$ are the frequency components of the output signal and the input voltage, respectively. Also, $E_r(\omega)$, $D(\mathbf{x}, \omega)$, $E_t(\omega)$ and $B(\omega)$ are response functions of the transducer reception, the wave characteristics in the specimen, the transducer transmission and the other electric equipment, respectively.[3] It is noted that $D(\mathbf{x}, \omega)$ corresponds to the numerical solutions shown in the previous sections.

A corner echo from a rectangular corner observed by the same measurement system is taken as a reference signal. Then the reference signal may be expressed as

$$O_{cor}(\mathbf{x}, \omega) = B(\omega)E_r(\omega)D_{cor}(\mathbf{x}, \omega)E_t(\omega)I(\omega) \quad (10)$$

where $D_{cor}(\mathbf{x}, \omega)$ denotes the response function representing the reflection from the corner point. For the SH wave propagating along the free surface, the corner echo can be easily computed as the wave from the image point with respect to the vertical surface at the corner. Hence $D_{cor}(\mathbf{x}, \omega)$ can be calculated analytically. From eqs.(9) and (10), we have

$$O(\mathbf{x}, \omega)/O_{cor}(\mathbf{x}, \omega) = D(\mathbf{x}, \omega)/D_{cor}(\mathbf{x}, \omega). \quad (11)$$

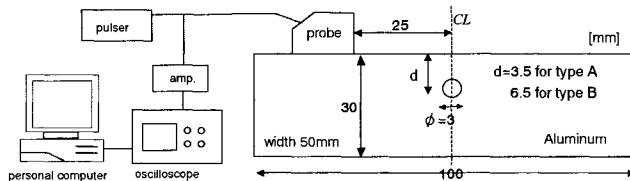


Fig. 8. Experimental setup and dimensions of test blocks.

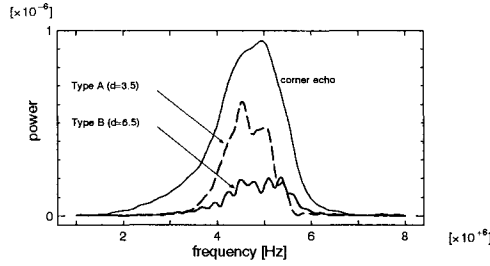


Fig. 9. Power spectra of measured A-scope data.

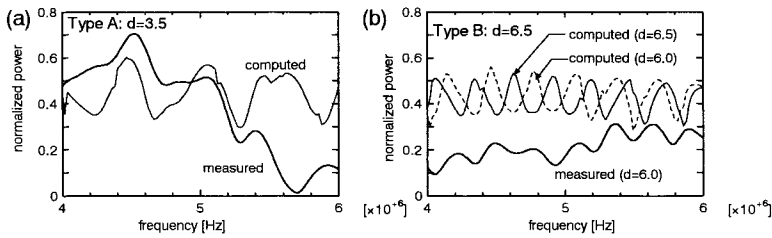


Fig. 10. Normalized power spectra((a)type A specimen, (b)type B specimen)

The left hand side of the above equation is obtained experiment and the right hand side is calculated numerically. In this way, the experiments can be compared with the numerical solutions.

The absolute values of $O(x, \omega)/O_{cor}(x, \omega)$ (measured) and $D(x, \omega)/D_{cor}(x, \omega)$ (computed) are shown for two types of specimens in Fig.10(a) and 10(b), respectively. In Fig.10(b), computed results for the model of $d=6.0$ is also shown. For both types of specimens, numerical simulation fails to predict the shape of spectra. However, computed results show periodic variations as a function of frequency, and similar variations can be observed in experimental results.

As the intervals of the maxima and minima appeared in the power spectra are obviously different between two specimens, it is expected that the depth of cavity can be deduced from the frequency periodicity (Δf [Hz]). Fig. 11 shows Δf as a function of the depth of cavity d . It is shown that Δf obtained from numerical results decrease monotonically as d increases, and a good agreement between computation and experiment is obtained for the type B specimen. Considering the sensitivity of Δf to the change of d , this relation may be used for the estimation of a depth of a subsurface defect.

A-scope waveform

In the numerical examples shown in the previous section, the time variation of the traction on the probe contact surface is prescribed by the Ricker wavelet. In experiments, however, it is very difficult to determine the real time variation of the traction. In this section, the

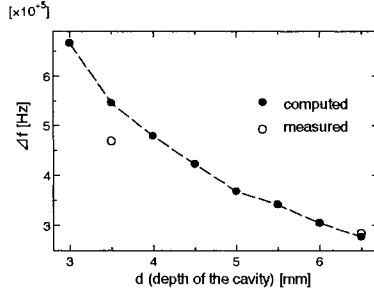


Fig. 11. Relation between depth of cavity(d) and period(Δf).

unknown time variation of the traction is determined indirectly by using the reference corner echo to simulate A-scope waveforms measured in experiments.

The response function $D_{cor}(\mathbf{x}, \omega)$ for the reference corner echo may be expressed by

$$D_{cor}(\mathbf{x}, \omega) = u(\mathbf{x}, \omega) = 2 \int_{B'_S} U(\mathbf{y}', \mathbf{x}, \omega) t(\mathbf{y}', \omega) ds_{y'} \tag{12}$$

where $U(\mathbf{y}', \mathbf{x}, \omega)$ is the fundamental solution in an unbounded medium and B'_S and \mathbf{y}' are the image boundary and the image point of B_S and \mathbf{y} with respect to the vertical plane at the rectangular corner, respectively. Aside from the phase delay $k_T \Delta s(\mathbf{y}')$, the distributed traction is assumed to have the same time variation everywhere on the probe contact surface. Then $t(\mathbf{y}', \omega)$ may be expressed by

$$t(\mathbf{y}', \omega) = \exp(-ik_T \Delta s(\mathbf{y}')) T(\omega). \tag{13}$$

Substituting eq.(13) into eq.(12) yields $D_{cor}(\mathbf{x}, \omega) = \bar{D}_{cor}(\mathbf{x}, \omega) T(\omega)$, where

$$\bar{D}_{cor}(\mathbf{x}, \omega) = 2 \int_{B'_S} U(\mathbf{y}', \mathbf{x}, \omega) \exp(-ik_T \Delta s(\mathbf{y}')) ds_{y'}. \tag{14}$$

Using eq.(10) based on the linear system theory, the unknown characteristics of the time variation and measurement equipment may be represented as follows:

$$T(\omega) B(\omega) E_r(\omega) E_t(\omega) I(\omega) = O_{cor}(\mathbf{x}, \omega) / \bar{D}_{cor}(\mathbf{x}, \omega). \tag{15}$$

The response function $D(\mathbf{x}, \omega)$ for the specimen with a cylindrical cavity has the same form as $D_{cor}(\mathbf{x}, \omega)$, i.e.,

$$D(\mathbf{x}, \omega) = \bar{D}(\mathbf{x}, \omega) T(\omega) \tag{16}$$

where $\bar{D}(\mathbf{x}, \omega)$ represents the numerical solution obtained by the combined method with the assumption of $T(\omega) = 1$. From eqs.(9), (15) and (16), the frequency components $O(\mathbf{x}, \omega)$ of the observed waveform can be evaluated in the following form

$$O(\mathbf{x}, \omega) = O_{cor}(\mathbf{x}, \omega) \bar{D}(\mathbf{x}, \omega) / \bar{D}_{cor}(\mathbf{x}, \omega). \tag{17}$$

The A-scope waveform $o(\mathbf{x}, t)$ in the time domain can be reconstructed by applying the inverse Fourier transform to $O(\mathbf{x}, \omega)$.

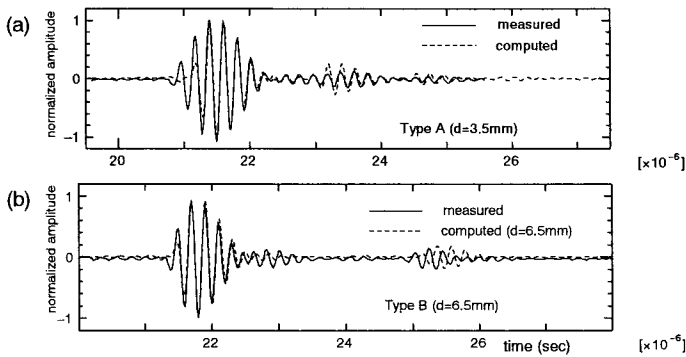


Fig. 12. Comparison between observed A-scope waveforms and simulated ones for the (a) type A specimen and (b) type B specimen.

Fig.12 compares measured and computed A-scope waveforms. Their amplitudes are normalized with respect to their maximum value. For the type A specimen, the phases of the measured and computed wave forms show relatively a good agreement, but some differences are observed at the initial part of the big echo around $21\mu\text{sec}$. For the type B specimen, the first big echoes of numerical and experimental results fit well, however, the phases of subsequent small echoes are not reproduced well by the numerical simulation.

CONCLUSIONS

An efficient numerical method which combines BEM with ray theory was developed to simulate an ultrasonic testing of a thick plate. The method can save computational time by reducing the number of boundary elements used in BEM analysis, and particularly useful when many transmission points are need to be considered. Numerical examples which simulate pulse-echo tests with SH-wave probes were shown and the results for a surface SH-wave probe were compared with the experimental data. Although agreements between numerical results and experiments are not fully satisfied, it was shown that the periodicity appeared in power spectra may be used to evaluate the depth of subsurface defects. Since all numerical results shown in this paper were based on a simple probe model, a more appropriate modeling technique will be necessary to have better agreement between numerical and experimental data.

REFERENCES

1. Hirose, S.(1999) Review of Progress in QNDE, D.O.Thompson and D.E.Chimet (eds). Plenum, New York, Vol.18,pp.87-93. New York.
2. Banerjee, P.K.and Butterfield, R.(1981).Boundary Element Method in Engineering Science. McGraw-Hill, London.
3. Schmerr, L.W.Jr.(1998). Fundamentals of Ultrasonic Nondestructive Evaluation. Plenum. New York.

THE USE OF SURFACE WAVES FOR THE NON DESTRUCTIVE TESTING OF CONCRETE STRUCTURES

O. ABRAHAM*, **H. PEDERSEN****, **G. HEVIN*****, **X. KERGADALLAN******, **Ph. CÔTE***

* Laboratoire Central des Ponts et Chaussées

BP 19 - 44340 Bouguenais - France

** Laboratoire de Géophysique Interne et Tectonophysique
Université Joseph Fourier - BP 53X - 38041 Grenoble - France

*** EDF - Division R&D, Dpt REME, Gpe CND

6 quai Watier _ 77401 Chatou Cedex - France

**** SEG, Savoie Technolac - BP 230 - 73375 Le Bourget du Lac Cedex - France

ABSTRACT

The use of surface waves for the survey of pavements and sub-surface soils is becoming more and more widespread in the civil engineering community. In this paper we present, through our ongoing research work on the subject, two recent field applications of Non Destructive Testing (NDT) methods for concrete using surface wave: the mechanical characterisation of surface damaged concrete structures and the determination of the depth of an opening crack.

In the first example, rather than using the common SASW (Spectral Analysis of Surface Waves) set-ups, we use multiple filter and phase velocity analysis as used in Earth physics and here applied to a large number of sensors. This multiple filter and phase velocity analysis is combined with seismic refraction methods to characterise three 3mx4mx0,8m concrete slabs with, on top, a layer of light weight concrete with three different thicknesses (0.05m, 0.1m and 0.2m).

In the second example, the depth of opening cracks is recovered using the crack low pass filter effect on surface wave propagation.

For both cases numerical results obtained with the boundary element method (IBEM) are also presented.

KEYWORDS

Surface waves, concrete, dispersion curves, IBEM, crack depth measurement

INTRODUCTION

The use of surface waves to study the mechanical characteristics of the sub-surface is becoming more and more widespread in the field of civil engineering. The study of surface waves can provide information on the shear wave velocity as a function of depth which is necessary to calculate G profiles. Surface waves have the advantage that they do not require a shear source. Thus it is an interesting alternative approach to methods that use shear wave propagation. Furthermore [1] evaluated that a point force, in a homogeneous half space, radiates 67% of the energy as a Rayleigh wave, while 26% is carried by the shear wave and 7% by the compressional wave. Moreover, surface waves propagate radially along circular wave fronts on the surface. Consequently, surface waves dominate over the body waves at the surface and are therefore easy to excite and to record.

The main characteristic of surface waves that is used in the following is the fact that their penetration depth depends on their wavelength. The longer the wavelength, the deeper is the penetration depth of the medium. Thus a medium having characteristics changing with depth, will modify the surface wave propagation. If the mechanical properties vary with depth surface wave velocity will vary with frequency. This phenomenon is called dispersion; it is described by dispersion curves, i.e. the values of the surface wave velocity as a function of frequency. On the other hand, if an obstacle exists in the near surface, surface waves will react differently depending on their wavelength compared to the obstacle geometry.

These two aspects are discussed in the following.

APPLICATION OF SURFACE WAVES FOR MECHANICAL CHARACTERISATION

To determine the velocity dispersion curves, the experimental set-up and data processing often rely on the well documented SASW method (Spectral Analysis of Surface Waves) [2,3]. SASW has the advantage of requiring only two sensors but it has several disadvantages:

- the experimental procedure is fastidious,
- with two sensors it is not possible to separate surface wave modes,
- The body waves, above all the shear waves, add noise to the results,
- the sensors are in the near field in the standard experimental set-up, even though, in the inverse problem, it is a far field forward model that is often used [4].

In our present research work, we are currently evaluating Non Destructive Testing (NDT) methods that combines surface waves study as well as seismic refraction using several sensors. This objective has lead us to carry out both numerical and experimental studies.

Indeed, when it is possible, the data collected during a seismic refraction survey [4,5], can be judiciously used for the determination of the surface waves dispersion curve as the compression wave velocity (with the density) are parameters that intervene in the a priori model and forward modelling of the inverse problem. Furthermore seismic refraction can be used to determine the thicknesses of the layers. In refraction set-ups data from several sensors are collected (currently 24) at one time. There is no need with this type of set-up, as opposed to the SASW, to move source and sensors from one point to another depending on the wavelength one expects to measure. In addition, multi-sensors recording set-ups will overcome most of the problems listed above [5].

Numerical results and signal processing

The signal processing technique for the multi-sensor recordings is composed of three steps :

1. the determination of the group velocity dispersion curve,
2. the selection of one mode of the surface wave,
3. the determination of the phase velocity dispersion curve.

Figure 1a shows the seismogram obtained numerically for a undamaged concrete half space that is overlaid by a layer of 0.1m which is indicative of damaging. For the calculation of the synthetic seismograms we chose to use a boundary element method (IBEM) because it is very easy to introduce an impact at the surface and it has the advantage of making possible an undulating geometry (cf. the second example) of the layer - half space interface [6]. In the IBEM, the full wavefield is calculated so the complexity of interfering waves in the near field is taken into account. Figure 1b gives the theoretical dispersion curves computed with [7] for three different overlying thickness layer and Figure 1c shows the phase velocity dispersion curve calculated with the seismogram presented Figure 1a according to the three steps mentioned above.

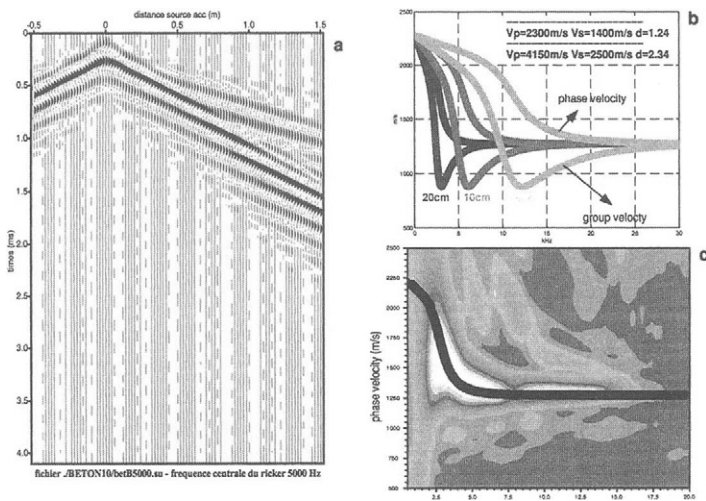


Fig. 1. Numerical results obtained with IBEM for an half space ($V_p=4150\text{m/s}$, $V_s=2500\text{m/s}$, $\rho=2.34\text{t/m}^3$) overlaid by a layer of lower mechanical impedance ($V_p=2300\text{m/s}$, $V_s=1400\text{m/s}$, $\rho=1.37\text{t/m}^3$) (a) seismogram for a 0.1m layer (b) dispersion curves for three different overlying layer thicknesses (0.05m, 0.1m and 0.2m) (c) phase velocity computed from the seismogram (1a) with the corresponding theoretical curve superimposed.

In [4] we show that dispersion curves calculated from sensors located in the far field (Figure 1c) better match the theoretical dispersion curves that ones calculated in the near field.

In the following, we show our first experimental results obtained on two layer concrete test slabs.

Experimental results

Figure 2a shows the seismogram recorded on a 3mx4m concrete test slab of 0.75m thickness overlaid by a 0.1m layer of light concrete whose mechanical characteristics are assumed equal to those used for the numerical computation. The sensors are Bruel & Kjaer n°4393 accelerometers. The source, located near one edge of the slab, is a steel ball with a diameter of 0.02m that was selected because its frequency content matches the frequency band where the dispersion curves vary (below 12kHz) without approaching the resonance frequency of the accelerometers.

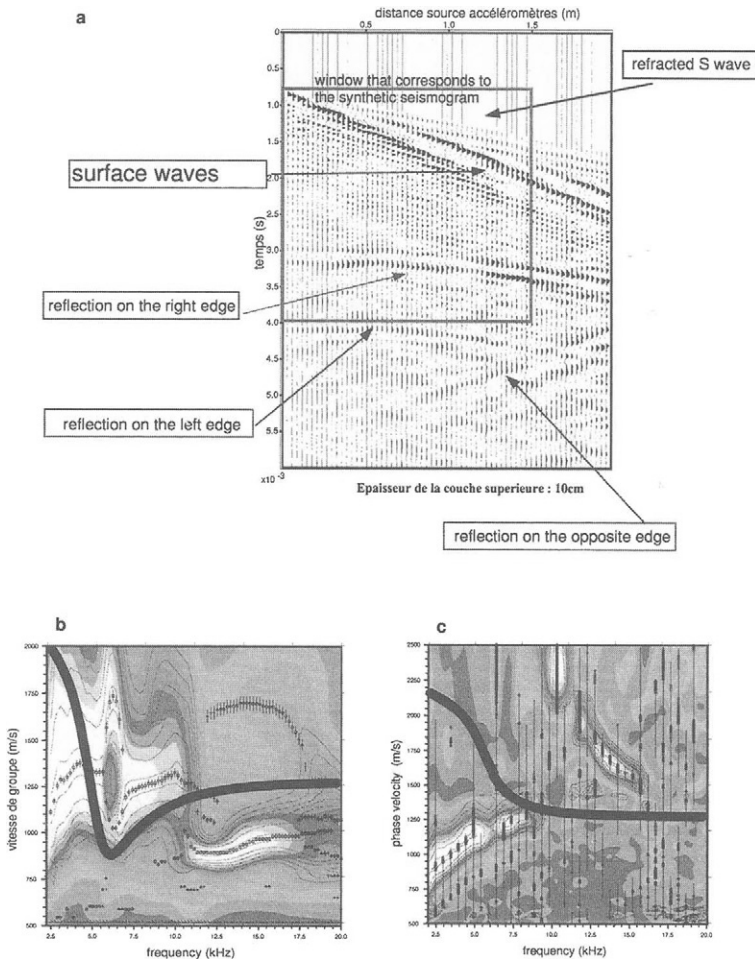


Fig. 2. Experimental results obtained for a two layer concrete test slab (a) seismogram (b) experimental group velocity calculated in the window shown in figure (a) in thick line is superimposed the theoretical dispersion curve (c) experimental phase velocity dispersion curve.

Note that the seismogram is more complex than the numerical one mainly due to the finite geometry of our propagating medium. The reflections of the surface waves on the three edges are clearly visible. Note also that we must work with wavelengths smaller than the thickness of the slab so that frequencies below 2.5kHz should not be taken into account.

Figure 2b shows the group velocity in a time window selected before the first reflection and Figure 2c the phase velocity obtained with a multiple filter techniques [7,8]. Even though their global trend corresponds to a medium with a velocity that increases with depth, the experimental dispersion curves do not match the numerical ones. The same discrepancy is obtained for two other slabs with overlying layers of 0.05m and 0.2m. Our current work is focused on the explanation of this phenomenon which might be due to:

- concrete segregation while curing,
- a source frequency content not as adequate as expected,
- the influence of the soil even for wavelengths of the order of but smaller than the thickness of the slab.

For the last possible explanation quoted numerical work is required to calculate the dispersion curve from synthetic seismograms as the current modelling technique we are using [7] cannot cope with system having high velocity layers above the half space.

APPLICATION OF SURFACE WAVES FOR GEOMETRY CHARACTERISATION

Introduction

The determination of the depth of an opening crack in concrete, even though described in official state norms [9], is often not obvious and can lead to an underestimation of the depth when the crack is partially closed [10]. We propose an alternative approach [10,11] using surface waves to measure the depth of an opening crack. In the steel NDT community, surface waves are used in the time domain to reach this goal. The principle can be explained with Figure 3 which shows a seismogram calculated with the IBEM [6] for a crack of 0.09m depth in concrete. The surface waves arriving on the crack is diffracted by its tip and the time that separates the directly transmitted surface wave and the diffracted one is directly proportional to the depth.

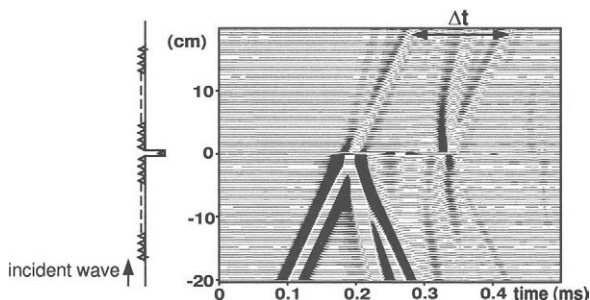


Fig. 3. Synthetic seismogram calculated with IBEM for a crack of 0.09m.

Unfortunately, as concrete is not a homogeneous medium with regards to the wavelengths we are considering and because our source signal is not as sharp as that used in numerical calculations, it is difficult to work in the time domain with experimental data. A solution is to work in the frequency domain as described below.

Frequency domain approach

As the depth penetration of surface waves depends on the wavelength, the low frequencies of the surface wave train incident on a crack, will be less affected than the high frequencies. A large amount of the low frequency energy will be directly transmitted below the crack whereas the main part of the high frequencies will be reflected back. The crack can therefore be viewed as a low pass filter whose cut off frequency is related to the depth of the crack [10].

The filter role of cracks can be characterised with the computation of the spectral ratio of the transmitted signal (U_t) divided by the incident signal (U_i). The mean of this ratio, calculated with several sensors located before and after the crack, is presented for three crack depths in Figure 4. Experimental and numerical (obtained with IBEM) results are superimposed. The relation between the depth of the crack $h(\text{cm})$ and the wavelength corresponding to the cut off frequency $\lambda(\text{cm})$ obtained by analysis of the synthetic seismograms [10]:

$$h(\text{cm}) = \lambda(\text{cm})/2.46 - 1.4$$

The cut off frequency is determined using the slope of the spectral ratio U_t/U_i . This slope is almost equal to 1 in the low frequency range and decreases quite abruptly towards zero ± 0.075 . We define the cut off frequency as the frequency for which the slope is equal to -0.075 after this minimum.

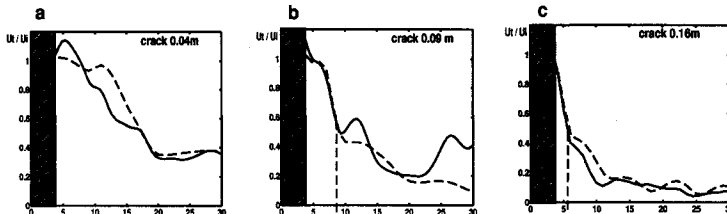


Fig. 4. Experimental (solid line) and numerical (dotted line) results obtained for three crack depths (a) 0.04 m (b) 0.09m (c) 0.16m

The experimental results were obtained on artificial cracks of 0.005m width in a concrete slab of 6m x 4m. The experimental cut off frequency is $8.37 \pm 0.8 \text{ kHz}$ for the depth of 0.09m, that is $0.097 \pm 0.019 \text{ cm}$. For the depth of 0.16cm the measured cut off frequency is equal to $5.67 \pm 0.5 \text{ kHz}$ which gives a depth of $0.16 \pm 0.034 \text{ cm}$. In the case of the crack of 0.04m depth, the experimental results do not match the numerical ones mainly because the cut off frequency expected is near the resonance frequency of the accelerometers and because of the damping of high frequencies due to the high level of heterogeneity in the concrete.

The method was applied on numerical and experimental seismograms to cracks filled with water and cracks partially closed. It is shown in [10] that surface waves yield information of

the overall depth of the crack. In the case of partially closed cracks, the nearest contact from the surface can be measured by analysis of the body waves [9] and an estimation of the whole crack depth obtained by analysis of the surface waves as presented here. The two methods are therefore complementary.

We illustrate the method described in [9] and our method on a last example (Figure 5) where measurements were carried out on a real crack on a bridge [10]. In the second location (point 2), the depth of the crack measured according to [9] is equal to $0.19 \pm 0.035\text{m}$ (Figure 5a) and the surface waves give a value of $0.15 \pm 0.027\text{cm}$ thus confirming the previous result (Figure 5b). On another location (point 1), the depth measured using surface waves method is significantly higher than with technique [9] (Figure 5c). This is confirmed by a visual inspection of the crack on one side of the concrete so we concluded that the crack is partially closed at this location.

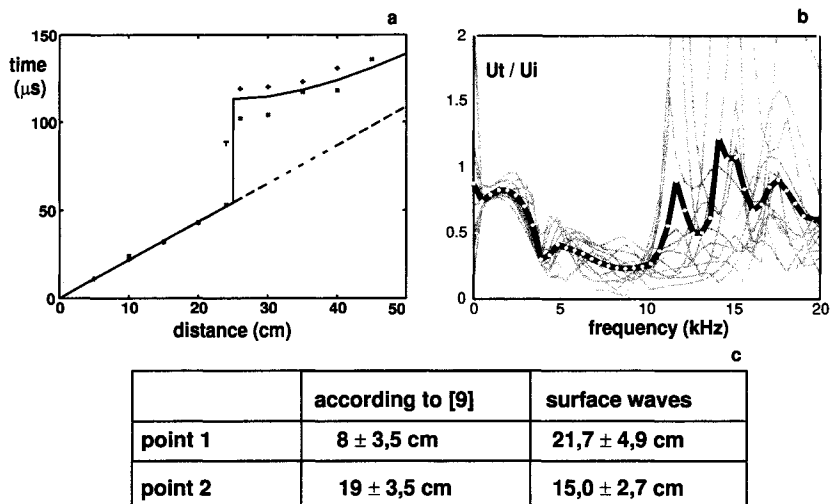


Fig. 5. Results obtained on a bridge (a) according to the method proposed in [9] for location 1 (b) with the surface waves method for location 1. Results above 10kHz should not be taken into account as the signal to noise ratio is poor due to experimental condition (c) table summarising results from two locations.

CONCLUSION

Concrete test slabs were built to carry out experiments for the use of surface waves in the mechanical and geometrical characterisation of concrete structures. Preceding our experimental work we currently perform numerical calculations with the IBEM to design new Non Destructive Methods and study all the parameters that influence their efficiency and

precision. In the case of mechanical characterisation this procedure has led us to couple seismic refraction and the study of the dispersion of surface waves. In the case of geometry characterisation, more precisely the determination of open crack depth, a frequency domain method has been elaborated and evaluated.

REFERENCES

1. Miller G. F., Pursey H. (1955). In: *Proceedings of the Royal Society, London. Serie A*, Vol. 233, pp. 55-69.
2. Stokoe K.H., Wright S.G., Bay J.A., Roësset J.M. (1994). In: *Proceedings of the XIIIth ICSMFE*, pp. 15-25, R.D. Woods (Ed.). Oxford & Ibh Publishing Co. Pvt. Ltd., New Delhi, India.
3. Matthews M.C., Hopes V.S., Clayton C.R.I. (1996). In: *Proc. Instn Ci. Engrs Geotech. Engng.*, Vol. 119, pp. 84-95.
4. Abraham O., Pedersen H., Côte Ph. (1998). In: *Proceedings of the IVth Meeting of the Environmental and Engineering Geophysical Society (European Section)*, pp. 395-398. Barcelona, Spain.
5. Jongmans D., Demanet D. (1993). In: *Engineering Geology*, Vol. 34, pp. 105-113.
6. Pedersen H. A., Maupin V., Campillo M. (1996). In: *Geoph. J. Int.*, Vol. 125, pp. 545-558.
7. Herrmann, R. (1986). *Computers programs in seismology*, St. Louis University, MO, USA.
8. Dziewonski A., Bloch S., Landisman M. (196). In: *Bull. Seism. Soc. Am.*, Vol. 59, pp. 427-444.
9. British Standard (1986). In: *Testing concrete*. BS 1881 : Part 203.
10. Hévin G. (1998) *Utilisation des ondes de surface pour l'auscultation des structures en génie civil : application à la caractérisation des fissures de surface*. PhD Thesis, University J. Fourier, Grenoble, France
11. Hevin G., Abraham O., Pedersen H., Campillo M. (1998). In: *NDT&E Int.* Vol. 31, No. 4, pp. 289-297.

FRACTURE MECHANICS APPROACH TO CRACK DEPTH DETERMINED THROUGH ULTRASONIC METHOD

T. KAMADA, M. KUNIEDA and K. ROKUGO
*Department of Civil Engineering, Gifu University,
1-1 Yanagido Gifu 501-1193, Japan*

ABSTRACT

In general, the evaluation of crack depth in concrete members through the ultrasonic method is carried out by using the propagation time of the ultrasonic pulse diffracted at a crack tip. However, it is well known that the fracture process zone (FPZ) with a large number of micro-cracks exists around and ahead of the main crack tip. Therefore, it is important to clarify the influence of cracks on the propagation of ultrasonic pulses in order to confirm the validity of the ultrasonic method for crack depth determination. In this study, the crack depth determined through the ultrasonic method was compared with those measured by dyeing and estimated by finite element analysis (FEM Analysis) with a tension softening diagram.

KEYWORDS

Ultrasonic method, concrete, crack depth, fracture process zone.

INTRODUCTION

The quantitative evaluation of crack depth and width is important for the diagnosis of the structural integrity of the concrete structures. The cracks inside the concrete members cannot be recognized with the visual observation, but can be detected with the ultrasonic method. Many reports [1-3] have been given for evaluating the crack depth by the ultrasonic method. In these works, testing methods using the propagation time of ultrasonic pulses diffracted at the crack tip have been adopted. A large number of micro-cracks are produced in the fracture process zone (FPZ), which develops around and ahead of the main crack tip [4,5]. The influence of cracks on the propagation of ultrasonic pulses should be clarified. In this study, the crack depth under the loading and unloading conditions was predicted through the ultrasonic method, and was compared with the measured crack depth after dyeing. In addition, the crack depth was estimated by finite element analysis (FEM Analysis) with a tension softening diagram, and the results were compared to those obtained through the ultrasonic method.

Table 1. Mixture proportions of concrete

G_{max} (mm)	W/C (%)	Unit content (kg/m ³)				Ad.* ⁴
		Water	Cement* ¹	Fine agg.* ²	Coarse agg.* ³	
15	50	172	341	787	1029	1.024

*1 : High early strength portland cement (specific gravity: 3.12)

*2 : Fine aggregate (specific gravity: 2.58, fineness modulus: 2.93)

*3 : Coarse aggregate (crushed stone, maximum size: 15mm,
specific gravity: 2.62, fineness modulus: 6.72)

*4 : Admixture (AE water reducing agent)

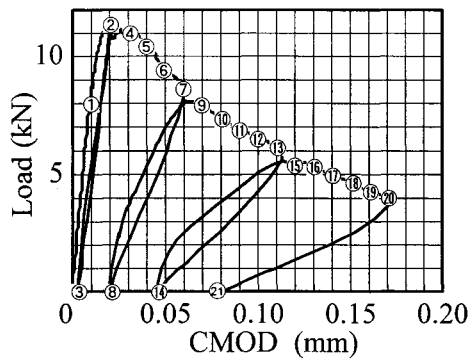


Fig. 1. Measurements of ultrasonic velocity

OUTLINE OF EXPERIMENTS

Specimens

The size of the specimen was $100 \times 100 \times 400$ mm. The mixture proportions of concrete are shown in Table 1. The maximum size of coarse aggregate was 15 mm. Water curing was carried out for 28 days, and the four-point bending test was performed. At the center of the specimen, a notch (depth: 20 mm) was made by a concrete cutter before the loading test.

Detection of Crack Depth Using Ultrasonic Method

The propagation time of the ultrasonic pulse was measured by the two-probe transmission method at 0.01mm intervals of CMOD (crack mouth opening displacement) as shown in Fig. 1. Fig. 2 shows the location of the probes. When the applied load was removed to nearly 0 from CMOD of 0.02, 0.06, 0.11 and 0.17 mm, the measurement was carried out. Therefore, the measurement was done twenty-one times in all. The crack depths were calculated from the pulse propagation times by using the Tc-To method [3] as the ultrasonic crack depths.

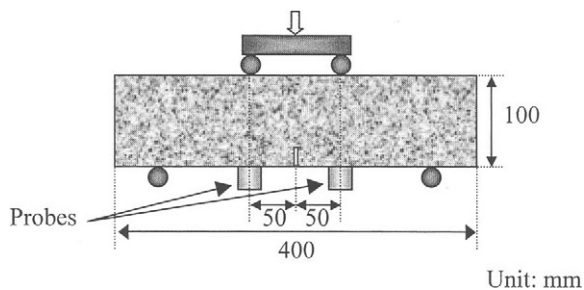


Fig. 2. Test setup

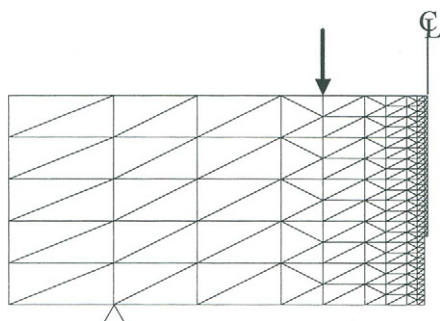


Fig. 3. Mesh for FEM analysis

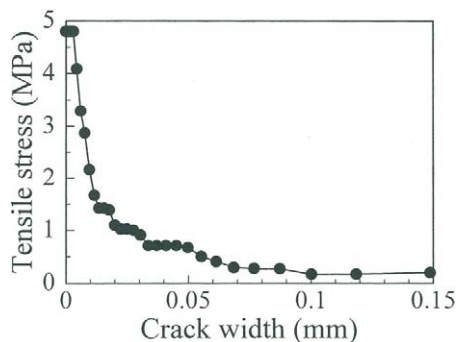


Fig. 4. Tension softening diagram for FEM analysis

Detection of Crack Depth by Dyeing

The crack surfaces in eleven specimens were dyed with red ink after being unloaded. Three specimens were adopted for each unloading from CMOD of 0.02, 0.06 and 0.11 mm, and two specimens for unloading from CMOD of 0.17 mm. The ratio of the dyed section area to the cross section area of a specimen was calculated by image analysis. The averaged crack depth was named the dyed crack depth. In addition, the maximum and minimum depths of the dyed cracks were also measured.

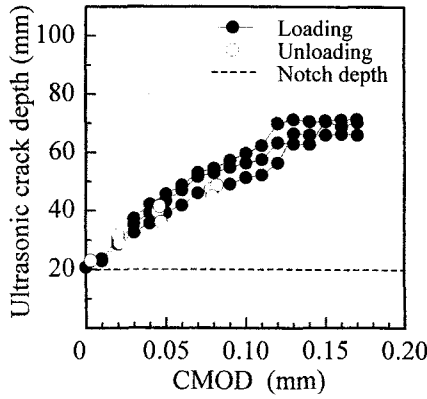


Fig. 5. Ultrasonic crack depth

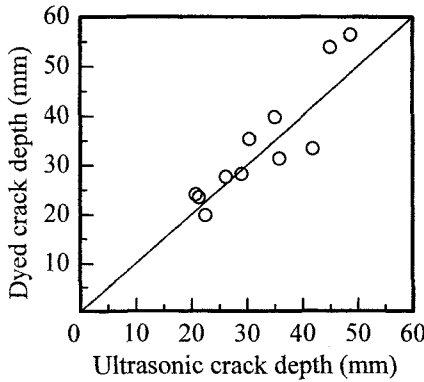


Fig. 6. Dyed and ultrasonic crack depths

Determination of Crack Depth through Analysis

FEM analysis combined with a fictitious crack model [6] was carried out to determine crack depth. Considering the symmetry of the specimen and the loading geometry, a half of the specimen was analyzed as shown in Fig. 3. The tension softening diagram (Fig. 4) obtained from the experimental load-CMOD curve was adopted as a constitutive model for tension. The tip of the analytical crack was taken to the point, where the stress agrees with the tensile strength, that is, the initial tensile stress of the tension softening diagram.

EXPERIMENTAL AND ANALYTICAL RESULTS

Ultrasonic Crack Depth and CMOD

The ultrasonic crack depths versus CMOD are shown in Fig. 5. The crack depths after

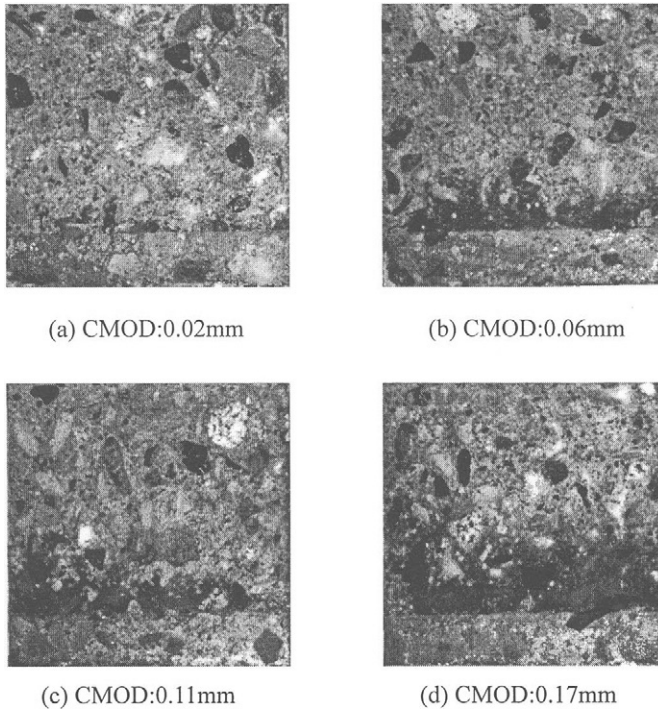


Fig. 7. Cross section of specimen and dyed section

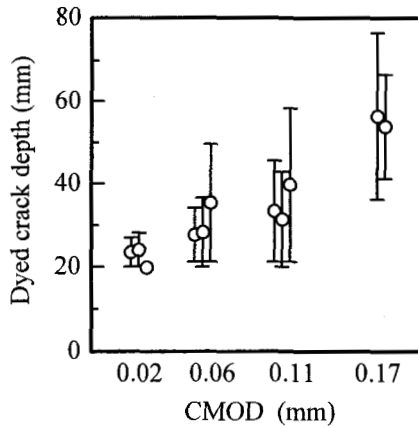


Fig. 8. Maximum and minimum dyed crack depth

unloading were also plotted with CMOD values not before but after unloading. The ultrasonic crack depth after unloading became smaller than that before unloading. After unloading, the propagating path of the ultrasonic pulse seems to become shorter due to closing

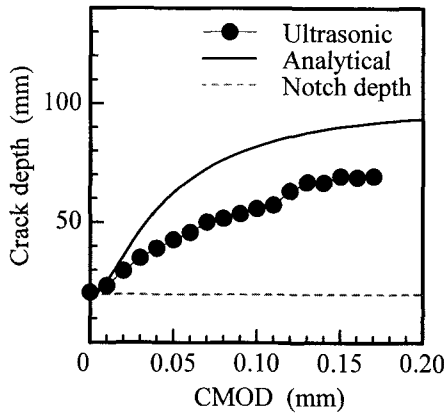


Fig. 9. Ultrasonic and analytical crack depth

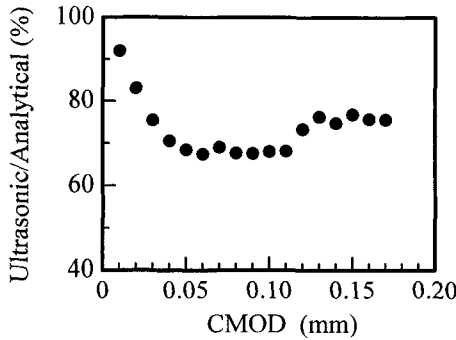


Fig. 10. Ratio of ultrasonic crack depth to analytical one

of cracks in FPZ.

Ultrasonic Crack Depth and Dyed Crack Depth

Fig. 6. shows the relation between the ultrasonic crack depth and the dyed one. Good agreement between these two kinds of depth was observed, when the crack depth was less than 40 mm. When the depth was over 40 mm, the dyed crack depth was larger than the ultrasonic crack depth. One of the reasons of this difference may be that the ultrasonic crack depth was determined from the propagation time of the pulse passing through the shortest path in the specimen. Examples of dyed fracture surfaces are shown in Fig. 7. The depth of the dyed cracks in the specimen was not constant [7]. The maximum and minimum depths of the dyed cracks in each specimen are shown in Fig. 8. As the CMOD became larger, the difference between the maximum and minimum crack depths became large.

Ultrasonic Crack Depth and Analytical Crack Depth

Fig. 9. gives the relation between the ultrasonic and analytical crack depths. The ultrasonic crack depth was about 70% of the analytical one, as shown in Fig. 10. Although the analytical crack was assumed to be in constant depth, and to be open up to the crack tip, however, the depth of the real crack was not constant, as shown in Fig. 7. The ultrasonic crack depth was measured only at the center in specimen width.

CONCLUSIONS

The crack depth obtained through the ultrasonic method was compared with the analytical crack depth and the dyed crack depth, and the following conclusions were obtained:

- (1) The ultrasonic crack depth measured after unloading became smaller than that before unloading. The propagating path of the ultrasonic pulse seems to become shorter due to closing of cracks in FPZ.
- (2) Good agreement between the ultrasonic crack depth and the dyed one was observed when the crack depth was less than 40 mm. When the depth was over 40 mm, the dyed crack depth was larger than the ultrasonic crack depth. This difference may be caused by that the ultrasonic crack depth depends on the shortest pass in the specimen.
- (3) The ultrasonic crack depth was about 70% of the analytical one. The main reason of this difference may be that the analytical crack was assumed to be in constant depth and to be open up to the crack tip.

REFERENCES

1. British Standards Institution (1974) *Recommendations for Non-destructive Methods of Test for Concrete - The Measurement of the Velocity of Ultrasonic Pulse in Concrete*, BS 4408, Part 5.
2. Kamada T., Iwanami M. Nagataki S. and Otsuki N. (1996) *J. of Materials, Concrete Structures and Pavements*, No.538/V-31, 81.
3. Amasaki S. and Akashi T. (1981) *Transactions of the JCI*, 3, 113.
4. Otsuka T. (1992) In: *Fracture Mechanics of Concrete Structures*, Z. P. Bazant (Ed.). Elsevier Applied Science, London and New York, pp.485-490.
5. Otsuka K., Date H. and Kurita T. (1998) In: *Fracture Mechanics of Concrete Structures*, H. Mihashi and K. Rokugo (Eds). AEDIFICATIO Publishers, pp.3-16.
6. Hillerborg A., Modeern M. and Petersson P. E. (1976) *Cement and Concrete Research*, 6, 773.
7. Swartz S. E. and Refai T. (1989) In: *Fracture Toughness and Fracture Energy*, H. Mihashi, H. Takahashi and F. H. Wittmann (Eds). Balkema, pp.509-520.

This Page Intentionally Left Blank

DETECTION OF ULTRASONIC PULSE ECHO THROUGH STEEL BAR IN CONCRETE CRACK DEPTH MEASUREMENT

TAKAYOSHI HIRATA and TAKETO UOMOTO
*OBAYASHI Corporation. Technical Research Institute, and
Center for Collaborative Research, University of Tokyo, Japan*

ABSTRACT

The aim of improving the reliability of an ultrasonic crack depth survey of reinforced concrete structures, the authors proposed a method of eliminating the effect of reinforcement near the surfaces of concrete structures and investigated the effect of ultrasonic frequency employed for such a survey. As a result, a possibility of detecting reinforcement near concrete surfaces was indicated. It was also found necessary to select an ultrasonic frequency suitable for crack depth measurement.

KEYWORDS

Ultrasonic measurement, concrete crack depth, frequency, reinforced concrete, waveform

INTRODUCTION

In Japan, the lessons learnt from the 1995 Hyogoken-Nambu earthquake and the issue of concrete deterioration in structures constructed in the 1970's have led to a demand for evaluation existing concrete structures [1]. With such a social demand as a background, nondestructive testing has been acquiring importance as a technique for maintaining existing structure [2].

The authors took up the subject of crack depth measurement by ultrasonic testing from among techniques for examining cracking, one of the indices to deterioration of concrete structures. Thanks to its safety and simplicity, ultrasonic testing has accumulated a substantial track record, but generally speaking, its reliability has not been rated high as a tool for crack detection of reinforced concrete structures. This may not only stem from ultrasonic nondestructive testing instruments, but also from the nonuniformity of reinforced concrete structures and the complexity of crack configurations.

Accordingly, the authors explored a method of eliminating the effect of reinforcement embedded near the surfaces of reinforced concrete structures on the ultrasonic crack depth detection, with the aim of improving the reliability of such a detection technique. Basic investigation was also conducted on the effect of ultrasonic frequencies employed in the test.

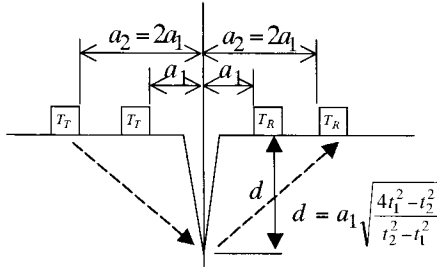


Fig.1 Modified BS method

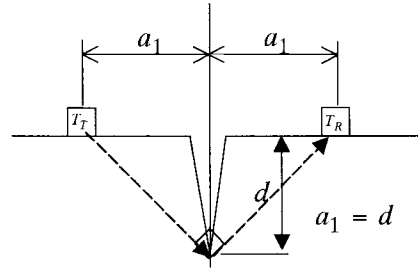


Fig.2 Right angle diffracted wave method

MAJOR ULTRASONIC MEASURING METHOD AND PROBLEMS

The Tc-To method and modified BS method (Fig. 1) are typical examples of the “time of flight difference” method, in which a transmitting probe and receiving probe are set across a crack and the crack depth is determined from the propagation time of pulses diffracted near the crack tip. The problems of these methods are as follows:

- 1) When cracks surface touch in the concrete or when reinforcing steel bars crosses a crack, pulse echoes through the cracks touch surface or the reinforcing steel bars are received instead of the diffracted wave near the crack tip, leading to underestimation of the crack depth.
- 2) The calculated ultrasonic velocity varies depending on the distance between the probes.

Another simple method of measuring crack depth in concrete is the method using right angle diffracted wave (Fig. 2) proposed by Yamaguchi et al [3,4,5], in which diffracted waves propagating in directions perpendicular to the travelling direction are measured. The problems of this method are as follows:

- 3) Since Poisson’s ratio of concrete is not constant, the diffraction angle may not be perpendicular depending on the concrete conditions.
- 4) Measurement is made where the diffracted waves reverse, but the location may vary depending on the sensitivity of the probes.

Moreover, crack configurations may be complicated, such as two or more cracks close to one another or one crack ending and the other beginning from nearby. Also, the minimum crack width measurable by these methods is unknown. These encumber crack depth measurements of concrete in actual structures.

PROPOSAL OF A METHOD OF ELIMINATING THE EFFECT OF NEAR-SURFACE REINFORCING STEEL BAR

Most reinforced concrete structures encase reinforcing steel bars within 100 mm from the surfaces. When measuring the depth of a crack crossed by a reinforcing steel bar located near the measuring point, ultrasonic pulses propagate or are diffracted through the bar as shown in Fig. 3, instead of a round the crack tip. This reduces the propagation time, resulting in underestimation of the crack depth. This phenomenon can cause a gross error in the evaluation of crack depth, being one of the major factors impairing the reliability of crack depth surveys by ultrasonic testing. The authors therefore propose a method of measuring crack depths while

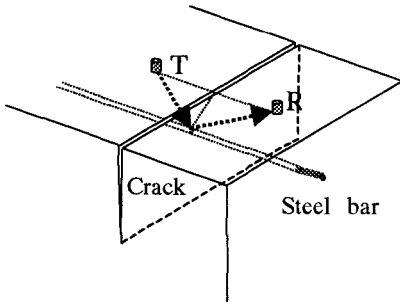


Fig.3 Diffracted wave by way of reinforcing steel bar

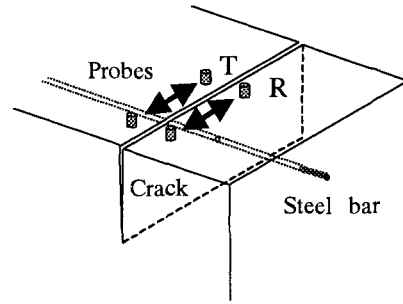


Fig.4 Investigate of the steel bar position

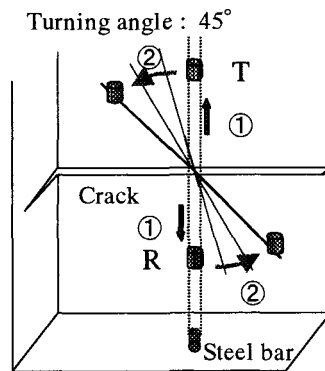


Fig.5 Turning of the probes

judging if the received ultrasonic echoes come through a reinforcing steel bar and eliminating the effect of the reinforcing steel bars.

The measurement procedure and the mechanism of detecting reinforcing steel bars are as follows: Begin by placing the transmitting and receiving probes near and across a crack to measure the depth. Move the probes along the crack maintaining the distance between each other while guessing the reinforcing steel bar line as shown in Fig. 4, until they reach a position where the propagation time is shortest and the ultrasonic echo is highest. This brings the two probes right above a surface reinforcing steel bar. These steps are unnecessary if the positions of surface bars are known by means of other nondestructive tests, such as the pulse reflection method using one probe or the reinforcement radar method. When the location of the surface bar is found, employ the right angle diffracted wave method. Progressively widen the distance between the two probes from near the crack to find the distance at which the rise of the echo sufficiently reverses. This right angle diffracted wave method is very convenient for grasping the diffraction depth of longitudinal ultrasonic waves. Finally, at the position where the rise of the echo is sufficiently reversed, turn the two probes by 45° around the intersection point of the crack and the straight line connecting the probes, while maintaining the distance between the probes constant as shown in Fig. 5. If the pulse propagates or is diffracted through the bar, then the propagation distance is extended, the rising time of the echo is delayed, and the rise of the

echo decreases as the probes are turned. If the pulse is diffracted a round the crack tip, then the propagation distance does not change, resulting in no delay in the rising time of the echo nor any appreciable loss in the height of the echo. This operation can therefore raise the possibility of judging the effect of reinforcing steel bars.

When the presence of reinforcement is recognized, widen the distance between the probes while maintaining the angle of 45° to the reinforcement line to find the positions where the rise of the echo is reversed, at which the crack depth is measured by the right angle diffracted wave method. It is considered preferable to measure the crack depth accurately by such methods as the modified BS method at positions out of the effect of right angle diffracted waves.

TEST PROCEDURE

Ultrasonic reflectoscope

The recent trend of nondestructive testing has been towards the use of the frequency components and phase information of ultrasonic signal waves. The measurement of test frequency becomes more and more important also from the aspect of improving the reproducibility of the ultrasonic test results. This type of digital ultrasonic test instrument was therefore used in these tests (Photo 1). The principal performances of the instrument are given in Table 1. Digital ultrasonic test instruments have strong points as given below when compared with analogue instruments. It should also be taken into consideration that different instruments, including probes, could lead to different test results.

- 1) Errors resulting from visual reading of scales are minimized.
- 2) Test conditions and results can be electronically logged and easily reproduced.
- 3) Digital instruments also have other functions, such as measurement of echo frequency, facilitating data processing.

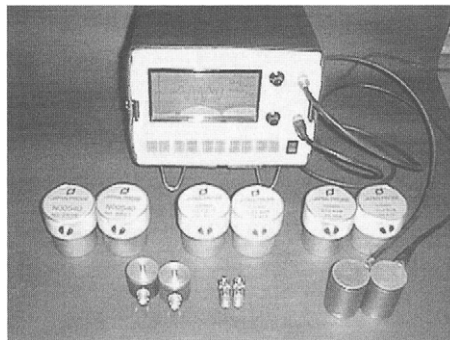


Photo.1 Digital ultrasonic test instrument (TR-300)

Table 1. Principal performance of digital ultrasonic test instrument

Pulse voltage (V)	-350 , -700
Pulse width (μ sec)	5,10,20,50,100,200,2000
Pulse form	Rectangle wave
Sampling length (μ sec)	1600
Sampling time(μ sec)	0.1
Interface	RS-232C Output

Probes

Four types of circular normal incidence probes with a frequency of 50, 100, 200 and 500 kHz were used in the tests. The performances of the probes are given in Table 2. When the longitudinal ultrasonic velocity through concrete is constant, the wavelength decreases as the frequency increases. In concrete with a longitudinal sonic velocity of 4,000 to 4,500 m/s, the

Table 2. Performances of probes

Frequency (kHz)	50	100	200	500
Type	Circular normal incidence probe			
Active element ingredient	PZT	PZT	PZT	PbNbO ₃
Band type	Narrow	Narrow	Narrow	Broad
Active element diameter (mm)	35	40	40	40
Near field length (mm)	3.1	8.1	16.2	41.3
Angle of beam spread in concrete (degree)	198.6	86.3	43.1	19.4
-6dB echo angle of beam spread in concrete (degree)	82.3	35.8	17.9	7.0

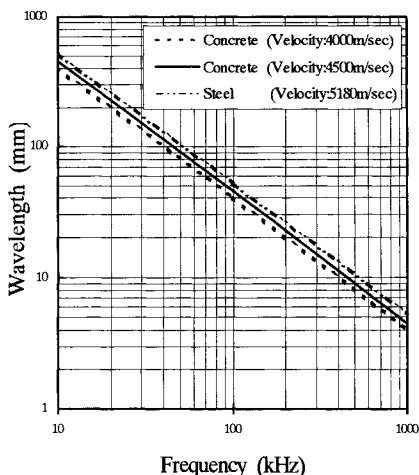


Fig.6 Frequency and wavelength

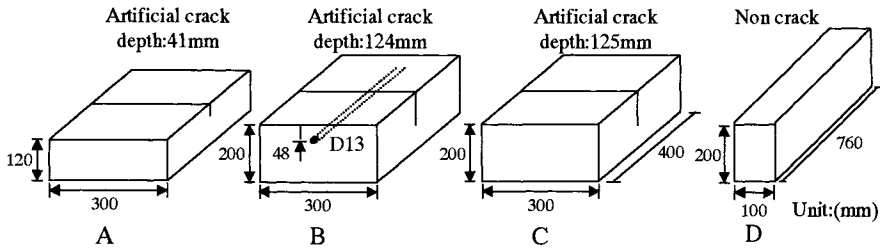


Fig.7 Concrete Specimens

Table 3. Mixture proportions of concrete and results of test

Specimen	W/C (%)	s/a (%)	Unit weight (kg/m ³)					Compressive strength 28days (N/mm ²)	Static Young's modulus E1/3 (×10 ⁴ N/mm ²)	Dynamic Young's modulus (×10 ⁴ N/mm ²)	Poisson's ratio
			W	C	S	G	Adm.				
A,B,C	55	47	163	296	853	1003	0.74	42.7	2.95	4.09	0.18
D	50	46	175	350	807	987	1.05	43.8	3.30	4.73	0.21

wavelength of a longitudinal wave ranges from 10 mm to 100 mm in the frequency range of 50 to 500 kHz shown in Fig. 6. Ultrasonic waves with a short wavelength generally have a good resolution and are suitable for detecting small defects. However, an excessively short wavelength is prone to attenuation by Rayleigh scattering at aggregate particles, being unable to propagate through concrete. An increase in the frequency of probes increases the near field distance, in which the sound pressure does not diminish monotonically with the distance, while decreasing the angle of ultrasonic beam spread.

Specimens and measuring method

Four types of specimens were prepared with artificial cracks as shown in Fig. 7. Two types of mixture proportions were adopted as given in Table 3. The crack depths were measured by bonding probes with surfaces of specimens smoothed with a sander using a glycerin-based couplant. Measurements were made by three methods: the symmetrical permeation method, right angle diffracted wave method and modified BS method.

RESULTS AND DISCUSSION

Detection of near-surface steel bars

Measurements for detecting steel bars near the surfaces of concrete were made using Specimens A and B and 100-kHz probes were employed. There is a artificial crack of the depth 41mm in Specimen A, and D13 steel bar is going through the artificial crack of the depth 124mm in Specimen B. By applying the right angle diffracted wave method, the probes were brought to the points where the rise of the echo is reversed for the first time, and were turned around the point of intersection of the crack and the straight line connecting the probes (see Fig.5). The measurements during this process are shown in Fig. 8. When the pulse is diffracted through a

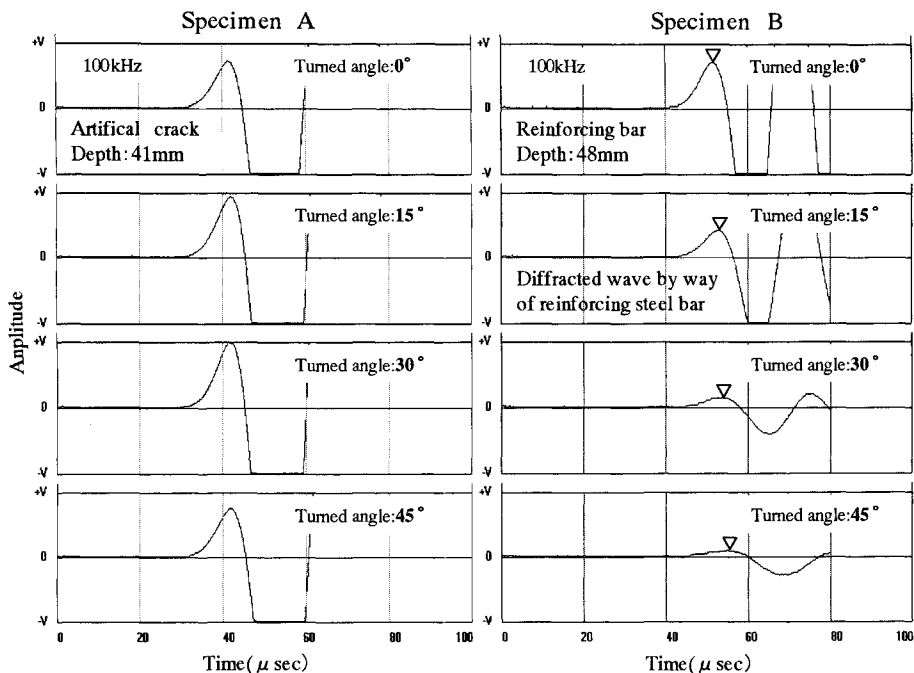


Fig8. Waveforms by tuning of the probes

reinforcing bar, the rise of the echo was delayed and the echo height was reduced as the rotation angle of the probes increased. When the pulse is diffracted round the crack tip, no delay was observed in the rising time, despite slight scatter in the echo height. Accordingly, reinforcing steel bars encased near concrete surfaces are considered to be detectable by this measuring method.

Effect of ultrasonic wave frequency

The effect of frequency on the ultrasonic velocity in Specimen D was investigated by the symmetrical permeation method using four types of probes with different frequencies. The measurements are shown in Fig.9. The effects of frequency on the measured crack depth were also investigated by the right angle diffracted wave method and modified BS method. The results are shown in Fig. 10.

No appreciable effect of the frequency of probes was observed, though the ultrasonic velocity slightly decreased as the frequency increased. The rise amplitude decreased as the probe frequency increased, but the 500 kHz probes could not be measure. This suggests that reduced amplitude may not accurately reflect the propagation time, resulting in an inaccurate measurement of crack depth. The frequency of the probe should therefore be adequately selected. As for the effect of probe frequency on the crack depth measurement, there was no clear tendency in the error, but the differences were marginal.

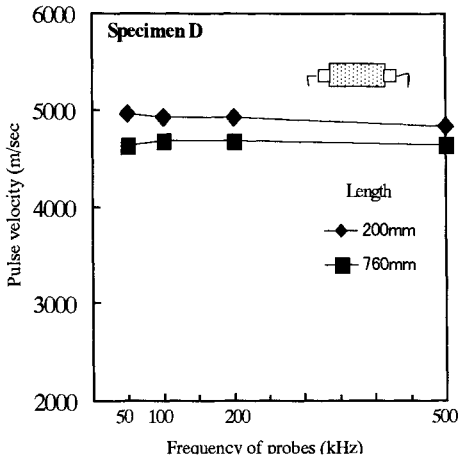


Fig.9 Ultrasonic pulse velocity of concrete

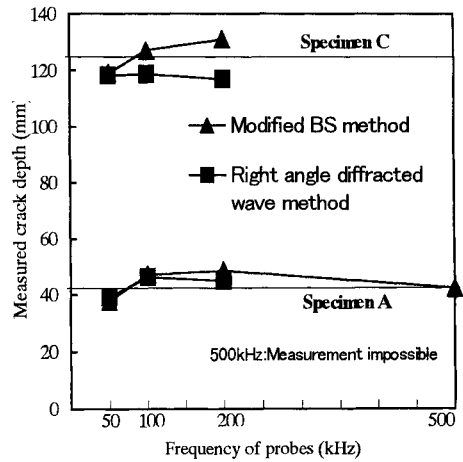


Fig.10 Relationships between measured crack depth and frequency of probes

CONCLUSIONS

Basic investigation was conducted on the method of eliminating the effect of reinforcing steel bars embedded near the surfaces of reinforced concrete structures. The effects of ultrasonic frequency to be used for the tests were also investigated. The following findings were obtained:

- 1) There is a good possibility of detecting reinforcing bars near concrete surfaces by the proposed method. It is considered necessary to define the limits of application of this method under various conditions and to refine and optimize the measuring method.
- 2) The frequency of the probes to be used for crack depth survey is considered to have no appreciable effects on the measurements in the range where the ultrasonic pulse is receivable. It was also found necessary to select a frequency in consideration of the attenuation of ultrasonic energy in the concrete, as the propagation time cannot be accurately measured with an excessively low echo.

REFERENCES

1. KEMI, T. (1998). *Journal of JSNDI*, Volume 47, Number 9, Japan, pp.617-619.
2. UOMOTO, T. (1998). *Journal of JSNDI*, Volume 47, Number 9, Japan, pp.620-623.
3. YAMAGUCHI, T.,HIRONO,S. and MIZOBUCHI,T.(1993). *Proceed of International Conference NDT in Liverpool*, pp.519-529.
4. YAMAGUCHI, T.,MARUMO,F., YAMAGUCHI, T. and OKAMURA,K.(1996). *Journal of JSNDI*, Volume 45, Number 10, Japan, pp.742-748.
5. YAMAGUCHI, T. (1998). *Journal of JSNDI*, Volume 47, Number 9, Japan, pp.636-642.

**NEW ULTRASONIC COMPUTERIZED TOMOGRAPHY TECHNOLOGIES
FOR NONDESTRUCTIVE TESTING AND DIAGNOSTICS
OF BRIDGES WELDED STRUCTURES**

V. KOSHOVY, Z. NAZARCHUK, E. KRIVIN, V. KURIY, I. ROMANYSHYN
Karpenko Physico-Mechanical Institute of National Academy of Sciences of Ukraine.
5, Naukova Street, Lviv, 290601, Ukraine, Fax: (380)322 64 94 27; E-mail:
koshovy@ah.ipm.lviv.ua

ABSTRACT

This paper presents new nondestructive testing (NDT) technologies of welded metal structures based on the principles of ultrasonic computerized tomography (USCT). These NDT technologies opens a new approach to technical diagnostics, taking into account not only the presence of defects, but also the material state in product volume. Especially it concerns those products which have the complex inhomogeneous internal material structure caused by diverse technological processes. Spatial inhomogeneous material state in a product volume is weak-controlled in natural conditions. Among these products, including bridge structural elements, there are welded sheet products.

In paper new NDT technology of welded joints, which uses USCT principles, is presented. This NDT technology is a material characterization technology. It allows to determine in real time the material characteristics spatial distribution (SD) in a product volume including scalar and tensor characteristics.

Peculiarities of USCT NDT technology which uses a mirror-shady method of US sounding of thick-sheet products have been theoretically investigated including numerical simulation. Theoretical results allowed to optimize parameters of data collection scheme and propose new tomographic reconstruction algorithm, optimal for NDT technology.

On the bases of theoretical researches a model of the US NDT tomograph had been developed. Proposed NDT technology was experimentally investigated on welded specimens. A set of restored experimental tomographic images of the material physicomaterial characteristics (PMC) SD in the weld and basic material of the welded sheet product is presented. It is shown that a real joint weld is characterized by a strong mechanical characteristics inhomogeneity in a weld volume. Relative changes of the material PMC, which influences the result of the product diagnostics, may reach 30% and more.

Information about the main technical characteristics and application fields of the developed US NDT tomograph have been represented.

KEYWORDS

Ultrasonic nondestructive testing, mirror-shady method, tomography, reconstruction, material physico-mechanical characteristics, spatial distribution, welded sheet products.

PROBLEM FORMULATION

US NDT of welded structures, as a rule, is employed to determine the defects presence, their coordinates, types, dimensions, orientation, and also to estimate the averaged (on US wave spread direction) values of the material PMC. In time the same, for welded joints the inhomogeneous distribution of the material PMC and material deflected mode (MDM) parameters is typically. Namely MDM inhomogeneity determines the predefective material state (PDSM). So, material domains with anomalous level of residual stresses are the most probable domains for crack-like defects. Therefore one of the ways of improvement of US NDT and technical diagnostics (TD), that consists in estimation of the PDSM and forecast of product working life, is connected with determination of the material PMC SD and inhomogeneous MDM parameters by tomographic methods.

Application of the tomographic methods in US NDT has some peculiarities, which embarrasses the use of traditional approaches of transmission tomography. For a guarantee of high testing productivity and US tomographic system universality to the controlled product geometry the authors propose to carry out data collection by beam projections, reconstruction - by inverse projecting, forming of sum image (SI) and SI projections filtration. Besides, SI can serve as a searching image on basis of which the anomalous domains, being subject of a more detailed testing, are being determined.

Assessment of the material PMC SD is being fulfilled by determination of the material acoustic characteristics (AC) SD (spread velocities and fading of a diversity types of US waves), connected by analytic or phenomenological relations with the sought material PMC, and the subsequent computation of the material PMC SD on their base.

A majority of bridge welded structural elements belong to a class of sheet products, access to which is one-sided. For sheet product testing with one-sided access a mirror-shady method (MSM) is the most adequate and has been selected. However, a limited entry view of sounding US signal is a peculiarity of this method. Thus, it is impossible to provide a complete data collection during tomographic reconstruction.

It has been shown, that data collection scheme is optimal if beam projections collection is carried out by transducer scanning on the product surface at different angles φ [1]. According to that data collection scheme, in case of one sounding view for each product volume element, all the projections are directed on cone formative with an angle which is equal to US signal entry angle.

Data collection scheme peculiarities and inversion formulae during one-viewed data collection «in cone» were not investigated. Selection of US sounding signal entry view and establishment of the effective application fields of US tomographic NDT facilities have not been also fulfilled. US tomographic facilities for products NDT including welded joints have not been developed. Therefore all these problems should be solved.

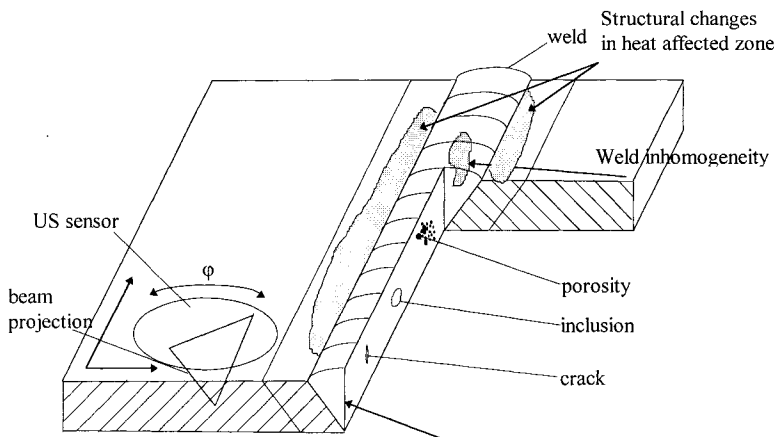


Fig.1. Data collection scheme during testing of welded sheet product.

THEORETICAL RESULTS.

An analysis of data collection scheme possibilities can be carried out by a projecting theorem. Final data collection results by beam projections can be represented by parallel projections set of the explored volume at diverse projecting directions:

$$f(\vec{R}_m, \vec{m}) = \int_{-\infty}^{\infty} g(\vec{R}_m + \vec{m}t) dt, \quad \vec{R}_m \in S_m^{\perp}, \quad (1)$$

where $g(\vec{r})$ is sought SD, $\vec{m} = (\cos\varphi \sin\theta, \sin\varphi \sin\theta, \cos\theta)^T$ is orth, assigning the projecting direction, S_m^{\perp} is plane, perpendicular to \vec{m} and passing across the coordinates origin. Let $G(\vec{\rho}) = \mathfrak{T}_3\{g(\vec{r})\}$ - be a three-dimensional Fourier transformation. According to projecting theorem Fourier transformation of projection $f(\vec{R}_m, \vec{m})$ determines values of function $G(\vec{\rho})$ in section, passing through coordinates origin and perpendicular to \vec{m} , i.e.:

$$\mathfrak{T}_2\{f(\vec{R}_m, \vec{m})\} = G(\vec{\rho}_m), \quad \vec{\rho}_m \in S_m^{\perp}. \quad (2)$$

Completeness of data collection is being provided under condition that \vec{m} is being turned in some plane from 0 to π .

According to a mirror-shady scheme of data collection the projecting results can be represented as sum of two parallel projections $f(\vec{R}_m, \vec{m})$ and $f(\vec{R}_n, \vec{n})$:

$$\mathfrak{T}_2\{f(\vec{R}_m, \vec{m})\} + \mathfrak{T}_2\{f(\vec{R}_n, \vec{n})\} = G(\vec{\rho}_m) + G(\vec{\rho}_n),$$

where $\vec{n} = (-\cos\varphi \sin\theta, -\sin\varphi \sin\theta, \cos\theta)^T$.

During data collection on a sheet product the complete data collection is impossible, because of the limited transducer size. The possibilities of data collection scheme are limited by the angles change of sounding direction ($0 \leq \varphi \leq \pi$, $0 \leq \theta \leq \theta_{\max}$). It yields from the projecting

theorem that one can obtain spectral components $G(\vec{\rho})$ with an exception of the cone components $\gamma = \frac{\pi}{2} - \theta_{\max}$ (Fig. 2).

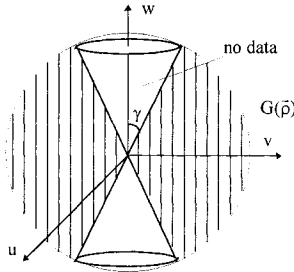


Fig. 2. Results of data collection by a mirror-shady method.

For reconstruction of the inhomogeneities SD along a sheet products thickness the sufficient high-frequency material PMC SD in the planes, parallel to product surface is needed. The welded sheet products have just those properties.

From a projecting theorem we draw an important conclusion, that maximum of information about the inhomogeneity SD is obtained in case when an entry angle (view) of the US sounding signal is maximum. Therefore at that data collection scheme one can choose only one sounding view. Thus, a sounding scheme, which is characterized by the sounding angle $0 \leq \varphi \leq \pi$, $\theta = \theta_{\max}$, is optimal when used in practice.

Consider reconstruction of the inhomogeneity SD at one-viewed data collection « in cone». It has been showed [1] that SI

$$b(\vec{r}) = \hat{K}_3^{\theta_0} \{g(\vec{r})\} = \int_{-\infty(2\pi)}^{\infty} \int g(\vec{r} + \vec{m}k) \delta(\vec{m} \cdot \vec{n}_{\theta_0}) d\Omega dk,$$

where $K_3^{\theta_0}$ is inverse projecting operator, $\vec{n}_{\theta_0} = (-\cos \varphi \cos \theta_0, -\sin \varphi \cos \theta_0, \sin \theta_0)^T$ one can represent as:

$$b(x, y, z) = g(x, y, z) *** \frac{\delta(z \sin \theta_0 - \cos \theta_0 \sqrt{x^2 + y^2})}{\sqrt{x^2 + y^2 + z^2}}. \tag{3}$$

Inversion formulae one can obtain in spectral domain. From relation (3) it is obtained:

$$B(u, v, w) = G(u, v, w) \cdot \begin{cases} \frac{4\pi}{\sqrt{u^2 + v^2 - w^2} \operatorname{tg}^2 \gamma_0}, & |w \operatorname{tg} \gamma_0| < \sqrt{u^2 + v^2}, \\ 0, & |w \operatorname{tg} \gamma_0| \geq \sqrt{u^2 + v^2} \end{cases}, \tag{4}$$

From relation (4) we can reconstruct only function G^* , which characterizes the sought function with some distortions:

$$G^*(u, v, w) = \begin{cases} G(u, v, w), & |w \operatorname{tg} \gamma_0| < \sqrt{u^2 + v^2}, \\ 0, & |w \operatorname{tg} \gamma_0| \geq \sqrt{u^2 + v^2} \end{cases}.$$

From relation (4) we obtain:

$$g^*(x, y, z) = \frac{1}{4\pi} \mathfrak{F}_3^{-1} \left\{ \mathfrak{F}_3 \{ b(x, y, z) \} \sqrt{u^2 + v^2 - w^2 ctg^2 \theta_0} \right\}. \quad (5)$$

Relation (5) shows that operations of three-dimensional Fourier transformation are necessary for reconstruction of a sought function in the classical case of tomographic reconstruction. Therefore a reconstruction algorithm on the basis of operations of inverse projecting of SI projections was proposed:

$$g^*(\vec{r}) = -\frac{1}{(4\pi)^2} \left(\frac{\partial^2}{\partial x^2} + \frac{\partial^2}{\partial y^2} - ctg^2 \theta_0 \frac{\partial^2}{\partial z^2} \right) \hat{K}_3^{\theta_0} \{ b(\vec{r}) \}. \quad (6)$$

NUMERICAL SIMULATION.

Numerical simulation has been carried out for determination of the effective application of the proposed data collection scheme and reconstruction algorithms, for choice of the sounding view and estimation of the reconstruction possibilities. The following function have been chosen as the model SD:

$$g(x, y, z) = A \left(1 + \alpha \cos \frac{\pi k_x}{L_x} x \cos \frac{\pi k_y}{L_y} y \cos \frac{\pi k_z}{L_z} z \right), \quad (7)$$

where $x \in [0, L_x]$, $y \in [0, L_y]$, $z \in [0, L_z]$. A controlled domain was being divided into voxels. Collection of beam projections was being modeled by calculation of the averaged values of function (7) along US signal spread directions during scanning by transducers on a product surface. Scanning step along line coordinates and angle φ was being chosen with consideration of the given function spectrum. Using the calculated beam projections the volume SD was being reconstructed. To control this process the vertical sections were being visualized. In Fig. 3 the SD (7) in the vertical sections at $k_x = k_y = 3$, $k_z = 1$ have been represented.

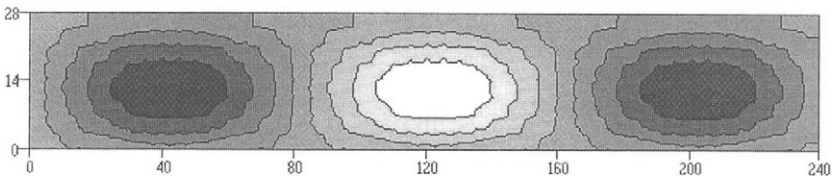


Fig. 3. Model inhomogeneity distribution.

Estimation of sounding view influence. Data collection was simulated at US signal entry under views $\theta_0 = 35^\circ; 60^\circ; 75^\circ$. The reconstructed images of a section, shown in Fig. 3, have been represented in Fig. 4, which demonstrates that reconstruction quality along product thickness is being improved with entry angle θ_0 increase.

Simulation results, obtained using data, collected at two views (35° and 60°), have been represented in Fig. 5. Comparison of Fig. 4,b and Fig. 5 confirms a conclusion about the possibility of use of only one view during data collection.

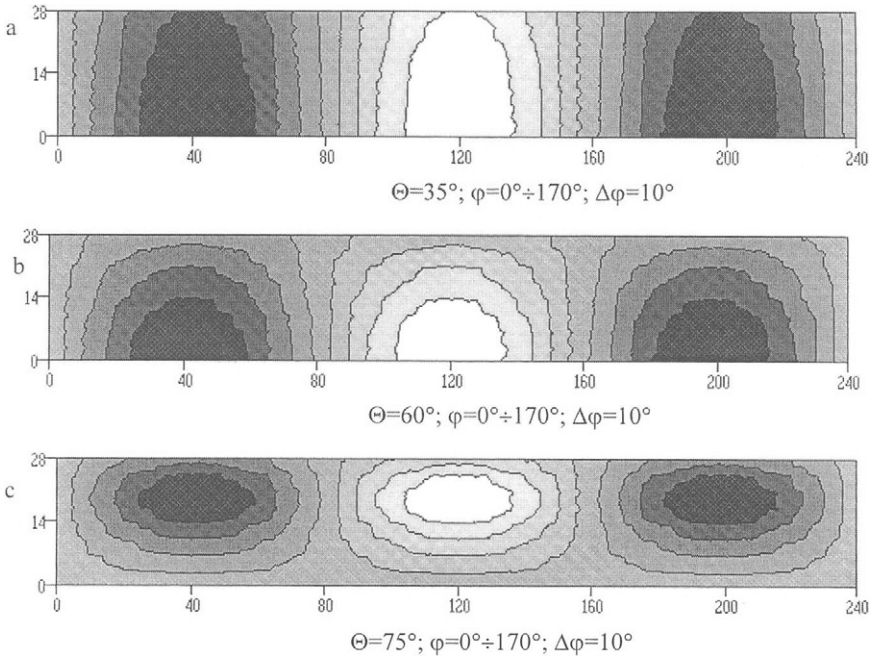


Fig. 4. Result of function reconstruction in the vertical section of a sheet product at the diverse entry angles during data collection.

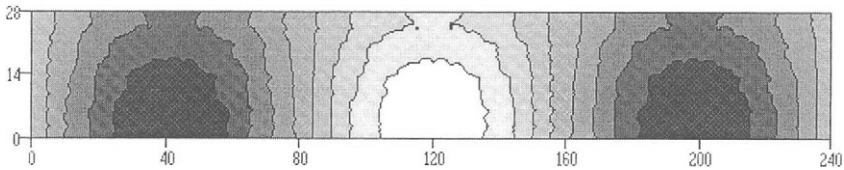


Fig. 5. Result of function reconstruction in the vertical section of a sheet product at two entry angles during data collection $\Theta=35^\circ; 60^\circ$

Estimation of reconstruction possibility along sheet product thickness. One-viewed ($\theta_0 = 60^\circ$) data collection have been simulated and possibility of the SD reconstruction depending on spectral composition of the reconstructing function have been investigated (Fig.6).

Numerical simulation confirmed a possibility of the inhomogeneity SD reconstruction in case of the sufficient high-frequency change of inhomogeneity in planes, parallel to sheet product surface, that allowed to determine the material PMC SD in welded joints.

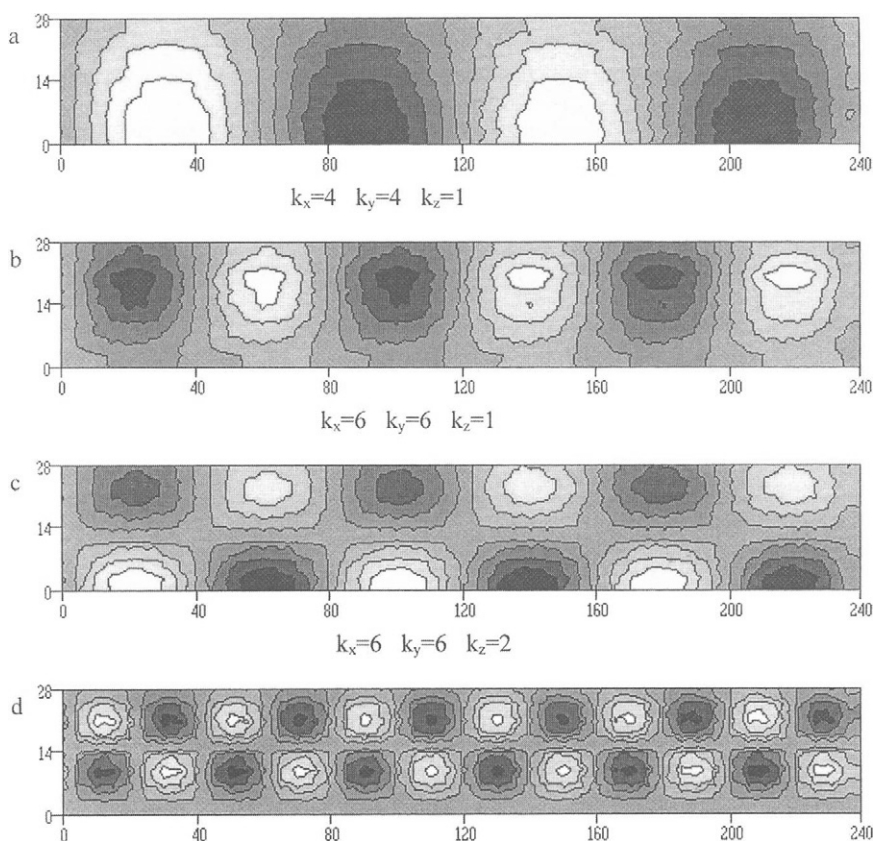


Fig. 6. Function reconstruction in the vertical section of a sheet product at the various relations between the spatial spectral components in a specimen plane.

EXPERIMENTAL RESULTS.

Experimental researches have been carried out with the use of the experimental model of the US NDT tomograph, aimed at NDT determination in the thick sheet products of the SD (on a product volume) of the material acoustical characteristics (spread velocities and fading of the longitudinal and transverse US waves) and the related material PMC, such as elastic (elasticity moduli), strength, technological (hardness), structural (grain size, degree of intercrystalline corrosion) characteristics and parameters of inhomogeneous MDM (stress tensor, its invariants).

The main US NDT tomograph technical characteristics:

- ◆ sounding by longitudinal, transverse and surface US waves;
- data collection method: mirror-shady; multiangle viewing;

- ◆ measuring parameters: US signal spread time (relative measuring error less than $10^{-4}\%$) and amplitude;
- ◆ data processing method: computerized 3D-tomography with beam scheme of data collection;
- ◆ reconstructing spatial distributions (US images): orthographic (averaged on thickness); tomographic (arbitrary oriented sections).

For illustration of US NDT tomography possibilities the experimental results of the SD reconstruction of the material PMC in steel sheet specimen of thickness 28 mm with V-similar weld have been represented in the figures below (restored orthographic images - Fig. 7 and Fig. 8; restored tomographic images - Fig. 9 and Fig. 10).

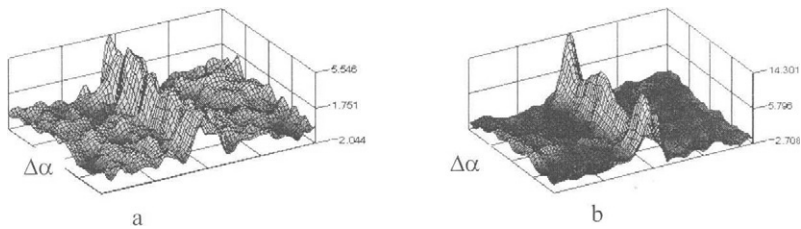


Fig.7. Restored orthographic images of the US waves attenuation change (dB/m) in a control plane of the welded specimen at 2.47 MHz (a- transverse wave, b- longitudinal wave).

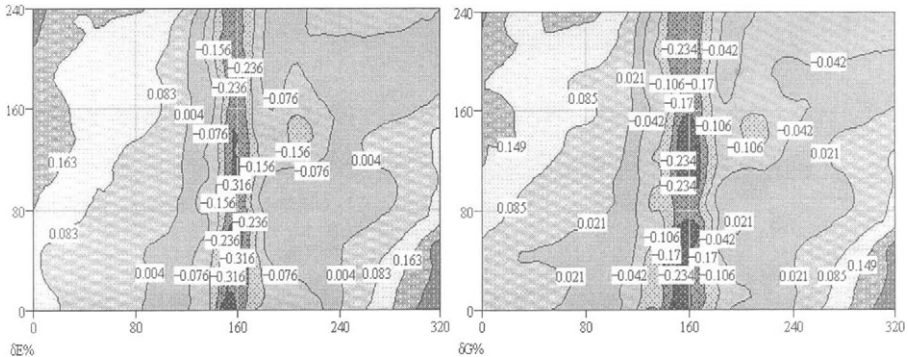


Fig.8. Restored orthographic images of the spatial distribution of relative change of Young's modulus $\delta E\%$ and shear modulus $\delta G\%$ in a control plane of a welded sample at 2.47 MHz.

Combined image of the spatial distribution of defects and the material PMC is very informative and creates new possibilities for technical diagnostics. These possibilities may be realized by means of US NDT tomography. For example Fig. 11 represents the restored by US tomograph combined image of the spatial distribution of defects and Young's modulus change in the welded plate.

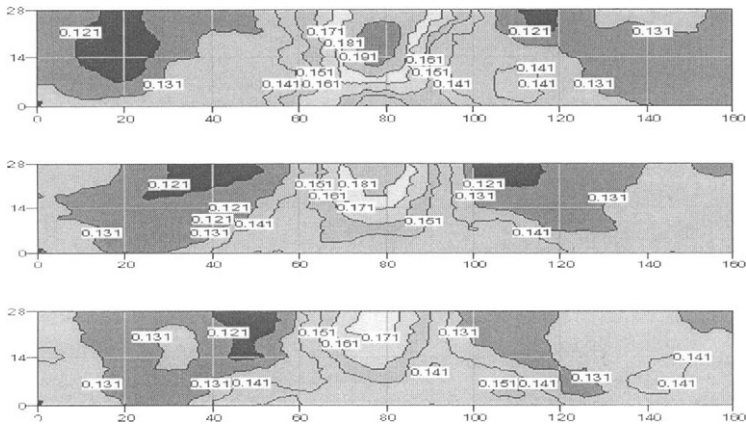


Fig. 9. Restored tomographic images of the spatial distribution of grain size D (mm) in the vertical sections of the V-similar welded plate across the weld (distance between sections is 120 mm).

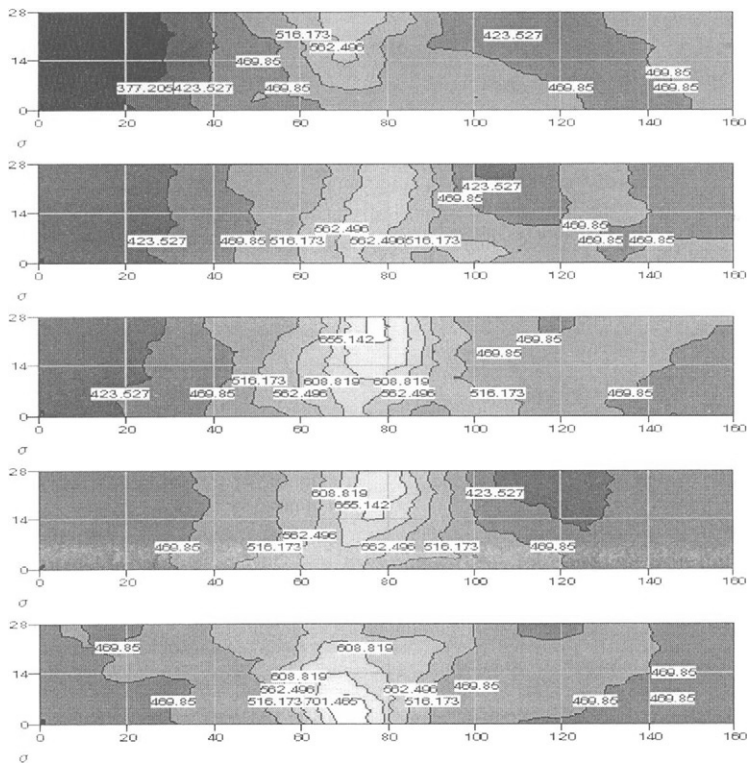


Fig. 10. Restored tomographic images of the spatial distribution of the ultimate resistance σ_v (MPa) in the vertical sections of the V-similar welded plate along the weld (distance between sections is 5 mm).

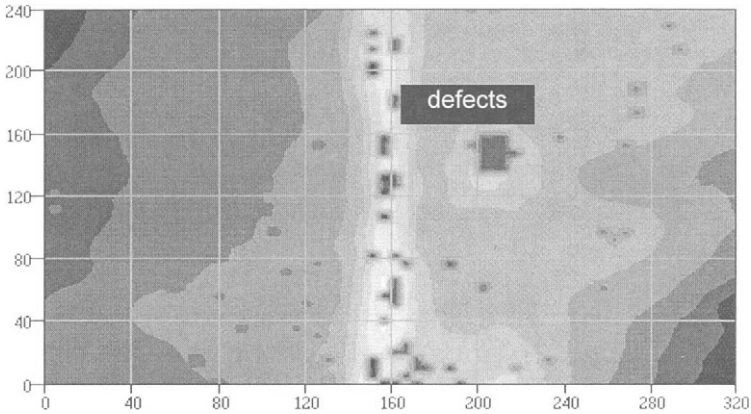


Fig. 11. Restored combined image of the spatial distribution of defects and Young's modulus change in the welded plate.

Fields of application of the US NDT tomography:

- ◆ material experimental researches, related to spatially-inhomogeneous material structure changes and inner stresses: cracking, intercrystalline corrosion, material fatigue, material state after mechanical, thermo-mechanical and other types tooling, taking down of residual stresses in welded joints, etc.;
- ◆ ultrasonic NDT of diverse products aimed at the material predefective state determination (for example, material degradation in thick-walled pipes of power, chemical, oil and gas installations, volume distribution of residual stresses in welded structures, etc.).

CONCLUSIONS

Use of the developed ultrasonic tomographic NDT technology and facilities, which allow to determine by US NDT methods the spatial distribution of the material physico-mechanical characteristics in a product volume with a strong inhomogeneous inner structure, have been stated and proposed in the paper for NDT of the welded sheet products possibilities of US NDT tomographic technologies were theoretically investigated and confirmed by experimental results on reconstruction of the spatial distribution of some material physico-mechanical characteristics (Young's modulus, grain sizes, etc.) in steel plate with V-similar weld.

The present work was fulfilled in the Karpenko Physico-Mechanical Institute of National Academy of Sciences of Ukraine within the frame of Project #612 of Science and Technology Center in Ukraine.

REFERENCES

1. Koshovy V.V., Krivin D.E., Krivin E.V., Romanyshyn I.M. Tomography of sheet products// *Defectoscopya*.- 1998, №9.- P.-20-27.(in Russian).

High Elevation Inspection Vehicle

N.TAMURA and K.TAKADA

*Technology Center of Metropolitan Expressway
3-10-11, Toranomon, Minato-Ku, Tokyo, 105-0001, Japan*

ABSTRACT

The bridge often damages supports and when the damages occurring around supports. These places are blind spots from ground. We often use the staging and the mobile platform when inspecting to the bridge. It isn't always possible to confirm that they watch the damage, which occurred in the part of superstructure and part of the beam of the pier. It is " The Height Elevation Inspection Vehicle " that developed to solve such a problem. The characteristic of this vehicle is to have loaded the vehicle rear with the stretch pole system of about 15m of the maximum extension. This system consists of stretch pole, which can turn and horizontal arm that can stretch from 1.5m to 3m, and this horizontal arm has high sensitive camera equipment for the inspection on the arm tip. This report is the introduction of this system.

KEYWORDS

Inspection, stretch poles, carbon fiberglass, convex

Introduction

Since the Metropolitan Expressway opened to traffic in 1962, It has had to bear a significant rise in both traffic load and vehicle size, and its burden of responsibility continues to grow every year. Our most important task is to preserve the good condition of structure and make improvements. Therefore, maintenance management or the inspection work of the structure is important. 80% of the Metropolitan Expressways are overpass. And, many bridges are being constructed in the limited space or over the road. So we have to inspect the limited space. We inspect structure on foot every year, by mechanical staging every about 5 years, and by on the staging every about 15 years. There are blind spots where we can't inspect by on foot with the binocular from under the bridges. There are blind spots like supports. There are many damages occur in supports or around supports. We had to develop the machine that can cope

with limited space, with the mobility for early detection of damage. Therefore, we developed the Height Elevation Vehicle.

System outline

1) The Height Elevation Inspection Vehicle.

We made the vehicle as small as possible in order to cope with small features under the bridge. In addition, we remodeled the base car by adopting two tons track. The inside of the vehicle is divided into driving room, operation room and the hangar. The control machine, monitoring system, and recording device are arranged in the operation room, where we work. The hanger has stretch poles, generator, and tools.

2) The mechanism to inspection for high location.

The mechanism to inspection for high location on the vehicle is composed of the multiple step-type pole, which can stretch 15 m long vertically, horizontal arm, which can stretch 3m long, and camera equipment for the inspection which is in the tip the horizontal arm.

We adopted the poles and arms made of Carbon Fiberglass, because these materials need to be lighting weight for vehicle. Considering when we store them in the vehicle, the pole is 13-step structure, the arm is structure 3-step structure. And we adopted "the steel sheet of curved surface" system as stretching drive form. This system is called "Convex" by using this system, we can adjust subtle movement when working. The stretch speed of pole is 4m/min, and speed of the arm is 6m/min. As the pole's shaft can turn a full 360°, the inspection camera can be set up easily by this mechanism, regardless of its vehicle position. The camera for the inspection attached to the tip of the stretch arm is 3CCD digital camera with 12 times zoom lens. Light and microphone are beside the camera in order to watch things in the dark, and record the extraordinary sound.

3) Image monitor and data record device.

The image monitor (high resolution 14 inches) in the operation room can offer the real-time picture through the camera, and we can remake the picture from record device timely. The data record device has two types, which are DV-type and S-VHS type. and we can use each of them depending on the purpose.

Digital data can be possible to print out and access to personal computer, moreover if you connect it to the communication machines, you can transmit the data to the office and so on.

Examination item

1) *Stretch poles.*

We adopted the poles and arms made of carbon fiberglass in order to lighten weight themselves. We were worried about the action such as deformation and shaking caused by it's character of the material, therefore we experiment by using the similar pole on advance through the experiment. Through the experiment, we verified the influence of the formation caused by deflection of weight, vibration character, and attenuation. We did the confirmation of using carbon fiberglass for the pole.

The Convex form was adopted for the stretch drive of the pole. At first, stretch poles pushed up the first-step pole by the Convex. And them do the next-step pole and the next-step until the 12th-step pole, has done them, extension is completed.

It is desirable that the Convex stands up to the big shaft power under the straight-line condition, and it also desirable to easy to rewind. Take "r" radius of arc, take "t" board thickness. If a circular arc-opening angle is fixed, buckling strength is in proportion to r^3t , and a torque of rewinding is in proportion to rt^3 . We verified the strength of section by FEM analysis and buckling examination.

A technical countermeasure was necessary in the following point before adopting it in this vehicle though the stretch pole itself of the Convex form was existent technology.

2) *Stretch drive device.*

We had to make height of vehicle low as much as possible to enter under the bridge. This restriction forced to increase the number of the pole steps, and miniaturize size of drive device. Become new matter to consider as the releasing part for "Convex" is narrow, we adopted the way to release "Convex" interposing it between a pair of arc-shaped roller. (refer to fig-2)

In the case of these arc-shaped rollers of 1 pair, the surface speed is uneven because the radius of the rollers are uneven as for convex roller, as for convex roller, the surface speed is fast at the center part, and is slow at the edge.

While Convex is put between convex roller and concave roller, so, it always cases vertical slip and it's possible to wear out them. Therefore, we made various types of rollers and experimented. As the result of the experiment, we adopted "the rubber roller have the looser curve than circle "which has looser curve than Convex has curve. As the parts of this vehicle,

furthermore being the safe side, we also installed the brake to prevent vertical slip
 As for the turn mechanism of the pole, we adopted the way to turn pole in itself by using "rade gear" for turning attached to pole base on the vehicle. Because we gave up putting devices for turning on the top of the pole due to its limitation of weight and size of hanger.

The specification of the inspection system (vehicle)

1) Vehicle.

Vehicle's dimension	entire length 5.13m, full width 1.71m, overall height 3.08m (at the time of the poles storage).
Weight of Vehicle	2.0ton
Vehicle's total weight	4.5ton.
Minimum radius of gyration	4.6m
Riding capacity	5 persons
Total emission	2,693cc.

2) Loading mechanism.

Poles	slide height $H=2.90\sim 14.80\text{m}$. maximum diameter 280mm, minimum diameter 110mm. Left-right 275° each degree of the turn angle. Rise speed 4m /min Turn speed 8m /min
Arms	slide length $L=1.5\sim 3.0\text{m}$. maximum diameter 110mm, minimum diameter 73mm. Arm angle $0^\circ \sim 20^\circ$ (manual-operation) stretch speed 3m /min, 6m /min

Pole and arm stretch form.

Convex drive form (plate strip spring steel).

The range of camera turn

angle $\pm 180^\circ$ tilt angle $\pm 90^\circ$

Safety device surveillance camera, supersonic sensor for the contact prevention,
control device for level.

3) Measuring part.

Camera	1/2inch 3 plate charge coupled device(Color).
Horizontal resolution	750TV scanning line

Lens	12 times zoom
Microphone	directional microphone.
4) <i>Data recorder</i>	
Recording method	digital record, S-VHS.
5) <i>Video Display Unit</i>	
During measurement	real-time video display
During playback	tape rapid feed, a head is provided at the time of the regeneration, it functions, image print.

Summary

This vehicle is effective when inspecting narrow spot. With this vehicle, we can inspect the narrow places at the back of the bridge where we used to have difficulties investigating from under the bridge. Moreover, it is also available for investigating features and follow-up. so this is very useful as the method of regular inspection, and these inspection devices attach to the vehicle. This vehicle has good mobility, and the picture taped by this device can be good inspection when examining bridges afterward. So, these features show that this vehicle is good for emergency. From now on, we will verify these things on practical field test.

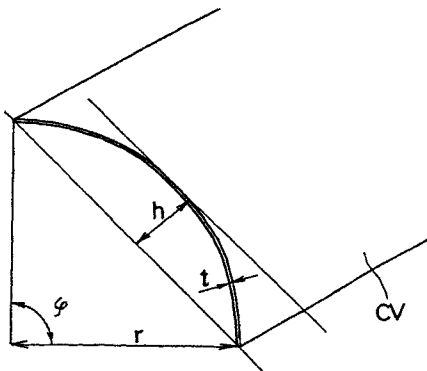


Figure-1 squint view of convex

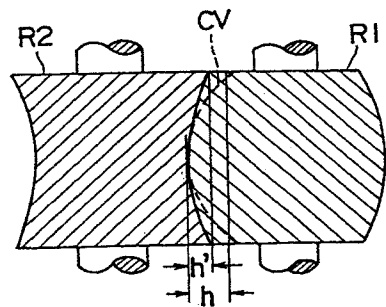


Figure-2 section of the rotation roller

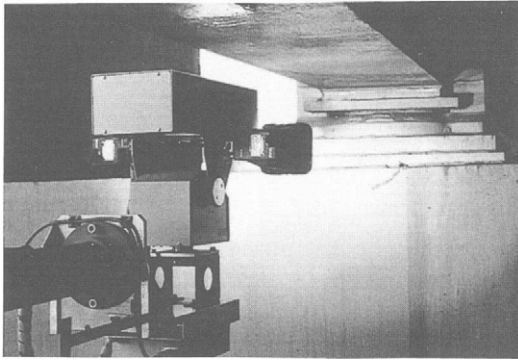


Figure-3 view support

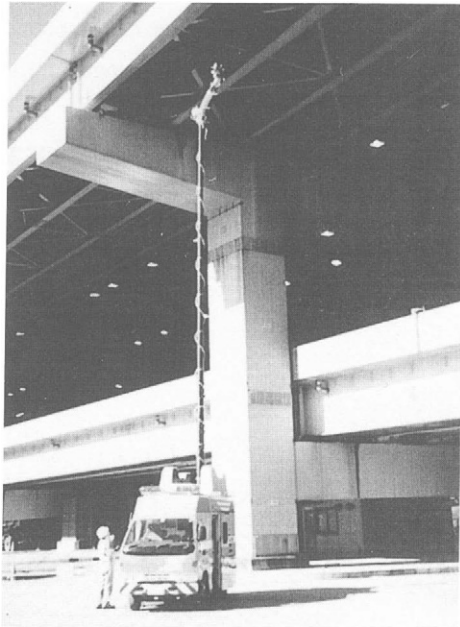


Figure -4 Height Elevation Inspection Vehicle

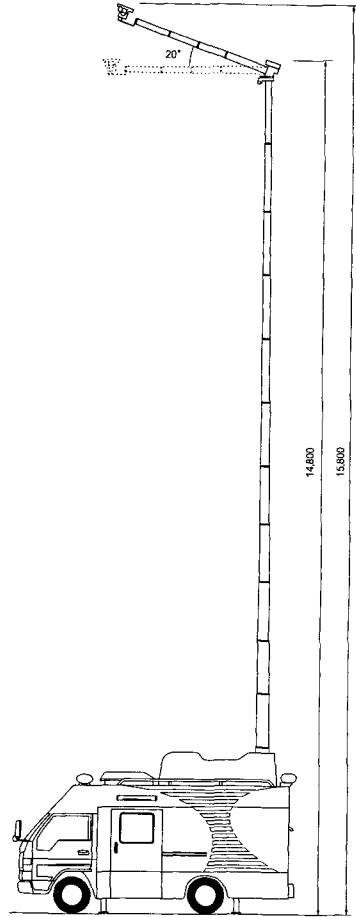


Figure -5 side appearance figure

Reference

Column Research Committee of Japan: handbook of structural stability, colona.co, 1971
B.CURVED PANELS condition No.194 fig.2 Chu, K .H & Krishnamoorthy, G.. Buckling of open cylindrical shells, Proc. ASCE, ME, No2, pp.177~205(April,1967)

ANALYSIS OF CONCRETE USING LIBS

H. WIGGENHAUSER, G. WILSCH, D. SCHAURICH and J. WÖSTMANN
*Federal Institute for Materials Research and Testing,
D-1205 Berlin, Germany*

ABSTRACT

The application of laser induced breakdown spectroscopy (LIBS) to determine the composition of building materials is shown for concrete as an example. The characterisation of the building material is done by measuring the content of the three elements Calcium, Aluminium and Silicon. The results are included in a Rankin diagram.

KEYWORDS

LIBS, spectroscopy, concrete, chemical analysis, Rankin diagram

INTRODUCTION

Measurement of the composition of building materials can be done with high precision using the tools of the analytical chemistry. The measurements are done in the laboratory, the samples must be prepared, typically dissolved. Direct measurements in the solid phase, e.g. XFA (X-ray fluorescence analysis) are not typically available and mobile systems are not available for use on site. LIBS is an analytical method which has the potential to accurately determine the concentration of selected elements [1, 2]. LIBS also can be configured for mobile use on site [3].

LIBS has successfully been used to measure the distribution of salts in building materials [2], such as NaCl in brick specimens. Depth profiles can be measured with high geometrical resolution and contamination of material with heavy metals can be detected [2, 3].

The analysis of the concrete composition, the amount and type of the cement, the size and size distribution of aggregates, and the measurement of the w/c ratio are some of the testing tasks for the assessment of existing structures or for quality control during construction. Because of the natural variation of the material composition in inhomogeneous materials such as concrete,

the exact determination of the values is not always possible, not even with the high precision methods of the analytical chemistry.

Oxide	Portland cement	Iron- portland cement	Blastfurnace cement	Trass cement	Portland oil- shale cement	Fly ash cement	Cinder Sand	Fly ash	Rhein. Trass
CaO	61 - 69	52 - 66	43 - 60	43 - 58	53 - 58	46	35 - 48	3 - 6	ca. 7
SiO ₂	18 - 24	19 - 26	23 - 32	25 - 28	19 - 21	30	24 - 40	44 - 50	ca. 56
Al ₂ O ₃	4 - 8	4 - 10	6 - 14	6 - 9	5 - 7	10	5 - 17	25 - 29	ca. 18
Fe ₂ O ₃	1 - 4	1 - 4	0,5 - 3	2,5 - 3,5	3 - 6	6	0,5 - 3	7 - 14	ca. 6
Mn ₂ O ₃	0 - 0,5	0 - 1	0,1 - 2,5	0,1 - 0,3	0,1 - 0,2	-	-	-	-
MgO	0,5 - 4	0,5 - 5	1 - 9,5	1 - 3	1,5 - 2,5	1,5	2 - 13	1 - 3	ca. 2
SO ₃	2 - 3,5	2 - 4	1 - 4,5	2 - 3	2,5 - 3,5	2	0 - 3	0,5 - 5	ca. 0,5

Table 1: Typical composition of some cements [5]

The characterisation of cement in the Rankin diagram is done by measuring the content of three (or five) elements (Ca [+Mg], Si, Al [+Fe]) and by printing the values for their oxides in the Rankin diagram.

Using LIBS, the element concentration can be determined point by point on the surface. The oxide values are then calculated using stoichiometric relations.

The composition is determined at each point, while scanning over the surface of the specimen.

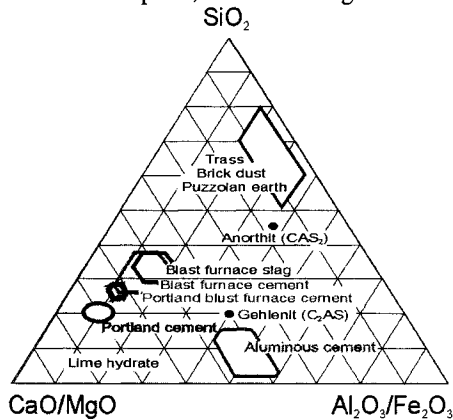


Figure 1: Rankin diagram with cement types

Plotting each single result into the Rankin diagram, the point distribution visualises the typical inhomogeneity of the specimen.

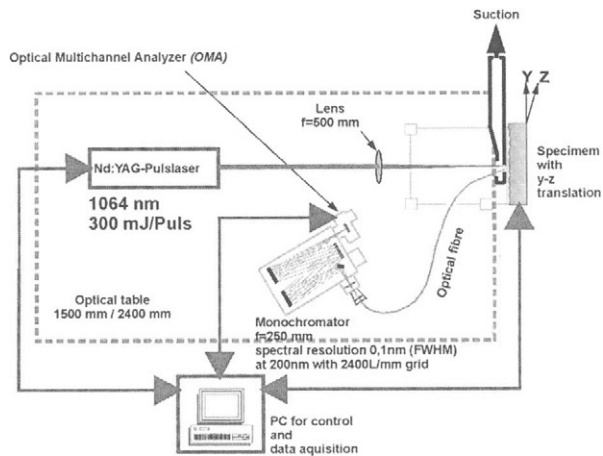


Figure 2: Experimental set-up for LIBS experiment

THE METHOD

In figure 2 the experimental set-up for LIBS experiment is shown. The excitation source is a pulsed NdYAG laser ($\lambda = 1064$ nm, energy = 300 mJ/pulse, pulse duration 10 ns, vaporised mass approx. 10 μg /pulse for concrete). The optical detection system is a monochromator ($f = 250$ mm, 2400 L/mm grating, resolution 0.1 nm) with an optical multichannel analyser. The

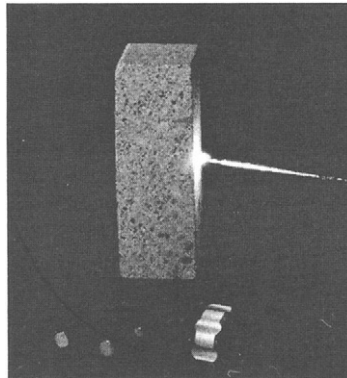


Figure 3: Laser vaporisation of concrete and plasma generation

plasma emission is collected through the open end of an optical fibre and guided to the entrance slit of the monochromator. The set-up is mounted on an optical table. A simple lens with a focal length of 500 mm focuses the laser light to generate the energy density to vaporise the substance. The length of the focus allows to measure samples with an uneven surface, e.g. broken concrete.

The focussed laser beam (energy density in the focus > 2 GW/cm^2) vaporises a few micrograms of the sample. In the generated plasma (figure 3) the temperature is very high, the chemical bonds are broken and the atoms are highly excited. In the following cooling process

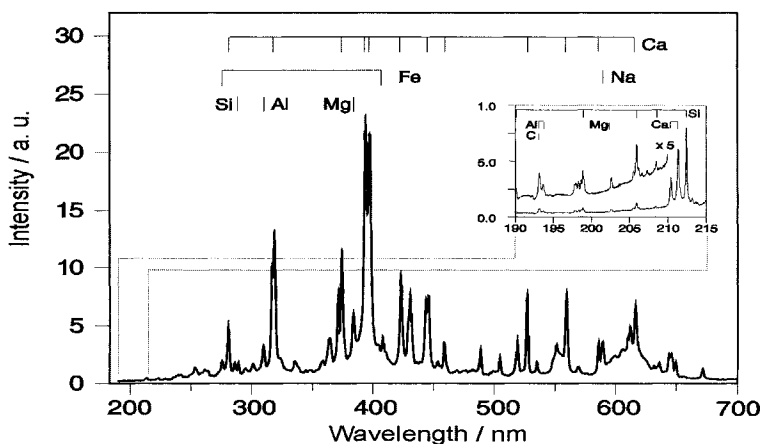


Figure 4: Typical LIBS spectrum with wavelength indication of Ca, Si, Na, Al, Mg, Fe and C. The inset shows a high resolution enhancement of a small wavelength range.

the atoms emit their characteristic fluorescence while relaxing into their ground state. These characteristic radiation is used to identify the elements. The intensity of the radiation depends on the abundance of the element and is used for the quantification.

Measurements are only taken in a time window of a few microseconds, some microseconds after the laser pulse. The use of this technique increases the signal to noise ratio and permits measurements also at a high background light level, e.g. in daylight. In the laboratory, the specimen can be moved in the plane perpendicular to the laser beam using a biaxial frame. Line scans are taken when the specimen is moved during the experiment. Several line scans can be combined to area scans which can be used to visualise the distribution of one element over an area.

The laser pulse also causes some dust to be emitted which attenuates the laser beam. Therefore an air flow system has been installed which removes the dust.

For each laser pulse a spectrum is recorded (figure 4), typically 10 spectra are averaged. A total of 127 spectra can be collected, which are typically taken equidistant along a line, and stored for post-processing.

The spectral range chosen for concrete analysis lies between 190 nm and 215 nm. In this range lines of the important elements Ca, Si, Al, C, Mg are present and used for analysis. However, the spectral overlap of the Aluminium lines (193.00, 193.24, 193.48 nm) and the Carbon lines (193.09 nm) requires a careful separation of lines through curve fitting procedures. Especially at carbonated specimens with high intensity carbon lines, this separation of C- and Al-lines can be complicated. Special numerical procedures take care of this problem.

The line intensities are normalised and weighted to get quantitative results. A reference specimen with known composition is used to calculate the weighing factors.

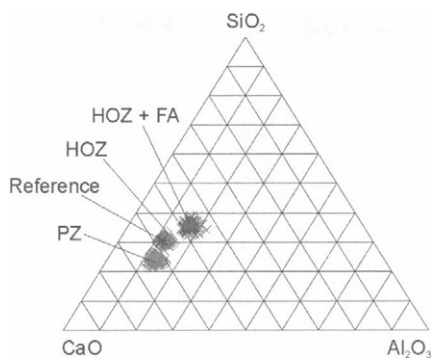


Figure 5: Rankin diagram with results from cement paste material made of portland cement (PZ), blast-furnace slag cement (HOZ) and blast-furnace slag cement with 30% fly ash (HOZ+FA).

RESULTS

Specimens made from cement only, without aggregates or added sand, have been analysed to test the system. The cements used are portland cement (PZ), blast-furnace slag cement (HOZ) and HOZ with added fly ash (HOZ+FA). The results of the quantitative analysis, using a HOZ-specimen as reference, are visualised in figure 5. Each measurement is analysed and the corresponding value is plotted in the Rankin diagram. The results for each specimen lie very close and show, that cement can be distinguished using this analysis.

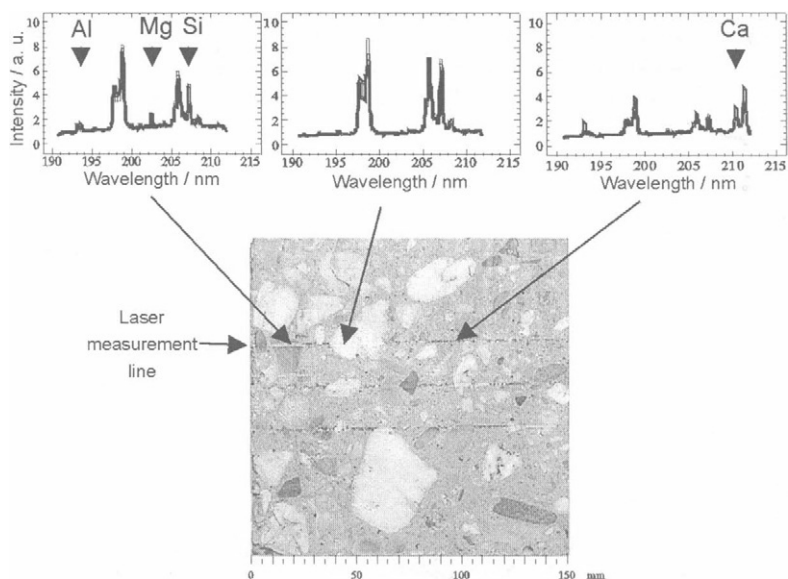


Figure 6: Photograph of the cutted surface of a specimen showing traces of measured lines. Above: typical spectra at three different points (dark aggregate, left; bright aggregate, middle; cement paste, right).

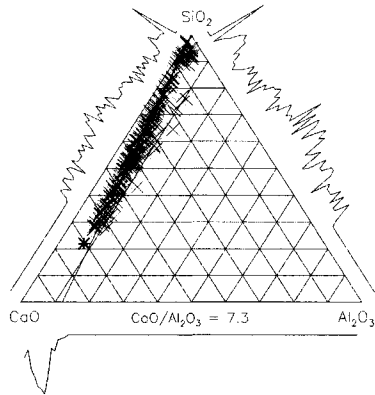


Figure 7: Rankin diagram with results from concrete specimen made of Portland cement. The results are distributed along a line between the position of pure SiO₂ and the position for cement paste. The star indicates the position of the reference measurement.

The analysis is more difficult when concrete specimens are used for the investigation. Casted surfaces are different from broken or cutted surfaces because they present more cement. Instead, the latter ones have more exposed aggregates of different sizes.

Figure 6 shows a photograph of a concrete surface with aggregates. Above, the spectra obtained at three different points along a line are shown to demonstrate the change in line intensities for the elements which are used for analysis. Obviously, the "dark" aggregates have higher content of Mg and Al than the other aggregates.

Depending on the amount of aggregate hit with the laser pulse, the silicon amount varies. Then, no longer the silicon value is a measure of the cement type. The values obtained from measurements of concrete will vary between the two extremes: pure SiO₂ and cement paste. All points in the Rankin diagram lie between the SiO₂ corner and the position of the cement

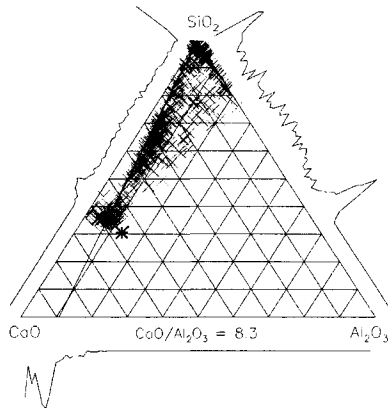


Figure 8: Rankin diagram with comparison of measurements taken on a cutted surface (red hashes) and a casted surface (blue crosses).

used in the specimen (figure 7). Along the axis of the triangle, the histogram distribution is plotted as an additional characterisation of the specimen.

A comparison between the measurements on a cutted surface (red hashes) and one from the casted side (blue crosses) is shown in figure 8. Naturally, the element paste covering the aggregates on the casted surface prevents the aggregates to be directly hit by the laser light. This results in a shift of the measured values towards the position of the pure cement material. In this figure, also the influence of aggregates with an Aluminium content is apparent. The points for the cutted side are distributed in a triangle whose corners are given by the value for the pure SiO_2 , the value for the measurement with maximum Aluminium content and the value for cement paste.

The results from concrete specimens which differ only by the concrete type are shown in figure 9. Again, on each specimen along two lines across the cutted (crosses) and the casted

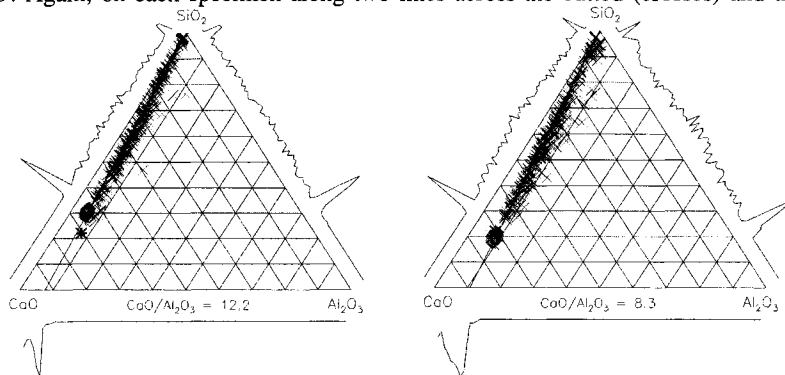


Figure 9: Comparison of Rankin diagrams with LIBS results from specimens which differ only by cement type. Left: Furnace blast slag cement. Right: Portland cement. Measurements were taken on a cutted surface (red hashes) and a casted surface (blue crosses) on both specimens.

(hashes) side, respectively, have been measured. The results from the side with exposed aggregates show very little difference. From the opposite side, the values show a distinct shift relative to the reference material. Also, the slope of the line along which the values are grouped, show a difference in slope as indicated at the bottom of the triangle by the $\text{CaO}/\text{Al}_2\text{O}_3$ ratio.

SUMMARY AND OUTLOOK

The experiments and the results show the successful application of LIBS for concrete analysis. The element types can be distinguished by visualising the results in the Rankin diagram. The scattering of the results is caused by the natural inhomogeneity of the concrete. The difference between different concretes can be smaller than the scattering of the results obtained from one sample. A methodology how to perform LIBS measurements on building materials is needed. The visualisation in a Rankin diagram might be substituted by a different procedure.

The advantage of LIBS is in the ability to measure samples in the solid phase. Samples must not be prepared and can be measured on site with mobile LIBS equipment [3].

The use of new Echelle spectrometers will enable the simultaneous determination of more elements and to exclude side effects by cross checking different lines of the same element.

REFERENCES

1. Wiggensauser, H., Salzmann, M., Wilsch, G. and Schaurich D. (1995).
Analysis of Concrete with Laser Induced Breakdown Spectroscopy (LIBS)
In: *Proceedings of the International Symposium Non-Destructive Testing in Civil Engineering (NDT-CE)*, G. Schickert and H. Wiggensauser (Eds.). DGZfP, Berlin, Vol. 1, pp. 529-537
2. Wiggensauser, H., Wilsch, G. and Schaurich D. (1997).
LIBS for Non-Destructive Testing of Element Distributions on Surfaces
In: *Proceedings of the International Conference NDT in Civil Engineering*, J. H. Bungey (Ed.). Liverpool, Northampton, The British Institute of NDT, pp. 577 – 589
3. Yamamoto, K., Cremers, D., Ferris, M. and Foster, L. (1996). Detection of Metals in the Environment Using a Portable Laser-Induced Breakdown Spectroscopy Instrument, *Applied Spectroscopy*, **2**, pp. 222-233
4. Pakhomov, A., Nichols, W. and Borysow, J. (1996). Laser-Induced Breakdown Spectroscopy for Detection of Lead in Concrete, *Applied Spectroscopy*, **7**, pp. 880-884
5. Verein deutscher Zementwerke (1979), *Zementtaschenbuch 79/80*, Bauverlag, Wiesbaden, p. 28

HIGH RESOLUTION SEISMIC IMAGING AS A NDT TOOL FOR THE SHALLOW SUBSURFACE SURVEY

B. PIWAKOWSKI and CH.LEONARD

*Groupe Acoustique-Electronique, Ecole Centrale de Lille (IEMN DOAE UMR 8520 CNRS)
59651 Villeneuve d'Ascq, BP48, Cedex. France*

ABSTRACT

The paper presents the successful application of the high resolution seismic reflection imaging (HRS) to survey of the shallow subsurface environment. Recent progress in this domain has been made both as regards the measurement system, the signal processing and interpretation techniques. It is shown that the HRS may be considered as the particular CND technique, adapted for detection in ground. Furthermore, it completes the use of the ground penetrating radar, for cases where its operation is no longer applicable. The enclosed field examples cover the different civil engineering applications, such as the stratigraphy of the shallow subsurface, the detection and location of the underground voids and the detection of the collapsed and filled-in grounds. It is shown that the HRS may be successfully used for the evaluation of risk of cavity collapse, as well as for the verifying the quality of filling of collapsing cavity with the cement mixture.

KEYWORDS

High resolution seismic, acoustic imaging, voids, detection, shallow stratigraphy, faults, cavities, non destructive testing.

INTRODUCTION

The seismic reflection method, a powerful geophysical exploration technique, that has been in widespread use in the petroleum industry for more than 60 years [1], has been also used since 30 years for targets shallower than 30 m. Advances in microelectronics have resulted in construction of seismographs and microcomputers allowing for cost effective acquisition and processing of seismic data, relative to the test drilling have permitted the appearance of the high resolution seismic reflection (HRS) technique, adapted for the imaging at shallow depths. The HRS may be compared to the ground penetrating radar (GPR), which is in widespread use in civil engineering [2]. The radar uses the electromagnetic pulse which is radiated into ground, propagates to the target, reflects, propagates back and then is detected by the receiving antenna (Fig.1.a). In the HRS, the electromagnetic pulse is replaced by the acoustic one and this involves the practical differences between these methods: the GPR may operate only in the medium with relatively low absorption of electromagnetic waves (i.e. dry, no electrically conducting grounds)

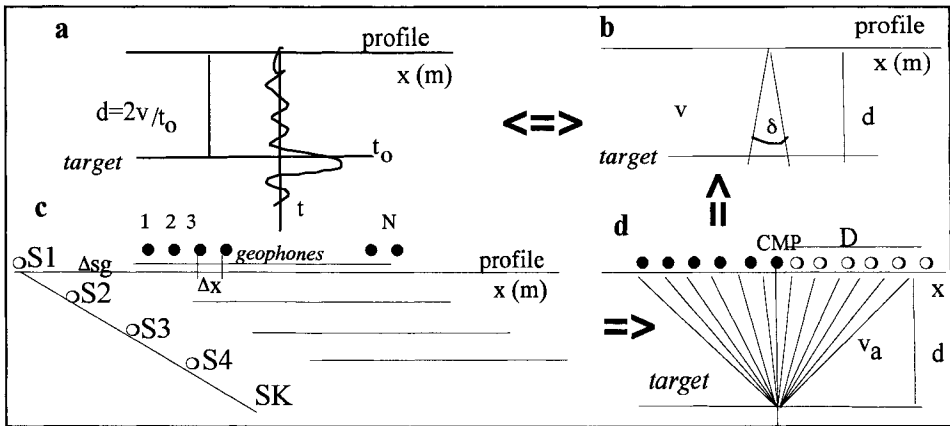


Fig.1. Operation of the Ground Penetrating Radar and High Resolution Seismic Imaging; (a) output single trace signal; (b) Both systems are equivalent to a point probe, characterised by angular resolution δ ; (c) Geometry of the acquisition in seismic imaging (d) Synthetic aperture of dimension D focused at depth d .

and detects the targets which display an electric contrast. The HRS may operate in media which enable the acoustic waves to propagate and detects the targets which display the acoustic impedance contrast.

The above difference leads to important differences in operational procedure. The GPR is commonly a closed shape device enabling the output image to be obtained directly in the field and any complicated signal processing is not required in principle. It may be modelled as a point probe characterised by angular resolution $\delta = \lambda_c / L$ where λ_c is the electromagnetic wavelength and L is the antenna lateral dimension (Fig.1.b)

At the same time the operation of the HRS is more complicated. The high absorption of the ground, which strongly increases with frequency, requires the use of the very low frequencies. The spectrum exploited in practice varies from several dozen Hertz (deeper imaging, depths of several hundreds of meters) to several hundred Hertz (high resolution shallow imaging, depth of dozen of meters). This implies the use of specific seismic sources to generate the acoustic waves (explosives, weight-drops, vibrators, [3]) and of the geophones (acoustic velocity sensors) as the receivers [1,4]. The use of the synthetic aperture methods for the resolution enhancement requires the use of the specific geometry for the acquisition of the data. An example of such geometry is illustrated in Fig.1.c. The acoustic field is recorded along the sounded profile by the N -channel Δx spaced acquisition array, for the start position $S1$ of the seismic source. The source and the receiving array are moved by Δx and the acquisition is repeated K times. The obtained records are then processed in laboratory. The results of processing are equivalent to sounding with the point acoustic probe, moving along the profile, focused at a given depth at a given position known as CMP point (Common Middle Point). The probe is characterised by the angular resolution $\delta = \lambda_a / D$, where λ_a is the acoustic wavelength and D is the dimension of the synthetic aperture (Fig.1.d) used in the processing. The set of traces presented as a function of CMP position gives the final output image. The distance between the traces (ΔCMP) is a function of the acquisition geometry. In the light of this discussion, the HRS may also be

considered as the particular realisation of the sonar or of the ultrasonic non destructive testing (NDT) probe, adapted for the detection in ground.

In fact the GPR and HRS are similar in concept: both use the reflections from a target and their resolution is given by the similar formulas. For both systems, the depth of the target is found by using formula $d=vt_0/2$ where t_0 is two-way vertical travel time and v is the propagation velocity (Fig.1.a). As well the depth resolution, δ_r , may be estimated as to be equal to $1/4\lambda_{s,e}$ [5]. In practice, the angular resolutions of both techniques are quite comparable, but since the GPR exploits much shorter wavelengths, its available depth resolution δ_r is at least ten times better. The case histories presented in the following sections show the use of the HRS in civil engineering, in detecting the ground stratigraphy, faults, voids.

ACQUISITION AND PROCESSING

For the all examples presented in this paper the acquisition of the seismic data was carried out using a 24 or 48 channel seismograph and 100 Hz geophones which provided the low-cut filtering of the seismic data. End-off geometry (as illustrated in Fig.1.c) was applied; the closest offset Δs_g ranged from 1 to 20 m, depending on the position of the optimum offset window [6]. The geophone spacing Δx was set in order to fulfill the spatial sampling requirements. A silenced "betsy gun" (designed in the laboratory) firing 12-gauge hunting cartridges, similar to the one presented by Miller et al.[3] was used as a source. It performs well for depths less than 50 meters and can be operated directly at the surface, thus avoiding the drilling of shot-holes. The processing included the high resolution "optimum offset window" operations flow [7,8].

PRACTICAL EXAMPLES

Shallow stratigraphy

The aim of the survey presented in this section is the imaging of the structure of cliff. The experiments were conducted on North Sea coast in northern France, along two profiles **A** and **B** [9]. The obtained seismic sections are shown in Fig.2. Figure 2.c shows the well-logging data of this site and the comparison with the results obtained. Profile **A** is located parallel to the cliff. Its vertical setting is 7 meters above the limestone layer (P2). Profile **B** was set perpendicular to the cliff at an altitude of about 20 meters above P2.

As seen in Fig.2, both seismic sections display, as expected, the horizontally layered structure of the site, which relates the markers noted as A, B-C, D, F-G, H. It can be noted that practically all expected layers are detected. The obtained depth resolution δ_r may be estimated as 3 m for this survey. Profile **A** was located between two military post-war bunkers along the path covered with filled-in ground. Since the unloaded ground induces high absorption of seismic waves and perturbs their spatial correlation, the "bunker" and "path" induced effects limit the depth of imaging. The influence of the left bunker is seen in zone $180 < \text{CMP} < 195$, where reflections F, G, H are disturbed. Note that the depth of imaging obtained for profile **B**, which was realized in better conditions, is nearly two times greater (for the same power of seismic source). The deepest marker K-L. is detected only within the narrow interval because, in this zone, the design of the acquisition geometry favoured deeper imaging.

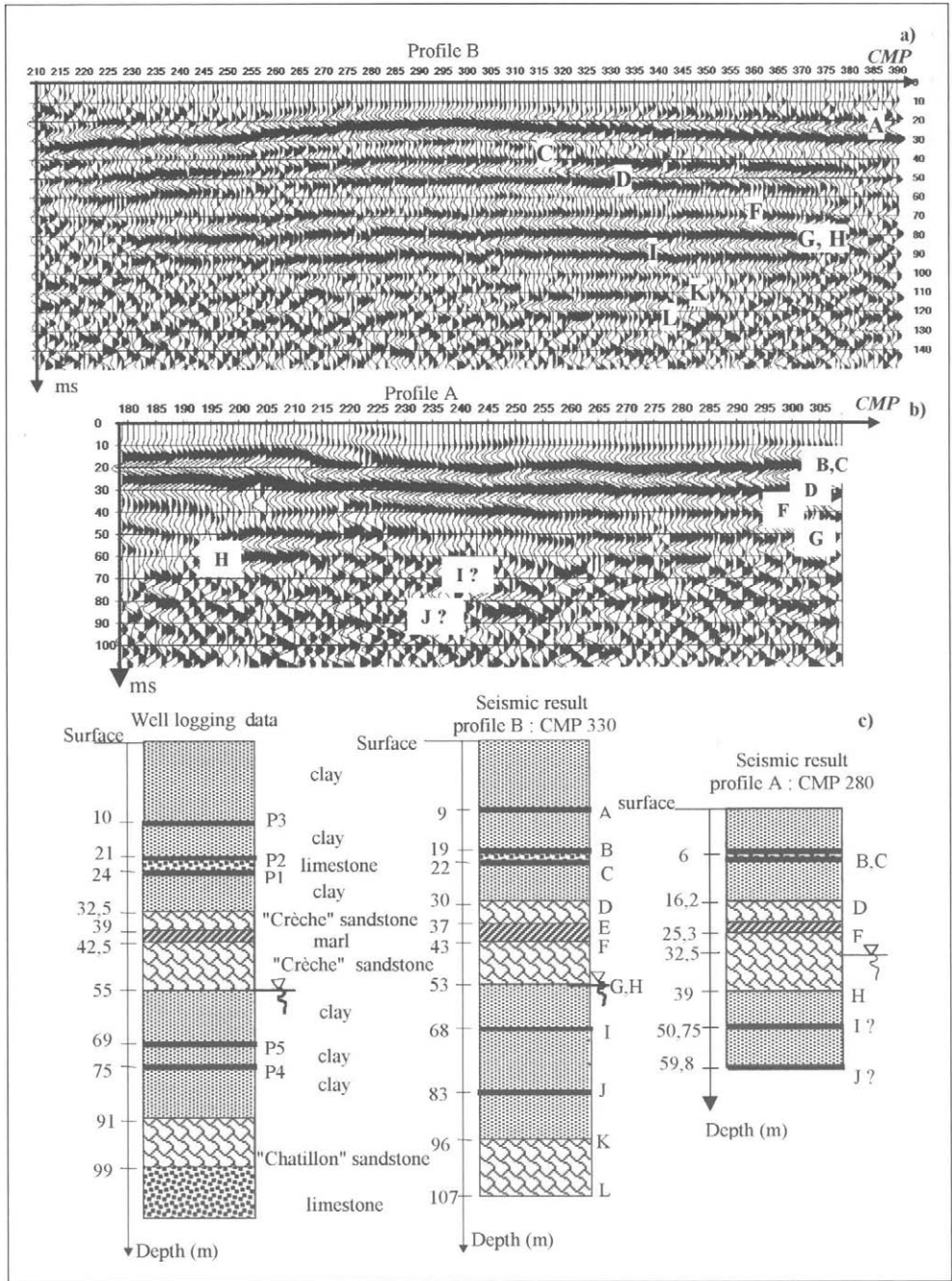


Fig.2. Seismic stratigraphy of the structure of cliff ($\Delta\text{CMP}=0.5$ m); **(a)** profile *B*; **(b)** profile *A*; **(c)** well logging data and the interpretation of the results from sections (a) and (b).

Mapping of old chalk pits

This section presents the successful application of the HRS for the indirect detection and location of old abandoned chalk-pits, in the north of France. Some positions of these voids, which form a network of tunnels are mapped, whereas others are unknown and represent a real danger for both population and building activities. The tunnels typically occur in chalk at a depth of 8-15 m and are followed by a water table and a chalk layer (Fig.3.c). The detection of those cavities has been performed in an indirect way, i.e. by means of the detection of the cavity-induced perturbations of the seismic image of the regular geological structure (which should be known in advance) [10]. The detection procedure includes two stages:

(1). The HRS survey of the profile, respecting the basic principles of this technique. This stage reveals two principal markers: the water table (B) and the interface chalk/marl (C).

(2). Interpretation and classification of the direct and indirect signs of the cavity occurrence. In fact, the reflectors B and C, which represent quasi-stationary well-correlated events can be used as the reference signals for the observation of the abnormal indirect signs. The numerous experiments conducted at the areas with known cavity positions allowed us to construct the "cavity symptoms list" including all the signs correlated with the cavity occurrence. These symptoms are, respectively, the amplitude perturbation of B (see Fig.6.a), the amplitude drop of the high frequency version of B, the spatial correlation drop of B, the spectral modifications of B, the masking of reflector C, the spatial correlation drop of C. In most situations the masking of reflector C, illustrated in Fig.3, is so seen clearly that cavity can be interpreted directly from the seismic section. In other situations, these signs are poorer as they should be considered together, so as to improve the reliability of detection. In order to help the interpretation, all symptoms are expressed in a binary scale (0 - 1) and their weighted sum is assumed to be equal to the risk of the cavity presence (CR). This signal may be plotted directly as a function of CMP, thus enabling an easy interpretation and presentation of the results.

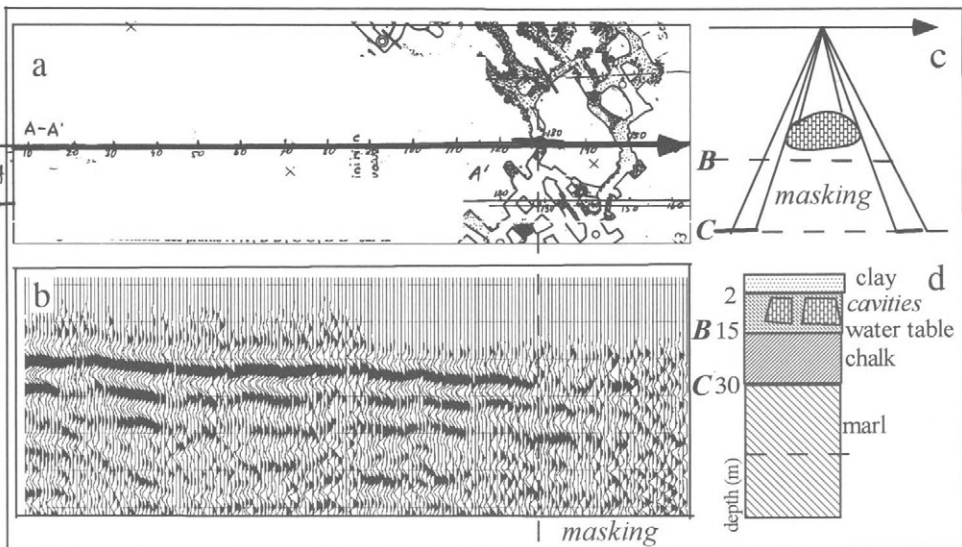


Fig. 3. Tunnel detection by means of "masking effect"; (a) Tunnel map and location of the prospected profile; (b) Seismic image of chalk/marl interface (marker C, $\Delta\text{CMP}=0.5$ m): masking of this marker, well correlated with the tunnel position, is observed; (c) Symbolic illustration of the "masking" effect. (d) Geological well logging data in the region of experiments.



Fig.4. Detection of underground voids (geological conditions as in Fig.3.a) - test for the method reliability performed at the site where the presence of tunnels was a priori unknown. The obtained Cavity Risk criterion is superimposed over the map of the known tunnels. The results obtained by seismic was tested by drilling.

The successful application of the procedure is presented in Fig.4, which shows the criterion CR obtained along four profiles. This work was performed without any a priori knowledge of the cavities position. The results obtained were checked by drilling. The figure shows that the borehole tests confirm 80% of detections (since the cavities never occupy more than about 75% of the surface, these results can be considered as very favourable). Moreover, the precision of evaluation of the depth of void is greater than 15%.

Mapping of collapsed structures and/or of filled-in ground deposits

Since the unloaded ground induces high absorption of seismic waves and perturbs their spatial correlation, the ground collapses and the filled-in ground areas should appear in the seismic section as the zones of poor and badly correlated signals. The presence of such grounds in the shallow, near surface structures is often the reason of the poor HRS data quality, when the imaging aims at the deeper structures (problem mentioned in Fig.2.b). However, as shown in this section, this feature may also be useful for the detection of the collapsed ground.

The experiment illustrated in Figure 5 was conducted along a profile which included a collapsed surface, located in the interval $CMP < 250$. The study aimed to check if this collapse was of natural origin or was induced by the collapse of an underground tunnel (the second possibility was highly probable in the experiment zone [11]). The observation of the image obtained shows that the seismic signals are clearly observed only within the zone $CMP (250-273)$, indicating the presence of the intact geological structure. A decay of the signal exactly within the interval $CMP < 250$ confirms the hypothesis of a collapsed ground. An additional decay zone is also observed for $CMP > 274$. Since this zone is not associated with any collapsed structure observed

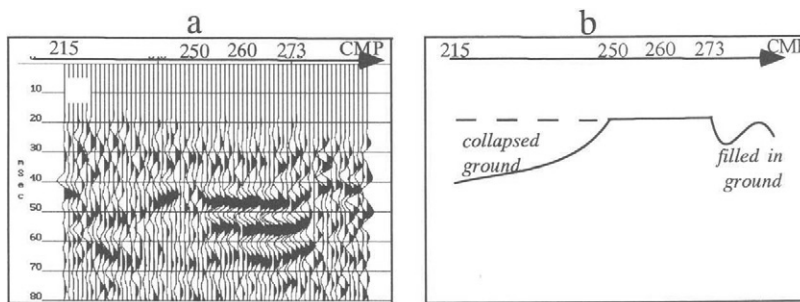


Fig.5. Examples for the detection of the collapsed and filled in ground; (a) Seismic image obtained; ; (b) Position of the profile in relation to the collapsed zone.

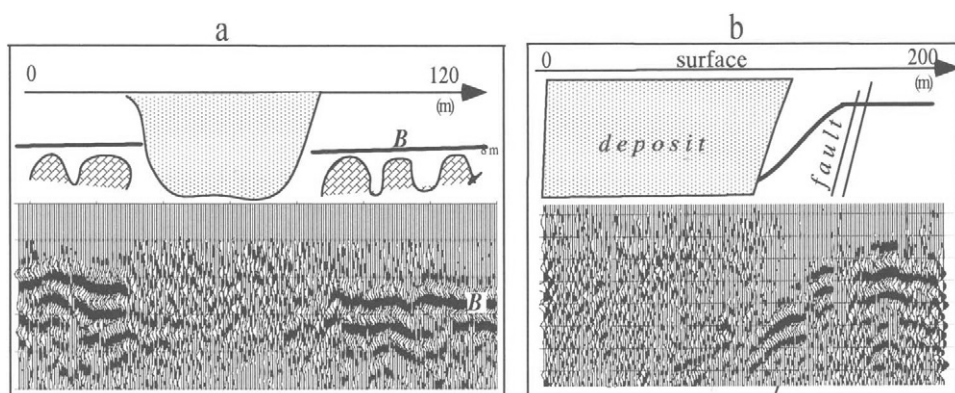


Fig.6. Examples for the detection of the collapsed and filled-in ground; (a) Seismic section of profile Q2 (see Figs.3a and 4) showing the marker B and its interpretation: the strong discontinuity observed within zone $150 < \text{CMP} < 170$ represents the collapsed filled-in cavity; (b) The seismic image obtained along the profile crossing the old waste deposit and its interpretation

at the surface, it is interpreted as being related to building activities which involved the filled-in ground.

The second example shown in figure 6.a shows the image of an underground cavity, one of those detected during the experiments shown in Fig.4. The image which presents the marker B (see Fig.3.a) includes clearly seen discontinuity ($150 < \text{CMP} < 170$), dominated by coherent noise. We emphasize that, as is illustrated in figure 6.a, the whole profile contains the voids, but only a part the profile displays such discontinuity. In fact, as was explained by the local inhabitants, this discontinuity represents the image of the void that had been collapsed after the bomb impact during World War. The cavity was filled in after the war. Note that the non-intact voids which around the filled-in zone, do not induce such effects.

The third example (Fig.6.b) shows the cross section of the old waste deposit, not exploited for more than a hundred years. In this case the HRS was used in order to locate the limit of the deposit. According to previous interpretations, the limits sought are found by interpreting the presence of uncorrelated signals. The image obtained also shows that the location of the deposit was associated with the natural dipping structure of the ground.

Evaluation of risk of the collapse of an underground cavity

During the erosion of an underground cavity the parts of the ceiling which are the object of the degradation, fall down, thus involving so-called "lifting void" phenomena. When the void "approaches" the ground surface and the subsurface layers are not rigid enough, there is a risk of the surface collapse. This risk may be evaluated by an estimation of the actual depth of the void.

Figure 7.a. shows the image of the subsurface obtained along the profile located over the old chalk pits. The geological structure of this site is shown in Fig.7.d. The voids occur in the chalk structure (C), under the sequence of the tuff. The aim of this study was to define the lateral limits of the voids and to check for the risk of its collapse.

The profile (Fig.7.a) reveals zones $60 < x < 103$ m with strong discontinuity of marker C. This is interpreted as the symptom of existence of the cavities (the reflection from the tuff/chalk interface interferes with the reflections from void of an opposite sign). At the same time, the absence of marker E within zone $70 < x < 90$ m indicates that, in this area, the cavities perturb the water table. This shows that the void is rising and reaches (or has already crossed) the depth level of 18 m. Finally the $70 < x < 90$ zone was classified as the area of risk [12].

The profile also reveals the high quality of the non-perturbed signals which represent water table E and chalk C, for $x > 105$ and $x < 60$. Thus, this interval is interpreted as the absence of voids. The interpretation of this survey is summarized in Figure 7.c.

To prevent collapse, the voids were filled with a mixture of sand, cement and water. In order to check the quality of this operation, the second seismic survey was conducted along the same profile (Fig.7.b). When compared with the previous result, the additional signal R is observed. It is difficult to interpret its origin, but its presence may be seen as the confirmation that acoustic waves have penetrated the void and that the mixture has filled it completely.

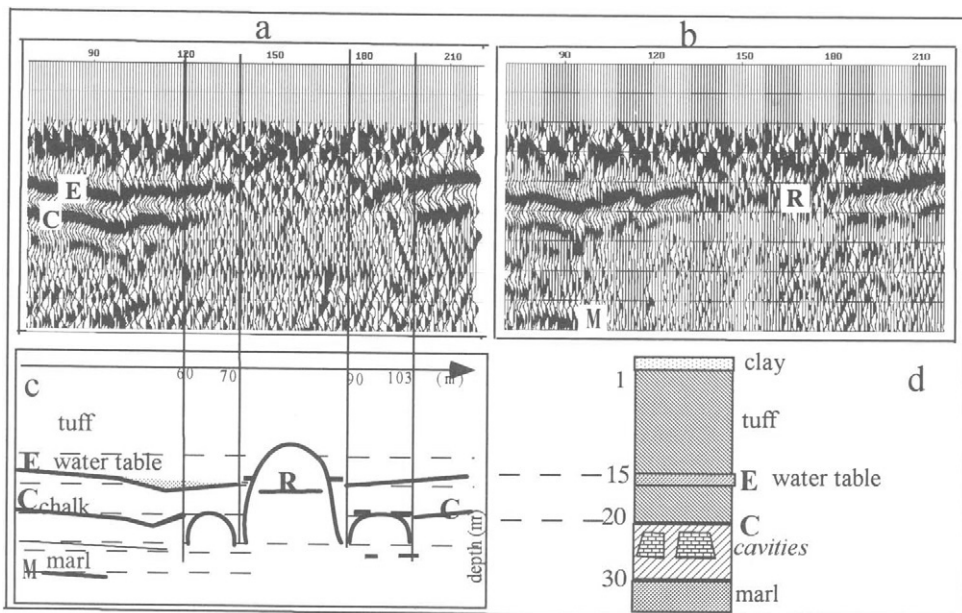


Fig.7. Evaluation of the risk of collapse of underground void. (a) Seismic image showing two main markers E and C; $\Delta CMP = 0.5$ m; (b) same as (a) but after the filling-in the cavities (c) Interpretation of section (a): the discontinuity of E is interpreted as the "lifting void" phenomena; (d) well-logging data.

Archaeological research

This example concerns the use of HRS in the archaeological field [9]. The objectives of this study was to find the position of an underground tunnel linking the 15th century castle with the 12th century keep constructed 500m away (the occurrence of this tunnel is not sure). The results of the research are summarised in Fig.8. The tunnel is expected to occur in the sand layer, above the sand/clay interface, at a depth not greater than 4 m. According to previous discussions, the only expected symptom of tunnel is the masking of marker A. This problem would be more suitable for a GPR application, but because the high humidity level of the ground, the radar could not be applied at this site.

In order to increase the reliability of detection the different processing flows are used in this case. Two versions of processing are presented in Figure 8. The first one emphasises the marker A, even if its signal is relatively weak, thus enabling to follow its continuity. The second one emphasises the anomalies of the signal. The results obtained show that the depth of interface A varies from 3 to 6 meters.

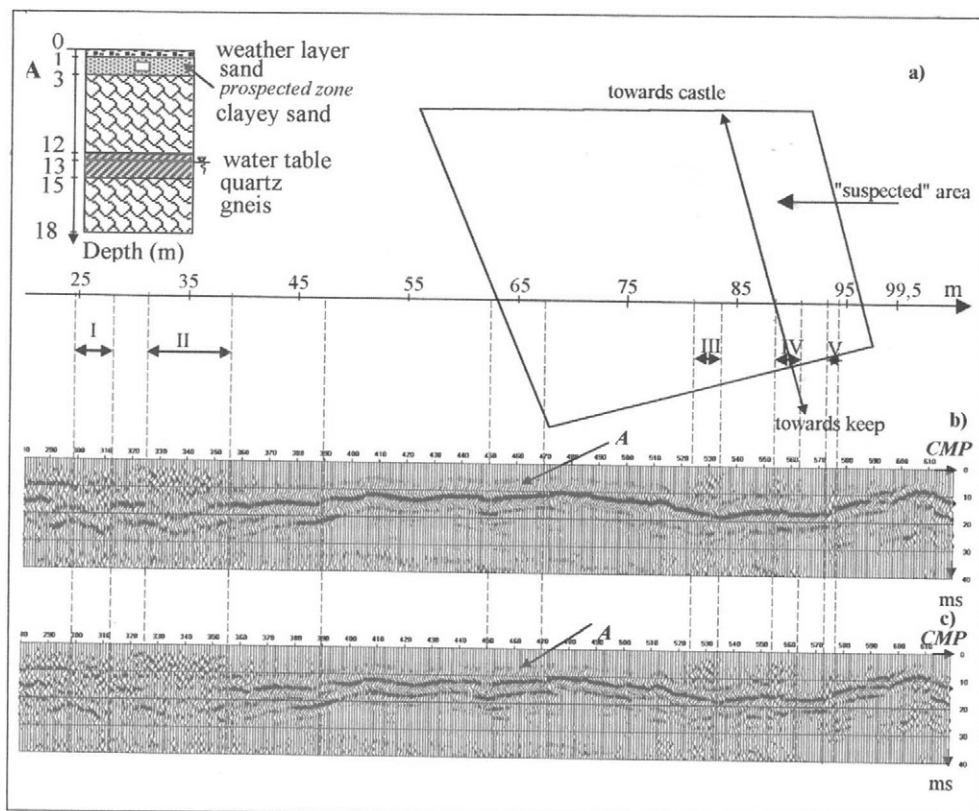


Fig 8. Example of use of HRS in archaeological domain. (a) geological structure and the most suspected area of tunnel occurrence; (b) Seismic images of marker A for two different signal processing. Zones I, II, III, IV and V have been selected as possible positions of the tunnel.

Five perturbation zones, which may be interpreted as the tunnel symptoms, have been selected. Zones I and II represent the "filled-in ground" symptoms (see Figs 5 and 6) and may be related to the construction of a house (which occurs several meters from the profile) but it may not be excluded, that those effects mask the existence of tunnel. Note that the filled-in zone occurs beyond marker A and therefore masks partially its signal. In fact there is not any reason to suppose that A is not continuous there

CONCLUSIONS

The high resolution seismic technique completes the use of the ground penetrating radar, for cases, where its operation is no longer applicable i.e. in wet, electrically conducting soils and at greater depths.

The seismic imaging proved to be efficient, in particular for the stratigraphy of the shallow subsurface, for the detection and location of the underground voids and for the detection of collapsed and filled-in terrain. It has been successfully used for the evaluation of risk of cavity collapse as well as for the verification of the filling of this cavity with the cement mixture.

ACKNOWLEDGEMENT

The authors are very grateful to *Service d'Inspection des Carrières Souterraines de Douai* for her kind help and assistance in presented research concerning the use of the HRS in the detection of underground voids.

REFERENCES

1. Dobrin, M.B., (1983) *Introduction to Geophysical Prospecting*. Mc Graw Hill N.Y.
2. Ward, S.H. (1990), *Geotechnical and Environmental Geophysics*, Society of Exploration Geophysicists,
3. Miller, R.D., Pullan, S.E., Waldner, J.S., & Haeni, F.P., (1986) *Geophysics* **51** (2067-20)
4. Knapp, R.W., Steeples, D.W., (1986) *Geophysics* **51**, (283-294).
5. Mari, J-L, Arens, G., Gaudiani, P., Chapellier D.. (1998) *Méthodes de géophysique de gisement appliquées au génie civil* Publications de l'Institut Français du Pétrole, éditions TECHNIP, Paris
6. Cook, J.,C. (1985) *Geophysics*, **30** (527-538).
7. Mari, J-L., Glangeaud, F., Coppens, F., (1997b) *Traitement du signal pour géologues et géophysiciens*. Publications de l'Institut Français du Pétrole, éditions TECHNIP, Paris
8. Yilmaz O, (1987) *Seismic Signal Processing*, Society of Exploration Geophysicists,
9. Leonard, Ch., (1999) *Phd thesis in preparation*, Université de Lille France.
10. Piwakowski, B., Tricot, J.C., Leonard, C., Ouarradi, N., Delannoy, B., 1997 In *Proceedings of 3rd Congress of Environmental & Engineering Geophysical Society*, Arthus, Denmark.
11. Piwakowski, B., Watelet, J-M., Moreaux, D., (1997) in *European Journal of Environmental and Engineering Geophysics*, **2** (2), (109-120)
12. Piwakowski, B., Moreaux, D., (1995) In: *Proceedings of 2ème rencontre du Réseau de Laboratoires GEO*, Aussois, France

DETERMINATION OF THERMOPHYSICAL PARAMETERS OF BUILDING COMPONENTS AND BUILDINGS

A. DONATH

*Brandenburg Technical University Cottbus / Department of Applied Physics
P.O.Box 101344, D-03013 Cottbus*

ABSTRACT

The knowledge of the thermophysical parameters of materials and building components is the basis of all calculations of the thermal behaviour of a building. The parameters must be determined both under natural climatic conditions and under conditions of use. Measurements can be carried out on separate components and on buildings in situ.

The searched parameters are the heat loss coefficient U , the solar heat gain factor g , surface temperatures, heat fluxes, the air tightness, the air exchange rate, flow velocities etc. Both at measurements in the laboratory and at measurements in situ non-destructive methods are used. At laboratory measurements the building component (e. g. the window) should be usable after the test. At measurements in situ the building or the building component must not be damaged.

The methods are infrared-thermography, Blower-Door measurements, tracer-gas measurements, flow velocity measurements (heat-wire method and Laser-Doppler anemometry), hot box measurements and well-known temperature and heat flux measurements.

The paper tries to give a general view of some non-destructive thermal investigations on building components and buildings.

KEYWORDS

Thermophysical parameters, building components, buildings, heat transfer coefficient, air change rate, convection, infrared thermography

INTRODUCTION

The calculation of the thermal behaviour requires the knowledge of the thermophysical parameters of materials and building components.

In the planning phase of construction the thermophysical parameters have to be known for meaningful and useful techniques of energy saving.

New materials and components are often used in new houses. Investigations of these materials and components are necessary to describe the behaviour both under natural climatic conditions and under conditions of use. The thermophysical parameters of materials must be determined in the laboratory and the behaviour must be investigated on test facades under real climate conditions.

For the reconstruction of buildings the thermal conditions must be known to apply effective methods of heating energy reduction. If the thermal parameters are unknown, they must be measured on the building.

The material parameters can be calculated in many different measurements under laboratory conditions. Measurements of the thermal conductivity, the heat capacity or the density of materials are usual. These parameters enable the calculation of the thermal behaviour of walls and other simple building constructions.

Difficulties arise for the determination of the thermal behaviour of complete building components. The thermophysical behaviour is caused by complex physical effects. The dynamic energy transfer is influenced both by thermal conductivity, convection, radiation and by the boundary conditions (weather and user conditions).

All these influences can be regarded separately or the energy transfer of the building component and the building can be determined within a complex measurement.

Non-destructive test methods are especially important. At laboratory measurements the building component should still be usable after the test. At measurements in situ the building component or the building itself must not be damaged.

At the Department of Applied Physics at the BTU Cottbus the behaviour of materials, building components and buildings are investigated. The thermal and moisture parameters can be measured in the laboratory, on test applications or on buildings. Many projects are conducted in co-operation with manufacturer of building materials and components.

Some methods to determine the thermal behaviour of building components and buildings are described in the paper. Results of measurements illustrate these methods.

In the first part of the paper investigations of the thermal behaviour of separate building components are presented.

In the second part some methods for investigations of buildings (In-Situ methods) are illustrated. These are methods to determine the heat transfer coefficient of facades, the Blower Door and tracer-gas techniques to determine the air exchange rate and the infrared thermography.

MEASUREMENTS ON SEPARATE BUILDING COMPONENTS

Heat Transfer Coefficient

A common method to determine the thermal conductivity of materials is the hot plate method. Two plates with different temperatures produce a constant heat flow in the specimen. This heat flow can be measured with a heat flow meter or by measurement of the heating power of an electrical heating. The heat transfer coefficient of the specimen can be calculated with the thickness of the probe.

The heat transfer coefficient of a building component can be measured in similar manner. Is there a temperature gradient on the building component the heat flux q and the temperature difference ΔT can be measured and the heat transfer coefficient (U-value) can be calculated with:

$$U = \frac{\Delta T}{q} \quad (1)$$

The heat flux can be measured by a heat flux meter. Then the U-value represents the local value. Under steady state conditions within a double climate the U-value can be calculated with the constant values of the temperature difference and the heat flux. Figure 1 shows the measurement

on a roof window. This window with an inclination of 45° and a pane area of $0.8 \text{ m} \times 0.6 \text{ m}$ was installed within an insulation frame between two rooms with different temperatures. The room temperatures, the surface temperatures and the heat flux were measured continuously. To eliminate the fluctuations of the measured data the mean values was calculated. The local heat transfer coefficient U in the example is $1.46 \text{ W/m}^2\text{K}$.

For the determination of the U -value of used windows (quality control) the building component can be disassembled of the building and after the measurement reintegrated in the building.

A measurement of the overall heat transfer coefficient of a building component is possible with the hot box method. At the guarded hot box method the metering box is surrounded by a guard box in which the environment is controlled to minimize the heat flow through the metering box walls q_{env} and the lateral heat flow in the specimen q_{lat} . If $q_{\text{env}} = 0$ and $q_{\text{lat}} = 0$ the total heat flow through the specimen will then be equal to the heat input to the metering box. The energy transfer through the specimen corresponds to the electrical power of the metering box heating. Figure 2 illustrates the measuring principle.

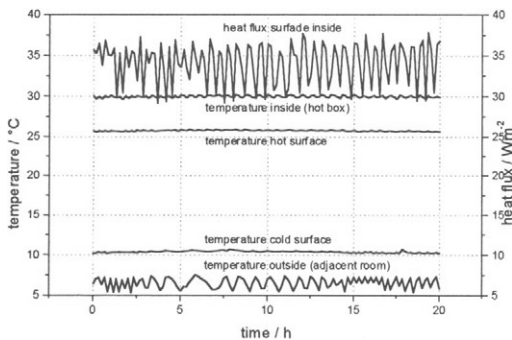


Figure 1: Measurement of the local U -value of an inclined window

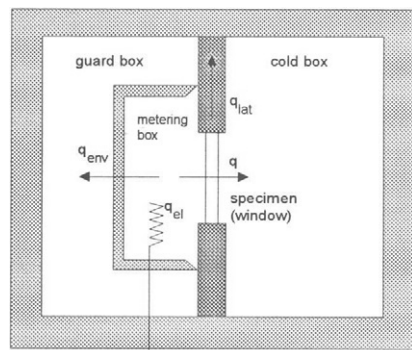


Figure 2: Measuring principle of the hot box method

The calculated overall heat transfer coefficient of the window (window with frame and reveal) is 2.94 W/K , which corresponds to an average heat transfer coefficient of $4.09 \text{ W/m}^2\text{K}$. This value clarifies the influence of the frame and the edges of the window.

The results of the measurements are the requirement of further calculations of the energy consumption of the building or of decisions for the exchange of windows in a building.

Measurements under steady state conditions do not consider the influence of real weather data or using conditions. Therefore the dependence of the heat transfer on convection and solar radiation can not be determined. This is only possible by means of an outdoor test-site. Thereby the investigated building component is an external wall of an air-conditioned room. The outside conditions are the weather conditions and the room climate can be controlled to simulate different using conditions. The Figure 3 illustrates the cross-section of an outdoor test-cell. These (so-called) PASSYS test-cell (PASSYS = Passive Solar Systems and Component Testing) includes a well-insulated test room with a floor area of 13.8 m^2 and a volume of 38 m^3 (Research Project PASSYS [1], Donath et al [2]). The south wall of the test room is the investigated building component with a size up to 2.7 m to 2.7 m . This is the size of a real building facade. Disassembled facades or separate building components can be installed in this test room and different thermophysical parameters can be determined simultaneously. The PASSYS test equipment contains a weather station to determine real weather data.

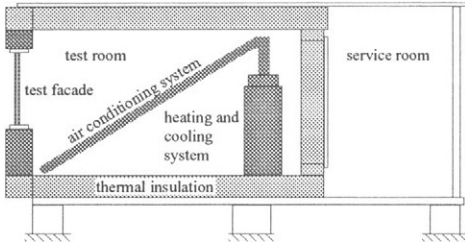


Figure 3: Longitudinal cross-section of a PASSYS test-cell

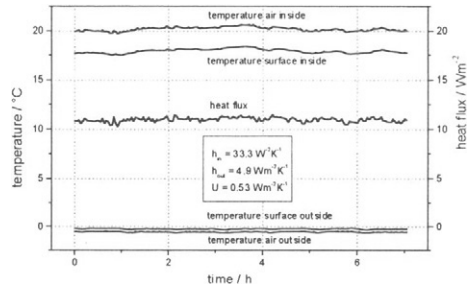


Figure 4: Measurements of the heat transfer in a PASSYS test-cell

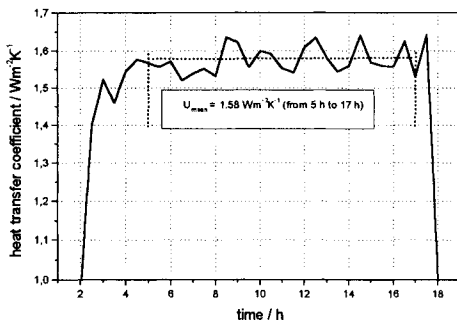
With these test cells as well local measurements as measurements of overall values of the component are possible. The real outside weather conditions and particularly the real solar radiation enable the determination of the effective U-values and of solar gains of the building component. The energy consumption of the room in consideration of the solar gains can be measured. The searched g-value can be calculated by means of a thermal model and parameter identification.

The Figure 4 shows the measurements on a vertical window. The temperatures reflect the influence of the outside temperatures and the solar radiation. The inside and the outside heat transfer coefficient (h_{in} and h_{out}) was measured. The overall heat transfer coefficient of the facade is $0.7 \text{ W/m}^2\text{K}$.

MEASUREMENTS ON BUILDING COMPONENTS OR BUILDINGS IN SITU

Heat Transfer Coefficient

Measurements of the local heat transfer coefficient are possible in the same way as described above. The heat transfer coefficient U can be calculated with Equation (1) if the temperature difference between inside and outside and the heat flux are measured. Supposed are measurement values within a period of relative constant temperature difference and without influence of solar or other thermal radiations. The Figure 5 shows results of a measurement on an inclined roof window.



The local heat transfer coefficient can be calculated as mean value with respect to the effect of the solar radiation. If there is solar radiation on the surface the temperatures of the glass panes increase and the heat flux decreases. The heat transfer coefficient attains very low or negative values (see the beginning and the end of the measurement). Therefore the correct heat transfer coefficient is calculable only while undisturbed periods (e.g. at night).

Figure 5: Measurement on an inclined roof window

Convection Measurements

In many cases the energy losses are influenced by the heat transfer between a surface and air. Especially on windows and lower insulated building components the energy transfer depends on the convection effects.

To calculate the heat transfer by convection the velocity and the temperature profile have to be known. Due to the low fluid velocities measurements of the free convection require methods with high resolution. An appropriate method is the Laser-Doppler anemometry. By using of a Laser-Doppler anemometer one obtain well-located 1-, 2- or 3 dimensional velocity profiles. An additional advantage is the possibility of measurements within enclosures, e. g. between glasses of a window.

The Figure 6 illustrates the principle of Laser-Doppler measurements on an inclined roof window. The Figure 7 shows the vector plot of the convection on an inclined window inside above the window board. The window board influences the velocity profile and thereby the heat transfer coefficient.

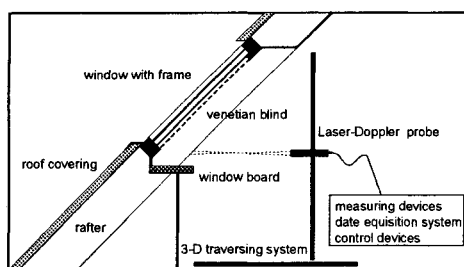


Figure 6: Equipment of Laser-Doppler flow measurements

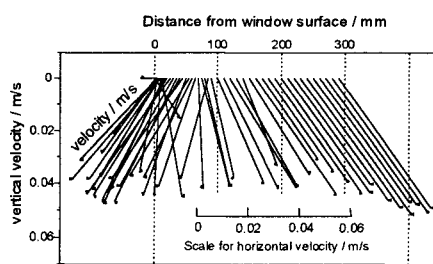


Figure 7: Two-dimensional vector plot of the flow velocity on an inclined window

The flow velocities near the surface on a vertical window (Height 1.0 m, Width 0.8 m) in different heights are shown in Figure 8. The window was inside of a frame that forms a recess of 100 mm around the pane. For that reason the convection is different from the free convection on a simple vertical plate. From these measurement data can be calculated the local heat transfer coefficient. The average heat transfer coefficient between $x = 500$ mm and $x = 900$ mm is $h_x = 2.95 \text{ W / m}^2 \text{ K}$ (Donath [3]).

An example of a measurement of the convection in a vertical rectangular enclosure shows Figure 9 (Width 1.2 m, Height 2.4 m). The results of velocity measurements are the typical one for a boundary layer regime in enclosures. The profile is unsymmetric about $y = \frac{1}{2} D$ due to the variation of viscosity with temperature. A second reason is the convection in z -direction. Hence in addition to the convection between the hot and the cold glass pane there is a secondary convection from the centre of the enclosure to the edges. The edges are non-adiabatic and therefore there are heat losses to the frame.

Measurements of the convection can help to calculate the heat resistance of the window (with frame) and to minimize the heat losses of the building component.

Beyond that the correlation between the heat transfer coefficient and the velocity profile distribution can be deduced (Donath [3]).

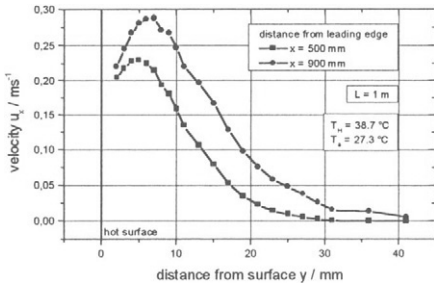


Figure 8: Velocity profile of free convection in different heights

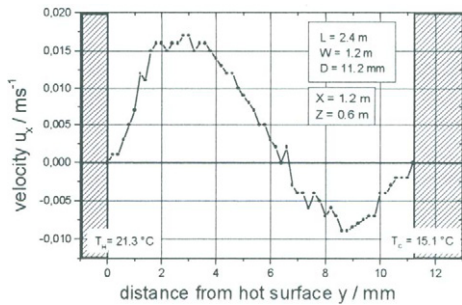


Figure 9: Velocity profile of a Double-glassed window

Infrared Thermography

Many investigations can be supported by infrared thermography. An example is the investigation of the convection in correlation with the effect of solar blinds. Although the air flow is not visible the thermal effect on surfaces can be uncovered. The Figure 10 shows the infrared image of the inner surface of an inner venetian blind on an inclined roof window. The window is south orientated with an inclination of 48 °. The solar radiation on the surface is $I_{surf} = 600 \text{ W/m}^2$. The image shows that the highest temperatures not only occur on the upper edge but also near the centre of the window. The reason of this effect is the convection between the inner glass pane and the venetian blind. These measurements are used to develop effective solar blinds and improve the thermal comfort near windows and solar charged building components.

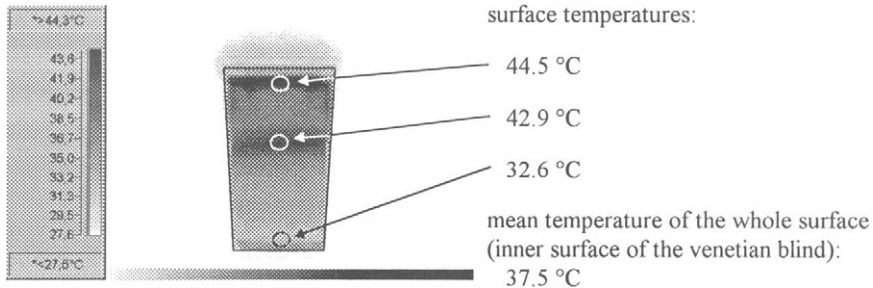


Figure 10: Infrared image of the inner surface of a venetian blind on an inclined roof window

Air Change Rate and Air Permeability

Infiltration and ventilation in dwellings generally obtain 1/3 to 1/2 of the space conditioning energy. As energy conservation improvements to the thermal envelope continue, the fraction of energy consumed by the conditioning of air may increase. Air-tightening, while decreasing energy requirements, has the tendency to decrease the ventilation. These results in reducing the

air quality and increases the risk of moisture problems. Therefore the air change rate and the air permeability are defined in standards. The measurements of the real values on building components and buildings are necessary to evaluate the quality of a building component or a building, to calculate the energy demand of a building or to estimate the thermal behaviour of a building.

Blower-Door-Method. The Blower-Door consists of a variable-speed fan, mounted in an adjustable panel that temporarily fits in a doorway. Pressure gauges connected to the fan measure the rate of airflow required to maintain the building at a certain pressure. At this method the air flow at desired pressure differences between the house (room) and outside is recorded. Measurements are taken by controlling the speed of a fan until the pressure difference is constant. Typically, testing is done between 10 Pa and 60 Pa. If the room volume is considered, the air change rate at 50 Pa can be calculated with $n_{50} = \dot{V}_{50} / V_R$. For higher accuracy the average value of measurements at overpressure and low pressure can be calculated. In the example is $n_{50} = 8,7$ 1/h (see Figure 12).

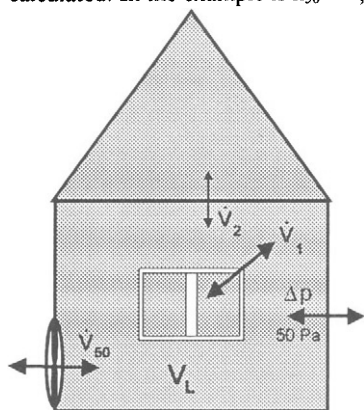


Figure 11: Principle of Blower-Door measurements

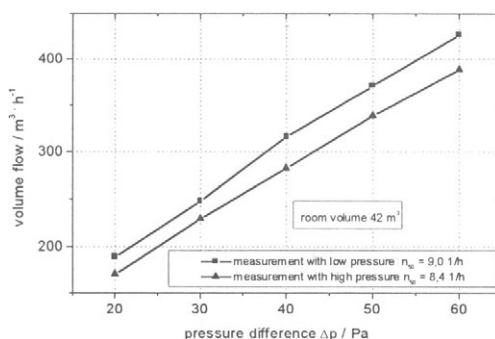


Figure 12: Results of a Blower-Door measurement

The air change rate n_{50} can be converted in the air change rate at normal conditions (see below). Blower-Doors are also useful for identifying specific leaks. By forcing air in or out the leaks become more apparent. If there are temperature differences between inside and outside the thermal effect can be observed with an infrared camera.

Results of Blower-Door measurements can be used to calculate the coefficient of air permeability of joints. The required values of the air permeability of windows are defined in standards ([4]). The air permeability describes the volume of air interchanged by joints between outside and inside at a pressure difference at 10 Pa.

The air flow rate is:

$$\dot{V} = a \cdot l \cdot \Delta p^n \quad \text{in } \text{m}^3/\text{h} \quad (2)$$

with

$$\dot{V} \quad \dots \text{ air flow rate in } \text{m}^3/\text{h}$$

- a ... air permeability of joints
- l ... length of joints
- n ... exponent to define the non-linearity between the pressure difference and the air volume
- Δp ... pressure difference in daPa

Then the coefficient a can be calculated for the results of 10 Pa measurements as:

$$a = \frac{\dot{V}_{10\text{Pa}}}{l}$$

If there are measuring results at different pressure differences the coefficient can be identified by fitting to the measuring data. An assumption is the total tightness of the test room (except the window to be measured).

Tracer-Gas Measurements. By introducing of a tracer-gas (e.g. N₂O) the trend of concentration can be measured (e.g. by gas-chromatography). These values are correlated with the „natural“ air change rate. If C₀ is the concentration at t = 0 the concentration is

$$C = C_0 \cdot \exp(-\beta \cdot t) \tag{3}$$

Then the air change rate can be calculated with

$$\beta = (\ln C_0 - \ln C) / t \tag{4}$$

The tracer-gas measurements quantify the air change rate at normal conditions, that is it gives results for the specific weather conditions at the time. An advantage is that the measurement does not change the natural pressure and the air flow circumstances in the room or the building. Figure 14 shows the time depending gas concentration. By using of equation (4) the air change rate is calculable.

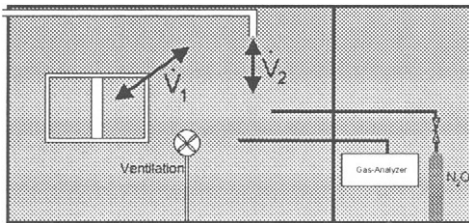


Figure 13: Principle of tracer-gas measurements

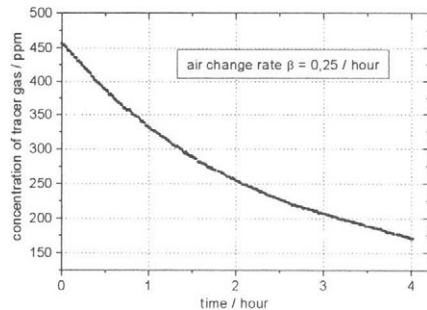


Figure 14: Tracer-gas measurement in an office

Assuming some simplifications the results of tracer-gas and Blower-Door measurements can be compared. A reasonably good estimation of the average infiltration rate at normal conditions (and for a typical single-story house) can be obtained by dividing the air change rate at 50 Pa by 20, that is:

$$\beta = \frac{n_{50}}{20} \tag{5}$$

This equation ignores many details of the infiltration process, e.g. the influence of wind and pressure fluctuations, the conditions of convection and the types of leaks. If the leakage exponent or the building height are different from the default assumption corrections must be applied (Sherman[5]).

In the example above the air change rate of $n_{50} = 8,7$ 1/h results in an air change rate at normal conditions of $\beta = 0,44$ 1/h. The differences between this measurement and the tracer-gas measurement indicate the influences of the specific weather and air flow conditions at the time of the experiments.

CONCLUSIONS

The described test methods are suitable to determine the thermal parameters and to characterize the energy transfer of building components and buildings. These parameters are the basis of calculations of the thermal behaviour of buildings and to develop energy effective building constructions. The measurements have to consider the real boundary conditions and user conditions. The use of certain methods depends on the concrete problem. The investigation of building components in the laboratory is quasi non-destructive. The component can be used after the test. The described measurements on the building itself are non-destructive, however not free from inconveniences for the occupants. But the measurements are only temporary and do not influence the building construction or the building.

ACKNOWLEDGEMENT

The author would like to thank U. Maschke, C. Lanzke and A. Kraus for their help to perform the measurements.

REFERENCES

- [1] Commission of the European Communities Directorate - General XII for Science, Research and Development, The PASSYS Project, Final Reports, and PASLINK (Consolidation of the Operational Structure of the PASSYS Test Sites and the PASSYS Test Procedures, Final Reports.
- [2] Donath, A., Gutschker, O., Rogäß, H., Maschke, U., Test of passive and active solar building components, In: International Symposium Non-Destructive Testing in Civil Engineering, Berlin, September 26 - 28, 1995, pp. 1291 - 1298.
- [3] Donath, A., The use of the Laser-Doppler anemometer to investigate the heat transfer by convection on building components, In: Proceedings of the International Conference Non-Destructive Testing in Civil Engineering, Volume 2, Liverpool, 1997, pp 611 - 622, J. H. Bungey (Ed).
- [4] DIN 18055, German Standard. Windows, air permeability of joints, water tightness and mechanical strain, requirements and testing, Oct. 1981
- [5] Sherman, M. H., Estimation of infiltration from leakage and climate indicators, In: Energy and Buildings 10, pp 81 - 86, 1987

This Page Intentionally Left Blank

MEASUREMENT OF A SPATIAL DISTRIBUTION OF RADON EMANATIONS
THROUGH A FRACTURE – A NEW NON-DESTRUCTIVE TESTING TECHNIQUE OF
CONCRETE MATERIALS

T. Hatsukari and N. Tsuchiya

Department of Geoscience and Technology, Graduate School of Engineering,
Tohoku University, Sendai 980-8579, JAPAN

ABSTRACT

New measuring method of natural radioactivity of concrete materials was investigated by using Imaging Plate(IP). IP is a two-dimensional radiation detectors based on photostimulated luminescence, and it has high sensitivity to every kinds of radiations. Fractures in concrete were visualized as a radiation image. Radon α -ray, including alpha disintegration of thoron and their daughter nuclides, were detected by the imaging plate, even though they occurred with other kinds of ionizing radiation emanating from the concrete, such as β - and γ -rays from concrete. Radiation dose through fractures in the concrete, particularly radon emanation, was strongly related to fracture surface area. Emanation of radon families from concrete may be accelerated, depending on fracture character. Measurement of radon α -ray using the IP could prove to be a effective non-destructive testing technique to characterize concrete failure associated with the development of fractures.

KEYWORDS

Photostimulated luminescence, radon, α -ray, γ -ray, Imaging Plate, fracture, concrete failure, non-destructive testing, two-dimensional radiation measurement.

INTRODUCTION

Radon(Rn) and Thoron(Tn) are one of the natural radioactive nuclides, and such radioactive

noble gases radiate α -ray in the process of their decay. Rn (half life 3.83 day) and Tn (half life 55.6 second) are the only gases in radioactive decay series. Rn can easily move in air and is able to be dissolved into solution. Due to its high mobility and relatively long half life, Rn has been shown to be a good indicator of atmospheric cycling [1,2], to access radiation in living spaces [3] and to predict the occurrence of earthquakes [4-6].

Recently, two-dimension measurement of extremely weak radiation have been carried out by using an Imaging Plate, which acts as a visual detectors of radiation based on the principle of photostimulated luminescence. If IP is able to detect Rn α -rays emanating from fracture in concrete materials, then it has the potential to become an effective non-destructive testing technique to evaluate mechanical failure in concrete buildings. However, no systematic investigations have until now been carried out to investigate the effectiveness of IP as a Rn detector.

In this paper, a radiation image of a fractured concrete floor was performed using the IP. The applicability of IP as a non-destructive testing technique is then described.

PRINCIPLE OF THE IMAGING PLATE

Photostimulated luminescence and the Imaging Plate

The mechanism of photostimulated luminescence (PSL) is shown as follows (Fig.1): When photostimulated phosphors are excited by radiation, electrons are elevated into the conduction band and trapped in the unstable energy level. If the phosphors are re-excited by a light beam, and luminescence is obtained at a shorter wave-length than that of the incident beam, i.e. photostimulated luminescence results.

The photostimulated phosphors coated on the IP are barium fluorobromide doped with Eu^{2+} ($\text{BaFBr}:\text{Eu}^{2+}$). The mechanism of $\text{BaFBr}:\text{Eu}^{2+}$ is described as follows [7, 8] (Fig.2).

Recording radiation image. Excitation by radiation such as α -ray, β -ray, γ -ray, X-ray, and UV light, produces electrons and holes in the crystals of the photostimulated phosphors. The holes are caught by Eu^{2+} ions which are the detector emitting light in the crystals, and Eu^{2+} ions are converted into Eu^{3+} ions. Electrons are excited to the conduction band and trapped at the two levels of F-centers (halogen ion vacancies). It is the $\text{F}(\text{Br}^-)$ and $\text{F}(\text{F}^-)$ sites, which form the color center under the stable conditions. The radiation image is recorded as a latent image in the IP, and in principle the quantity of trapped electrons is in direct proportion to the dose.

Reading latent image. Using He-Ne laser beams as an incident beam (633 nm), trapped electrons are released to conduction band, and then recombine with the holes captured by Eu^{3+} . The Eu^{3+} ions are reverted to excited Eu^{2+} ions and Eu^{2+} luminescence is observed as a photostimulated Luminescence (390 nm). The latent image of radiation can be seen by measuring the position and intensity of photostimulated luminescence on the IP.

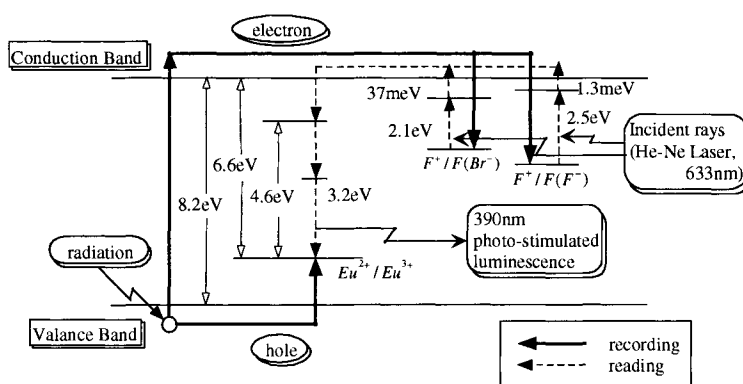


Fig.1 Luminescent mechanism of photostimulated phosphors (BaFX:X=Br,I)

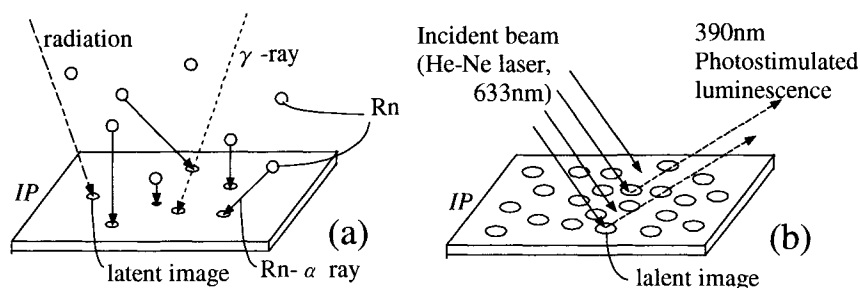


Fig.2 Principle of recording and reading radiation image using the IP; (a) Recording radiation image, (b) Reading latent image.

Characteristics of the Imaging Plate

The IP is a sheet type detector and visual sensor of radiation. It is coated with PSL phosphors (BaFBr:Eu²⁺), which is enable to measure a two-dimensional radiation image. The IP has a high sensitivity to all kinds of radiations, including α -ray, β -ray, γ -ray, X-ray, ultraviolet radiation, heavy ion ray and neutron ray. The IP has the following characteristics, as a radiation detector [9].

- ① Very high sensitivity
- ② Large detection area (e.g. $20 \times 25 \text{ cm}^2$ per sheet)
- ③ Wide energy range
- ④ High position resolution (minimum is $25 \mu\text{m}$)
- ⑤ Wide dose rate characteristic
- ⑥ High speed reading

- ⑦ Reusable
- ⑧ Simple to use without a requirement for chemical treatment in a darkroom
- ⑨ Digital image for data processing

EXPERIMENTAL DETAILS

A trial measurement of R_n , emanating from a fracture in concrete, was performed in a covered overpass corridor connecting the second level floors of the main building and annex of the Department of Geoscience and Technology, Tohoku University. The floor is made from concrete and contains rock aggregates. The floor surface is covered with 2.0 mm thick ceramic tiles. Figure 3(a) shows overview of the overpass corridor, which was under repair of outside wall in the course of this study.

The open fracture is observed in the floor. The average aperture of the fracture is approximately 3 mm and the length is 2.72 m extending across the corridor. There is a displacement of about 2 mm between the two sides of the fracture. The fracture is considered not to extend entirely through the floor, but its depth is uncertain. Figure 3(b) shows photographs of the fracture and floor surface.

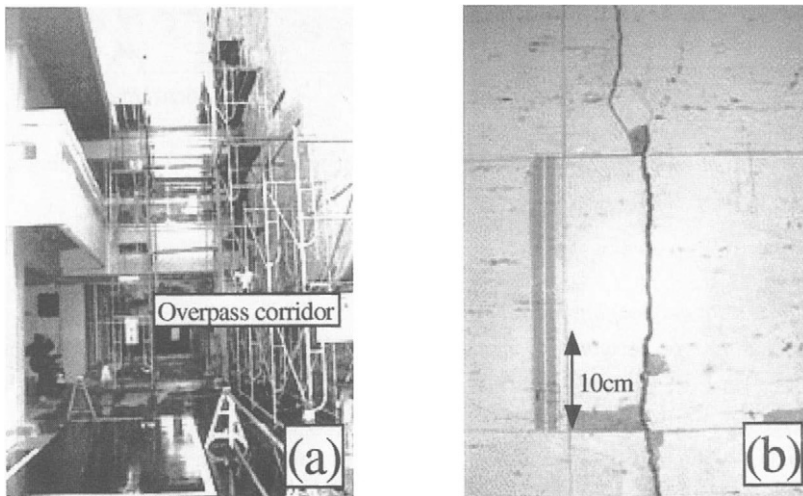


Fig.3 Photographs of experimental site; (a) view of covered overpass corridor, (b) floor and fracture.

The IP used here is BAS-SR (Fuji Photo Film Co., 25mm×20mm). The reading apparatus is BAS-2500 (Fuji Photo Film Co.). The software for reading the IP is Image Reader v1.4j (Fuji

Photo Film Co.). The reading condition of the IP is as follows: dynamic range of dose 10^5 , latitude level 4, digital image level 16 bits (65536). The resolution is $50 \mu\text{m}$. The software for analyzing the radiation image is Image Gauge v3.0 (Fuji Photo Film Co.). The intensity of photostimulated luminescence is expressed by the PSL value, which is arbitrary and is unique to the BAS systems. PSL is defined as follow [10];

$$P = (Z/100)^2 \times (4000/S) \times 10^{(L(Q/G-1/2))}$$

where P is PSL value, Z is the resolution, S is the sensitivity, L is the latitude, G is the number of gradation, Q is the QL value which is the original digital image data within 16 bits.

The IP was covered with clean plastic wrap, coated with silicon oil, which was effective in capturing Rn gas. The IP was wrapped in a blackout polyethylene bag to prohibit exposure to the sun and fluorescent lights. [11]

The IP, coated with silicon oil and inside the dark bag, is put on the floor, and two types of measurement subsequently were carried out. One measurement is with an aluminum absorber insetted between the IP and the floor. The other test is without the aluminum absorber. The thickness of the aluminum absorber is $45 \mu\text{m}$, which means α -rays from concrete buildings were completely absorbed. Based on these experiment conditions, the α -ray image could in principle be obtained by subtracting the radiation image of the test with aluminum absorber from the results for the test that without aluminum absorber.

Exposure time was 24, 48 and 72 hours. A selected area of $28 \times 2 \text{mm}^2$, including part of the fractured in the floor, was analyzed.

RESULTS

Measurement of the fracture

Figure 4 shows radiation images using IP, without aluminum absorber (Fig.4a) and with aluminum absorber (Fig.4b). The fracture is evident as the near-vertical line of dark PSL spots on both images of Fig.4(a) and (b). The PSL value, however, when the aluminum absorber was used, is lower than that when the aluminum absorber was not used from Fig.4. Even though the radiation image of the fracture is weak, such as in the case where the aluminum absorber was used, the fracture figure is evident. This fact suggests that the main radiation image of the fracture was created by γ -rays.

α -ray image of the fractured floor

After subtracting the radiation image with aluminum absorber from that without aluminum absorber, α -ray image could be obtained. Figure 6(a) shows a selected radiation image of α -ray on the fracture, indicating in Fig.5.

The area size in Fig.6 is expressed by pixel, where 20 pixels are equal to 1 mm. Right side axis corresponds to 28mm side in Fig.5, and left one is 2 mm side.

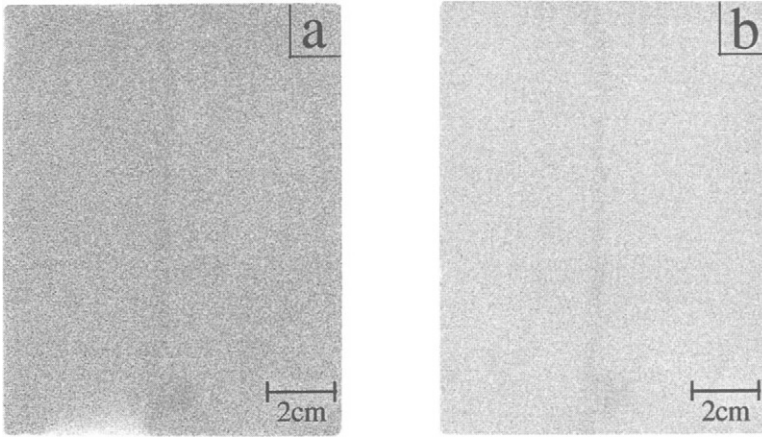


Fig.4 Radiation image of the floor including fracture. (a): without aluminum absorber; (b): with aluminum absorber.

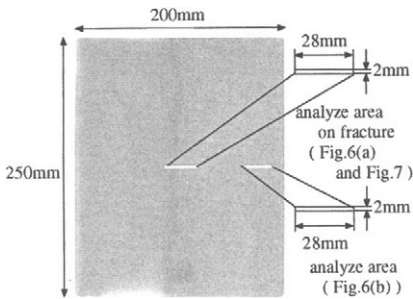


Fig.5 Index map of selected areas for analysis

High PSL spots can suggest α -ray image due to strong stopping power of α -ray compared to γ -ray. The maximum α -ray range of natural radioactive nuclides is approximately $50 \mu\text{m}$ in concrete materials. If α -ray is radiated from surface or inside of the concrete, it is considered to be difficult to cause high PSL spots because of high energy loss. If Rn were absorbed on the surface of IP, α -ray disintegration of Rn and its daughter nuclides gave high PSL spots.

Figure 6(b) shows α -ray image of a different area without fractures. Comparing Fig.6(a) to (b), the number of high PSL spots of Fig.6(a) where is the area on the fracture is larger than that of Fig.6(b). Thus, the main source of Rn, indicating high PSL spots, is considered to be Rn emanated through the fracture.

High PSL spots were also recognized in Fig.6(b), even though the number of spots was lower than that in Fig.6(a). Rn maybe move through a gap between IP and the floor, and a part of Rn maybe environmental Rn as a background. Figure 7 shows PSL maps of α -ray under different exposure conditions. Figure 7(a) is 24 hours exposure, (b) is 48hours which is the same to Fig.6(a), and (c) is 72hours. With increasing exposure time, the number of α -ray spots also increased. Figure 8 shows relationship between exposure time and the number of α -ray spots. The number of high spots is proportional to exposure time.

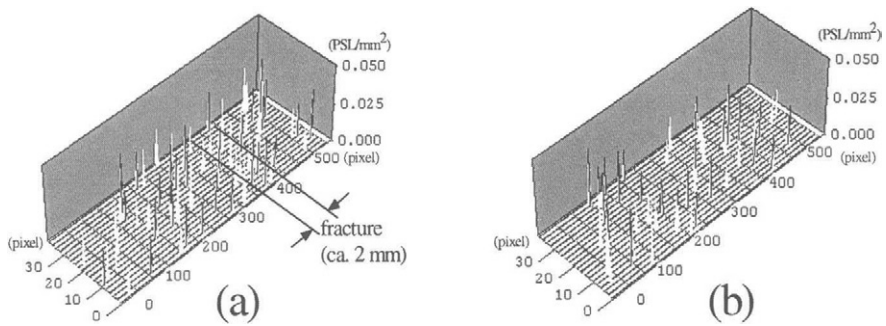


Fig.6 PSL map of α -ray spots obtained after subtraction of γ -ray image from the original radiation image. (a): area across the fracture, (b): area without the fracture, indicated in Fig.5.

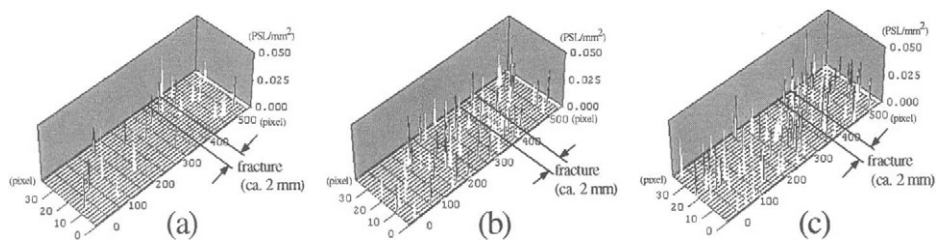


Fig.7 PSL maps of α -ray spots. (a): 24hours exposure, (b): 48 hours, and (c): 72 hours.

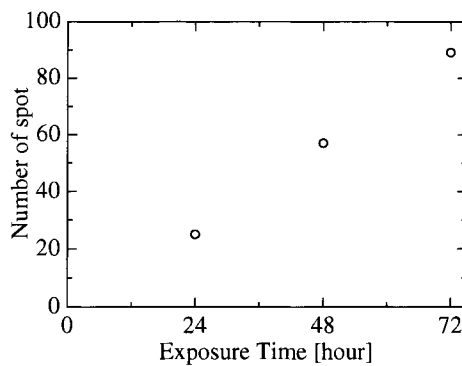


Fig.8 Relationship between exposure time and the number of spots

CONCLUSIONS

Spatial distribution of radiation of concrete floor including fracture was measured by using the Imaging Plate. The following conclusions were obtained;

- (1) Low-level radioactivity of the concrete materials could be obtained by IP, and fracture was recognized as a radiation image.
- (2) α -ray image was created through subsequent experiments. One is with aluminum absorber and the other is without absorber. α -ray image is represented as the high PSL spot map.
- (3) The main α -emitter indicated by high PSL spots is considered to be Rn which emanated through the fracture.
- (4) The Imaging Plate was developed as a two-dimensional radiation detector, and it is applicable to new non-destructive testing techniques of concrete materials.

ACKNOWLEDGMENTS

The authors would like to express our gratitude Professor Emeritus M. Takabe of Tohoku University for introduction of the IP. This research has been financially supported by joint research program with Japan Nuclear Cycle Development Institute.

REFERENCES

1. Rangarajan, C., Gopalakrishnan, S., Chandrasekaran, V. R. and Eapen, C. D. (1975) *J. Geophys. Res.* 80, 845.
2. Liu, S. C., McAfee, J. R. and Cicerone, R. J. (1984) *J. Geophys. Res.* 89, 7291.
3. Fujimoto, K., Kobayashi, S., Uchiyama, M., Doi, M., Nakamura, Y., (1997) *Hoken Butsuri (Health Physics)* 32, 41.*
4. Kanai, Y. (1991) *Chishitsu News* 446, 33.*
5. Igarashi, G. (1996) *Chikyukagaku (Geochemistry)* 30, 1.*
6. Wakita, H. (1996) *Hoken Butsuri (Health Physics)*, 31, 215.*
7. Takahashi, K., Kohda, K., Miyahara, J., Kanemitsu, Y., Amitani, K. and Shinoya, S. (1984) *J. Lumi.* 31&32, 266.
8. Iwabuchi, Y., Mori, N., Takahashi, K., Matsuda, T., and Shinoya, S. (1994) *Jpn. J. Appl. Phys.* 33, 178.
9. Takebe, M. (1996) *Ouyou Butsuri (Applied Physics)* 65, 601*.
10. Fuji Photo Film Co. (1993) BAS Technical Information, No.1.*
11. Ishii, K., Tsuchiya, N., Takebe, M. (1999) *Radioisotope*, 48, 441.*

* : in Japanese with English abstract

EVALUATION OF CONCRETE WITH FRP SHEET UNDER ACCELERATED DEGRADATION ENVIRONMENTS

Hattori, A*, Etoh, A**, Ohnishi, Y*** and Miyagawa, T*

* *Dept. of Civil Eng., Kyoto University, Sakyo-ku, Kyoto, Japan*

** *Public Works Bureau, Nagoya City, Naka-ku, Nagoya, Japan*

*** *Dept. of Civil Eng., Nishimatsu Construction Co., Ltd., Nishi-ku, Yokohama, Japan*

ABSTRACT

In this study, mortar and concrete specimens with several types of FRP sheets under accelerated sewerage and freezing and thawing environments respectively were investigated. After 1 month of sulfuric acid solution immersion for the mortar specimen and freezing and thawing of 90 cycles for the concrete specimen, SEM observation, element distribution analysis, measurements of ultrasonic pulse propagation velocity, dynamic elastic modulus and acoustic emission were conducted. Flexural loading and pull-off loading tests were also carried out. These non-destructive and destructive experiment results were summarized to know the applicability of the non-destructive evaluation methods. Degradation processes of repair and strengthening of concrete by the FRP sheet under the accelerated degradation environments were also discussed.

KEYWORDS

Concrete, repair and strengthening, fiber sheet, resin, FRP, sulfuric acid, freezing and thawing, durability

INTRODUCTION

Degradation of repair and strengthening by the fiber sheet may be caused by deterioration of concrete, FRP layer and/or interfacial property between them. In order to evaluate the degradation of concrete structures with the FRP layer, it is important to confirm applicability of various non-destructive inspection methods as well as destructive methods used from outside of the FRP layer surface. In this study, several types of the FRP layers using some combinations of the fiber sheet and the resin were applied for mortar and concrete specimens. A surface with the FRP layer of the mortar specimen were immersed into sulfuric acid solution, which was an accelerating environment simulating the sewerage facilities, for 1 month. Concrete specimens were placed in 90 cycles of freezing and thawing environment. After these degradation accelerations, the mortar specimen was investigated by surface and cross section observation using scanning electron microscope (SEM) with the element distribution analysis and measuring ultrasonic pulse propagation velocity and acoustic emission (AE). Flexural loading test was also carried out. The ultrasonic pulse propagation velocity and dynamic elastic modulus were measured for the concrete specimens. Pull-off and flexural loading tests were also conducted. These non-destructive and destructive experiment results were summarized to know the applicability of the non-destructive evaluation methods. Degradation processes of repair and strengthening of

Table 1 Properties of fiber sheets and resins (for mortar specimens)

Fiber sheet	Carbon fiber (High strength type)	Carbon fiber (High modulus type)
Designation	HS	HM
Tensile strength (kN/mm ²)	4900	4200
Elastic modulus (kN/mm ²)	230	436
Elongation (%)	2.1	1.0
Weave Density (g/m ²)	300	300

Resin	Epoxy (Normal type)	Epoxy (Acid proof type)	Epoxy (Flexible type)
Designation	N	A	F
Tensile strength (kN/mm ²)	42.7	25.0	20.6
Elastic modulus (kN/mm ²)	2.2	0.98	0.88
Elongation (%)	3.0	8.0	20

Table 2 Properties of fiber sheets and resins (for concrete specimens)

Fiber sheet	Carbon fiber	Glass fiber (E-Glass)
Designation	C	G
Tensile strength (kN/mm ²)	3480	1470
Elastic modulus (kN/mm ²)	230	72.5
Weave Density (g/m ²)	200	300

Resin	Epoxy (Normal type)	Epoxy (Flexible type)
Designation	N	F
Tensile strength (kN/mm ²)	42.9	13.7
Elastic modulus (kN/mm ²)	N/A	N/A

For **Table 1** and **Table 2**:

- Types of fiber sheet and resin for mortar and concrete specimens differ from each other.
- Specimens were named with combinations of fiber sheet and resin used for FRP layer; ex. HS-N, C-N, and specimens without FRP layer were named "0-0".

concrete by the FRP sheet under the accelerated degradation environments were also discussed.

EXPERIMENT OUTLINE

Mortar specimen test

On a side surface of the 40×40×160mm standard mortar specimen, 1 layer of fiber sheet was axially applied. The material properties used in the FRP layer is shown in **Table 1**. Mix proportion of the mortar is shown in **Table 3**. In order to accelerate degradation, some of the mortar specimens were immersed in 20°C 10% sulfuric acid solution for 1 month.

Table 3 Mix proportion of mortar

Flow (mm)	Unit mass (g/l)		
	W	C	S
162	225	450	1350

Table 4 Mix proportion of concrete

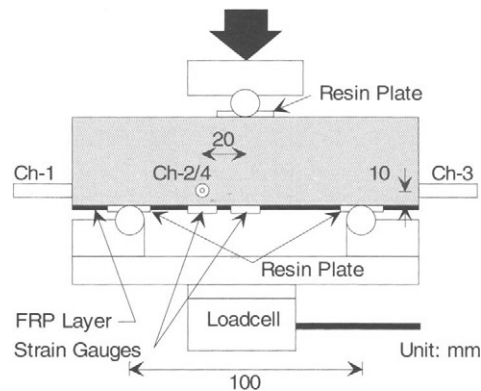
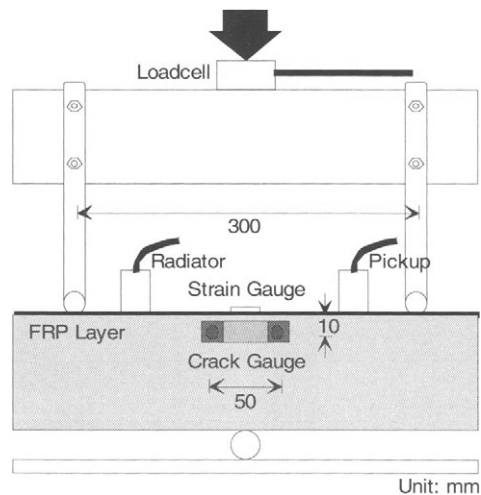
N.M.S. (mm)	Slump (cm)	Air (%)	W/C (%)	s/a (%)	Unit mass (kg/m ³)				W.R.A. (cc/m ³)	A.E.A. (cc/m ³)
					W	C	S	G		
15	8±1	3.3	55	49	168	305	861	942	763	610

Those immersed were applied thick epoxy coating on the surfaces other than that with the FRP layer. The following investigations were conducted for the mortar specimens.

SEM observation and element distribution analysis. In addition to visual observation, observation of surface and cross section by SEM (Acceleration voltage: 20kV, Working distance: 28mm) was conducted. During the SEM observation, element distribution analysis of cross section in a line of depth direction from the FRP layer surface was carried out on elemental sulfur (S). Neutralization depth of cross section was also measured by using the phenolphthalein solution.

Ultrasonic pulse propagation velocity. By the symmetric method (the radiator and pickup: 50mm diameter, 50kHz, 160mm distance), ultrasonic pulse propagation velocity was axially measured between both end surfaces.

Flexural loading. The loading state is shown in Fig. 1. The unidirectional monotonic loading, and the unidirectional cyclic loading were conducted. In the cyclic loading, load was applied up to $0.5P_{cr}$, $1P_{cr}$, $2P_{cr}$, ... (where P_{cr} : flexural cracking load) and then unloaded down to small load every time. Load, FRP layer surface strain at span center (gauge length: 5mm) and AE (sensor:

**Fig. 1** Flexural loading test (Mortar)**Fig. 2** Flexural loading test (Concrete)

150 kHz resonant type, gain: 40dB for both pre and main amplifier, discriminate level: 1V) were measured. In the AE measurement, the ring down counting was carried out. In addition, Ferocity ratio ($= P_{AE}/P_{LAST}$, P_{LAST} : last load, P_{AE} : load when AE count increases remarkably in the next loading) which shows stability of the Kaiser effect and the unidimensional position rating of the AE source were also carried out.

Concrete specimen test

On a side surface of the 100×100×400mm concrete specimen, 1 layer of fiber sheet was axially applied. The material properties used in the FRP layer is shown in **Table 2**. Mix proportion of the concrete is shown in **Table 4**. Average compressive strength was 37.9N/mm². In order to accelerate degradation, some of the concrete specimens were given 90 cycles of freezing and thawing according to ASTM B method. The following investigations were conducted for the concrete specimens.

Ultrasonic pulse propagation velocity. By the symmetric method (the radiator and pickup: the same as above, 400mm distance) applied between both end surfaces, and by the surface method (100, 200, 350mm distances between centers of the radiator and pickup) applied on the FRP layer, ultrasonic pulse propagation velocity was axially measured.

Dynamic elastic modulus. Measuring the first resonance frequencies of the longitudinal and flexural vibration, dynamic elastic modulus was obtained. When measuring the flexural vibration frequency, specimens were placed so that the FRP layer came to lower end.

Pull-off loading. By using a steel attachment of 40×40mm adhesion area, the pull-off strength was obtained.

Flexural loading. The loading state is shown in **Fig. 2**. The unidirectional monotonic loading was conducted. Load, FRP layer surface strain at span center (gauge length: 5mm), crack width at span center by a π shape crack gauge (gauge length: 50mm) were measured. Ultrasonic pulse propagation velocity was also measured during loading in the same method as above. The loading was continued until a generation of the diagonal crack, and then it was monotonously unloaded afterwards.

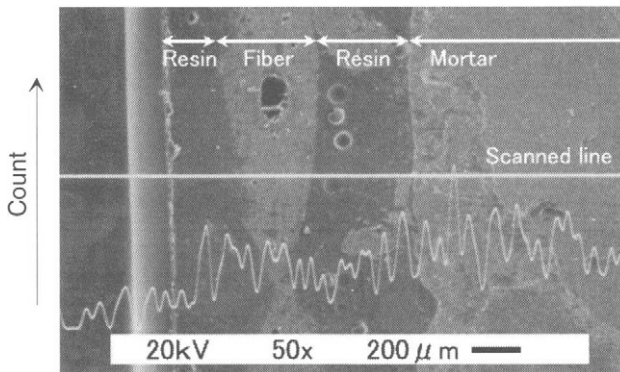


Fig. 3 Distribution of sulfur (S) (Mortar, Not immersed)

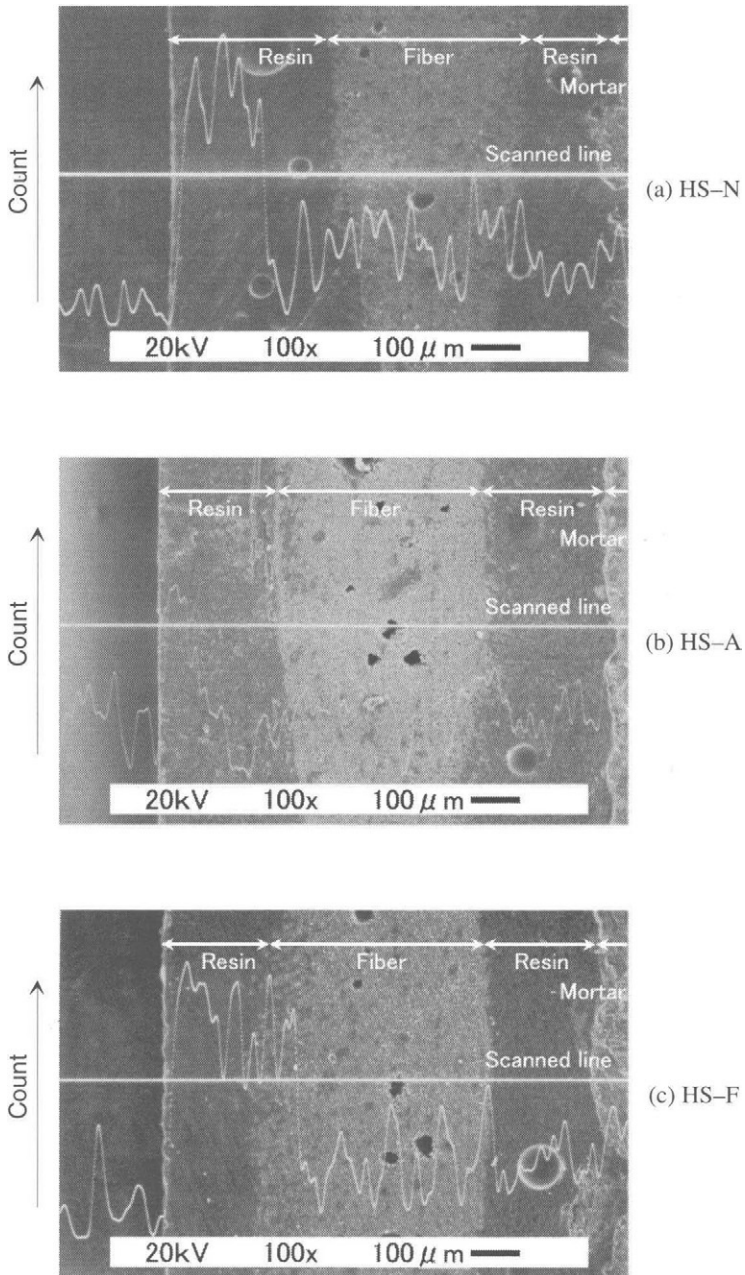


Fig. 4 Distribution of sulfur (S) (Mortar, Immersed)

RESULTS AND DISCUSSIONS

Mortar specimen test

SEM observation and element distribution analysis. Since the neutralization depth was all 0mm, the mortar was not influenced by the sulfuric acid immersion. Visible changes such as cracks were not recognized by the visual and SEM observation in the FRP layer. However, infiltration depth of sulfur (S) by the element distribution analysis increased clearly from those without immersion. Therefore, the infiltration depth can be adopted as an index of influence of sulfuric acid environment. While the infiltration depth was small in the acid proof resin (A), it advanced close to the surface of the fiber bundle of the carbon fiber sheet in the flexible resin (F), as shown in Fig. 3 (not immersed) and Fig. 4 (immersed). This means that cutoff performance is better as the cross-link density of resin is larger. The infiltration depth is correspondent to reduction of tensile strength and weight increase tendency [1] after immersion in the same resin.

Ultrasonic pulse propagation velocity. Significant differences were observed according to the material combinations of the FRP layer, as shown in Fig. 5. The influence of the fiber sheet was more remarkable than that of the resin. The velocity was also affected by the position of the radiator and pickup; that is, the velocity increased as they were placed closer to the FRP layer in the both end surfaces. The reasons may be that the fiber sheet itself might have high velocity when its high elastic modulus is considered, that the fiber sheet stiffened the mortar, and that the resin fulfilled pores near the surface of the mortar. The velocity decreased a little after the immersion.

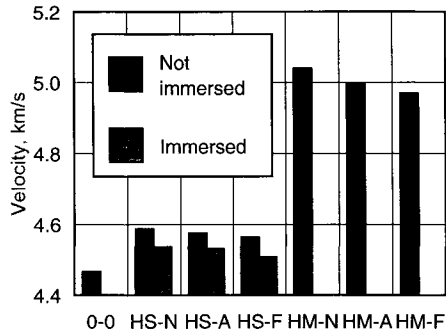


Fig. 5 Ultrasonic pulse propagation velocity (Mortar)

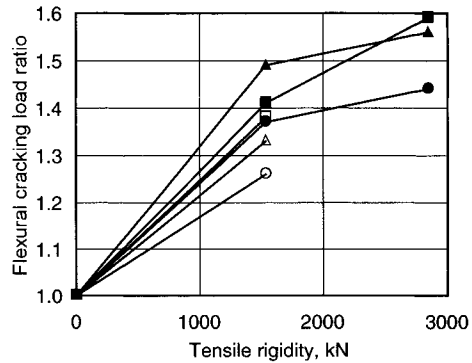


Fig. 6 Flexural cracking load ratio (Mortar)
 ■, ●, ▲: Not immersed, Resin=N, A, F
 □, ○, △: Immersed, Resin=N, A, F

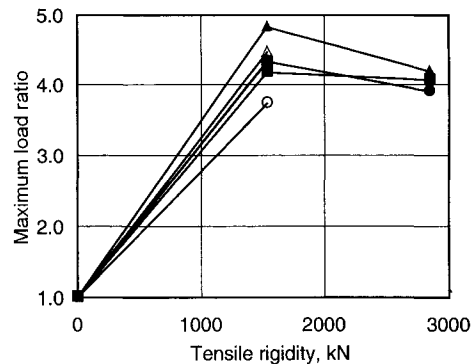


Fig. 7. Maximum load ratio (Mortar)
 ■, ●, ▲: Not immersed, Resin=N, A, F
 □, ○, △: Immersed, Resin=N, A, F

Degradation of elastic modulus of the resin surface may cause the velocity reduction.

Flexural loading. After a flexural crack was generated near the span center, cracks due to diagonal tension stress generated in both sides of the flexural crack. The diagonal cracks developed to the FRP layer, and then they caused debonding of the FRP layer, when the maximum load was obtained. Making the tensile rigidity of the FRP sheet to be the x -axis, the ratio of the flexural cracking load to the non-reinforced specimen is shown in Fig. 6, and the ratio of the maximum load is shown in Fig. 7. Although the flexural cracking load was higher in the high modulus carbon sheet (HM), the maximum load was lower. Since the stress at an equal strain is larger due to the high elastic modulus, the high modulus carbon sheet (HM) could restrain cracks. On the contrary, the high modulus carbon sheet (HM) required large bond strength, so the debonding might easily occur. The FRP layer surface strain of the high modulus carbon sheet (HM) was one half of that of high strength carbon sheet (HS). The strain was small when the flexible resin (F) was used. In the case of the flexible resin (F), slip might occur in wide area. After the immersion, the flexural cracking

load decreased as much as 15% when the the flexible resin (F) was used. Degradation of the resin may be the reason. However, the maximum load reduction and the strain reduction at the same load were not significant.

AE measurement in flexural loading. With increase in the precedence load, the Ferocity ratio decreased, as shown in Fig. 8. The specimens became an unstable condition. After the immersion, the Ferocity ratio decreased significantly at $P_{LAST}/P_{cr}=1$. Therefore, the Ferocity ratio is effective for degradation estimation. On the contrary, the Ferocity ratio did not decrease in the immersed specimens at $P_{LAST}/P_{cr}=2$. This means that degradation which made the Ferocity ratio decrease greatly occurred at $P=P_{cr}$ by the immersion. In the unidimensional position rating, remarkable AE arose near the span center when the flexural crack was generated, as shown in Fig. 9. Afterwards, AE generation frequency is small for some time. Then the generation area extended with load increase, which means the generation and development of the diagonal and debonding cracks were caught by the AE measurement. However, the effect of material type and immersion were not clear.

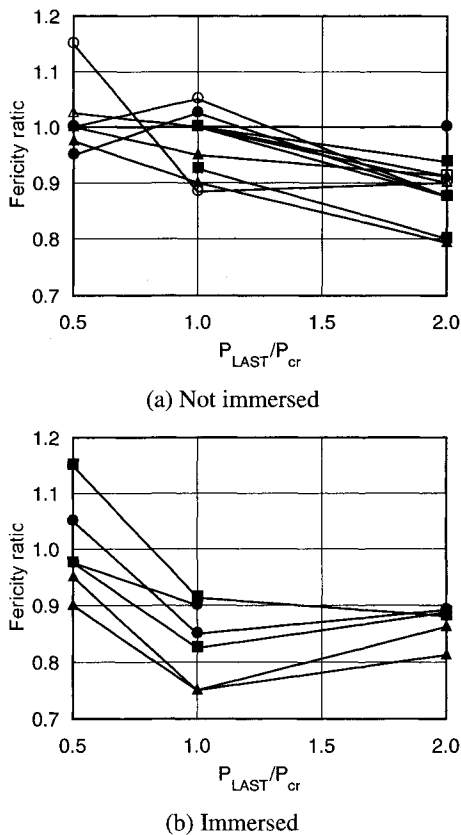


Fig. 8 Ferocity ratio (Mortar)

■, ●, ▲: HS, Resin=N, A, F
□, ○, △: HM, Resin=N, A, F

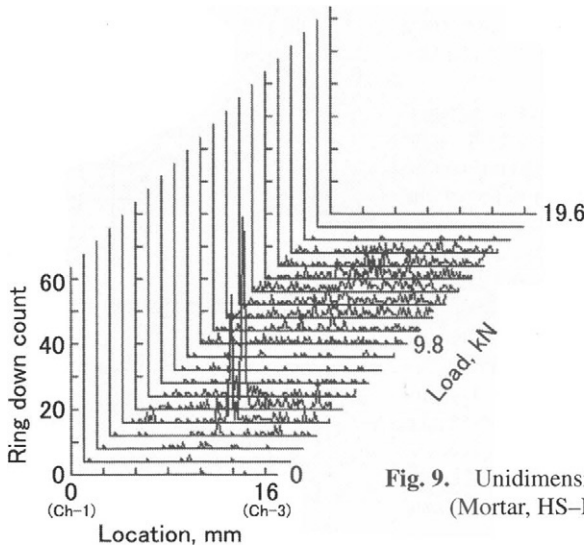


Fig. 9. Unidimensional position rating (Mortar, HS-N, Immersed)

Concrete specimen test

Ultrasonic pulse propagation velocity.

Although the FRP layer tended to make the propagation velocity lower, 1 layer of FRP did not perfectly inhibit the propagation of the ultrasonic pulse as shown in Fig. 10. However, the influence of the materials of the FRP layer on the velocity was not clear. After the freezing and thawing of 90 cycles, either measuring method did not indicate significant difference.

Dynamic elastic modulus. The dynamic elastic modulus relative to the non-reinforced specimen tended to be larger in the case of carbon fiber sheet (C) than glass fiber sheet (G), and in the case of the normal resin (N) than the flexural resin (F), as shown in Fig. 11. These tendencies were especially clear in the flexural vibration. However, the influence of the freezing and thawing was not clear.

Pull-off loading. Since the tensile fracture of the mortar part of the concrete base was observed in all specimens, all FRP layers had sufficient pull-off strength. The pull-off

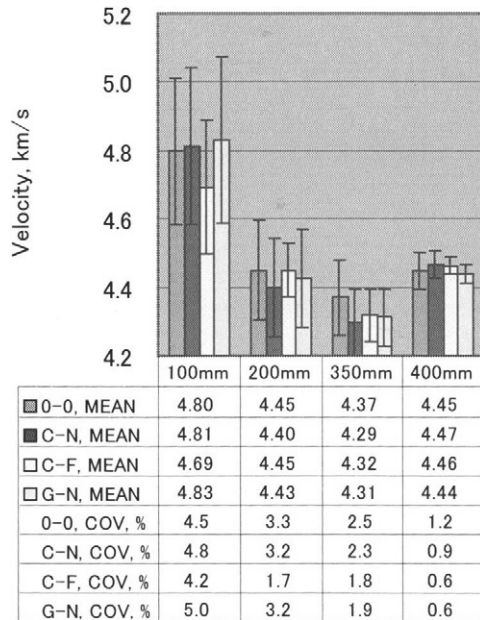


Fig. 10. Ultrasonic pulse propagation velocity (Concrete, 0 Cycle)

strength is shown in **Fig. 12**. The material properties of the FRP layer hardly appeared in the normal specimen since the pull-off strength was decided by the destruction of the concrete as mentioned above. On the contrary, in the specimen after 90 cycles, pull-off strength decreased in about 20%. Degradation of the concrete by the freezing and thawing might be the reason. The decrease was especially significant in the flexible resin (F). The flexible resin (F) of small elastic modulus could not sufficiently suppress the microcracks by the freezing and thawing cycles, so degradation of the concrete might be easy to progress.

Flexural loading. The flexural cracking load increased with tensile rigidity increase of the fiber sheet. However, it tended to be smaller in the case of the flexible resin (F) than normal resin (N). Even when carbon fiber sheet (C) of high tensile rigidity was used together with the flexible resin (F), the flexural cracking load was almost the same as the specimen with the glass fiber sheet (G) and normal resin (N). After the freezing and thawing of 90 cycles, the flexural cracking load decreased. Especially this tendency was remarkable in the flexible resin (F). This result was similar to the result of the pull-off loading test result.

Ultrasonic pulse propagation velocity in flexural loading. Large change could not be recognized at either distance of the symmetric method and surface method until the flexural cracking load, as shown in **Fig. 13**. On the contrary after the flexural cracking, while the influence of the flexural crack could hardly be recognized in the symmetric method (400mm distance), it could be detected by reduction of the velocity in the surface method (100, 200mm distance). In addition, restoration of the velocity was small even if the crack width decreased to some

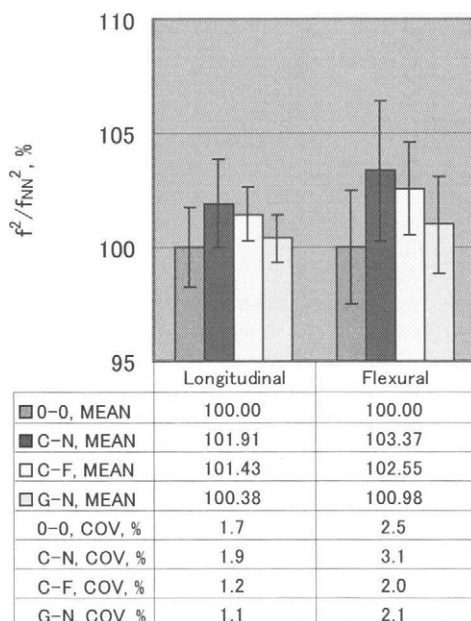


Fig. 11 Relative dynamic elastic modulus (Concrete, 0 Cycle)

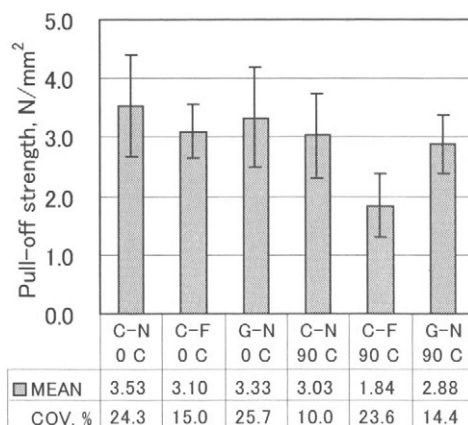


Fig. 12 Pull-off strength (Concrete)

extent after unloading. Although influence of the flexural crack appeared the most remarkably in the case of 100mm distance, 200mm distance may be sufficient since 20% reduction of the velocity was observed.

CONCLUSIONS

In this study, several non-destructive and destructive tests were conducted for mortar and concrete specimens with FRP sheet subjected to sulfuric acid solution immersion and 90 cycles of freezing and thawing respectively. The main results obtained in this study are summarized as follows:

- (1) In the sulfuric acid solution environment, degradation of the FRP layer can be grasped by the element distribution analysis of sulfur (S).
- (2) The ultrasonic pulse propagation velocity of the mortar of 40×40 mm cross section by the symmetric method receives material influence of the FRP layer. However, the influence is small in the 100×100 mm cross section.
- (3) The ultrasonic pulse propagation velocity by the surface method is significant under the existence of 1 layer of FRP. It is detectable for existence of the flexural crack under the FRP layer.
- (4) The dynamic elastic modulus in $100 \times 100 \times 400$ mm concrete receives the material influence of the FRP layer, especially in the case of the flexural vibration.
- (5) AE measurement can detect propagation of diagonal and debonding cracks of the FRP layer as well as generation of the flexural crack. Degradation under sulfuric acid solution environment can be expressed by Ferocity ratio.
- (6) While the flexural cracking load increases as tensile rigidity of the fiber sheet is bigger, influence of the resin is not clear. However, by immersion of 10% sulfuric acid solution for 1 month, 15% reduction was observed in the case of the flexible resin. Severe degradation can cause reduction in the flexural cracking load.
- (7) Even if significant decreases of ultrasonic pulse propagation velocity and/or dynamic elastic modulus are not observed, the freezing and thawing cycles can affect the pull-off strength and/or the flexural cracking load. Although degradation of concrete seems to be a cause on this, type of the resin and/or its degradation level affect the degree of degradation of concrete.

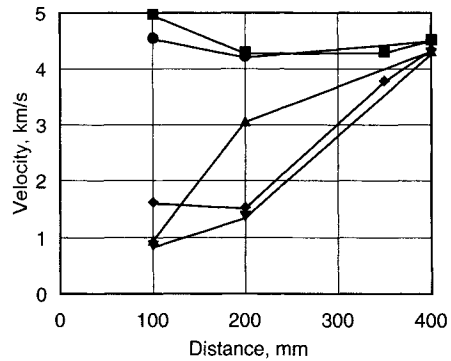


Fig. 13 Ultrasonic pulse propagation velocity (Concrete, C-N, 0 Cycle)
 ■: 0.0kN (before loading),
 ●: 9.8kN,
 ▲: 18.5kN (just after a flexural cracking load),
 ▼: 15.2kN,
 ◆: 0.0kN (after loading)

REFERENCES

1. Hattori, A., Yamamoto, T., Kashi, S. and Miyagawa, T. (1998) Journal of Construction Management and Engineering, No. 599/V-40, pp.59-69.

SPECTRAL IMAGING OF IMPACT ECHO TECHNIQUE FOR GROUTED DUCT IN POST-TENSIONING PRESTRESSED CONCRETE BEAM

T. WATANABE and M. OHTSU

*Department of Civil Engineering, Kumamoto University,
Kurokami 2-39-1 Kumamoto, Japan*

ABSTRACT

An impact echo technique recently draws an attention as nondestructive evaluation of defects in concrete structures. Since it is found that the technique is available to identify embedded defects, an application to the evaluation of grouted ducts in post-tensioning prestressed concrete structures is promising. Although a variety of attempts are reported, it is realized that identification of resonance frequencies due to ungrouted ducts is not easy. To improve the impact echo, a specimen containing an ungrouted duct is tested. Theoretically, frequency responses of the specimen depend on the size of the member, and the location of the void and P-wave velocity, because wave motions in concrete structures are characterized by material properties, incident waves, and the representative length. The frequency response is investigated in respect to the relationship between the wavelength and the depth of the duct. Then, applying scanning procedure, spectral imaging is conducted. Results show that the procedure is quite effective to identify the ungrouted ducts.

KEYWORDS

Impact-echo technique, frequency response, impact test, spectral imaging

INTRODUCTION

An impact-echo technique is a kind of pitch-catch procedure in ultrasonics. The technique has been developed for nondestructive evaluation of defects in concrete [1]. It may lead to the conclusion that an application to the evaluation of grouted ducts in post-tensioning prestressed concrete (PC) structures is promising. A variety of publications are reported, so far which suggest that it is not easy to identify peak frequencies due to ungrouted ducts. Concerning a similar procedure, a concept of ultrasonic spectroscopy was studied [2]. The procedure was already applied to estimation of grouted ducts in post-tensioning tendon under construction [3] and a limited success was reported. To

improve and apply the impact-echo technique to identification of ungrouted ducts, a basic research is conducted. Further, a spectral imaging is developed for classifying grouted ducts and ungrouted ducts.

IMPACT-ECHO TECHNIQUE AND RESONANCE FREQUENCY

Theoretically, frequency responses of a PC member depend on the size of the member, the location of the void, and P-wave velocity. This is because that wave motions in concrete structures are characterized by material properties, incident waves and the characteristic lengths. Concerning the frequency responses of post-tensioning ducts, the following two relationships between the wavelength and the depth of the duct are known [1],

$$f_T = 0.96C_p / 2T \tag{1}$$

$$f_{void} = 0.96C_p / 2d \tag{2}$$

Where f_T is the resonance frequency of the plate thickness T , and f_{void} is the resonance frequency of the duct at the depth d . C_p is the velocity of P-wave. 0.96 is a shape factor determined by the geometry and is not directly related with the theory. The presence of these resonance frequencies is illustrated in Fig. 1, along with the resonance frequency of grouted steel duct, f_{steel} .

Concerning dynamic motions of concrete members, the dimensional analysis has been carried out [4]. Among such parameters as frequency f , characteristic length L , and wave velocity v , the following non-dimensional parameter is obtained.

$$\alpha = f \cdot L / v \tag{3}$$

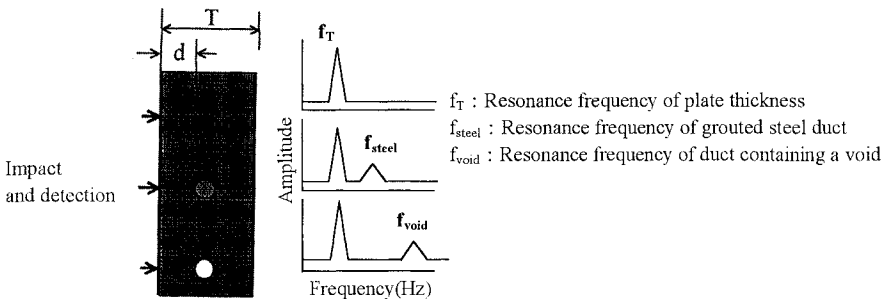


Fig.1 Frequency responses of post-tensioning concrete.

In the case that α is larger than 1, it is found that the frequency response is significantly influenced by the characteristic length. Considering the case that α is equal to 1, L is replaced by the depth of a void (duct hole) d , and v by P-wave velocity C_p , the following relationship is obtained.

$$f^*_{\text{void}} = C_p/d \quad (4)$$

Thus, three characteristic frequencies, are f_T , f_{void} and f^*_{void} are defined.

SPECIMEN

A specimen containing a grouting duct was tested. Dimensions of the specimen are $250 \times 250 \times 1000$ mm and the diameter of the duct is 30mm, as shown in Fig.2. Mixture proportion of concrete is given in Table 1. Mechanical properties of moisture-cured at 20°C for 28days are shown in Table 2. Thus, resonance frequencies f_T , f_{void} , and f^*_{void} are computed as 8.6kHz, 19.1kHz, and 39.9kHz, respectively.

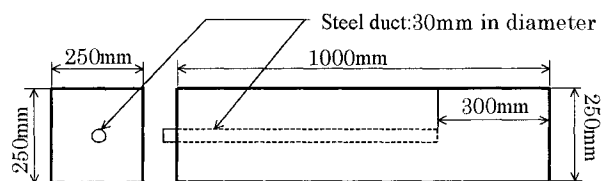


Fig.2 Specimen.

Table1. Mixture proportion of concrete.

Maximum gravel size (mm)	W/C (%)	s/a (%)	Weight for unit volume(kg/m^3)				Admixture (cc)	Slump (cm)	Air (%)
			Water	Cement	Fine aggregate	Coarse aggregate			
20	50	48	172	344	830	1021	104	3.0	6

Table2 Mechanical properties of concrete.

Tensile strength (MPa)	Compressive strength (MPa)	Young's modulus (GPa)	Poisson's ratio	P-Wave velocity (m/s)
2.76	33.07	27.37	0.20	4496

EXPERIMENT

First, frequency response of the impactor was examined. Based on several trial and errors, shooting an aluminum bullet was selected as the impactor. The aluminum bullet is illustrated in Fig.3. The aluminum bullet was shot by employing air compressor and a cylindrical hollow guide of 11mm diameter, as the distance between the surface of the specimen and the tip of the aluminum bullet was kept 100mm. Wave motions due to the aluminum bullet were detected by an accelerometer of broadband type up to 50kHz at the surface of the specimen. Fourier spectrum of the acceleration was analyzed by FFT. The receiver for the impact echo, which is commercially available, was first applied. But it was realized that the frequency range could not cover the frequency f_{void} . A result of FFT is shown in Fig.4. The frequency range of sensitivity is limited to around 30kHz. Therefore, the accelerometer system mentioned-above was adopted.

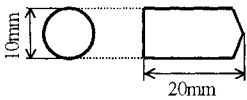


Fig.3 Aluminum bullet for an impactor.

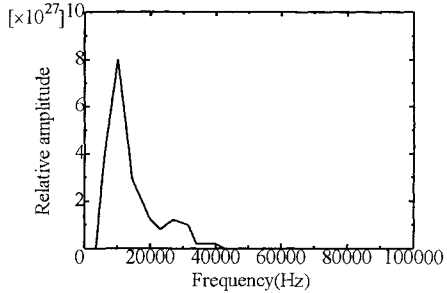


Fig.4 Frequency spectra detected by the impact-echo device.

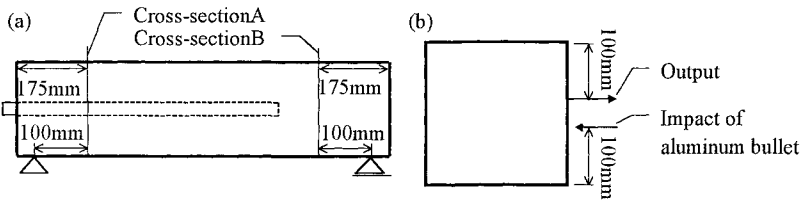


Fig.5 Impact test : (a)elevation view and (b)cross-sectional view.

The tests were performed at cross-sections A and B, which are shown in Fig.5. Waveforms detected and their Fourier spectra analyzed by FFT are given in Figs.6 and 7. According to Fig.6, waveforms do not clearly show any effects of the duct. In Fig.7, one particular peak frequency is observed around 8kHz at both cross-sections A and B. It could correspond to the resonance frequency of plate thickness f_T as indicated by arrow. At cross-section A, another resonance frequency is observed

around 40kHz, which probably was regarded as the resonance frequency of the duct containing the void, f_{void} . The resonance frequency regarded as f_{void} (19.1kHz) cannot be observed at the both cross-sections, because there exist many other peak frequencies near f_{void} .

In the impact-echo technique, it is reported that only particular resonance frequencies are observed in the spectra of detected waveforms [1]. But this is obviously not the case. As seen in Fig.7, many peak frequencies due to reflection, diffraction, resonance and so forth are normally observed. It implies that an applicability of the resonance frequencies in Fig. 1 may be marginal.

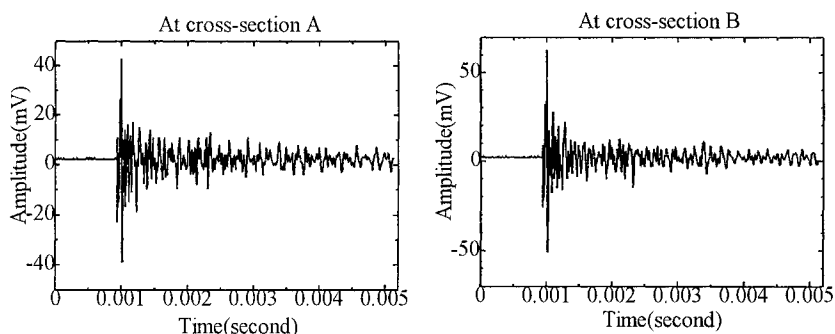


Fig.6 Waveforms due to aluminum-bullet.

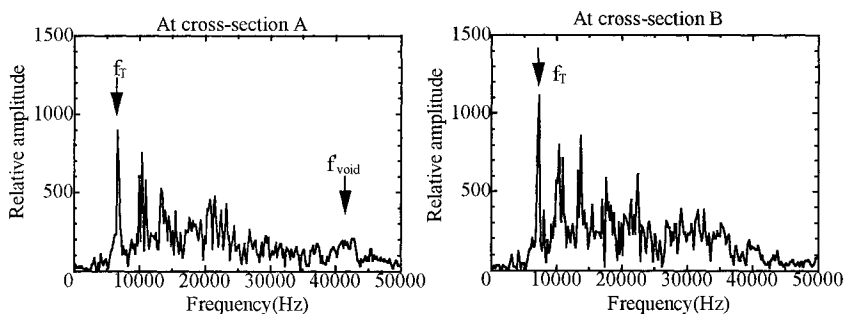


Fig.7 Fourier spectrum by FFT of impact waves due to the aluminum-bullet.

SPECTRAL IMAGING

The peak (resonance) frequencies could consist of reflections from the boundary surfaces of the specimen and from the duct containing the void. In order to identify the locations of reflectors, spectral imaging is developed. First, cross-sections of the specimen divided into squares elements. An analytical model divided into 100 square elements is shown in Fig.8. Then, the resonance frequencies due to reflections from the center of the elements are computed. In this case, the travel

distance from the input to the output via the center of the element is calculated as indicated in Fig.8, and the total distance, R is

$$R=r_1+r_2 \tag{5}$$

Next, the resonance frequencies due to reflections at the element location are virtually computed as,

$$f_1=C_p/(R/2), \quad f_2=C_p/R, \quad f_3=C_p/2R, \quad f_4=C_p/3R, \dots \tag{6}$$

In the frequency spectrum, spectral amplitudes corresponding to the above frequencies in eq.6 are summed, and the intensity of reflections at each element is determined.

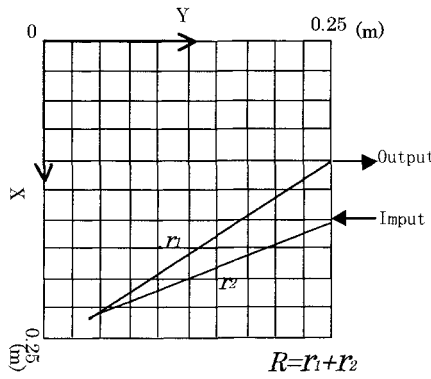


Fig 8 Spectral imaging model.

The effect of mesh division of the cross-section is studied. Results of the spectral imaging at the cross-section divided into 25 and 100 are shown in Fig.9 and 10. There exist no particular reflectors. The duct hole is indicated at cross-section A. These results suggest that the size of elements is too large to resolve the reflector due to the duct hole. A relationship between the P-wave velocity and the sampling time of detected waveform is studied and then characteristic length is obtained as,

$$\Delta x=1/2C_p \Delta t \tag{7}$$

C_p is the velocity of P-wave, Δt is the sampling time. In this case, Δx becomes 11mm. In the case that the size of the square elements is longer than Δx , it becomes difficult to resolve the particular reflectors. In the cases of the cross-section divided into 25 and 100 square elements, Δx becomes 50mm and 25mm respectively, which are clearly longer than $\Delta x=11$ mm.

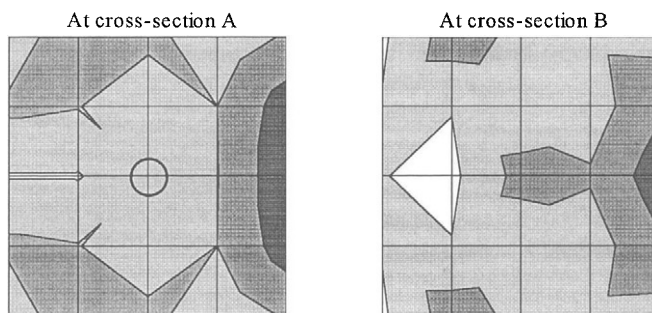


Fig.9. Results of the imaging at the cross-section divided into 25 square elements.

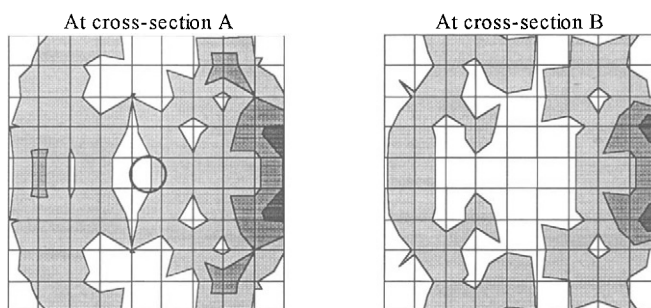


Fig.10. Results of the imaging at the cross-section divided into 100 square elements.

Results of spectral imaging at the cross-section divided into 625 and 2500 are shown in Fig.11 and 12. In these cases, the sizes of square elements are 10mm and 5mm, respectively, which are shorter than $\Delta x=11\text{mm}$.

In Fig.11, due to the presence of the duct-hole, high intensity regions of the spectral amplitude are clearly observed at cross-section A. In Fig.12, the pattern of intense regions is almost the same at both cross-section A and cross-section B. Thus, there exist no particular reflectors due to the duct hole. In the case the size of square elements is comparable to Δx in eq.7, it is possible to resolve the particular reflectors due to a void. When the element size is even shorter than Δx , however, the resolution becomes poor.

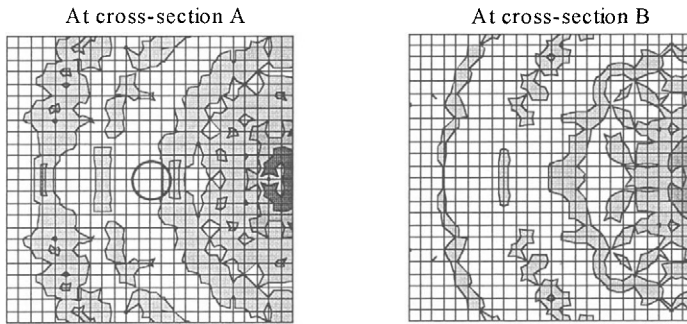


Fig. 11. Results of the imaging at the cross-section divided into 625 square elements.

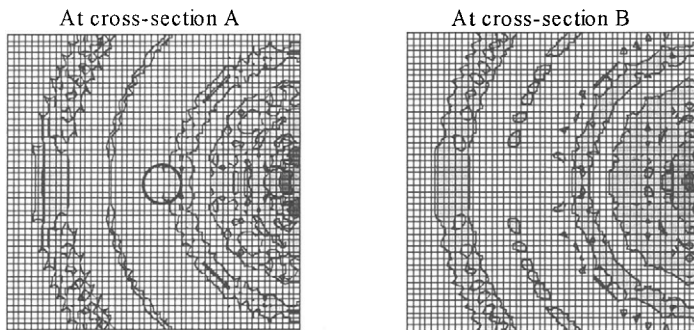


Fig. 12. Results of the imaging at the cross-section divided into 2500 square elements.

CONCLUSION

Based on the impact-echo technique, the resonance frequency due to the duct containing a void is investigated by using aluminum bullets. Conclusions are summarized as follows:

- (1) By the impact test using aluminum bullets, the resonance frequencies due to the plate thickness and the duct containing a void are confirmed. Generally speaking, results demonstrate the difficulty to identify the resonance frequency of the duct containing voids only from the spectrum.
- (2) In order to clarify that the reflections at the cross-section, spectral imaging is developed. It is clarified that the reflector near the duct containing a void is effectively visualized in the case the size of square elements is properly selected.

(3) In the case that the size of square elements is comparable to the characteristic length Δx which obtained from relationship between the P-wave velocity and the sampling time, the feasibility to resolve the particular reflectors due to duct containing a void is confirmed.

REFERENCES

1. Sansalone, M.J. and Streett, W.B.(1997). *Impact-Echo*. Bullbrier Press, Ithaca, N.Y.
2. Sakata, Y. and Ohtsu, M.(1995), "Crack Evaluation in Concrete Members based on Ultrasonic Spectroscopy," *ACI Materials Journal*, **92**(6), 686-698
3. Sakata, Y. and Ohtsu, M.(1993), "Evaluation of Grouted Ducts in Post-Tensioning Prestressed Concrete using the Ultrasonic Spectroscopy" Proc. of FIP Symposium: Modern Prestressing Techniques and Applications, Kyoto, **III**, 1591-1598
4. Ohtsu, M.(1996), "On High-Frequency Seismic Motions of Reinforced Concrete Structures," *J.Materials, Concrete Stru. and Pavements*, JSCE, **544**, 277-280.

This Page Intentionally Left Blank

**USE OF A TIME-FREQUENCY ANALYSIS APPROACH
IN IMPACT ECHO METHOD
EXAMPLE OF APPLICATION : DETECTION OF FAULTS IN CONCRETE SLABS**

O. ABRAHAM¹, Ch. LEONARD^{2,3}, Ph. CÔTE¹, B. PIWAKOWSKI²

¹Laboratoire Central des Ponts et Chaussées, BP 19, 44340 Bouguenais, France.

²Groupe Electronique-Acoustique (IEMN DOAE UMR 9929 CNRS), Ecole Centrale de Lille,
BP 48, 59651 Villeneuve d'Ascq CEDEX, France.

³Laboratoire de Mécanique de Lille (URA CNRS 1441), EUDIL, 59651 Villeneuve d'Ascq
CEDEX, France.

ABSTRACT

The "impact echo method" (IEM) has been developed in the eighties for non destructive testing of concrete structures. The basic principle of IEM is to study in the frequency domain the multiple reflections of the compression wave between the surface and a fault.

The objective of paper is to present an original time-frequency analysis procedure (TFA) which enables the automatic research of an optimum temporal window of observation. This technique helps to interpret impact-echo data when the current method fails or when the diagnosis is not obvious. The use of TFA is illustrated on the example of the detection of the fault in concrete slab. TFA is presented both through the analysis of numerically computed signals, calculated with the finite element method, and through the analysis of signals recorded experimentally. The detection possibility is studied as a function of the size of the fault in regard to the wavelength and as a function of its form. The results obtained from computations and from experiments display an excellent agreement. The main parameters that influence IEM are identified. The advantage of TFA is clearly shown by comparing with the results obtained by the "classic" IEM technique.

KEYWORDS

Impact echo, time frequency analysis, concrete, non destructive testing

INTRODUCTION

The non destructive impact-echo method is characterized by a frequency analysis of the transient seismic response of a structure to an impulse load. Impact-echo is classically used for the detection of voids and the measurement of thicknesses, or more generally, for the detection of interfaces between materials with different mechanical impedances.

This method has been developed in the National Bureau of Standards (USA) and in Cornell University (USA) in the middle of the eighties for concrete non destructive testing [1-3].

BASIC EQUATIONS

The impact-echo method relies on the study of the echoes in the frequency domain of the P-wave from the surface of a slab and a fault parallel to the surface inside it. The change from the time domain to the frequency domain, namely a breakthrough for the method [4], is the foundation principle of impact-echo method. For instance, for the search of the thickness e of a concrete slab supposed to be a homogeneous isotropic elastic medium, if v_p is the P-wave velocity, the time t_e required for a return travel from the top to the bottom is:

$$t_e = 2e/v_p \quad (1)$$

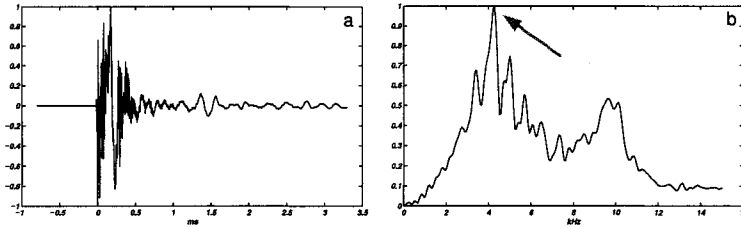


Fig. 1. Experimental results for a slab of thickness e equal to 0.5m : (a) in the time domain (b) in the frequency domain.

In the time domain, the periodical arrival of the P wave, of period t_e , are difficult to distinguish because of the numerous wave groups that overlap (Figure 1a). On the other hand, in the frequency domain, the "thickness resonance frequency" f_e is clearly visible (Figure 1b). Its expression is :

$$f_e = v_p/2e \quad (2)$$

A void at depth d will be characterized by a frequency f_d equal to:

$$f_d = v_p/2d \quad (3)$$

The impact-echo method requires a calibration to recover a measure of depth in meter. If the thickness e is known in some place and if the frequency f_e has been measured, then v_p can be calculated with Equation (1). And, if a frequency f_d is measured somewhere else, the depth d of the defect can be determined with Equation (3).

IMPACT ECHO : SIMPLIFIED MODEL APPROACH

The main parameters that influence the performance of impact-echo are: the geometry of the structure and of the fault (size and shape), the fault depth, the materials mechanical impedance, the materials absorption coefficient, the source function, the sensor response.

In order to better understand the influence of those parameters, we focus our attention on the determination of the thickness of a slab taking into account the P-wave only. The finite element modelling, in the next paragraph, will introduce the full wave field generated by an impact and consider the case of an embedded void.

Let us consider an infinite slab of dynamic impedance Z ($\rho=2400\text{kg/m}^3$, $v_p=4500\text{m/s}$, $e=0.5\text{m}$) overlying a half space (Z'). If the slab is excited by a Dirac pulse which is perpendicular to its surface, if there is no material absorption and no geometrical spreading, and if $Z' \ll Z$, then the signal $y(t)$ recorded close to the source is a periodic series of Dirac pulses of period $t_e=2e/v_p$ (Figure 2a). The Fourier spectrum of $y(t)$, $Y(f)$, is a series of Dirac pulses of period $f_e=v_p/2e=4.5\text{kHz}$ (Figure 2b). The first maximum is the expected resonance frequency needed to calculate the thickness e with Equation (2). The other maxima are multiples of f_e that may either confirm or deteriorate the diagnosis if the first maximum is visible or not.

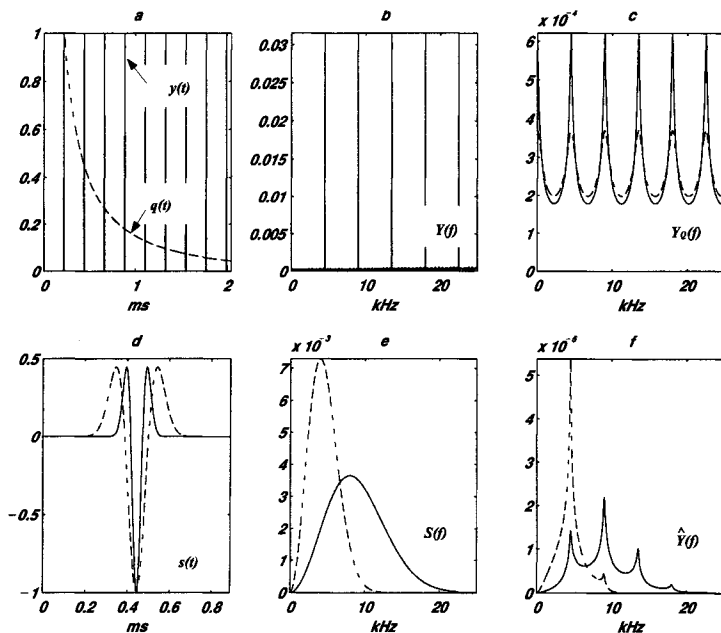


Fig. 2. Results of obtained with the simplified model (a) solid line: "Brush function" $y(t)$ displaying the series of periodic Dirac pulses; dotted line: attenuation function $c_Q(t)$ for $Q=50$ (b) Spectrum $Y(f)$ of $y(t)$ in the case without attenuation (c) Output spectrum $Y_Q(f)$ in the case where attenuation is considered; solid line: $Q=50$; dotted line: $Q=5$ (d) dotted line: Ricker source wavelet $s(t)$ with a central frequency 4kHz; solid line: 8kHz (e) Spectra of the Ricker

source wavelet $S(f)$; dotted line: central frequency of: 4kHz; solid line: 8kHz (f) final spectrum $Y_Q(f)$ for absorption $Q=50$; dotted line: central frequency: 4kHz; solid line 8kHz.

Then, we introduce geometrical spreading and a material absorption function that are gathered in the function $q(t)$ equal to [5-7]:

$$q(t) = \frac{e^{-\frac{\omega(t-t_0)}{2Q}}}{t / t_0} \quad (t > t_0 > 0) \tag{4}$$

Q is called the quality factor (used by [8]) and t is the traveled time (t_0 is a reference time where the amplitude is known). The multiplication of the signal $y(t)$ with the attenuation function $q(t)$, gives:

$$y_Q(t) = y(t) \cdot q(t) \quad (t > t_0 > 0) \tag{5}$$

Figure 2a shows the function $q(t)$ normalized on the first P-wave reflection ($t_0=2e/v_p$) for $Q=50$. In the frequency domain, we have (Figure 2c):

$$Y_Q(f) = Y(f) * Q(f) \tag{6}$$

where $Q(f)$ is the Fourier spectrum of $q(t)$. The influence of material attenuation is crucial for soils [5-7]. For concrete a common value for Q is 50 [9]. This value is an apparent value of Q including all types of attenuation (intrinsic attenuation and diffusion by the aggregates). The maxima in the frequency domain of $Y_Q(f)$ are wider with $Q=5$ than with $Q=50$ (Figure 2c) or in the case without attenuation considered (Figure 2b). As the attenuation increases, it becomes more and more difficult to isolate the first maximum.

Now, if the source generated signal wavelet is $s(t)$, then the recorder signal becomes:

$$\hat{y}(t) = y_Q(t) * s(t) \tag{7}$$

And, in the frequency domain, we have:

$$\hat{Y}(f) = Y_Q(f) S(f) \tag{8}$$

The results presented in Figure 4f are obtained for a wavelet function $s(t)$ equal to:

$$s(t) = [1 - 2(pf_{Ri}t)^2] \exp[-(pf_{Ri}t)^2] \tag{9}$$

with a central frequency, f_{Ri} , of 4kHz or 8kHz (Figures 4d and 4e. With an impact source centered around 4kHz, the maximum of the Fourier spectrum is clearly the thickness resonance frequency. With a source centered at a higher frequency (8kHz), the maximum is a multiple of the thickness resonance frequency ($2f_e$) and Equation (2) cannot be used to recover the thickness.

With this model, we see that the attenuation properties of the material, the source function and the thickness can be combined in a way that prevents a reliable diagnosis with the impact-echo method. The maximum source energy should be centered around the frequency expected. In practice, the source function should be wide enough in the frequency domain in

order to detect the resonance frequency changes. This remark appears in the literature under a recommendation of an optimal choice of the size of the steel ball source [2] for it is one of the parameters that controls the frequency content of the source signal.

TIME FREQUENCY ANALYSIS OF THE SIGNAL

The aim of a time frequency analysis of the signal of length N is to follow the frequency content of a signal that varies with time. The signal is windowed by a window. Then, the window center is moved and a new Fourier transform is calculated. This process requires a trade off between time and frequency resolution. If the window is small, the time resolution will be high but it will be to the expense of the frequency resolution.

Figure 3a shows the signal $r(t)$ calculated near the impact point for a void of radius $R=0.3m$ at depth $d=0.3m$ with a Ricker central frequency of 6kHz with the finite element method [5]. The Fourier spectrum of $r(t)$ (Figure 3b), $R(f)$ is dominated by the Rayleigh wave with an energy centered around the central frequency of the source function. The thickness resonance frequency, f_d , is not visible. Figure 3c shows the normalized amplitude of the Fourier transform of $r(t)$ in the time frequency domain. The normalisation of the spectra overcomes the attenuation of the signal and puts forward the energy that arrives after the Rayleigh wave. The void depth resonance frequency is clearly seen after the 4th window.

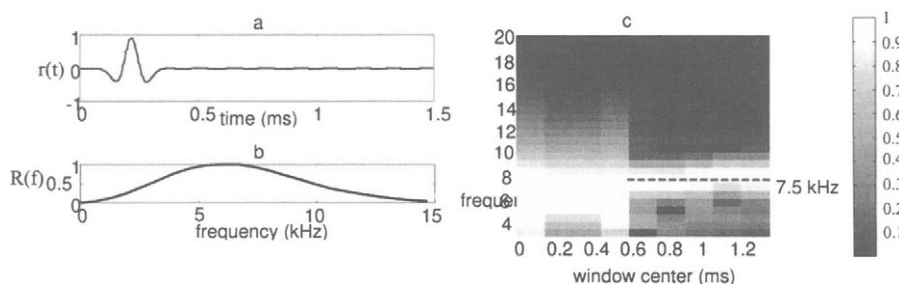


Fig. 3. (a) Signal calculated near the impact point for a void of radius $R=0.3m$ at depth $d=0.3m$ (b) spectrum (c) time frequency plot

EXPERIMENTAL VERIFICATION : APPLICATION ON A CONCRETE TEST SLAB

A concrete test slab 2m x 4.5m was built to study the impact-echo method (before filling with concrete). The slab has three different thicknesses: step A (2m x 2m) is 0.5m thick, step B (2m x 1.5m) is 0.35m thick and step C is (2m x 1m) 0.2m thick.

A polystyrene bloc of 0.3m x 0.6m was put on the bottom of each step near one edge. The thickness of the bloc in step A is 0.15m, 0.15m in step B, and 0.1m in step C. The top of the bloc in step A (resp. B) is at a depth equal to the thickness of step B (resp. C).

Figure 4 (a,b,c) shows the Fourier spectra of 10 trials are superimposed as well as their mean above the middle of each step. The thickness resonance frequencies are clearly.

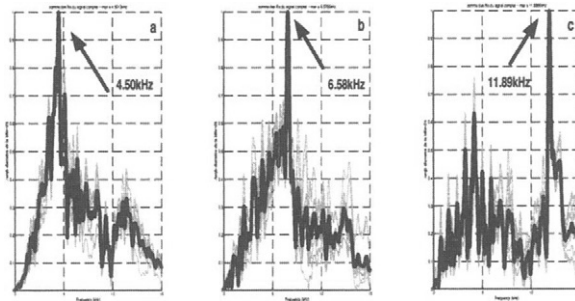


Fig. 4. Spectra of the measured signals above the middle of each step (a) 0.50m (b) 0.35m (c) 0.20m.

The source signal appears to be centered around 4kHz to 6kHz. This explains the reason why the Fourier transforms are very clear for step A and step B, whereas, for step C, the frequency content of the source can be seen as a undesirable "noise" before the thickness resonance frequency (the maximum source energy is not necessarily centered around the resonance frequency expected).

The same experiment is carried out above the polystyrene bloc in step B. Figure 5a gives the frequency spectrum of the whole signal. There are several peaks that dominate. One around 3kHz and one around 12kHz. Figure 15b is the corresponding time frequency. The time frequency plot help choose the right frequency to obtain more information on the default. The frequency that dominates at the beginning of the signal after the Rayleigh wave is equal to 11.5kHz which give the correct void depth, actually 0.2m.

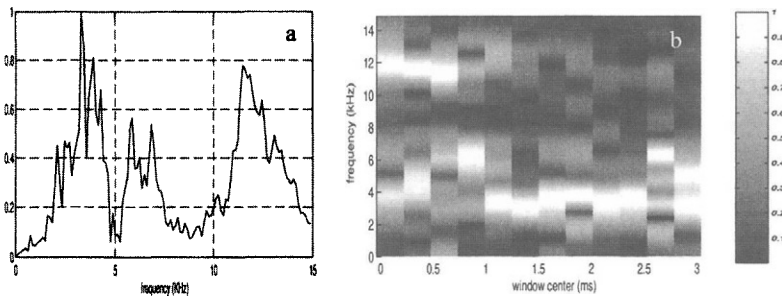


Fig. 5. Results above the polystyrene bloc included in the 0.35m thickness step (a) spectrum of the measured signal. The bloc depth resonance frequency, with $v_p=4600\text{m/s}$, is equal to 11.5kHz (b) Time frequency graph of the signal

CONCLUSION AND PERSPECTIVE

In this paper the influence of all the parameters that condition the use of the impact-echo method have been reviewed, through a clear signal processing model for P-wave propagation and with the finite element method for the full waveform study. In addition, a new signal processing method, based on the time frequency analysis of the signal, has been presented. It can help better interpret the results when the current method is not giving clear results, for instance when there are several maxima with similar magnitude in the Fourier spectrum of the whole signal.

REFERENCES

1. Carino, N.J. (1984) Laboratory study of flaw detection in concrete by the pulse echo method. *American Concrete Institute*, Detroit, Michigan, USA, SP 82-28, 557-579.
2. Carino, N.J., Sansalone, M., Hsu, N. (1986) Flaw detection in concrete by frequency spectrum analysis of impact-echo waveforms. *Int. Advances in Nondestructive Testing*, 12, 117-146.
3. Sansalone, M., Carino, N.J. (1988) Impact-echo method. *Concrete International*, 38-46.
4. Sansalone, M. (1997) Impact-echo : the complete story. *ACI Structural Journal*, 94(6), 777-786.
5. Léonard, Ch., Piwakowski, B., Shahrour, I., Abraham, O., Côte, Ph. (14-17 sept. 1998) Application of the "impact-echo method" to the detection of underground cavities. Part I : theory and finite element modeling. *Proceeding of the EEGS*, Barcelona, Spain, 343-346.
6. Abraham, O., Côte, Ph., Leonard, Ch., Piwakowski, B., Shahrour, I. (14-17 sept. 1998) Application of the " impact-echo method " to the detection of underground cavities. Part II : field experiments. *Proceeding of the EEGS*, Barcelona, Spain, 347-350.
7. Léonard, Ch. (1999) Détection des hétérogénéités du sous-sol par méthodes sismiques. *PhD thesis in preparation. Université des Sciences et technologies de Lille*.
8. Aki, K., Richards, P. G. (1980) Quantitative seismology, Theory and Methods. *W.H. Freeman and Company*, SF (USA).
9. Kharrat, Y. (1997) Auscultation des structures en béton par tomographie sonore de vitesse et d'atténuation. *Thèse d'habilitation*, Sherbrooke University, Canada.

This Page Intentionally Left Blank

AUTOMATED IMPACT-ECHO AND METHOD IMPROVEMENT: 2- AND 3-D IMAGING OF CONCRETE ELEMENTS

C. COLLA, G. SCHNEIDER and H. WIGGENHAUSER
*BAM - Federal Institute for Materials Research and Testing,
Division VII.3, Unter den Eichen 87, D-12205 Berlin, Germany*

ABSTRACT

The development of advanced NDT methods for structure/infrastructure investigation and assessment is today an important topic in Civil Engineering, not only for the construction industry but also for infrastructure stock owners that could use NDT as a tool for evaluating structural safety as well as for performance criteria assessment.

Point-measurement Impact-Echo (IE) has been used to investigate concrete elements and structures giving often encouraging results. Nevertheless IE data can easily lead to misinterpretation and require skilled personnel. This has been so far a limitation to a wider employ of the method. Instead, the use of scanning IE developed at BAM implements the method by giving complete and detailed information about the object under test. Furthermore an automated procedure has been developed for data collection. A description of the automated IE technique and its benefits is given, so that it is highlighted how this new approach is aimed at easing data interpretation and thus widening a reliable use of the technique in the practice.

First, example laboratory applications on concrete specimens will be shown and data collection described for the plotting of 2-D and pseudo 3-D re-elaboration of the element sections. Secondly, site examples from testing railway high-speed tracks will be shown.

KEYWORDS

Impact-Echo, Concrete, Post-tensioning, Duct, Railway, Sleeper, Infrastructure, Assessment, NDT.

INTRODUCTION

In the assessment of concrete elements and structures, Non-Destructive Testing (NDT) techniques are being used to investigate integrity and locate defects. Non invasive techniques such as NDT techniques are clearly to be preferred in that they maintain the integrity of the structure. Additionally these methods offer in general the advantage of rapidity at the data collection phase, with minimum activity/traffic disruption, and with possibility of large areas coverage on the element. Nevertheless there is today a requirement for the development of NDT techniques which can provide quantitative instead of qualitative results. Therefore, on demand from a market with great expanding potential, research is moving towards development of reliable and easy to use NDT techniques for evaluating structural safety as well as for assuring concrete products quality. With these objectives, a procedure has been

developed at BAM to improve the measuring capabilities of the Impact-Echo (IE) technique [1, 12].

IE has been used since a number of years to evaluate concrete condition by locating voids and discontinuities in concrete and to determine concrete thickness, duct cover and delaminations. The method has often given encouraging results [2, 3, 4, 5, 7, 8, 11] and, thanks to commercially available IE systems, almost everybody is enabled to carry out the tests. Nevertheless, not always the results have been conclusive and reproducible. Especially in the presence of complex element geometry (box-girder bridge, multiple ducts, crossing reinforcements), the interpretation of the experimental results is not always unequivocal and can easily lead to misinterpretation [9, 10]. The requirement for skilled personnel that can provide a reliable and thorough interpretation of the IE data has been perhaps so far a limitation to a wider employ of the method.

Traditionally, IE is a point method: the operator, based upon his/her experience with the method and knowledge of the structure, or at random, selects a number of measurement points for testing. With this method of local, punctual readings, important information can be missed when the points are badly selected or not enough. For example when the target of the investigation is to detect a flaw or other internal feature of small dimensions or a small variation in the element geometrical dimensions. In addition, the output of these punctual readings is single frequency spectra, whose interpretation and comparison is made difficult by a number of factors. Mainly these include variations in spectra peaks amplitude due to uneven coupling of the transducers, small frequency shift of the peak position due to influence of vibration of the element under investigation, and due to geometrical location of the measurement point on the element. To address these problems the research work reported herein was initiated.

IMPACT-ECHO PRINCIPLE

IE is a wave propagation based technique, which uses frequency domain analysis for data interpretation. Frequency spectrum analysis is performed on the waveform obtained from a mechanical elastic impact applied on the surface of the concrete element via a metal tip (instrumented hammer or steel ball). By applying such point impact, a transient stress pulse is generated and propagates into the concrete as compressional, shear and surface waves. The compressional and shear waves, which travel through the material, are partly reflected by any internal interface or discontinuity such as reinforcements, ducts, defects and delaminations. These waves are almost completely reflected if the second material is air, such as in the presence of a void or at the external boundaries of the element under investigation. The principle of IE testing is based on multiple reflections of an acoustical wave between the testing surface and any internal reflector. A receiver located besides the impactor picks up the reflected waves. A waveform is so built up in the time domain by the first and subsequent reflection arrivals.

The interpretation of time domain data can be time consuming and uncertain if the geometry of the test object is complex and/or if the reflectors are located close to each other. Therefore, analysis of the data is performed in the frequency domain. The transient resonance frequencies contained in the time domain waveform are plotted in a frequency spectrum (a graph of amplitude versus frequency components) obtained by performing a Fast Fourier Transformation on the time signal recorded (Fig. 1). The relevant peaks in each spectrum are identified and the corresponding depth (d) of each reflector would be calculated by dividing the

wave velocity (v) by the measured frequency of the echo signal (f): $d = v/2f$. From this procedure follows an interpretation of the structural characteristics and conditions of the element.

RESEARCH OBJECTIVES

Due to the complex information contained in the data, researchers and industrial users experience difficulty in unequivocal interpretation of single frequency spectra. So much that, in

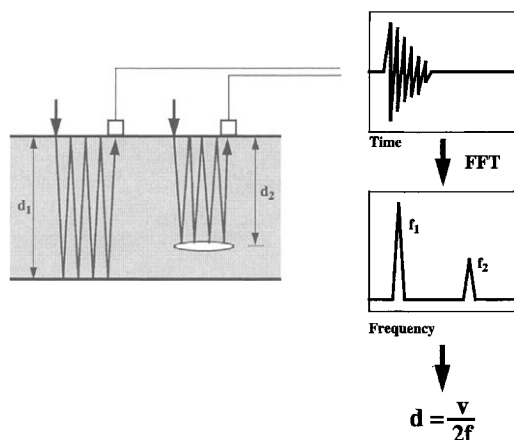


Fig. 1. Impact-Echo principle

case of complicated test situations, it is considered useful to aid data interpretation by comparing experimental with simulated data or by predicting the IE response through numerical modelling [6, 13]. In any way, an overall, complete interpretation of the situation of the concrete element can be made more difficult by the fact that only local, punctual readings have been collected and the direct comparison of the frequency spectra is hard, because of the problems described above.

Moreover, because of coupling problems that may be experienced at the impactor/surface or receiver/surface interface, the wanted frequencies may not be excited and a high level of noise is registered. The frequency of the impact produced has a considerable influence on the resolution of the method, in that a high frequency component signal will be capable of detecting smaller defects or closer to the surface. Nevertheless it is not easy to produce a high frequency signal because the impact of the hammer causes the surface to crumble and a lower frequency of excitation is achieved. Therefore a clear dominant frequency necessary to measure in the near field may not be excited. Two cases can then happen: 1) spurious data are occasionally collected; 2) relevant peaks are of difficult or impossible identification because hidden between the “noise peaks” produced by vibration of the tested element.

The consequence is that the single frequency spectra are not directly comparable because: a) it is uncertain whether the amplitude variations of the relevant peaks are due to coupling problems or to changes in the structural conditions. b) Nor it is evident in single reading spectra whether shifts in frequency are due to interference with peaks caused by the geometrical dimensions and bonding conditions of the element or to the presence of an anomaly in the concrete. In fact it is reported in literature that the presence of a “target” inside the element can also be indirectly detected by observing an apparent increase in “thickness” at the backside of the element.

The IE research work at BAM aims at addressing the problems above described and in particular at easing data collection and interpretation by proposing a procedure for collecting a complete set of data so to plot a 2-dimensional cross sectional representation of the concrete element under investigation.

INSTRUMENTATION AND DATA COLLECTION PROCEDURE

A commercial IE instrumentation (Olson Engineering IE-2) [14, 15] was used for data collection and run through in-house built software. The Olson hand-held unit, containing impactor and receiver, was mounted on an in-house built X-Y system frame with own driving programme. The frame allows for the position of the testing unit to be controlled exactly and to be recorded automatically in the file header with considerable time saving, without need for taking site notes or manual marking on the concrete surface. An in-house developed data display and analysis program was used for data collection, real time display and data analysis, including digital signal processing, imaging and plotting.

It was noticed during initial IE experiments, that measurements were difficult to reproduce and that coupling had a strong influence on the data collected. Mounting the IE unit on the X-Y frame and ensuring, via a pneumatic cylinder, a firm constant force of the unit against the testing surface (fig. 2), a considerably reduced operator influence from experimental factors was achieved and so it was obtained a reproducible experimental procedure. During data

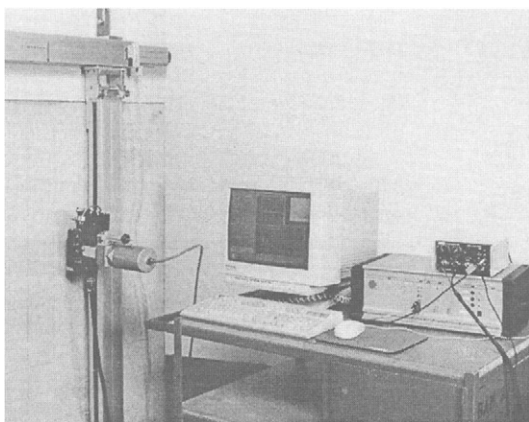


Fig. 2. Automated IE testing equipment with frame.

collection, a computer program controls the stepping motors of the frame system and the valve for the air pressure cylinder which presses the IE unit against the surface. Furthermore, at each point the average of a selectable number of single readings is recorded (typically 3 to 5). The advantage of adopting this procedure is that more uniform data are collected (the spectrum amplitudes are more comparable) and reproducibility of measurements can be achieved on horizontal and vertical surfaces.

The other advantage of mounting the system on a frame is that measurements can be automatically taken along survey lines and with pre-selected spacing between the single measurements. The evident consequence of collecting measurements along lines is that data can be plotted in 2-dimensional cross-sectional images, allowing for a complete and immediate view of the element situation, and for an easier interpretation. This is to direct advantage of the engineer responsible for the structure, and who is often not a specialist in NDT. Thanks to the frame, measurements can be programmed along lines in any direction, almost removing the necessity for the presence of personnel. At present, the length of the two frame axes permits to move the IE unit in an area of 1.5 m x 2 m with a precision better than 1/10 mm. By collecting data on an array of parallel lines, testing areas can also be covered, thus permitting a 3-dimensional elaboration and plotting of the data.

With the instrumentation and software presently available for this research work, digital data are collected using an A/D converter (frequency range 10 Hz to 18 kHz) and displayed simultaneously in real time on the computer screen both as time series and frequency spectra. The data from each measurement line are build up in real time also as B-scans (cross sections perpendicular to the testing surface, as it is known for ultrasonic tests) and are visible on the laptop/computer screen. B-scans are 2-dimensional plots of data, which present on the

horizontal axis the position of the reading station and on the vertical axis frequency. Different tones of grey represent values of the frequency amplitude. If the velocity of wave propagation in the element is known, B-scans of position vs. depth (or thickness) can be plotted. Files containing the collected waveforms are saved on the hard drive and data sets can be processed and plotted to easily identify features of interest in the data.

LABORATORY EXPERIMENTAL WORK

Experimental IE work was carried out in the laboratory on concrete specimens with simple geometry, as described in table 1. No surface preparation was performed before the experiments took place. The specimen dimensions are also shown in figure 3 and 4 together with the position of the IE measurement lines.

Table 1. Summary description of laboratory specimens.

No.	Size (WLT) [cm ³]	Description
1	100 x 100 x 16/20	Plate with a step and a steel pipe (\varnothing 4 cm) parallel to the step. Concrete with max. aggregate size of 8 mm, no reinforcement.
2	200 x 150 x 50	Concrete specimen with reinforcement in one half side (along long axis) and a duct (diameter 10 cm). Maximum aggregate size 8 mm.

Data collection was carried out in scan mode i.e. measurements were taken along lines made up of equidistant points (in these cases, 1 cm spaced). More extended experiments were carried out on specimen 2 to cover a large area. Here, IE data were collected in more than 20 parallel lines in a grid of 5 cm by 1 cm, covering areas of 115 cm x 90 cm (see fig. 4). The velocity of propagation of the sound wave in the specimens was determined by calibration on the same object (with IE or other NDT technique). The thickness corresponding to a given frequency is calculated through the equation given above.

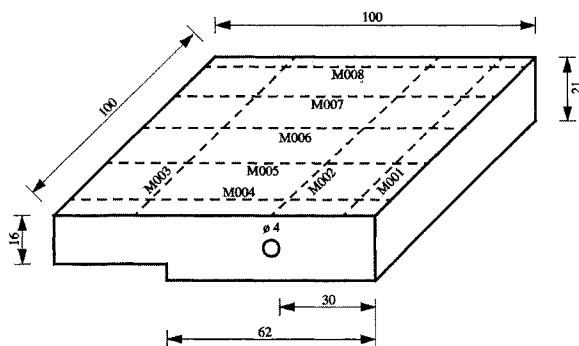


Fig. 3. Sketch of specimen 1

Specimen 1

On this specimen (Fig. 3), the targets of the testing were the location of the duct and the difference in plate thickness. Because of the thin concrete cover over the duct a direct measurement of it was not possible with the instrumentation described above, therefore other effects caused by this feature were searched.

Figure 4 visualises the data collected along a line across the specimen (M004 in fig. 3) with the data plotted in measurement position vs. thickness. The line, 65 cm long, is made up of 65 single readings, 1-cm spaced. The B-scan represents an IE vertical section of the specimen, where the signal from the backface of the plate is clearly identified by the horizontal dark line

at 22 cm (between stations 15 and 65), and the thinner part of the plate at 17 cm (between stations 1 and 10). These values are slightly greater than the true value, because of the wave velocity employed (4400 m/s) determined by laservibrometer and ultrasound techniques.

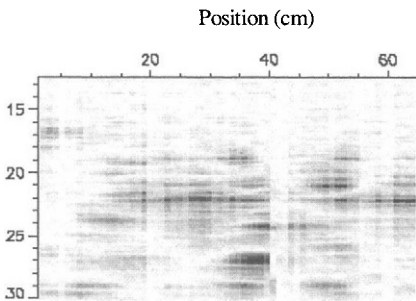


Fig. 4. IE data from specimen 1, along line M004

The pale vertical lines are caused by data readings characterised by uneven coupling due to surface anomalies where the hammer tip hits the surface. As it can be seen, these readings still contain some information but this information can only be read and correctly interpreted thanks to the adjacent readings. The correct interpretation of these poor readings when isolated from the rest of the file would prove to be a challenge.

There are other important features in this graph which have very practical consequences for IE testing:

- At the change of thickness no clear signal was detected for either thickness. Only a few centimeters away from the step the thickness is detected, but overlapped by additional thickness indications.
- Apart from the clear backside reflection, additional dark "spots" appear at greater and smaller thicknesses and overlapping with the backside signal. These features are not randomly distributed but form instead diagonal lines across the image when this is plotted in thickness. The magnitude of these signals can be the same as for the backside signal. These additional signals cannot correspond to internal features in the specimen and they are caused by the element geometry and bonded conditions. It is clear that from random point measurements, it would be almost impossible to reliably distinguish between the true signals and other of the plate specimen effects.
- At the position of the pipe (around station 40), this screens the direct measurement of the backside. Furthermore, the diagonal lines due to geometrical effects above described and crossing the backside reflection signal at the pipe position, seem the more intense. An increased signal intensity is measured at a much greater apparent thickness. It is almost as if the sound waves are focussed by the pipe. In this case the position of the pipe could not be read directly but as apparent increased specimen thickness. Its location is also revealed by the geometrical effect lines.

Specimen 2

Specimen 2 (Fig. 5) has a built-in duct with concrete cover of 15 cm from one side. Previous IE tests did not locate the duct [9]. A large set of data was collected on this specimen: 27 parallel lines with 90 points, each 1 cm spaced. At each point, the average of three single measurements was collected. This 3-D array of data was used to visualise projection slices through the specimen. Figure 6a shows the B-scan in the XZ plane, fig. 6b the B-scan in the YZ plane and fig. 6c the C-scan in the XY plane. All figures are plotted in frequency i.e. dark grey tones represent higher intensity of the frequency signal.

The XZ and YZ projections show no indications of a direct measurement of the duct but they reveal the backside specimen echo. This is not a single straight line at the thickness of the specimen as expected, but it is a collection of several slightly shifted reflection horizons.

Both these projections reveal a multitude of geometrical effects due to the specimen dimensional characteristics. When plotted in frequency, like in this case, these effects appear as

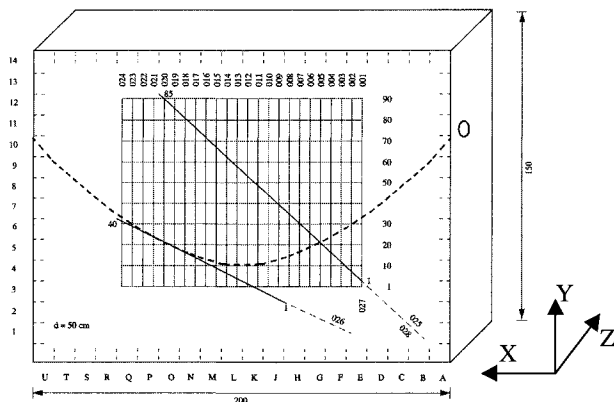


Fig. 5. Sketch of specimens 2.

curved lines that start at higher frequencies near the edges of the specimen, to decline towards lower frequencies in the middle of the specimen. When these curves pass in proximity of the peaks due to features of interest (like, in this case, the backside reflection) their peaks overlap and merge causing a shift in the position of the peak. This effect is particularly clear in the YZ plane of fig. 6b:

the middle portion of the vertical line representing the backside reflection is shifted towards higher frequencies. This causes an incorrect reading of the specimen thickness: in this case a reduced thickness.

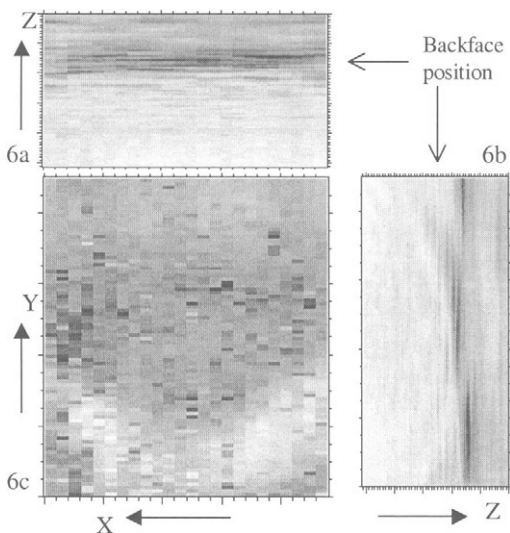


Fig. 6. Result of scanning IE testing on specimen 2

The shift of the backside reflection visible in the YZ plane towards the bottom middle third of the image is due to the presence of the duct. As already described for specimen No. 1, the presence of the duct screens a correct reading of the specimen thickness and shows up as an increased specimen thickness.

Figure 6c is a projection created with a sub-set of data: by plotting only the frequency range corresponding to a depth between 20 and 50 cm, a depth slice is visualised. This image indirectly reveals the presence of the curved duct in the bottom half of the picture as a lower intensity of the specimen thickness signal. Whilst the presence of the duct is also detectable in the YZ plane, a depth slice in the XY plane reveals also the curvature of the duct.

Creating a projection through the data set using only data beyond the element thickness results in fig. 7 which shows clearly the position of the duct in the XY-plane. This is again an indirect reading of the duct. What happens is that the back side signal is screened by the presence of the duct, the path for the waves is longer around the duct and the backside signals appear „behind“ the specimen. These findings confirm the measurements on specimen 1 where the steel pipe had the same effect at a much thinner specimen.

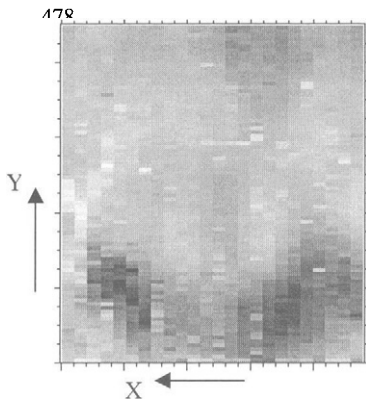


Fig. 7. C-scan in the thickness range 56 to 58 cm.

SITE WORK

IE tests were carried out on non-ballasted trackforms, for the investigation of the bonding condition of concrete railway sleepers with the underlying carrying layer. Measurements were collected along lines on the surface of the railway system, as from the sketch in fig. 8. Lines run transversely to the direction of the track and are all collected on the sleepers, except for line 2, which is positioned between sleeper 1 and 2, thus directly on the concrete carrying layer. This line is made up of 100 stations, approximately 2 cm spaced. In each other line between the rails, the stations are 1 cm spaced, for a length of approximately 58 cm. Two small files were also collected on the head of sleepers 1 and 2.

From tests on the carrying layer (29 cm thick), a peak maximum corresponding to the reflection from the underside was identified at 7 kHz allowing

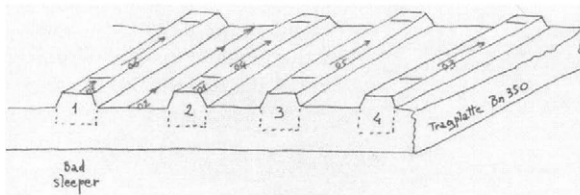


Fig. 8. IE lines location and site photo.

collected. It is evident that sleeper 1 is not bonded to the underlying layer, because it does not present a reflection at the underside of the carrying layer (4 to 5 kHz region), whilst this is a clear peak on sleeper 2. On this sleeper, a weak reflection at 8.1 kHz, represent the bottom of the sleeper (24 cm thick). Figure 10 compares data from the 4 sleepers: it is clear that file 06

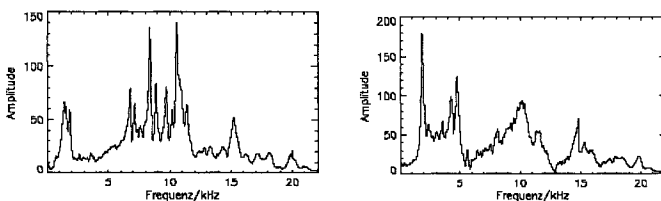


Fig. 9. Average plot from sleeper head No. 1 and 2

of 12,9 kHz represents the reflection from the underside of the sleeper (17,5 cm). The next reflection, from the underside of the carrying layer, should be expected at 6,6 kHz, keeping into account the different velocities in the two layers. This peak is not present in file 06 and

belongs to the sleeper with bad bonding. In fact, this is the only file presenting a maximum in the 12 kHz region, and no peaks in the 6 kHz region. With a velocity of 4200 m/s in the sleeper, a freq.

constantly present in files 04, 05, 03. When debonding under the sleeper is present, almost all of the wave energy is reflected at the bottom of the sleeper; instead, when there is bonding, the wave propagates also in the carrying layer giving then a reflection at the bottom of this layer.

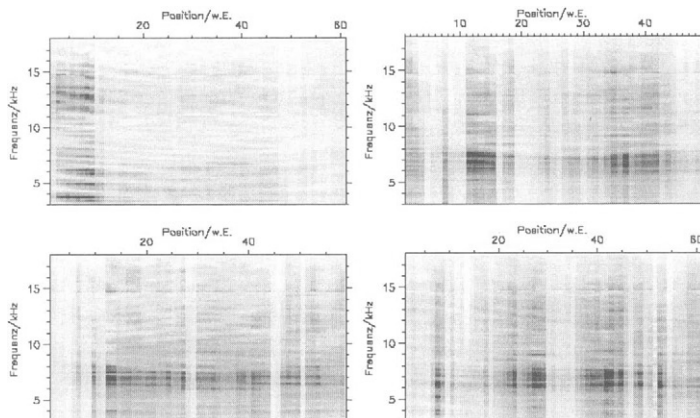


Fig. 10. B-scans from sleeper 1 and 2 (top), 3 and 4 (bottom).

CONCLUSIONS AND FURTHER WORK

It was discussed how local IE readings require the need for skilled personnel to avoid mislead in data interpretation, and a procedure was proposed for easing data collection and interpretation and to evaluate the object thoroughly. By automating the data

collection phase a higher reproducibility of measurements can be achieved; the work also aimed at collecting more reliable data independently from the operator. Furthermore, by collecting more complete sets of data, it is possible to plot cross sectional representations of the element under investigation. It was described how 2D projection images and depth slices, not only locate the position of features of interest embedded in the concrete, but also reveal their shape. This is of evident advantage to the engineer or manager of the structure, who can so see visualised the information needed. The improved understanding of the IE results will be reflected in a greater confidence in the technique's possibilities and use.

It was also shown that plotting IE data in 2D images allows to visually distinguish relevant data information from noise, geometrical effects or false readings, therefore easing data interpretation. It was seen that geometrical effects play an important role in IE (it is intended to study this further) and how they affect correct data interpretation by overlapping with peaks of interest and distorting depth information. In particular it was described how features such as ducts and pipes mask information related to deeper features, like in the case of the backside reflection, which will appear thicker than in reality. Therefore, result considerations underline the necessity to do IE measurements in scan mode to avoid incorrect interpretations.

It can be foreseen that the automated measurements as described in this paper with the use of the frame, because they do not require the presence of personnel during data collection, could be usefully employed for remote controlled measurement applications.

ACKNOWLEDGEMENTS

The authors wish to acknowledge the helpful assistance and co-operation of colleagues from BAM division VII.3 during laboratory and site testing.

REFERENCES

1. Colla, C., Schneider, G. and Wiggerhauser, H. (1999). Automated Impact-Echo: method improvements via 2- and 3-D imaging of concrete elements. In: *Proc. VIII Int. Conf. Structural Faults and Repair -99*, M. Forde (Eds.). CD-Rom Engineering Technics Press, London, UK.
2. Krause, M., Bärmann, M., Frielinghaus, R., et al. (1997), "Comparison of pulse-echo methods for testing concrete", *NDT&E International*, Vol. 30, 4, 195-204.
3. Ghorbanpoor, A. (1993). "Evaluation of post-tensioned concrete bridge structures by the Impact-Echo technique", Publication No. FHWA-RD-92-096, Federal Highway Administration, U.S.A.
4. Martin, J., Hardy, M., Usmany, A. and Forde, M.C. (1997). Impact-echo assessment of post tensioned concrete bridge beams. In: *Proc. 7th Int. Conf. Structural Faults and Repair-97*, vol. 1, pp. 341-354; M. Forde (Eds.). Edinburgh, UK.
5. Carino, N.J., Sansalone, M. and Hsu, N.N., (1986). Flaw detection in concrete by frequency spectrum analysis of Impact-Echo waveforms. In: *International advances in Nondestructive Testing*, 12, 117-146.
6. Sansalone, M., and Carino, N.J. (1986). *Impact-echo: a method for flaw detection in concrete using transient stress wave*. National Bureau of Standards Report NBSIR 86-3452, Gaithersburgh, Maryland.
7. Sansalone, M. and Carino, N.J. (1989). Detecting delaminations in concrete slabs with and without overlays using the impact-echo method. *ACI Materials Journal*, March-April, pp. 175-184.
8. Sansalone, M. and Streett, W.(1995). Use of the impact-echo method and field instrument for non-destructive testing of concrete structures. In: *Proc. Int. Symp. Non-destructive Testing in Civil Engineering (NDT-CE)*, pp. 495-502, Berlin, Germany.
9. Krieger, J., Krause, M. and Wiggerhauser, H. (1998) *Erprobung und Bewertung von zerstörungsfreien Prüfmethoden für Betonbrücken*, BAST, Bergisch Gladbach, Germany.
10. Krieger, J., Krause, M. and Wiggerhauser, H. (1998). Tests and Assessment of NDT methods for concrete bridges. In: *Structural Materials Technology III, Proceedings of SPIE*, Vol 3400, pp. 258-269. Medlock, R. D. and Laffrey, D. C. (Eds.).
11. Sack, D. and Olson, L. (1994). In-situ Nondestructive testing of buried precast concrete pipes. In: *Proc. ASCE Materials Engineering Conferences*, San Diego, CA.
12. Colla, C., Milman, B., Wöstmann, J., Mielentz, F., Henschen, J. and Wiggerhauser, H. (1999). Combined NDT for system assurance in railway construction: Impact Echo, Ultrasonic and Radar techniques. In: *DGZfP Fachtagung Bauwerksdiagnose – Praktische Anwendungen Zerstörungsfreier Pruefungen*, pp. 179-190. German Society of NDT, DGZfP-Berichtsband 66-CD, Munich, Germany.
13. Martin, J. (1997). Non-destructive testing of metal ducted post-tensioned bridge beams using sonic Impact-echo techniques. PhD Thesis, University of Edinburgh, UK.
14. Olson Instruments, Inc (1998). Freedom NDT PC, Impact Echo (IE-1/IE-2) concrete testing system, TFS V. 1.66. Reference Manual.
15. Olson Instruments, Inc (1998). Supplemental operating instructions: BAM remote IE testing system, special pupose IE-2 Impact Echo testing system. Reference Manual.

APPLICATION OF GROUND PENETRATING RADAR FOR EVALUATION OF SUB-SURFACE AIRFIELD PAVEMENT CONDITIONS

K. R. Maser

Infrasense, Inc.

14 Kensington Rd., Arlington, MA 02476 USA

and

I. Sande

Carlbro Pavement Consultants

Fuglesangsalle 16

DK-6600 Vejen, Denmark

ABSTRACT

The paper describes applications of Ground Penetrating Radar (GPR) to identify and quantify delamination, stripping, and voids in airport pavement. The applications have been carried out at airports in Denmark and Norway. At Copenhagen Airport, two conditions were addressed. The first was a delaminated anti-skid surface layer of asphalt, about 25 mm thick. The delaminated areas could not be seen from the surface, and there was concern that spalling asphalt could cause damage to airplane engines. The objective of the GPR survey was to identify the locations and extent of this condition. A second condition was the presence of stripping (and associated asphalt disintegration) within the pavement structure. At the Stavanger Airport in Norway, the condition of concern was settlement due to voids under the concrete slab. The objective of the GPR survey was to determine the cause and extent of the problem. GPR was selected for both projects because it provides subsurface data, which can be obtained quickly and without interruption of service. The equipment used in these projects is non-contact, and collected from a survey vehicle, which drives continuously across the pavement. The paper describes: the equipment used, the method of data collection, the procedures and principles used for processing the data, the results of the survey; and the correlation of survey results with known conditions. The use of the results by each agency for planning future maintenance and rehabilitation is also discussed.

KEY WORDS

Ground Penetrating Radar, GPR, Pavement, Airfield, Runway

INTRODUCTION

The maintenance of airport pavement is an ongoing job in airports around the world. The demands on airport pavements have increased as a result of heavier wheel loads from the larger passenger and cargo planes. Airport pavements continue to age and exhibit various distresses that need to be treated as a result of the high volume of traffic on airport runways. Many airports have old pavement whose complete structure is not well defined or documented.

Pavement condition data is important for prediction of remaining life and for planning, designing, and evaluating rehabilitation work. It is important to obtain pavement information using a method that will cause the least disturbance and interruption of service. For this reason, Ground Penetrating Radar (GPR) is being implemented on a more regular basis for airport pavement evaluation. GPR is a subsurface measurement technique that can determine pavement layer thickness, and identify local variation in moisture content, problems, and anomalies in the pavement structure. Since GPR can be done at normal driving speeds it is particularly useful for evaluating airport pavement.

PRINCIPLE OF GROUND PENETRATING RADAR

Ground Penetrating Radar operates by transmitting short pulses of electromagnetic energy into the pavement using an antenna attached to a survey vehicle (see Fig. 1 and 2). These pulses are reflected back to the antenna with an arrival time and amplitude that is related to the location and nature of dielectric discontinuities in the material (air/asphalt or asphalt/concrete, reinforcing steel, etc). The reflected energy is captured and may be displayed on an oscilloscope to form a series of pulses that are referred to as the radar waveform. The waveform contains a record of the properties and thicknesses of the layers within the deck, as shown schematically in Fig. 1.

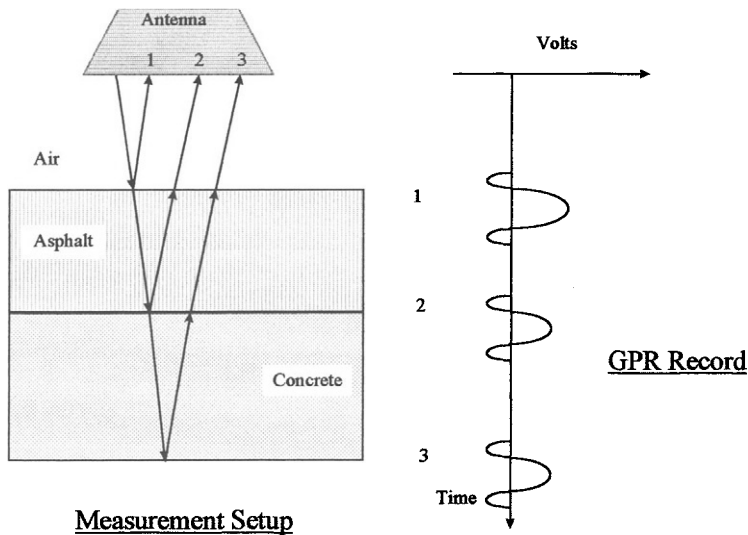


Fig. 1 - Principle of GPR Pavement Evaluation

The presence of disturbances in the asphalt structure, such as delaminations or stripping, will alter the GPR record from what would normally be expected. Similarly, voids under the concrete slab will also produce anomalies. The anomalies in the GPR record created by these conditions can be identified and tracked by the user, using both manual and automated methods. Previous work has shown that this method can be successful when the method of analysis is calibrated using data from areas where the damage is known to have occurred (Scullion, 1994; Maser, 1996). The result of this process is a linear or a plan area map of the conditions detected. These results provide information on the location and total quantity of damaged pavement.

DATA COLLECTION

The equipment used in this work is shown in Fig. 2. The radar system uses a 1 GHz air-coupled horn antenna positioned from 0.3 to 0.5 meters (12-18 inches) above the pavement surface. This is a non-contact arrangement, which allows for surveys to be carried out at any normal driving speed. Typical horn antenna systems generate 50 scans per second, with a pulse width of approximately 1 nanosecond. The radar analog signal is transmitted to a PC-based data acquisition system where it is digitized and stored to hard disk, and later archived to zip disk or CD-ROM. A fifth wheel or DMI (distance measuring instrument, typically operated off of the vehicle transmission) provides position pulses, which are encoded into the digitized radar for location referencing. Pulse Radar Inc., of Houston, TX manufactured the equipment used in the reported work.



Fig. 2 - 1 GHz Horn Antenna GPR Equipment used for Airfield Runway Surveys

A GPR runway survey is carried out by travelling down the runway with a series of longitudinal passes typically spaced transversely at 1 meter. Thus, a runway 20 meters wide would be surveyed by conducting 20 parallel passes of the same length, each offset one meter transversely from the other. Since airport work must often be carried out at night, it is sometimes difficult to maintain a straight linear survey path. To address this need, a special

arrangement was designed to facilitate night surveying. The arrangement is shown in Fig. 3. An outrigger boom has been designed, which is supported on one end at the survey vehicle and on the other end by two independent wheels. A video camera is mounted onto the boom, and a video monitor is positioned in the vehicle within view of the driver. For each survey pass, the camera is positioned over the white paint stripe down the center of the runway. The driver can then maintain a fixed offset from the centerline by observing the centerline on the video monitor. For each subsequent survey pass, the camera is repositioned so that the offset is changed to the appropriate position. Runway lights are turned on during this process to illuminate the white stripe.

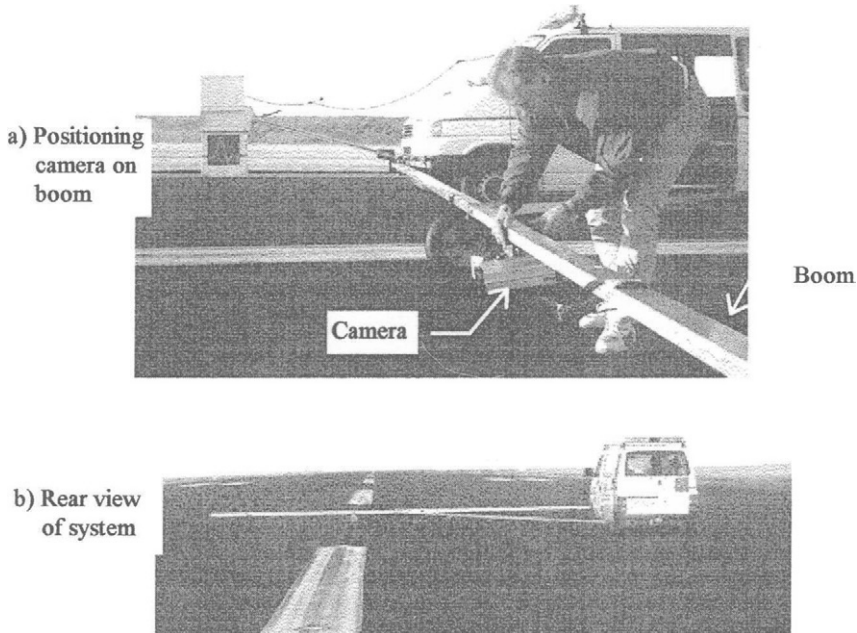


Fig. 3 - Survey System for Night Surveys on Runways

COPENHAGEN AIRPORT

Two different situations of concern occurred in the asphalt runway pavement, which are described below.

Delamination of the Anti-Skid Layer

The problem here, initially addressed in the summer of 1996, was the delamination of a thin anti-skid layer of asphalt approximately 25 mm in thickness (see Fig. 4). The delaminated areas could not be seen from the surface, and there was concern that spalling asphalt could cause damage to airplane engines. The area of concern was 20 meters wide by 500 meters long in runway 04R-22L. The objective of the GPR survey was to identify the locations and extent of the delamination condition within the area of concern.

In order to determine the ability of the GPR system to reveal this condition, the GPR data was collected over the area as described above, and the data was evaluated at specific locations where delamination was known to exist from core data. The evaluation at these locations showed that the dielectric contrast between the anti-skid layer and the structural asphalt layer became more pronounced at the delamination locations. This contrast was then used as an indicator to analyze the remainder of the data.

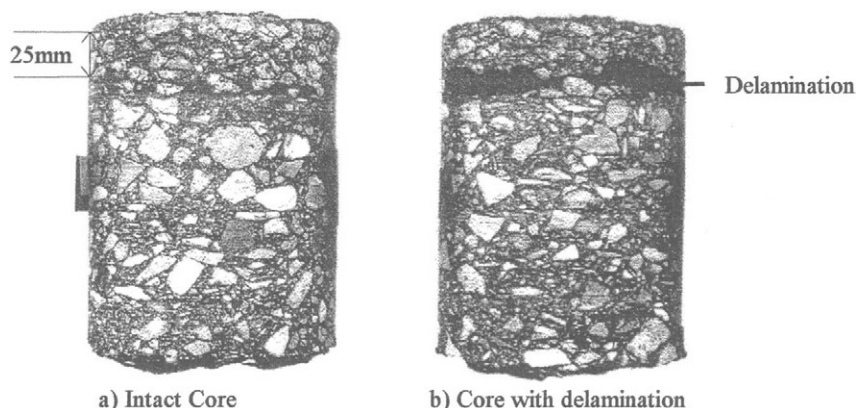


Fig. 4 - Cores from Area Showing Delamination of Anti-Skid Layer

Data analysis using this algorithm was carried out using **DECAR[®] (DECK CONDITION ASSESSMENT USING RADAR)**, software which was originally developed for bridge decks but whose use has been extended to airfield pavement. An example of the results of the analysis is shown in Fig. 5.

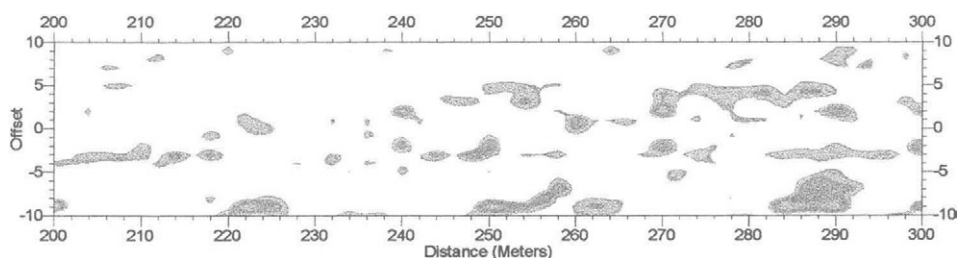


Fig. 5 - Sample of Processed GPR Output Showing Locations of Delamination

The horizontal axis in the Fig. 5 plot shows the longitudinal distance from the start of the runway, and the vertical axis shows the offset from the centerline of the runway. A total of five plots similar to Fig. 5 were generated to cover the entire area of interest.

The areas indicated in Fig. 5 are presented in color, where the color level represents the value of the dielectric contrast between the anti-skid layer and the layer below. The more intense

the color, the higher the probability that delamination is occurring. Based on the data analysis, the total area where delamination is likely to occur is 18.1% of the surveyed area.

Subsequent to the presentation of the above results, additional 18 cores were taken. The cores were located in areas where delamination was predicted, as well as in areas which were considered sound. All core results agreed with the GPR findings.

Based on the results of the GPR survey, the airport authorities decided to wait a year to see if the problem had stabilized or if it was progressing. In the summer of 1997, the airport authority conducted a repeat survey to investigate whether or not the delaminated area was increasing. The data was collected and analyzed in an identical fashion. The results for 1997 showed that 29.6% of the surveyed area was likely to be delaminated; therefore, the estimated area of delamination increased by over 50% in one year. The airport authorities are currently planning to remove the entire anti-skid layer in the area of concern. This decision will address the delamination problem.

Stripping Within the Asphalt Layers

Stripping of an asphalt layer occurs when the bitumen is “stripped” from the aggregate due to the interaction of moisture with the aggregate. There are certain aggregates that are particularly susceptible to this process, and these are referred to as “stripping aggregates”. Sometimes stripping occurs within an asphalt layer, and sometimes it occurs at the boundary between two asphalt layers, causing debonding.

At Copenhagen Airport, problems associated with stripping were identified in the “touchdown” area of runway 04R-22L. The area of concern was in the center of the runway, 20 meters wide by 900 meters long. Fig. 6 below shows core samples, which display the type of damage that was occurring to the asphalt pavement.

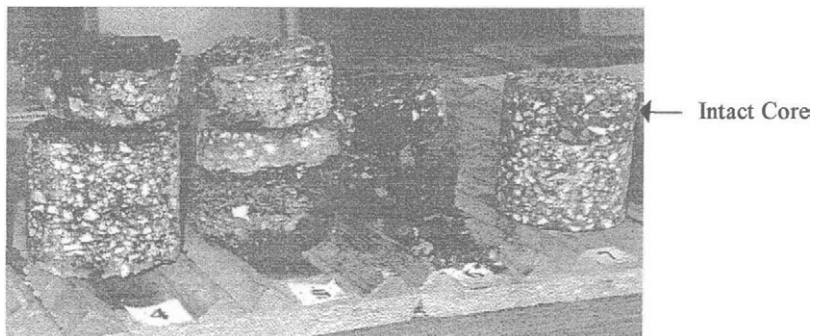


Fig. 6 - Examples of Cores Showing Stripping (No.'s 4, 5, and 6)

A GPR data analysis approach was employed similar to that used for the debonding of the anti-skid layer. Stripping was identified as a layer with reduced dielectric permittivity. Previous studies have shown (Scullion and Rmeili, 1997) that the occurrence of stripping results in increased void content, which leads to an anomalous reduction in the dielectric constant of the

stripped layer. Using this algorithm, a threshold dielectric level was established so that the areas identified as stripped matched the results from available cores. A typical result of this survey is shown in Fig. 7. The figure also shows the match between the GPR results and the core data.

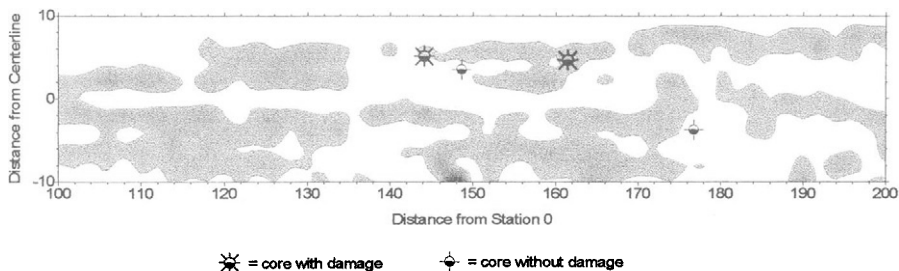


Fig. 7 - Map of Potential Areas of Pavement Stripping

The airport authority plans to utilize this GPR data in conjunction with a Falling Weight Deflectometer (FWD) and other results to develop a rehabilitation plan for the runway. Follow-up GPR surveys will be conducted to continue to monitor the problem.

Pavement Layer Thickness Variations

As part of the stripping study, the airport authority conducted a pavement thickness evaluation to determine if tire loads were causing differential deformations in the pavement layers. In order to carry out this evaluation, pavement layer thickness measurements carried out in 1997 were repeated in 1998 to evaluate the progression of pavement deformation over time. The data was collected transverse to the runway axis at various stations. A typical result of this evaluation is shown in Fig. 8 below.

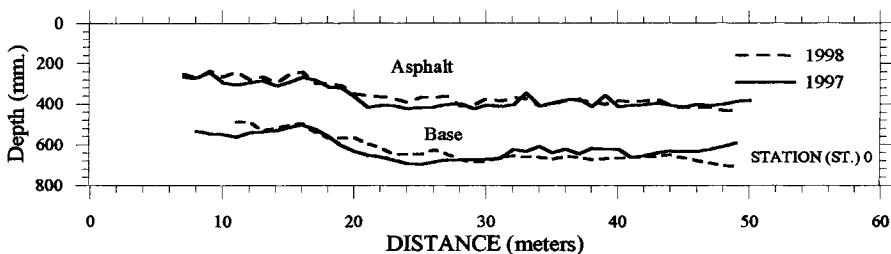


Fig. 8 - Cross Sectional Thickness Plot at Station 0, Runway 04R-22L

In Fig. 8, the horizontal axis is the survey distance transverse to the runway, and the vertical axis is the depth below the pavement surface. Note that the main runway pavement goes from 8 to 50 meters in the cross section.

The results of this survey show that there are small differentials, which have developed over the year, but none of the differentials appear to be significant from a pavement damage point of view.

A second objective of this survey was to examine variations in the base dielectric constant as a means of evaluating moisture infiltration problems, which would be associated with pavement damage. The results of this analysis, however, were dominated by overall changes, which appeared to be related more to seasonal changes than to local pavement conditions.

VOIDS UNDER RUNWAY PAVEMENT AT STAVANGER AIRPORT IN NORWAY

The Stavanger Airport runway in Norway, originally built during World War II, extends over 2,000 meters long. Sand, gravel and approximately 15-20 centimeters of concrete originally built up the main runway. About 15 years ago between 5 and 15 centimeters of asphalt was added over the concrete, and in some areas the concrete was broken down before overlaying with asphalt.

In the mid 1980's, the airport authorities began to see settlements on the airport shoulder where asphalt had suddenly disappeared (see Fig. 9). These areas were repaired, but the problem reoccurred and repair of the damaged areas had to be continued. In 1996, the airport authority had to repair over 300 square meters, including small settlement areas. The airport authorities believe that these settlements are due to voids under the concrete caused by a drainage condition that removed the sand materials. This belief was supported by excavations at specific locations which revealed voids on the order of 20 cm. in height by 10 meters in length. Based on this mechanism, there was some concern about the possibility of the pavement collapsing into a void under a wheel load.



Fig. 9 - Example of Pavement Settlement due to Voids

In order to address the safety issue, as well as formulate an effective rehabilitation plan, the airport authority wished to have more detailed information on the cause, location, and extent of the pavement settlement and voiding under the concrete.

In the summer of 1996, a survey was conducted to estimate the location and extent of voided areas. GPR was selected as the method of investigation since it can be applied without interruption of service, and because it is the only method available that has the capability of detecting the conditions of interest. The data was collected using multiple parallel passes as described earlier. Due to the qualitative nature of the problem, the GPR data was analyzed visually, and the findings were plotted on plan view maps. An example output map is shown in Fig. 10.

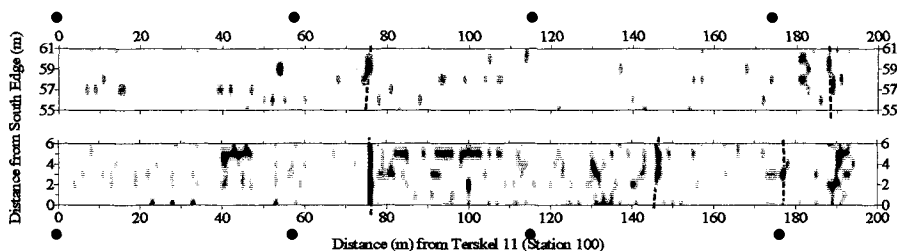


Fig. 10 - Map Showing Void Locations

In Fig. 10, the horizontal axis shows the distance along the runway, and the vertical axes show the offset from the south edge of the runway. Since these were shoulder areas, there are two areas with a 50 meter width in between representing the main runway area. The highlighted areas in Fig. 10 are color coded to represent different degrees of probability of the existence of voids. The areas that appear darkest are the most likely void locations. Other features identified in the survey were subsurface utilities. The black dots around the periphery of the plot are light poles that were used for reference.

The results of the analysis showed that there will be additional future settlements, predicted mostly on the south shoulder. Based on these results, the airport authority has now adopted a plan in which they will repair the worst areas first, without having to break down the entire shoulder. This knowledge has resulted in substantial cost savings for Stavanger and the ability to plan their work schedules accordingly.

CONCLUSIONS

The results of this work have shown that delamination, stripping, voids, and thickness variations in airport pavement can be detected with Ground Penetrating Radar. The equipment used is non-contact, and allows for surveys to be conducted at night without interference with airport operations. The results provide valuable data for airport pavement management and rehabilitation programs.

ACKNOWLEDGEMENT

The authors would like to acknowledge Mr. Povl E. Anderson and Mr. Hans Henrik Bünner of Copenhagen Airport, and Mr. Geir Lange from the Norwegian Airport Authorities for their assistance and cooperation in conducting this work.

REFERENCES

1. Scullion, Tom, "Ground Penetrating Radar Applications on Roads and Highways", Texas Transportation Institute Research Report 1923-2F, November 1994.
2. Maser, Kenneth, R., "Condition Assessment of Transportation Infrastructure using Ground Penetrating Radar", *Journal of Infrastructure*, V2 (2), ASCE, June 1996.
3. Scullion, Tom, and Elias, Rmeili, "Detecting Stripping in Asphalt Concrete Layers using Ground Penetrating Radar", Preprint 97-0508, 1997 Annual Meeting of The Transportation Research Board, Washington, DC.

STATEWIDE BRIDGE DECK SURVEY USING GROUND PENETRATING RADAR

K. R. Maser
Infrasense, Inc.,
14 Kensington Rd. Arlington, MA 02476 USA
and
M. Bernhardt
Burgess & Niple, Ltd.
5085 Reed Road, Columbus, OH 43220 USA

ABSTRACT

The Arizona Department of Transportation (ADOT) implemented a statewide bridge deck Ground Penetrating Radar (GPR) survey of 134 bridges. The deck component of this inspection was carried out using GPR, coupled with coring, half-cell corrosion potential tests, and chloride sampling. The GPR survey provided the first round of data, producing maps for each deck showing potential areas of concrete deterioration and depth of reinforcement. These maps were then used by field inspection crews to locate the subsequent tests, and to determine sample depths for chloride testing. The GPR field data was collected at normal driving speed without lane closures or interference to traffic. The total data collection effort for the 134 bridge decks, including mobilization throughout the state, consumed 35 field days. Data analysis was carried out at a rate of up to 15 bridges per week, so that the GPR maps were available for the field crews in time for their work. The project provided ADOT with 100% coverage data on deck condition and depth of rebar on over 1.5 million square feet of bridge, at considerably less cost than alternative methods.

KEYWORDS

Ground Penetrating Radar, GPR, Bridge Deck Survey, and State Wide

INTRODUCTION

The overall objective of the work described in this paper was to provide deck condition data for Arizona's statewide bridge deck condition survey. The specific objective of the GPR survey has been to locate and quantify deteriorated and delaminated concrete, and to determine the depth of reinforcing. The GPR survey and data analysis has been carried out in advance of on-deck inspection in order to support the on-deck inspection activity. "Specifically, the GPR data was

used in the field to focus the engineers' field inspection activities, including coring, half-cell testing and chloride ion sampling. Additionally, the GPR survey minimized the need for time-consuming chain drag surveys.

A total of 134 bridge decks representing 1.5 million square feet of deck were surveyed with GPR under this project. The decks have been classified according to the type of superstructure as described in Table I. With the exception of the concrete slab, the typical decks thickness range from 6 ½ to 8 inches, with a top rebar cover of 1 ½ to 2 inches. The dominant reinforcement for the girder and T beam decks is transverse, and tends to be uniformly spaced throughout the deck. The concrete box decks also have significant longitudinal steel, whose density varies with longitudinal position depending on the location of the supports. The concrete slabs vary in thickness from 14 to 18 inches depending on the span length. They also have a tapered thickening as they approach the supports. Primary steel in the concrete slabs is longitudinal.

Table I - Summary of Bridge Types

Bridge Type	Number in survey	Description
IBC	65	Steel Girders With A Concrete Deck
CTB	14	Concrete "T" Beam Supporting A Concrete Deck
CG	15	Pre-Stressed Concrete Girders Supporting A Concrete Deck
CB	7	Concrete Box Girder, In Which The Deck Is The Top Flange
CS	33	One-Way Concrete Slab
Total	134	

PRINCIPLES OF GPR FOR BRIDGE DECK EVALUATION

Ground Penetrating Radar operates by transmitting short pulses of electromagnetic energy into the pavement using an antenna attached to a survey vehicle. The principles for GPR as applied to bridge deck evaluation have been well documented elsewhere, and will not be repeated here (see Maser and Roddis, 1990; SHRP C-101). GPR was originally developed for overlaid decks, since access to the concrete surface via other traditional methods is limited. For overlaid concrete decks, the variation of the dielectric constant of the concrete is used to determine deterioration. Concrete with high moisture and chloride content, as associated with corrosion damage and

punky concrete, will produce highly variable reflections at the overlay/concrete boundary. This reflection is due to the higher dielectric permittivity associated with the moisture and chloride.

With one exception, all of the decks included in the ADOT survey were bare concrete with no overlay. For non-overlaid decks, the concrete surface tends to dry out and the moisture related variations are not necessarily observed. For these types of decks, the attenuation (loss of signal strength) of the radar signal, as measured from the bottom of the deck, is used as the alternate measure of concrete deterioration. Contaminated and damaged concrete will cause the GPR signal to dissipate and lose strength as it travels through the deck and reflects back from the bottom. An alternative to the bottom reflection for this measurement is the reflection from one of the levels of reinforcing steel. The use of rebar reflection as a measure of attenuation requires that the density of steel be uniform in the longitudinal direction.

Deteriorated concrete will show a higher dielectric constant (Carter, et. al., 1986; Maser, 1990; Maser, 1991; Maser and Rawson, 1992). The quantity of deterioration is then inferred from the percentage of deck area exceeding a threshold dielectric constant. For bare concrete decks, the concrete dielectric constant may not be an adequate indicator of concrete condition due the surface drying. In this situation, the concrete attenuation is calculated using the reflection amplitude either from the bottom of the deck, or from a rebar level (SHRP C-101, Volume 7; AASHTO TP36). The reflection from the deck bottom or rebar is normalized by the surface reflection, and areas of low reflection amplitude are identified with deterioration.

The arrival time of the reflection from the top rebar is used to calculate rebar depth. A previous study with the Wyoming Transportation Department has shown that the longer paths to the side rebar require an adjustment factor of 0.88 to obtain an accurate correlation (Maser, 1994b). This factor has been incorporated into the analysis presented in this paper.

DATA COLLECTION

GPR data was collected during the period from December 11, 1998, until April 24, 1999. The actual number of survey days during this period was 35. The other time was associated with resolution of equipment problem and work on other projects. The survey log is shown in Table 2. The GPR equipment and operator were provided Terracon, Inc. of Lenexa, KS. The GPR equipment was a dual 1 GHz horn antenna system manufactured by Pulse Radar, Inc. of Houston TX and is shown in Figure 1. The radar antennas were oriented with transverse polarization, so that reflections from transverse reinforcement would be maximized in order to calculate the depth of reinforcement, and reflections from the concrete boundaries would be highlighted. The vehicle was equipped with an electronic distance measuring instrument (DMI) mounted to the drive shaft which provided continuous distance data as the GPR data was collected.



Fig. 1 - Field Setup of GPR Equipment

The GPR survey was carried out at normal driving speeds, which ranged from 20-30 mph on secondary roads to 35-55 mph on major arteries and interstate highways. Each survey was carried out by conducting a series of longitudinal passes each at fixed offset from the curb. The overall objective of the survey layout was to generate passes at 3 foot transverse spacing from curb to curb. The actual location of each pass was determined approximately by visually reference using lane markers and other visual reference points. Data collection for each pass was initiated about 100 feet before the vehicle reached the actual start of the deck. The actual beginning of the deck is identified in the GPR data, as discussed in the data analysis section.

The data was collected using the Pulse Radar system, which was operated from inside the survey vehicle. Data was digitized and stored to hard disk as the survey progressed. The DMI distance data was continuously recorded into each GPR record, so that each GPR data scan had an associated distance. Manual markers were placed in the data at the beginning and end of each deck. Normally, the beginning and end of the deck can be observed directly in the GPR data (see Figure 2). However, for situations where this was not clear, the markers provided location backup. For the bulk of the survey, the air temperatures during data collection ranged from near freezing in the Flagstaff and northern areas, ranging within the mid 60's and 70's (°F) in the southern areas, and the conditions were generally damp.

DATA ANALYSIS

The bridge deck analysis is carried out using Infrasense's DECAR[®] software, which calculates and maps areas of high attenuation and dielectric constant, and estimates total deterioration quantities. The computation is based on the percentage of concrete attenuation and dielectric constant values, which exceed a threshold.

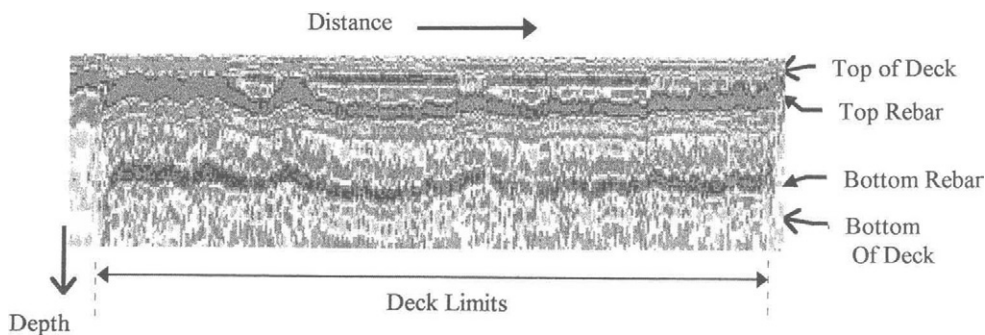


Fig.2. Data Sample - Typical Girder/Slab Deck

Note that the start of the bridge deck is very clear in the GPR data. This fact allows for data collection at driving speed without having to start specifically at the beginning of the deck. Note also that the top rebar and deck bottom are very clear in the radar data. This is typical for slab-on-girder decks. The picture is somewhat different for one way slabs, where the concrete is thicker and the reinforcing is not transverse. An example of this type of deck is shown in Figure 3. Note that the bottom of the deck is not as clear, and the thickening at the supports is evident in the data. Note also that the top reinforcement is not as clear, since it is mainly longitudinal, and it is not easily picked up with the antenna orientation used. Also, note that the reinforcement is more evident in the areas around the piers, where it is heavier to withstand the negative moments.

In these concrete slab decks the method of analysis had to be altered to take into account the thickening of the deck. In the thickened areas, the GPR signal becomes weaker due to attenuation. Therefore, this signal can not be used as a reference for concrete conditions. In these cases, the analysis was only considered valid in the areas where the concrete was uniform, and the other areas were "blacked out" on the GPR condition maps.

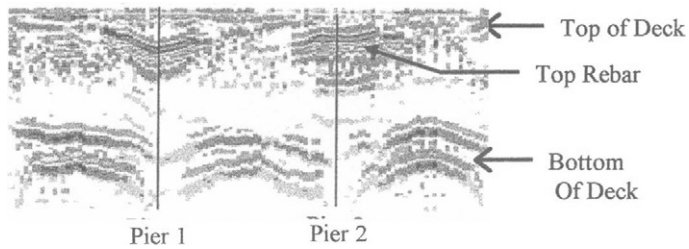


Fig. 3. Sample GPR Data - Typical 3-Span One-Way Slab Bridge

RESULTS OF DATA ANALYSIS

The analyzed data is presented in the form of contour plots and total percentages, as shown in Figure 4. Two types of contour plots have been prepared: (1) plots of top rebar depth; and (2) plots of potential areas of deteriorated concrete. The plots of rebar depth are generated directly from the output of the processing, and are presented as contour intervals spaced at 0.5 inches. Accompanying the rebar depth contour plots are percentages of the total deck area which fall into the following 3 categories: $\% < 1.0$ inch; $1.0 < \% < 1.5$ inch; and $\% > 1.5$ inch. These statistics identify the severity of shallow rebar in the deck structure.

The potential areas of deteriorated concrete are identified by a threshold, which is calculated from the mean value. The indicators used for identifying potential deterioration are the surface dielectric constant and the attenuation of the radar signal through the deck, as discussed earlier. Experience from other work (Maser, 1990; Maser and Rawson, 1992) has shown that a threshold of 20% from the mean value is a reasonable value. This threshold has been used for the plot and for the computation of the total estimated area of deteriorated concrete.

The results of the GPR survey have been correlated with chloride and half-cell measurements, and with selected decks where chain dragging was carried out for comparison. A correlation between GPR deterioration quantities and chain drag quantities for eight concrete slab and steel girder decks is shown in Figure 5. The figure shows reasonably good correlation, with a slope of 0.89 and an R-squared of 0.69.

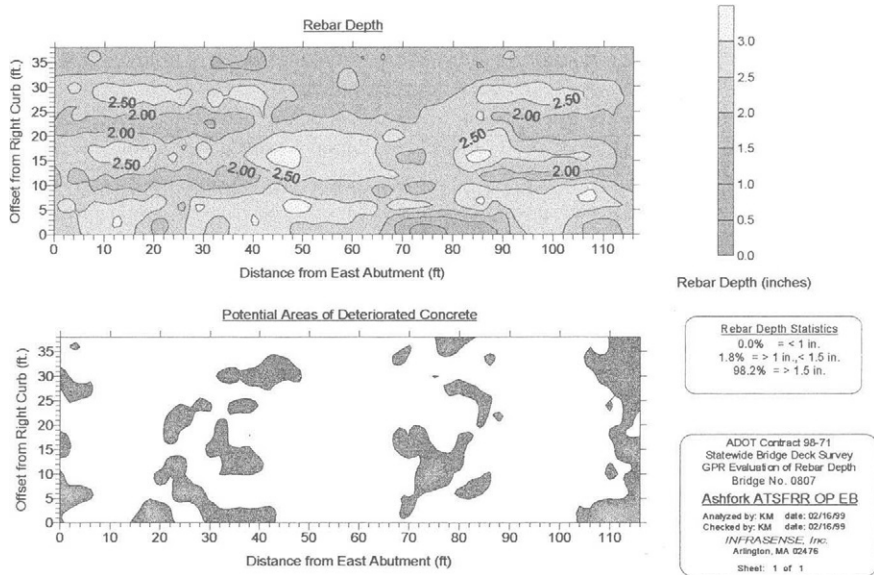


Fig. 4. Standard Output of GPR Data Analysis

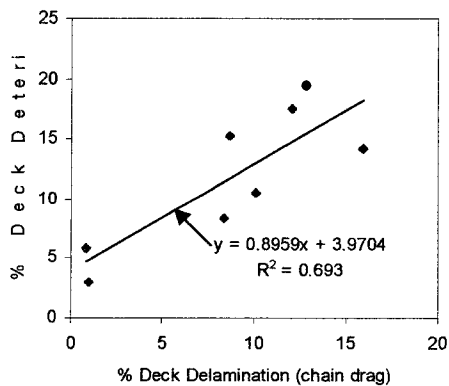


Fig. 5. GPR vs. Chain Drag for Percent Deck Deterioration (concrete slab and steel girder decks)

CONCLUSIONS

The ADOT GPR project, as described herein, demonstrated the value of GPR as an initial screening tool for an in-depth bridge deck inspection program. The GPR data can be collected quickly without lane closures, and the GPR data maps can be provided to field crews in advance of the detailed inspection. The availability of the rebar depth and deterioration maps minimizes the amount of time that crews spend on the decks, thus reducing project cost and risk to field personnel

REFERENCES

1. Maser, K.R. and Rawson, A. (1992) NETWORK BRIDGE DECK SURVEYS USING HIGH SPEED RADAR: CASE STUDIES OF 44 DECKS. Transportation Research Record No. 1347. Transportation Research Board. National Research Council.
2. Maser, K.R. (1990) "New Technology for Bridge Deck Assessment" Phase I and II Final Report, New England Transportation Consortium, Center for Transportation Studies, Massachusetts Institute of Technology, Cambridge Massachusetts.
3. Maser, K.R., and Roddis, W.M.K (1990) "Principles of Radar and Thermography for Bridge Deck Assessment", ASCE Journal of Transportation Engineering, V116 (5), Sept./Oct.
4. Carter, C. R., Chung T., Holt, F. B., Manning D. (1986) "An Automated Signal Processing System for the Signature Analysis of Radar Waveforms from Bridge Decks", *Canadian Electrical Engineering Journal*, V11 (3), pp. 128-137.
5. Maser, K.R. (1994b) "Evaluation of ground penetrating radar applications of pavement and bridge management" Report FHWA/WY-94/01, Wyoming Transportation Department, January.
6. Alongi, A.J., Clemena, G.G., and Cady, P.D. (1993) "Condition Evaluation of Concrete Bridges Relative to Reinforcement Corrosion – Volume 3: Method of Evaluating the Condition of Asphalt-Covered Decks" Strategic Highway Research Program Report SHRP-S-325, Washington D.C.

USING GROUND PENETRATING RADAR TO EVALUATE PAVEMENT STRUCTURES

I. L. AL-QADI and A. LOULIZI,

The Via Department of Civil and Environmental Engineering, Virginia Tech
Blacksburg, VA, USA

M. D. OOSTERBAAN

Haley & Aldrich, Inc., Cape May, NJ, USA

ABSTRACT

The use of ground penetrating radar (GPR) in pavement evaluation has been developed over the past 30 years. In rigid pavements, GPR is reported as a feasible method to locate dowels, estimate thickness variations, and detect voids or loss of support under slabs. In flexible pavements, GPR has been used to detect moisture in hot-mix asphalt (HMA) layers and to locate moisture in aggregate or treated base layers. Ground penetrating radar is also used to locate thickness changes in individual structural layers. This is one of the most important applications of GPR in pavements. These data are useful for overlay design, predicting pavement life, and as input for other testing techniques such as Falling Weight Deflectometer (FWD). Ground penetrating radar technology was used to assess the causes of the distressed condition of the 2680-m-long road at the National Wildlife Visitor Center in Laurel, Maryland. The 3.4-m-wide roadway was failing prematurely, and a number of localized full-depth repairs were required in the first four years after the road was constructed. Two types of GPR systems were used to evaluate the structural profile of the road. The first is an air-coupled system operates at a center frequency of 2 GHz. The second system is a ground-coupled GPR with a monostatic antenna operates at a center frequency of 900 MHz. Data were collected from the inner and outer wheel paths using both systems. For the 2-GHz system, data were collected along the length of the road at a speed of approximately 25 km/h and stationary at 100 m intervals. The stationary measurements were taken because a "time jitter" in the pulse was noticed by the authors. For the 900-MHz system, data were collected along the road at a speed of approximately 8 km/h. The 2-GHz system was capable of predicting, using some calibration cores, the HMA layer thickness, while the 900 MHz system was used to predict the total pavement thickness (HMA and base layers). The results of the GPR surveys indicated significant deficiencies in as-built thickness of each layer and the total pavement thickness in comparison to the design thickness. The ground-coupled system was successfully used to detect moisture trapped in the base layer. The moisture accumulation was thought to be the result of an inappropriate base and subgrade drainage. The results have been verified by visual survey, ground-truth cores, and the results of FWD tests.

KEYWORDS

Ground penetrating radar, nondestructive evaluation, flexible pavements, hot-mix asphalt, base material, drainage.

INTRODUCTION

Radar (Radio Detection and Ranging) is an application of electromagnetic (EM) energy. In the early 1900s, the principle of radar was found to be applicable for detecting airborne objects. This principle consists of transmitting EM waves and receiving the reflected signals from any object in the path of the beam. During the second World War, rapid development of radar technology took place because of its application in the military. It was later discovered that different objects interfere differently with EM energy. The main material properties that have an adverse effect on the electric and magnetic fields that constitute the EM wave are permittivity, conductivity, and permeability. It was also discovered that EM waves travel in free space with a constant speed comparable to the speed of light. With these discoveries, radar could be used to detect airplanes, ships, and clouds. In 1926, Hulsenberg used the same principle to detect buried objects; this was the first application in which EM waves were “intentionally” transmitted through solids [1]. In 1929, ground penetrating radar (GPR) surveys were performed in Austria to sound the depth of glacier [2].

Ground penetrating radar technology was forgotten until the late 1950s, when a U.S. Air Force plane crashed into the ice in Greenland as it tried to land because the radar system was “seeing through the ice” and misread the actual altitude. This event initiated investigations into the ability of radar to “see” into the subsurface strata, especially for mapping ice depth, subsoil properties, and locating water tables. In the late 1960s, some advances in radar technology were made through NASA lunar investigations when a GPR system was built and flown to the moon to characterize its surface electrical properties. During the Vietnam War, the US Army developed a radar system called “Combat Radar” for locating mines, tunnels, and bunkers. This radar system, through further research, led to the development of other ground probing radar systems used to identify and profile subsurface geological features. Since the 1970s, GPR has been used in many applications, including locating sewer lines and buried cables [3], measuring the thickness of sea ice [4], and profiling the bottom of lakes and rivers [5]. Since the 1980s, GPR has been used for different applications to assess civil infrastructure.

For the roadway project described in this paper, GPR was used to evaluate the variation in the thickness of the structural layers and to predict any internal flaws of a newly constructed road that failed very prematurely. The road was designed in 1990 and constructed in 1993/1994. It is a 4.3-m-wide one-way road that has a total length of approximately 2680 m. The pavement design required a stable subgrade of compacted native soils, placement, and compaction of 254-mm granular base, and placement and compaction of 102-mm HMA. The road surface shows several types of increasing surface distresses with continuing use. The distresses include fatigue cracking, raveling, rutting, shoving, and mix segregation. In some areas, subgrade soils have pumped through the pavement during wet seasons, and after ground freezing, potholes have formed. Ground penetrating radar, along with FWD testing, visual surveys, and coring, was used to examine the integrity of the structural capacity of the road in order to prepare a work plan for reconstructing the pavement to provide a 20-year design life that accommodates the anticipated traffic. In this paper, the use and effectiveness of GPR technology are discussed.

SYSTEM AND PRINCIPLE OF OPERATION

The GPR system used in this study is of the pulsed type. Figure 1 shows its major components. Trigger pulses are generated in the control unit by the radar circuitry. These pulses are sent through the control cables to the antenna, where each trigger pulse is transformed into a bipolar transmit pulse. These transmitted pulses encounter different materials in the subsurface with different dielectric properties. At the interface, signals are reflected back to the surface, where the receiving antenna will detect them; they are then sent to the control unit where they are processed and displayed. The air-coupled mode system used in this study utilizes a pair of 2-GHz horn antennae, while the ground-coupled mode system uses a 900-MHz transceiver (a device that transmits and receives electromagnetic signals).

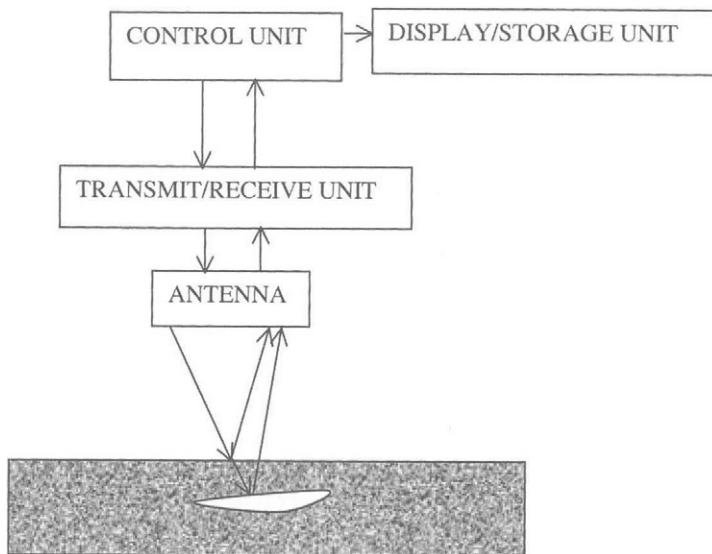


Fig. 1. Components of a pulsed GPR system.

In the air-coupled mode, the horn antennae were mounted behind a truck at a distance of 457 mm above the surface, and the truck was driven at 25 km/h. For the ground-coupled mode, the transceiver was attached to the back of the truck (insuring its full contact with the ground), and was towed at a speed of 8 km/h. The control unit generates 32 scans per second. This translates into approximately one scan every 200 mm for the air-coupled system, and one scan every 70 mm for the ground-coupled system.

There is a trade-off between penetration depth and resolution. As the frequency of the GPR system decreases, the penetration will increase; however, the resolution will decrease. This means that the 2-GHz air-coupled GPR system has a better resolution than the 900-MHz ground-coupled system, but its penetration depth is smaller. Knowledge of how to adjust the gain of the GPR system is usually important.

In this study, air-coupled system was used to estimate the thickness of the HMA layer, while the ground-coupled system was used to estimate the total thickness of the pavement structure (HMA and base layers), and also to locate areas where moisture was present inside the pavement structure. The data were stored as they were collected.

Figure 2 shows a schematic diagram of the reflections of a GPR signal from a layered pavement structure. R_0 is the reflection from the air/HMA interface, R_1 is the reflection from the HMA/base material interface, and R_3 is the reflection from the base/subgrade interface. Figure 3 shows the GPR output resulting from these reflections. To calculate the layer thickness, the following equation is used:

$$h = \frac{c\Delta t}{2\sqrt{\epsilon_r}} \quad (1)$$

where c is the speed of light (3×10^8 m/s), Δt is the two-way travel time, and ϵ_r is the dielectric constant (relative permittivity) of the layer.

For example, if the first layer is HMA with a dielectric constant of 5 and the pulse measured time Δt is 1.5×10^{-9} s, then the HMA layer thickness, using Equation (1), would be 100 mm. The same procedure is used to find the thickness of the other layers. Therefore, prior knowledge of the dielectric constant for all the pavement materials is needed to accurately determine the thicknesses. Typical values for the dielectric constant for different materials are shown in Table 1 (at a frequency of 1 GHz). If the materials contain moisture, these values will be increased significantly (e.g. soil with free moisture). The dielectric constant of the layers could be estimated using calibration cores.

If a layer thickness is smaller than the resolution ability of the GPR system, then the reflection from that layer will overlap the reflection from the previous layer; hence, it will be difficult to accurately distinguish that layer from the one above it.

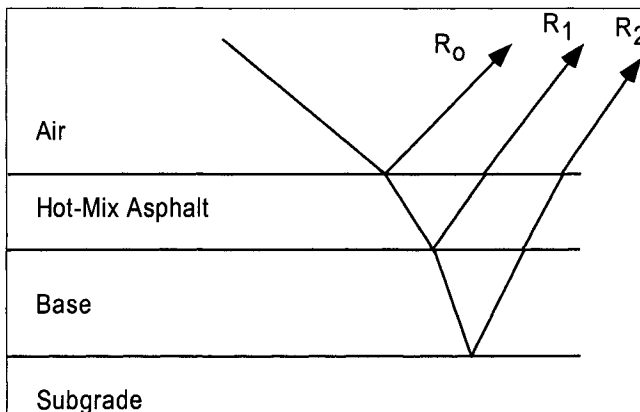


Fig. 2. Reflections from the interfaces in pavements.

The amplitude of the reflected signal depends on the contrast between the dielectric constants of the two materials. The reflection coefficient is given by Equation (2):

$$R = \frac{\sqrt{\epsilon_{r1}} - \sqrt{\epsilon_{r2}}}{\sqrt{\epsilon_{r1}} + \sqrt{\epsilon_{r2}}} \quad (2)$$

where R is the reflection coefficient, ϵ_{r1} is the dielectric constant of material 1, and ϵ_{r2} is the dielectric constant of material 2.

To determine if moisture exists in the pavement structure, changes in amplitude of the reflected signal were monitored. When moisture is present, the amplitude of the reflected signal becomes high due to the strong contrast between the dielectric constant of water and that of the pavement materials. When moisture is not present, the amplitude of the reflected signal would be much lower since the contrast between the dielectric constants of the pavement materials is usually small (see Table 1).

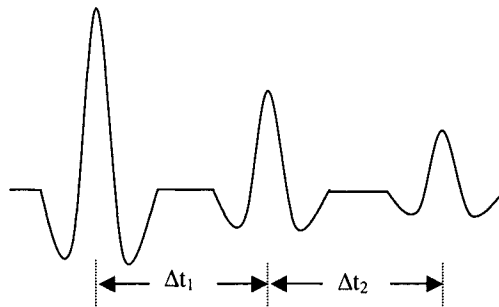


Fig. 3. Radar scan obtained from the pavement section shown in Figure 2.

Table 1. Real part of the dielectric constant at 1 GHz for pavement-related materials

Material	ϵ_r
Air	1.0
Clay soil (dry)	2.4
Loamy soil (dry)	2.5
Sandy soil (dry)	2.6
Hot-mix asphalt	3-6
Granite	4-6
Concrete	3-15
Limestone	4-8
Water	81

Radar data may be visualized in three different ways. In the oscilloscope mode, each scan (or waveform) is plotted separately, showing the reflected signal amplitude versus time (or depth). In the wiggle mode, all the sequential scans are graphically stacked to create a profile of the pavement structure showing the horizontal distance, time (or depth), and the amplitude of the reflected signals. In the color linescan mode, an intensity-modulated image is obtained by assigning different colors to different intensity ranges. This will also lead to a profile of the pavement structure showing the horizontal distance, time (or depth), and the intensity of

the reflected signals. In this mode, different color transforms could be used in order to highlight low-reflected signals or high-reflected signals.

RESULTS AND DISCUSSION

Data were first taken using the air-coupled system in the inner and outer wheel paths at 25 km/h; stationary measurements were also taken every 100 m to verify the effect of a “time jitter” in the pulse, which was noticed by the authors. Figures 4 and 5 show typical data obtained with this system. The wiggle trace is overlapped over the color linescan to help in the data interpretation. For this particular data, a weak reflection is represented by dark green (homogeneity in the scanned material, which leads to no wave reflection), while red and dark blue represent great changes in the dielectric properties. From these figures, one can notice the high variability encountered in the pavement structure. Due to this variability, calibration cores were needed for better interpretation. Since some cores were also needed for material testing, the GPR data helped in selecting core locations that would best provide ground truth measurements to calibrate the data evaluation. The cores corroborated the structural variability seen in the GPR scans. It was found that some sections had one layer of HMA over the subgrade (no base layer), and layer thicknesses varied significantly along the length of the road.

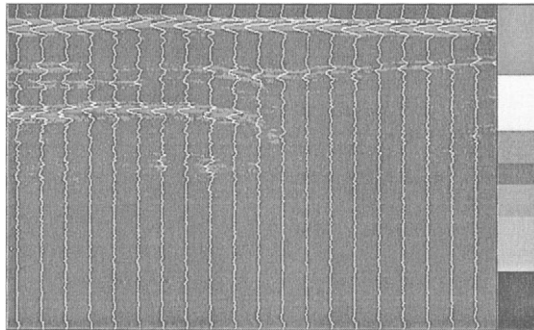


Fig. 4. Variability in the pavement structure (air-coupled system data, inner wheel path).

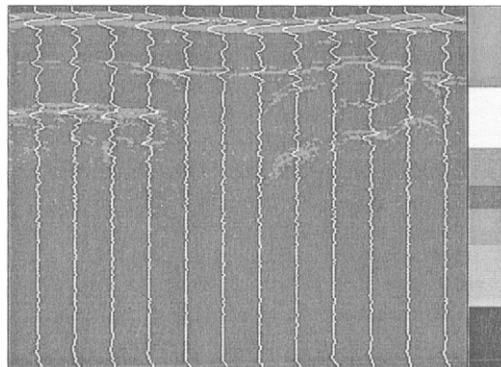


Fig. 5. Variability in the pavement structure (air-coupled system data, outer wheel path).

Data were then collected using the ground-coupled system in the inner and outer wheel paths. The calibration cores were used to calculate the dielectric constant of the HMA layer and the base layer. The same values were used in the nearby area of the cores. However, because of the high variability in the pavement structure of the road, this assumption could affect the accuracy of the results. Using Equation (1), the assumed dielectric constant and the measured travel times were used to calculate the layer thicknesses.

Figures 6 and 7 show the pavement profile along the road for the outer and inner wheel paths, respectively. Figures 8 and 9 show typical data taken by the 900-MHz system. Moisture was detected by this system along the road either deep in the subgrade or at the interface between the layers. This means that there was a drainage problem, which has been verified by identifying clogged ditches. The presence of moisture in the pavement structure would greatly reduce the structural capacity of the pavement. Moisture in the base or subgrade lowers the pavement support; in addition, loads may induce pore pressure, which ultimately results in pavement deterioration. Moisture is also known to cause stripping of the HMA, and thus raveling, which reduces its capacity to support loads.

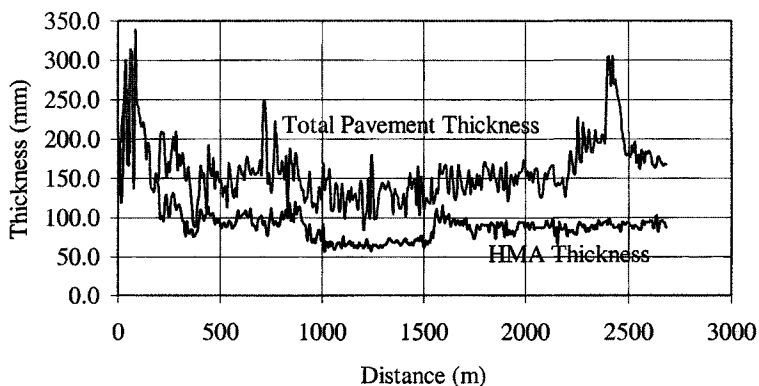


Fig. 6. Pavement profile for the outer wheel path.

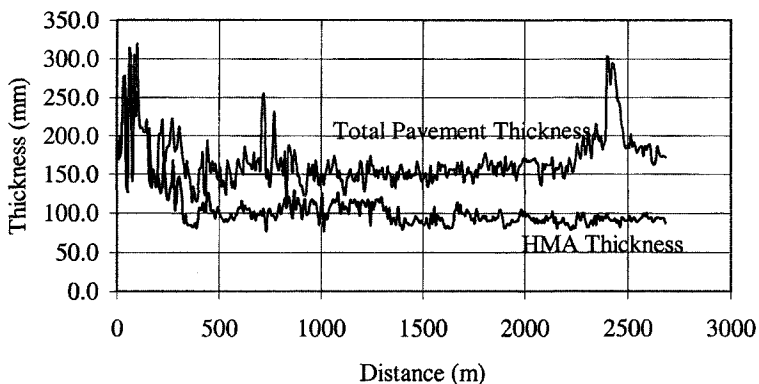


Fig. 7. Pavement profile for the inner wheel path.

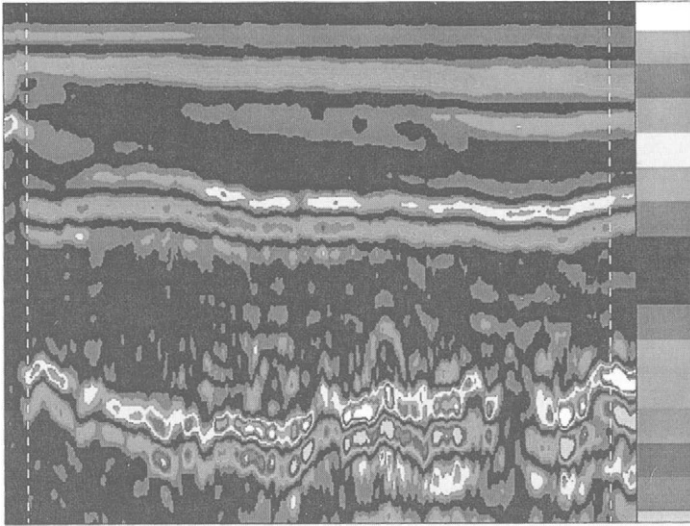


Fig. 8. High moisture content in the subgrade (900-MHz system, outer wheel path)

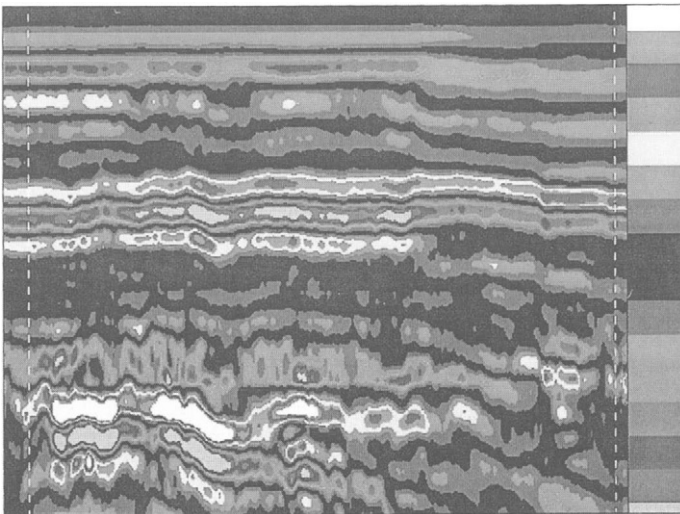


Fig. 9. High moisture content in the HMA/base interface and in the subgrade (900-MHz system, outer wheel path)

FALLING WEIGHT DEFLECTOMETER SURVEY

The falling weight deflectometer (FWD) is one of the nondestructive devices that has recently gained widespread acceptance (since the introduction of the static Benkelman beam at the

WASHO Road Test in the early 1950s) for the structural evaluation of pavement deflection response [6]. This device drops a calibrated mass onto a circular plate (radius 152.4 mm) in contact with the pavement surface. The magnitude of the applied load and the vertical deformation response of the pavement surface at the center of the loaded plate and at eight locations (203, 305, 457, 610, 914, 1219, 1524, and 1829 mm) offset from the loaded axis are recorded. Two types of analysis may be performed on FWD data. The simplest and most direct analysis relies on computing a Surface Modulus, E_0 , defined as the applied load divided by the measured axial deformation at the center of the loading plate. This value is analogous to a spring constant (N/m) and provides a gross measure of the overall structural value of the pavement system, including the subgrade. A more sophisticated analysis is possible using various techniques of back-calculation, which seek to match the observed pavement response to that returned by a mathematical model of layered linear elastic half-space. This technique generally relies upon varying the linear elastic moduli of the component material layers until a satisfactory match to the observed surface deflection is achieved.

A Dynatest FWD system was used to perform the structural evaluations of the road. Figure 10 shows the measured deflections by the first three sensors along the road using a load of 4400 kg. Comparing this figure with the GPR predicted thicknesses, shown in Figures 6 and 7, it is clear that the regions of high measured deflections correspond to deficiencies in pavement thicknesses. The thicknesses as predicted by GPR were used as input for ELMOD (back-calculation software). With the GPR input, the variability in the back-calculated moduli of all the road layers was reduced, and therefore less iteration was required.

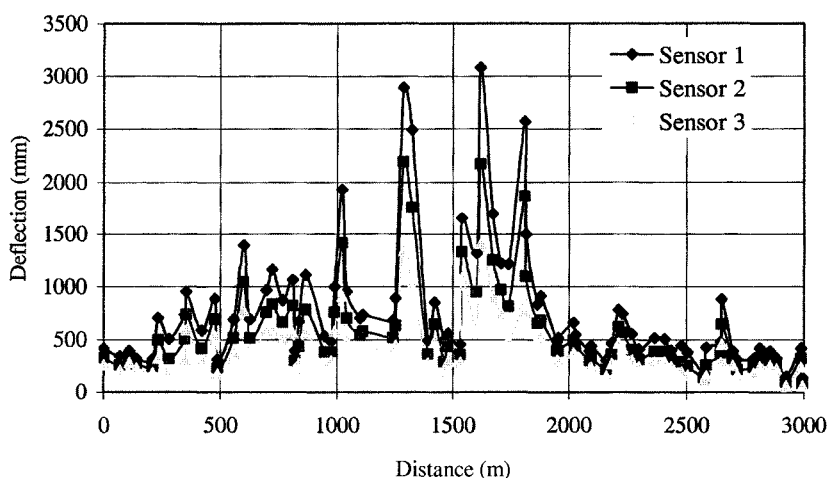


Fig. 10. Measured deflections along the road using a 4400-kg load.

The results of the layer thickness as obtained from the GPR show that the road has an average HMA thickness of approximately 95 mm, and an average base thickness of approximately 65 mm; both have high standard deviations. These results show significant deficiencies in the pavement thickness as compared to the design thickness (102 mm HMA and 254 mm Base).

SUMMARY

Ground penetrating radar systems (air-coupled at 2 GHz and ground-coupled at 900 MHz) have successfully been used to estimate layer thicknesses of a distressed flexible pavement, and detect variation in the pavement cross-section profile along the length of the tested lane. In addition, the 900-MHz system was used to detect moisture trapped in the base layer due to inappropriate drainage. The collected data have been verified by visual survey, obtained cores, and FWD testing. The GPR proved to be a good tool to reveal the cause of surface distresses, however, the appropriate system and frequency band must be used.

ACKNOWLEDGEMENTS

The authors would like to acknowledge the interest and support provided by Mr. David Washburn, Office of Engineering, U. S. Fish and Wildlife Service, Hadley, Massachusetts, and Ms. Susan McMaon, Refuge Manager of the Patuxent Research Refuge, Laurel, Maryland during the investigation and analysis of the roadway.

REFERENCES

1. Horne, W. A. (1993). In: *Hydraulic Engineering 93 Conference*, pp. 1888-1893, W. S. Hsieh, S. T. Su, and W. Feng (Eds), July 25-30, Vol. 2.
2. Olhoeft, G. R. (1988). In: *Proceedings of the Symposium on the Applications of Geophysics to Engineering and Environmental Problems*, pp. 462-520, March 28-31, Golden, CO.
3. Morey, R. M., and Harrington, W. S. Jr. (1972), *Feasibility Study of Electromagnetic Subsurface Profiling*, Report EPA-R2-72-082, U. S. Environmental Protection Agency, October, Washington, DC
4. Campbell, K. J., and Orange, A. S. (1974). In : *Polar Research*. Vol. 17, No. 31.
5. Morey, R. M. (1974). In: *Proceedings of the 13th Annual Canadian Hydrographic Conference*, Canada Center for Inland Waters, Burlington, Ontario, Canada.
6. Graves, C. R., and Drnevich, V. P. (1991) *Transportation Research Record 1293*, pp. 12-23, National Research Council, Washington, D.C.

GPR CALIBRATION FACILITY

I. L. Al-Qadi, S. Lahouar, and A. Loulizi
The Via Department of Civil and Environmental Engineering and
University Center for Transportation Research, Virginia Tech
Blacksburg, VA, USA

ABSTRACT

Ground penetrating radar (GPR) technology has been used for the past 30 years for a variety of applications to assess pavement performance and structure. The main issue after all these years remains: "How well does GPR work and under what conditions?" Results show that GPR works well for some situations, but is not an appropriate tool for other situations. GPR is currently not used on a routine basis by the US Departments of Transportations (DOTs) due mainly to difficulties encountered in data interpretation, as well as the expenses involved for conducting GPR surveys. Data interpretation difficulties are mainly attributed to the fact that images obtained from the reflected signals are dependent on the GPR frequency used, and the dielectric properties of the structural materials. To calibrate GPR systems and to better interpret collected data (signals), a project is currently underway at the Virginia Smart Road in Southwest Virginia. Twelve different flexible pavement sections and one continuously reinforced concrete pavement section, comprised of different layers/materials, are incorporated in the test facility. These sections provide a unique opportunity to explore the feasibility of using GPR to assess pavements, and to verify its practicality. Thirty-one copper plates are placed at different layer interfaces throughout the pavement sections. The copper plates serve as a reflecting material and thus allow the determination of the dielectric constant of the layers over the GPR frequency range. Two GPR systems were considered in the preliminary evaluation: an air-coupled system with a pair of horn antennae operating at a center frequency of 1 GHz, and a ground-coupled system operating at a center frequency of 900 MHz. This paper presents preliminary results from both GPR systems. Early results revealed the capability of each system's penetration and their capability to distinguish between layers. Due to the low dielectric contrast between pavement layers, especially base/subbase layers, the copper plates serve as means to indicate that adequate energy reached those deep layers. Reflection at the interface between layers with similar dielectric constants will be used to fine-tune GPR data analyses as the layer materials' dielectric constants and layer thicknesses are determined at the Smart Road.

KEYWORDS

Ground penetrating radar, flexible pavements, nondestructive evaluation, hot-mix asphalt, base layer.

BACKGROUND:

Ground Penetrating Radar (GPR) has been used for the last 30 years as a Non-Destructive Evaluation (NDE) technique to evaluate and assess pavement structures and their performance. This technique is based on sending electromagnetic waves through the surveyed structure and then analyzing the reflected signal. The authors present the theory of GPR elsewhere [1]; however, the three simplified basic equations currently used to interpret GPR data are the following:

$$h = \frac{c\Delta t}{2\sqrt{\epsilon_r}} \quad (1)$$

$$\gamma = \frac{\eta_2 - \eta_1}{\eta_2 + \eta_1} = \frac{\sqrt{\epsilon_{r1}} - \sqrt{\epsilon_{r2}}}{\sqrt{\epsilon_{r1}} + \sqrt{\epsilon_{r2}}} \quad (2)$$

$$\beta = \frac{2\eta_2}{\eta_2 + \eta_1} = \frac{2\sqrt{\epsilon_{r1}}}{\sqrt{\epsilon_{r1}} + \sqrt{\epsilon_{r2}}} \quad (3)$$

where h is a layer thickness or the depth to a buried object or hidden defect, c is the speed of light (3×10^8 m/s), Δt is the two-way travel time measured by the GPR unit, ϵ_r is the material's relative permittivity or dielectric constant, η is the material's electrical impedance, γ is the reflection coefficient, and β is the transmission coefficient.

Ground penetrating radar has been used for a variety of pavement applications, including measuring pavement thickness, locating voids beneath pavements, detecting excess moisture, and evaluating geosynthetic effectiveness. Currently, the thickness of pavements is determined by using cores or test pit excavations. These methods are time consuming and expensive, they provide information at test locations only, and they disturb the pavement structure, which may initiate future deterioration. Maser [2] used GPR (RODAR) and PAVLAYER software to investigate the as-built conditions of pavements. The results of the pavement analysis were compared with several cores and test pits. An accuracy of $\pm 7.5\%$ was found for hot-mix asphalt (HMA) layers ranging from 51 mm to 500 mm in thickness, and $\pm 12\%$ for granular base layers ranging from 150 mm to 330 mm in thickness.

Ground penetrating radar is also used to detect voids under jointed concrete pavement since reflection from the concrete slab/base interface is affected by the presence of air and/or water, which distinguishes areas where voids exist from sound areas. While some studies reported the success of GPR for such an application [3,4], other studies showed limited success. In fact, the first author, as part of SHRP H-103, evaluated three short-pulse GPR systems, from different manufacturers, at the Pennsylvania Transportation Institute's test track. Artificial voids were dug underneath a known-thickness rigid pavement, and some were filled with water to wet the surrounding areas. None of the three GPR personnel were able to locate the voids. Sheftick and Bartoski [5] conducted a similar evaluation after eight years. Without knowledge of the slab thickness and/or the dielectric properties of the concrete, GPR operators may interpret the collected data erroneously.

Loulizi et al. [6] used a ground-coupled GPR system with a center frequency of 900 MHz to evaluate the effectiveness of geosynthetics when used as separators in secondary flexible pavement roads. Reflections from the subgrade/base interface of nine different sections were monitored to determine any soil movement at the interface. It was found that the amplitude of the reflected signal at the interface is higher when geotextile separator was used. Using Equation (2), it was found that a lower dielectric contrast occurs in the control sections due to contamination of the base layer with the migrated fines from the subgrade, and thus the development of a transition layer.

Al-Qadi and Loulizi [7] used GPR on different rehabilitated pavement sections in Kernersville, North Carolina (USA) to evaluate the effectiveness of geosynthetics as moisture barriers. They established a spatial layout of the areas where moisture accumulated in the pavement structure by monitoring the high amplitude reflected signals. High-reflected signals were attributed to the presence of moisture because of the high dielectric contrast between water and pavement materials (the dielectric constant of water is around 81, while the dielectric constant of dry pavement materials ranges from 4 to 8). Moisture presence was reported in the sections without the geosynthetics in the base and subgrade. In the sections with geosynthetics, moisture was trapped over the geosynthetic material, and therefore, with a good transversal drainage in the surface layer, moisture damage could be significantly reduced.

The application of GPR in pavement assessment has proven to be a powerful nondestructive testing tool. It is expected that there will be a growing interest and demand for GPR surveys. However, a number of limitations exist that are related mainly to interpreting the results of GPR testing:

- The images obtained from the reflected signals (using signal-processing packages) are not photographs of the features that are beneath the surface being investigated. The images show the amplitude of the GPR-reflected signals from the interfaces with different dielectric properties. These amplitudes are plotted in colors using user-defined color codes. Therefore, a considerable amount of experience and operator skill may be required to interpret sub-surface radar results correctly.
- Extensive amount of data.
- Determination of the exact location of a reflecting feature beneath the surface relies upon a prior knowledge of the dielectric properties of the material. These dielectric properties are also frequency dependent, and therefore a frequency domain method of analysis is required to accurately measure thicknesses.
- Change of the dielectric constant with depth mainly because of the presence of moisture.
- Losses in the pavement materials, especially with the presence of moisture or conducting subgrade soils.
- Reflections from thin layers may overlap depending on the GPR system resolution.
- Insufficient dielectric contrast between layers may hinder the detection of the layers underneath.

To address some of these limitations, field calibration testing is currently being conducted at the Virginia Smart Road facility.

THE VIRGINIA SMART ROAD

The Virginia Smart Road in southwest Virginia is a unique, state-of-the-art, full-scale research facility for pavement research and evaluation of Intelligent Transportation Systems (ITS) concepts, technologies, and products. The Smart Road is the first facility of its kind to be built from the ground up with its infrastructure incorporated into the roadway. When completed, the Smart Road will be a 9.6-km connector highway between Blacksburg and I-81 in southwest Virginia, with the first 3.2 km designated as a controlled test facility, which has already been constructed. This connection will serve an important role in the I-81/I-73 transportation corridor. After construction, provisions will be made to route traffic around controlled test zones on the Virginia Smart Road to allow for ongoing testing. The construction of the Virginia Smart Road project has been made possible through a cooperative effort of several federal and state organizations, including the Virginia Department of Transportation, the Virginia Transportation Research Council, the Federal Highway Administration, and Virginia Tech.

In addition to a one continuously reinforced concrete pavement section, the flexible pavement part of the Virginia Smart Road test facility includes 12 (heavily instrumented) sections. As noted in Table 1, each section is approximately 100 m long. Seven of the 12 sections are located on a fill, while the remaining five sections are located in a cut. Different layers, accurately surveyed for thickness, are used in each section (all designations are in accordance with Virginia Department of Transportation specifications):

Table 1. Sectional profile of different pavement sections at the Virginia Smart Road

Section	Length (m)	Wearing Surface (38mm)	BASE BM-25.0 (mm)	BASE SM-9.5A (mm)	OGDL (mm)	21-A Aggr. Cem. Stab. (mm)	21-B Aggr. (mm)
A	371	SM-12.5D/CP	150/CP	0	75/CP	150/CP	175/CP
B	90	SM-9.5D/CP	150	0	75	150	175/ GT/CP
C	87	SM-9.5E/CP	150/CP	0	75	150	175/ GT
D	117	SM-9.5A/CP	150/CP	0	75	150/CP	175/ GT
E	76	SM-9.5D	225/CP	0	0	150	75/ GT/CP
F	94	SM-9.5D	150/CP	0	0	150/CP	150/CP
G	90	SM-9.5D	100/CP	50/CP	0	150	150/ GT/CP
H	90	SM-9.5D	100	50/CP	75/CP	150	75
I	98	SM-9.5A*/CP	100/CP/GM	50	75/CP	150	75
J	92	SM-9.5D	225	0	75/SR/CP	0/GT	150/CP
K	86	OGFC^	244/SR/CP	0	75/CP	0/GT	150
L	104	SMA-12.5/CP	150/GM	0	75/CP	150	75

CP: Copper plate

SR: Stress Relief Geosynthetic

^ 19-mm-thick over 19-mm SM-9.5D

* Low lab compaction

GT: Woven Geotextile/Separator

GM: Galvanized Metal Mesh

- Wearing surface: Seven types of wearing surface are used (SM-9.5A, SM-9.5A with low laboratory compaction, SM-9.5D, SM-9.5E, SM-12.5D, SMA-12.5, and open-graded friction course (OGFC)). Five of these seven mixes are SuperPave™ mixes. All mixes,

with the exception of the OGFC, were constructed at 38-mm-thick; OGFC was constructed at 19-mm-thick.

- Intermediate HMA layer: BM-25.0 at different thicknesses, ranging from 100 to 244 mm.
- Three sections have the SuperPave™ SM9.5A fine mix placed under the BM-25.0 to examine the benefits of such a design on reducing fatigue cracking.
- Open Graded Drainage Layer (OGDL): Out of the 12 sections, three sections were built without OGDL. Seven sections are treated with asphalt cement, and two are treated with Portland cement. The thickness of this layer is kept constant at 75 mm throughout the project.
- Cement Stabilized Subbase: A 21-A cement-stabilized layer is used in 10 sections at a thickness of 150 mm.
- Subbase layer: A 21-B aggregate layer was placed over the subgrade at different thicknesses with and without a woven geotextile.

The Virginia Smart Road offers a unique opportunity to explore the feasibility of using GPR to accurately measure layer thicknesses and monitor pavement performance over time. To achieve this objective, copper plates were embedded in the road at different layers. Copper with a conductivity of 5.7×10^7 Siemens/m is a very good conductor, and therefore was chosen to serve as a reflecting material. Copper sheets (914 x 1219 x 0.7mm) were placed at several locations in all tested sections, as shown in Table 1; Figure 1 shows a copper plate placed on top of subgrade in section B. These copper plates serve as a tool to measure the dielectric properties of the pavement materials over the GPR frequency range (100 MHz to 3000 MHz). Another benefit of the copper plates is that they indicate where the interface between each pair of layers occurs. As stated earlier, some of the pavement materials do not have significant differences in their dielectric properties, and therefore a very small amount of energy will be reflected back from their interface. Sometimes this reflected energy is obscured by the radar system noise; therefore, accurate determination of the interface becomes difficult.

PRELIMINARY DATA

Over the next three years, data will be collected periodically over different environmental conditions using an air-coupled GPR operating at a center frequency of 1 GHz, and a ground-coupled system operating at a center frequency of 900 MHz. Other systems may be considered for evaluation in the near future. The periodic collection will allow monitoring of any changes occurring inside the pavement that might affect the GPR response. Data were collected as the different layers were constructed. Figure 2 shows a line-scan representation of the GPR data obtained over section A using the 900 MHz ground-coupled antenna. The data were taken over the BM-25.0 layer while driving at a speed of approximately 8 km/h. In this figure, the x-axis represents the scan number (or distance along the road) and the y-axis represents the reflection time or depth. In this representation, the amplitude of the reflected wave is quantified and then depicted using a color table (left of Figure 2) that maps each discrete value of the amplitude to a distinct color.

Reflections from the copper plates at the subgrade/21-B, 21-B/21-A, 21-A/OGDL, and OGDL/BM-25.0 interfaces are clearly seen. Figure 2 shows a weak contrast between the subgrade and the 21-B materials, as well as the 21-B and 21-A materials. The copper plates clearly define the interfaces. This indicates that enough energy is reaching the subgrade, but

due to low dielectric contrast, energy is not reflected back. Figure 3 represents the oscilloscope waveform of the scan obtained over the copper plate at the 21-B/21-A interface in section A (location 2 in Figure 2). In this waveform, peak 1 represents the reflected signal from the 21-A/OGDL interface, while peak 2 represents the reflected energy from the copper plate at the 21-B/21-A interface.



Fig. 1. Copper plate under 21-B material in section B.

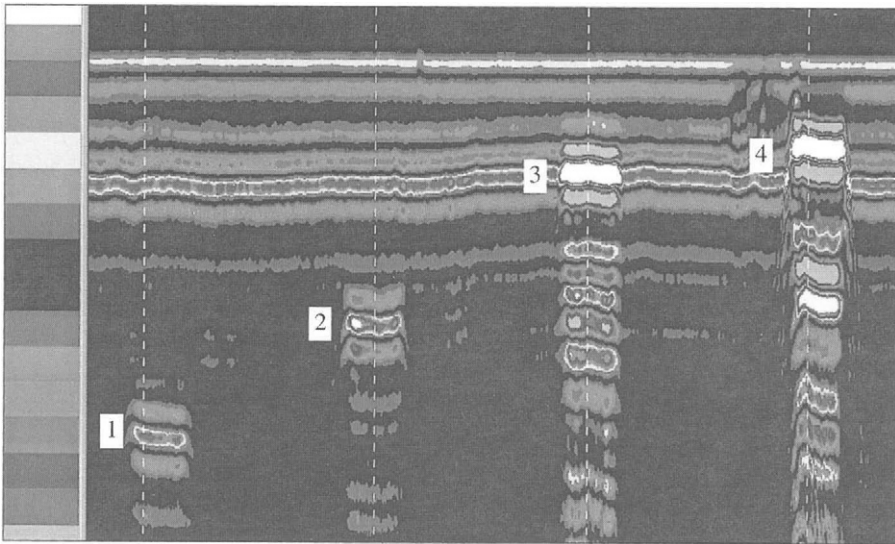


Fig. 2. Radar scans over section A using the 900 MHz ground-coupled antenna: reflections from the copper plates at interfaces (1) subgrade/21-B, (2) 21-B/21-A, (3) 21-A/OGDL, and (4) OGDL/BM-25.0.

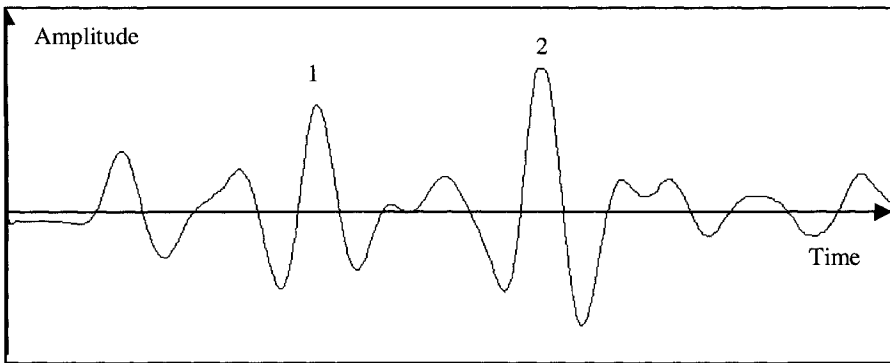


Fig. 3. Reflected waveform obtained using the 900 MHz ground-coupled antenna over section A: (1) 21-A/OGDL interface, and (2) copper plate at 21-B/21-A interface.

Figure 4 shows the GPR output obtained with the air-coupled system over the same section. As stated earlier, the air-coupled system has a lower penetration depth than the ground-coupled system, and therefore less energy is reflected from the interfaces. In order to highlight these weak reflections, non-linear color-coding was used. All copper plates at the different interfaces are clearly visible. Figure 5 shows the scan obtained at location 2 in Figure 4. Figure 6 shows the data obtained from section J with the air-coupled system, while Figure 7 shows a single scan from the same section.

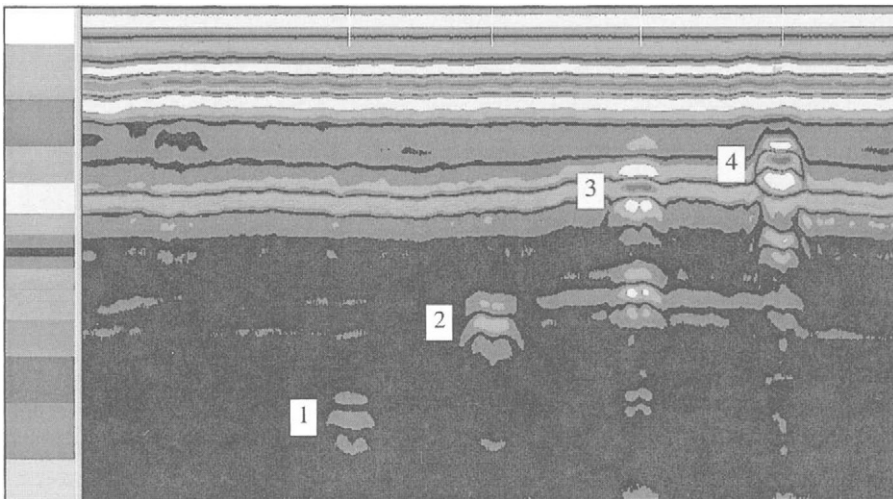


Fig. 4. Radar scans over section A using the 1 GHz air-coupled antenna: reflections from the copper plates at interfaces (1) subgrade/21-B, (2) 21-B/21-A, (3) 21-A/OGDL, and (4) OGDL/BM-25.0.

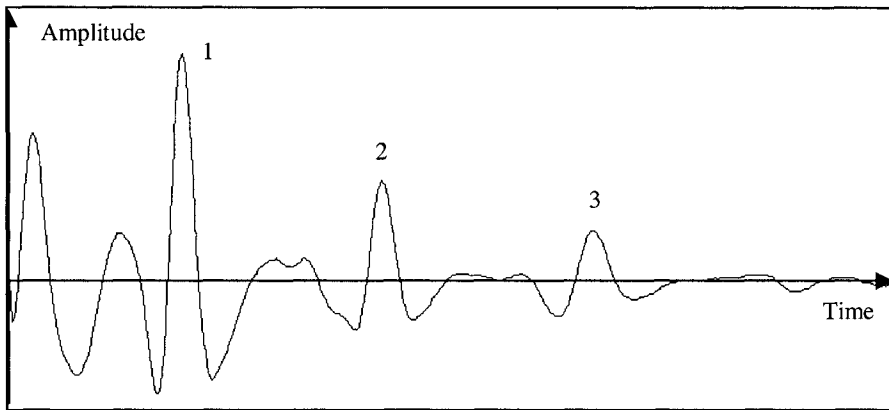


Fig. 5. Reflected waveform obtained using the 1 GHz air-coupled antenna over section A: (1) surface, (2) 21-A/OGDL interface, and (3) copper plate at 21-B/21-A interface.

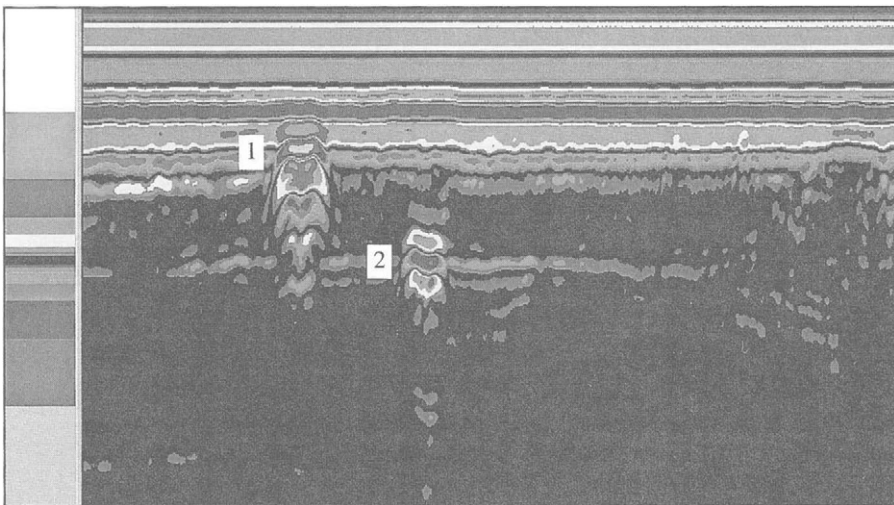


Fig. 6. Radar scans over section J using the 1 GHz air-coupled antenna: reflections from the copper plates at interfaces (1) 21-B/OGDL, and (2) subgrade/21-B.

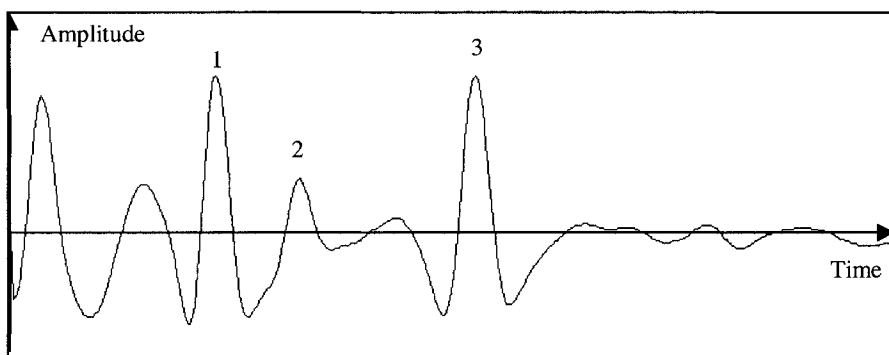


Fig. 7. Reflected waveform obtained using the 1 GHz air-coupled antenna over section J: (1) surface, (2) 21-B/OGDL interface, and (3) copper plate under 21-B layer.

SUMMARY

A new facility, the Virginia Smart Road, has recently been constructed for pavement and ITS research. The facility includes a one continuously reinforced concrete pavement design and 12 different flexible pavement designs (including different materials and layer thicknesses), which positions it as a unique facility for GPR calibration. To accomplish this calibration, 31 copper sheets were embedded at different layer interfaces during construction, and 1 GHz and 900 MHz GPR systems were used for preliminary testing. Early results revealed the capability of each system's penetration and its capability to distinguish between layers. Due to the low dielectric contrast between pavement layers, especially base/subbase layers, the copper plates serve as a means to indicate that adequate energy reached those deep layers. Reflection at the interface between layers with similar dielectric constants will be used to fine-tune GPR data analyses.

ACKNOWLEDGEMENT

This research is part of the Virginia Smart Road Pavement Research Project sponsored by the Virginia Transportation Research Council, the Virginia Department of Transportation, and the Center for Innovative Technologies.

REFERENCES

1. Loulizi, A., and Al-Qadi, I. L. (1997). In: *Recent Advances in Bridge Engineering*, pp. 335-345, U. Meier, and R. Betti (eds.), July.
2. Maser, K. R. (1996). In: *Structural Materials Technology: An NDT Conference*, pp. 61-67, P. E. Hartbrower, and P. J. Stolarski (eds.), February.
3. Clemena, G.G., Sprinkel, M. M., and Long, R. R. (1987) *Transportation Research Record* 1109, pp. 1-10, Washington, DC.

4. D'Angelo, J. A. (1986). *Portland Cement Concrete Pavement Stabilization*. Federal Highway Administration, Washington D.C.
5. Sheftick, D. E., and Bartoski, T. A. (1997), *Study of Void Detection Methods And Slab Stabilization Procedures*. Research Project 86-102, Pennsylvania Department of Transportation, Bureau of Construction and Materials, Harrisburg, PA. June.
6. Loulizi, A., Al-Qadi, I. L., Bhutta, S. A., and Flintsch, G. W. (1999). In: *Transportation Research Board 78th Annual Meeting*, No. 991316, Washington DC, January 10-14.
7. Al-Qadi, I. L., and Loulizi, A. (1999). In: *Structural Faults and Repair 8th International Conference*, in a CD, M. C. Forde (ed.), London, England, July 13-15.

DIELECTRIC PROPERTIES OF CONCRETE AND THEIR INFLUENCE ON RADAR TESTING.

DR. M. N. SOUTSOS, PROFESSOR J. H. BUNGEY, DR. S. G. MILLARD,
DR. M. R. SHAW, AND DR. A. PATTERSON.

*Department of Civil Engineering, The University of Liverpool,
Liverpool L69 3GO, United Kingdom.*

ABSTRACT.

Sub-surface radar is becoming increasingly popular as an inspection method. Interpretation can be enhanced if uncertainties about the dielectric properties of the concretes under investigation are removed. The need for reliable data to identify possible variations of the dielectric properties of different concrete mixes and their condition on site has led to a systematic laboratory based experimental programme under the auspices of a major Brite-Euram III Framework 4 project. Some key results from this recently completed work are presented in this paper with practical implications related to field surveys of structural concrete.

KEYWORDS

NDE, Radar, Permittivity, Conductivity, Concrete, Pulverised Fuel Ash, Gound Granulated Blast Furnace Slag, Moisture, Temperature, Fibres.

INTRODUCTION.

Sub-surface radar has become established over the past ten years as a valuable inspection tool for use as part of non-destructive surveys of structural concrete. Applications range from determination of major construction features, including element thickness and location of metallic reinforcing bars and ducts, to location of voids, honeycombing, delamination, cracking and moisture ingress. Such applications have been reported in many technical papers and are reviewed and illustrated in Concrete Society Technical Report No. 48 [1]. Interpretation is largely qualitative and based on comparative study of radargrams produced by scans across an area of interest, with appropriate calibration by drilling or physical exposure.

Efforts to enhance quantitative interpretation capabilities, and to extend viable applications, have encompassed physical model testing, numerical modelling and development of signal processing and analysis techniques, including neural networks [2]. All of these rely upon the availability of information about the dielectric properties of the concrete. Development of such information has formed a focus of research by the Authors over several years [3] with support

from EPSRC and has continued under the auspices of a recently completed Brite-Euram project from which the results here have been obtained.

The impulse radar signal generated by a transmitting antenna at the concrete surface propagates through the material with a speed which is related to the relative permittivity ϵ_r and with attenuation principally influenced by the apparent conductivity σ . Reflections from internal interfaces, at which there is a defined change in these properties, return to the surface and are detected by the receiving antenna. Refractions will also occur at these interfaces, depending upon the magnitude of the property changes, and part of the signal will continue to penetrate to greater depth. The relevant theory has been considered in detail elsewhere [4, 5].

This paper presents results on the influence of mix design, more specifically the concrete strength, and cement replacements like pulverised fuel ash (PFA) and ground granulated blast furnace slag (GGBS). Steel fibres are increasingly being used in overlays and they are expected to lead to differences in dielectric properties. The condition of the concretes in structures may vary according to environmental factors such as wetting and drying cycles and temperature variations. Dielectric properties of concretes may therefore be affected not only by the moisture level at the time of testing but also by whether the concrete has previously been allowed to dry. In addition concretes may have honeycombing due to poor compaction or may have areas of high salt concentrations. It would be useful to an inspecting engineer if radar can detect either of these features.

EXPERIMENTAL PROGRAMME.

Dielectric Determination

A coaxial transmission line accommodating a concrete sample 200mm long and 101mm diameter has been developed to provide frequency domain measurements over the range 10MHz to 1GHz when used in conjunction with a Hewlett Packard HP8753B Network Analyser, see Fig. 1. This encompasses the frequency range of most commercially available field systems in use for testing concrete. The basic development of the equipment, and the interpretation of measurements to provide values of ϵ_r and σ at discrete frequencies has been described elsewhere [3, 6].

Concrete Mixes and Scope of Testing.

Table 1 shows the concrete mix proportions used for the transmission line specimens. The ordinary Portland cement mixes were designed to give three target strength levels (20, 40 and 60 MPa). Three specimens for each target strength were cast but were cured differently; they were either left to air dry or were fully saturated for ten months so that they could be compared with the third set that was oven dried and resaturated.

The effects of salt impregnation, honeycombing due to poor compaction, cement replacements and the inclusion of fibres in the concrete have also been studied.

Materials.

All the concrete mixes contained Staffordshire Pink 10mm gravel aggregate with Hope Quarry sand. Ordinary Portland cement was supplied by "Castle", pulverised fuel ash by Powergen

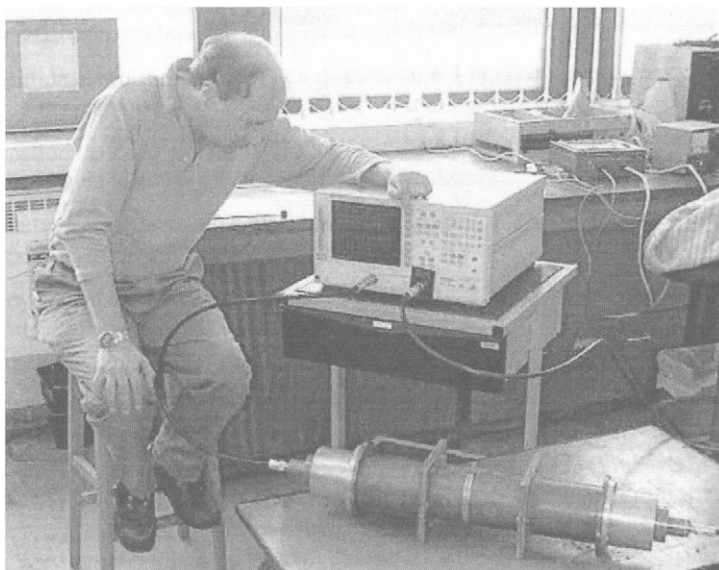


Fig. 1 The Transmission Line connected to the Hewlett Packard HP8753B Network Analyser.

Ltd., ground granulated blast furnace slag by Appleby Group Ltd., and microsilica (CSF) by Elkem Materials Ltd.. Steel fibres were from Bekaert and they were of type Dramix ZP30/.50 whilst the superplasticizer (SPA) used was naphthalene based and supplied in powder form by Tillman (Netherlands).

Casting and Conditioning Procedures.

Specimens were cast in a vertical orientation using the central portion of the split cylindrical outer casing of the transmission line as the mould. This was fixed to a base plate with the central brass core attached and placed on a 50MHz vibrating table. Concrete was placed by trowel in 3 layers and compacted until no further air bubbles were discernible on companion cubes (approx. 2-3 minutes). The top surfaces of the cylindrical specimens were trowelled to give a smooth finish. After casting, the mould was covered with damp hessian and polythene until stripping at 24 hours. Specimens were then wrapped in damp hessian and polythene sheeting for a further 3 days before weighing and the start of the specified curing regimes.

Honeycombed concretes were based on reduced sand and paste contents. Steel fibre concretes required particularly careful casting, and incorporated a layer of heavy duty plastic coated cloth waterproof tape wrapped around the brass core to prevent electrical short-circuiting by the fibres during testing.

Specimens 7 - 9 were not allowed to air-dry, but were stored under water at approx. 20°C until required for testing, when they were wiped dry, weighed and wrapped in cling film prior to fixing into the transmission line. They were removed from the transmission line, re-wrapped, re-weighed, and returned to water storage immediately after testing. For the remaining specimens, transmission line test were carried out over a range of moisture levels, which were

Table 1: Transmission Line Specimens – Mix Designs.

Ref. No.	Nominal Strength level (N/mm ²)	Variable to be investigated	Free W/C ratio	Cement/Binder kg/m ³	10mm Gravel	Sand
1, 4, 7	20	Curing	0.82	225	1085	890
2, 5, 8	40	Curing	0.59	340	1070	715
3, 6, 9	60	Curing	0.44	455	1085	735
10	20	Salt	0.82	225	1085	890
11	20	Salt	0.82	225	1085	890
12	40	Honeycombed	0.49	165	1462	0
13	40	Honeycombed	0.37	180	1462	240
14	40	30% PFA	0.41	305/130	1050	700
15	40	70% GGBS	0.47	120/285	1075	715
16	40	16% PFA	0.61	310/60	1060	705
17	100	CSF/PFA/SPA	0.35	420/105/42	1215	470
18	25	30kg Fibres	0.69	300	1210	650
19	35	50kg Fibres	0.58	390	1135	610

achieved by a combination of air and oven drying. Air drying of specimens was in a laboratory atmosphere at approximately 20°C and 34% RH, with specimens resting on wooden blocks to facilitate air circulation. All specimens were weighed immediately prior to placement into the transmission line and were removed and returned to air storage immediately afterwards. Once air dried specimens were seen to be losing no further weight, oven drying was commenced at approximately 35°C and was increased to a maximum of 80°C as moisture contents reduced. Specimens were removed from the oven and allowed to cool to approx. 20°C prior to testing.

To differentiate between the effects of cement hydration and moisture content during early ages, some mature specimens were resaturated after oven drying and were re-tested using the transmission line at a range of moisture contents. Resaturation of these specimens was achieved by immersion in potable tap water, with appropriate periods of wetting time determined by trials on companion 100mm cubes. For transmission line testing during the resaturation process, specimens were treated in a similar manner to that described above for Specimens 7 - 9, except that they were left wrapped in cling film for 24 hours before testing to allow differential moisture levels to equilibrate within the specimen.

The influence of temperature changes upon dielectric measurements was studied by temperature conditioning of Specimens 4 and 6. This involved placing the specimen together with the transmission line assembly in a freezer at approx. -10°C or in an oven at approx. 50°C overnight. 24 hours before testing, the transmission line was assembled with a thermocouple attached to the outer surface adjacent to the concrete sample and placed in an insulating box which was again placed in the freezer or oven overnight. Polystyrene end caps were placed over the end of the transmission line during transfer for measurement with the Network Analyser, which was located in a nearby building. Temperatures were measured both before and after the test, whilst weighing was undertaken after dismantling of the transmission line and return of the specimen to ambient temperatures (typically about 2 hours).

The influence of external chloride contamination on dielectric measurements was investigated

by using a vacuum impregnation technique. An oven dried concrete sample plus companion cubes were placed in the vacuum chamber and subjected to a pressure of 0.05 bar overnight. A solution prepared from an appropriate amount of aqueous sodium chloride dissolved in tap water was admitted and the specimen kept immersed for 6 hours before removal, weighing and storage. The target % chloride ions by weight of cement were 1% for Specimen 10 and 0.5% for Specimen 11. Salt concentrations were evaluated by measuring the increase in weight following impregnation by a solution of known concentration. Confirmation of these salt concentrations were obtained by the extraction of drilling dust on the transmission line specimens, and the use of the "Quantab" method, at the conclusion of testing.

The volume of water in each transmission line specimen was calculated from the difference between the weight of the specimen immediately after the transmission line test and the weight of the specimen after it had been oven dried. The percentage of water by volume could then be calculated from the ratio of the volume of water to the volume of the specimen.

3 No. companion 150mm cubes were used for strength measurements. These were tested after 28 days of moist curing to provide compressive strength values relating to each transmission line specimen.

RESULTS

The general relationship between relative permittivity, conductivity, frequency and moisture obtained for each specimen are illustrated in Fig. 2, which may be regarded as typical. It can be seen that the frequency dependence of the relative permittivity between 500MHz and 1GHz is relatively small, particularly for the dry specimens, although permittivities may increase significantly at lower frequencies. It should be noted that previous work [3] suggests that single

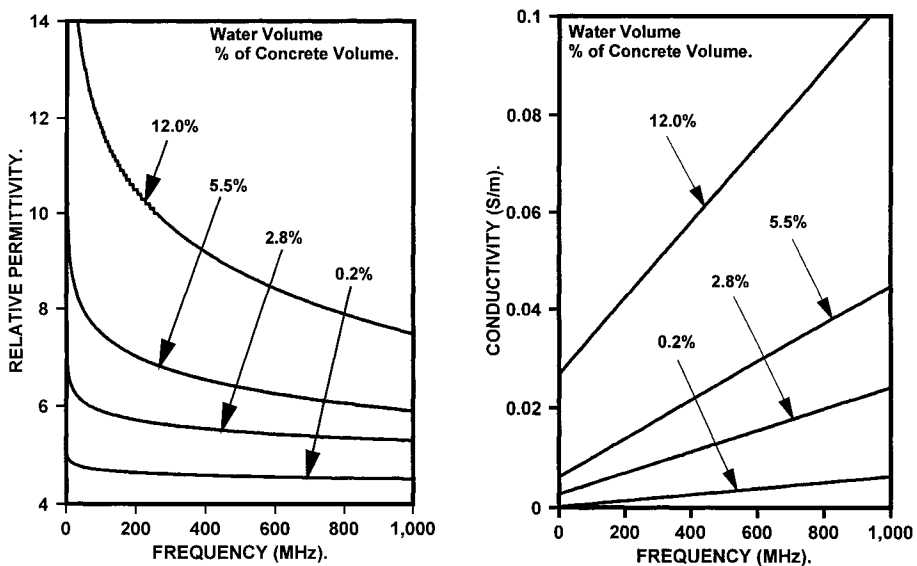


Fig. 2. Typical variations of permittivity and conductivity with frequency and moisture content.

frequency values at 500MHz may best represent the results obtained by a 1GHz broadband impulse antenna on concrete. Thus subsequent typical comparative plots are given for 500MHz.

Moisture content appears to be the dominant factor in determining the relative permittivity and conductivity of all concretes. Both of these properties increase with increasing moisture, as might be expected, indicating the dominant effect of matrix rather than aggregate (except where steel fibres are present).

Whilst relative permittivities increase approximately linearly over the whole range, as typically shown by Fig. 3, there is a tendency for conductivities to experience greatest change in the region above about 6 to 7% water volume. These % water volumes are associated with mature concretes in wetter conditions than achieved by air-drying in a laboratory environment.

The specimens shown in Fig. 3 are of same concrete mix but have received different conditioning regimes. In general, results fit together in a single curve although a number of general features are noted when all such plots are studied:

- There is a tendency for the initial value of permittivity and conductivity to lie slightly above the curve produced by subsequent drying and resaturation. This is possibly due to incomplete hydration effects at the time of initial testing.
- There is a tendency in some cases for the slope of the permittivity curve to decrease marginally decrease at very high moisture contents.
- Results for continuously saturated specimens are not invariant with age, but no consistent pattern emerges.

Figure 3 also illustrates the minor effects caused by temperatures in the range 0°C to 40°C on

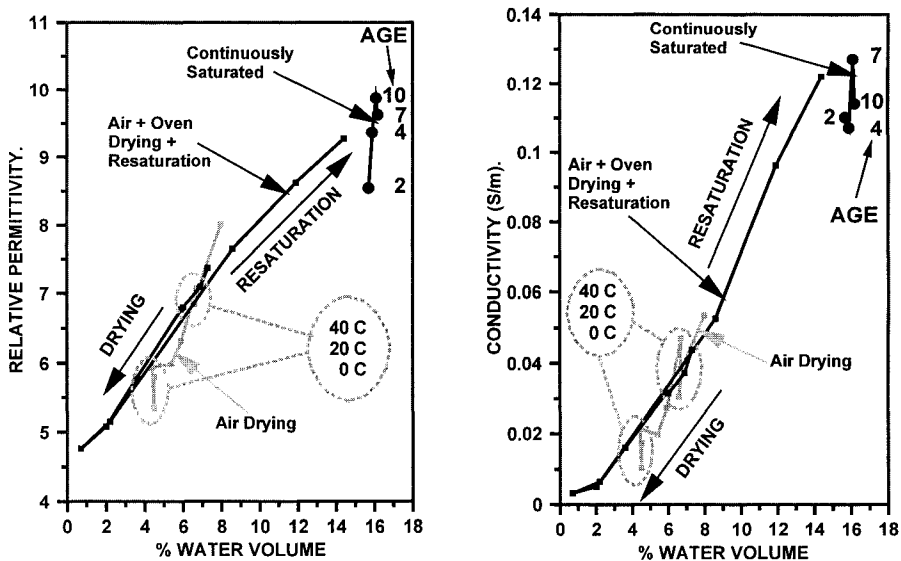


Fig. 3. Relative permittivities and conductivities with varying water volume (60MPa OPC Concrete). (All values are at 500MHz).

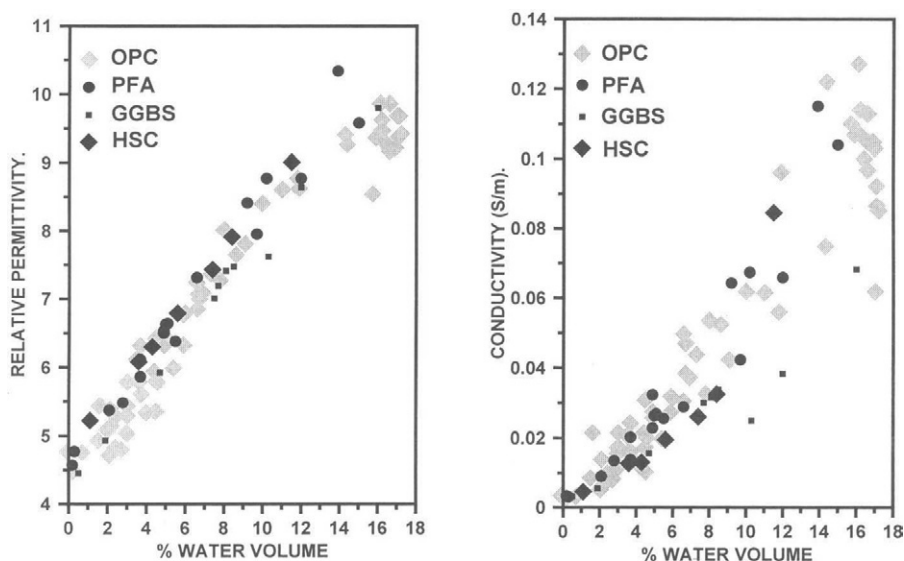


Fig. 4. Relative permittivities and conductivities for OPC, PFA, GGBS and high-strength concretes (HSC). (All values are at 500MHz).

air-dry concrete. The greatest effect noted here is on conductivity where a small increase can be seen as temperature increases, for moisture contents at approximately 7% by volume. There is, however, no significant change in permittivity with temperature.

Figure 4 combines all the results obtained for 10mm gravel concretes and the close grouping of permittivities for all concrete strength levels, irrespective of any cement replacement materials or chemical admixtures in the mix, is a key feature. A range of ± 0.5 can be seen at all moisture levels. It is noted however that conductivities for GGBS concrete appear to be reduced in comparison with similar plain concretes although PFA effects are minor.

The influence of steel fibres upon both permittivity and conductivity is very significant, see Fig. 5, leading to substantially increased values in each case with increasing fibre content. These were such that it was impossible to analyse results at frequencies above 500MHz, leading to the view that testing of such concretes in field situations is likely to be restricted to low frequency antennas.

The effects of salt content on the relative permittivity at 500 MHz were negligible, as can be seen in Fig. 5, (even in low strength concrete), although increased conductivity was noted as moisture content increased. It is clearly the dissolved salt content which is important. Al-Qadi [7] has suggested that greatest sensitivity to salt is at very low frequencies, thus at normal radar frequencies it is not possible to quantify salt content from permittivity measurements. Salt contamination may however in practice often be associated with high moisture contents, as in leaking bridge decks subjected to de-icing salt for example. In these circumstances, the increased conductivity may assist identification of such regions through increased signal attenuation.

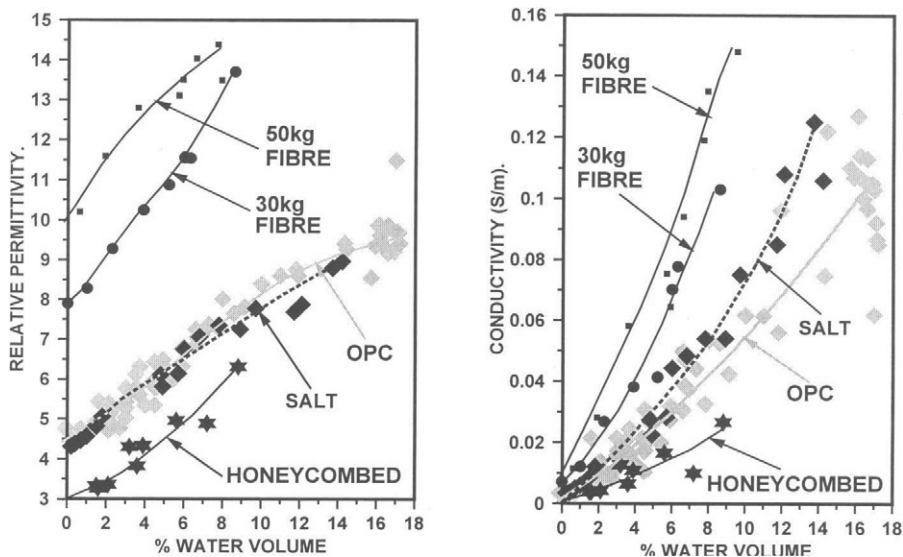


Fig. 5. Relative Permittivities and Conductivities for Fibre, Honeycombed and Salt impregnated Concretes (all values are at 500MHz).

Honeycombing was found to reduce both the relative permittivity and conductivity in comparison to similar strength but normal density concretes. It should be noted that it was not possible to obtain higher moisture contents than those shown in Fig. 5 due to the inability of the specimens to retain water as a result of their porous nature. On the other hand, transmission line tests were not possible at very low moisture contents due to disintegration of the specimens caused by oven drying.

CONCLUSIONS

The co-axial transmission line system has successfully and fully enabled the determination of the dielectric properties of laboratory concrete samples and a comprehensive set of data has been established for future reference. Specific conclusions arising from this work, within the ranges considered, are that:

1. Relative permittivity and conductivity both reduce with decreasing moisture content.
2. Differences due to mix constituents or strength level have minor influence compared to the effects of moisture (except when steel fibres or honeycombing are present). The influences on conductivity are however greater than on permittivity.
3. Resaturation appears to produce similar values for permittivity and conductivity to those obtained during drying.
4. Salt impregnation does not affect permittivity but slightly increased conductivities may be expected.
5. Steel fibres increase both permittivity and conductivity and such concretes are unlikely to be testable with higher frequency antennas.
6. Results for the specimens tested over a range of temperatures suggest that there is only

a small effect in relatively dry concrete. Supplementary tests on saturated concrete indicate similarly small effects on permittivity but suggest that the conductivity may increase with temperature.

The results of this work provide extensive and comprehensive reference data relating to the influence of variables considered upon the relative permittivity and electrical conductivity of concrete mixtures and conditions likely to be encountered in practice. The single frequency results have successfully permitted comparisons of the effects of the different parameters. Relationships between these discrete single frequency values and those obtained by broad-band commercially available field testing antennas are currently being investigated by comparison with results obtained on similar concretes by Building Research Establishment.

ACKNOWLEDGEMENTS

The authors gratefully acknowledge the financial support of the EU through Brite-Euram Project BE95-2109 "Subsurface Radar as a Tool for Non-Destructive Testing in the Construction and Building Industries". The helpful collaboration of the Partners in this project is also acknowledged, together with the contribution of Dr B. A. Austin of the Department of Electrical Engineering and Electronics in developing the transmission line equipment and providing access to support instrumentation used in the work.

REFERENCES

1. Concrete Society (1997), *Guidance on radar testing of concrete structures*, Tech. Rep. 48.
2. Shaw, M.R., Molyneaux, T.C.K., Millard, S.G., Bungey, J.H. and Taylor, M.J. (1998), In: *Proc. GPR 98*, University of Kansas, USA, pp. 449-454.
3. Bungey, J.H., Shaw, M.R., Millard, S.G., Soutsos, M.N. and Austin, B.A. (1997), *Insight*, 39, 7, 474.
4. Bungey, J.H. and Millard, S.G. (1993), *Proc. Inst. Civil Engineers, Structures and Buildings*, 99, 173.
5. Daniels, D. J. (1996), *Surface Penetrating Radar*, Inst. Electrical Engineers.
6. Shaw, M. R. (1998), *Advances in Cement Research*, 10, 4, 187.
7. Al-Qadi, I. L., Loulizi, A., Haddad, R., and Riad, S. M. (1997), In: *Proc. Structural Faults and Repair*, 2, 423-429, (M.C. Forde), Eng. Technics Press, Edinburgh, UK

This Page Intentionally Left Blank

RADAR INVESTIGATION OF HISTORICAL STRUCTURES

CH. MAIERHOFER, J. WÖSTMANN and D. SCHAURICH
*Federal Institute for Materials Research and Testing,
D-12205 Berlin, Germany*

ABSTRACT

In this paper, three case studies are presented of non-destructive radar investigations of the internal structure and moisture content of historic brick- and stonework. Part of this work was performed in the frame of a Brite EuRam project titled "Subsurface Radar as a Tool for Non-Destructive Testing and Assessment in the Construction and Building Industries".

KEYWORDS

Non-destructive testing, radar, cultural heritages, brickwork, stonework, masonry

INTRODUCTION

In the last ten years, the impulse radar technique has been increasingly adopted and applied for the non-destructive evaluation of the inner wall structure and moisture content of historic buildings. This includes the location of foundations [1], the investigation of the internal structure of pillars [2], masonry bridges [3] and stonework [4] and the assessment of old sluices [5]. Despite the inhomogeneous structure of historical brick and stone masonry which still remains a problem for data interpretation, several structural features could be detected. The great advantages of this technique are that it is completely non-destructive and the measurements can be performed quickly without a special coupling of the antenna to the surface.

In this paper, three case studies will be presented which demonstrate further important fields of the application of radar to the evaluation of structures and moisture condition of Cultural Heritages. Two of these case studies had been part of the Brite EuRam project No BE 95-2109 with the title "Subsurface Radar as a Tool for Non-Destructive Testing and Assessment in the Construction and Building Industries".

EXPERIMENTALS

For the impulse radar measurements, the GSSI SIR 10 A system was used together with the nominal 500 and 900 MHz antennas. This method is based on the propagation of short electromagnetic impulses which are transmitted into the building material using a dipole antenna. The impulses are reflected at interfaces between materials with different dielectric properties, i. e. at the surface and backside of walls, at detachments, voids, etc. When the transmitting and receiving antennas, which are often contained in the same housing, are moved

laterally over the surface of the object under investigation, radargrams (colour or grey scale intensity charts over position of the antenna and wave travel time) are produced. For more information about this technique, see [6].

CHURCH OF S. MARIA ROSSA IN MILAN, ITALY

The Church of S. Maria Rossa was built in different phases from IX-Xth cent. to XIIIth cent. over older buildings [7]. Some modifications and repair were made in 1783 and 1966. The present building shows parts of various ages. Excavations under the floor allowed to find portions of floors, mosaics and fragments of walls of the previous roman (ageing IInd cent. a C.) and paleocrisian buildings (Vth cent.). The walls were made of solid bricks and lime mortars. The Church was originally all frescoed, but at present it is possible to see only some traces of the ancient decoration. The water table is high, nearly superficial, in the area where the Church is situated. The Church is at present under the street level (see Fig. 1), close to an artificial channel (Naviglio). Furthermore the soil leans against the Church walls in the north side on the Naviglio channel. The area of the Church is characterised by the presence of several small channels built for agriculture necessities. All these factors produce a great presence of moisture which rises by capillary through the walls. Two photographs from the Church are shown in Fig. 2.

For structural as well as for moisture investigations, radar measurements were performed at three areas which are marked in the plan view in Fig. 1. For the determination of depth resolved moisture distribution, microwave transmissions measurements in thin boreholes using two small dipole antennas were accomplished [8]. At **area 1**, the brickwall is almost the original one with a texture of solid brick and hydrated lime mortars. The thickness of the walls is about 52 cm. This area is localised under the street level, in direct contact with the soil. Thus, a very high moisture content was expected. In the radargrams recorded with the 500 MHz antenna as shown in Fig. 3 left, reflections from the backside are hardly visible due to the very high moisture content and due to the presence of soil directly at the backside, which has a similar dielectric constant as the wet brick material. From some of these very weak reflections, a mean integrated real part of the complex permittivity of about 12.8 could be calculated with an absolute error of 1.0. Extrapolating the calibration curves of [9], this corresponds to an absolute moisture content of about 25 vol%. In Fig. 3 right, the depth re-

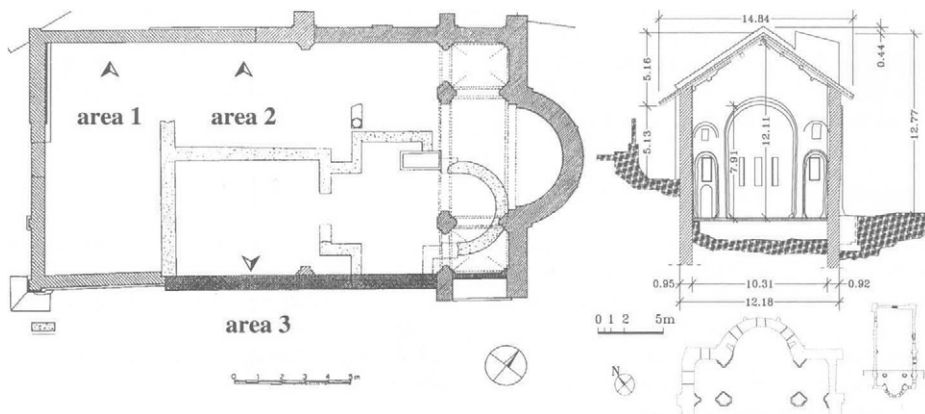


Fig. 1. Plane view and section of the Church of S. Maria Rossa. The location of the three areas investigated are indicated by arrows.

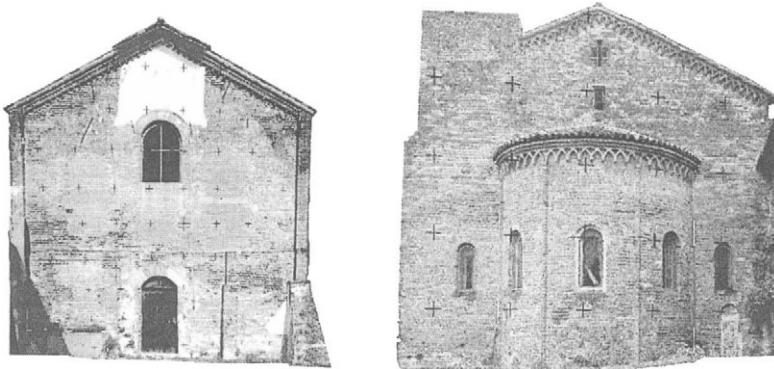


Fig. 2. The Church of S. Maria Rossa.

solved real part of the complex permittivity determined with the microwave borehole system is presented. Here, the real part of the complex dielectric constant increases up to 17 in the middle of the wall while it decreases to 11 and below at the front and back sides. The mean real part is equal to 12.4, which is close to the value obtained by radar. Both values are included in Fig. 3 right as parallel lines.

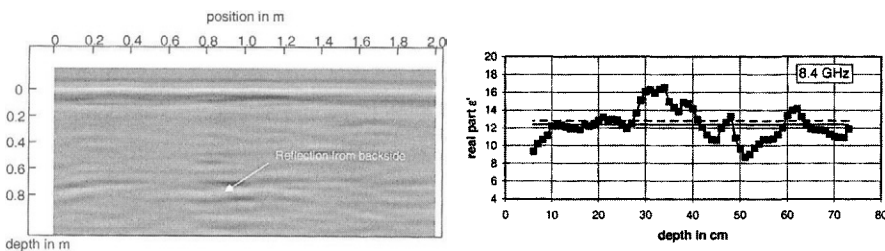


Fig. 3. Radargram recorded with the 500 MHz antenna (left) and depth resolved distribution of the dielectric constant and thus the moisture content as determined with the microwave borehole system (right) at area 1.

Area 3 is localised in the most ancient part of the Church dating IX-Xth century, located at the south side. Close to this area there is an infilled door. This work was done during the repairs of 1966. The brickwork is characterised by new brick and cement mortars. Figure 4 left shows the radargram of a horizontal scan in the middle of area 3, recorded with the 900 MHz antenna. On the right side of the radargram, the reflection from the backside is very clear. Thus, the depth scale of the radargram was calibrated from the known thickness of the wall of 60 cm (length of the boreholes). From the backside reflection, a real part of permittivity of about 4 was calculated. On the left side of the radargram, no backside reflection is visible but a very strong reflection occurs at a depth of approximately 20 cm. This reflection might be due to a detachment at the interface of the new brick material to the old material. After the radar measurements, a brick was removed from this area and a void was found with a thickness of about 25 cm. Thus it can be concluded that this region consists of two leaves: The internal leaf is made of new brickwork having a thickness of about 22 cm while the external leaf has a greater depth and is made of old brick material. The depth resolved real part which was

determined at 10.4 GHz is demonstrated in Fig. 4 right. This shows a maximum value of the real part of 5.8 at a depth of 11 cm and a mean value of 5.1 being relatively dry.

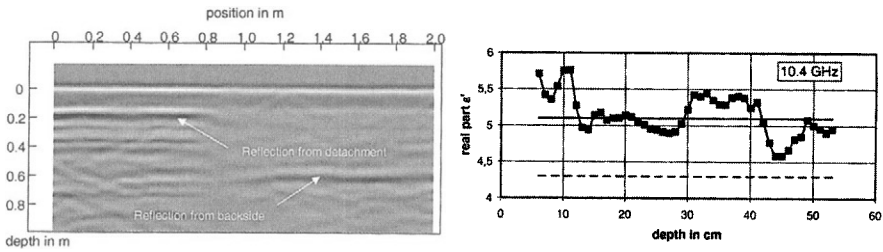


Fig. 4. Radargram recorded with the 900 MHz antenna and depth resolved distribution of the dielectric constant and thus the moisture content as determined with the microwave borehole system at area 3.

More details about the investigations at the Church can be found in [10].

PETERSHOF IN HALBERSTADT, GERMANY

The Petershof in Halberstadt, Germany, is a former episcopal see which was built from 1035 to 1059. In 1552 and 1566, the Romanesque building was replaced by a Renaissance castle. The chapel called Petrikapelle was changed to the today's hall building during the 14th century. Below the main building, there are several barrel vaults, which go back to the Romanesque. In 1650, the building was utilised by the government of Brandenburg. In the 19th and 20th century until the end of the Second World War, the Petershof was the seat of the Inferior Court. Then, the building was used as a prison and also as the Public Record Office. Since several years now, the building is empty and has to be refurbished for further use.

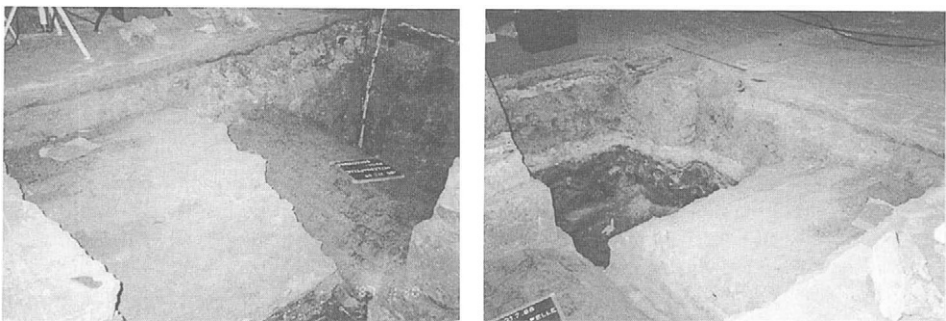


Fig. 5. Two barrel vaults below the floor of the chapel of the Petershof.

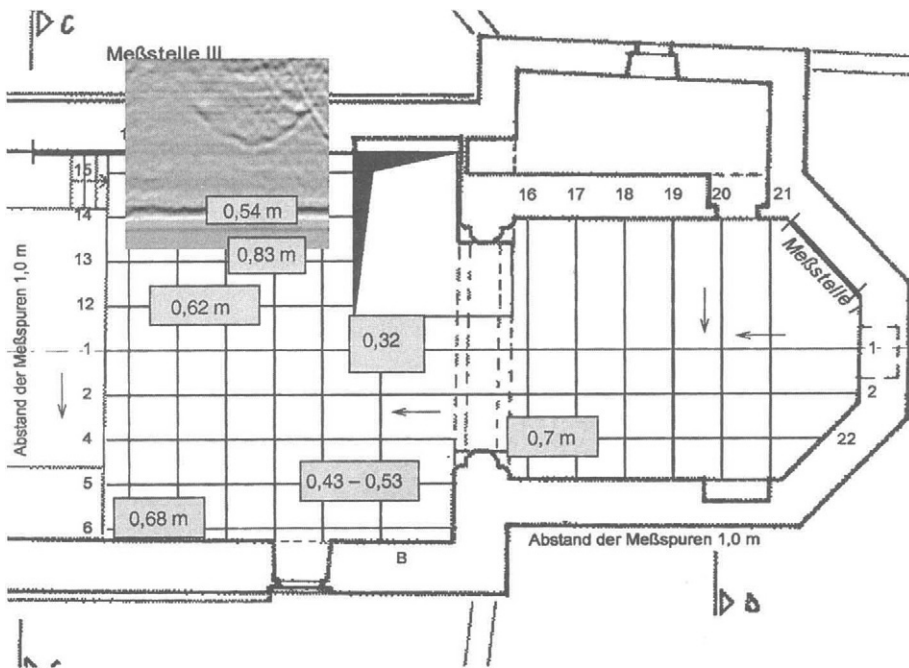


Fig. 6. Position and size of the barrel vaults (grey rectangles) below the floor of the chapel localised with radar. The values in the rectangles are information about the depth of each vault. The radargram is an example showing a large hyperbola representing one vault at a depth of 0.54 m.

For this refurbishment, the structure and moisture content of stonework and subsurface ground floor had to be investigated. Below the floor of the chapel, two barrel vaults were found by careful digging. These vaults are shown in Fig. 5. It was expected that further vaults are existing, therefore a grid of traces was recorded with radar using the 500 MHz antenna as displayed in the plan view in Fig. 6. Several vaults were localised with radar, which are all shown as grey rectangles in Fig. 6. In this plan, also one radargram of a vault is displayed as an example. The reflection from the vault appears as a large hyperbola at a depth of about 0.54 m.

ALTES MUSEUM IN BERLIN, GERMANY

The Altes Museum in Berlin, Germany, was built from 1822 to 1830 by Karl Friederich Schinkel (see Fig. 7). For the planning and preparation of restoration, the internal structure of the brickwork of the rotunde in the centre of the building, had to be investigated non-destructively by radar. The main aim was the location of voids and larger hollow spaces which might be used as installation wells.

All radar measurements were performed with the 500 MHz antenna in reflection configuration along both sides (surfaces) of the exterior walls of the rotunde in horizontal traces. These horizontal traces are all included in the plan view of the rotunde in Fig. 10 as arrows and are marked by numbers. The height of the traces related to the ground floor of the rotunde was 1 m.



Fig. 7. Left: Portico facade of the Altes Museum as shown from the Lustgarten [11]. Right: Perspective from the inside of the rotunde [11].

In the following, two selected radargrams are presented. Figure 8 shows the radargram of trace No. 4 which was recorded from the inside of the rotunde along a distance of 16.6 m. In this radargram, many reflections are visible. Five of them as marked with letters can be easily related to hollow spaces:

- a: Reflection directly below the surface reflection along a distance from 0.96 to 2.6 m: This reflection can be related to a niche which was used for the room heater (radiator).
- b: Reflection at a depth of 1.5 m at a distance of 6.4 m. This reflection occurs at the inner side of the staircase.
- c, d: Reflections at depths of 1.9 and 1.13 m at distances of 9 and 12.5 m. These reflections can be related to small chambers inside the brickwork.
- e: Reflection at a depth of 1.55 m at a distance of 13.7 to 14.6 m: Reflection at the backside of the wall.

Figure 9 shows a radargram containing the traces No. 12, 13 and 14 which were recorded at the backside of the same wall as trace No. 4. Here, seven reflections can be related to the following structures:

- a: Reflection from a depth of 1.57 cm, which can be related to the backside of the wall (comparable to reflection e in Fig. 8)
- b, c, d, e: Reflections from depths between 0.1 and 0.3 m and in distances of 10.37, 11.38, 13.19 and 15.1 m related to the beginning of the trace. From the shape of the hyperbolas it can be concluded that these reflections belong to regular voids or to vertical pipelines (electricity, water etc.).
- f, g: Reflections from a depth of 0.3 m at a distances between 13.7 to 14.6 m and 17.9 to 18.8 m: These reflections belong to two small chambers (comparable to the reflections c and d in Fig. 8).

All pipelines and hollow spaces inside the brickwall of the rotunde which were detected by radar are visualised in Fig. 10. In addition to the known chambers and structures, three additional chambers and several voids and/or pipelines could be localised. In some areas, the actual thickness of the wall could be determined. In all radargrams, the reflections were very clear which is a hint for homogeneous and dry brickwork. In some radargrams additional weak reflections could be observed deep inside the brickwork which were not related to any structures and which might not be relevant for the restorations.

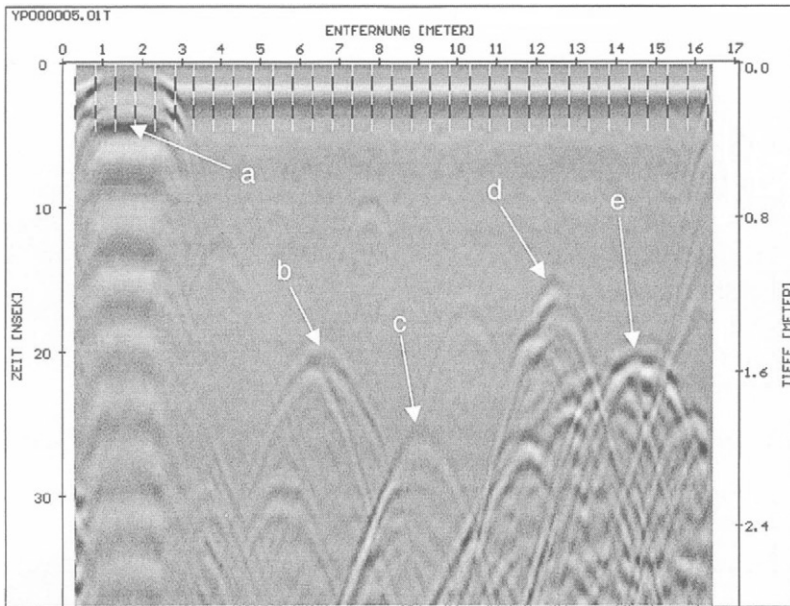


Fig. 8. Radargram of trace No. 4 recorded with the 500 MHz antenna from the inside of the rotunde.

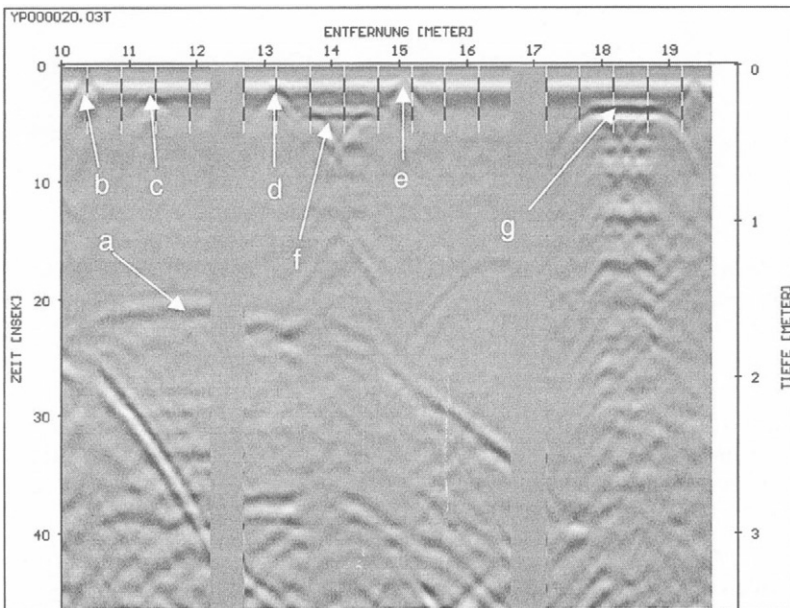


Fig. 9. Radargram of the connected traces No. 12, 13 and 14 recorded with the 500 MHz antenna from the outside of the rotunde.

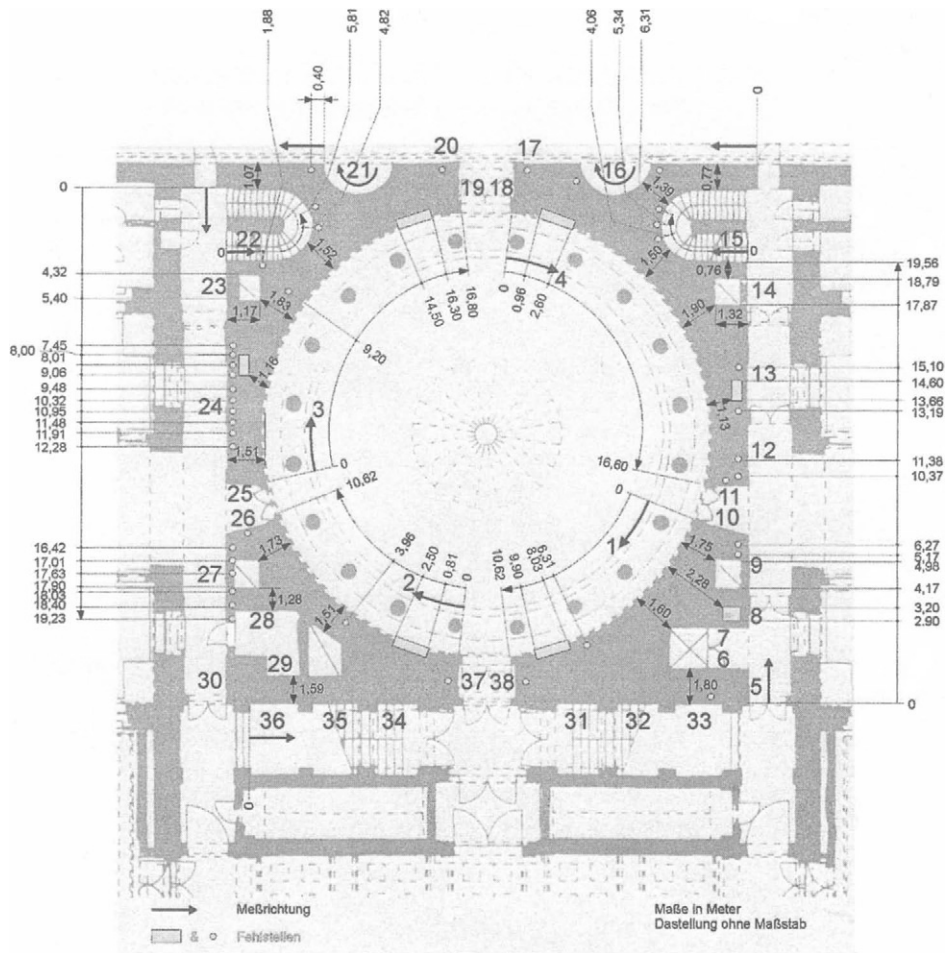


Fig. 10. Plan view of the rotunde inside Altes Museum showing the radar traces and the localised voids and larger hollow spaces.

ACKNOWLEDGEMENTS

Part of this work was founded by the European Commission as a Brite EuRam Project No. BE 95-2109 in the 4th Framework Programme. The title of the project was “Subsurface Radar as a Tool for Non-Destructive Testing and Assessment in the Construction and Building Industries”.

The investigations at the Church of S. Maria Rossa were performed in close co-operation with the working group of Prof. L. Binda from Politecnico di Milano, Italy.

The radar measurements at Altes Museum were supported by the Bundesamt für Bauwesen und Raumordnung, Germany.

REFERENCES

1. Kahle, M., Illich, B. and B. Serexhe: Erkundung des Untergrundes der Kathedrale von Autun mit dem Radarverfahren, Universität Karlsruhe, Jahrbuch, 1990
2. Bernabini, M., Pettinelli, E., Pierdicca, N., Piro, S. and L. Versino: Field experiments for characterisation of GPR antenna and pulse propagation, *Journal of Applied Geophysics*, Vol. 33, 1995, pp. 63-76.
3. Colla, C., Forde, M. C. and P. C. Das: Radar imaging in composite masonry structures, Forde, M. C. (ed.), *Proc. of 7th Int. Conf. on Structural Faults and Repair*, Edinburgh: Engineering Technics Press, Vol. 3, 1997, pp. 493-504.
4. Binda, L., Lenzi, G. and A. Saisi: NDE of masonry structures: Use of radar test for the characterisation of stone masonries, Forde, M. C. (ed.), *Proc. of 7th Int. Conf. on Structural Faults and Repair*, Edinburgh: Engineering Technics Press, Vol. 3, 1997, pp. 505-514.
5. Maierhofer, Ch., Krause, M. and H. Wiggenhauser: Non-destructive investigation of sluices using radar and ultrasonic impulse echo, Forde, M. C. (ed.), *Proc. of 7th Int. Conf. on Structural Faults and Repair*, Edinburgh: Engineering Technics Press, Vol. 3, 1997, pp. 467-474.
6. Daniels, D. J.: *Surface-Penetrating Radar*, London: The Institution of Electrical Engineers, 1996.
7. Lucarelli, C. and M. Nastase: Aspetti preliminari al progetto di recupero di „Cascina Chiesa Rossa“, L'evoluzione del complesso e l'approccio sperimentale alla fase di rilevamento, M.Sc. Thesis Work supervised by Binda, L., Guzzetti, F., Faculty of Architecture, Politecnico of Milan, Milan
8. Rudolph, M., Schaurich, D. and H. Wiggenhauser: Feuchteprofilmessungen mit Mikrowellen in Mauerwerk, Wiggenhauser, H., Müller, H. S. and N. Girlich (eds.), *Tagungsbericht Feuchtetag 21.09.1993*, Berlin: DGZfP, 1993, pp. 44-56.
9. Maierhofer, Ch., Leipold, S. and H. Wiggenhauser: Investigation of the influence of moisture and salt content on the dielectric properties of brick materials using radar, *Proceedings of the 7th International Conference on Ground Penetrating Radar (GPR)*, Kansas, USA: Radar Systems and Remote Sensing Laboratory, University of Kansas, Vol. 2, 1998, pp. 477-484.
10. Maierhofer, Ch., Leipold, S., Schaurich, D., Binda, L. and A. Saisi: Determination of the moisture distribution in the outside walls of the S. Maria Rossa using radar, *Proceedings of the 7th International Conference on Ground Penetrating Radar (GPR)*, Kansas, USA: Radar Systems and Remote Sensing Laboratory, Vol. 2, 1998, pp. 509-514.
11. <http://www.quondam.com/fos>

This Page Intentionally Left Blank

ESTIMATION OF THICKNESS AND WIDTH OF VOID UNDER CONCRETE SLAB USING RADAR IMAGE PROCESSING

S. K. PARK

*Assistant professor
Department of Civil Engineering,
University of Taejon,
96-3 Yongwoon-tong, Tong-ku,
Taejon 300-716 Republic of Korea*

T. UOMOTO

*Professor
Center for Collaborative Research
University of Tokyo,
22-1, Roppongi, 7-chome, Minato-ku
Tokyo 106-0032 Japan*

ABSTRACT

The presence of voids under concrete slabs (such as pavements) or behind tunnel linings results in the deterioration. One method of detecting such voids by non-destructive means is radar. This research is devoted to easily evaluating the efficiency of such non-destructive tests with radar. As a foundation to this ongoing research, which aims to detect only voids and estimate the cross-sectional size (thickness and width) of voids using radar, a new method based on radar image processing is carried out with various void sizes and depths.

The regression relationship between void size (thickness and width) which has different depth and the amplitude characteristics of the radar return is considered in a new method of this research. For the purpose of examining this regression relationship, experiments with change of void depth, surface area and thickness were carried out. Finally, the threshold value for image processing which aims to represent only voids to be fitted size (width) can be obtained.

As a result, a proposed method in this study has a possibility of detecting only voids and estimating void size (thickness and width) with good accuracy.

KEYWORDS

Radar, Void thickness, Void width, Concrete slab, Image processing

INTRODUCTION

The presence of voids under concrete slabs (such as pavements) or behind tunnel linings is very likely to result in settlement or structural collapse. However, a characteristic of such voids is that they cannot be detected easily by visual inspection. To effectively locate voids using non-destructive methods is not easy, but one method using radar has been proposed. The advantage of radar is that it can be used to survey a broad area at relatively high speed. Consequently, radar can be regarded as the optimum method for detecting voids under the pavements or behind tunnel linings.

More than simply judging the existence of voids under pavements or behind tunnel linings, this research aims to develop an analysis technique of non-destructive test (NDT) capable of evaluation of void size. In order to achieve these goals, the following issues are investigated in this research: (i) an identification system for the size and location of voids from image data; (ii) the prediction of void thickness and width by low-resolution radar. The results of this work verify the possibility of a labor-saving NDT system using radar. Subsequently, experiments are conducted to detect the thickness and width of voids under non-reinforced concrete pavements (or tunnel linings).

ANALYSIS METHOD AND EXPERIMENTAL

Basic Principles and Concepts

Materials under concrete pavements or behind tunnel linings are commonly composed of soil or rock material. The relative dielectric constant of a void, which represents electrical properties of a material, is 1, and that of soil or rock material is in the range of about 10~30. As the electrical property of a void under concrete pavements or behind tunnel linings is different from that of surrounding materials, it shows high amplitude of electromagnetic radar return. The relative dielectric constant of metallic material such as steel bar being almost infinity, the shape of reflected radar pulse of metallic material is clearly distinguished from that of a void. Also, each wave shape appears differently in same medium, the reflected radar pulse of metallic material may be distinguished from that of a void in advance.

From the above characteristics, if the signal from a void in radar image can be thresholding by the threshold value of certain amplitude of radar return, both the detection of just a void and the size of a void can be displayed in image. Though those shapes of voids are confined to co-axial ones, it is reported that the generally discovered shapes of voids under pavements are nearly co-axial.

Fig. 1 shows the results of displaying the gradient vectors for radar image of voids in Fig. 10(a) into a vector larger than a definite value. Fig. 2 shows the results of three-dimensional transformation of these light and shade distribution of images. In Fig. 1, it may be known that only the most strongly reflected group located at the nearest distance between a void and an antenna remains finally. This group becomes an assembly of signals reflected after the vertical incidence of electromagnetic wave on the surface of a void. Therefore, if this group may be thresholding by defining threshold value so that only the images which are correspondent to the size (width) of a void can be remained, just a void and its width may be displayed on image. These concepts may be understood easily by thresholding of light and shade distribution reflected from a void (radar image of Fig. 2) as shown in Fig. 3.

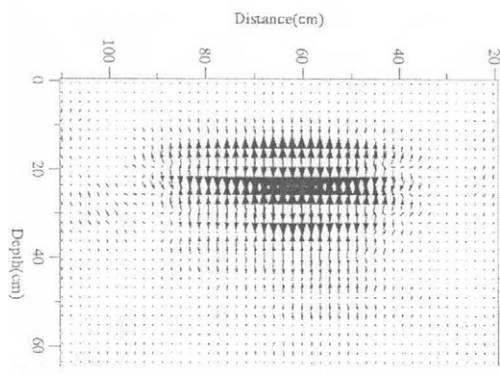


Fig. 1. Gradient vectors for radar image of voids

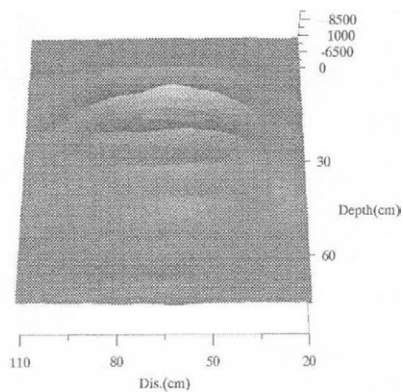


Fig. 2. Three dimensional image of a void

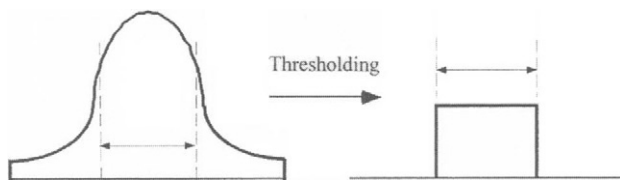


Fig. 3. Concept of thresholding

In the present study, we selected and tested the influential factors of embedding depth, size and thickness of voids, characteristics of attenuation compensation of radar, and so on. The relationship equation was induced to define the threshold value to perform the mentioned thresholding through the integration of test results for each factor. As various influences of each factor were considered, this equation may be applied, regardless of void size and embedding depth, and so forth. But, in the application of the present solution, it is assumed that surrounding medium has comparatively constant electrical property, and also detectable voids are confined to ones having co-axial shape.

Estimation of Void Thickness

A void under concrete slabs (such as pavements) or behind tunnel linings will cause radar returns (reflected radar pulses) to appear as shown in Fig. 4. Since the dielectric constant of concrete or soil is greater than that of air, the reflection coefficient at a concrete/void or soil/void interface is positive. However, the reflection coefficient at a void/soil interface is negative. Thus, the reflected pulses from these two boundaries are of different polarities, as indicated in Fig. 4.

The time separation between the pulses from the top and bottom of the void is proportional to the void thickness in the direction of incidence. The relationship between an air void thickness, $D(\text{cm})$, and pulse separation $t(\text{nanoseconds})$ is as follows[1]:

$$t = \frac{2D}{v} = \frac{2D\sqrt{\epsilon_r}}{c} = \frac{D\sqrt{\epsilon_r}}{15} \quad (1)$$

where ϵ_r is the relative dielectric constant of the medium and c is the speed of light ($3 \times 10^8 \text{ m/s}$).

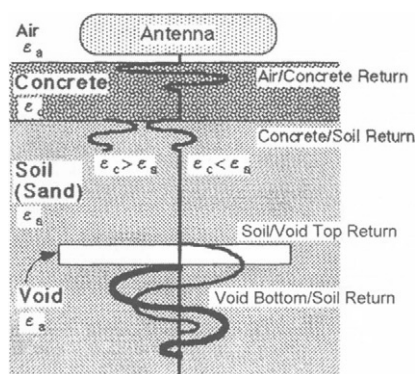


Fig. 4. Behavior of radar returns at multiple boundaries.

The radar used in this study (central frequency: 600MHz) has a pulse length of about 1.7 nanoseconds. Thus, a void thickness must be greater than 26cm if the reflected radar pulses from the concrete or soil/void and void/soil interfaces are not to overlap in time. Since many voids are expected to be less than 26cm, the radar returns from the top and bottom of the void will overlap. However, the amplitude of the composite pulse will vary depending on the time separation between the two pulses. Thus the amplitude characteristics of the radar return can be used to estimate void thickness even if actual radar returns from the top and bottom of the void cannot be distinguished.

The regression relationship between void thickness and the amplitude characteristics of the radar return is considered in this study. For the purpose of examining this regression relationship, the following experiments were carried out. The experimental design is indicated in Table 1.

First, the regression relationship between the maximum amplitude characteristics of the radar

return and void depth was examined under conditions of constant thickness and surface area. Next, to be examined was the regression relationship between the maximum amplitude characteristics of radar return and the void surface area under conditions of constant thickness and depth. Last, the regression relationship between maximum amplitude and void thickness was examined under conditions of constant depth and surface area. The equation given below was obtained by arranging the regression equations as above using a proportional expansion of each equation. In particular, equation (2) includes the parameters STC. STC is a function compensating for the exponential attenuation of electromagnetic waves according to additive propagation distance (depth) in a dielectric medium. This function is useful in that it allows detection of the radar return from objects at comparatively deep locations. However, it has different properties depending on the actual radar apparatus used. Equation (2) allows STC to be applied to any radar apparatus.

$$T_{STC_x}(cm) = \left[\frac{4020 - R_{m/STC1} \frac{A}{1.6 \times 10^6 B} e^{-0.0378D(cm)}}{49.1} \right] \tag{2}$$

where, T_{STC_x} is the estimated value of void thickness and R_{m/STC_x} is the maximum amplitude of the radar return from the void when parameter STC is not applied. Coefficients A and B can be calculated by equation (3), which is obtained from the relationship between maximum amplitude of the radar return and the void depth when STC is applied. D is the void depth.

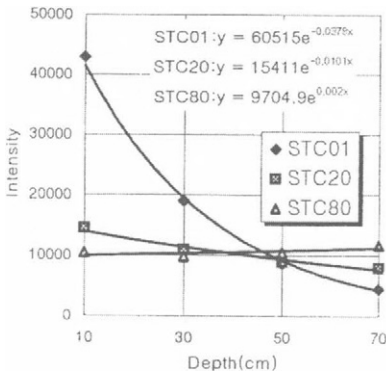


Fig. 5. Relationship between maximum amplitude characteristics of radar return and void depth when STC 1, 20, and 80 are applied

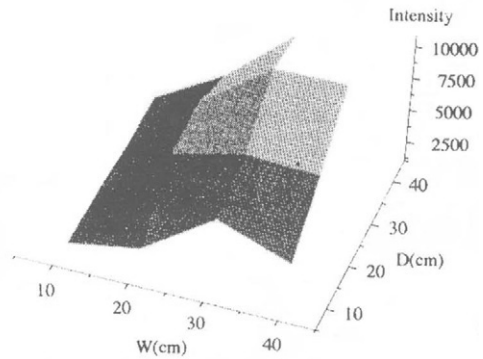


Fig. 6. Relationship between maximum amplitude characteristics of radar return and void surface area

$$R_{m/STC_x} = Ae^{-BD(cm)} \tag{3}$$

where, R_{m/STC_x} is the maximum amplitude of the radar return from the void when STC is applied. The values of STC used this study range from 1 to 80. The larger this number becomes, the greater the attenuation compensation. The relationship between the maximum amplitude of the radar return and void depth is compared in Fig. 5 for representative STC values of 1, 20, and 80. As is clear from this Fig., the maximum amplitude of radar return varies not only with void depth

but also with STC. Thus, a suitable STC has to be chosen according to the properties of the radar apparatus in use when this function is applied.

Table 1. Experimental design for estimation of void thickness and width (W, D, and H are defined in Fig. 7)

	Void condition (Unit: cm)	
	Fixed factor	Variable factor
Change in void depth	W40,D40,H10	Depth 10,30,50,70
Change in void surface area	Depth30,H10	
	W10	D10,20,30,40
	W40	D10,20,30,40
	D10	W20,30,40
	D40	W20,30,50
	W20	D20
	W30	D30
	W50	D50
Change in void thickness[H]	Depth30, W40,D40	H2,10,20,30

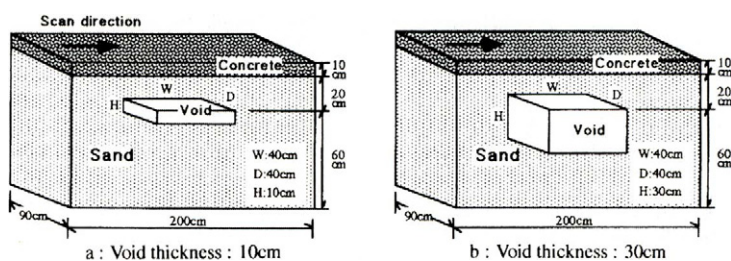


Fig. 7. Examples of experimental conditions for detecting voids of square plane form (co-axial type) and of different thicknesses (10cm, 30cm) under non-reinforced concrete slab

This method is valid only for the estimation of void thickness when the void surface area is greater than $W40\text{cm} \times D40\text{cm}$. [Definitions of W and D are given in Fig. 7.] The reason for this is that the maximum amplitude of the radar return from voids of this surface area is uniform, as shown in Fig. 6. Thus, void thickness can be estimated from equation (2) regardless of the influence of void surface area only if the void surface area is greater than $W40\text{cm} \times D40\text{cm}$.

Experimental Conditions

Experiments on the detection of voids (estimation of thickness and width) under concrete slabs (such as pavements) or behind tunnel linings were performed as shown in Fig.7 under experimental design of table 1. As one example, Fig. 7 shows the experimental conditions in the case of voids with a square plane form (co-axial type) and various thicknesses (10cm, 30cm) under a non-reinforced concrete slab.

Mix conditions of the concrete slab were w/c; 55%, s/a; 46%, slump; 5cm, maximum aggregate size; 22mm and compressive strength at 28days; 240kg/cm^2 . In all cases, the water content of the sand in the material under the concrete slab was from 1.7 to 3.4%.

Measurement system

Ground probing radar was used for measurements in this experiment. The frequency of this radar is from 20 MHz to 1GHz (central frequency: 600MHz) and the antenna system is a 3-dipole type.

Image Processing to detect the signal and size(width) of a void

Fig. 8 shows a flowchart of the procedure of image processing by thresholding to detect the signal and size of a void from measured radar image. The details of the procedure are as follows.

(1) Performance of preliminary test for medium to be detected

It should be performed to measure the sample voids that are arranged in constant depth to define representative characteristic values under the real condition of measurement. Being difficult to form these arranged voids realistically, those sample voids should be made artificially of the medium of which the relative dielectric constant is nearly zero, for example styrofoam, etc. If the relative dielectric constant of the artificial medium is n , it should be corrected in the ratio of n to 1.

(2) Definition of threshold value of the amplitude of radar return from a void

After test for a sample void under the real condition of measurement, the threshold value of the amplitude of radar return from a void is defined to obtain, in the axis of distance, the signal of the size of a void which is almost equal to its size in test. Because the depth and thickness of a sample void from the threshold value determined by the equation (2) become a standard value, the width of the void in the optional field condition can be naturally known from the result of image processing, and then the thickness can be calculated by the equation (2)

(3) Input of information and threshold value of a sample void and Correcting the equation as a proper one under the measurement condition

The equation is corrected to meet properly the measurement condition by making use of the information(thickness and depth) and the threshold value of a sample void.

(4) Performance of operation of measurement

The operation of measurement in the field is performed through the above procedure.

(5) Removal of reflected waves from continuous boundary layer

In radar image obtained by the mentioned procedure, reflected waves from continuous boundary layer such as concrete slab or lining, is removed by the common method which can remove surface wave.

(6) Judgement for possibility of discrimination of voids and Application of threshold value

The obtained radar images are reprocessed according to the distinguishable degree of a void. If the distributed domain of voids can be known from a measured image(able to discriminate voids), the threshold value may be defined in advance by inputting the depth of the domain of voids to the equation (2) that is gone through the above procedure (2) and (3). If the depth of voids cannot be defined in advance(unable to discriminate voids), voids may be automatically detected by the discriminative application of the threshold value for each depth from the equation (2).

(7) Thresholding of images by weight function

From the above threshold value, all images are processed by thresholding using the weight function that define images over the threshold value as 0(black) and images under the threshold value as 1(white).

(8) Correction of depth of voids

For the detective apparatus by radar, the depth of voids should be corrected properly to field condition by a sample void. As radar apparatus, according to its type, displays the depth of an objective by assuming that the relative dielectric constant of medium is a constant value, the depth of the objective may be displayed differently from its real depth, and, therefore, this operation is performed to correct these effects.

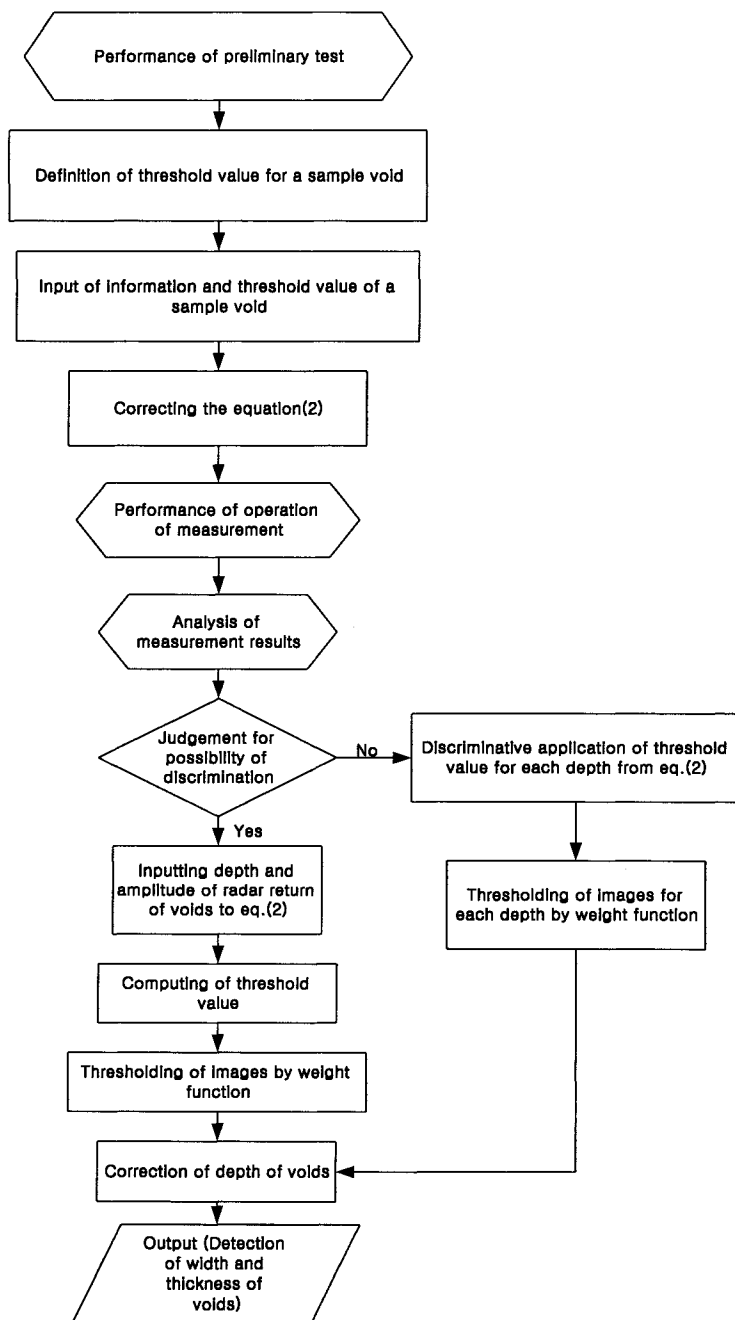
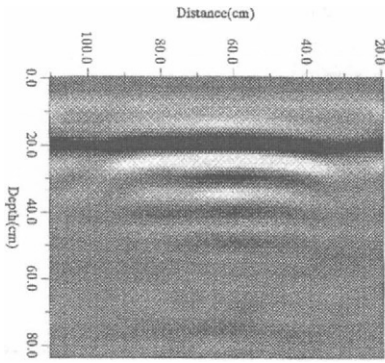
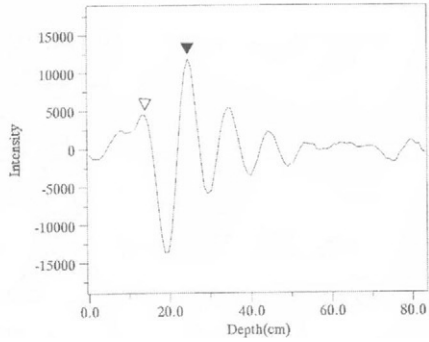


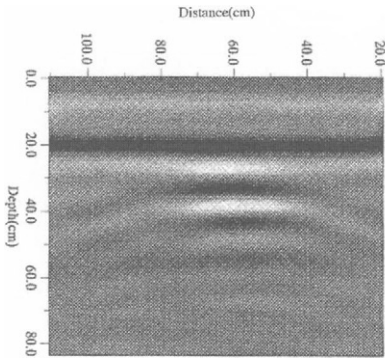
Fig. 8. Flowchart of the procedure of image processing by thresholding to detect the signal and size of a void from measured radar image



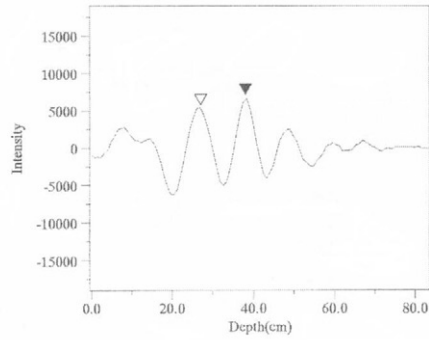
(a) W40,D40,H10,Depth 10cm



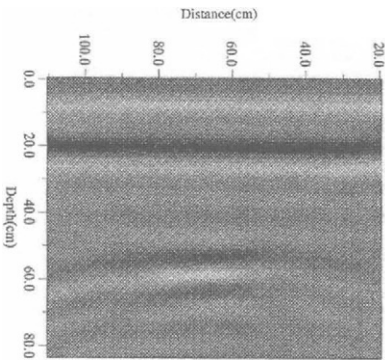
(b) Maximum amplitude of radar return from void of (a)



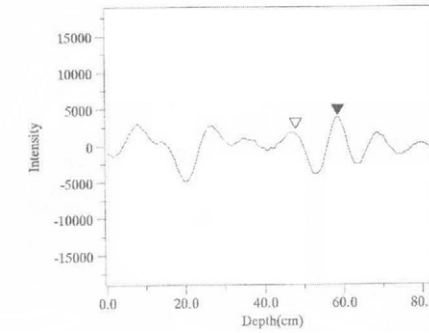
(c) W40,D40,H10,Depth 20cm



(d) Maximum amplitude of radar return from void of (c)



(e) W40,D40,H10,Depth 30cm



(f) Maximum amplitude of radar return from void of (e)

Fig. 9. Examples of radar images in case of different depths (10,20 and 30cm from surface)

RESULTS AND DISCUSSION

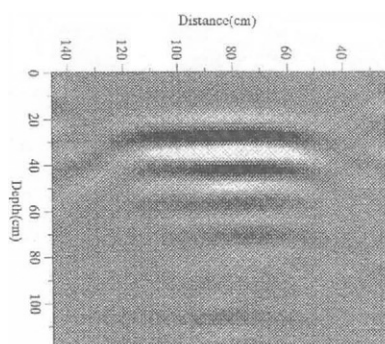
Results of image processing and discussion

Fig. 9 shows the radar image for a representative case (change in void depth) among the results of

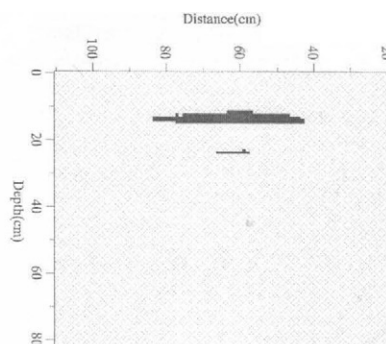
Table 2. Results of detection of a void size (width) by image processing for each condition (unit:cm)

	Experimental Conditions	Void size (Width)	Results	Relative error	Average error
Change in void depth	W40,D40,H10				
	Depth 10	40	40	0	
	30	40	36	-4	-1.5
	50	40	39	-1	
Change in void surface area	W10,D40,H10	10	-	-	
	W20,D40,H10	20	23	+3	+3.5
	W30,D40,H10	30	34	+4	
Change in Void thickness	W40,D40,H20	40	34	-6	-4.0
	W40,D40,H30	40	37	-3	

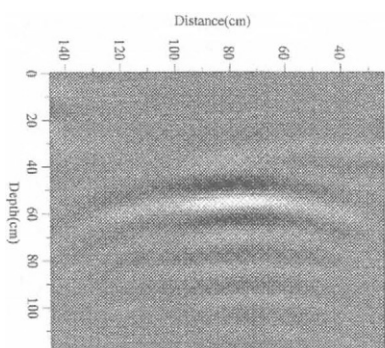
measurement obtained under the former experimental condition. Fig. 10 shows the result of image processing for Fig. 9 through the mentioned procedures. Table 2 shows the result of detection of a void size (width) by putting together the results of image processing for each condition. As shown in this result, it shows good result that the average of the errors for relative values of the size (width) of a void is -1.0cm and the average of absolute values is 2.8cm. Therefore, it is analyzed that the solution for the detection of voids suggested in the present study is effective.



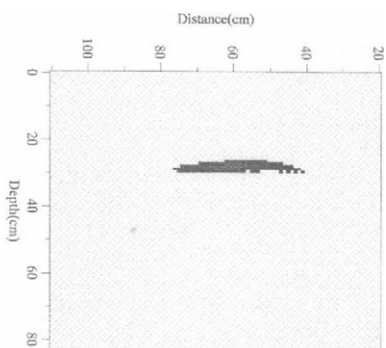
(a) Removal of surface wave in Fig. 9(a)



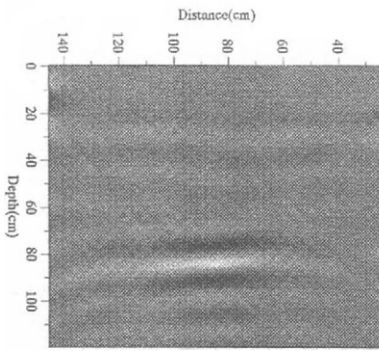
(b) W40,D40,H10,Depth 10cm



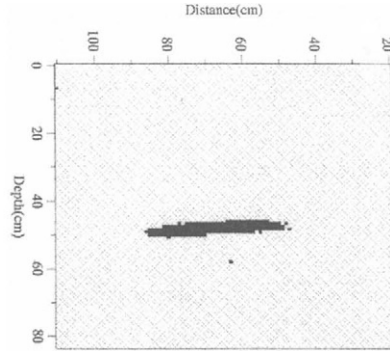
(c) Removal of surface wave in Fig. 9(c)



(d) W40,D40,H10,Depth 20cm



(e) Removal of surface wave in Fig. 9(e)



(f) W40,D,40,H10,Depth 30cm

Fig. 10. Results of image processing for Fig. 9

CONCLUSIONS

1. The availability of a new method for detecting voids under non-reinforced concrete slab has been verified. The precision of the results obtained by this proposed method is considered acceptable. It shows good result that the average of the errors for estimated values of the size (width) of a void by the proposed equation in this study is -1.0cm and the average of absolute values is 2.8cm . Therefore, it is analyzed that the method for the detection of voids (or the estimation of size of it) suggested in the present study is effective.
2. In the case of estimating void size (thickness and width), it should be noted that the new method is only available for co-axial shape voids, such as voids with a square plane form, and is valid only for the estimation of void thickness when the void surface area is greater than $W40\text{cm}\times D40\text{cm}$. But, this method is can be applied for the detection of just a void and the estimation of void width by image processing when the void surface area is greater than $W20\text{cm}\times D40\text{cm}\times H10\text{cm}$.

ACKNOWLEDGEMENTS

This study was carried out at the University of Tokyo, Uomoto laboratory. The authors would like to thank Mr. D. Sakamoto of Fujita Corporation and other collaborators for their kind contribution in performing the experiments.

REFERENCES

1. J.R.Moore, J.D.Echard and C.G.Neill, *Radar Detection of Voids under Concrete Highways*, IEEE International Radar Conference, pp.131~135, 1980
2. S.K.Park, T.Uomoto, *Estimation of The Volume of Three-Dimensional Subsurface Voids Using Three-Dipole Radar*, Concrete Library of JSCE, No.33, June 1999
3. S.K.Park, T.Uomoto, Radar image Processing for Detection of Shape of Voids and Location of Reinforcing Bars in or under reinforced concrete, *Insight*, Vol.39, No.7, The British Institute of Non-Destructive Testing, July 1997

Evaluation of Concrete Strength using Radar Method on Structures

S. Oota, T. Fujiwara, K. Matsuyama and Y. Kanemoto
Research and Development Center, Nippon Koei Co., Ltd.
2304 Takasaki, Kukizaki-machi, Ibaraki 300-1259, Japan

ABSTRACT

This paper introduces research and development of the method of evaluating concrete strength using ground-penetrating radar. It has been presumed that concrete strength can be estimated from the propagation velocity of radio waves and attenuation thereof. Concrete strength is a very important factor for the assessment of deterioration and the residual load carrying capacity of concrete structures.

Ground-penetrating radar can provide a complete inspection along each scan line, obtain quantitative and continuous data, save time, and make the investigation work safe.

KEYWORDS

Ground-penetrating radar, concrete strength, electric properties of concrete

1. Purpose of study

The purpose of this study is to develop a method of evaluating concrete strength using ground-penetrating radar.

2. Backgrounds of study

Concrete strength is a very important factor for the assessment of deterioration and residual load carrying capacity of concrete structures. The rebound number method and ultrasonic pulse velocity method are used to evaluate concrete strength, but they are point-by-point tests. Continuous nondestructive test methods are useful to investigate the concrete properties of tunnels, bridges and pavements, which have long concrete structures. Ground-penetrating radar (in this report, it will be called "radar") can provide a complete inspection along each scan line, obtain quantitative and continuous data, save investigation time and make the investigation work safe. It is difficult to estimate the strength of honeycombed concrete using the rebound number method and ultrasonic pulse velocity method, and it is very hard to obtain core samples for the unconfined compressive strength test by boring works.

Therefore, this study developed an estimation method for low strength concrete, in particular.

3. Principle of method of estimating concrete strength using radar

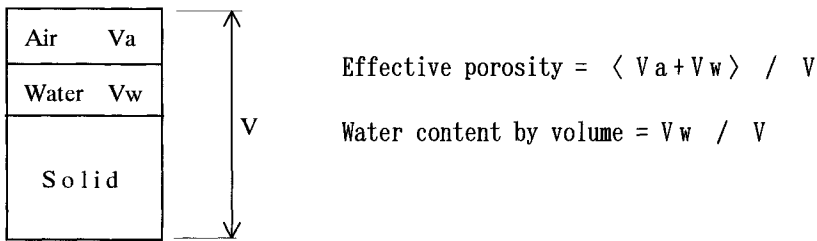
This study assumes that concrete strength can be estimated from the propagation velocity of radio waves and the attenuation ratio of radio waves. The radar method utilizes electromagnetic waves for measuring the electrical properties of concrete. The properties of electromagnetic waves propagating through various materials can be expressed using values of complex dielectric constant. Electromagnetic waves propagate at a speed specific to the material and attenuate at a

ratio specific to that material. Table 1 shows the electrical properties of concrete and major contributing factors. In other words, this method attempts to derive water content and effective porosity of concrete based on the propagation velocity and attenuation ratio of electromagnetic waves measured using the direct wave measurement method developed for this study as described in chapter 4. To achieve this, the following two technical problems need to be solved:

- (i) Establishment of technology to measure effective porosity of concrete using radar
- (ii) Investigation of the relationship between concrete strength and effective porosity

Table 1. Electrical properties of concrete and relevant major factors

Electrical properties	Propagation velocity of radar wave	Attenuation ratio of radar wave
Corresponding dielectric constant	ϵ' (real part)	ϵ'' (imaginary part)
Measuring method	Direct wave method	
Major factors	Water content by volume	Effective porosity, saline content, aggregate ratio



4. Improved method to estimate propagation velocity of electromagnetic waves in a medium

Conventional measuring techniques using radar can not accurately measure the propagation velocity (V) of electromagnetic waves in concrete. For this reason, in tunnel investigations, drilling has been performed in actual surveys at intervals of approximately 200m, for checking the lining thickness and time required for wave propagation. Propagation velocities (V) were obtained from these measurements, assuming that V is constant in the 200m section. It has therefore been impossible to obtain accurate values at regions having water inflow, etc., where the water content of lining concrete varies greatly so. More frequent drilling was required for these regions. Furthermore, drilling is usually conducted at high locations, which causes problems such as poor working environment due to carbon dioxide emitted from generators.

A new technology has been developed for more accurate radar measurements and improved working environment. Figure 1 shows the conventional transmission-receiving system for underground radar, and Fig.2 shows the improved system. The newly developed technology involves estimation of the propagation velocity of radar waves in a medium, and is used for deriving the propagation velocity of electromagnetic waves by measuring the waves directly transmitted between the transmission and receiving antennas. This is very difficult by the conventional technology, since the distance between the transmission and receiving antennas is very short and the transmission time to be measured is in the order of several nanoseconds.

In the transmission-receiving system developed for the present study, electric energy in the form of an impulse generated by the transmitter is diverged by the electric distributor in part into a coaxial cable of length $2L - \Delta L$, and the remaining substantial part into a coaxial cable of length L, the latter

being delivered to the transmission antenna. Here, the impulse is converted into radio energy and then radiated into the ground. A part of the radiated energy is received directly by the receiving antenna (direct wave), while another part by the receiving antenna after being reflected by underground objects (reflected wave). The waveform produced is converted by the receiving antenna into electrical energy again, sent to the electrical synthesizer, where it is combined with the waveform of the impulse that was diverged initially. Figure 3 shows a model waveform. As seen in the figure, the waveform of the basic wave T_r via the coaxial cable of length $2L - \Delta L$ appears first, followed by that of the direct wave T_1 and then by the reflected wave T_2 . Here, the value $T_r - T_0$ is obtained by dividing the difference ΔL of coaxial cable length by the propagation V_c of ratio waves through them. By improving the system, propagation velocity V_g of radio waves through a medium can be estimated using Eqn.1 below. This technology enables accurate estimation of propagation velocity, which is not affected by fluctuation of the circuit or other reasons.

$$\begin{aligned}
 V_g &= D / \{ (T_1 - T_r) - (T_0 - T_r) \} \\
 &= D / \{ (T_1 - T_r) - (L / V_c) \}
 \end{aligned}
 \tag{1}$$

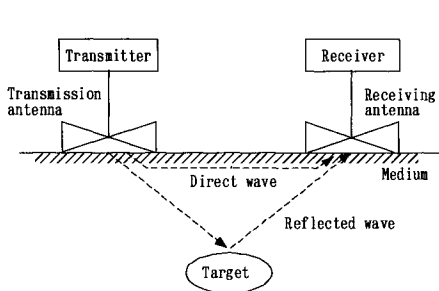


Fig.1. Transmission-receiving system for estimating velocity of electromagnetic radio waves using conventional underground radar

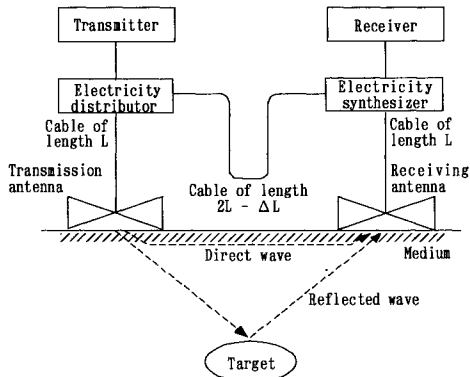


Fig.2. Transmission-receiving system for estimating velocity of electromagnetic radio waves using the technology developed for this study

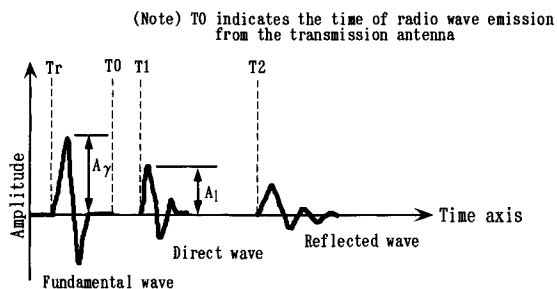


Fig.3. Model wave forms received using the technology developed for this study

5. Fundamental laboratory test

(1) Preparation of concrete specimens with different void ratios

When a lining is made of lean concrete or when lining concrete has been exposed to deteriorating conditions (such as streams or water inflow) for a long period of time, the concrete becomes porous (the void ratio increases) due to accumulated micro-cracks and leaching of cement. In order to reproduce concrete that has deteriorated over a long period of time, specimens ($\phi 10\text{cm} \times 20\text{cm}$) made of concrete with the composition shown in Table 2 were prepared.

Table 2. Mixing conditions for the concrete

Items	Mixing conditions
Maximum size of coarse aggregate	20mm (crushed aggregate)
Required strength	150,180,210 kgf/cm ² (based on the air content of 5%)
Required slump	10 ± 2cm
Required air content	5 ± 1,10 ± 1,15 ± 1,20 ± 1%

(2) Relationship between the effective porosity

An unconfined compression test was performed using the concrete specimens in order to investigate the relationship between the effective porosity and strength. The same investigation was performed for drilled cores sampled from an existing tunnel. Figure 4 shows the relationship between the effective porosity and the strength of the concrete specimens. The relationship between the effective porosity and the strength of drilled cores sampled from an existing tunnel is illustrated in Figure 5. These figures indicate the tendency that concrete strength of the prepared specimens and drilled core samples decreases linearly as the effective porosity increases. It has also been shown that the effect of the amount of cement on the concrete strength decreases as the air content increases.

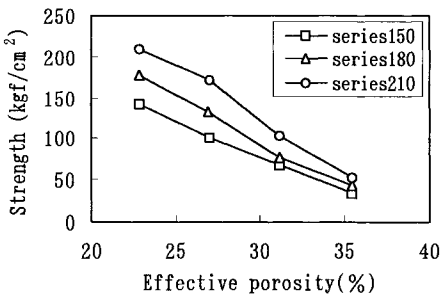


Fig.4. Relationship between the effective porosity and the strength of concrete specimens

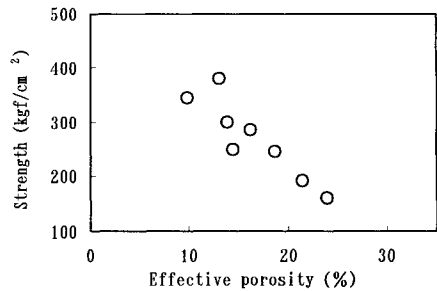


Fig.5. Relationship between the effective porosity and strength of the drilled core sampled from an existing tunnel

(3) Electric properties of concrete specimens

The basic experimental system shown in Photograph 1 for measuring electrical properties of concrete specimens was assembled, and used for measuring the specimens placed in connection jigs of the horn type. In order to clarify the electrical properties of concrete with various water contents, the specimens were dried naturally, and the measurement continued for a year. Figures 6 and 7 show the relationship between the complex dielectric constant (real and imaginary parts) and water content under a constant air content. These figures show that the complex dielectric constant, which indicates the electrical property of concrete, varies linearly as water content changes, when the air content is constant. Also, the effect of required concrete strength (the amount of cement) is insignificant. These results indicate that when the effective porosity of concrete is constant, the complex dielectric ratio is fairly consistent, regardless of the composition (the amount of cement)

Figures 8 and 9 show the relationship between the effective porosity and complex dielectric constant for a series of specimens prepared to fulfill the required strength of 180 kgf/cm². Figure 8 shows that the relationship between the real part of the complex dielectric constant and the water content is fairly linear, and even though the slope of the graphs changes slightly with the change of the air content, its effect is minimal. Figure 9 on the other hand, shows that the slope of the graphs for the imaginary part of the complex dielectric constant - water content relationship varies considerably with the changes of air content. These results indicate that the real part of the complex dielectric constant corresponds to the water content of concrete, while the imaginary part corresponds to the effective porosity. Thus, it has been shown that the information needed for estimating concrete strength (i.e. the water content and effective porosity) can be obtained through the measurement using radar.



Photograph 1. Basic experimental system

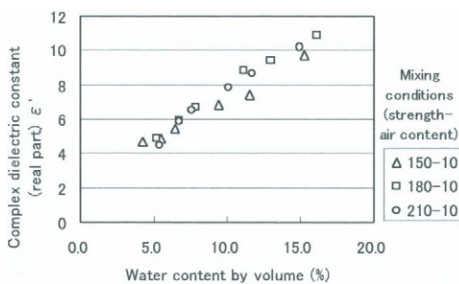


Fig. 6. Relationship between real part of complex dielectric constant and water content by volume

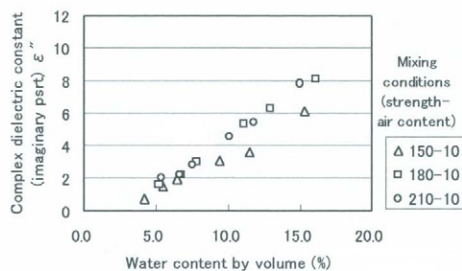


Fig. 7. Relationship between imaginary part of complex dielectric constant and water content by volume

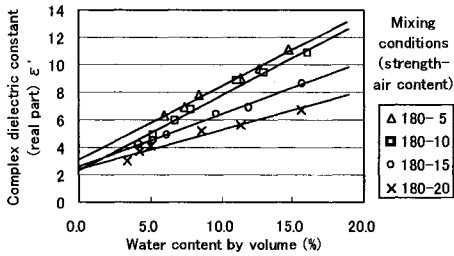


Fig.8 Relationship between real part of complex dielectric constant and water content by volume

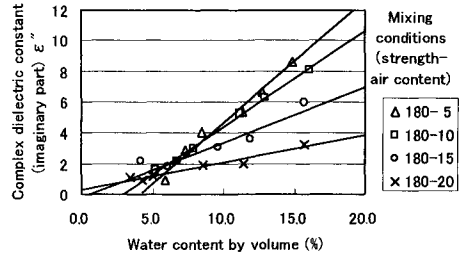


Fig.9 Relationship between imaginary part of complex dielectric constant and water content by volume

6. Field tests

In laboratory tests, it became clear that the measurement accuracy of the complex constant (real and imaginary part) was improved by increased water content. The field test was therefore carried out on an actual concrete structure which is sometime covered by water.

(1) Type of radar antenna

Photograph 2 shows the antenna and control unit. The antenna is a bistatic dipole antenna and monocycle transmitter with 800MHz frequency, and is moved in contact with the surface of the structure to be surveyed. The radar equipment, as shown in Figure 2, could measure the propagation velocity of radar waves.



Photograph 2. Antenna and control unit

(2) Concrete core drilling and radar measurement

Concrete core drilling and radar measurement were carried out at the same points on the dewatered concrete structure. After radar measurement at 12 points, 12 concrete cores were obtained by boring.

(3) Results of test

1) Laboratory test

The relationship between the water content by volume and the concrete compressive strength are shown in Table.3. The concrete strength obtained by unconfined compressive tests was less than 110kgf/cm², and all the data of water content by volume were over 15%.

Table 3. Results of laboratory test

Core No.	Unconfined compressive strength (kgf/cm ²)	Water content by volume (%)
1	77.3	26.26
2	78.5	25.96
3	79.5	23.75
4	104.5	21.09
5	93.6	21.98
6	61.5	18.69
7	109.6	24.04
8	66.1	28.38
9	49.1	26.41
10	10.7	31.87
11	27.2	27.15
12	53.7	29.82

Figure 10 shows the relation between compressive strength and effective porosity, using data for another concrete structure. This figure indicates the concrete strength decreases linearly as the effective porosity increases.

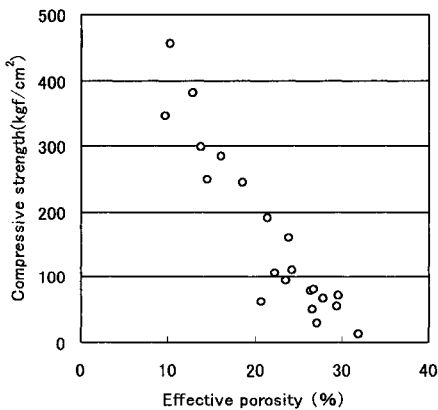


Fig. 10. Relationship between compressive strength and effective porosity on actual structure

2) Relationships between electrical property and strength of concrete

Relationships between the electrical properties (velocity of ratio wave propagation and attenuation coefficient^(*)) and the unconfined compressive strength are shown in figure 11.

The concrete strength decreases linearly as the velocity of ratio wave propagation and the attenuation coefficient^(*) increase respectively.

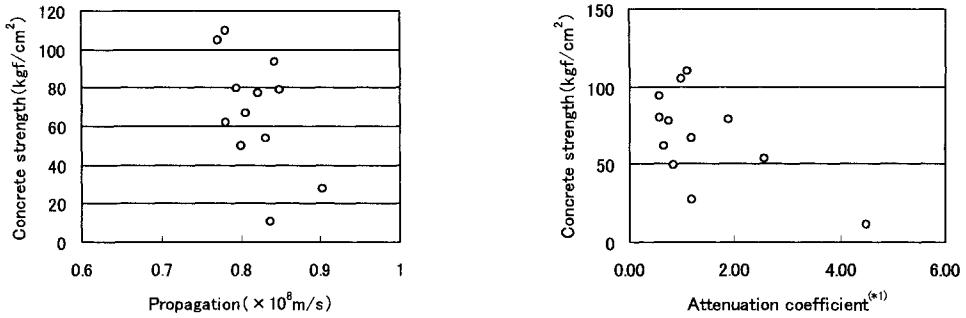


Fig. 11. Relations between electrical properties and concrete strength

Attenuation coefficient^(*): refer to figure 3
 Attenuation coefficient^(*)
 = amplitude of direct wave / amplitude of fundamental wave = A1/Ar
 The attenuation coefficient^(*) is affected by the characteristics of the radar measuring equipment, because the cable length and attenuator of the transmission-receiving system are different in each equipment. We have to investigate the attenuation characteristics by only concrete in the next study, to be able to discuss the relationship and difference between the results of laboratory and field tests.

3) Assumed equations of concrete strength

Equation (I) was obtained by laboratory tests, and equation (II) by field tests.

$$y = -74.5 + 14.2X_1 + 11.1X_2 \dots\dots\dots (I)$$

$$y = 486.8 - 4.8 \times 10^{-6} X_{1'} - 17.7X_{2'} \dots\dots\dots (II)$$

where,

- y : Unconfined compressive strength of concrete (kgf/cm²)
- X₁ : Real part of complex dielectric constant
- X₂ : Imaginary part of complex dielectric constant
- X₁ : Propagation velocity of electromagnetic wave
- X₂ : Attenuation coefficient^(*) of electromagnetic wave

In order to investigate the accuracy of the results of laboratory and field tests, figure 12 was made. Figure 12 shows the relationship between the real strength obtained by tests and the assumed unconfined compressive strength of concrete calculated by equations (I) and (II). In this calculation, the numerical values of X₁, X₂, X_{1'} and X_{2'} were obtained by tests. Figure 12 is for the data of water content of 15% or over by volume, because all the data of water content of concrete core in the actual structure were 15% or over. It is clear that the concrete strength can be evaluated by the radar method within about ± 25 kgf/cm² accuracy for a water content exceeding 15%.

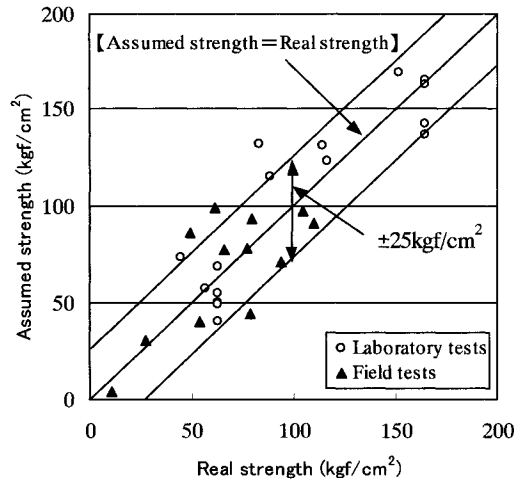


Fig. 12. Accuracy of results of laboratory and field tests

7. Future Studies

- ① In order to clarify the limitations of this method of evaluating concrete strength using radar, more field tests on actual concrete structures having strength of more than 100kgf/cm² will be carried out.
- ② In order to clarify the attenuation characteristics of only concrete of an actual structure, the attenuation of the cable and attenuator of the radar circuit system used in the field tests will be investigated.

Reference

1. Oota, S., Fujiwara, T., Matsuyama, K., Kanemoto, Y.(1998), Inspection and Assessment system for waterway tunnel by NDT, Symposium for Inspection and Assessment of Structures , July 1998, Japan Society of Civil Engineers

This Page Intentionally Left Blank

RADAR TECHNIQUE FOR DETECTING VOIDS UNDER CONCRETE PAVEMENT

K. Matsuyama and S. Oota

*Research and Development Center, Nippon Koei Co., Ltd.
2304 Inarihara, Kukizaki-machi, Inashikigun, Ibaraki, Japan*

M. Kawamorita and I. Tamura

*The Second District Port Construction Bureau, Ministry of Transport
5-57 Kitanakadori, Naka-ku, Yokohama-shi, Kanagawa, Japan*

ABSTRACT

In Haneda airport, land subsidence has occurred due to reclamation. The existence of voids under the surface of the pavement results in the deterioration of pavement. To effectively detect the voids by a non-destructive technique, a radar technique is proposed. In this study, a model pavement was cast for investigations. Radar measurement against the model was carried out to monitor the change of height of voids. It was found that the radar frequency of 800 MHz is the most suitable for NC slabs. Characteristics of radar wave propagation with increase of the height were clarified and formulas for estimating of void thickness were proposed.

KEYWORDS

radar, void, concrete pavement, airport, reclamation

1 INTRODUCTION

In order to deal with the rapid increase in aviation demand in the Tokyo metropolitan area and to solve noise problems of airplanes, The Second District Port Construction Bureau, Ministry of Transport has been undertaking the offshore development project of the Tokyo International Airport (Haneda Airport). The construction site extends over extremely soft ground which was reclaimed with sludge dredged adjacent to the present airport. Therefore, estimation and countermeasures against differential settlement after completion of the project have become a very serious problem [1,2].

Principal airport facilities such as runways, aprons, and taxiways are strictly maintained; their surfaces must be flat for safe takeoff and landing of aircraft. Furthermore, it is necessary to maintain uninterrupted operation of the airport. Asphalt (AS), normal concrete (NC), and prestressed concrete (PC) are generally used for airport pavements. Damages such as voids under pavement and cracks on pavement surfaces may occur due to differential settlement of the ground. If such voids and cracks occur, they will obstruct airplane and other traffic. Crack inspections are usually carried out visually. Pavement excavation is carried out for void inspections. These are certain methods to confirm the existence of voids. However, it requires a great deal of labor for excavation and it is difficult to cover a wide area

without damaging the pavement. For this reason, it is necessary to develop an effective method for inspecting voids under pavement.

2 REQUIREMENTS FOR VOID INSPECTION

The requirements for inspection of voids under pavement at airports are as follows;

- 1) It does not damage the pavement.
- 2) It is continuous.
- 3) It is quantitative.
- 4) It does not take a long time for measurement.
- 5) It is safe.
- 6) It is economical.

A nondestructive technique meets these requirements.

3 RADAR TECHNIQUE

To develop an effective method for inspection of voids under pavement, we conducted a comparative study of non-destructive techniques. The results are shown in Table 1. Table 1 shows that radar, laser measurement and infrared thermography are effective methods for inspecting voids. Laser measurement is an effective inspection for cracks and deformations on the pavement surface. Radar and infrared thermography are more effective methods than laser measurement. In these methods, infrared thermograph is affected by rain and snow, because the method determines the distribution of surface temperature. Radar is not much influenced by weather, and it is used for void inspection for tunnels and road pavement. Therefore, radar is considered as the most suitable method for inspecting voids under pavement at airports.

Table1 applicability of nondestructive test for surveying on pavement

Name of a method	Information about pavement					Void under pavement		Applicability	
	Crack	Deformation	Thickness	Strength	Rebar	Size	Thickness	Efficiency	Safety
Ultrasonic	△	×	×	○	×	×	×	△	○
Surface Wave	×	×	○	○	×	△	○	△	○
Radar	×	×	○	×	○	○	○	○	○
Laser	○	○	×	×	×	×	×	○	△
X ray	×	×	△	×	△	△	△	△	△
Fiber scope	×	×	△	×	×	○	○	△	○
Acoustic Emission	○	×	×	×	×	×	×	△	○
FWD	×	×	×	×	×	○	△	△	△
Infrared thermography	△	×	×	×	×	○	△	○	○

4 APPLICABILITY OF RADAR FOR VOID INSPECTION

In Haneda airport, three types of pavement are employed.

1) Asphalt pavement (AS)

(15 cm thick, no rebars)

2) Prestressed concrete pavement (PC)

(Slab is 25 cm thick, there are rebars and PC bars)

3) Normal concrete pavement (NC)

(Slab is 44 cm thick, no rebars)

On sample pavements of AS, PC and NC, tests of five radar antennas of different frequency were carried out (Photo 1 and Photo 2). The results are shown in Table 2. Using a suitable antenna, it is possible to survey NC and PC pavements. The survey measures the thickness of pavement, thickness of covering concrete, interval of rebars and existence of voids. On AS pavement, it is possible to survey the thickness of the pavement.

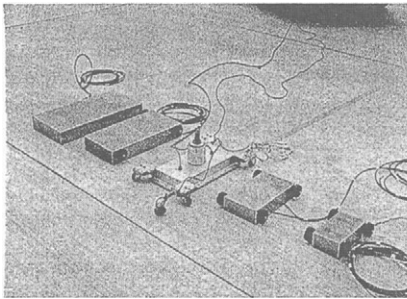


Photo1 radar antenna



Photo2 test at airport

Table2 applicability of radar antenna for surveying on pavement

	NC pavement	PC pavement	AS pavement
Frequency of antenna	600, 800 MHz	800, 1000MHz	600, 800 MHz
Possibility for surveying under rebar	○	○	—
Possibility for surveying under pavement	△	△	△
Thickness of covering concrete	○	○	—
Pitch of rebars	○	○	—
Diameter of rebar	×	×	—

○ : yes

△ : possible

× : impossible

— : out of the subject(no rebars)

5 ACCURACY OF VOID DETECTION BY RADAR

5.1 Purpose of test

We tested the ability of radar to detect voids under airport pavement. The NC is the thickest slab among AS, NC and PC. The NC slab does not follow the bend due to occurrence of voids under the slab. For these reasons, we tested the accuracy of void detection by radar using NC slab.

This test investigated the following;

- 1) Suitable frequency of radar antenna for detecting voids under NC slab
- 2) Limitations of radar for detecting void thickness
- 3) Ability of radar to detect voids quantitatively

We made an NC slab model and carried out radar measurement for varying void thickness.

5.2 NC slab model

The NC slab model was based on the specifications for construction of airports. The size of the NC slab is 2.0×2.0×0.44 m (Photo 3). Reinforcing bars (D10) are arranged at 25 mm pitch. The thickness of covering concrete is 13 mm. The mix proportion of the concrete is shown in Table 3. After placing fresh concrete, the model was cured by spray curing. The period of the curing was three months, whereupon hydration of concrete had almost finished and the electrical properties had stabilized. Properties of the concrete strength are shown in Table 4. The base of the NC slab model was made with materials shown in Table 5 (Photo 4). Comparing the data of radar measurement on the NC slab model and the NC slab in the airport, we confirmed agreement of these data and the accuracy of the NC slab model.

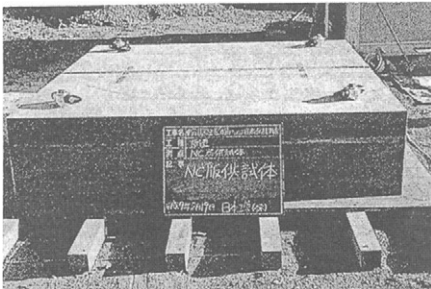


Photo3 NC slab model

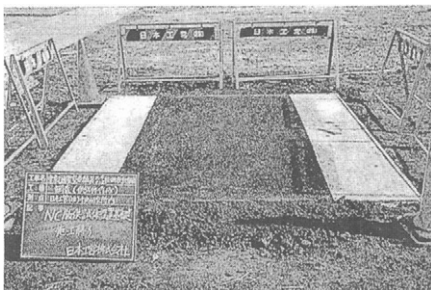


Photo4 basement of NC slab model

Table3 mix proportion of NC slab concrete

Dmax (mm)	Slump (cm)	Air (%)	W/C (%)	S/a (%)	Unit Weight (kg per 1m ³ of concrete)			
					Water	Cement	Sand	Gravel
40	6.5	4.5	40.5	35.7	152	375	640	1135

Table4 result of bending test

Specimen No.	Weight (kg)	Strength (N/mm ²)	Average (N/mm ²)	Nominal strength (N/mm ²)
1	28.65	6.35	6.22	5
2	28.58	6.17		
3	27.96	6.13		

Table5 materials for basement of NC slab model

	Material	Thickness (mm)
Base course	asphalt with aggregate	120
Subbase course	crushed stone	320
Prepared Subgrade	soil	—

5.3 Accuracy of void detection

In the accuracy test, the thickness of voids was adjusted by inserting steel between the NC slab model and base. The NC slab model was lifted up by a 25 ton crane. The conditions of this test were as follows (Photo 5) ;

- a) Type of radar antenna
dipole antenna
- b) Frequency of antenna
400, 600, 800, 1000, 1500 MHz
- c) Thickness of void
0, 1, 2, 3, 5, 10, 20, 30 cm
- d) Pitch of measurement 1 cm
- e) Length of measurement 1 m

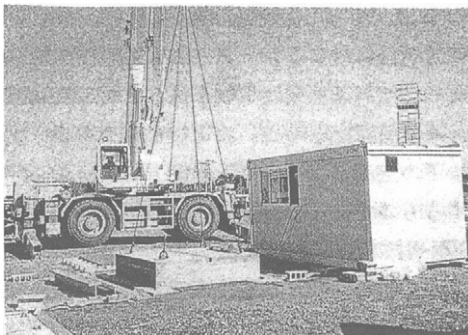


Photo5 accuracy test

6 RESULTS OF THE TEST

6.1 Suitable frequency for void detection

Graphic recorder outputs for scans over the NC slab model are shown in Fig. 1. Graphic recorder outputs using a high frequency antenna are sensitive around the surface and radar waves are attenuated greatly. On the other hand, graphic recorder outputs using a low frequency antenna are vague and radar waves are attenuated only a little. Considering these characteristics of every antenna, 800 MHz is the most suitable frequency of radar antenna for detecting voids under the NC slab model (Table 6).

6.2 Minimum thickness of void detected by radar

In the case of 10 cm void thickness, the received signal using the 800 MHz radar antenna is shown in Fig. 2. In the signal, the peak marked with a double circle changes with increase of thickness of the void. This peak was generated by a phase difference between concrete and void. This characteristic was observed from 2 cm thickness of void. For the same reason, a change of the graphic recorder output was observed from 5 cm thickness of void. Therefore, the minimum thickness of void detected by radar is 2 cm in the signal and 5 cm in the graphic output.

6.3 Quantitative detection of void under NC slab model

The received signal using 800 MHz is shown in Fig. 2. Peaks of the signal are marked A to K. The relation between width of the peak of A to K and thickness of the void is shown in Fig. 3. Widths of peak H and I change with increase of void thickness (Fig. 4). We approximated the relation as an exponential function, and obtained formulas for estimating the thickness of void under the NC slab model (Fig. 5). The relation between estimated thickness of void and actual thickness of void is shown in Fig. 6. It is possible to estimate the thickness of a void of less than 6 cm using the peak of I. The peak of H is able to provide an estimate of the thickness of a void of less than 20 cm. Using these peak I and H appropriately, it is possible to estimate the thickness of voids under the NC slab model.

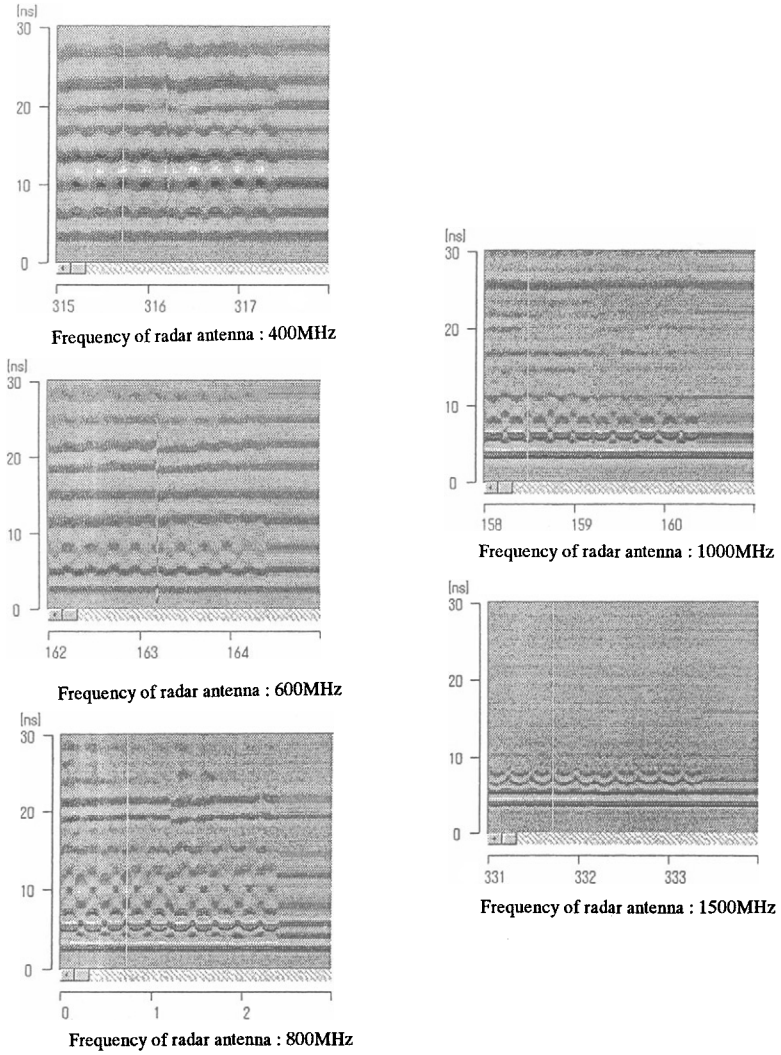


Fig.1 graphic recorder outputs (thickness of void is 0 cm)

Table6 result of accuracy test

	400 MHz	600 MHz	800 MHz	1000 MHz	1500 MHz
sharpness of picture at rebar	×	△	○	○	⊙
sharpness of picture under NC slab	×	△	⊙	△	×
applicability of void detection	×	△	⊙	○	△

⊙ : very good △ : poor
 ○ : good × : very poor

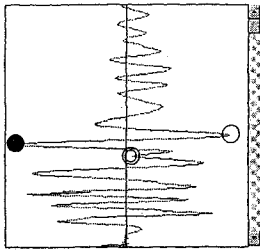


Fig.2 a received signal (800 MHz, 10 cm of void thickness)

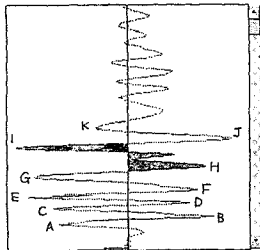


Fig.3 peaks of a received signal

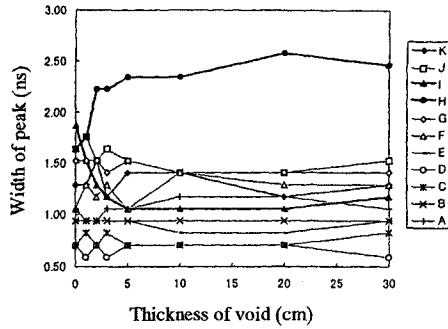
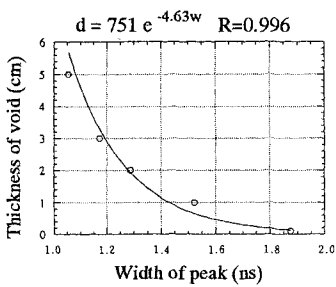
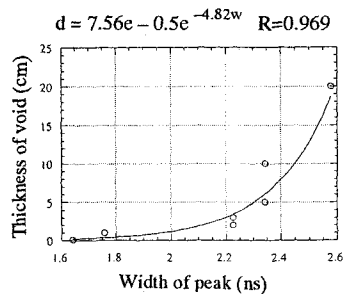


Fig.4 relation between width of peak and thickness of void



d : Thickness of void, w : Width of peak, $e=2.7182...$

Fig.5(a) formula of void thickness using peak I



d : Thickness of void, w : Width of peak, $e=2.7182...$

Fig.5(b) formula of void thickness using peak H

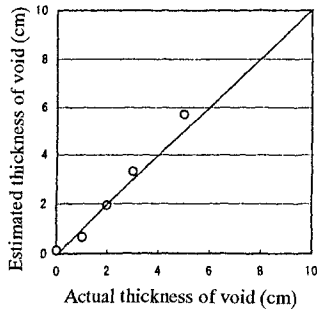


Fig.6(a) relation between estimated thickness and actual thickness (peak I)

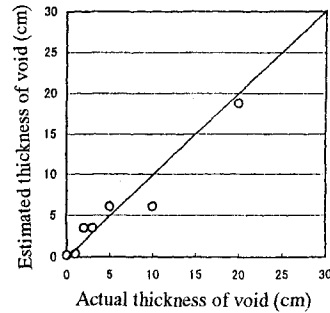


Fig.6(b) relation between estimated thickness and actual thickness (peak H)

7 CONCLUSIONS

We conclude the radar application for void detection under NC slabs as follows;

- 1) The radar method is the most suitable for detecting voids under pavement at airports.
- 2) 800 MHz is the most suitable frequency for void detection under NC slabs.
- 3) It is possible to detect voids of over 2 cm thickness using 800 MHz radar antenna.
- 4) It is possible to estimate the thickness of voids using peaks of H and I in the received signal.

By placing the outputs of radar measurement and visual test on the surface of pavement, it could be possible to detect deterioration early on. By storing the outputs of radar measurement at regular, prediction of the generation and growth of the void could be possible.

8 FUTURE WORKS

8.1 Improve the performance

It was shown that radar can detect voids of over 2 cm. In designing the NC slab, thickness is decided by ultimate destruction. When the NC slab is in the ultimate limit state, the deflection of the NC slab is 1.5 mm due to differential settlement. Therefore, the radar can not easily detect voids which makes the NC slab reach ultimate destruction.

However, due to differential settlement, cracks and voids have occurred in NC slabs in service, so it is necessary to conduct radar measurements on an actual NC slab and to study the relation between the output of radar and actual voids under the NC slab.

8.2 Study of efficiency of measurement

For efficient void detection over a large airport area, it is necessary to investigate the extent of voids under the NC slab by integrating the radar technique with GPS (Global Positioning System).

REFERENCES

- [1] Y. Mori, S. Soda, T. Tsuchida (1993), "Observation of Differential Settlement in Offshore Development Project of Tokyo International Airport", *Soils and Foundations* Vol.33, No.2, pp.116-125.
- [2] S. Hitachi, M. Shiomi, N. Ikeda, T. Tsuchida (1995), "Observation and estimation of differential settlement in Tokyo International Airport Offshore Expansion Project", *Compress Consol Clayey Soils* Vol.1, pp.629-634.
- [3] J. H. Bungey, S. G. Millard, M. R. Shaw (1994), "The influence of reinforcing steel on radar surveys of concrete structures", *Constructions and Building Materials* Vol.2, No.2, pp.119-126.
- [4] J. H. Bungey, S. G. Millard (1995), "Detecting Sub-surface Features in Concrete by Impulse Radar", *Nondestructive Testing and Evaluation* Vol.12, pp.33-51.

GPR EXPERIMENTS USING SMALL TUB AND APPLICATION FOR DETERMINING FRACTURE

H. IMAI and J. KAWAKAMI

*Civil Engineering Technology Development Dept.,
Taisei Research Institute, Taisei Corporation,
344-1 Nase-cho, Totuka-ku, Yokohama, Kanagawa Pref., Japan*

ABSTRACT

Electromagnetic(EM) wave characteristics are obtained by experiments using a small tub with silica sand are carried out and the results reveal phase changes of EM reflection waves at the boundary of sand and water filling in an acrylic pipe buried in the tub. Signal processing and migration for the EM wave field provides precisely an image with the pipe size and its depth. For the purpose of more expanding the use of EM waves to civil engineering, the method is developed to determine the dip angle, the strike angle and the depths of boundaries under the ground. Experiments of the method at a granite quarry, at least 3 open cracks are found and they are confirmed from the rock section at the quarry.

KEYWORD

electromagnetic wave, reflection method, exploration of fracture/crack

INTRODUCTION

Recently, the technology based on electromagnetic waves has been used not only in archaeology but also in civil engineering., for examples, EM wave tomography of underground, locating the life lines buried at underground as gas or water pipes, finding air pockets under roads, *etc.* Moreover, recently, radar system installed on the shield machine which excavates a tunnel at urban area and the system is utilized to find the life lines as gas or water pipes and the metal or woody old piles existing ahead of the machine.

In this paper, the basic theory on the propagation and the reflection of electromagnetic waves are introduced at first and, followed by the description of the experimental results at small tub and at the field of granite quarry.

THEORY

Electromagnetic wave is described as an energy wave and its propagation is the phenomena made by the chain of electric field and magnetic field which are generated each other by the other. This is confirmed by Hertz and its formulation is done by Maxwell.

Propagation

Maxwell's equations describe completely the characteristics of EM waves are as follows:

$$\nabla \times \mathbf{H} = \mathbf{J} + \frac{\partial \mathbf{D}}{\partial t} , \quad (1)$$

$$\nabla \times \mathbf{E} = -\frac{\partial \mathbf{B}}{\partial t} , \quad (2)$$

$$\nabla \cdot \mathbf{D} = \rho , \quad (3)$$

$$\nabla \cdot \mathbf{B} = 0 , \quad (4)$$

where ρ , \mathbf{J} , \mathbf{H} , \mathbf{D} , \mathbf{E} and \mathbf{B} are, respectively, the electric charge [C/m³], the electric current density [A/m²], the magnetic field intensity vector [AT/m], the electric displacement vector [C/m²], the electric field intensity vector [V/m], the magnetic flux density vector [T], also, $\rho = 0$ and $\mathbf{J} = \mathbf{0}$ in the air, vacuum or silicate rock. Vectors \mathbf{H} , \mathbf{D} , \mathbf{E} and \mathbf{B} are related to the electromagnetic field. Also,

$$\mathbf{D} = \varepsilon \mathbf{E} , \quad (5)$$

$$\mathbf{B} = \mu \mathbf{H} , \quad (6)$$

$$\mathbf{J} = \mathbf{J}_0 + \sigma \mathbf{E} , \quad (7)$$

where ε , μ , σ are the dielectric constant or permittivity [F/m], the magnetic permeability [H/m], and the electric conductivity [S/m] (equal to the inverse of resistivity) of the material, respectively. In general, $\mathbf{J}_0 = \mathbf{0}$ because there is no origin of electric current in the case of investigating under the ground. Using Eqs.(1)-(7), \mathbf{E} and \mathbf{H} are defined by

$$\nabla \times \mathbf{H} = \sigma \mathbf{E} + \varepsilon \frac{\partial \mathbf{E}}{\partial t} , \quad (8)$$

$$\nabla \times \mathbf{E} = -\mu \frac{\partial \mathbf{H}}{\partial t} , \quad (9)$$

$$\nabla \cdot \mathbf{E} = 0 , \quad (10)$$

$$\nabla \cdot \mathbf{H} = 0 . \quad (11)$$

Doing differential calculus and using a formula: $\nabla \times \nabla \times \mathbf{A} = \nabla(\nabla \cdot \mathbf{A}) - \nabla^2 \mathbf{A}$,

$$\nabla^2 \mathbf{E} = \sigma \mu \frac{\partial \mathbf{E}}{\partial t} + \varepsilon \mu \frac{\partial^2 \mathbf{E}}{\partial t^2} , \quad (12)$$

$$\nabla^2 \mathbf{H} = \sigma \mu \frac{\partial \mathbf{H}}{\partial t} + \varepsilon \mu \frac{\partial^2 \mathbf{H}}{\partial t^2} . \quad (13)$$

are obtained. Thus, \mathbf{E} and \mathbf{H} satisfy the same differential equation. As a general solution concerned with \mathbf{E} , the following equation can be assumed:

$$\mathbf{E} = \mathbf{E}_0 \exp\{i(\omega t - kx)\} \quad (14)$$

where \mathbf{E} is propagating along x direction with its initial intensity vector \mathbf{E}_0 and $i = \sqrt{-1}$. Putting Eq.(14) into Eq.(12),

$$\nabla^2 \mathbf{E} + k^2 \mathbf{E} = \mathbf{0} , \text{ where } k^2 = \varepsilon \mu \omega^2 - i \sigma \mu \omega . \quad (15)$$

As k is a complex, $k = \alpha - i\beta$ ($\alpha > 0, \beta > 0$) is assumed. Then,

$$\mathbf{E} = \mathbf{E}_0 \exp(-\beta \mathbf{x}) \exp\{i(\omega t - \alpha \mathbf{x})\}, \tag{16}$$

and so α is related to phase velocity and β is related to attenuation factor, and

$$\alpha = \omega \sqrt{\frac{\epsilon \mu}{2}} \sqrt{\sqrt{\left(\frac{\sigma}{\epsilon \omega}\right)^2 + 1} + 1}, \quad \beta = \omega \sqrt{\frac{\epsilon \mu}{2}} \sqrt{\sqrt{\left(\frac{\sigma}{\epsilon \omega}\right)^2 + 1} - 1}. \tag{17}$$

In the case of exploration under the ground or inside of rock, $\sigma \approx 10^{-3}$, $\omega \approx 10^6$ and $\epsilon \approx 10$. Then, $(\sigma / \epsilon \omega)^2 \ll 1$ can be set in Eq.(17). Also, $\mu = \mu_0$, $\epsilon / \epsilon_0 = \epsilon_r$ and $c = 1 / \sqrt{\mu_0 \epsilon_0}$, where μ_0 , ϵ_0 , ϵ_r and c are magnetic permeability in vacuum ($\mu_0 = 4\pi \times 10^{-7} [\text{C}^{-2} \text{N s}^2]$), dielectric constant or permittivity in vacuum ($\epsilon_0 = 10^7 / 4\pi c^2 [\text{C}^2 \text{N}^{-1} \text{m}^{-2}]$), dielectric permittivity in the material (e.g. rock) and ray velocity in vacuum ($c = 3 \times 10^8 \text{ m/s}$), respectively. Using these assumptions and expansion formula, Eq.(17) is approximated as

$$\alpha \approx (\omega / c) \sqrt{\epsilon_r}, \quad \beta \approx (\sigma / 2) \sqrt{\mu / \epsilon}. \tag{18}$$

Therefore, the phase velocity V is described as

$$V = \omega / \alpha = c / \sqrt{\epsilon_r}. \tag{19}$$

Reflectivity

The assumption of $\sigma \approx 0$ is a good approximation for exploration under the ground or inside of rock. Then, Eqs.(8) and (9) are

$$\nabla \times \mathbf{H} = \epsilon \frac{\partial \mathbf{E}}{\partial t}, \quad \nabla \times \mathbf{E} = -\mu \frac{\partial \mathbf{H}}{\partial t}. \tag{20}$$

Considering components of vectors \mathbf{E} and \mathbf{H} , the coordinates is right hand system with their order. Also it is found that $\mathbf{E} \cdot \mathbf{H} = 0$, which means that $\mathbf{E} \perp \mathbf{H}$ in homogenous material. Using Eqs.(8), (9) and (16) with the assumption of $\sigma \approx 0$,

$$|\mathbf{H}| / |\mathbf{E}| = \sqrt{\epsilon / \mu}. \tag{21}$$

is obtained. Fig.1 shows incidence, reflection and transmission of EM wave. By the continuation condition:

$$\begin{aligned} E_{in} + E_{ref} &= E_{tra} \quad \text{and} \\ H_{in} - H_{ref} &= H_{tra}, \end{aligned} \tag{22}$$

reflection coefficient R and transmission coefficient T are formulated as follows:

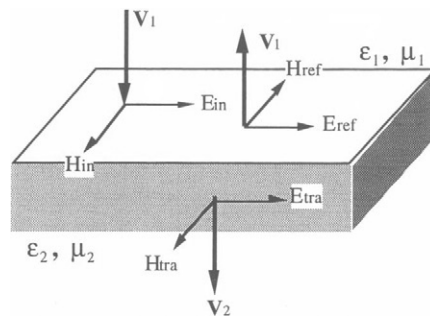


Fig.1. Schematic illustration of EM incident wave resultant in both reflection and transmission at the boundary of EM wave velocity change from V_1 in material 1 to V_2 in material 2.

$$R = \frac{E_{ref}}{E_{in}} = \frac{\sqrt{\epsilon_1/\mu_1} - \sqrt{\epsilon_2/\mu_2}}{\sqrt{\epsilon_1/\mu_1} + \sqrt{\epsilon_2/\mu_2}}, \quad T = \frac{E_{tra}}{E_{in}} = \frac{2\sqrt{\epsilon_1/\mu_1}}{\sqrt{\epsilon_1/\mu_1} + \sqrt{\epsilon_2/\mu_2}}, \quad (23)$$

where $\mu_1 = \mu_2$ in the present case, then, the above equations are simplified to below:

$$R = \frac{\sqrt{\epsilon_1} - \sqrt{\epsilon_2}}{\sqrt{\epsilon_1} + \sqrt{\epsilon_2}}, \quad T = \frac{2\sqrt{\epsilon_1}}{\sqrt{\epsilon_1} + \sqrt{\epsilon_2}} \quad (24)$$

Fig.2 shows R as a function of ϵ . The abscissa is the dielectric permittivity in the material 1 and the ordinate is the reflection coefficient derived from dielectric permittivity of materials 1 and 2.

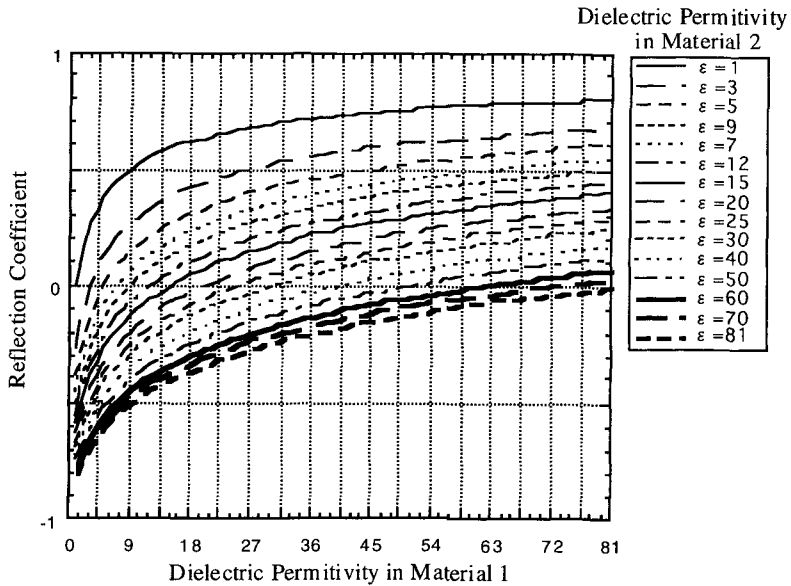


Fig.2. Nomogram of reflection coefficient derived from dielectric permittivity of materials 1 and 2. When it is negative, phase change (reverse) occurs in wavelet reflected from the boundary of materials 1 and 2.

According to Eq.(24) or Fig.2, for example, when the material 1 is completely dry rock or sand (e.g. $\epsilon=4$) and the material 2 is water ($\epsilon=81$), $R = -0.64$, therefore, the phase change occurs in reflection wavelet at the boundary.

EXPERIMENTS BY USING SMALL TUB

Reflected Waves

For the purpose of confirming the above characteristics in reflection EM waves, experiments are carried out by using a small tub as shown in Photo.1 and 2. The small tub is filled with silicate

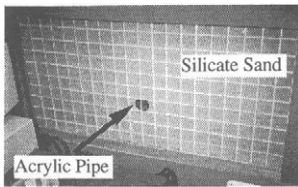


Photo.1. The condition of pipe buried in silicate sand in a small tub.

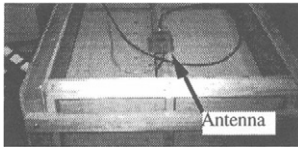


Photo.2. Wave Guides as 3 GHz antennas.

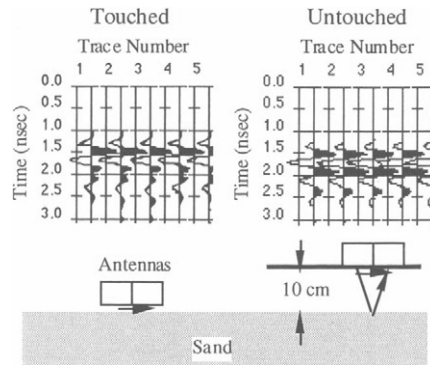


Fig.3. Phase distortion in direct wavelets in the right case where antennas are untouched by 10 cm to silicate sand results in the possibility of misunderstanding the shape and position of direct wavelet.

sand and acrylic pipes are buried inside. In the experiments, two wave guides as antennas of sending and receiving EM waves with frequency of about 3 GHz. The velocity is estimated as 17.8 cm/nsec (*i.e.* $\epsilon = 2.8$) from the observed reflection wave data. And the data were obtained by moving antennas by 2 cm through 100 cm. Therefore, the data of each run consists of 51 traces. As shown in Fig.3, the shape of direct wavelet is recognized as zero phase wavelet, when antennas touch the sand surface. In the case as shown right side in Fig.3, however, it is possible to cause misunderstanding by the distortion in the shape of direct wave, as if direct wavelets have big amplitudes with reverse phase compared with wavelets as shown left side in Fig.3. Fig.4 shows the wavelets which propagated directly and two kinds of wavelets reflected, from the boundary of sand-to-air, and, from the boundary of sand-to-water. These data are obtained when antennas are touched to the sand surface, by using a air-filled acrylic pipe and a water-filled one buried inside at the same depth. At the boundary of sand-water, phase change in reflection wavelets can be confirmed as shown in the right side of Fig.4.

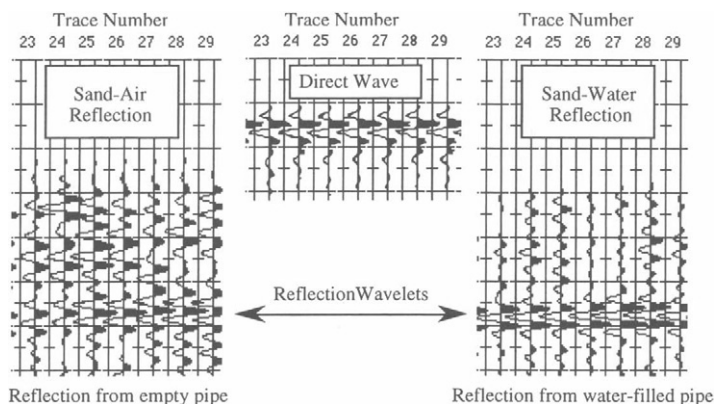


Fig.4. Direct wavelets (center) and phase change in reflection wavelets from the sand-water boundary (right) and no change from the sand-air boundary (left).

Migration Processing

Reflection wave traces are treated by the usual signal processing methods which are used in seismology in general (e.g., filtering, deconvolution, migration). Though these methods are not described in detail in this paper, examples of applications using migration processing developed by Stolt [1] are shown in Fig.5. In this experiments, water-filled acrylic pipes with 10 cm in diameter were buried in the tub at the depths of 20 cm, 40 cm and 60 cm, respectively. Traces of raw data, which means the data have never been processed, are shown at the upper part of Fig.5, where the reflected wavelets form in the line of hyperbolas. By using migration processing, each acrylic pipe can be imaged into the corresponding traces at the same depth as shown at the lower part of Fig.5. The time-depth conversion is made by multiplying the half of travel time and the velocity of EM wave.

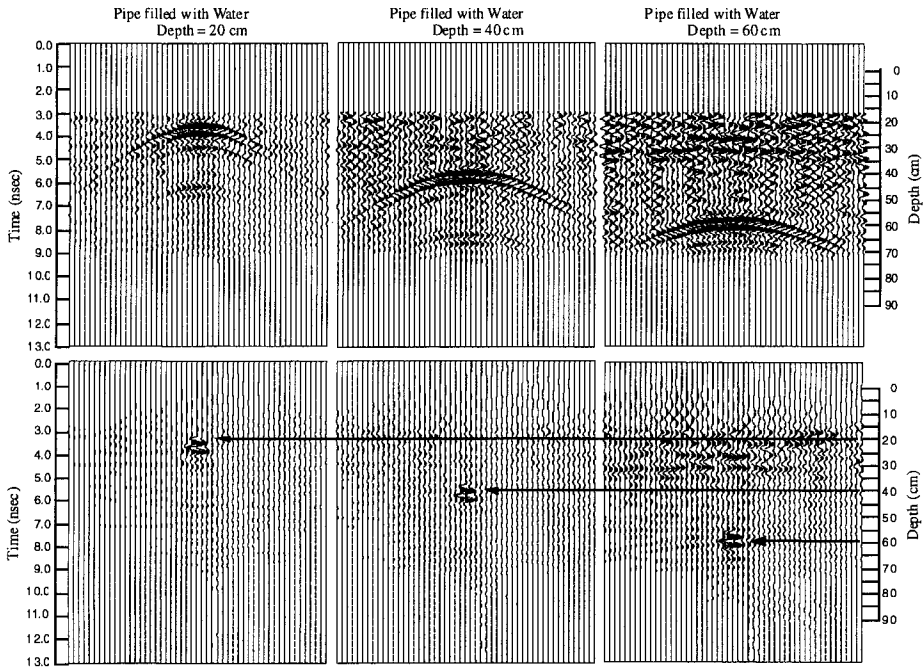


Fig.5. Imaging process by using migration technique for the buried acrylic pipes filled with water at depths of 20 cm, 40 cm and 60 cm.

APPLICATION TO FIELD TEST

Reflection Plane Determination by Circle Line

The strike angle (α), the dip angle (β) and the distance to the reflection plane (L) under the ground as the representative of fractures are obtained from data by a circle line observation. As shown in Fig.6, the definitions of the parameters are drawn in X-Y-Z 3D coordinates of which the

origin is O and Y axis is taken in depth direction. Reflection plane is formed by points A, B, C and D. Line PR is the cross line between the reflection plane ABCD and the plane YOZ. The observation point E is moving around the origin O with a distance r and a rotating angle θ measured counterclockwise from O-X axis. In this case, coordinates of points P, Q, R and E are $(0, L, 0)$, $(-L \tan \alpha, 0, 0)$, $(0, 0, L \tan \beta)$, and $(r \cos \theta, 0, r \sin \theta)$, respectively. Then the reflection plane is determined by the points P, Q and R as follows:

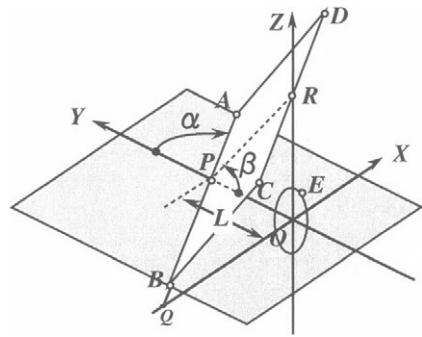


Fig.6. Coordinate system and parameters representing a reflection plane.

$$h_{\theta} = \frac{|r \cos \theta \tan \beta - r \sin \theta \tan \alpha + L \tan \alpha \tan \beta|}{\sqrt{\tan^2 \beta + (\tan \alpha \tan \beta)^2 + \tan^2 \alpha}}$$

(25)

where h_{θ} is the distance between the observing point E with rotating angle θ and the reflection plane PQR. Fig.7 shows the simulation of reflection wave arrivals in the observation traces obtained by using Eq.(25). Therefore, the parameters (α, β, L) relative to the reflection planes can be determined automatically by using Least Square Method with Eq.(25).

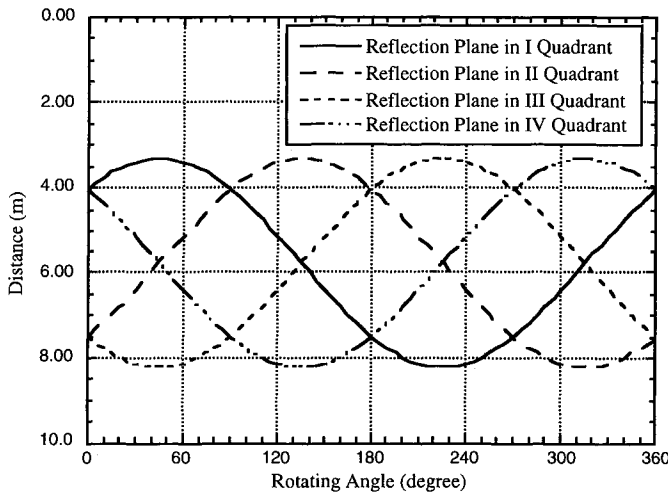


Fig.7. Reflection wave arrivals in traces expected from the position of reflection planes, assumed that $\alpha=135, \beta=45$ in I quadrant; $\alpha=45, \beta=45$ in II quadrant; $\alpha=45, \beta=-45$ in III quadrant; $\alpha=135, \beta=-45$ in IV quadrant, with $r=3$ and $L=10$.

As known from Fig.7, the nearest position and the farthest position are 180 degree apart from each other. Therefore, the parameters (α, β, L) can be determined when 2 points are designated in the traces. When 3 points are designated, moreover, the reflection plane can be specified as a plane facing three spheres with radii obtained by Eq.(25). This technique is used when determining reflection planes by hand on a computer display as shown below.

Field Experiments

Field experiments with GPR's of which antennas are 150 MHz, 350 MHz, 1 GHz were carried out by using a circle line with the radius 4 m at a granite quarry as shown in Fig.8. Among the data in this paper is focused the data obtained by 350 MHz antenna and the traces are processed by the migration technique as shown in Fig.9. Photo 3 of cross section at the wall was taken from the direction as shown in Fig.8. In this photo, three fractures are recognized, shown as A, B and C within about 9 m from the top to the bottom.

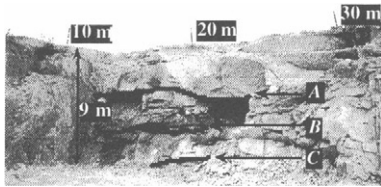


Photo 3. This was taken from the direction shown in Fig.8.

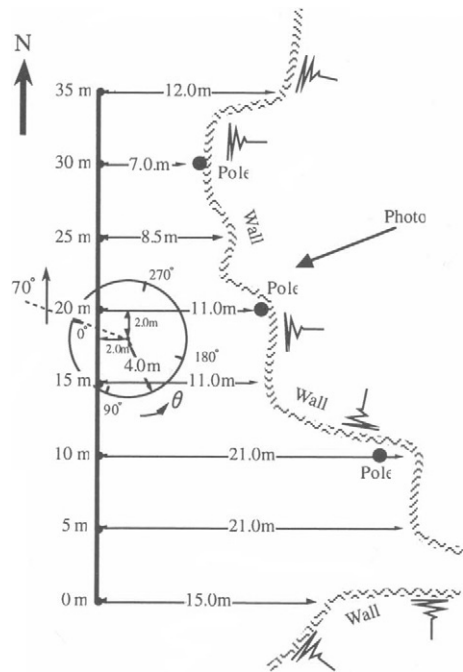


Fig. 8. Layout of a circle line at the bench of granite quarry.

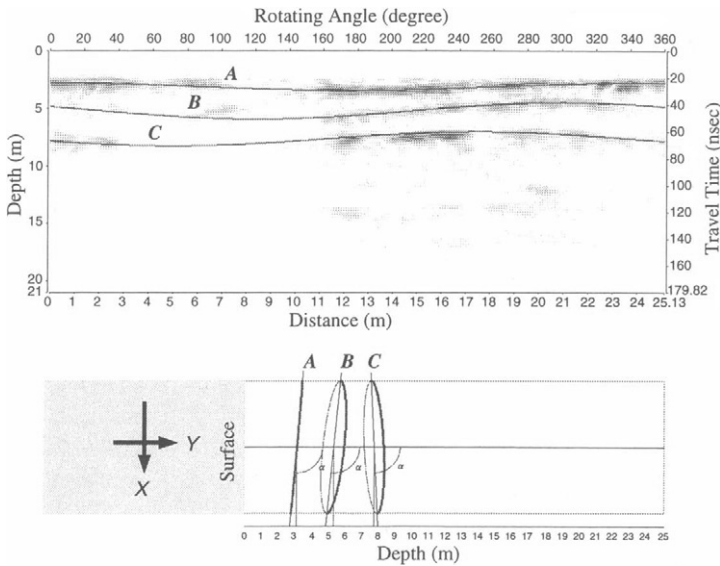


Fig.9. Tree fractures are determined as A, B and C by designating 2 points or 3 points in the traces (upper), and interpretation of the reflection planes in 3D display method (lower).

The parameters of the three fractures are determined by designating 2 points or 3 points in the traces as shown in Fig.9. Also it is found that all reflection planes include water, because of phase investigations. At the lower part of Fig.9, the thick lines represent the data from this side and the thin lines represent the data from the other side and the straight lines are the cross lines between the reflection planes and X-Y plane. The strike and dip angles in degree and distance of the reflection planes: A, B and C are obtained as

A: 94.8, 89.6, 3.1 m,

B: 95.5, 80.9, 5.3 m,

C: 87.2, 81.7, 7.7 m,

respectively. The results are consistent to the fractures A, B and C, found by watching, shown in Photo 3.

APPLICATION TO CIVIL ENGINEERING

Here, the application of this technique into the field of tunnel excavation by TBM (Tunnel Boring Machine) can be considered. When the antennas of GPR mount to a TBM cutter face, the antennas move along a circle line with the radius determining the distance between the antennas and the TBM rotation center and the obtained reflection data can be used to determine the faults or the fracture zones existing ahead of tunnel face.

CONCLUSIONS

At first the basic equations are described assuming parameters so as to apply Maxwell's equations to the current study. Using a small tub with silicate sand and acrylic pipes filling with air or water, phase changes are confirmed at the sand-water boundary inferred from reflection coefficient derived from the basic equations. Next the methods to determine the reflection planes existing under the ground are developed with the circle line and it is found that the method is good enough to determine the reflection planes existing under the ground.

REFERENCES

1. Stolt, R.H. (1978) *Geophysics*, 43, 23.

This Page Intentionally Left Blank

DETECTION OF STEEL REINFORCING BARS INSIDE CONCRETE USING RADAR

HONG C. RHIM

*Department of Architectural Engineering, Yonsei University
Seoul 120-749, Korea*

ABSTRACT

An imaging scheme has been developed and proposed for the use of radar in detecting steel reinforcing bars embedded inside concrete. The scheme utilizes the measured data of electromagnetic properties of concrete and impedance mismatch between concrete and the steel bar. In the paper, the electromagnetic properties of concrete measured over a frequency range from 1 to 6 GHz are also presented. The results provided a ground work in improving imagery from radar measurements for nondestructive testing of concrete structures.

KEYWORDS

Radar, concrete, steel reinforcing bar, nondestructive testing, electromagnetic properties

INTRODUCTION

For the radar method to be successfully used, it involves the understanding of concrete as a material with electromagnetic properties [1], the modeling of electromagnetic wave propagation inside concrete [2], and the utilization of different features of radar systems for civil engineering applications [3, 4]. In addition, proper signal processing schemes need to be developed which can provide a spatial distribution of electromagnetic reflectivity sufficient to characterize the object probed [5].

The use of radar is becoming more popular in the nondestructive testing of concrete structures. However, the interpretation of radar measurement data are still dependent on the experience of the operator. In some cases, time to depth conversions are guess work based upon assumed material properties. Without knowing an exact value of the electromagnetic properties of concrete, the rest of interpretation process can be incorrect.

In this paper, the electromagnetic properties of concrete are measured prior to the radar measurements. Both real and imaginary parts of the properties are measured using open-ended coaxial probe method [6]. Then, the radar measurement data are processed using the electromagnetic properties and impedance mismatch of concrete and a steel bar. The imaging results successfully identified the bar.

MEASUREMENTS OF ELECTROMAGNETIC PROPERTIES OF CONCRETE

Characterizing the electromagnetic properties of concrete is essential to the enhancement of accuracy and reliability in nondestructive testing using electromagnetic techniques, such as radar method. The electromagnetic properties of concrete affect radar measurements in many ways. The velocity and attenuation of the wave are influenced by the electromagnetic properties. Thus, the establishment of a data base for the properties is needed for a frequency range that a radar is operating.

For the measurements, a measurement technique using an open-ended coaxial probe and automatic network analyzer have been applied. Both real and imaginary parts of complex permittivity are measured over the frequency from 1 GHz to 6 GHz as shown in Fig. 1 and Fig. 2.

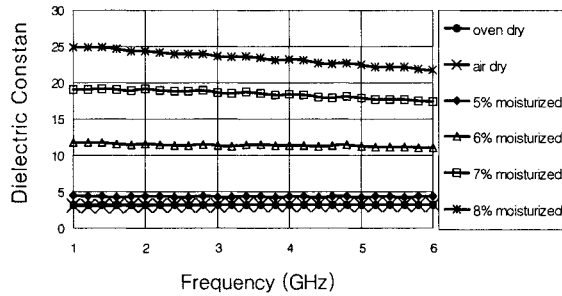


Fig. 1. Measured Dielectric Constant of Concrete

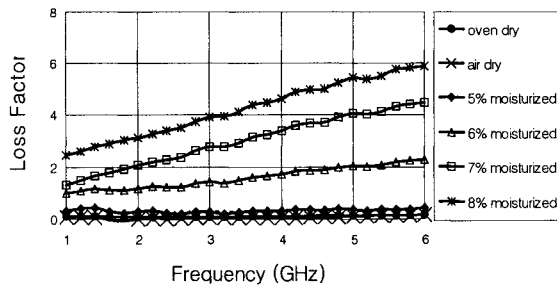


Fig. 2. Measured Loss Factor of Concrete

Moisture content is varied as it affects the properties significantly. The measured data showed the frequency dependency of the properties. The importance of the moisture variation is also demonstrated quantitatively. It is expected that the results obtained from this study will serve as a basis for the development of the radar method as a useful nondestructive testing techniques.

At a given moisture content, the dielectric constant does not change much over the measured frequency range. However, the change of the dielectric constant is significant when the moisture content varies as in Fig. 1. In Fig. 2, the loss factor of concrete measured is shown. The loss factor increases as the frequency increases. The effect of moisture content on loss factor is clearly shown in the results.

RADAR MEASUREMENTS OF CONCRETE SPECIMENS

Concrete targets used for the measurements have the dimensions of 1,000 mm (width) x 1,000 mm (height) x 140 mm (thickness) with different inside configurations. A specimen with a steel reinforcing bar is modeled for a simplified reinforced concrete structure. Concrete specimens are cast with water/cement/sand mix ratio of 1 : 2.22 : 5.61 by weight. Portland cement of Type I was used. The age of the specimens at the time of the measurements was 4 weeks. The radar system used for the measurements has a center frequency of 1 GHz and bandwidth of 1 GHz. Measurement scheme is illustrated in Fig. 3

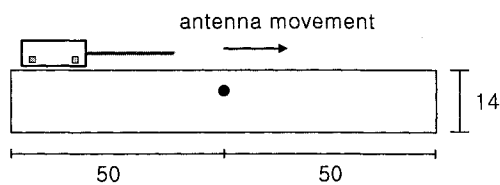


Fig. 3. Dimensions of Concrete Specimen for the Radar Measurements in cm

RESULTS AND DISCUSSION

An imagery obtained by processing raw data from the measurements is shown in Fig. 4. The imagery represents a typical output from a commercially available radar system. Improvement is made by using the measured electromagnetic properties of concrete. Thus, the vertical scale (range direction) in Fig. 4 is exact.

In Fig. 5, the data in Fig. 4 has been processed using a signal processing scheme developed and the mismatch between concrete and the steel bar is now clearly seen. Locating the bar is much easier compared to Fig. 4.

CONCLUSION

The radar method has been studied experimentally by improving the output of measurements by utilizing dielectric constant and impedance mismatch of concrete and steel bar. It has been shown that the developed technique significantly enhances the accuracy of the output compared to raw data. Further study includes the investigation of concrete specimens with multiple steel reinforcing bars.

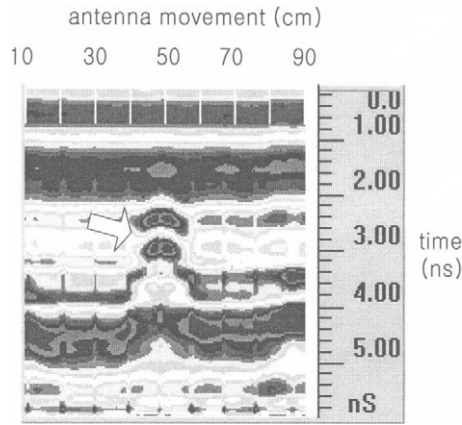


Fig. 4. Display of Radar Measurement

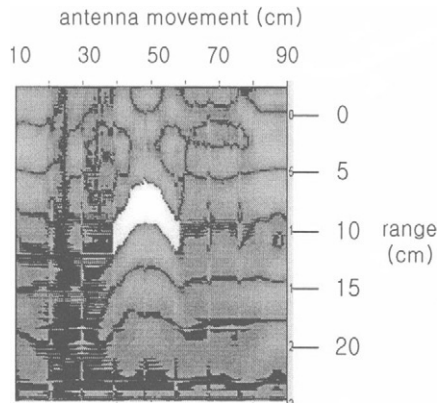


Fig. 5. Radar Imaging with Improved Signal Processing Specimen

ACKNOWLEDGEMENT

This work was supported by Korea Earthquake Engineering Research Center (KEERC) funded by Korea Science and Engineering Foundation (KOSEF). Computational facilities were provided by Advanced Building Science and Technology Research Center (ABSTRC) in the College of Engineering, Yonsei University, Seoul, Korea.

REFERENCES

1. H.C. Rhim and O. Buyukozturk. (1998). In: *ACI Materials Journal*, Vol. 95, pp. 262-271.

2. O. Buyukozturk and H.C. Rhim. (1995). In: *International Journal of Cement and Concrete Research*, Vol. 25, pp. 1011-1022.
3. H.C. Rhim. (1995). In: *Experimental Techniques*, Society for Experimental Mechanics, Vol. 19, pp. 21-22.
4. H.C. Rhim, O. Buyukozturk, and D.J. Blejer. (1995). In: *Materials Evaluation*, American Society for Nondestructive Testing, Vol. 52, pp. 295-299.
5. Dean L. Mensa. (1981). *High Resolution Radar Imaging*. Artech House, Inc., Dedham, Massachusetts.
6. Hewlett-Packard Company. (1992). *Basics of Measuring the Dielectric Properties of Materials*. Hewlett-Packard Application Note 1217-1.

This Page Intentionally Left Blank

**IN-SITU STRENGTH ASSESSMENT OF CONCRETE
- THE EUROPEAN CONCRETE FRAME BUILDING PROJECT -**

DR. M.N. SOUTSOS, PROF. J.H. BUNGEY*,
PROF. A.E. LONG**, AND DR. G.D. HENDERSON**.*

** Department Of Civil Engineering,
The University Of Liverpool, Liverpool L69 3GO,
** School Of Civil Engineering
The Queen's University Of Belfast, Belfast BT9 5AG.*

ABSTRACT.

A full scale seven-storey insitu advanced reinforced concrete building frame was constructed in the Building Research Establishment's Cardington laboratory encompassing a range of different concrete mixes and construction techniques. This provided an opportunity to use in-situ non-destructive test methods, namely the Lok and CAPO tests, on a systematic basis during the construction of the building. They were used in conjunction with both standard and temperature-matched cube specimens to assess their practicality and their individual capabilities under field conditions. Results have been analysed and presented to enable comparisons of the performance of the individual test methods employed.

KEYWORDS

In-situ non-destructive tests, strength development, temperature matched curing, maturity, temperature, pull-out test, Lok and CAPO tests.

INTRODUCTION.

In most countries in the world the quality of the concrete in a structure is assessed indirectly by measuring the strength of cubes or cylinders which are made from the concrete supplied to the site. Whilst this is well accepted by industry, it has its limitations in that problems are not detected until it may be too late for economical remedial action as testing is generally carried out at 7 and 28 days. In addition, these procedures can be the subject of abuse - either by making cubes prior to the addition of water to the mix or, in extreme cases, by the contractor supplying cubes from a specially prepared mix which will meet the specifications. Fortunately, the latter practices seldom if ever arise in the United Kingdom, but all these shortcomings could be eliminated by measuring the strength properties of the concrete in-situ and at an early age. This also permits the effectiveness of compaction and curing processes to be incorporated in providing a reliable indication of the condition of the finished product.



Fig. 1 : The in-situ concrete frame building project at Cardington.

Another advantage to be gained from in-situ testing is that the speed of the overall construction programme can be increased if an accurate assessment of the early-age in-situ strength is made because this allows a much faster ‘turn-around’ for formwork and back-propping.

This report describes work undertaken as part of the insitu concrete frame building project at Cardington. The overall objective of that project was to re-engineer the business process of such buildings in order to reduce costs, increase speed and improve quality. The need, established through industry-based studies, was addressed by a thorough re-appraisal of the supply chains and construction processes. A full scale seven-storey insitu advanced reinforced concrete building frame, see Fig. 1, designed to Eurocode 2 by Buro Happold was constructed in the BRE Cardington laboratory encompassing a range of different concrete mixes and construction techniques. This provided a focus for a number of construction-phase research investigations involving several Universities and including that reported here, which was concerned with the practicality on site and the individual capabilities of non-destructive test methods.

The in-situ concrete test building at Cardington provided an ideal opportunity to establish a benchmark for alternative systems of concrete strength assessment to cube testing for early age strength monitoring.

EXPERIMENTAL PROGRAMME.

An important feature of the Project was the need to balance the ‘research’ requirements of the Academic Institutions involved, with the practical and commercial requirements of the Contractor (Byrne Bros.) to complete the work with a minimum of delay and disruption.

Compromises were necessary on both sides, and one consequence was the limitations that were necessary upon the number of tests performed. These numbers were relatively small in comparison with those typically associated with laboratory based studies, and in some instances were further curtailed as a result of operational circumstances. Some conflict of requirements between the five Universities involved in parallel projects was also inevitable.

Test Methods.

Previous studies by Bungey [1] have established that surface hardness testing is unreliable at early ages, and that whilst Ultrasonic Pulse Velocity measurements can yield good early age strength estimates usage is usually precluded by the need for access to two opposite faces. Where testing is required on one face, penetration resistance testing is quick and suitable for large members such as slabs, but this again has been shown to be unreliable at low strength values. Internal fracture tests are generally recognised as having high variability and are thus similarly considered unsuitable for early age work. The previous studies concluded that pull-out testing, maturity testing and temperature-matched curing were the most reliable and practicable techniques at low strength levels. It is on this basis that these three techniques were selected for use in this programme of work.

Pull-out testing involving preplanned inserts cast into the pour is particularly suitable for direct insitu measurements of early age strength utilising cut-out panels in shutters where appropriate. The Danish Lok-Test system was selected for this project since this is the version which has gained greatest commercial acceptance worldwide. A companion CAPO-Test system is also available in which tests may be conducted on hardened concrete without preplanning, except to avoid reinforcement, utilising drilling and under-reaming with specialist equipment. This was also used in the project to provide supplementary information and to permit a controlled comparison of the two techniques under 'field' conditions. One key feature of these pull-out methods is the good sensitivity to compressive strength and the relative insensitivity of correlations to mix variables such as aggregate type.

Maturity and Temperature Matched Curing techniques are both well established and are based upon measurements of within-pour temperatures. Both can provide reliable results but suffer from potential practical disadvantages [1]. They were adopted for this project to permit overall comparison with the two partially-destructive techniques, and to assist interpretation of results as well as further examination of the benefits of test combinations.

Scope Of Variables.

The flat slab insitu concrete frame was designed to encompass a range of different concrete types and construction procedures. The six different mixes that were covered in this study are detailed in Table 1. It must be noted that the ready-mixed concrete supplier reserved the right to make adjustments, during construction, to the mix proportions originally submitted for approval, e.g., to make savings when the target mean strength was proving to be higher than what was needed, see Table 1, Mixes C37N-10 and C37N-11. It is understood that these adjustments are a norm during the construction of a project. The principal variables for the concretes covered by this study were: concrete grade (C37 and C85), admixtures (plasticiser and superplasticiser) and aggregate type (gravel and limestone).

Table 1: Concrete mixes used for the construction of the in-situ concrete frame building project.

		CONCRETE TYPES AND DRY BATCH WEIGHTS (per m ³).					
		C85MS	C85MK	C37N-10	C37N-11	C37P	C37F
		Microsilica	Metakaolin	Normal	Normal	Plasticised	Flowing
Location							
	Column	2→3	1→2		3→6		
	Slab			1, 2	5	3	4
Portland Cement (kg)		400	400	380	355	330	335
Sand (kg)		732	717	755	785	815	810
20-5mm Coarse Aggregate (kg).							
	Limestone	1170	1146				
	Gravel			1025	1025	1010	1010
Admixtures (ml)							
	Plasticiser¹	1232	1232			990	
	Superplasticiser	8800	8800				5000
CRMs (kg)							
	Microsilica	40					
	Metakaolin		40				
	GGBS						
Fibres (kg)							
Free W/C		0.25	0.32	0.50	0.53	0.52	0.52
Target							
Slump (mm)				100	100	100	
Flow (mm)		550	600				550

Tests were performed on columns at different heights (top, middle and bottom), and on slabs, both adjacent to columns and in mid bay (top and bottom). The selected test methods were each used at similar locations to further permit assessment of their practicality on site e.g. speed, relative cost, disruption and accuracy, and to assist determination of an optimum balance between insitu tests and cube testing.

Insitu tests using the Lok and CAPO, were undertaken at 1 day (or as soon as practicable), 3 days, 7 days and 28 days. Temperature measurements were made (by BRE) from the time of casting at several locations on columns at a depth of 25 mm below the surface and on slabs at 25 mm above soffits and 50 mm below top surfaces. Results for corresponding temperature-matched cured cubes (based on sensors at a depth of 50 mm below the tops of slabs midway between columns), air cured and water cured cubes were also made available. These were designed to enable comparisons of insitu strength with cubes experiencing differing curing regimes.

Data Collection.

During the development of the work programme, extensive discussion and pre-planning was undertaken with the staff of BRE, leading to the programme outlined above. Preparation of correlations between measured property and strength is a key issue for insitu testing, and it is recommended that for normal practice these should be prepared in advance of the construction

starting date. In this case, however, bearing in mind the number of mixes involved, the short time-scale for preparatory work, the BRE intention to set up a laboratory on site, and the need to avoid duplication of effort, correlation specimens were cast on-site during concreting of the structure. In each case these comprised four 200mm timber moulded cubes (Lok-tests), four 200mm timber moulded cubes (CAPO-tests) and one 150mm cube containing a temperature probe connected to a data logger (maturity). Results from these specimens were compared with cube results provided by BRE. Records of ambient temperature and humidity were also made.

RESULTS AND DISCUSSION.

The objective of an in-place test is to obtain an estimate of the properties of concrete in the structure. Very often the desired property is the cube compressive strength. To make a strength estimation it is necessary to have a known relationship between the result of the in-place test and the strength of the concrete for the particular concrete mix concerned. Correlation specimens, air-, water- and temperature matched cured cubes, cast on site by BRE during concreting of the main structure, were tested by STATS Ltd.

Strength Correlations.

Lok-Test Strength Correlations. Historically, most strength relationships have been assumed to be straight lines, and ordinary least-squares analysis has been used to estimate the corresponding slopes and intercepts, as shown in Fig. 2, with results from this project. The Y intercepts and the slopes of the strength correlations vary considerably for each individual concrete mix, but the combined correlation for all mixes is surprisingly very close to the Manufacturer's correlation [2].

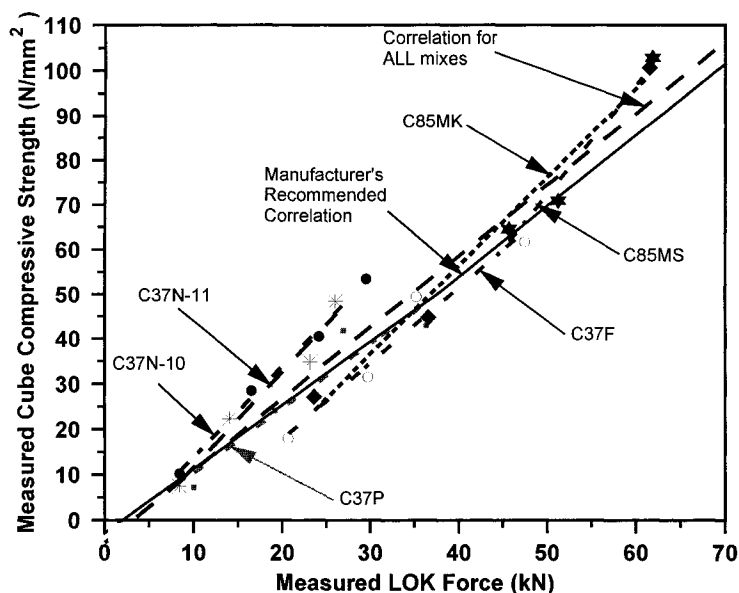


Fig. 2: Lok test strength correlations.

This line crosses the Manufacturer's recommended correlation at a Lok force of 10.5 kN but because of its different slope it starts deviating resulting in an estimated in-situ strength which is higher by 4.8 N/mm² at a Lok force of 37 kN. Beyond this Lok force the Manufacturer's recommended correlation has the same slope as the Cardington correlation but the Y intercept is lower by 4.8 N/mm². It was also found that grouping all the results together to obtain one strength correlation for all the mixes that were tested improved the confidence in the strength prediction; the 95% confidence interval was ± 4 N/mm² for a concrete strength of 43 N/mm². This single strength correlation, based on all the results, was therefore used for estimating the in-situ strength from Lok. These strength estimates will be discussed in the next section.

CAPO-Test Strength Correlations. The possibility of using the Lok-test correlation to interpret the CAPO-test results has been investigated. It was found that because of the similarity of the best-fit line, for all normal strength concretes, with that obtained for the Lok-test, one strength correlation can be used for both the Lok and CAPO-tests

Maturity Strength Correlations. The ambient temperature inside the Cardington hangar varied between 5 and 10°C during the construction period. The air-cured cube temperatures dropped to the ambient temperature within 2-days after casting. This resulted in almost linear relationships between the maturity, expressed in °C Hours, and time after casting in days. The compressive strength was plotted against the natural logarithm of the maturity to determine equations relating the two. These equations have been plotted on normal axes as shown in Fig. 3. It is clear that, as expected, one strength correlation *cannot* be used for all concrete mixes. The same maturity, say 12000 °C Hours, corresponds to 47 and 104 N/mm² for mixes C37N(modified) and C85MS respectively. Fig. 3 also shows that modifications to the concrete mix proportions of the C37N concrete affected the maturity strength correlation. Individual strength correlations for each mix were therefore used to estimate the in-situ strengths, described in the next section.

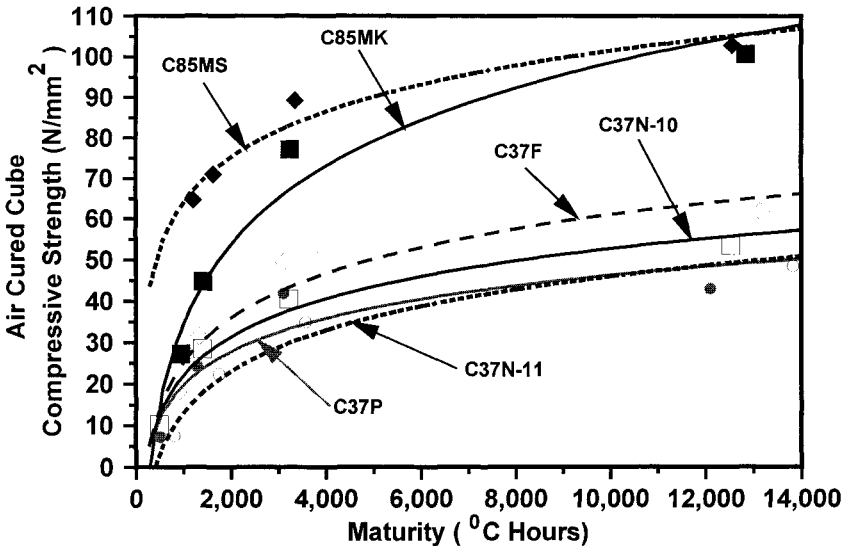


Fig. 3: Maturity strength correlations.

In-Situ Strength Estimates.

The strength correlations determined in the previous section have been used to estimate the in-situ strengths based on measurements on the structure. These are compared to strengths obtained from air-, water- and temperature matched cured cubes.

Lok-test strength estimates. Fig. 4 shows the estimated strengths for columns and slabs, versus the measured compressive strengths obtained from air-cured companion cubes. The average coefficients of variation from the equality line are: (a) 27.9 % for the concrete mixes used in the columns and 22.2 % for the strength of the mixes used in the slabs. It must be noted that some deviation from the equality line is expected from the in-situ strength results. This is because of the difference in the compaction and temperature curing regime of the concretes in a structural element and in air-cured cube moulds. The peak temperatures in the column and in the air-cured cube for the C85MS concrete were 41 and 16°C respectively. Similar trends were obtained for the other mixes but the temperature difference was smaller, e.g., for the C37N-10 the peak temperatures were 24°C and 14°C in the column and in the air-cured cube, respectively. The ambient temperature was approximately 8°C.

The in-situ strengths should ideally be related to strengths obtained from temperature matched cured cubes. The average coefficient of variation from this equality line was found to be 13.9%. Unfortunately, this comparison was only possible for the C37 mixes, as no temperature matched cured cubes for the C85 concretes were available for testing.

In-situ strength estimates quoted above included different locations on structural elements; top middle and bottom for columns and top and soffit for slabs. In the columns with the C85MK and the C85MS mixes the highest strength was obtained at mid-height. The average strength

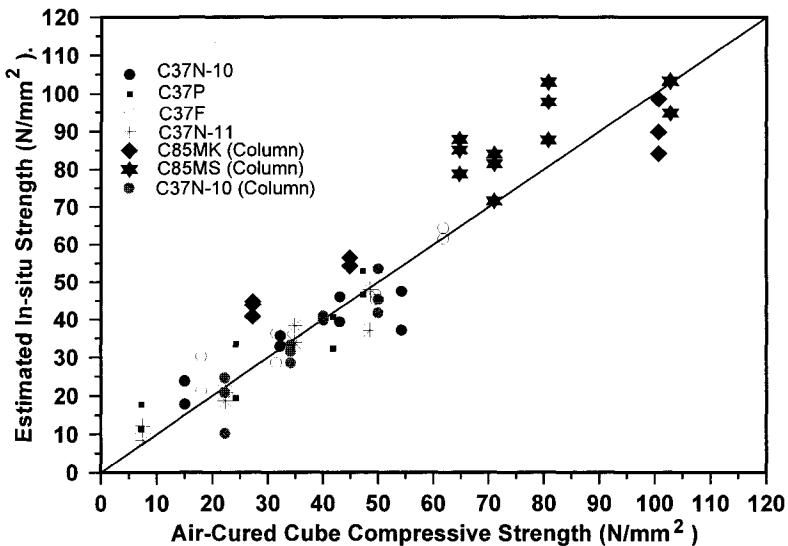


Fig. 4: Estimated in-situ compressive strengths using one Lok-test strength correlation for all the mixes tested.

for all ages at the top of columns was 3.3 % lower than at mid-height, while the strength for the bottom of columns was considerably lower at 5.0 %. Only one column cast with the C37N-10 concrete mix was tested and the highest strength was obtained at the top. The average strength differences, for all ages, were 4.6% and 8.0% lower from the top, for mid-height and bottom respectively. These differences appear to be due to different insertion times of the poker vibrator.

The average difference between the top and soffit strengths of slabs at mid-bays was 13.6 %, the highest compressive strength being at the soffit. This difference is however affected by the location; the strength difference increases to 34.8% for concrete placed adjacent to columns.

CAPO-test strength estimates. The similarity of the strength correlations for the Lok and Capo tests was discussed in the previous section. The estimated in-situ strengths showed similar average coefficients of variation about the equality line with air-cured cube compressive strengths as those of the Lok test; 16.0 % and 22.2 % for the CAPO and Lok test respectively. The small difference in these values may be due to the fact that CAPO tests were only performed on the lower strength (C37) concretes and did not include the C85 concretes. It may therefore be concluded that the CAPO test may be used to complement data obtained by the Lok test since the same correlation can be used.

Maturity strength estimates. Individual strength correlations only have been used to convert maturities into in-situ strengths. Fig. 5 shows the estimated in-situ strengths plotted against the compressive strengths obtained by testing air-cured companion cubes. Coefficients of variation from the equality line are 16.3% and 21.9% for columns and slabs respectively. Similar trends as with the Lok-test results were found, i.e. (a) early-age in-situ strengths are higher than

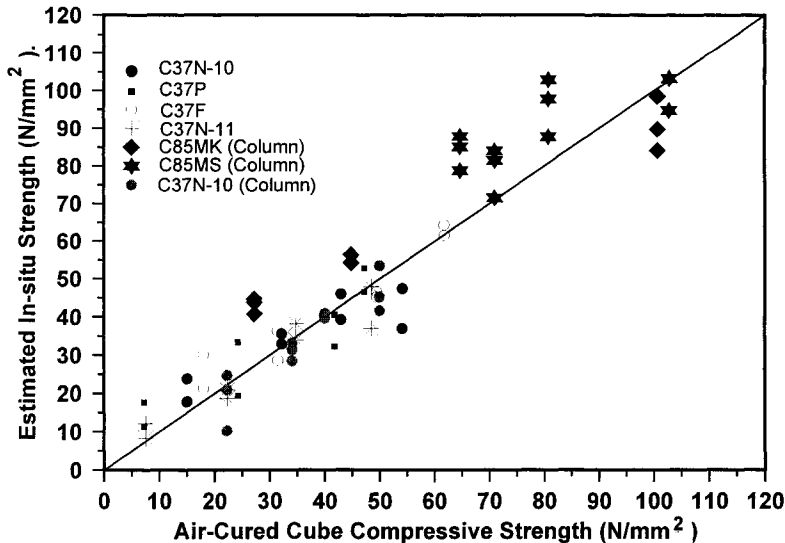


Fig. 5: Comparison between the estimated in-situ compressive strengths (using individual maturity strength correlation for each of the mixes tested) and the air-cured cube compressive strengths.

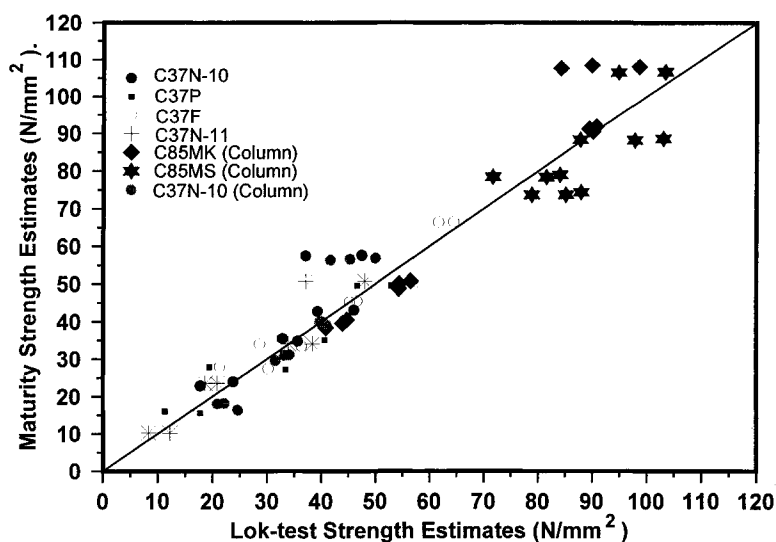


Fig. 6: The strength estimates from the maturity measurements are plotted against the Lok-test estimates.

compressive strengths of air-cured cubes but are similar to water-cured cube compressive strengths, (b) the 28-day in-situ strengths are lower if compared to the water-cured cube compressive strengths, and (c) the in-situ strengths should ideally be related to strengths obtained from temperature matched cured cubes. Unfortunately, as mentioned earlier, temperature matched cured cubes were only available for the C37 concretes that were used in the slabs.

The above trends and their similarities with the Lok-test results implied that the strength estimates from the two tests might be similar. The strength estimates from the maturity measurements are plotted against the Lok-test estimates in Fig. 7. The strength predictions from the two tests show a very good correlation for the C37 concrete mixes. The scatter of results about the equality line appears to increase with higher strengths.

CONCLUSIONS AND RECOMMENDATIONS.

The project created a massive amount of data, some of which are presented in this paper. The main conclusions are:

- There are definite advantages in being able to rely on the manufacturer's recommended strength correlation, as was the case with the Lok and CAPO tests, in the absence of a specific strength correlation. Concrete mixes to be used on site may not be finalised until just before the construction start date. In this case if the appropriate facilities exist on site, specific confirmatory strength correlations can be developed if deemed necessary from companion cubes cast during concreting of the structure; thus minimising the cost of expensive pre-construction laboratory work.
- The norm for determining when to strike has been to use, on small sites, cubes that are air-

cured alongside the structure, and only on bigger sites, temperature matched cured cubes. Air-cured cubes have been used on the assumption that their maturities do not differ significantly from those in the structure. In this project, however, the in-situ maturities at the early-age of one day were considerably higher (by a factor of 2.4 in some cases) than those of air-cured cubes.

- Relating maturity to Lok-test strength estimates offers a way of validating the values and thus increases the confidence of the strength estimates obtained from each test. The values estimated should be within ± 5 N/mm². If any results fall outside this equality line band width then further tests may be performed using the CAPO test apparatus. If maturity measurements consistently overestimate the in-situ strength as determined by the Lok or CAPO tests then it is likely that the concrete mix proportions have changed.

AKNOWLEDGEMENTS:

The authors gratefully acknowledge the helpful collaboration of the Building Research Establishment, Byrne Bros., and Ready Mixed Concrete Ltd.

REFERENCES:

1. Bungey, J. H. (1989). In: *Non-Destructive Testing*, J. Boogaard and G. M. Van-Dijk (Ed.). Elsevier, Amsterdam, pp. 1243-1248.
2. Petersen, C. G. (1997). In: *Proceedings of the International Conference on NDT in Civil Engineering*, J. H. Bungey (Ed.), Brit. Inst. NDT, pp. 77-96.
3. Natrella, M. G. (1963). *Experimental Statistics*. National Bureau of Standards, USA.

IDENTIFICATION OF CONVECTIVE HEAT TRANSFER COEFFICIENT FROM FIELD TEST

Takayoshi SHIINA, Noriyuki NISHIDA
*Technical Research Institute, Nishimatsu Construction Co., Ltd.,
2570-4 Shimotsuruma, Yamato, Kanagawa 242-8520, Japan*

Kunihito MATSUI
*Department of Civil and Environmental Engineering, Tokyo Denki University,
Ishizaka, Hatoyama, Hiki-gun, Saitama 350-0394, Japan*
and

Theodore F. SMITH
*Department of Mechanical Engineering, The University of Iowa,
Iowa City, IA 52242, U.S.A.*

ABSTRACT

Nonlinear temperature distributions in concrete structures are a cause of thermal cracking that results in shortening of the useful life of these structures. To predict a possible occurrence of cracking, accurate estimations of thermophysical properties of concrete in-situ as well as the convective heat transfer coefficient are required. Among the various variables, the convective coefficient in particular plays a key role. Field tests on concrete specimens have been conducted and specimen temperatures and meteorological data have been acquired. Using these sets of data, a procedure to identify all necessary parameters is developed in this paper.

KEYWORDS

Gauss-Newton method, convective heat transfer coefficient, thermal cracking, field tests, thermal analysis.

INTRODUCTION

Techniques for estimating the possible occurrence of thermal cracking in concrete structures have been established and are used in practice. It is well known that concrete cracking poses a serious problem for concrete structures from a viewpoint of their functionality and durability. Nonlinear temperature distributions in a concrete body due to heat released by cement hydration are a cause of thermal cracking at an early age of the concrete and may result in shortening the useful life of concrete structures. Temperature distributions in a concrete body are affected by a number of parameters. A thermal analysis of concrete is normally conducted using standard values of these parameters given in references or concrete codes. However, the temperatures that are computed using reported values for these parameters often do not agree well with the experimental data. This lack of agreement is because the properties of in-situ concrete differ from those of laboratory tests due to the difference in the environment and casting conditions.

Chikahisa et al.[1] evaluated a convective heat transfer coefficient by using the simplex method. The authors [2, 3] proposed a Gauss-Newton method to estimate the values of five parameters (thermal conductivity and specific heat of concrete, convective coefficient, and experimental

constants of adiabatic temperature rise Q_{∞} and γ) using construction site data. However, discrepancies between predicted and actual measured surface temperatures often occur. Furthermore, among the identified parameters, the convective coefficient may differ greatly from that given in references. This is due to the fact that the coefficient is identified without considering the effects of solar radiation, infrared radiation, and latent heat on the concrete surface.

The factors affecting the temperature distribution within concrete may be divided into two types. The first are the thermal characteristics of concrete that are affected by aggregate types and concrete mixture (e.g., density, thermal conductivity, specific heat, thermal diffusivity, emittance, and solar absorptance). The second are climatic conditions of surroundings (e.g., ambient air temperature, relative humidity, and velocity; solar radiation; infrared radiation from surrounding atmosphere; and rainfall).

In this paper, a boundary model at the concrete surface that considers climatic factors is proposed. We have conducted field tests using concrete specimens and have automatically monitored concrete spatial and temporal temperatures as well as meteorological data. An inverse analysis algorithm for estimating all necessary thermal parameters from the data is developed, and the effectiveness of the algorithm is demonstrated.

ENERGY BALANCE AT CONCRETE SURFACE

The net radiation Q_{RNET} at the concrete surface is the sum of the solar flux Q_{SNET} and infrared radiative flux Q_{INET} , and is given by

$$Q_{RNET} = Q_{SNET} + Q_{INET} \quad (1)$$

Equation (1) is termed the radiant energy balance equation and can be rewritten as

$$Q_{RNET} = (Q_{Sdown} - Q_{Sup}) + (Q_{Idown} - Q_{Iup}) \quad (2)$$

Q_{Sdown} is the global solar radiation that is the sum of the downward components of direct and diffuse solar radiation. Q_{Sup} is the reflection of global solar radiation at the concrete surface. Q_{Idown} is the downward infrared radiation from the atmosphere to the concrete surface. Q_{Iup} is the upward infrared radiation and is the sum of upward radiation emitted from the concrete surface in the infrared spectrum and the reflection of downward infrared radiation at the concrete surface. The terms in parentheses in Eq. (2) represent the absorbed solar radiation and the net radiant energy exchange between the atmosphere and concrete surface.

The net non-radiative flux Q_{NNET} is expressed as

$$Q_{NNET} = Q_{CH} + Q_{LH} \quad (3)$$

Equation (3) is the sum of the convective flux Q_{CH} between the concrete surface and the surrounding air and the latent heat flux Q_{LH} due to water evaporation from the fresh concrete surface.

The sum Q_{EB} of Eqs. (1) and (3) is termed the energy balance equation and is written as

$$Q_{EB} = Q_{RNET} + Q_{NNET} = (Q_{SNET} + Q_{INET}) + (Q_{CH} + Q_{LH}) \quad (4)$$

Equation (4) illustrates that the fundamental energy balance for the concrete surface is divided into four terms: solar and infrared radiative fluxes, convective heat flux, and latent heat flux.

MODELING OF CONCRETE TEMPERATURE PREDICTION

Governing equation

The internal temperature distribution of concrete is modeled using the one-dimensional, transient heat conduction equation

$$\rho C \frac{\partial T(z,t)}{\partial t} = K \frac{\partial^2 T(z,t)}{\partial z^2} + \dot{Q}(t) \quad (5)$$

where ρ is density [kg/m^3], C is specific heat [$J/kg \cdot ^\circ C$], K is thermal conductivity [$W/m \cdot ^\circ C$], $\dot{Q}(t)$ is heat generation for cement hydration in concrete [W/m^3], z is the depth below the concrete surface [m], t is time [hr] and $T(z,t)$ is internal temperature distribution [$^\circ C$] of concrete at depth z and time t .

The heat generation rate is written as

$$\dot{Q}(t) = \rho C Q_\infty \gamma e^{-\gamma t} \quad (6)$$

where Q_∞ is ultimate adiabatic temperature rise [$^\circ C$], γ is a constant for the rate of temperature rise [$1/day$] and t is time [day]. This cement hydration model is considered only for the early age of the concrete.

Boundary condition between concrete surface and surroundings

The boundary condition between the concrete surface and surroundings is expressed by

$$K \frac{\partial T(0,t)}{\partial z} + Q_{EB} = 0 \quad (7)$$

where Q_{EB} is the rate of energy transfer between the concrete surface and surroundings per area [W/m^2]. The energy balance at the concrete surface in Eq. (7) is expressed by the following equation:

$$Q_{EB} = Q_{SNET} + Q_{INET} + Q_{CH} + Q_{LH} \quad (8)$$

where Q_{SNET} is the net solar radiative flux [W/m^2], Q_{INET} is net infrared radiative flux [W/m^2], Q_{CH} is the convective flux [W/m^2], and Q_{LH} is latent heat flux [W/m^2].

Solar radiative flux

The short-wavelength solar radiation absorbed at the concrete surface is calculated using

$$Q_{SNET} = (1 - \alpha) S \quad (9)$$

where α is solar reflectance for the concrete surface and is called the solar albedo, and S is the global solar radiation energy per unit area incident on the concrete surface [W/m^2].

The albedo is calculated by dividing the reflected global solar radiation at the concrete surface Q_{Sup} by the global solar radiation Q_{Sdown} , which is the sum of the downward component of the direct solar radiation and the diffuse solar radiation, all measured quantities. Then,

$$\alpha = \frac{Q_{Sup}}{Q_{Sdown}} \quad (10)$$

The albedo depends on such factors as the physical properties of the material, the roughness and color of the surface, and the solar angle.

Infrared radiative flux

The infrared radiative exchange between a horizontal flat concrete surface and the sky can be estimated by [4]

$$Q_{INET} = \varepsilon \sigma (T_{sky}^4 - T_{sur}^4) \quad (11)$$

where ε is a radiative property of the concrete surface termed the total hemispherical

emittance and applies to the infrared spectrum, σ is the Stefan-Boltzmann constant ($5.6686 \times 10^{-8} [W/m^2 \cdot K^4]$), T_{sky} is the equivalent blackbody temperature of the atmosphere [K] and is termed the sky temperature, and T_{sur} is the concrete surface temperature [K].

It is known that the sky temperature changes considerably with atmospheric conditions. Several equations have been proposed to relate the sky temperature for clear skies to the measured meteorological variables.

Swinbank [5] relates the sky temperature to the local air temperature using a simple relationship, and Brunt [6] relates the sky temperature to the water vapor pressure. Bliss [7] relates the sky temperature to the water vapor content of the air and/or air temperature. The result of his investigation can be expressed in terms of the local air temperature and dew point temperature. Berdahl and Martin [8] used extensive data from the United States to relate the sky temperature to the dew point temperature, dry bulb temperature, and time using the expression

$$T_{sky} = T_{air} \left[0.711 + 0.0056T_{dp} + 0.000073T_{dp} + 0.013 \cos \left(\pi t / 12 \right) \right]^{0.25} \quad (12)$$

where T_{air} is the local air temperature [K], T_{dp} is the dew point temperature [$^{\circ}C$], and t is time [hr]. The expression covers dew point temperatures ranging from -20 to $30^{\circ}C$. The range of the difference between sky and air temperatures is from $5^{\circ}C$ in a hot, moist climate to $30^{\circ}C$ in a cold, dry climate. Equation (12) is adopted in the ASHRAE Handbook [9].

The emittance is a radiative property of the concrete surface and its value has a range of $0 \leq \varepsilon \leq 1$. This property provides a measure of how efficiently a surface emits radiant energy relative to that of a blackbody. It depends strongly on the surface material, surface temperature, and finish condition (e.g., roughness and color). The value of emittance is given by

$$\varepsilon = \frac{Q_{Iup} - Q_{Idown}}{Q_{bc} - Q_{Idown}} \quad (13)$$

where Q_{Iup} and Q_{Idown} are the measured upward and downward infrared radiative fluxes, and Q_{bc} is calculated from

$$Q_{bc} = \sigma T_{sur}^4 \quad (14)$$

Equation (14) is the infrared radiation emitted by a blackbody ($\varepsilon = 1$) according to the Stefan-Boltzmann law. Because $\varepsilon \leq 1$, the radiant energy emitted by a real surface is less than that of a blackbody at the same temperature.

Convective heat transfer flux

The convective heat transfer between the concrete surface and its surroundings is described by

$$Q_{CH} = h(T_{air} - T_{sur}) \quad (15)$$

which is known as Newton's law of cooling. In Eq. (15), h is the convective coefficient [$W/m^2 \cdot ^{\circ}C$]. For $T_{air} < T_{sur}$, energy transfers from the concrete surface to the adjacent air.

The convective coefficient for forced convection is expressed as a linear function of wind speed using

$$h = A + B \cdot v \quad (16)$$

where v is wind speed [m/sec] and parameters A and B are constants.

Latent heat flux

The latent heat flux is due to water evaporation from a fresh concrete surface. It is known that the magnitude of evaporation from surface depends on the air temperature, relative humidity,

and wind speed as well as the temperature of fresh concrete surface. Furthermore, the temperature change in fresh concrete, amount of plastic shrinkage, and plastic shrinkage cracking depend to a large extent on the rate of evaporation from the fresh concrete surface, which influences the amount and microstructure of the hydration product and the strength and durability of the concrete. The latent heat flux is a significant factor that affects the concrete temperature.

The latent heat flux is expressed by [10]

$$Q_{LH} = 0.0865 \Delta H (P_0 - P_a)(0.253 + 0.201v) \quad (17)$$

where ΔH is the latent heat of vaporization for water [kJ/kg]; P_0 is the saturated water vapor pressure at the concrete surface temperature [kPa]; and P_a is the water vapor in the surrounding air [kPa]. Equation (17) is called Menzel's formula.

ΔH is given by a regression formula of experimental data between temperature and vaporization heat. [11]

$$\Delta H = 2503.526 - 2.454 \cdot T_{sur} \quad (18)$$

where ΔH has units of [$^{\circ}C$].

OUTLINE OF FIELD TESTS

Concrete mixture and test specimens

Field tests have been conducted on concrete specimens shown in Fig. 1 starting at 11 a.m. on Nov. 7, 1997. The tests have been continued over a one-year period during which time the concrete body temperature, heat flow at the concrete surface, and meteorological data are recorded at a time interval of 30 minutes. The concrete mixture and aggregate are shown in Table 1. The concrete has a compressive strength $30 N/mm^2$, and its initial temperature is $21.4^{\circ}C$. Test specimens are of 6 types that are described in Fig. 1 and Table 2. The convection at the concrete surface for type B and C are forced and natural, respectively. The infrared

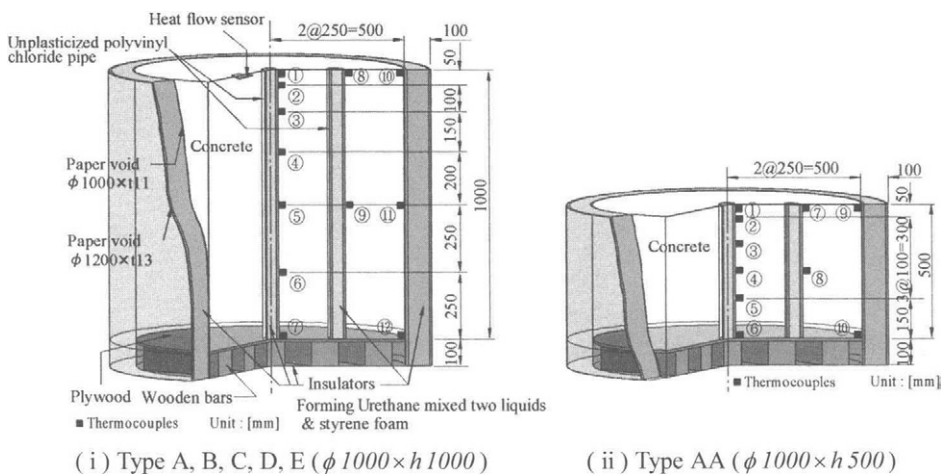


Fig. 1. Location of thermocouples and heat flow sensor

Table 1. Mixture of concrete

G_{max} [mm]	Slump [cm]	W/C [%]	Air [%]	s/a [%]	Unit weight [kg/m ³]				
					W	C	s	G	A
20	12 ± 2.5	50.0	4.5 ± 1.5	45.9	164	328	819	983	1.230

G : coarse aggregate, W : water, C : normal portland cement, s : fine aggregate, A : admixture

Fine aggregate ($s1$: Pit sand, $s2$: Crushed sand)

$s1$; fineness modulus: 1.61, specific gravity: 2.58, water absorption: 2.43%

$s2$; fineness modulus: 3.19, specific gravity: 2.61, water absorption: 0.84%, solid volume perc.: 55.6%

Coarse aggregate ($G1$: crushed stone)

$G1$; fineness modulus: 6.46, specific gravity: 2.64, water absorption: 1.01%, solid volume perc.: 58.0%

Ratio of aggregate mixing (mass mixing) $s1 : s2 = 20 : 80$

Table 2. Effective items and boundary conditions of surface

Type	Effective items *1 S I W V	Boundary condition of surface *2	Number of sensors *3	Note
A	S I W V	$Q_{EB} = Q_{SNET} + Q_{INET} + Q_{CH} + Q_{LH} -$	12	Exposed
B	I W V	$Q_{EB} = Q_{INET} + Q_{CH} + Q_{LH}$	12	Covered by roof
C	I V	$Q_{EB} = Q_{INET} + Q_{CH} + Q_{LH}$	12	Covered by roof with side
D	S I W	$Q_{EB} = Q_{SNET} + Q_{INET} + Q_{CH}$	12	Covered by vinyl sheet
E		$Q_{EB} = 0$	12	Simulated adiabatic condition
AA	S I W V	$Q_{EB} = Q_{SNET} + Q_{INET} + Q_{CH} + Q_{LH}$	10	Exposed

*1 S: global solar radiation, I: infrared radiation, W: wind, V: vaporization of water

*2 See Eqs. (7) and (8).

*3 See Fig. 1.

Table 3. Measured items and its' instruments

Items	Unit	Instruments	Location
Concrete temperature	°C	Thermocouples	
Air temperature	°C	Thermohygrometer	
Relative humidity	%	Thermohygrometer	
Dew point temperature	°C	Dew point thermometer	
Wind direction & velocity	m/sec	Breeze type anemometer	1, 2 and 3m height
Solar radiation	W/m ²	Albedometer	Type A
Infrared radiation	W/m ²	Pygeometer	Type AA
Heat flux	W/m ²	Heat flow meter	Type A, C and D
Precipitation	mm	Rain gauge	

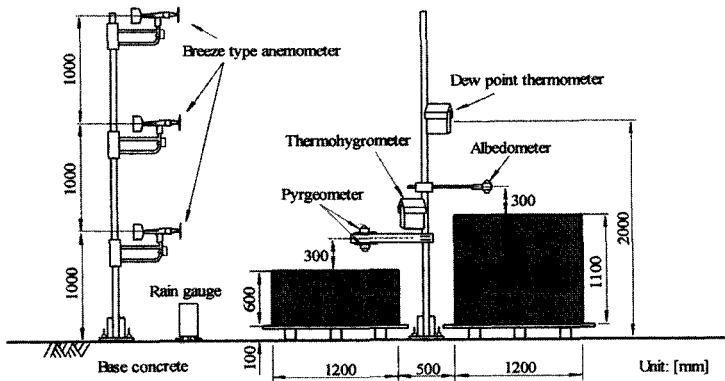


Fig. 2. Diagram of meteorological observation

radiative flux Q_{NET} occurs between the horizontal concrete surface and the adjacent air. Therefore, the sky temperature in Eq. (11), is changed to the ambient air temperature T_{air} . The shape of the specimen is cylindrical and all surfaces except the top surface shown in Fig. 1 are covered with insulation. Thus, a one-dimensional thermal analysis in the depth direction can be applied.

Measured items and measurement procedure

The concrete internal temperatures are measured using thermocouples. The deployment of thermocouples is shown in Fig. 1. It is difficult to measure the concrete surface temperature by a thermocouple affixed to the concrete surface, because the effects of solar and infrared radiation depend on material and its color, etc. A non-contacting type thermometer has deficiency in accuracy. Referring to reference [12], a thermocouple was installed at a location of 0.5 cm below the concrete surface, and its value was regarded as the concrete surface temperature. The measured temperature data of all specimens have noise due to an unstable supplied voltage. A heat flow meter, which directly measures conductive heat flux, was installed 1 cm below the concrete surface.

The measured variables and their instruments are shown in Table 3. A diagram of meteorological observations is illustrated in Fig. 2. Meteorological data were scanned every 6 seconds for 30 minutes and their averages computed to represent the measured data for the 30-minutes time interval.

METHOD OF INVERSE ANALYSIS

The temperature distribution in a concrete body is a function of thermal properties X and time t and can be expressed as $T_i(X, t)$, where subscript i refers to the location of i th thermal sensor. X is an unknown vector composed of six parameters X_1, X_2, X_3, X_4, X_5 , and X_6 that represent the thermal conductivity and specific heat of concrete, constant values of A and B for the convective coefficient from concrete to air in Eq. (16), and parameters Q_∞ and γ for the hydration heat generation model in Eq. (6).

The remaining parameters in the model are considered as known. The six unknown parameters are determined using the least square method to achieve agreement between computed and measured temperatures at the thermocouple sensor locations. The temperature measurements are taken at N locations and are defined by $u_i(t), (i = 1, \dots, N)$. A least square functional is defined by

$$f(X) = \int_{t_0}^{t_1} \sum_{i=1}^N \{u_i(t) - T_i(X, t)\}^2 dt \quad (19)$$

where t_0 and t_1 are the lower and upper limits of time used for the analysis. The unknown parameters $X_i (i = 1, \dots, N)$ are determined so as to minimize Eq. (19). Because Eq. (19) is a nonlinear least square problem, an iterative computation is required to achieve the minimum of Eq. (19). To introduce the Gauss-Newton method, the following linear approximation

$$T_i(X + \Delta X) = T_i(X) + \sum_{j=1}^6 \left(\frac{\partial T_i}{\partial X_j} \right) \Delta X_j \quad (20)$$

is utilized. Inserting Eq. (20) into Eq. (19), we want to determine ΔX_j such that the functional attains a minimum assuming X is given. The necessary condition is written as

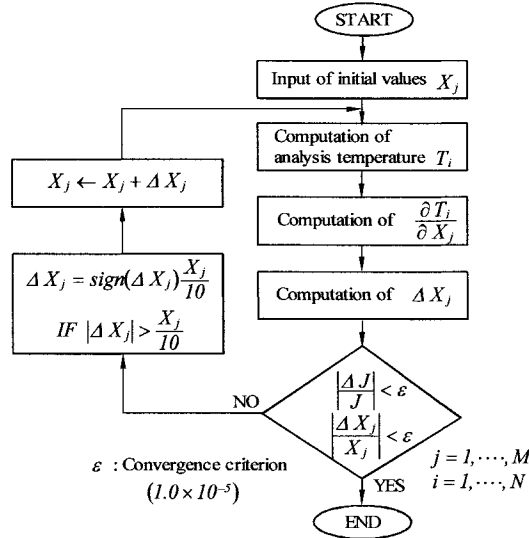


Fig. 3. Flow of an inverse analysis

$$\sum_{j=1}^6 \left\{ \int_0^t \left(\sum_{i=1}^N \frac{\partial T_i}{\partial X_j} \frac{\partial T_i}{\partial X_j} \right) dt \right\} \Delta X_j = \int_0^t \sum_{i=1}^N \{u_i(t) - T_i(X, t)\} \left(\frac{\partial T_i}{\partial X_k} \right) dt \quad (21)$$

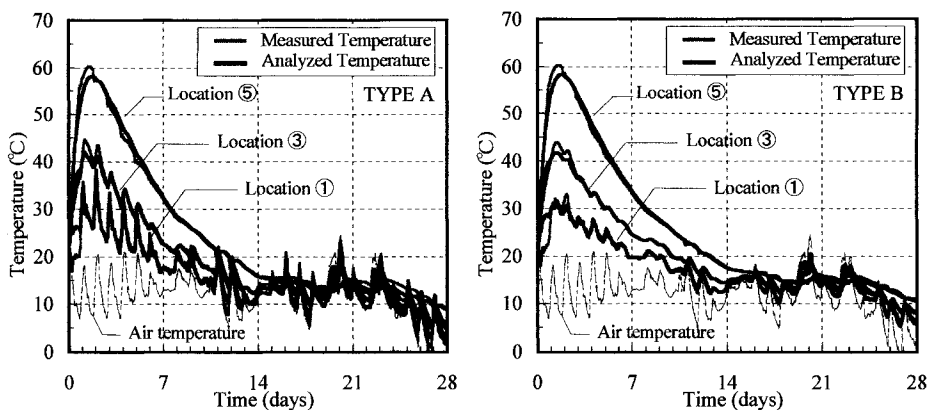
$(k = 1, \dots, 6)$

Equation (21) is a set of linear equations with respect to ΔX_j . The coefficient matrix is referred to as a normal matrix that often manifests singular or nearly singular characteristics. Taking numerical instability into consideration, a singular value decomposition is employed to solve for ΔX_j ($j = 1, \dots, 6$). The flow of the computations is shown in Fig. 3. In the figure the maximum allowable change for $|\Delta X_j|$ is set at 10 % of X_j , because the linear approximation in Eq. (20) has to hold.

RESULTS OF INVERSE ANALYSIS

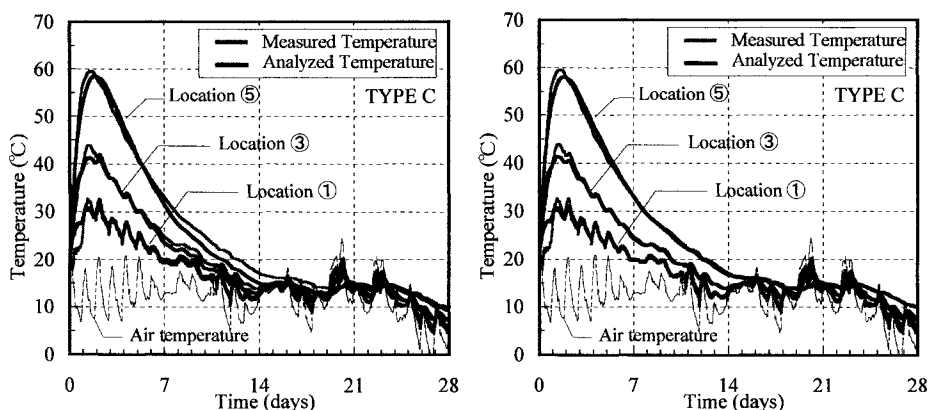
For evaluating the validity of the method from field test data, we used four sets of thermal data for the test specimens: type A, B, C, and AA. Ten or twelve thermal sensors are embedded in the concrete specimens and their locations are shown in Fig. 1. However, all the data for the thermal sensors are not used in the inverse analysis. The time periods of duration for the thermal analysis are 7, 14, and 28 days for the measuring time that has extended over one year after the concrete placing. The thermal sensors used for the inverse analysis are ①, ③, ⑤ of type A, B, C and ①, ③, ④ of type AA in Fig. 1.

The known variables for the thermal analysis of emittance and albedo are calculated from Eqs. (13) and (10) using meteorological data. The mean values of these variables are 0.34 and 0.77. The six unknown variables $K, C, A, B, Q_\infty,$ and γ are initially assumed according to the JSCE concrete code[13]. Boundary conditions for the exposed concrete surface are shown in Table 2, and the bottom and sides are adiabatic. Six thermal parameters are estimated from



(a) Results of measured data within 28 days (b) Results of measured data within 28 days

Fig. 4. Comparison between measured and analyzed temperature (Type A and B)



(a) Results of measured data within 7 days (b) Results of measured data within 28 days

Fig. 5. Comparison between measured and analyzed temperature (Type C)

the field test data of concrete. The results of the inverse analysis are presented in Table 4 along with their initial values.

Figure 4 and 5 show the comparison between the measured and computed temperatures. The latter temperatures were computed using the numerical values of the parameters found from the inverse analysis. It may be stated the both temperatures show very good agreement for the measured time period. If a strong instability lies in an inverse problem, the computational process will show a slower convergence rate, will converge to different values, or will even diverge. The results depend on the following factors: 1) number of sensors and their locations, 2) duration of measurement, and 3) computational algorithm involved in the analysis. The effect of each factor is now examined.

Duration of measured data

Three different time periods for measured data, namely, 7, 14, and 28 days, are considered for

Table 4. Results of inverse analysis for different time periods of measured data

Type	Duration [days]	K		C		A		B		Q _∞		γ	
		[W/m ² ·C]		[J/kg·°C]		[W/m ² ·°C]		[W/m·sec·C]		[°C]		[l/day]	
		initial	results	initial	results	initial	results	initial	results	initial	results	initial	results
A	7		4.94		1250		2.3		3.0		69.8		0.816
	14	2.70	4.80	1256	1480	3.0	2.3	4.0	3.0	48.9	61.5	1.262	0.947
	28		4.84		1567		2.4		3.2		59.4		0.994
B	7		5.24		1309		2.2		2.8		70.7		0.806
	14	2.70	5.17	1256	1627	3.0	2.1	4.0	2.7	48.9	60.5	1.262	0.969
	28		5.16		1687		2.1		2.7		58.8		1.008
C	7		5.97		1430		6.5		—		76.1		0.771
	14	2.70	5.84	1256	1718	13.0	6.6	—	—	48.9	62.1	1.262	0.903
	28		5.78		1710		6.7		—		62.2		0.903
AA	7		4.23		1178		2.1		2.8		82.1		0.610
	14	2.70	4.45	1256	1212	3.0	2.2	4.0	2.9	48.9	81.8	1.262	0.575
	28		4.50		1214		2.2		2.8		81.3		0.570

Table 5. Convergent values of number of sensor locations (Type B, 7 days)

Case	Locations in Fig. 1 (a)	K [W/m ² ·C]	C [J/kg·°C]	A [W/m ² ·°C]	B [W/m·sec·C]	Q _∞ [°C]	γ [l/day]
1	①②③④⑤⑥⑦	5.85	1584	2.0	2.5	61.2	0.923
2	①②③④⑤	5.05	1252	2.2	2.9	72.4	0.783
3	③④⑤⑥⑦	7.76	2030	1.6	2.0	58.0	1.026
4	①③⑤	5.24	1309	2.2	2.8	70.7	0.806
5	①⑤⑦	5.70	1649	2.0	2.6	57.8	0.992
6	③④⑤	5.89	1576	2.0	2.5	64.6	0.929
7	④⑤⑥	8.28	2136	1.5	1.9	58.9	1.063
8	⑤⑥⑦	22.01	3570	0.8	1.1	59.4	1.024
9	①⑤	5.06	1352	2.2	2.9	67.5	0.866
10	①⑦	5.79	1474	2.0	2.6	60.8	0.834
11	⑤⑦	25.5	3742	0.8	1.0	59.5	1.007
12	①	—	—	—	—	—	—

— : not converged

each specimen type for estimating the parameters. The results of the inverse analysis for these time periods are presented in Table 4 along with their initial values. Changes in the results for a time period greater than 14 days are not significant. These results are mean values over the time period for each variables; however, slight variations within the time periods for the measured data, and Q_∞ and C in particular, are found using different initial values. This is because the thermal properties change depending on the time and temperature of the concrete body. Type A and B in Fig. 4 demonstrate very good agreement. Fig. 5 shows inconsistency, because the identified parameter values are different depending on the time period.

Noise in measured data

Even if slight or strong noise is present in the measured data, the computed temperatures from the identified parameters should exhibit a good agreement with the measured temperatures. In the field tests, all measured data have noise due to an unstable supplied voltages and natural fluctuations in environmental conditions. Despite the noise, converged results are obtained for each specimen.

Convergence rate and number of measuring locations

The necessary number of sensors and their locations, and the status of convergence are

Table 6. Values of A and B for convective heat transfer coefficient in Eq. (16)

Authors	Year	A	B
ASHRAE Handbook [9]	1987	5.7	3.8
Watmuff [14]	1977	2.8	3.0
Australian Standard [15]	1989	3.1	4.1
Molineaux [16]	1994	3.1	2.1
Yang [17]	1997	6.0	3.7
Current	1999	2.2	3.0

investigated by conducting the inverse analysis using the Type C data in Fig. 5.

The results presented in Table 5 show that the number of sensors and their locations influence the identified results.

The cases that do not converge are observed not to include the temperature data at the location ①, which is embedded just below the concrete surface. For the inverse analysis to be successful, the data at 3 locations at least are required including the location ① and ⑤. When the thermal parameters including the convective coefficient of concrete need to be identified, thermal sensor ① at the concrete surface is found to be extremely important. The data for sensor ① includes thermal effects of external factors related to climatic parameters such as solar radiation, infrared radiation, and air temperature.

Convective coefficient

The convective coefficient can be expressed as a linear function of wind speed as shown in Eq. (16). The constant values of A and B in Eq. (16) proposed in the past are shown in Table 6 show a wide variation. The values of A and B are also determined from the inverse analysis using the measured data.

For the constants in the convective coefficient correlation identified by the inverse analysis in Table 4, the following equation was obtained

$$h = (2.2 \pm 0.1) + (3.0 \pm 0.2)v \quad (22)$$

The values of A and B in Eq. (22) are similar to those of Watmuff in Table 6. When the boundary condition at the concrete surface considers only convective heat transfer, the identified constants are higher than the standard values given in references or concrete codes.

CONCLUSIONS

An inverse analysis procedure based on the Gauss-Newton method was developed to identify the six thermal properties of concrete from measured temperatures in the concrete body and meteorological data. These limited preliminary studies yield the following conclusions:

1. An identification procedure based on the Gauss-Newton method serves as an effective tool for estimation of the thermal properties in concrete.

2. It is possible to identify a more accurate forced convective coefficient by applying the meteorological data to the boundary condition of the concrete surface.
3. Stable convergence is observed when the time period of measured data is more than 14 days.
4. The results change slightly with the length of the time period for the measured data and the number of sensors and their locations.
5. It is desirable to have at least three locations that include the locations at the top and center to identify the thermal parameters of new cast concrete from measured data.

REFERENCES

1. Chikahisa, H., Tsuzaki, J., Arai, T. and Sakurai, H. (1992). In: *Journal of Concrete Engineering and Pavements, JSCE*, No.541/V-17, pp.39-47. (in Japanese)
2. Matsui, K., Nishida, N., Dobashi, Y. and Ushioda, K. (1993). In: *Transactions of the Japan Concrete Institute*, Vol.15, pp.131-138.
3. Nishida, N., Ushioda, K. and Matsui, K. (1999). In: *Proceedings of the International Conference Held at The University of Dundee, Concrete Durability and Repair Technology*, Concrete 5, Dundee, Scotland, UK, 6-10 September, pp.81-92.
4. Duffie, J.A. and Beckman, W.A. (1991). *Solar Engineering of Thermal Processes*, 2nd Ed., John Wiley & Sons, New York.
5. Swinbank, W.C. (1963). In: *Quart. J. R. Meteor. Soc.*, 89, 339.
6. Brunt, D. (1932). In: *Quart. J. R. Meteor. Soc.*, 58, 389.
7. Bliss, R.W. (1961). In: *Solar Energy*, 5, 103.
8. Berdahl, P. and Martin, M. (1984). In: *Solar Energy*, Vol.32, No.5, pp.663-664.
9. ASHRAE Handbook. (1987). *HVAC Systems and Applications*.
10. Berhane, Z. (1984). *ACI Journal Technical Note*, pp.560-565, Nov-Dec.
11. Incropera, F.P. and DeWitt, D.P. (1996). *Fundamentals of Heat and Mass Transfer*, 4th Ed., pp.846, John Wiley & Sons, New York.
12. Maruyama, T., et al. (1993). In: *Proc. of 5th Cold Region Pavement Conference under Japan-Canada Science and Technology Council, PICA*, pp.227-237.
13. JSCE. (1996). *Standard Specification for Design and Construction of Concrete Structures*, Part of Construction. (in Japanese)
14. Watmuff, J.H., Charters, W.W.S. and Proctor, D. (1977). *COMPLES*, No.2, 56.
15. Sheridan, N.R. (1989). *Australian Standard*, A53634.
16. Molineaux, B., Lachal, B. and Guisan, O. (1994). *Solar Energy*, Vol.53, No.1, pp.21-26.
17. Yang, S., Zollinger, D.G. and Rasmussen, R.O. (1997). In: *Proc. of 6th International Purdue Conference on Concrete Pavement Design and Materials for High Performance*, Vol.3, pp.161-191.

A Quality Control Method of Thick Embankment by a Falling Weight Test

Koichi Oniki, Katsutoshi Fujisaki & Keisaku Yasumoto
Kajima Technical Research Institute,
2-19-1, Tobitakyu, Chofu-shi, Tokyo, Japan

ABSTRACT

The thick-layer compaction method, in which the spreading depth of each layer is greater than the conventional depth of 30cm, has been considered a practical means of rationalizing fill work¹⁾. However, the conventional quality control method such as RI system standardized by the Japanese Geotechnical Society cannot be applied to this method. Focusing on a falling weight test as being fast and simple, this study explores feasibility in terms of correlation with the compaction characteristics of the ground and the vertical measurement range. As a result, Δt_v is adopt as a characteristic value of an acceleration wave, and this method was proved to be applicable to the thick-layer compaction method.

KEYWORDS

quality control, compaction characteristics, embankment, impact test, impact acceleration

INTRODUCTION

In view of rapid rationalization of civil engineering construction works, applicability of thick-layer compaction method, with a spreading thickness greater than the conventional thickness of 30cm, has been studied along with development of numerous large-scale compaction equipment. It has been clarified that a spreading thickness close to 60cm is possible for sandy or gravel soil and soft rocks¹⁾. However, it is difficult to apply conventional quality control methods such as RI system and sand replacement method for thick-layer compaction, since the measuring range in the depth direction in these methods is less than 30cm. Even though water replacement method can be applied for the purpose, greater amount of labor and time required for this method also pose difficulty. This study focuses on falling weight test as a prompt and simplified method for quality control of thick-layer compaction, and investigates its applicability in terms of correlation with characteristic values of ground compaction and measuring range in the depth direction.

CHARACTERISTIC VALUES OF ACCELERATION WAVE

In a falling weight test, estimation of characteristic values of ground compaction (density or strength) is attempted using characteristic values of acceleration wave upon the weight's collision onto the ground. The followings have been proposed as indices for quantitative assessment of characteristic values of acceleration wave upon the weight's collision onto the ground²⁾:

- (i) the maximum impact acceleration (a_{max})
- (ii) the time needed until the impact acceleration becomes 0 (Δt).

In this study, another parameter is considered,

- (iii) the time required until the decelerating velocity v becomes 0 (Δt_v). (See Figure 1.)

CORRELATION WITH CHARACTERISTIC VALUES OF GROUND COMPACTION

1. Estimation based on theoretical equations

Based on the results of observation on the ground surface after collision of the weight, a ground deformation model caused by penetration of the weight into the ground is shown in Figure 2²⁾. Using this model and numerical analyses, relationship between the characteristic values of acceleration wave and those of ground compaction (coefficient of sub-grade reaction K_{30}) was derived based on theoretical equations³⁾. As a result, It was revealed that relationship between the characteristic values of acceleration wave and those indicating ground condition, under various specifications of the falling weight test cases, can be approximated by Equations (1) through (2). Based on the information obtained by the theoretical equations above, the results of laboratory tests are summarized as follows:

$$a_{max} = \alpha_1(A\sqrt{h/m})K_{30} + \beta_1 \dots\dots\dots(1)$$

$$\Delta t_v = -\alpha_2(m/A)\log K_{30} + \beta_2 \dots\dots\dots(2)$$

where

α, β : coefficients characteristic to soil material

A: bottom surface area of the weight.

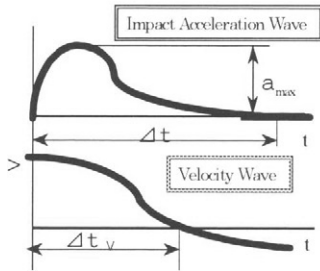


Fig.1 Characteristic Value of Acceleration Wave

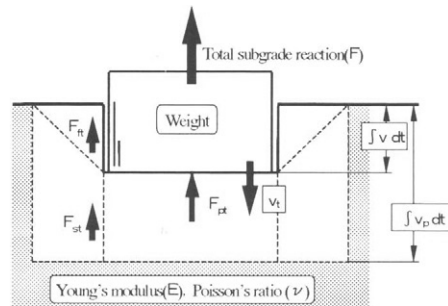


Fig.2 Model of Ground Deformation

2. Laboratory Investigation

Laboratory tests were performed in order to investigate the correlation between the characteristic values of acceleration wave and those of ground compaction for a falling weight test. Sample soil used for the tests was sandy soil with almost uniform grain size (the maximum grain size $D_{max}=2mm$ and uniformity coefficient $U_c=3.27$), and the maximum dry density $\rho_{dmax}=1.605g/cm^3$ when water content $w=18.5\%$, as shown in Figure 3.

Figure 4 shows relationship between the coefficient of sub-grade reaction (K_{30}) and dry density (ρ_d), derived after performing a plate bearing test on a uniformly compacted ground of a specific density at a constant water content ($w=7.5\%$) within a laboratory test mold (60cm in diameter and 60cm high). The results indicated positive correlation between dry density (ρ_d), and the coefficient of sub-grade reaction (K_{30}) of the sample soil used for the test.

The laboratory tests were performed using mass of the weight(m) and dropping height(h) as parameters, on a ground uniformly compacted in a mold at a specific density. The test conditions are summarized in Table 1.

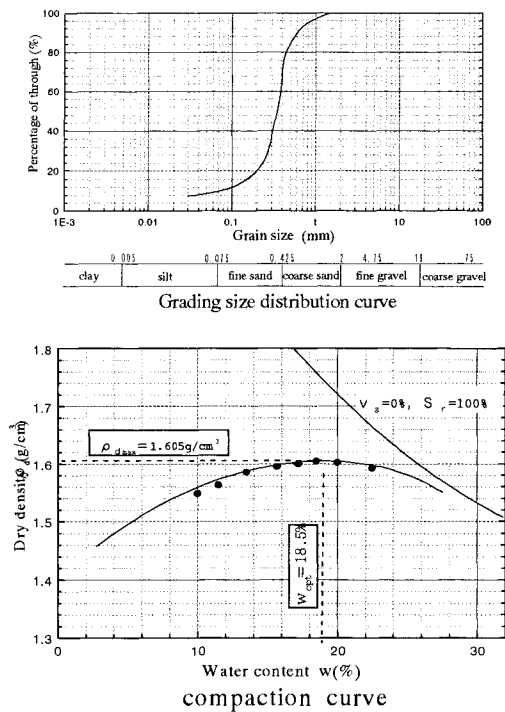


Fig.3 Characteristic of a Sample Soil

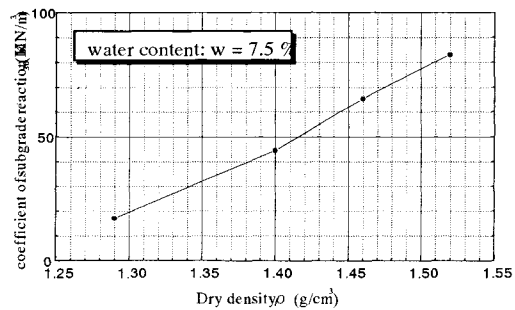


Fig.4 Relationship between ρ_d and K_{30}

Table 1 Laboratory Test Case(1)

Weight		h(cm)	w(%)	$\rho_d(\text{g/cm}^3)$
ϕ (cm)	m(kg)			
15.0	3.2,5.0	15,30,50	7.5	1.52

Figure 5 shows the test results. It was revealed that both a_{max} and Δt_v correlates well with the coefficient of sub-grade reaction (K_{30}) similar to the results obtained based on the theoretical equations, it was also shown that for materials whose dry density (ρ_d) correlates positively with the coefficient of sub-grade reaction(K_{30}), such as that used in the study, the two parameters a_{max} and Δt_v correlates also correlates well with the dry density(ρ_d). On the other hand, when impact acceleration a is close to 0, error of measurement becomes significant therefore making it difficult to read out the value of Δt accurately. Thus, we judged that Δt is not suitable as a parameter for actual quality control of thick-layer compaction.

Figure 5 shows that followings are possible in order to enhance measurement accuracy of the following parameters when diameter(ϕ) of the weight is constant:

- (i) for a_{max} , mass(m) should be made smaller or dropping height(h) should be made higher.
- (ii) for Δt_v , mass(m) should be made larger, regardless of dropping height (h).

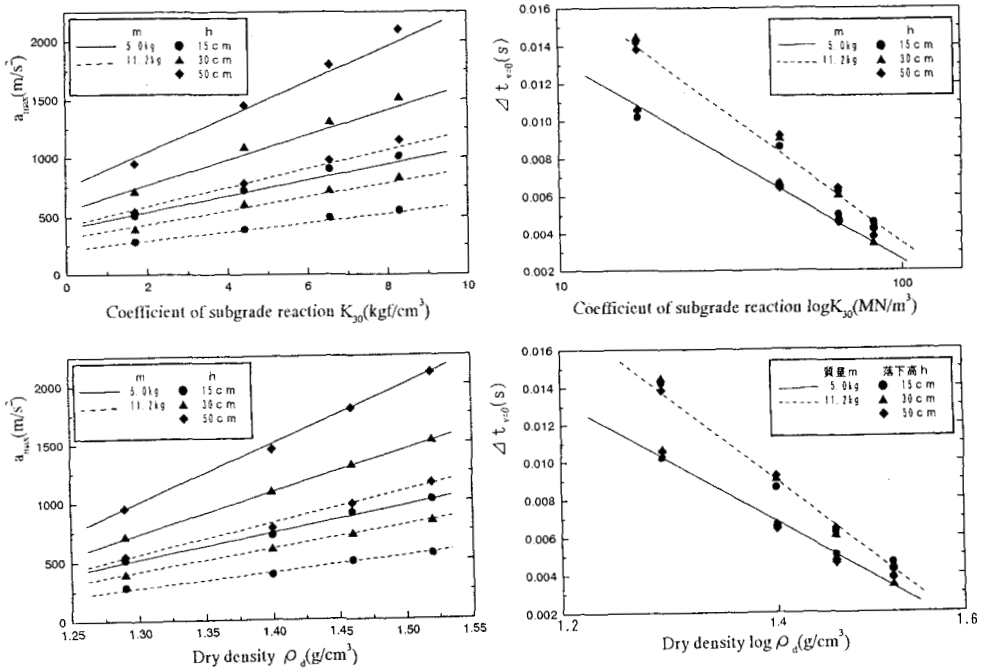


Fig.5 The result of Laboratory test(1)

If falling weight tests are to be applied for quality control in actual construction works, it is necessary that accuracy of characteristic values of ground compaction (K_{30}, ρ_d) obtained through the tests should be about the same with that for the conventional RI system (in the order of 10^{-2}g/cm^3). The accuracy of measurements for characteristic values of the ground compaction (K_{30}, ρ_d) under the test conditions was computed based on the test results shown in Figure 5 to reveal that the accuracy in the order of 10^{-1}MN/m^3 is maintained with respect to the coefficient of subgrade reaction (K_{30}) and that in the order of 10^{-2}g/cm^3 is maintained with respect to the dry density (ρ_d) under the following conditions:

- (i) for a_{max} , when the mass m equals 5.0 kg and dropping height h is greater than 30cm.
- (ii) for Δt_v , in all the cases.

Thus, it was confirmed that parameters a_{max} and Δt_v , among the characteristic values of acceleration wave, correlate well with characteristic values of ground compaction (K_{30}, ρ_d) under the test conditions of the study. Furthermore, trends similar to those obtained through studies on theoretical equations shown in Equations (1) through (2) were observed with respect to the relationship between the characteristic values of acceleration wave and those of ground compaction, under various specifications of the falling weight test cases.

MEASURING RANGE IN THE DEPTH DIRECTION

The measuring range in the depth direction(d) was obtained based on theoretical equations and laboratory tests, for the characteristic values of acceleration wave (a_{max} and Δt_v), which correlate well with those of ground compaction(K_{30} , ρ_d)

1. Estimation based on theoretical equations

In the study, the measuring range in the depth direction(d) for falling weight tests was assumed to be the propagation distance of impact wave through the ground in a specific time interval(δt) after the weight's collision onto the ground, as shown in Figure 6. Thus, it was decided that Equation(3) below, which was derived based on wave equations, is used for estimation of the range(d)

$$d = v_p \cdot \delta t \quad \dots\dots\dots(3)$$

where,

d: measuring range in the depth direction

v_p : propagation velocity of impact wave through the ground

E: a constant expressed as a function of Young's modulus (E) and poisson's ratio(ν)

$$E' = (1 - \nu)E / (1 - 2\nu)(1 + \nu)$$

ρ_i : wet density of the ground

δt : time interval after the impact acceleration started to accrue

Here, δt was defined as follows for each characteristic value of acceleration wave:

(i) for a_{max} , δt equals Δt_{a-max} which is the time required until impact acceleration a reaches the maximum value after the weight's collision onto the ground.

(ii) for Δt_v , δt equals Δt_v which the time required until decelerating velocity becomes 0 after the weight's collision onto the ground.

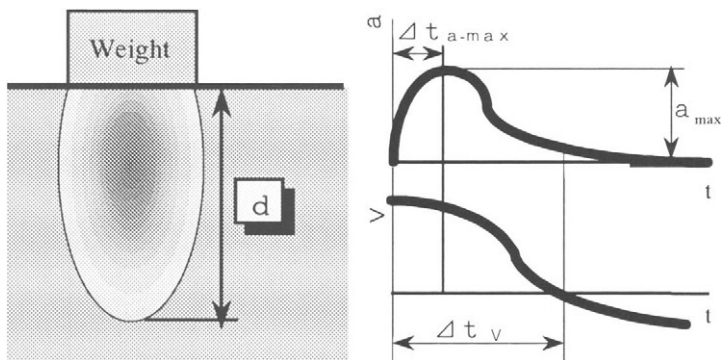


Fig.6 The Measuring Range in the Depth Direction

2. Verification through laboratory tests

Laboratory tests were performed assuming mass(m) of the weight and dropping height(h) as parameters. Here, thickness(H) of the ground compacted inside a mold at a constant dry density ($\rho_d=1.52g/cm^3$) was increased gradually to arrive at a value where characteristic values of acceleration wave (a_{max} and Δt_v) would not be influenced by effects from the bottom surface of the mold. The value of H was in turn defined as the measuring range in the depth direction. The test conditions are summarized in Table 2.

The test results are shown in Table 7. It was shown that measuring range in the depth direction (d) would take the following values:

- (i) for a_{max} , d was approximately 15 cm regardless of the values of m and h.
- (ii) for Δt_v , d was between 40 and 50cm when $m = 3.2\text{kg}$, and between 50 and 60cm when $m = 5.0\text{kg}$, regardless of the value of h. These values nearly equal to d obtained by substituting the values of $\delta t(\Delta t_{a-max}$ and $\Delta t_v)$ that correspond to each characteristic value of acceleration wave (Δt_{a-max} and Δt_v) which were read out from the test results for $H=60\text{cm}$ under the test conditions shown in Figure 7. This indicates that the method for setting the values of δt described above is valid.

From the above, it was confirmed that in order to enlarge the measuring range in the depth direction(d), Δt_v should be used as a characteristic value of acceleration wave. Furthermore, for Δt_v it is possible to enlarge the measuring range in the depth direction d if mass of the weight(m) is made larger when the weight diameter(ϕ) is constant, regardless of dropping height(h).

In this test, however, mold conditions have confined the ground thickness to only up to 60cm. The ground thickness should be at least about 1m thick, for more detailed investigation (on the limit of applicability of Equation(3), etc.).

Table 2 Laboratory Test Case(2)

Weight		h (cm)	w (%)	ρ_d (g/cm ³)	E (MN/m ³)	ν
ϕ (cm)	m (kg)					
15.0	3.2,5.0	15,30,50	7.5	1.52	1780	0.33

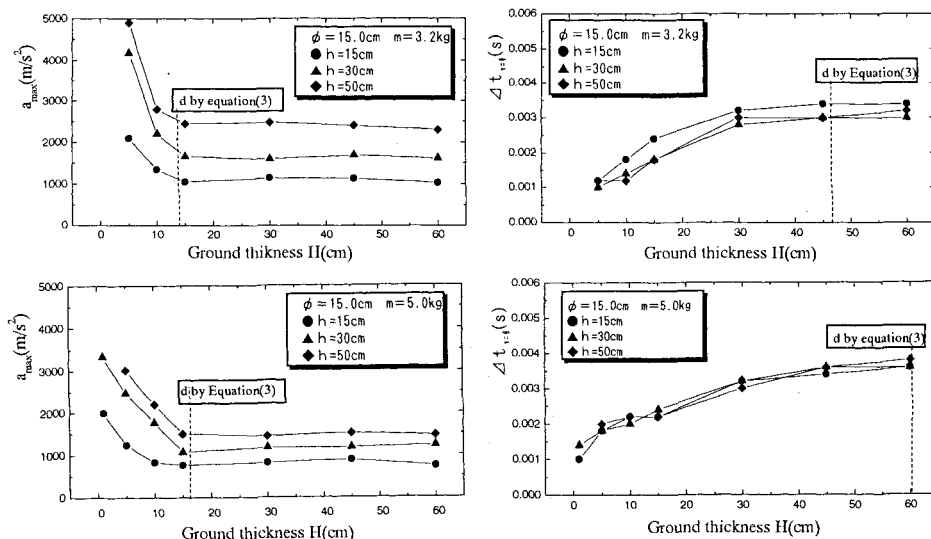


Fig.7 The result of Laboratory test(2)

A PROPOSED QUALITY CONTROL METHOD

In order to apply a falling weight test for quality control of thick-layer compaction, Δt_v should be used as a characteristic value of acceleration wave, and specifications of the test cases (weight diameter(ϕ), mass(m), and dropping height(h) and quality control standards should be determined taking into consideration the features of fill materials, depth for measurement, and correlation with characteristic values of ground compaction(K_{30}, ρ_d). Figure 8 shows a process for reaching the decision.

1. Specifications of the test cases

(1) Diameter(ϕ) of the weight

Diameter(ϕ) of the weight should be determined so as to avoid any effect from gravels, etc., upon collision, at the same time considering for the maximum particle diameter D_{max} of fill materials. Referring to the method adopted for determining diameter of a specimen ϕ and maximum particle diameter of fill material D_{max} in plate bearing tests, it was decided that ϕ should be greater than $5D_{max}$.

(2) Mass(m) of the weight

Mass(m) of the weight should be determined in accordance with measuring range in the depth direction(d) required for in practical application works. The measuring range in the depth direction(d) should be calculated using Equation(3) described, by substituting Δt_v , which corresponds with the quality control standard for characteristic values of ground compaction (K_{30}, ρ_d) obtained in a falling weight test performed along with field roller compaction test, into the said equation. In order to use Equation(3), it would be necessary to clarify beforehand the Young's modulus E and poisson's ratio n for the quality control standards of characteristic values of ground compaction (K_{30}, ρ_d), by triaxial compression test and other means.

(3) Dropping height(h)

Dropping height is known to have almost no effect on correlation with characteristic values of ground compaction and measuring range in the depth direction, it was decided that $h=30\text{cm}$ for ease of the test procedure.

2. Quality control standard for falling weight tests

For clarification of the quality control standard for falling weight tests, relationship between the characteristic values of ground compaction (K_{30}, ρ_d) and Δt_v was derived after performing falling weight tests assuming mass(m) as a parameter, along with field roller compaction tests, at four or five spots in a vicinity of the point where the characteristic values of ground compaction(K_{30}, ρ_d) had been measured through plate bearing tests and RI systems. Based on the above, it was decided that Δt_v corresponds to quality control standards for ground compaction would be the quality control standard for falling weight tests.

CONCLUSION

We have chosen falling weight test as a prompt and simplified method for quality control of thick-layer compaction, and studied its applicability (in terms of relationship with characteristic values of ground compaction and measuring range in the depth direction). The followings were clarified under the test conditions (on sample soils, dimensions of a mold, etc.).

(i) If a falling weight test is to be applied for quality control of thick-layer compaction, Δt_v , which has a large measuring range in the depth direction, should be used as the characteristic value of acceleration wave.

(ii) Accuracy of measurement of Δt_v is enhanced and its measuring range in the depth direction is enlarged if mass(m) of the weight is made larger when diameter(ϕ) is constant, regardless of dropping height(h).

(iii) Specifications of the test conditions should be determined as follows, for instance the diameter(ϕ) in accordance with the maximum particle diameter D_{max} of fill materials, and the mass(m) in accordance with required measuring depth.

(iv) Quality control standards for a falling weight test should be determined after duly considering the correlation with characteristic values of ground compaction ((K_{30}, ρ_d)), which are clarified based on a falling weight test performed along with field roller compaction test.

REFERENCES

- 1.Kato(1997):Effectiveness of large size compaction machine on the thickly spreaded embankment, Japan National Conference on Geotechnical Engineering,vol.32, pp.2235-2236.
- 2.Tateyama and Tanaka(1993):Evaluation of bearing capacity of unsaturated-compacted soil by behavior of a falling weight, Geotechnical Engineering Symposium, pp.91-98.
- 3.Oniki,Fujisaki and Yasumoto(1997):A Quality Control Method of Thick Embankment by a Falling Weight Test, Kajima Technical Research institute Annual Report, vol.45, pp.121-126.

This Page Intentionally Left Blank

COMPENSATED HALF-CELL POTENTIAL TECHNIQUE FOR NDE OF REBAR CORROSION

M. OHTSU and Y. TOMODA

Department of Civil Engineering and Architecture, Kumamoto University,
2-39-1 Kurokami, Kumamoto 860-8555, JAPAN

ABSTRACT

Concerning nondestructive evaluation (NDE) for corrosion of reinforcement (rebars) in concrete, the half-cell potential measurement can provide information on the probability of corrosion. It is reported, however, that the potentials measured are really sensitive to moisture content of concrete, thickness of concrete cover, surface coating, and internal defects (voids). As a result, the estimation on corrosion is somehow inconsequent. To compensate these effects, the boundary element method (BEM) is simplified for the data analysis. The potentials measured on the surface are analyzed and converted into those on the rebars. From the experiments, it is found that the ASTM criterion on the potential values are practically available for the estimation of corrosion in the case that the values are compensated. Further, the electric current analysis is performed from the compensated potentials. Results demonstrate that the corroded zone on rebars can be identified precisely. It is noted that a software developed for the compensation is so simple as to be readily implemented in a microcomputer.

KEYWORDS

Rebar corrosion, NDE, Half-cell potential, BEM

INTRODUCTION

For reinforcement of concrete, steel bars (rebars) are extensively employed. Chemically, rebars embedded are protected from corrosion by the surrounding alkaline of concrete. So far the concrete is as porous, chloride can penetrate into it and the passivity of the steel is destroyed. Due to salt attack, thus, chloride contamination of the concrete causes corrosion of rebars, which leads to cracking in reinforced concrete (RC) structures. In order to prevent from cracking,

nondestructive valuation (NDE) for corrosion of the rebars is desirable. At present, two techniques of the half-cell potential and the polarization resistance are commercially available. The former provides information on the probability of corrosion, while the latter is associated with the corrosion rate [1]. As for the half-cell potentials, the criterion for estimation of corrosion has been already coded in ASTM C876 [2], by employing a copper-copper sulfate half-cell electrode (C. S. E). It is reported, however, that the potentials measured are so sensitive to moisture content in concrete, thickness of concrete cover, surface coating that the estimated results are somehow inconsequent [3]. Further, the testing procedure is analytically investigated on the effect of internal defects [4]. It is found that the presence of internal void or cavity provides more negative values of the potential.

These undesirable effects on the half-cell potential measurement result mainly from the fact that the potentials are measured not on the rebars but on concrete surface. One compensation is to measure the potentials as near the rebars as possible, applying an embedded probe [5]. Another compensation is to determine the potentials at the rebars analytically. Previously the boundary element method (BEM) was applied [6]. The three-dimensional (3-D) analysis, however, was not only time-consuming but also impractical. Thus, the procedure was modified and the charge simulation method (CSM) was developed [7, 8]. The potentials measured on the concrete surface were quantitatively converted into those on the rebars. It was demonstrated that the ASTM criterion on the potential values converted were practically available for the estimation of corrosion, although the CSM still needed improvement.

In the present paper, the half-cell potential measurement is theoretically clarified. Simplifying the BEM, the CSM is improved and a compensated procedure is developed for the half-cell potential measurement. An applicability of the procedure is examined in reinforced concrete (RC) slabs of which rebars were corroded by an electrolytic test. Further, the electric current analysis is performed from the compensated potentials to identify the corroded regions of the rebars.

HALF-CELL POTENTIAL

Potential field and BEM

In the half-cell potential measurement, electrical potential $u(\mathbf{x})$ in the domain of concrete, D , is measured at the surface. The potentials in the concrete is satisfied with the Laplace equation,

$$\nabla^2 u(\mathbf{x}) / R(\mathbf{x}) = 0 \quad \text{in } D, \quad (1)$$

where ∇ is the gradient (nabla) operator and $R(\mathbf{x})$ are concrete resistivity at point \mathbf{x} in D . On

boundary conditions for eq. 1, concrete surface S is classified into the potential boundary S_p and the current boundary S_c . The surface, where the half-cell potentials are measured, corresponds to the potential boundary. Other surfaces are referred to as the current boundary where outward flow of the current is electrically free. These are presented,

$$u(\mathbf{x}) = E(\mathbf{x}) \text{ [C. S. E.]} \quad \text{on } S_p, \quad (2)$$

$$1/R(\mathbf{x}) \cdot \partial u(\mathbf{x}) / \partial \mathbf{n} = 0 \quad \text{on } S_c. \quad (3)$$

Here $E(\mathbf{x})$ are the potential values obtained by the copper-copper sulfate half-cell electrode [C. S. E.], and \mathbf{n} is the outward normal vector to the boundary surface.

Provided that the concrete near the rebar could be assumed as homogeneous, the resistivity R becomes constant and then the solution $u(\mathbf{x})$ can be represented by the boundary integral,

$$C \cdot u(\mathbf{x}) = \int_S \{G(\mathbf{x}, \mathbf{y}) [\partial u(\mathbf{y}) / \partial \mathbf{n}] - [\partial G(\mathbf{x}, \mathbf{y}) / \partial \mathbf{n}] u(\mathbf{y})\} dS. \quad (4)$$

C is the configuration coefficient. $C = 1$ in the case that the point \mathbf{x} is located inside the concrete, and $C = 1/2$ on the smooth surface. Points \mathbf{y} are located on the boundary S ($S = S_p + S_c$), surrounding the domain D . $G(\mathbf{x}, \mathbf{y})$ is the fundamental solution, as follows;

$$G(\mathbf{x}, \mathbf{y}) = 1/(4\pi r) \quad \text{for the three-dimensional (3-D) body,} \quad (5)$$

$$G(\mathbf{x}, \mathbf{y}) = 1/2\pi \cdot \ln(1/r) \quad \text{for the two-dimensional (2-D) body.} \quad (6)$$

Here r is the distance between points \mathbf{x} and \mathbf{y} .

Analytical procedure

The charge simulation method (CSM) is known as the indirect BEM. In the case that points \mathbf{x} are located inside D , eq. 4 is mathematically formulated as,

$$\begin{aligned} u(\mathbf{x}) &= \int_S G(\mathbf{x}, \mathbf{y}) [\partial u(\mathbf{y}) / \partial \mathbf{n} - \partial G(\mathbf{x}, \mathbf{y}) / \partial \mathbf{n} / G(\mathbf{x}, \mathbf{y}) u(\mathbf{y})] dS \\ &= \int_S G(\mathbf{x}, \mathbf{y}') f(\mathbf{y}') dS, \end{aligned} \quad (7)$$

where the boundary S is replaced by the virtual boundary S' . The virtual boundary is considered to circumvent the singularity ($r = 0$). The potentials measured are substituted into the left-hand of eq. 7, and the surface densities $f(\mathbf{y}')$ are determined, solving integral equations. Internal potentials $u(\mathbf{x})$ on the rebars are then computed from the surface densities, providing new $G(\mathbf{x}, \mathbf{y}')$ for the rebar locations. Here, one problem remains still unsolved with respect to the

location of the virtual surface, although an iteration procedure was proposed to minimize the error [8].

To improve the CSM, BEM formulation on the half-cell potential is alternatively simplified. Thus, the potential boundary, S_p , is only taking into account, because $\partial u(\mathbf{y})/\partial \mathbf{n}$ is normally equal to zero on the current boundary S_c . Then, eq. 4 becomes,

$$u(\mathbf{x}) = \int_{S_p} [-\partial G(\mathbf{x}, \mathbf{y})/\partial \mathbf{n}] u(\mathbf{y}) dS. \quad (8)$$

The potential boundary is divided into M surface elements of area ΔS . The potentials are measured at the center of the element as u_j and eq. 8 is digitized,

$$u_i = \sum_{j=1}^M -[\partial G_{ij}/\partial \mathbf{n}] u_j \Delta S. \quad (9)$$

The potentials at rebar surface, u_r , are computed, substituting the potential values u_j and area ΔS .

To identify the regions of corroded and non-corroded on the rebar, the current analysis is available [9]. From potentials u_i on the surface of the rebar, electric current at location x_k can be computed from,

$$I_k = \sum_{i=1}^N (u_k - u_i)/R \cdot DL_{ki}. \quad (10)$$

Here, the rebar is divided into N elements. The difference $(u_k - u_i)/R$ represents a current flow from x_i to x_k in the rebar, and DL_{ki} is the distance between x_k and x_i . R is a specific resistivity of concrete, which is assumed as constant as $10 \text{ k}\Omega\text{cm}$.

NUMERICAL ANALYSIS

Half-cell potential simulation

To study the potential field in the half-cell potential measurement, a two-dimensional (2-D) BEM analysis was carried out. A model analyzed is shown in Fig. 1. The boundary of a concrete block of 30 cm length and 6 cm depth is divided into 72 meshes of 1 cm length. The anode region and the cathode region are assumed at the bottom boundary as shown. The potentials were given as -0.4 V at the anode region and -0.2 V at the cathode region, setting

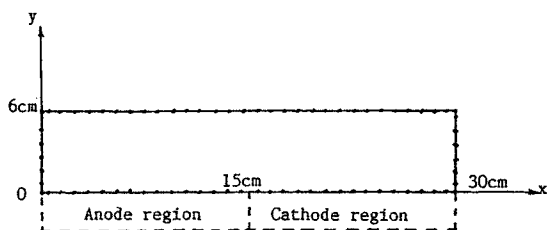


Fig. 1 2-D BEM model for potential analysis in concrete.

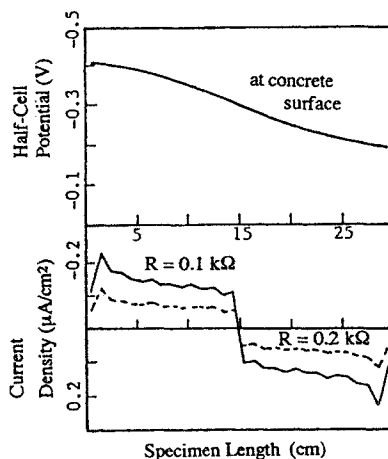


Fig. 2 Potential distribution at the top surface and current charge at the bottom.

-0.3 V offset potential. Two cases of concrete resistivity, $R = 0.1 \text{ k}\Omega$ and $R = 0.2 \text{ k}\Omega$, were analyzed. Results of the potentials at the surface and the current density at the rebar are shown in Fig. 2. Due to the change of concrete resistivity, the current densities at the rebar are varied, while potential distribution at the concrete surface is identical. This clearly shows that the potentials are independent of the resistivity in a homogeneous body. It implies that the effect of concrete resistivity on the half-cell measurement is not significant in the area where the concrete could be referred to as homogeneous.

Compensated procedure

To confirm an applicability of the procedure in eq. 9, a numerical experiment was performed by employing a three-dimensional model as shown in Fig. 3. An RC model of dimensions 3 cm x 25 cm x 40 cm, which corresponds to cover concrete, was analyzed. Potentials were given at the rebar elements as -0.1 V at the anode region and +0.1 V at the cathode region. Here, the offset potential was not taken into consideration. By using the BEM analysis, first, potentials at the concrete surface were determined. Some of results over the rebars are shown in Fig. 4 as dotted curves.

From these potential values on the top surface, the potentials at the rebars were determined from eq. 9. This means that the potentials on the rebar were recovered from only the potentials measured on the top surface. Results are shown in Fig. 4. A result of the rebar located at the end is shown in Fig. 4 (a), and that of the center in Fig. 4 (b). It is confirmed that the proposed compensation could reasonably recover the potential distribution at the rebar.

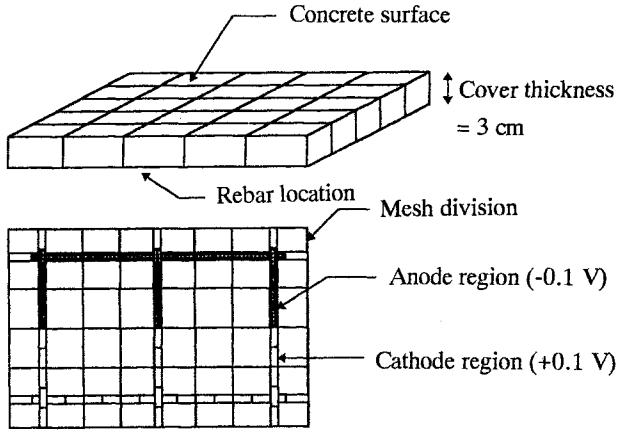


Fig. 3 3-D BEM model for the analysis.

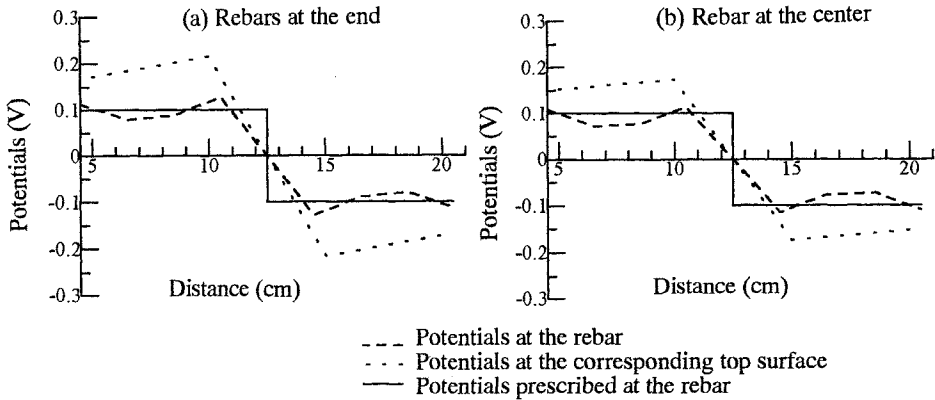


Fig. 4 Potential distributions at the top surface and at the rebar.

EXPERIMENT OF RC SLAB

Specimen

An applicability of the proposed compensation to an actual half-cell potential measurement was examined. An RC slab specimen of dimension 40 cm x 25 cm x 10 cm was made as shown in Fig. 5. Rebars of 10 mm diameter were embedded at 3 cm cover thickness. Mixture proportion of water : cement : sand : gravel is 0.5 : 1.0 : 2.41 : 2.97. The maximum size of aggregate is 20 mm. Uniaxial compressive strength of concrete was 46 MPa at 28 days. To accelerate an electrolytic corrosion, 3% NaCl solution was mixed for shaded portions of the model in the figure. The specimen was moisture-cured at 20°C for 28 days. After removal

from the mold, rebar surface out of the specimen and the top surface of concrete block were epoxy-coated to protect from corrosion.

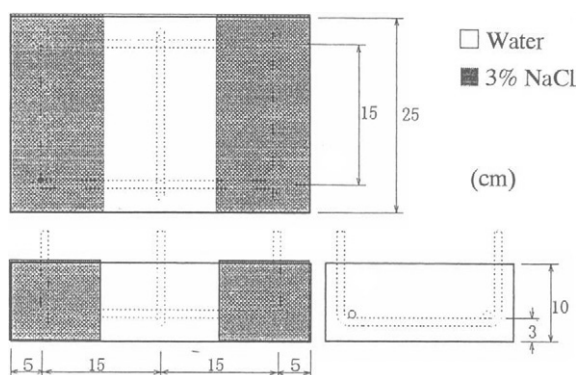


Fig. 5 Sketch of RC specimen.

Rebars in the concrete were artificially corroded by an electrolytic corrosion test. A test set-up is shown in Fig. 6. A copper plate was placed on the bottom of a tub. The specimen was mounted on the copper plate and 3% NaCl solution was filled up to the top surface of the specimen. By using a current supply, constant 100 mA electric current was charged between the rebars and the copper plate. To monitor corrosion of rebars, an AE sensor was mounted on the top surface of the specimen, and continuously AE generation was monitored [4]. The AE sensor was of 50 kHz resonance frequency. Total gain was 90 dB and frequency range was 1 kHz to 200 kHz.

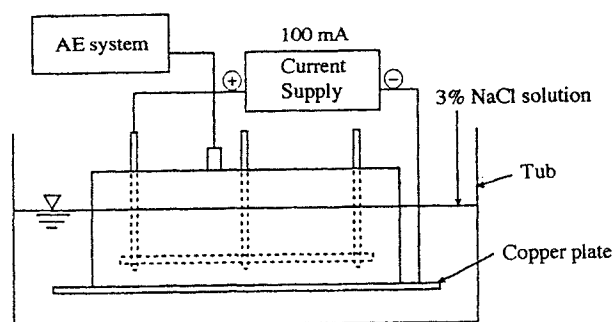


Fig. 6 Set-up for the electrolytic test.

Results and discussion

At 200 hr. elapsed, high AE activity and minor surface cracks were observed. Then, the electric charge was stopped. A contour mapping on the potentials observed at 200 hr. are

given in Fig. 7 (a). According to the ASTM criterion, potentials more negative than -0.35 V (C. S. E) indicate very high probability (more than 90%) of active corrosion. The potentials between -0.20 V and -0.35 V imply uncertainty on corrosion. The potentials less negative than -0.2 V suggest high probability of no corrosion. Results in Fig. 7 (a) suggest corroded portions corresponding to 3% NaCl solution mixed. Then, the specimen was broken and the rebars were removed to identify the corroded area. Results are shown in Fig. 7 (b). Comparing the results in Fig. 7 (a), the agreement between the concrete surface of the potentials more negative than -0.35 and the actually corroded region is fairly good.

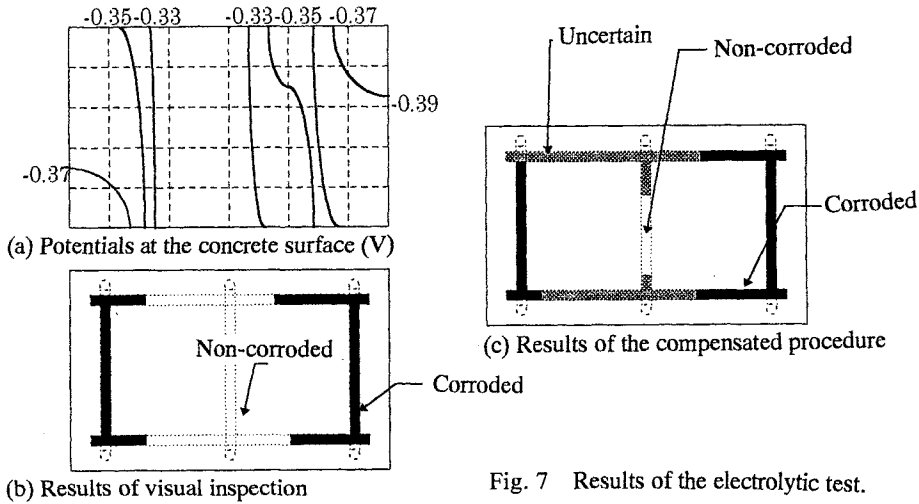


Fig. 7 Results of the electrolytic test.

By applying eq. 9, potentials at rebars were computed and then the ASTM criterion was applied to the potentials at the rebars. Results are given in Fig. 7 (c). Except for one portion at the left top, reasonable agreement between the actual corroded region and the estimated is observed. The result confirms that the procedure for compensation is useful for quantitative information on corrosion of the rebars,

Since the procedure for compensation could provide direct information on the potentials at the rebar, the current analysis of eq. 10 can be conducted to identify corroded regions of the rebar precisely. A result of the rebar located at the lower side in Fig. 7 (b) and (c) is shown in Fig. 8. Concerning the potentials at -0.35 V, the boundaries between corroded and non-corroded are a little different from those of visual observation. In contrast, agreement between the boundaries and the zero-current locations of the current analysis is remarkable. Thus, a reliable procedure to identify corroded regions of rebars is developed.

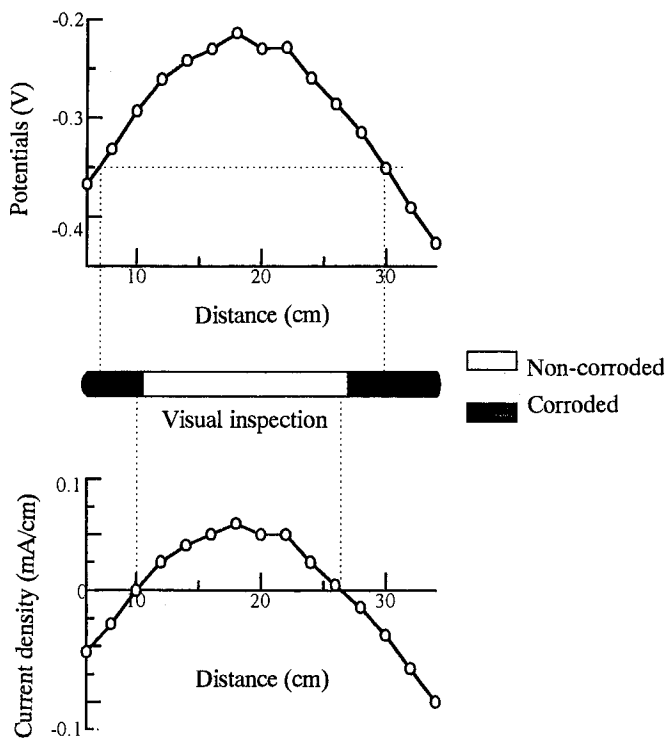


Fig. 8 Results of the rebar at the center.

CONCLUSION

A compensation procedure for the half-cell potential measurement is developed. Conclusions are summarized as follows:

- (1) In the numerical analysis by the BEM, it is found that the effect of concrete resistivity on the half-cell potential is not significant in an area where the concrete block is referred to as homogeneous. It is demonstrated that the proposed compensation could reasonably recover the potential distribution at the rebar, which is available for applying the ASTM criterion to the estimation of corrosion.
- (2) The potentials at rebars were compensated in the electrolytic test. Reasonable agreement between the corroded region estimated and that actually corroded is observed. A software is so simple as to be readily implemented in a microcomputer.
- (3) To identify corroded regions of the rebar, the current analysis is performed. Agreement of the corrosion boundaries with the zero-current locations is remarkable. Thus, a reliable procedure to identify corroded regions of rebars is developed, on the basis of compensation.

REFERENCES

1. Ohshiro, T., Tanikawa, S. and Goto, N.(1991), *Proc. of JCI*, **13**(1), 503.
2. ASTM C876 (1991), Standards Test Method for Half Cell Potentials of Reinforcing Steel in Concrete.
3. Misra, S. and Uomoto, T.(1990), *Proc. of JCI*, **12**(2), 825.
4. Ohtsu, M. and Yamamoto, T.(1997), *Construction and Building materials*, **11**(7-8), 398.
5. Tamura, H., Nagayama, M. and Shimozawa, K.(1992), *Proc. of JCI*, **14**(1), 763.
6. Otomaru, M., Murakami, Y. and Ohtsu, M.(1990), *Proc. of JCI*, **12**(1), 539.
7. Ohtsu, M. and Yamamura, H.(1991), *Proc. of JCI*, **13**(1), 527.
8. Yamamura, H. and Ohtsu, M.(1992), *Proc. of JCI*, **14**(1), 717.
9. Koyama, R., Yajima, T. and Uomoto, T. (1995), *Proc. of JCI*, **17**(1), 865.

ENVIRONMENTAL INFLUENCES ON LINEAR POLARISATION CORROSION RATE MEASUREMENT IN REINFORCED CONCRETE

S G MILLARD, D LAW, J H BUNGEY and J CAIRNS*
*Department of Civil Engineering, University of Liverpool,
Liverpool, L69 3BX, England*

**Department of Civil and Offshore Engineering, Heriot-Watt University,
Riccarton, Edinburgh, EH14 4AS*

ABSTRACT

The linear polarisation resistance (LPR) method can be used to measure the active rate of corrosion of steel reinforcement in concrete structures. However a single measurement may be sensitive to the ambient environmental conditions and thus may not be representative of the mean annual rate of corrosion. The LPR measurement may be dependent upon the temperature at the time of sampling and on any wetting/drying effects resulting from rainfall and wind or sunshine.

Recent studies have examined the behaviour of a series of reinforced concrete specimens subject to chloride contamination or carbonation induced corrosion in a controlled laboratory environment. LPR measurements taken at frequent intervals have been related to a wet/dry cycle imposed upon the specimens to promote corrosion activity. In addition similar studies have been carried out of an insitu reinforced concrete specimen exposed to the ambient weather conditions. The study is only partly completed, but interim results show the variability of LPR measurements and the influences the environment may exert on single spot measurements.

KEYWORDS

Corrosion, linear polarisation, environment, reinforcement.

INTRODUCTION

For several decades the Civil Engineering industry has relied upon half-cell potential mapping [1] to assess the scale of a corrosion problem in reinforced concrete structures located in aggressive environments. Whilst with care this technique can be used quite successfully to identify regions of the structure which may be suffering from corrosion attack, it gives no certain information about the rate at which corrosion may be occurring. An active corrosion site indicated by half-cell mapping may have steel reinforcement corroding at a serious rate or may be corroding so slowly as to be of negligible significance during the design lifetime of the reinforced concrete structure.

An ancillary test method which is sometimes used is the measurement of concrete resistivity. It has been suggested [2] that the presence of a low concrete resistivity in regions indicated as being actively corroding by half cell potential mapping can be used as an indicator that the rate of corrosion is probably quite high.

Whilst both techniques are relatively simple to carry out, they are both passive methods which can only be indirectly related to the active rate of corrosion. Hence the linear polarisation resistance (LPR) method, which measures corrosion rates directly, has seen a growth in popularity in recent years and is beginning to be used as an effective NDT technique for the evaluation of reinforced concrete structures at risk of corrosion attack. LPR measurements are routinely used by electro-chemists in laboratory corrosion rate studies. However, when the method is to be used in the field there is some concern about the variability of measurements and the influence of fluctuations in ambient environmental conditions on spot readings. An ongoing collaborative project undertaken at the University of Liverpool and at Heriot-Watt University is presently investigating the effect of various environmental influences upon LPR corrosion rate measurements. The project is not yet completed but some interim results will be presented in this paper.

LINEAR POLARISATION RESISTANCE METHOD

The corrosion of steel in concrete is a dynamic electrochemical process involving an exchange of ions between passive (cathodic) and active (anodic) locations on the surface of a steel reinforcing bar. The process is shown schematically in Fig. 1. A simple electronic circuit known as a Randles Circuit [3], shown in Fig. 2 can represent the corrosion interface. The resistance R_s represents the “solution resistance” which is the electrical resistance of the concrete cover between the reinforcing bar and the surface. C_{dl} is a double layer capacitance, which is provided by charged ions on the surface of the steel. R_p is the polarisation resistance at the surface of the steel and represents the ease with which charged iron ions can leave the metal surface and enter solution. The rate of active corrosion is inversely proportional to R_p .

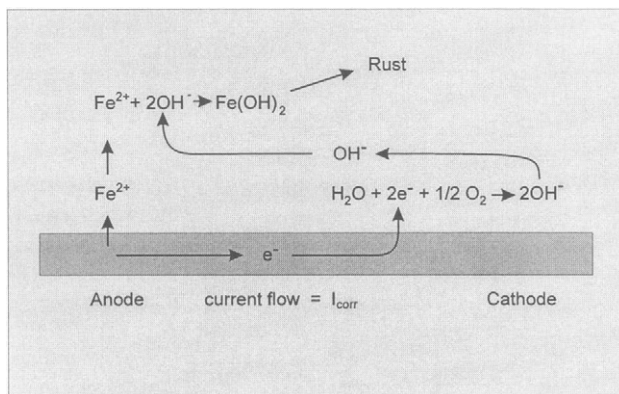


Fig. 1 The corrosion process of steel in concrete

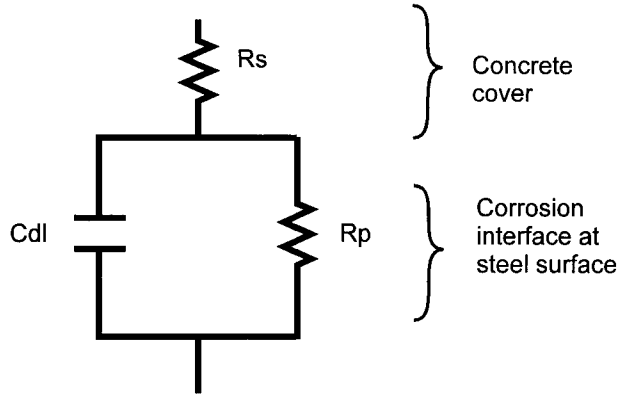


Fig. 2 Simple electronic circuit (Randles) for steel bar in concrete

To apply the LPR technique a small polarisation perturbation is applied to the steel reinforcing bar from the surface of the concrete and the resulting response is measured after a suitable time delay for equilibrium to be established. Using a potentiostatic method an overpotential, ΔE of between 10 mV to 30mV is applied to the corrosion potential, as shown in Fig. 3. After a delay, typically of about 30 seconds, the resulting current ΔI is recorded. In practice, both over and underpotentials are applied in order to maximise ΔI while minimising the disturbance to the steel potential.

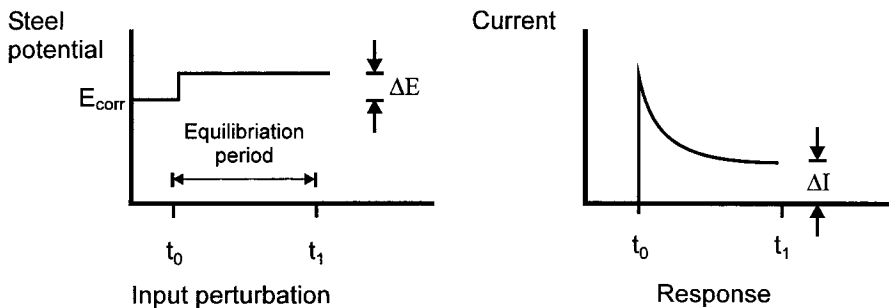


Fig. 3 Potentiostatic LPR measurement

Although the corrosion of steel in concrete is an electrochemical process and does not obey Ohm's law ($V=IR$), it has been shown [4] that Ohm's law will be approximately true if polarisation applied to the steel reinforcement does not exceed ± 30 mV. Thus the polarisation resistance R_p can be found from:

$$R_p = \frac{\Delta E}{\Delta I} \quad (1)$$

For steel in concrete, the solution resistance of the concrete cannot always be ignored. By applying a second AC perturbation at a high frequency, typically of 300 Hz, the double layer capacitance provides a short circuit bypass to R_p and hence a measurement of R_s alone can be made. This is subtracted from the overall potentiostatic resistance measurement to give R_p .

The polarisation resistance directly controls the rate of corrosion, I_{corr} that may be found using

$$I_{\text{corr}} = \frac{B}{R_p} \quad (2)$$

The value of B is normally assumed to be 25mV for actively corroding steel in concrete [5] and 50mV for a more passive situation [6]. Polarisation will normally only be applied to a small area, A of the reinforcing steel and the evaluation or assumption of a value for A can present some practical difficulties [7]. However if the polarisation can either be confined to a known area, or if a small section of reinforcement can be electrically isolated, then the density of the corrosion current can be found using

$$i_{\text{corr}} = \frac{I_{\text{corr}}}{A} \quad (3)$$

From this the average corrosion penetration (in cm/sec) may be evaluated from

$$p = \frac{Mi_{\text{corr}}t}{\rho zF} \quad (4)$$

Where M = gram atomic weight (=55.85g/mol for iron)

t = duration (in seconds)

ρ = density of iron (7.95 g/cm³)

z = number of electrons transferred per atom (e.g. 2 for $\text{Fe} \rightarrow \text{Fe}^{2+} + 2e^-$)

F = Faraday's constant (96500 C/mol)

Typical values for corrosion measurements are given in Table 1 [3].

LPR measurements are normally made using a three-electrode system, see Fig. 4. A stable reference electrode enables the corrosion potential and over-potential of the steel to be measured between the steel reinforcing bar and an auxiliary electrode placed on the surface of the concrete. LPR measurements can be shown to be an effective means of directly evaluating the rate of corrosion activity and hence the severity of risk to a reinforced concrete structure. However one particular concern is that corrosion is a dynamic process which may fluctuate both up and down with changes in ambient environmental conditions. If the degree of fluctuation is not known, or if ambient fluctuations are not compensated, then it may be difficult to place confidence in a particular LPR measurement when evaluating the corrosion risk to a structure.

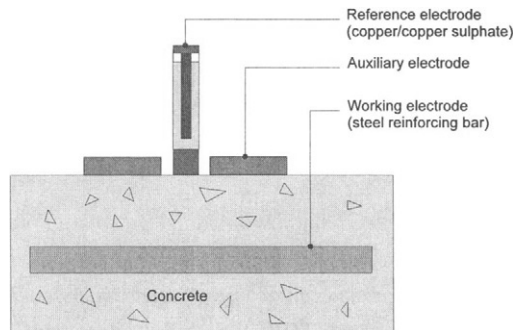


Fig. 4 Three-electrode LPR measurement

ENVIRONMENTAL INVESTIGATIONS

The current study is focused upon the effect of corrosion upon the bond of steel bars in concrete. The influence of carbonation of concrete is being studied together with the effect of chloride ingress through the cover zone, incorporating the effects of surface wetting and ambient temperature fluctuations. The study incorporates laboratory manufacture and conditioning of corrosion damaged bond specimens, supported by study of externally exposed corrosion specimens.

Laboratory studies

A series of 27 bond/corrosion specimens have been fabricated. Each specimen contains 16mm bond bars both confined by shear links and unconfined. Nine specimens contain deformed steel bond bars. A further nine contain plain round bond bars and the remaining nine contain hooked bond bars, Fig. 5, with a minimum concrete cover of 25mm. Bond tests were planned for just before cracking was predicted and after cracking was observed ~ 0.1mm and 0.5 mm crack width.

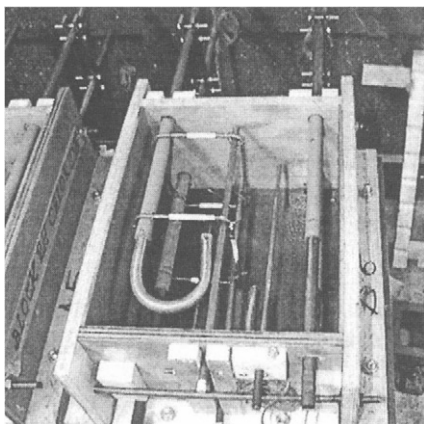


Fig. 5 Hooked bond bar corrosion specimen, before casting

In addition two small 6mm weight-loss bars were included in each specimen. These will enable a correlation between electrochemical corrosion measurements and actual weight loss at the end of the study. In addition, some specimens contain sensors to measure internal temperature and relative humidity of the concrete.

Three environmentally controlled cabinets were fabricated, each to control the corrosion conditioning of 9 specimens, see Fig. 6. These were designed to study carbonation, chloride attack and a non-corrosive inert atmosphere. Carbonation was achieved by placing specimens in a 100% CO₂ atmosphere after 14 days of conventional curing. Full carbonation to a depth beyond that of the steel bars was achieved in one month and was verified using phenolphthalein on test cubes. Following carbonation the specimens were placed in a normal atmosphere and were subjected to a 2-hour spray wetting cycle followed by a 22-hour fan assisted drying cycle to promote corrosion.

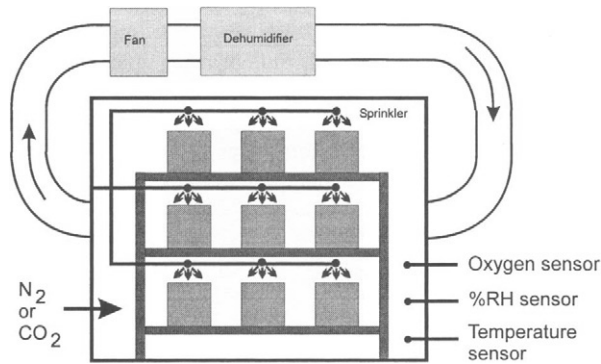


Fig. 6 Environmental control cabinet

Specimens in the chloride cabinet were not exposed to CO_2 in the same way but were spray wetted with a 1 molar sodium chloride solution under the same 24-hour cycle. The control specimens had the same wetting and drying cycle but were placed in an inert nitrogen environment to minimise any corrosion activity. An oxygen sensor was used to confirm the absence of oxygen in the nitrogen environment.

The temperature and relative humidity in each cabinet was regularly recorded every 60 minutes. LPR measurements on each of the 6 bars in each specimen were taken on a 3-week cycle.

Laboratory results

Over a period of 7 days, temperature and relative humidity measurements inside a concrete specimen were logged. It was seen that although the relative humidity in the environmental cabinets cycled as expected between 60% RH and 90% RH as the 24 hour drying and wetting cycle proceeded, the relative humidity inside the concrete specimens was invariant, Fig. 7. It should be noted that capacitive relative humidity meters lose their accuracy as a value of 100% is approached so that the actual value may in fact lie somewhere between 95% and 100%.

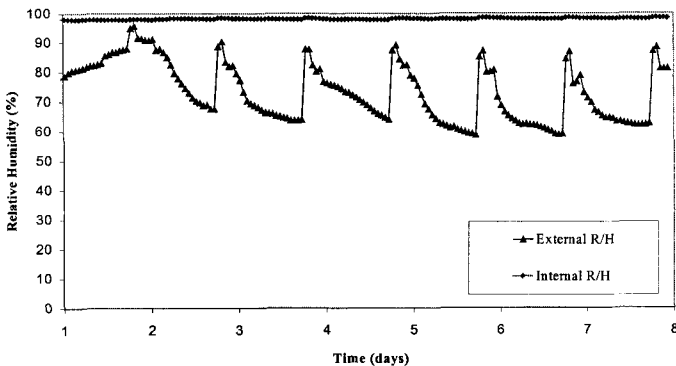


Fig. 7 Internal and external relative humidity of carbonation specimens

The temperature inside the concrete specimens however followed the external temperature very closely. The environmental cabinets were located inside the laboratory and hence ambient temperature changes were relatively small. However from Fig. 8 it can be seen that the two temperatures are always within 2 °C of each other. A short daily drop in temperature is seen as the cold water spray is activated for 2 hours.

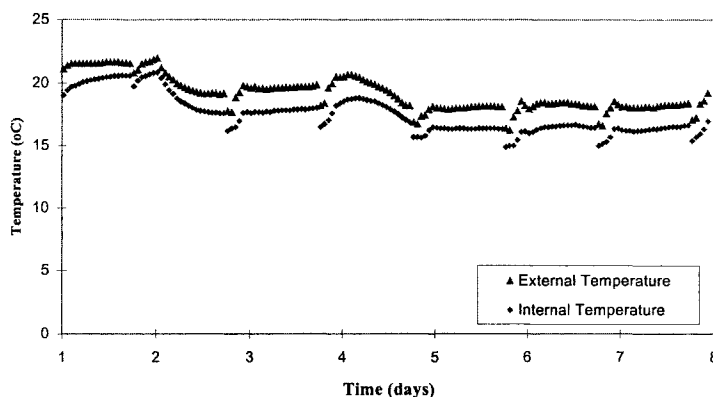


Fig. 8 Internal and external relative temperature of carbonation specimens

The effect of relative humidity and temperature on the LPR measurements is seen in Figs. 9 and 10. The influence of the concrete wetting and drying is seen clearly as the concrete solution resistance rises and falls in synchronisation with the spray and fan cycle. However this appears to have very little influence on the polarisation resistance. If the small temperature changes that were present in the laboratory are plotted against the rate of corrosion, it can be seen that there is a definite increase in the corrosion rate as the temperature rises. There is however significant scatter in these results, which cannot be accounted for. It can be seen that a corrosion rate of 1-2 $\mu\text{A}/\text{cm}^2$ places this steel in the “High” corrosion category in Table 1.

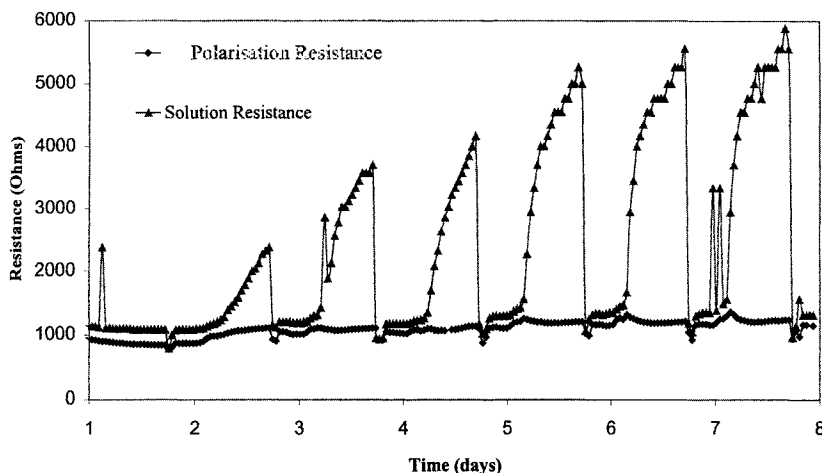


Fig. 9 Concrete solution resistance and steel polarisation resistance for carbonation specimens

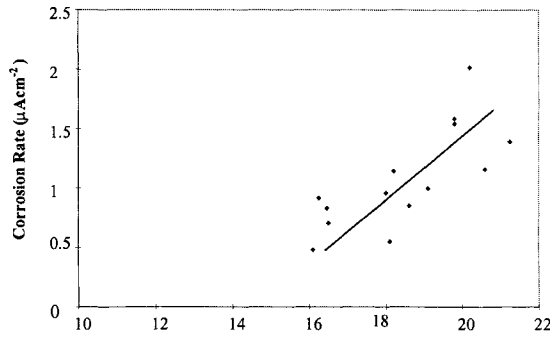


Fig. 10 Influence of temperature on corrosion rate on carbonation specimen

When the drying period was extended from 22 hours to 3 days, this did have an influence on the rate of corrosion. From Fig. 11 it is seen that the polarisation resistance begins to rise after 2 days of drying, indicating that the corrosion rate is reducing. During the wetting phase there is an immediate drop in R_p , indicating an increase in the rate of corrosion. Similar results were obtained from the chloride-contaminated specimens.

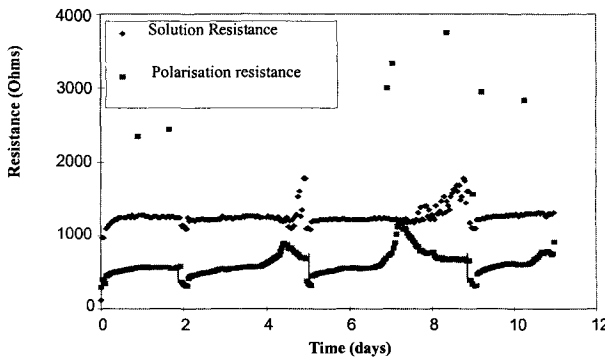


Fig. 11 Effect of extended drying period on solution resistance R_s and polarisation resistance R_p for carbonation specimens

Externally exposed corrosion specimens

To study the influence of ambient environmental fluctuations on externally located reinforced concrete, a 100 mm thick slab was cast containing a zone of concrete contaminated by chloride, mixed into the fresh concrete (5% NaCl by weight of concrete). The slab contained a number of 100mm lengths of reinforcing bar with a cover of 40mm, located in both the chloride contaminated and the uncontaminated zones as shown in Fig. 12. The slab was located in an external urban environment in Liverpool.

Results from external study

The trends shown in the environmental cabinets were replicated in the study on externally exposed reinforced concrete. Whilst the internal temperature of the concrete followed the

external temperature closely, the internal relative humidity remained above 95% in spite of fluctuations in the external relative humidity from 30% to 100%, Fig. 13.

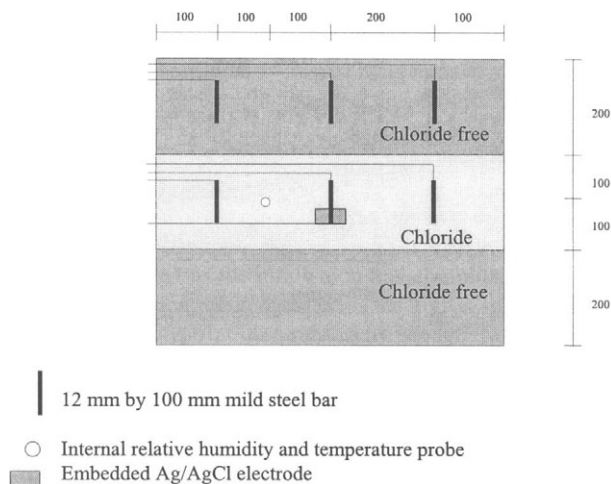


Fig. 12 External slab specimen

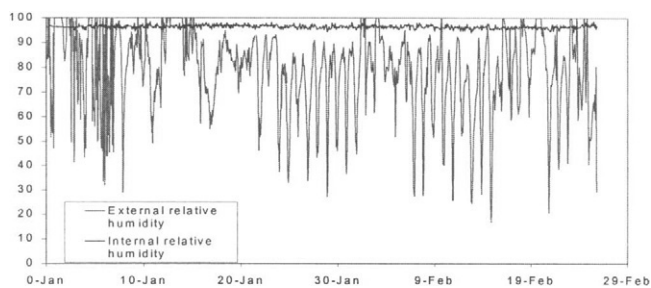


Fig. 13 Relative humidity of external slab specimen

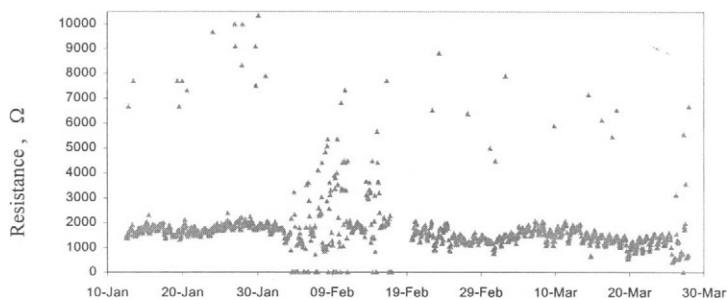


Fig. 14 Polarisation resistance (R_p) for external slab specimen

A study of the polarisation resistance, Fig. 14, of a bar in a chloride contaminated zone showed a mean value of about 1500Ω . Using Equations 2 and 3, this corresponds to a corrosion rate of $0.4 \mu\text{A}/\text{cm}^2$, placing it at present in a 'Low/Moderate' corrosion rate category, Table 1. However it can clearly be seen that there is significantly more scatter than seen in the environmentally controlled cabinets. The corrosion rate fluctuates between $0.06\text{--}1.2 \mu\text{A}/\text{cm}^2$. If a short section of the results is examined in more detail, Fig. 15 then the effects of diurnal temperature fluctuations can be clearly seen.

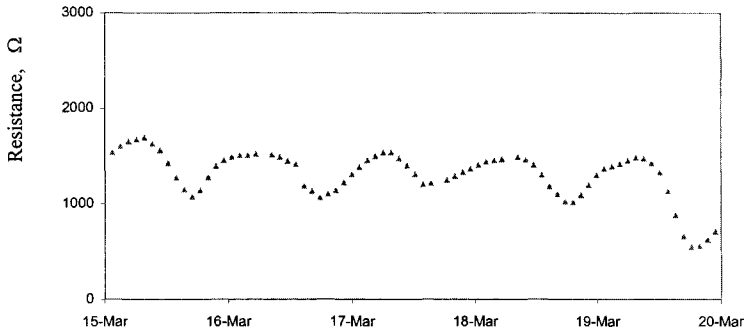


Fig. 15 Diurnal fluctuation of R_p with temperature

CONCLUSIONS

The study is continuing and the results presented are only interim results. Nevertheless results show that in a UK environment the concrete cover around reinforcing steel may never really dry out. Thus the presence of rainfall wetting the concrete surface may have little direct influence on the rate of corrosion. The ambient temperature however appears to have a significant influence on corrosion activity, with an increase in temperature causing an increase in the rate of corrosion. Whilst the LPR method promises to be a valuable technique enabling the rate of corrosion activity to be directly evaluated, it should nevertheless be used cautiously. It may be necessary to take a number of consecutive measurements to obtain a reliable measure of the mean corrosion rate.

ACKNOWLEDGEMENTS

The research programme was carried out with the financial support of EPSRC, Grant Ref. GR/L/27886. In addition, technical support was received from Magnox plc.

REFERENCES

1. Vassie PR (1991), 'The half-cell potential method of locating corroding reinforcement in concrete structures', *Application Guide 9*, Transport & Road Research Laboratory
2. Ewins AJ (1990) *British Jnl of NDT*, v. 32, no.3, 120
3. Millard SG, Gowers KR & Gill JS (1991) *ACI Special Publication*, SP 128-24, 373
4. Stern M & Geary AL (1957), *Jnl of the Electrochemical Society*, 1, 56
5. Hladky K, John DG & Dawson JL (1989) *Proceedings of NACE Corrosion 89*, 169/1-10
6. Alonso C & Andrade C (1988) *Advances in Cement Research*, 7, 155

7. Broomfield JP, Rodriguez J, Ortega LM & Garcia AM (1995) *American Society for Testing Materials*, STP1276, 15pp

Table 1 Typical corrosion rates for steel in concrete.

Rate of corrosion	Polarisation resistance R_p (Ωcm^2)	Corrosion current density, i_{corr} ($\mu\text{A}/\text{cm}^2$)	Corrosion penetration, p ($\mu\text{m}/\text{year}$)
Very High	2.5 to 0.25	10 to 100	100 to 1000
High	25 to 2.5	1 to 10	10 to 100
Low/Moderate	250 to 25	0.1 to 1	1 to 10
Passive	> 250	< 0.1	< 1

This Page Intentionally Left Blank

A RAPID FIELD TESTING METHOD FOR CHLORIDE ION CONTENT IN CONCRETE USING DRILLED POWDER

N. YUASA and Y. KASAI

Dept. of Architecture and Architectural Eng., College of Industrial Technology,
Nihon University, Japan
1-2-1 Izumi-cho, Narashino-shi, Chiba-ken, Japan

ABSTRACT

This paper deals with a rapid field-testing method of estimating chloride ion content in concrete using drilled powder.

First, all drilled powders of concrete were enabled to be gathered with a cover of the drill and a saucer. Next, the portable extraction device of chloride ion was developed to estimate chloride ion content in concrete on-site. The extracted chloride ion was measured with portable chloride ion meter or chloride ion testing paper estimated by Japan Institute of Construction Engineering. In comparison with the standard method using concrete core, the proposed method can not only evaluate the chloride ion content in concrete on-site but also be expected a great improvement in respect of the destruction extent, work amount and testing expenses.

KEYWORDS

Mini-destructive testing method, Concrete, Chloride ion content, Drill

INTRODUCTION

The reinforcing bar of a concrete structure needs to be protected from corrosion by chloride ions. Therefore, it becomes necessary to examine chloride ion content in the concrete. However, this measurement is conducted by gathering cores from concrete, and requires large amounts of energy and costs. And, destruction to the structure itself is not slight, and repairs become necessary after each examination. Further, for the results of chloride ion to be obtained, many processes and working hours are required. At present, such tests cannot be planned or conducted easily.

However, noting that concrete powder can be obtained easily by a portable drill also by mini-destruction [1,2,3], we would hereby like to introduce a rapid field testing method for chloride ion content in concrete using drilled powder, which our research group have proposed and developed. This testing method can be diffused widely both domestically and abroad, as the evaluation of the chloride ion content is possible in a field test using comparatively simple and inexpensive equipment.

OUTLINE OF TEST METHOD

Gathering of drilled powder and adjustment of samples

The sample for the measurement of chloride ion content has to represent the concrete of the object spot. Then, as a method of gathering all drilled powder using a portable hammer drill (hammer about ¥40,000.), a cover to be attached to the drill was made by a PET bottle, a wire and a transparent tape for packing as shown in Fig. 1 and Photo 1. Further, the total of the mass of powder sample gathered by drilling by a drill attached with a cover and the mass of the test body is confirmed by experiment to correspond to the mass of the test body before drilling.

Further, drilled powder was crushed using a mortar [outside diameter 120 mm, about ¥ 800 (porcelain)], until the grains cannot be sensed by finger touch, and this powder was used as a sample for the measurement of chloride ion content.

The trial manufactures of portable type chloride extractor and measuring of a powder sample and refined water

A portable type equipment shown in Fig. 2 was manufactured by way of trial in order to make an extract in the study field “soluble salt content” in JCI-SC4 “Analysis method of salt contained in hardened concrete” included in “Test method and standard regarding corrosion, anti-corrosion of concrete structure (draft)” by Japan Concrete Institute. This equipment, having a heater, can maintain the temperature of water at 50°C by thermo-regulator. Further, the equipment was so structured that the test tube could swing from right to left using a motor so that the sample of 1.0 g could be mixed fully with 5.00 ml of water in a test tube.

However, it was found that the concrete powder could not be fully mixed, as the powder tends to settle. Then, two plastic square bars were wound to the mouth of the test tube by a tape so that a further vibration may be given every time the test tube swings. Further, a mixing bar consisting of a wire of with a looped end, was inserted in the test tube to avoid sedimentation as shown in Fig. 3. Using this equipment, it was found that the full mixing of a sample was possible. Further, the material cost of the equipment was about ¥30,000.

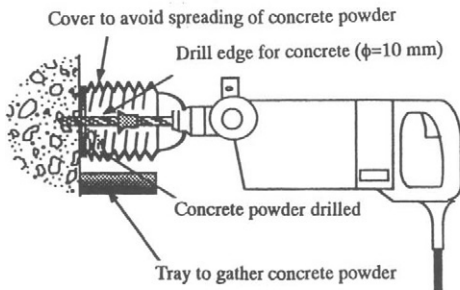


Fig. 1 Gathering of concrete powder by drill

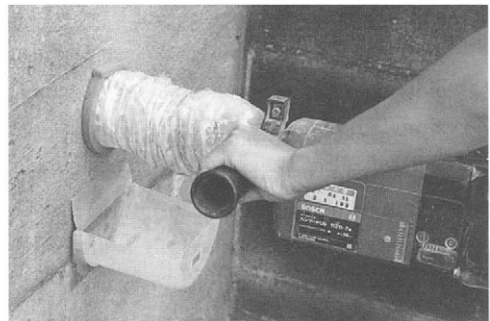


Photo. 1 Gathering of concrete powder by drill

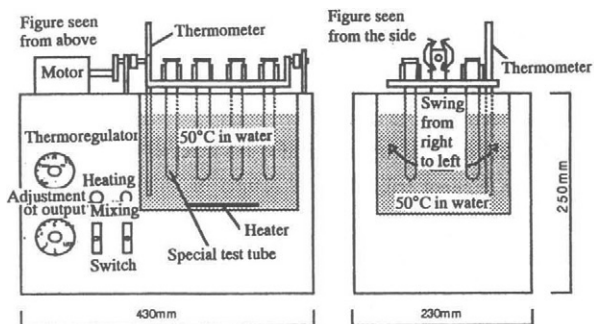


Fig. 2 Portable type chloride extractor

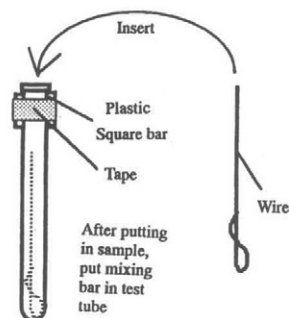


Fig. 3 Test tube

Measurement of sample and refined water, and extract and measurement of chloride

For the measurement of a concrete sample of 1.0 g and refined water, an even balance (basic weight 100 g, sensibility 100 mg, about ¥15,000), a measuring cylinder (capacity 10 ml, minimum division 0.1ml, about ¥600) were used considering portability, accuracy and inexpensiveness. Further, a measuring apparatus easily usable in field study or a disposable measuring apparatus of chloride ion content are necessary for the measurement of chloride ion content of concrete in the field. Further, accuracy, short measuring time and easy handling are required. In conclusion, soluble chloride ion content was measured in concrete (fresh concrete) mode using a measuring apparatus for chloride ion content or chloride judgement paper that have received the technical evaluation of the National Land Development Technical Research Center Foundation.

Soluble chloride in concrete is extracted using a chloride extractor manufactured by way of trial putting sample and refined water in a test tube. Here, measurement was decided to be effected by a chloride ion measuring apparatus (portable type, about ¥300,000.) made by Y Company of electrode-current measuring type. (Disposal chloride ion measuring apparatus of O company is about ¥9,000/36 pcs.) Fig. 4 shows the relationship between mixing time and the concentration of chloride ion extracted. By this, it was judged that even with 10 minutes of mixing, the extract of chloride ion is fully possible.

Study of the number of holes required to be drilled and mixing of samples.

Considering the diameter of the coarse aggregate, there may be cases where drilled powder including more aggregate content may become a sample because of having the drilled diameter ϕ 10mm. It, then, becomes necessary to evaluate chloride ion content based on the results of many drillings. However, considering the simplicity aimed at by this study, the fewer holes required to make an evaluation, the better. In order to use the concrete powder of at least three holes, a mean value of three drilled holes and a mean value of six drilled holes were compared. Fig. 5 shows the difference in these values. No big difference was observed. Many of the results measured showed a difference of within $\pm 10\%$. The number of holes to be used for evaluation was, therefore, decided to be 3, judging from the serious consideration of keeping the simplicity of the test.

Fig. 6 shows the necessary time, in case of the test of chloride ion content in one spot by two engineers, for the case ① to calculate a mean value obtaining chloride ion content for each hole of the three drilled holes and the case ② to obtain chloride ion content by first mixing, the drilled powder of the three drilled holes. Here, in order to gather quickly and exactly concrete powder in a layer of fixed depth, a stopper is attached to a drill edge as indicated in Photo 2. In case ①, to calculate a mean after obtaining values for each sample required about 75 minutes of measuring time, and in case ②, to mix powder when drilled, required a little over 35 minutes of measuring time. The latter enables simplification of work in addition to a considerable time reduction. Therefore, it was decided in principle to measure chloride ion content after mixing, drilled powder obtained from the three holes ②.

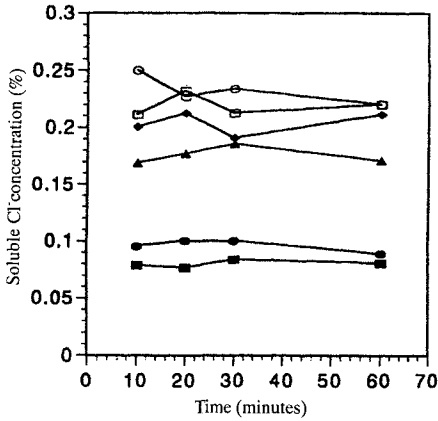


Fig. 4 Change of concentration according to elapse of time

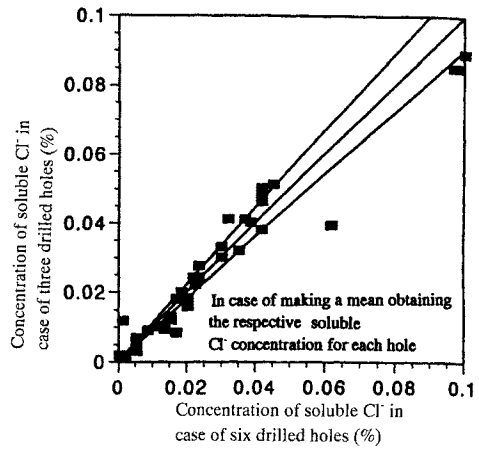


Fig. 5 The relationship between soluble Cl⁻ concentration (%) and the number of drilled holes in one spot.

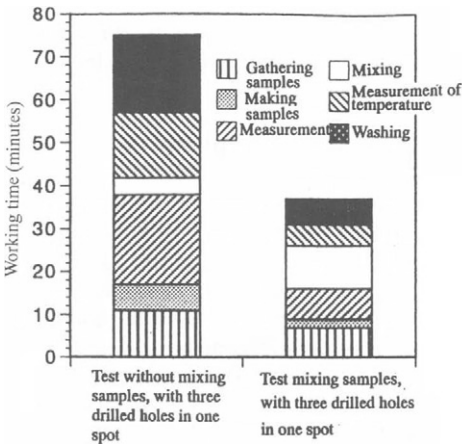


Fig. 6 Mixing of samples and shortening of test time

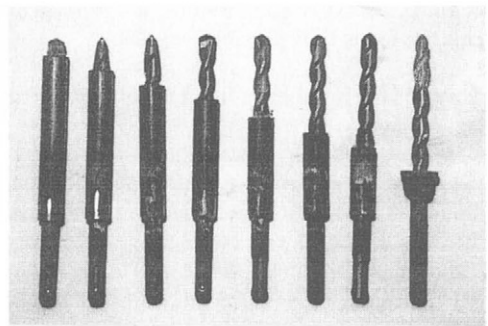


Photo. 2 The stopper attached to a drill edge

TEST METHOD PROPOSAL

From the study results conducted so far, "A rapid field testing method for chloride ion content in concrete using drilled powder" is proposed as follows.

A rapid field testing method for chloride ion content in concrete using drilled powder (draft)

1. Scope of application

This standard covers the rapid field testing method for chloride ion content of concrete structures using drilled powder. This test method applies to the vertical face of walls, columns and the joists of concrete structures. However, this standard can not be applied to the concrete using recycled aggregate.

Remarks: The standards quoted for these standards are shown as follows.

JIS Z 2300 Non-destructive test terms

JIS A 0203 Concrete terms

2. The definition of terms

The definition of terms used in this standard besides JIS Z 2300 and JIS A 0203 are as follows.

- (1) Drilled powder: Powder produced when a hole of about ϕ 10 mm is drilled into concrete using a hammer drill.
- (2) Soluble chloride ion: Chloride ion, which is soluble in warm water of 50°C contained in hardened concrete.

3. Test engineers for chloride ion content

Test engineers for chloride ion content (hereinafter called engineers) have to have sufficient knowledge regarding concrete structures and their deterioration.

4. Related studies

Chloride ion content is studied as a object. However, the following are studied as related matters both beforehand, and before and after the execution of the test for chloride ion content.

- (1) The outline of the object structure for the test: Address, year of construction, construction space, floor space, number of floors, use of structure, history, surrounding environmental conditions (especially information about distance from the sea, wind), direction the building faces, etc.
- (2) Concrete: Materials (especially the presence of use of sea gravel), mixing, etc.
- (3) Test spot: Inside or outside the structure ? In case outside the structure, is the structure exposed directly to rain water or not ?
- (4) The finished materials: The presence of the finished materials, in case there exist finished materials, their type and thickness, their age, cracks, presence and degree of delamination.
- (5) Others: Matters, which are deemed necessary for the test of chloride ion content.

5. Testing method for chloride ion content

(1) Test apparatus

Hammer drill: Portable and vibration type stipulated by JIS C 9605

Drill edge: Used only for concrete drilling and ϕ 10 mm.

Drill cover: Which can gather all drilled concrete powder used together with a receiving tray.

A receiving tray: A tray to gather drilled powder falling down, fixed in a position where the drilled powder falls down when drilling or when drill cover is removed.

Vernier calipers: Maximum measuring length 150 or 200 mm stipulated by JIS B 7507

Brush: Approximately 30 mm in width

Mortar: Approximately 120 mm in outside diameter

Test tube: ϕ 18 × 180 mm, capacity about 30 ml

Test tube holder: Holder to hold about 12 test tubes

Balance: Capacity 100g, sensitivity approximately 100 mg

Spoon for medicine:

Paper for medicine:

Water: Refined water

Measuring cylinder: Capacity 10ml

Chloride ion extractor: Portable type that can fully extract soluble chloride ion from concrete powder at temperature of 50°C.

Beaker: 50ml

Wiper: For chemical analysis

Measuring apparatus for chloride ion content: Technically evaluated by the Land Development Technical Research Center Foundation

(2) Weather at the time of testing:

The test should not be executed, when concrete is exposed directly to rain, or in strong winds.

(3) Handling of chloride ion content test:

- ① In case that there are tiles or mortar on the test spot, these must be removed so that the concrete is fully exposed.
- ② Drilled concrete powder in the layer of fixed depth of all three holes is all gathered using a drill and drill cover, receiving tray and brush.
- ③ Drilled powder sample gathered by mortar is crushed to the point that no grains can be felt by finger touch.
- ④ 1.0 g of the sample of drilled concrete powder is measured by a balance.
- ⑤ 500ml of refined water is measured by measuring cylinder.
- ⑥ Soluble chloride ion is extracted by chloride ion extractor for 10 minutes, putting measured sample and refined water in a test tube.
- ⑦ The solution of supernatant liquid in the test tube is transferred to a beaker, the concentration of chloride ion content is measured in concrete (fresh concrete) made by chloride ion content measuring apparatus.

(4) Calculation

Chloride ion content per unit mass of concrete is measured by the following equation (1). The results are shown to two significant figures.

$$Clc = Vw / \rho / Wc \times Clm$$

Here, Clc: Chloride ion content per unit weight of concrete (%)

Vw: Volume of refined water (ml) = 5.0ml

ρ : Density of water (g/ml) = 1.0g/ml

Wc: A sample weight (g) = 1.0g

Clm: The concentration of chloride ion measured (%)

6. Repair

After the test, the holes are filled by mortar or caulking compound.

7. Safety

To secure safety of engineers, The Occupational Safety and Health Law has to be observed. Further, engineers have to be given a rest at proper intervals.

8. Report

The following matters have to be stipulated in the report

- (1) Name and the address of the structure
 - (2) Outline of the structure
 - (3) Date of the test, weather
 - (4) Names of engineers
 - (5) The scope of test
 - (6) The results of related study
 - (7) The test results
 - (8) Other necessary matters
- Further, the report has to be kept for a necessary period.

APPLICATION EXAMPLES OF THIS CHLORIDE ION CONTENT TEST

When in dismantling No. 10 building of the College of Industrial Technology of Nihon University, this test method was applied. The equipment and tools used for the study were as shown in Photo 3. The dimension of the box to keep all, necessary equipment and tools such as the drill, electric cord reel, etc. except chloride ion measuring apparatus made by Y company, was about $45 \times 60 \times 40$ cm and the mass was about 23 kg. Further, the drill and electric drum weighed about 8 kg altogether, the chloride ion measuring apparatus made by Y company was about 6 kg, and total mass was less than 40 kg.



Photo. 3 The equipment, tools used for the test

Fig. 7 shows the process of a test to measure chloride ion content of 8 layers (every 1 cm from the surface) in one spot by two engineers. By this method, the measurement of chloride ion content of one spot (8 layers) was executed in about 90 minutes. Also, to measure 8 spots (only fixed layers) could be considered possible within the same period of time.

Fig. 8 shows a comparison between chloride ion content measured by using core and chloride ion content measured by the method using drilled powder. Although the value measured using drilled powder was a little larger, there was a tendency for the chloride ion content to decrease with

neutralization, and it was possible to approximately evaluate chloride ion content. This method is thought to be the optimum method for the first examination of chloride ion content. Further, according to writers studies in the past, the result that chloride ion content increases when using drilled powder is assumed to be because the drill edge drills more of the cement paste and avoids aggregate, as indicated in Fig. 9^[1] and Photo 4^[4].

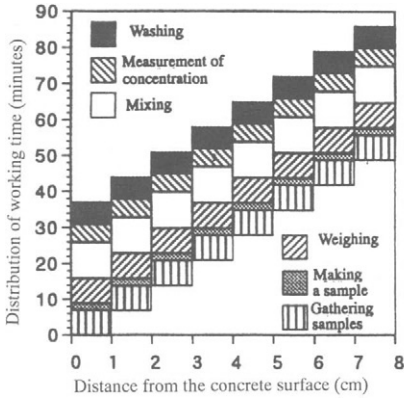


Fig. 7 Process of test (Samples from three drilled holes were mixed in one spot by two engineers)

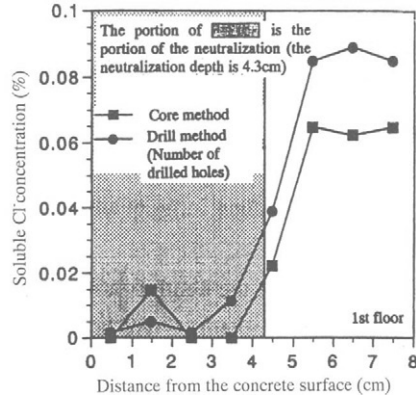


Fig. 8 A comparison of soluble Cl⁻ concentration between core method and drill method. (Examples of measurement of wall of 1st floor, No.10 building of this Faculty)

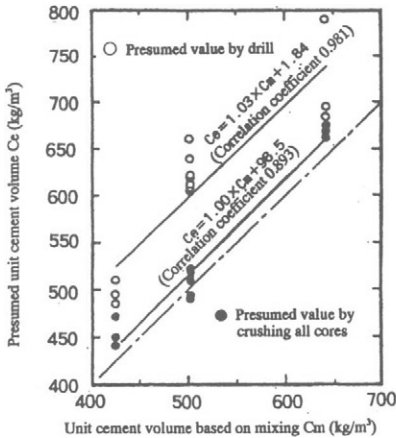


Fig. 9 Mixing value and presumed value of unit cement content



Photo. 4 Drilled situation

SUMMARY

Major findings can be summarized as follows.

- (1) All hole powders produced during drilling can be gathered by the cover installed at the drill.
- (2) The portable chloride extraction device was made.
- (3) Mixing time for the extraction of chloride ion in dilled concrete powder is 10 minutes.
- (4) The number of grinding holes was three at a place, and the powders obtained from these three grinding holes are mixed as a specimen.
- (5) "A Rapid Field Testing Method for Chloride Ion Content in Concrete using Drilled Powder" was tentatively specified.
- (6) With this method, chloride ion contents of eight samples can be determined by two workers in about 90 minutes.
- (7) Because the cement paste part rather than aggregate in concrete is selectively drilled, chloride ion content is likely to be measured greater than that using cores. So the proposed testing method is located as a suitable method for the preliminary inspection.

CONCLUDING REMARK

For the evaluation of the quality of a concrete structure and a diagnosis of durability of the structure, it is important how much data suitable for the object study can be obtained and how easily this data is obtained.

The test results obtained by concrete cores gathered from concrete structure and obtained by chipping are high in reliability. However, there are cases of problems from the viewpoint of structural durability, because this is in fact a destructive test, even though on a small scale. Further, even on a small scale, test costs are quite high, and tests are also resisted by the owner of the structure and large-scale work and repairs are involved.

It is possible to obtain large quantities data, and in many cases information at only one point can be obtained.

The test method of the test method of chloride ion content introduced here eliminate these problems. We hope that this method will be recognized widely both domestically and abroad.

REFERECES

1. Yoshio KASAI, Isamu MATSUI and Noboru YUASA: A trial for quality evaluation of structural concrete by easy test, Cement Association, Cement Concrete, No.559, pp.20-28, 1993.9
2. Yuji GOTOH, Humitoshi KOGA, Kaoru SAKAMOTO and Kozo TAKAHASHI: Regarding 2 or 3 methods related to durability evaluation of concrete structure, Cement Association, Cement Technology Annual Report, No.38, pp.321-324, 1984
3. Hiroo NAGANO, Tatsuyuki KAMIJYO, Takashi HIRATA: 2 or 3 trials to speed up of the study of salt content, Cement Association, Cement Concrete, No.492, pp.2-10, 1998.2
4. Yoshio KASAI, Isamu MATSUI, Noboru YUASA: Study regarding rapid study method to determine the quality of structural concrete (No.2 Examination of study method), Scholarship lecture meeting No. 23, College of Industrial Technology, Nihon University, pp.45-48, 1990.12

This Page Intentionally Left Blank

MACROCELL SENSOR SYSTEMS FOR MONITORING OF THE CORROSION RISK OF THE REINFORCEMENT IN CONCRETE STRUCTURES

M. RAUPACH and P. SCHIEßL

*Business Manager of S+R Sensortec GmbH, Aachen, Germany
Director of the Institute for Building Materials, Technical University of Munich*

ABSTRACT

Since 1990 a special macrocell system, the so-called Anode-Ladder-System, is used world-wide to monitor the corrosion risk of new concrete structures, besides other systems, which have been developed later. This sensor-system indicates the depth of the critical chloride content initiating corrosion, i.e. the critical depth of the reinforcement with respect to corrosion. Subsequently the time-to-corrosion can be determined, enabling the owners of buildings to initiate preventive protection measures *before* cracks and spalling occur. By measurement of the potentials and the electrical resistance of the concrete around the sensors an estimation of the humidity, the availability of oxygen and the corrosion behaviour after depassivation is possible.

To be able to monitor also the corrosion risk for existing structures a new sensor system has been developed called Expansion-Ring-System. It consists of 6 measuring rings (“anodes”) separated by sealing rings as parts of the main sensor and a “cathode-bar”, which are installed into small holes to be drilled into the concrete. The durable connection to the concrete is established by special patented expansion mechanisms for both sensors.

KEYWORDS

Corrosion, monitoring, steel, concrete, reinforcement, anode, cathode, sensor

INTRODUCTION

Corrosion of the reinforcement has become a major problem world-wide, especially for structures exposed to aggressive environments such as bridges, parking decks, tunnels, offshore structures or other buildings exposed to seawater or de-icing salts. As result, the repair costs nowadays constitute a major part of the current spending on the infrastructure.

Many new systems and materials have been developed to repair the damages and to increase durability, e.g. high performance concretes. However, there is only limited long-term

experience with these developments. Therefore sensor systems are needed enabling the owners of the structures to monitor the corrosion risk and to take protective measures *before* the damaging processes start.

As known, the costs for repair measures increase more than proportionally with time, when the reinforcement already has started to corrode. However, the traditional monitoring systems like reference cells only show the local onset of corrosion, but not the time-to-corrosion, which is measurable using the macrocell-systems.

THEORETICAL BACKGROUND

The development of the corrosion monitoring sensors was based on an extensive research program on the main factors influencing chloride induced macrocell corrosion of steel in concrete (see e.g. [1]-[5]). More than 500 concrete specimens with different concrete compositions have been investigated under varying environmental conditions. These investigations have been carried out using macrocell current measurements between anodically and cathodically acting steel surface areas.

The tests have shown, that this technique can also be used to monitor the ingress of aggressive substances like chlorides or carbonation by measuring electrical signals between different steel bars installed at defined locations.

The operation of a macrocell consisting of a piece of black steel (anode) and a noble metal (cathode) is shown in Fig. 1. In chloride free and non-carbonated concrete, both electrodes are protected against corrosion due to the alkalinity of the pore solution of the concrete (passive state). The electrical current between both electrodes is negligibly low under such conditions.

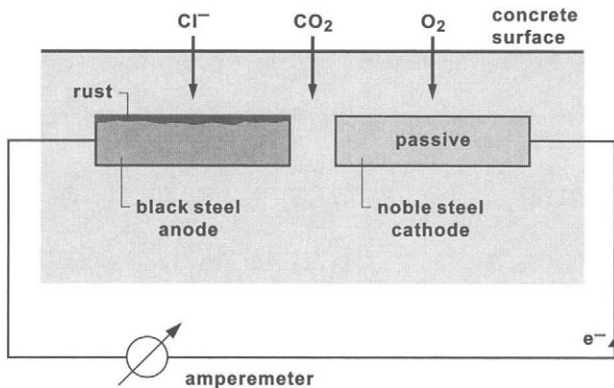


Fig. 1 Macrocell consisting of a black steel anode and noble metal cathode

If, however, a critical chloride content is reached, or if the pH-value of the concrete decreases due to carbonation, the steel surface of the so-called anode is no longer protected against corrosion. Provided that the selected cathode material is corrosion resistant in chloride

contaminated or carbonated concrete and sufficient moisture and oxygen are available, oxygen reduction takes place at the surface of the so-called cathode-bar. The local separation of anodically and cathodically acting areas leads to an electron flow between the black steel and the noble metal, which can easily be measured using an external cable connection.

Fig. 2 shows as the result of a demonstration test in the laboratory the electrical macrocell-currents flowing between a black steel anode and a stainless steel cathode embedded in two concretes with different w/c. The macrocells were embedded with a concrete cover of only 5 mm (0.20 in.) to initiate corrosion by applying a chloride solution on the concrete surface within a short period of time. The results of the macrocell current measurements showed that the critical chloride content reached a depth of 5 mm (0.20 in.) at the specimen with w/c = 0.7 about 80 days after concrete placement. This caused a significant increase of the macrocell current while the specimen with a lower w/c and a higher resistance against chloride diffusion remained passive.

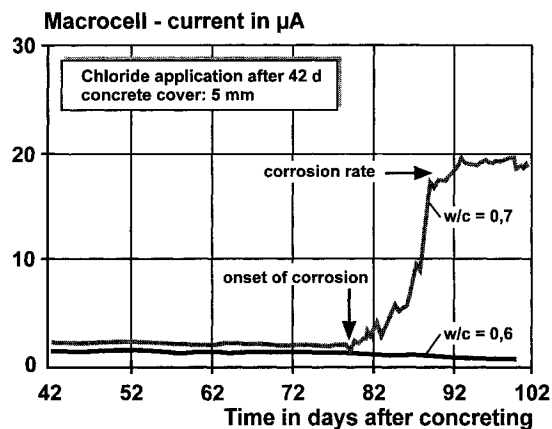


Fig. 2 Time-dependent behaviour of the galvanic currents

The basic measuring principle to monitor the time-to-corrosion is to place several electrodes into different depths related to the concrete surface and to measure the onset of corrosion of these electrodes one by one according to Fig. 3.

The measuring electrodes are made of steel with a similar composition as reinforcing steel to ensure that they will start to corrode at the same time, when a rebar at the same depth would start to corrode. Comparative tests have been carried out at the Institute for Building Materials Research of the RWTH Aachen, showing that there was no significant difference in the corrosion behaviour of the steel used for the measuring electrodes (anodes) and reinforcing steel also when using different degrees of pre-rusting before installation into the concrete specimens.

Using adequate calculation models the time-to-corrosion can be determined at any time related to the cover depth of the reinforcement.

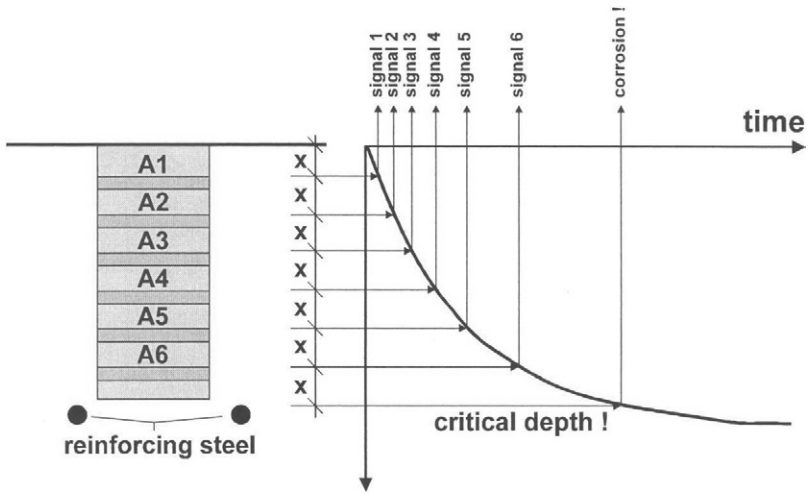
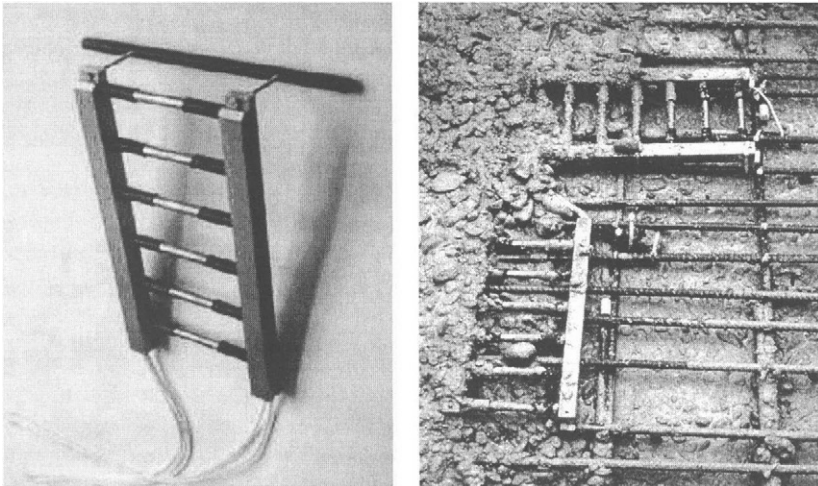


Fig. 3 Basic principle to determine the time-to-corrosion

DEVELOPMENT OF THE ANODE-LADDER-SYSTEM FOR NEW STRUCTURES

A typical layout of the corrosion sensor consisting of 6 single anodes is shown in Figs. 4 and 5. Each of the 6 black steel anodes is positioned 50 mm (2 in) from the next one to prevent interactions between the anodes.



Figs. 4 and 5 Photographs of the Anode-Ladder-System to monitor the corrosion risk of the reinforcement installed during construction

Figs. 4 and 5 also show that the cables are lead through stainless steel fixtures to the measuring device. The cable shafts within the stainless steel frame is filled with epoxy resin that acts as mechanical protection for the wires and the integrated PT 1000 temperature sensor. Two cables are connected with each single anode to get a redundant system. This allows the cables and cable connections to be checked after installation by short circuit tests.

The fixture is separated from the anodes by an insulation. This geometrical design of the sensor ensures that the concrete cover above every single anode is not affected by parts of the sensor, and that the penetration of chlorides into the concrete and the carbonation process are consequently also not influenced.

Since 1990 this so called Anode-Ladder-System has been used world-wide in different types of structures to monitor the corrosion risk for new reinforced concrete structures in aggressive environment [6]. More than 800 Anode-Ladders have been installed into tunnels, bridges, foundations and other structures exposed to aggressive environment in Germany, Austria, Denmark, Hong Kong, Japan, Croatia, Egypt, Switzerland, The Netherlands, Sweden, Taiwan and Australia and several installations are actually running. The actual state is given in the internet-homesite: www.sensortec.de.

Fig. 6. shows the results from the calibration tests of single reinforcement bars with the same geometry as of the single steps of the Anode-Ladders in high performance concrete with addition of different chloride contents mixed to the fresh concrete. As reference concrete a poor-quality concrete with water/cement-ratio of 0.7 has been investigated with a chloride content of 1.5 % / cement.

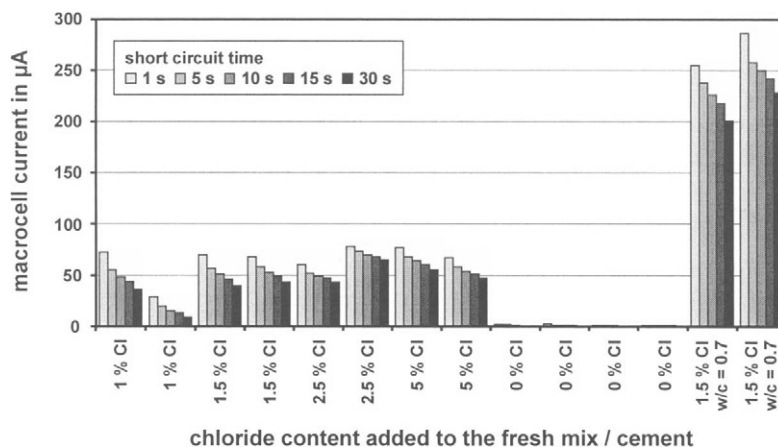


Fig. 6 Results from calibration tests of the Anode-Ladder-System in high performance concrete with different chloride contents and a concrete of poor quality

To investigate additionally the most suitable short circuit time between the single anodes and the cathode bar, five different short circuit times between 1 sec. and 30 sec. have been tested.

As expected, it was found that the high performance concrete without addition of chlorides showed very low macrocell currents lower than $15 \mu\text{A}$ independently from the short circuit time. On the contrary, when 1 to 5 % chlorides/cement had been added to the concrete, considerable macrocell currents in the range of $50 \mu\text{A}$ have been measured. The effect that the el. currents didn't increase with chloride content can be explained by the limited size of the cathode bar, because the cathodic process seems to be the rate controlling factor for the investigated corrosion conditions (see e.g. [7]).

However, as it is not intended to measure absolute corrosion rates, but the critical depth of corrosion, the size of the cathode bar is sufficiently large to separate between the passive and active state of the so-called anodes. The sensors within the reference concrete show much higher currents in the range of more than $200 \mu\text{A}$ as result of the poor concrete quality.

Regarding the most suitable short circuit time Fig. 6 shows that generally all selected times could be used to be able to differentiate between passive and active state. As for practical reasons a short measuring time is most convenient, a short circuit time of 5 seconds has been defined as standard short circuit time.

DESCRIPTION OF THE EXPANSION-RING-SYSTEM FOR EXISTING STRUCTURES

The Expansion-Ring-System consists of the Expansion-Ring-Anode and a cathode-bar. Both electrodes are inserted into holes, which have to be drilled into the concrete. Usually the hole to be drilled to fix the drilling equipment by a dowel is later used to insert the cathode-bar into the concrete. Fig. 7 shows the installation- and measurement-procedure schematically.

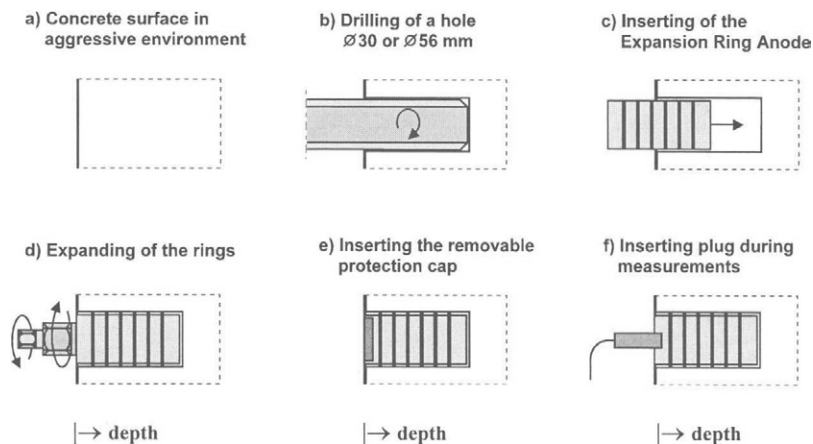


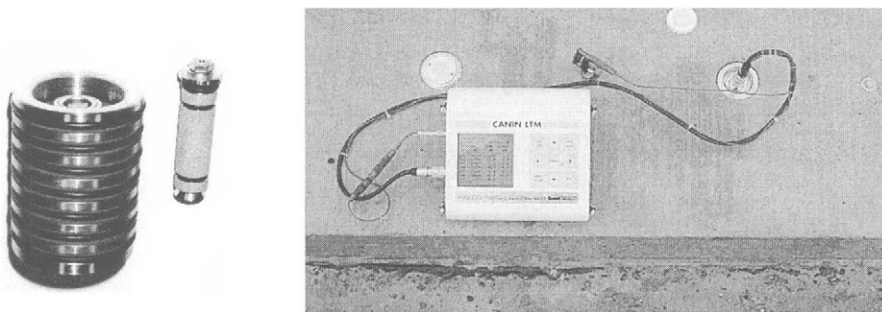
Fig. 7 Installation procedure of the Expansion-Ring-Anode

The main measuring sensor is the Expansion-Ring-Anode (see Fig.8). Similar to the six bars of the Anode-Ladder-System [6] the Expansion-Ring-Anode consists of six measuring rings in

different distances from the concrete surface, in 1 cm-steps from 1 to 6 cm. In this way the ingress of chlorides and/or carbonation from the concrete surface into the concrete and the subsequent corrosion risk of the reinforcement can be measured as it was shown in Fig.3.

Above, between and below these metal rings altogether seven insulation rings are established to seal the area between the rings, i.e. to prevent water or chlorides penetrating along the drilled surface deeper into the hole of the Expansion-Ring-Anode.

The cathode (see Fig. 8, at the right to the ring-sensor) consists of two pieces of a platinum-coated bar to be expanded by a special mechanism to ensure a durable contact to the concrete.



Figs. 8 and 9 Photographs of Expansion-Ring-Anode and cathode-bar as well as the system installed into a bridge cap during measurement with removed protection cap

The Expansion-Ring-Anode and cathode bar are connected to the concrete by turning nuts at the upper part of the sensors, leading to an expansion of the rings in a way that both sensors can be tightened sufficiently strong. During installation of the sensors the torque of the sensors will be measured to ensure that the tension between sensor and concrete is sufficient for a durable contact and not too high to induce problems of cracking of parts of the sensor or the concrete.

The distance between anode and cathode should be in the range of 5 to 15 cm. Additionally the electrolytic resistance between the rings can be measured to check the electrical contact between the rings and the concrete.

In the head of the Expansion-Ring-Anode a socket is integrated, which allows to insert a plug of the measuring instrument. Between the measurements a sealing cap is put onto the socket to protect it from corrosion. Cables lead from the measuring rings to this integrated socket inside of the Expansion-Ring-Anode. After production of the electrode all inner open spaces are filled with resin and sealing material to ensure that no water or chlorides can penetrate to the inner part of the sensor.

Laboratory tests have shown that the formation of rust at the first anodes after depassivation has an additional sealing effect. Therefore, the depth of the critical chloride front is not influenced by the presence of the sensors, because chlorides can only enter into the concrete besides the Expansion-Ring-Anode through the existing concrete.

MEASUREMENTS AND EVALUATION

To detect the onset of corrosion of the “anodes” (measuring bars or rings) the electrical currents, voltages, electrical resistances and temperatures of the installed sensors are measured using a specially developed hand instrument, e. g. one to four times a year.

As long as the critical chloride content and the carbonation depth have not reached the surface of the outer anode-ring, all electrical currents between the “anodes” and the “cathodes” are low. In the course of time the “anodes” will be depassivated one after the other. By measuring the electrical currents and voltages in regular intervals, the critical depth regarding reinforcement corrosion is measurable continuously.

To be able to estimate additionally the potential corrosion behaviour of the reinforcement after depassivation, the electrical AC-resistance-distribution of the concrete between the six single “anodes” is also measured. Generally the maximum possible corrosion rates decrease with increasing resistance of the concrete. Additionally the temperature is measured using an integrated PT 1000 sensor.

For the measurements an automatic portable instrument CANIN-LTM has been developed (see Fig. 9). Using this battery-powered instrument the electrical currents, potentials, electrolytic resistances and the temperature are measured automatically. The critical values are indicated simultaneously within the large display. The data of the measurements of 1.000 sensors can be stored and transferred to a personal-computer by the integrated serial port. For further evaluation of the data software is available, which builds up a database and shows the data versus time including alarm-values (see following section).

RESULTS OF LABORATORY TESTS

To investigate the correct functioning of the Expansion-Ring-System comparative tests have been carried out using concrete specimen with embedded Anode-Ladders. Expansion-Ring-Anode and cathode have been installed 137 days after placement of the concrete. At this stage the first two anodes of the Anode-Ladder indicated activity showing that the critical depth related to reinforcement corrosion was between 2 and 3 cm as the single anodes have been installed in 1 cm - steps. To achieve this situation a chloride solution containing 1 % Cl⁻ had been applied onto the concrete surface beginning from 1 week after placement of the concrete. After installation water has been applied onto the concrete surfaces in regular intervals (see Figs. 10 and 11) to investigate the influence of wetting and drying on the measured data.

Figs. 10 and 11 show the standard plots produced by the MACRO-software developed for the monitoring systems. To get a direct overview of all data, the time-dependent values of voltage of all anodes against the cathode, electrical currents 5 seconds after coupling of the anodes against the cathode, the AC-resistance at 100 Hz between neighboured anodes and temperature of the integrated PT 1000 sensor are plotted together on 1 page.

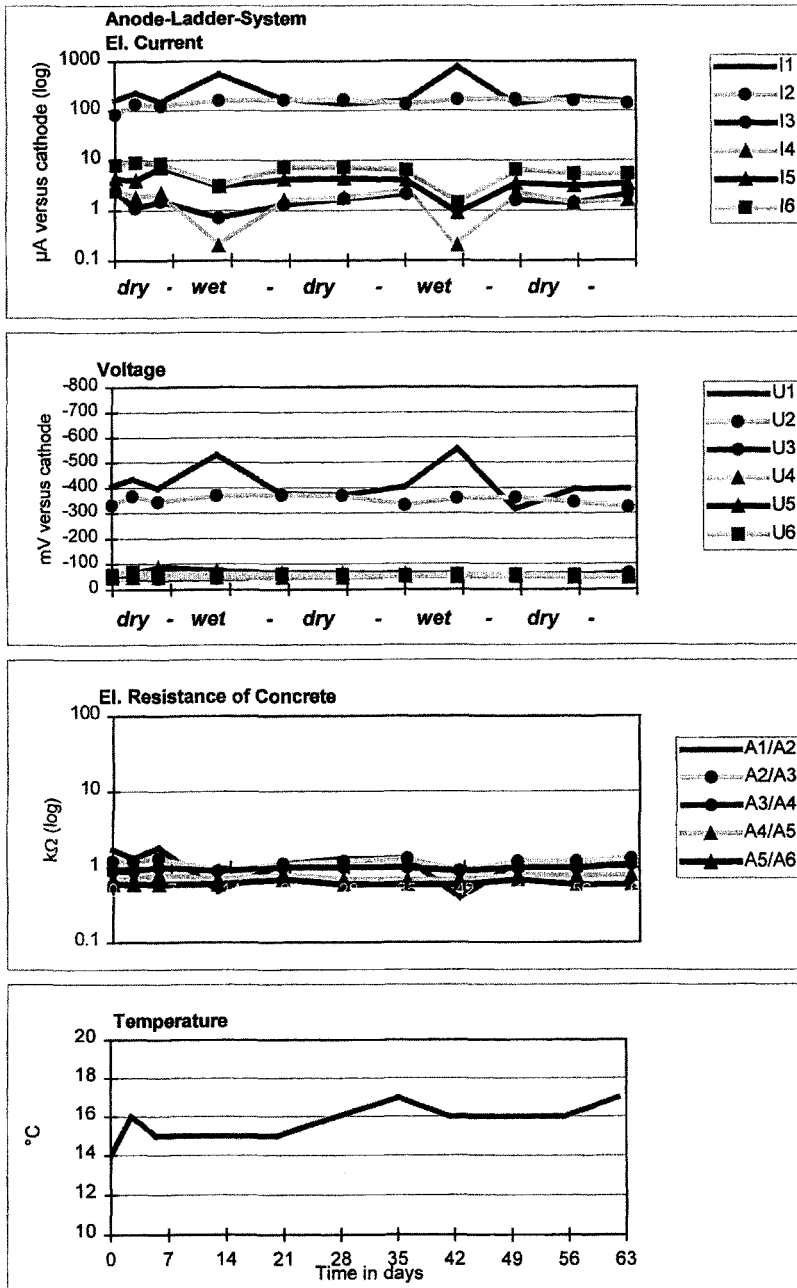


Fig. 10 Results from a laboratory test of the Anode-Ladder-System under cyclic water application (A1 is the single anode next to the concrete surface, etc.)

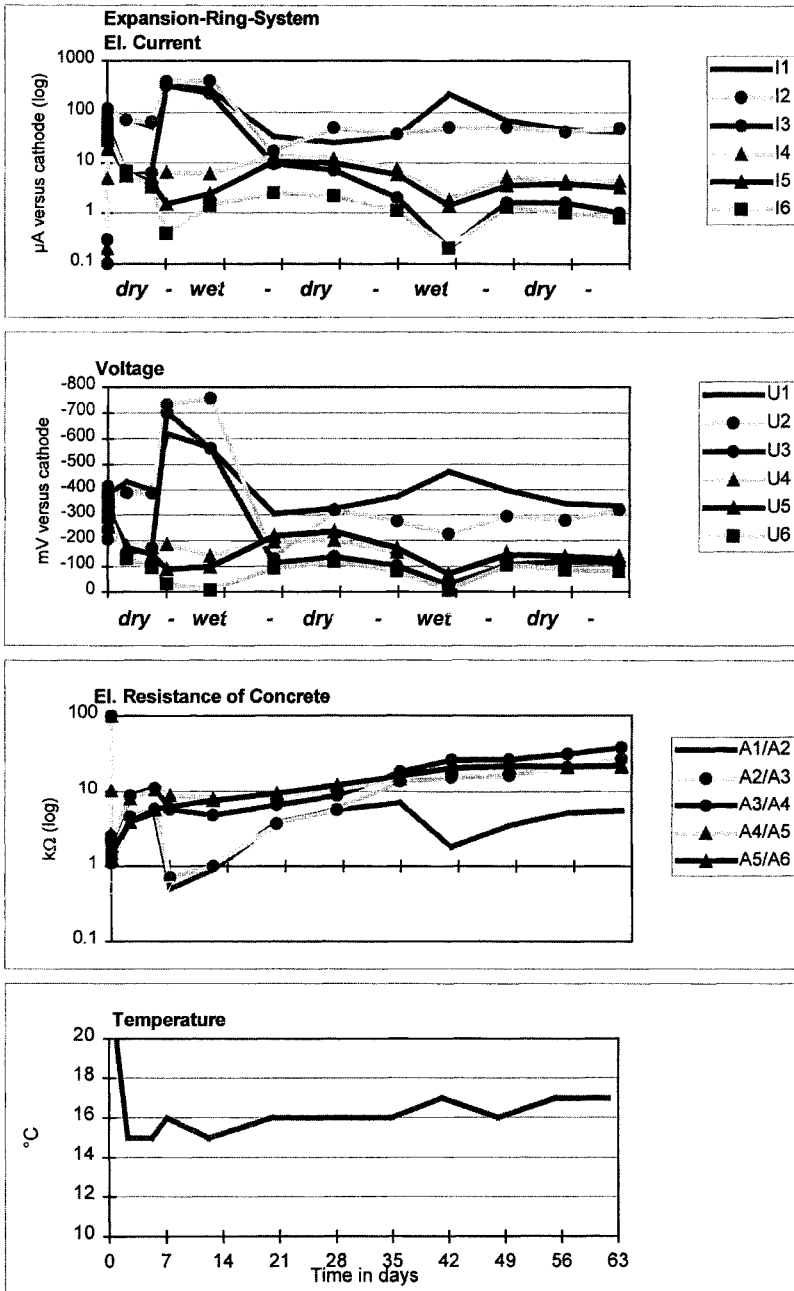


Fig. 11 Results of the Expansion-Ring-System installed near the Anode-Ladder; (compare to Fig. 10, A1 is the single anode next to the concrete surface, etc.)

As limit values for activity of the single anodes under usual conditions 150 mV and 15 μ A after a short circuit time of 5 seconds are used from experience. For special conditions regarding concrete composition or environment, e.g. for permanently submerged concrete, other limit values might be relevant, which can be determined individually by calibration tests using the same concrete under the same conditions.

Fig. 10 and 11 show the data taken from both sensor systems beginning at the time of installation of the Expansion-Ring-Anodes during cyclic application of the 1 % Cl⁻ solution, which can especially be seen at the data of the outer anodes near the exposed concrete surface. Voltages and currents of the Anode-Ladder show that the 2 outer anodes 1 and 2 are depassivated, while the remaining anodes 3-6 are passive (Fig. 10).

Fig. 11 shows that it takes about 1 month until voltages and currents of the single anodes of the Expansion-Ring-Anode above and below the critical depth separate clearly from each other. This can be explained by the fact that it takes a certain time until the surfaces of the rings passivate due to the alkalinity of the surrounding concrete and until the chlorides cause an activation. After this period the further ingress of chlorides can also be monitored.

The differences in the absolute values for the electrical currents and resistances are caused by the different geometry of both types of sensors. For these comparative tests an Expansion-Ring-Anode with a diameter of 30 mm has been used.

This preliminary test shows that the Expansion-Ring-System is suitable to monitor the critical depths related to corrosion of the reinforcement. The long-term-tests are still running and will be presented later.

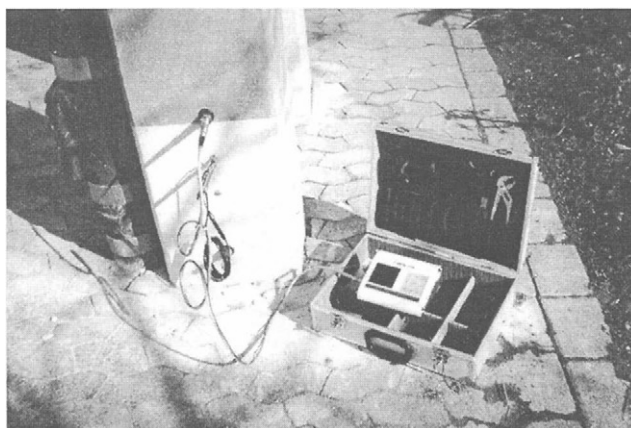


Fig. 12 Photograph of a prototype of the Expansion-Ring-System installed into a column of a parking garage to monitor the durability of the coating and the area above the coating

MONITORING OF THE DURABILITY OF REPAIR MEASURES

The Expansion-Ring-System can especially be used to monitor the durability of repair measures. Fig. 12 shows e.g. the installation of Expansion-Ring sensors into the columns of a parking structure, where a coating had been applied to prevent further ingress of chlorides and to dry the concrete increasing the electrolytic resistance of the concrete. The actual results show, that the concrete is drying out and no corrosion has to be expected. However, this situation is likely to change after several years.

OTHER FIELDS OF APPLICATION

The corrosion monitoring system has the following advantages compared to other monitoring methods:

- It is not only shown, whether the reinforcement corrodes or not, but it can also be estimated, *when* the reinforcement will start to corrode.
- The corrosion monitoring system shows directly the depth of the critical chloride content and not the absolute chloride contents. Compared to the measurement of chloride profiles this is a decisive advantage, because as known from experience the interpretation of absolute chloride contents is generally difficult. Therefore the installation of corrosion monitoring sensors can not be replaced only by taking concrete samples for chloride profiles.

The use of the corrosion monitoring system is especially economic in not accessible locations, e. g. at the outer surfaces of tunnels or in the tidal zones of pier shafts, etc..

When the corrosion monitoring systems are used as an effective integrated part of the maintenance program, the operating costs i.e. the inspection, maintenance and repair costs, can be reduced significantly. Interesting fields of application are the following:

- Reinforced concrete structures exposed to aggressive environments (offshore structures, buildings near the coast, bridges, parking structures, tunnels, foundations, etc)
- Areas with difficult or without access (outer areas of tunnels and pipes, foundations and tanks, piers, piles of bridges near the water level, etc.)
- Monitoring of the durability of special protection systems for new structures especially with a high designed service life, e.g. 100 years (high performance concrete, coatings, inhibitors, etc.)
- Monitoring of the durability of special repair systems (cathodic protection, desalination, coatings, inhibitors, etc.)

OUTLOOK

Experience from 10 years has shown that the Anode-Ladder-System is suitable to monitor the corrosion risk for the reinforcement in new concrete structures. Laboratory tests and first installations on site have shown, that it is also possible to monitor existing structures using the Expansion-Ring-System.

Since September 1998 the Brite Euram Project "Smart Structures" is running to develop an integrated monitoring system for concrete structures. One task of this project is the further development of the Expansion-Ring-System, especially optimisation of the installation procedure and testing in different concretes in laboratory and in critical locations of bridges. The further results will be presented within the next years.

REFERENCES

1. Schießl, P.; Raupach, M., *Second CANMET/ACI International Conference on Durability of Concrete*, Montreal, 1991, pp. 565-583
2. Schießl, P.; Raupach, M., *The Life of Structures: The Role of Physical Testing*. 2nd International Swedish Council for Building Research, Stockholm, 1989, Publ.-No. D9:89, pp. 226-233
3. Schießl, P.; Raupach, M., *Durability of Concrete; Aspects of Admixtures and Industrial By-Products*. 2nd International Seminar, Swedish Council for Building Research Stockholm, 1989, Publ.-No. D9:89, pp. 205-214
4. Schießl, P.; Raupach, M., *Corrosion of Reinforcement in Concrete*. International Symposium Wishaw, Warwickshire, UK, May 1990, London Elsevier, pp. 49-58
5. Schießl, P.; Raupach, M., *9th International Congress on the Chemistry of Cement*. National Council for Cement and Building Materials, New Delhi, November 1992
6. Schießl, P.; Raupach, M., *Concrete International* July 1992, pp. 52-55
7. Raupach, M. ; Gulikers, J., *EUROCORR 99 in Aachen*, August 1999, 16 pages

This Page Intentionally Left Blank

METHOD OF TEST FOR NEUTRALIZATION DEPTH OF CONCRETE IN STRUCTURE WITH DRILLING POWDER

Y. KASAI and N. YUASA

Dept. of Architecture and Architectural Eng., College of Industrial Technology,
Nihon University, Japan
1-2-1, Izumi-cho, Narashino-shi, Chiba-ken, 275-8575, Japan

T. MANO

Japan Testing Center for Construction Materials
5-21-20, Inari-cho, Soka-shi, Saitama-ken, 340-0003, Japan

ABSTRACT

A test method for neutralization depth of concrete with drilling powder has been developed. It can be applied very easily in site to wall and to column concrete by drilling a hole of diameter of 10 mm.

This method evolves measuring the drilled depth stopping drilling immediately the drilled powder discharged from the hole changes to a red color when the powder contacted to a phenolphthalein-ethanol solution soaked to a filter paper.

Accuracy is very high and these are no problems in practical use compared with conventional methods i.e. digging holes or boring cores.

KEYWORDS

Concrete in structure, Neutralization depth, Drilling test method, Rapid neutralization test.

INTRODUCTION

This test method was first proposed by the Ministry of Construction of Japan in 1988 [1] and the authors have been improved and developed [2]. The Japanese Society for Non-Destructive Inspection (NDI) composed of a committee for establishing a NDIS Test method for neutralization depth of concrete in structure with drilling powder, in 1998.

In this paper, some considerations on this test, an example of application, and finally, outline of NDIS "The method of test for neutralization depth of concrete with drilling powder-1999" [3] are presented.

FEATURES OF THE DRILLING METHOD

There is no standard method for the neutralization depth of concrete. The conventional methods and the drilling method are compared as follows.

(1) Digging a hole by a chisel: A test liquid with one percent of phenolphthalein ethanol solution, contained about 15 percent of water is sprayed on the surface of the dug hole. Neutralization depth is defined as the depth from the original surface to the red-colored portion of concrete.

(2) Core method: Sample core is washed well with tap-water, and surface water dried out in the air and test liquid is sprayed to core and neutralization depth is measured from original surface. Depth of 4 or 6 portions should be measured.

(3) Drilling method: The drilling method is very simple, easy and rapid compared to the conventional methods. The characteristics of the drilling test method are as bellow.

a) The only ϕ 10 mm holes are drilled, so defect of the structure is very small, and repair works are very easy with cement paste or cement mortar or caulking compound.

b) Number of testing spots can be increased.

c) Testing spots are mainly walls though columns and vertical plane of beams could be tested.

IMPORTANT FACTORS AFFECTING THE NEUTRALIZATION OF CONCRETE

The neutralization depth is influenced by the individual condition of structure and test spot.

(1) Conditions of structure

a) Neutralization depth becomes larger, when the age of structure is older.

b) The structures used for house or office, the neutralization speed of indoor of structure is faster than the outdoor, because in general indoor concentration of carbon dioxide (CO₂) is larger than that of outdoor.

c) The outdoor concrete get wet directly by the rain, the neutralization speed becomes slow because the moisture content of concrete is usually large, and moving of carbon dioxide gas is prevented by the moisture.

d) When the position of testing spots are lower than 20–30 cm from the ground line, the neutralization speed becomes very slow, because the concrete get wet by the rebounded rain or capillary suction water.

e) In general, concrete under soil or water does not get neutralization, although concrete in acidic soil or acidic water and acid gas neutralization is very faster.

(2) Quality of concrete and type of used cement

a) The neutralization speed of concrete is faster when water-cement ratio of concrete is larger.

b) When moisture curing of concrete is incomplete, neutralization speed becomes faster.

c) When blast furnace slag cement and fly ash cement are used, the neutralization speed becomes faster.

(3) Surrounding condition of structure

In the case of exterior wall, moisture content of concrete is smaller in west side or south side, so the neutralization speed is faster, and it is slow in east side and north side, and under the shadow of trees.

(4) Finishing Materials

a) When finished with mortar, neutralization of concrete starts after finishing mortar is neutralized. If there are clacks in mortar and separation boundary of concrete and mortar the neutralization progressed from the interface between mortar and concrete.

b) When exposed concrete is subsequently finished with mortar, the mortar does not neutralized though the neutralization depth of concrete is some time large.

(5) Testing apparatus or tools

• Hammer drill: A hammer drill should be used. A rotation drill can not make holes. Diameter of drill bit is fixed to 10 mm.

• Slide calipers and filter paper of ϕ 185mm or white hydrophilic neutral paper are needed.

- Chemical reagent: 1% of phenolphthalein-ethanol solution contained 15 % of water.
 - Test paper: It is made by a chemical reagent spread on the filter paper using a hand sprayer.
- Photo 1 shows spraying phenolphthalein-ethanol solution onto filter paper.

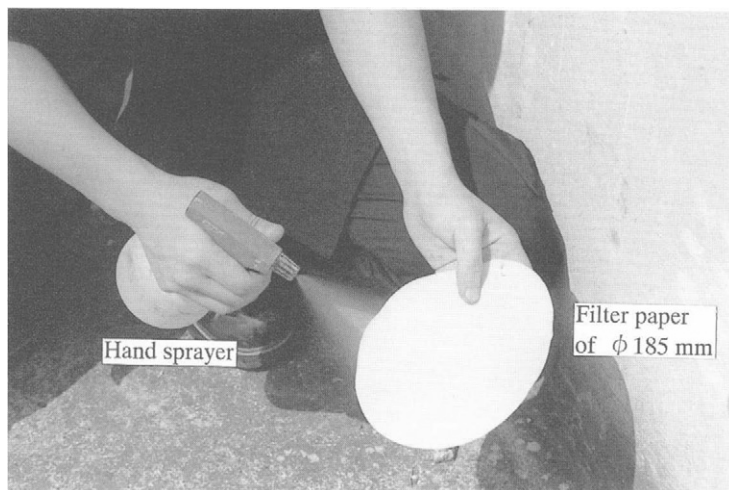
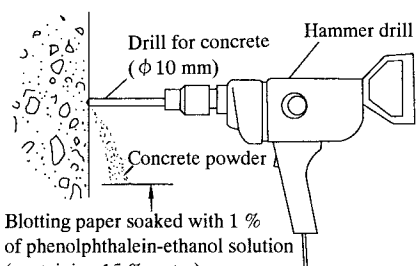


Photo 1 Spraying of phenolphthalein-ethanol solution onto filter paper

TESTING METHOD

Fig. 1 shows an illustration of neutralization depth test, and Photo 2 shows the testing situation. Two engineers are working for the test. One is drilling a hole using hammer drill attached it in right angle to concrete. Another one is receiving the concrete powder with a test paper slowly rotating under the drilling hole as shown in Photo 3.



Blotting paper soaked with 1 % of phenolphthalein-ethanol solution (containing 15 % water). This paper is turned so that concrete powder always falls on a new spot

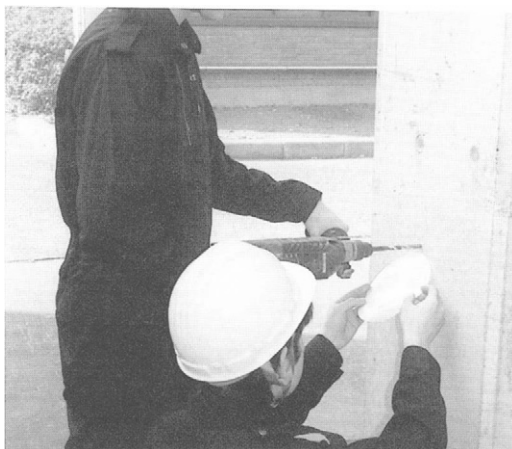


Photo 2 The neutralization depth test using drilled powder

Fig. 1 Testing image for neutralization depth with drilled powder

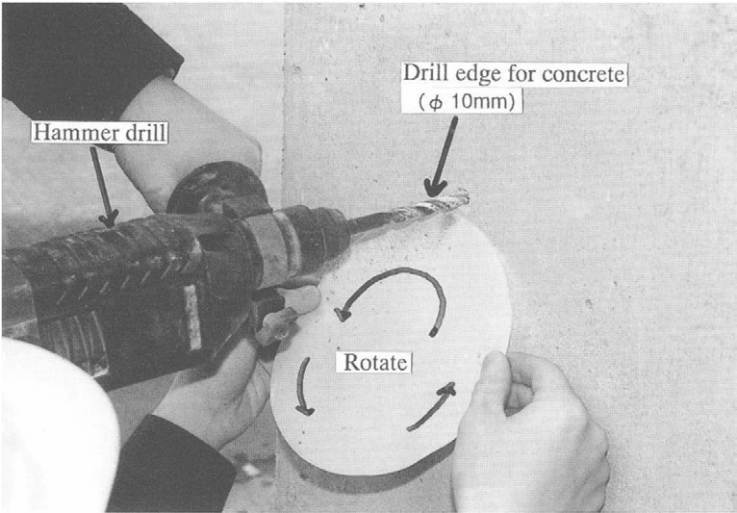


Photo 3 Drilling a hole and how to move paper

If the engineer could use an apparatus which receive concrete powder automatically, he could test only himself. Photo 4 shows a testing apparatus, which can test only one engineer.



Photo 4 The neutralization depth test using drilled powder for only one engineer

Before test, it is better to execute a preliminary test.

When testing, the ordinal rotation speed of drill and drilling speed of the hole may be maintained until it comes final stage of drilling, then switch the power on and off, so as to see the color of concrete powder turning to red. When the powder color turns to red, stop drilling immediately, and measure the depth of hole using depth bar of slide caliper as shown in Photo 5.

Drilling position should be decided after the discussion with the client. When the test spot is specified, number of testing holes are three with a distance of more than 5 cm.

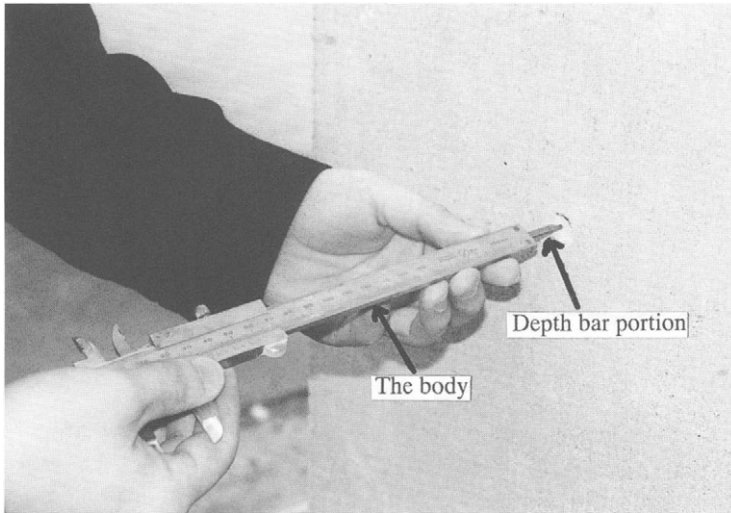


Photo 5 Measuring the depth of a hole

COMPARISON OF DRILLING AND CORE METHOD

Relationships between both methods are shown in Fig. 2. The neutralization depth measured by the drilling method is a little larger than that of core spreading method, because the drilled powder travels from drilling front to the exit.

However, close correlation can be found between the results, obtained with these two methods, and those obtained by the drilling method are generally safety side compare to the core method.

Table 1 shows test results of the neutralization depth obtained by drilling method and the conventional (core spreading) method with $10 \times 10 \times 40$ cm specimen under accelerate neutralization conditions.

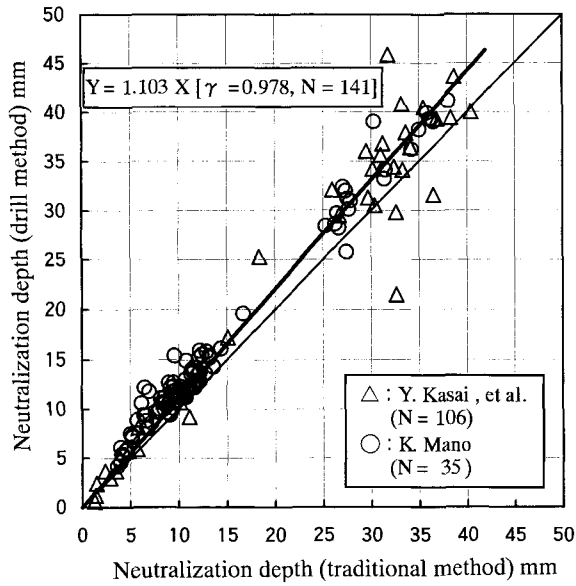


Fig. 2 Relation between the drilling method and the traditional method

Table 1 Comparison between test results of the neutralization depth obtained by drilling method (D.m.) and the traditional method (T.m.) in laboratory

Number	Number of measurements	Average of neutralization depth (mm)			Coef of variation		
		D.m.	T.m.	Difference*	D.m.	T.m.	Difference*
No. 1	7	5.4	4.3	1.1	18.5	11.2	7.3
No. 2	13	9.3	6.3	3.0	22.5	21.1	1.4
No. 3	13	11.6	9.2	2.4	18.1	17.2	0.9
No. 4	10	12.2	9.9	2.3	16.8	16.7	0.1
No. 5	13	12.2	10.6	1.6	16.2	15.9	0.3
No. 6	10	11.5	10.7	0.8	11.0	10.2	0.8
No. 7	10	12.6	11.5	1.1	11.0	11.5	-0.5
No. 8	10	14.0	11.6	2.4	22.2	22.2	0.0
No. 9	11	30.6	27.3	3.3	11.1	4.6	6.5
No. 10	9	37.8	35.0	2.8	7.2	6.5	0.7
Average	—	—	—	2.1	13.7	15.5	1.8

* difference = drilling method - traditional method

This table shows, the difference of the test methods is as follows.

- a) The neutralization depth obtained by drilling method is a little larger than that of the spread method. In the average value of the former is 2.1 mm larger than the latter. The differences are 0.8 mm in minimum and 3.3 mm in maximum.
- b) The neutralization depth obtained by the drilling method is 10 % larger than that of the spread method and there is no remarkable difference between them.
- c) The variance of drilling method is a little larger than spread method. The average of variance of drilling method is 1.8 % large than that of the spread method.

EVALUATION OF TEST RESULTS

A neutralization depth is an average of three measurements. When one depth is 30 % larger than the average, the one most likely to drill a coarse aggregate, in that case, one more new hole should be drilled and an average will be calculated for four depths including the new one. If there is any hole that has the neutralization depth over 30 % larger than the average, one more hole should be drilled and the neutralization depth is calculated as average value of the five depths. This average value is the final neutralization depth of the spot. This method for calculating the average value is due to an engineering judge to avoid increasing the number of drilling holes.

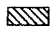
RECOVER

Tested holes will be recovered by mortar or other suitable material to maintain the durability and the appearance of the structure.

AN APPLICATION EXAMPLE OF THE NEUTRALIZATION DEPTH TEST

The neutralization depth test with drilling powder makes it possible to have more test spots than that with gathering cores, and makes it possible to indicate a distribution of the neutralization depth which has not previously been indicated. An example, east side, 2nd floor, a outside wall, not exposed directly to rain water of the College of Industrial Technology, Nihon University, constructed in 1968 (not existing at present) and studied in 1992 for the concrete structure is shown in Fig.3 [4].

This distribution of the neutralization depth was made on the whole wall with a representative area of 25×25 cm for one spot, and the results measured were processed by a computer. The results show that the higher the spot is located the greater the neutralization depth becomes. Further, reinforcement spots, the covering thickness of measured by non-destructive test using reinforcement probes, are shown on the same figure of the distribution of the neutralization depth. Thus, by the simultaneous use of the reinforcement probe, the corrosion risk degree of every spot of the reinforcement can be clarified without any great destruction.

 is the portion where the neutralization is thought to have reached the reinforcing bar

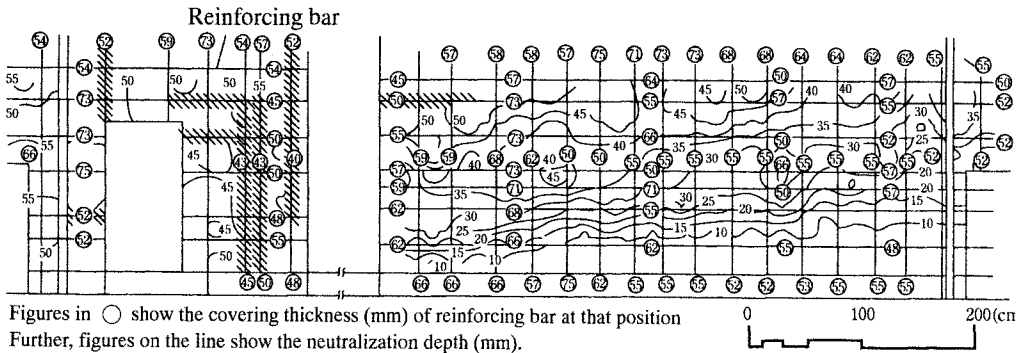


Fig. 3 The distribution of the neutralization depth and covering thickness [4]

OUTLINE OF “METHOD OF TEST FOR NEUTRALIZATION DEPTH OF CONCRETE WITH DRILLING POWDER” (NDIS 3419-1999)

This NDIS is established in August 1999. Outline of the test method is described as follows.

SCOPE OF APPLICATION

This standard test method is applied to test the neutralization depth of concrete in structures. The main application is to vertical face of walls, columns and the joists of concrete structures. However, this standard can not be applied to the concrete using recycled aggregate.

THE DEFINITION OF TERMS

The definition of terms used in this standard are as follows, and may also be referred to JIS Z 2300-1991 “Terms for non-destructive test” and JIS A 0203-1999 “Terms for concrete”.

- (1) Drilling powder: Powder exhausted from a hole of about 10 mm in diameter bored into concrete using a hammer drill.
- (2) The neutralization depth of concrete: The depth at which concrete does not color by one percent of phenolphthalein-ethanol solution, as a consequence of migration of the atmospheric carbon dioxide, other gas or acid liquid into the concrete, resulting concrete alkalinity.

TEST ENGINEERS

Test engineers for neutralization depth test (hereinafter called engineers) are those who satisfy the following conditions.

- (1) The color sense for red colors has to be normal. Further, the test methods for eyesight and color sense are based on NDIS 3413.
- (2) Engineers have to have sufficient knowledge regarding the concrete structure and its deterioration.

PRELIMINARY INSPECTION AND PREPARATION

The following are related studies to be done before the execution of the test for neutralization depth.

- (1) The out line of the structure: Location, construction year, scale of structure, building area, floor space, number of floors, use of structure, the history of the structure and outline of direction of the structure. Matters related to the materials and mixture of concrete.
- (2) The test spot: Inside or outside the structure. If the structure exposed directly to rain or not.
- (3) The presence of the finishing materials: If finished, their types and thickness, the age, cracks, presence of separation etc.
- (4) Other matters: Those necessary for the testing of neutralization depth.

EQUIPMENT

- (1) Test apparatus

Hammer drill: Portable and vibration type specified by JIS C 9605

Drill bit: To be used only for concrete drilling and 10 mm in diameter

Slide calipers: Maximum measuring length of 150 or 200 mm specified by JIS B 7507

Filter paper: Filter paper for chemical inspection specified by JIS P 3801

- (2) How to make the one percent phenolphthalein-ethanol solution

Phenolphthalein: Specified by JIS K 8001

Ethanol first class reagent: Specified JIS K 8102

Water: Distilled water or ion-exchanged water.

One percent phenolphthalein-ethanol solution can be made based on JIS K 8006.

- (3) How to make test paper

Test paper is a filter paper absorbed 1 % of phenolphthalein-ethanol solution applied with hand sprayer.

TEST METHOD

Lighting on testing and the lighting method

In order to evaluate the color of drilled powder by 1 % phenolphthalein-ethanol solution, the necessary light must be secured. When illumination of visual range and visibility are insufficient, e.g., at night or in rainy weather, etc., the test should not be executed. When the test is likely to be affected by unsatisfactory conditions, proper lighting is required. When necessary, the lighting method, the distance from the test face, and observation direction, etc., should be recorded.

Operation of neutralization test

- (1) When mortar or ceramic tiles are covered at the test spot, they have to be removed to expose the concrete.
- (2) Work have to done by two engineers. One engineer drills a hole slowly by holding the hammer drill right angle to the face of walls, columns and joists etc., of the concrete structure. The other engineer, before the drilling is started, watches and waits with holding the test paper in a position where the concrete powder can be expected to fall.
- (3) The test paper is rotated slowly so that the falling concrete powder does not accumulate only on one spot of the test paper, and drilling is to be stopped immediately when the fallen concrete powder turns to be red.
- (4) After pulling of the drill from the hole, the depth of the hole is measured in units of mm using the depth bar of slide calipers and is recorded as the neutralization depth.

Note: When concrete is finished by mortar or ceramic tiles, any the neutralization depth of concrete can be confirmed clearly, the finishing are not necessary to be removed.

CALCULATION OF NEUTRALIZATION DEPTH

- (1) Neutralization depth of a spot can be calculated by the average value of three holes.
- (2) If one hole of neutralization depth measured is over $\pm 30\%$ than the average value, there is the possibility of the test penetrating coarse aggregate. The neutralization depth is measured by opening another one hole, and calculate the average including new hole.
- (3) If there is the difference in neutralization depth between the average value and those of the four holes over $\pm 30\%$ from average, a fifth hole is to be drilled and the neutralization depth measured, and calculated the average value of five holes and it is considered the neutralization depth of the spot.

REPAIRS

After the test, mortar or a caulking compound is filled into the drilled hole.

REPORT

The following matters have to be stipulated in the report.

- (a) Name and address of the structure
 - (b) Outline of the structure
 - (c) Date of the test, weather
 - (d) Names of engineers
 - (e) Scope of the test
 - (f) Test results
 - (g) Results of related studies
 - (h) Other necessary matters
- Further, the report has to be kept for a necessary period.

ACCNOLEGEMENT

The authors are sincerely thanks to the NDI and the member of committee for consideration to establish NDI 3419-1999 Method of test for neutralization depth of concrete in structure.

REFERENCES

1. The Ministry of Construction of Japan. (1988). Development of rapid test method for neutralization depth report (Issued one), on the development of increasing resistibility of concrete the over-all Development Project of the Ministry of Construction, pp.397-400.
2. Kasai, Y., Matsui, I. and Yuasa, N. (1990) Rapid quality inspection of structural concrete, The 23rd, Scientific lecture meeting of section of architecture and architectural technology, College of industrial technology, Nihon University, pp.45-49.
3. NDI 3419-1999. (1999). Method of test for neutralization depth of concrete in structure with drilling powder and commentary.
4. Kasai, Y., Matsui, I. and Yuasa, N (1993) Evaluation of concrete qualities by rapid testing methods, Japan cement association, Cement & Concrete, No.559, pp.20-28.

ESTIMATION METHOD OF CORRODED PORTION OF REINFORCING STEEL BAR BY NATURAL POTENTIAL MEASUREMENT

E. TSUKAHARA, R. KOYAMA, T. HOSHINO, T. UOMOTO
*Department of Civil Engineering, University of Tokyo,
Tokyo, Japan*

ABSTRACT

Natural potential measurement is one of the simplest methods to evaluate corrosion of steel bars embedded in concrete. But natural potential has been used only to judge whether corrosion is occurring or not.

This study aims to establish the estimation method of corroded portion and amount of corrosion quantitatively by using natural potential. Amperage distribution is calculated using natural potential at the surface of steel bar, which was calculated from natural potential measurement data by FEM. Amounts of corrosion are estimated by integrating cumulative amperage by time. In these processes, all estimation methods are based on electrochemical theories.

It becomes possible to know more worthwhile information from estimation analysis based on the result of time-dependent measurement natural potential.

KEYWORDS

Natural potential, amperage, cumulative amperage, electrochemical theories, crack

INTRODUCTION

Electrochemical method is very convenient to evaluate corrosion of reinforcing steel bars embedded in concrete by non-destructive method. Natural potential measurement is one of the simplest methods to evaluate corrosion. But the relationship between corrosion and natural potential has not been clarified in details. According to the standard of ASTM, natural potential is only used to judge whether corrosion is occurring or not. This study aims to clarify the estimation method of corroded portion and amount of corrosion quantitatively by using natural potential measurement.

ESTIMATION METHOD FOR THE AMOUNT OF CORROSION BASED ON NATURAL POTENTIAL MEASUREMENT

Estimation of Natural Potential at the Surface of Steel Bar

The result of natural potential measurement does not show natural potential at the surface of steel bar. Therefore natural potential at the surface of steel bar was estimated from the result of natural potential measurement by FEM analysis [1].

The flowchart of natural potential analysis and the model of analysis were shown in figure1. This analysis is aimed to remove the effect of cover concrete and get therigorously natural potential at the surface of steel bar.

If concrete is considered as homogeneous material, the distribution of natural potential can be obtained from the solution of Laplace equation as shown below:

$$\frac{\partial^2 v}{\partial x^2} + \frac{\partial^2 v}{\partial y^2} = 0 \quad (1)$$

At first, the result of natural potential measurement at the surface of concrete is considered as a boundary condition for the equation (1). And then, natural potential at the surface of steel bar is estimated by reiterate calculation.

$$v = v_c \quad (2)$$

Where, v_c : natural potential measurement at the surface of concrete

Secondly, the boundary condition of the surface of concrete is shown as below by Fourier's law:

$$i = -\frac{I}{R} \frac{\partial v}{\partial n} \quad (3)$$

Where, i : current density on boundary
 R : resistance of concrete
 n : vertical vector

It is possible to say that this analysis is easy and effective method to estimate natural potential at the surface of steel bar from the result of natural potential measurement.

Estimation of Amperage Distribution and Amount of Corrosion

The boundary between cathode and anode is considered as the inflection point of natural potential distribution. The inflection point of natural potential distribution can be obtained from the amperage analysis. Because the relation between amperage and potential follows the law of Ohm, the amperage distribution can be estimated as shown below:

$$I_k = \int_0^L i_{kx} dx = \int_0^L \frac{v_{kx}}{R_k} dx \tag{4}$$

Where, I : total amperage into optional point k (A/cm)
 i_{kx} : current density into point k from each point x (A/cm²)
 v_k : potential difference per unit length of point k and each point x (V/cm)
 R_k : resistance of concrete on each point (kΩ · cm)

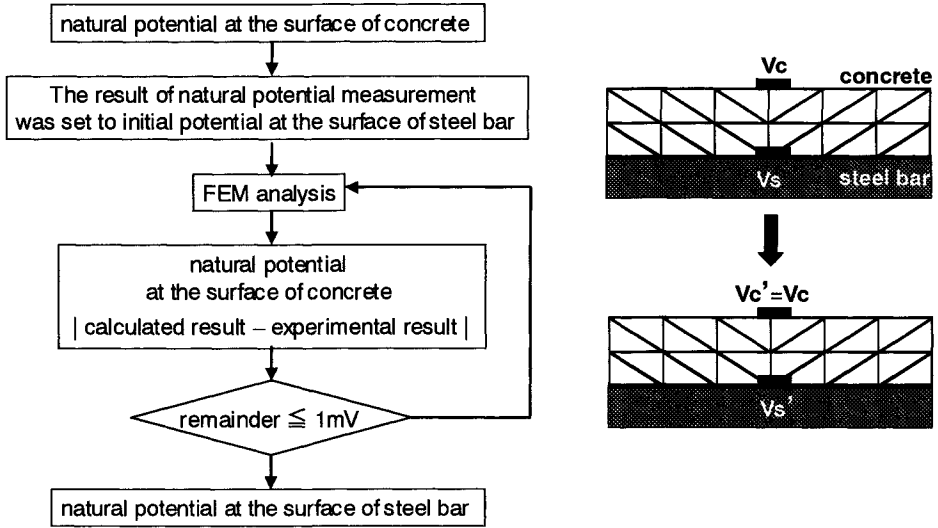


Fig.1 Flowchart and model for natural potential analysis

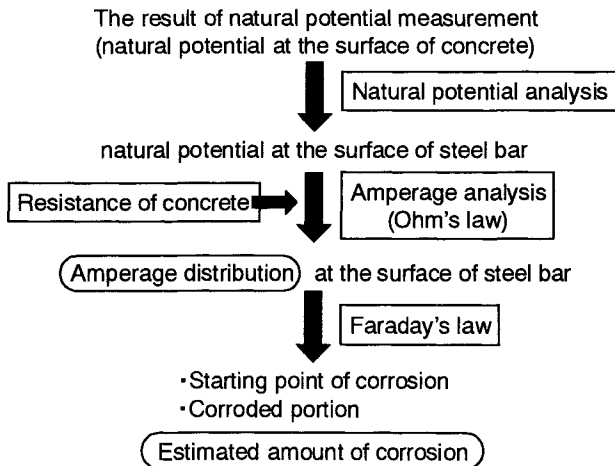


Fig.2 The flowchart of analysis

It was assumed that the resistance of the general concrete is constant value for $10k\Omega$. The current density in reinforcement at each point can be estimated from equation 5. Integrating equation.5 by time, the cumulative amperage is calculated. Amount of corrosion and cumulative amperage are proportional by Faraday's law. Therefore it is able to estimate the amount of corrosion from the cumulative amperage as shown below:

$$W_k = \int_0^t kI(t) dt \quad (5)$$

Where, W_k : amount of corrosion (g/sec)
 k : electrochemical equivalent

The flowchart of those analyses is shown in figure 2. By using electrochemical theories, it is possible to know the progress of the corrosion from the time-dependent measurement of natural potential.

RESULT OF ESTIMATION ANALYSIS

Environmental Condition of Specimen for Estimation Analysis

Specimens used for estimation analysis were exposed for 5 years in marine environment. Water cement ratio of concrete was 0.5. Beam specimens (10cm*10cm*120cm) were produced with 2 steel bars, which were 10mm in diameter and 110cm in length, and they were embedded at the depth of 20mm of cover. Cracks were generated at the center part of all specimens. During exposure duration, natural potential was measured continuously by saturated silver chloride electrode at the period of exposure for 1, 2, 3, 4, 5 years.

Natural Potential Analysis

The results of natural potential measurements are shown in figure 3, and the results of natural potential at the surface of steel bar by FEM analysis using equation (1)(2)(3) are shown in figure 4. Comparing figure 3 with figure 4, there are no big difference between experimental result and calculated result. Therefore, when cover concrete is within 20mm, it is possible to consider the result of natural potential measurement at the surface as natural potential at the surface of steel bar. But in case of large thickness of cover concrete, the result of natural potential measurement at the surface of concrete may not coincide with the values at the surface of steel bar. Therefore, it is important to remove the effect of cover concrete and estimate the natural potential at the surface of steel bar. Using this analysis, it is possible to calculate the amperage distribution, which is the next step to estimate corroded portion and the amount of corrosion of steel bar, exactly.

Amperage Analysis

The results of amperage analysis using calculated result of natural potential is shown in figure 5. In this figure, amperage in minus value is shown on the anode side and amperage in

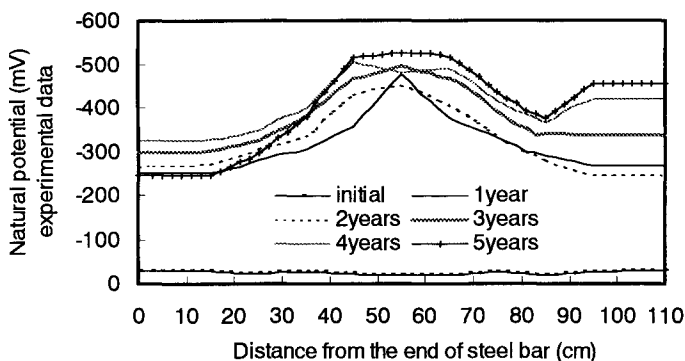


Fig.3 Distribution of natural potential measurements

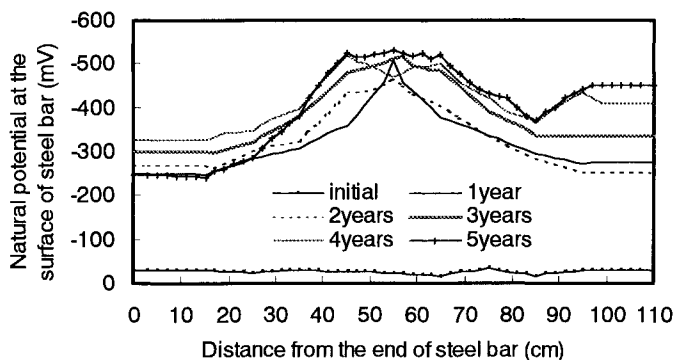


Fig.4 Distribution of calculated result of natural potential

plus value is shown on the cathode side. Therefore, the integrate value of amperage at each period have to become zero.

Observing the result of calculated natural potential is shown in figure 4, natural potential at each points of steel bar are shown in the anode values. But in figure 5, the position judged as corroded portion in experimental data of natural potential is not always shown in the anode. The gradually changes of anode area is observed in the amperage distribution. In center part of steel bar, the amperage is shown in high anode value in the period of 1 year. Because the anode area in figure 5 became large after 1 year exposing, corroded portion is seemed to expand gradually. At the right side of steel bar, the amperage is shown in the cathode in initial stage, but it changed to anode in the period in 4 and 5 years. Therefore, It seemed that corrosion is occurred after 3 years exposing.

From these results, though it is not enough to judge the corroded portion from the natural potential measurement, it is possible to estimate the inflection point between cathode area and anode area and the aspect of corrosion from the amperage analysis.

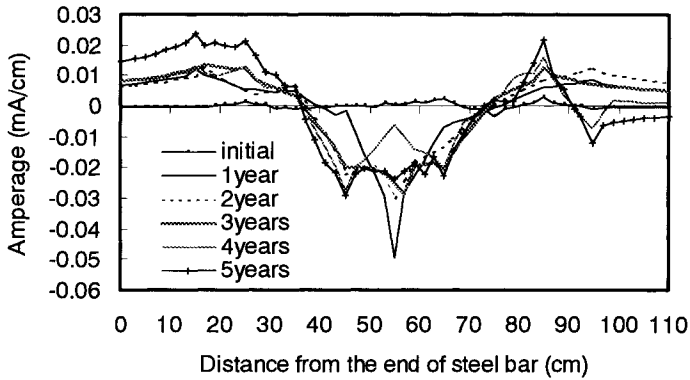


Fig.5 Amperage distribution

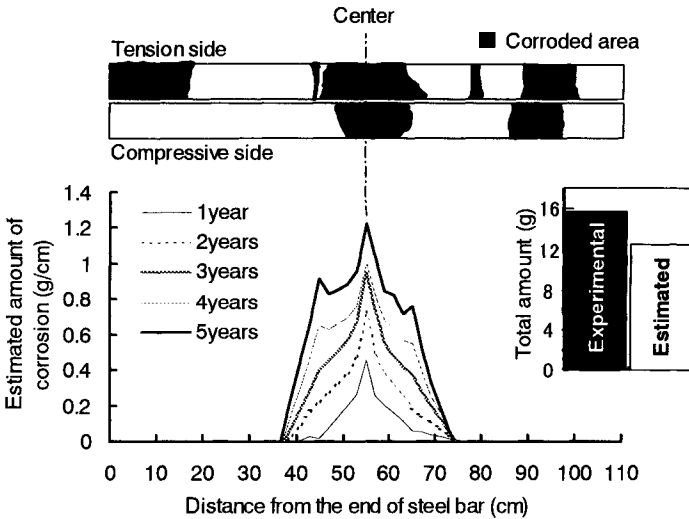


Fig.6 Corroded area and estimated amount of corrosion

Comparison Between Estimated Results and Experimental Results

The distribution of estimated amounts of corrosion calculated by equation (5) is shown in figure 6. Experimental measurements of corrosion area observed at both tension side and compressive side are also shown in figure 6. Corrosion area and estimated amount of corrosion were located in the almost the same position. It seemed that corrosion area was formed around the cracked portion. The results of total amount of corrosion both in experiment and estimation are coincide well. Estimated amount of corrosion in each point was calculated by integrating amperage in each point by time. Therefore, continuous

measurements are necessary to know amount of corrosion as exact as possible. It is considered that the error between estimated result and experimental result is based on the interval of the measurement. So in order to estimate the aspect of corrosion, both current amperage and estimated amount of corrosion should be used. In addition, it is considered that giving specific resistance would bring the exact estimation.

EFFECT OF CRACKS ON CORROSION

The effect of crack on corrosion is examined especially by numerical simulation [2]. This simulation is based on the experimental result of specimen exposed in cyclic wetting and drying environment for 13weeks. Using the relationship between natural potential and chloride ion content at each point of steel bar and equation (4), the amperage distribution can be calculated. The relationship can be shown as below [3]:

$$E = -a \times \ln(\text{NaCl.wt.\%}) - b \quad (6)$$

Where, E: Natural potential (V)
a, b: coefficient

The analyzed results of amperage distribution at different period of exposure is shown in figure 7 in case of the model which have 6.5cm as crack depth. The amperage of the cracked portion is anode at the initial stage, but it gradually changes to cathode. At the same time, though reaction rate becomes gentle than the initial stage, corrosion occurs at other parts of the reinforcement steel bar. Therefore, in the case of cracked concrete, it is considered that crack especially affects at the initial stage.

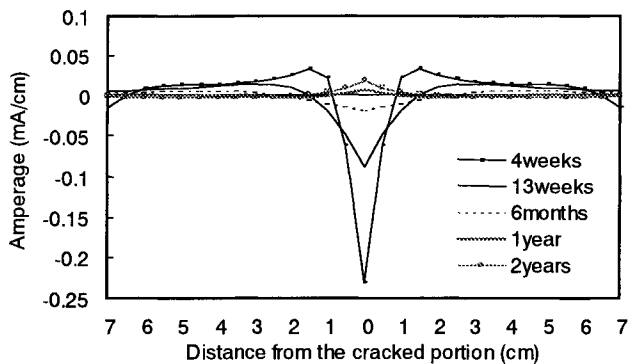


Fig.7 Calculated result of amperage distribution

CONCLUSIONS

Natural potential has been used only to judge whether corrosion occurs or not, but it become possible to obtain more worthwhile information from estimation analysis based on the result of natural potential measurement. In this study, estimation analysis is based on electrochemical theories with theoretical assumptions. It is concluded that corroded portion and aspect of corrosion can be estimated accurately by this estimation analysis with continuous time-dependent measurement of natural potential.

ACKNOWLEDGEMENT

The author would like to deeply appreciate Mr. Y. Kato and Mr. N. Nakayama for valuable support.

REFERENCES

1. Koyama, R., Yajima, T., Uomoto, T., Hoshino T. (1996): *Journal of Materials, Concrete Structures and Pavements*, No.550/V-33, pp.13-22, JSCE, Japan
2. Tsukahara, E., Uomoto, T. (1999): *Proceedings of EASEC-7*, Vol.2, pp.1496-1501, EASEC
3. Japan Concrete Institute (1996): *Report of Technical Research Committee on Concrete Repair (III)*

AUTHOR INDEX

ABE M.	135				
ABRAHAM O.	145	367	463		
AKTAN H.M.	245				
AL-QADI I. L.	499	509			
ARAZOE M.	239				
ARINO M.	79				
ASANO M.	79				
BERNHARDT M.	491				
BRANDES K.	127				
BUNGEY J. H.	41	519	583	625	
CAIRNS J.	625				
CASTRO P. F.	229				
CHA Y. H.	71				
COLLA C.	471				
COTE Ph.	367	463			
DEROBERT X.	145				
DONATH A.	425				
ETOH A.	443				
FERREIRA A. P.	229				
FISCHER U.	181				
FUJINO Y.	135				
FUJISAKI K.	605				
FUJIWARA T.	549				
GO Y.	109				
HARA N.	313				
HATSUKARI T.	435				
HATTORI S.	87				
HATTORI A.	443				
HAYASHI Y.	79				
HELMERICH R.	127				
HENDERSON G. D.	583				
HERTER J.	127				
HEVIN G.	367				
HIDA K.	151				
HIKICHI T.	151				
HILLEMEIER B.	99				
HIRAMA A.	253				
HIRATA T.	383				
HIROSE S.	357				
HOSHINO T.	671				
IMAI H.	567				
ITO Y.	239				
IWAKI K.	253				
IWANAMI M.	313				
JACOB A. F.	191				
JANNSEN B.	191				
KAARIAINEN H.	199				
KAISE S.	253				
KAITO K.	135				
KAMADA T.	375				
KAMEYAMA S.	347				
KANEMOTO Y.	549				
KASAI Y.	263	637	661		
KATO Y.	79				
KATSUKI F.	239				
KAWAKAMI J.	567				
KAWAMORITA M.	559				
KERGADALLAN X.	367				
KIMOTO K.	357				
KIMURA W.	79				
KIMURA T.	347				
KOIKE M.	347				
KOSHOVY V.	391				
KOYAMA R.	671				
KRAUSE M.	303				
KRIVIN E.	391				
KUNIEDA M.	375				
KUNIMOTO M.	263				
KURIY V.	391				
LAHOUAR S.	509				
LAW D.	625				
LEONARD Ch.	415	463			
LESCHNIK W.	209	219			
LI Z. W.	283	293			
LONG A. E.	583				
LORENZI A.	323				
LOULIZI A.	499	509			
MAIERHOFER Ch.	529				
MANO T.	263	661			
MANOME Y.	347				
MASER K. R.	481	491			
MATSUHASHI K.	87				
MATSUI K.	593				
MATSUYAMA K.	549	559			
MIELENTZ F.	303				
MIKAMI S.	117				
MIKI C.	13	357			
MILLARD S. G.	519	625			
MILMAN B.	303				
MITANI K.	253				
MIYAGAWA T.	443				
MIYAZATO S.	313				
MULLER W.	303				
NAKAGAWA K.	253				
NAZARCHUK Z.	391				
NESVIJSKI E.	323				
NESVIJSKI T.	323				
NISHIDA N.	593				
NOTO K.	79				
OHNISHI Y.	443				
OHTSU M.	161	273	293	453	615
OKAMOTO T.	161				
ONIKI K.	605				
OOSTERBAAN M. D.	499				

OOTA S.	549	559			
OSHIMA T.	117				
OTSUKI N.	313				
PARK S. K.	539				
PATTERSON A.	519				
PENDERSSEN H.	367				
PIWAKOWSKI B.	415	463			
RAHMAN M. S.	117				
RAUPACH M.	647				
RHIM H. C.	577				
ROGASS H.	181				
ROKUGO K.	375				
ROMANYSHYN I.	391				
RUDOLPH M.	199				
RUSSELL D.A.	245				
SAKAI Y.	61				
SANDE I.	481				
SATO N.	341				
SCHAURICH D.	199	407	529		
SCHEEL H.	99				
SCHIEBL P.	647				
SCHLEMM U.	209	219			
SCHMITZ V.	303				
SCHNEIDER G.	471				
SHAW M. R.	519				
SHIGEISHI M.	273				
SHIINA T.	593				
SHIMADA T.	87				
SHINYASHIKI N.	79				
SHIOTANI T.	293				
SHIOTSUBO M.	79				
SHIRAHATA H.	13				
SHKOLNIK I.E.	245				
SMITH T. F.	593				
SOUTSOS M. N.	519	583			
SUH J. H.	71				
TAKADA N.	117				
TAKADA K.	401				
TAKAHASHI T.	51				
TAMURA N.	61	401			
TAMURA I.	559				
TANAKA H.	171				
TANIGUCHI R.	87				
TODA H.	109				
TOKUNAGA T.	79				
TOMIZAWA S.	171				
TOMODA Y.	615				
TOMOKIYO T.	151	283			
TSUCHIYA N.	435				
TSUDA S.	79				
TSUKAHARA E.	671				
TULLA K.	199				
UCHIDA M.	161				
UOMOTO T.	1	79	151	171	283
	383	539	671		
WADAKA S.	347				
WATANABE T.	453				
WIGGENHAUSER H.	23	199	303	407	471
WILSCH G.	407				
WOSTMANN J.	407	529			
WU H.C.	245				
YAGIHARA S.	79				
YAMAGUCHI T.	331				
YAMAGUCHI T.	331				
YAMAZAKI T.	117				
YASUMOTO K.	605				
YAWATA T.	109				
YODA H.	135				
YOKOYAMA K.	109				
YOSHIKAWA O.	109				
YOSHIZAWA M.	283				
YUASA N.	263	637	661		
YUKAWA D.	273				
YUYAMA S.	283	293			

KEYWORD INDEX

acoustic emission	151	161	171	273	283	dielectric relaxation	79
	293					digital still camera	151 171
acoustic imaging	415					dispersion curves	367
acoustoelastic velocity-ratio	109					drainage	499
method						drill	637 661
acoustoelasticity	109					drying process	181
aggregates	313					duct	471
air change rate	425					durability	443
airfield	481					dynamic response	41
airport	559					elastic wave	87 313
ambient vibration	135					electric properties of concrete	549
amperage	671					electrochemical theories	671
anode	647					electromagnetic	567 577
array technique	303					embankment	605
automatic ultrasonic testing	13					exploration of fracture	567
system						fatigue	117 127 283
auto-regressive model	273					faults	415
base layer	509					FFT analysis	331
base material	499					fiber optic sensor	117
BEM	357	615				fibre	443 519
bolt	109					field tests	593
borehole magnetic survey	71					flexible pavements	499 509
boring method of concrete core	263					forward modeling	71
brickwork	529					fracture	145 293 435
bridge	99	127	491			fracture process zone	375
broadband angle probe	347					free water	79
building	209	425				freezing and thawing	443
b-value	293					frequency	313 383 453
calcium silicate hydrate	79					FRP	443
carbon fiberglass	401					geophysical method	51
cathode	647					GPR	481 491
cavities	415					ground granulated blast furnace	519
cement	79					slag	
chemical analysis	407					ground penetrating radar	145 481 491 499 509
chloride ion content	637						549
compaction characteristics	605					grouting condition	341
compendium	23					half-cell potential	615
compressive strength	79	239	253	263		heat flux density measurements	181
concrete	1	87	191	199	229	heat transfer coefficient	425
	263	293	313	323	367	high-resolution	51 415
	375	407	443	463	471	hot-mix asphalt	499 509
	519	577	637	647	661	hydration	79
concrete crack depth	383					IBEM	367
concrete failure	435					image processing	539
concrete members	161					imaging	145
concrete pavement	559					imaging plate	435
concrete slab	539					impact acceleration	605
concrete strength	549					impact acoustic	151 171
conductivity	519					impact echo	23 453 463 471
construction materials	199					impact test	453 605
convection	425					infrared thermography	425
convective heat transfer	593					in-situ test	253 583
coefficient						inversion	71
corrosion	273	625	647			laser doppler vibrometer	135
crack	161	331	375	367	671	leakage field	99
cultural heritages	529					LIBS	23 407
cumulative amperage	671					linear polarisation	625
damage detection	135					Lok and CAPO tests	583
damaged zones	145					magnetic anisotropy	61
data processing	145					magnetic method	99
depth estimation	71					magnetostriction	87
desorption enthalpy	181					magneto-strictive effect	61
detectability	13					maintenance	1 341
detection	415					masonry	529

